

Copyright

by

Bradley Allen Wood

1997

Investigation of Design and Repair Methods for Cantilever Bridge Bents

Volume II

by

Bradley Allen Wood, B.S., M.S.

Dissertation

Presented to the Faculty of the Graduate School of

the University of Texas at Austin

in Partial Fulfillment

of the Requirements

for the Degree of

Doctor of Philosophy

The University of Texas at Austin

December, 1997

Investigation of Design and Repair Methods for Cantilever Bridge Bents

Approved by
Dissertation Committee:

To My Wife

Acknowledgments

The research program presented in this dissertation was carried out at the Phil M. Ferguson Structural Engineering Laboratory at the University of Texas at Austin. This research was a part of the Texas Department of Transportation and the Federal Highway Administration Project 1364, "Design of Large Structural Members Utilizing Partial Prestressing." Additional funding for the author was provided by the University of Texas through a University Endowed Presidential Scholarship Award. Any opinions or recommendations expressed in this publication are those of the author and do not necessarily reflect the views of the sponsors.

I would like to thank my supervisor, Professor Michael E. Kreger, for his comments and his support. I would also like to thank the other members of my committee for their time in reviewing and commenting on this dissertation.

I would like to acknowledge, Scott Armstrong, Sarah Billington, and Ruben Salas for their contributions to the final recommendations of the project. I would also like to express my gratitude to Susan Scott who assisted in the construction and testing of the specimens for this project. Thanks are also extended to the student helpers Mohamed Najah and Mohamed Elmrbet for their time and effort.

It was a pleasure working with the Ferguson Lab faculty and staff, and I enjoyed the relaxed, but productive atmosphere.

Finally and most importantly I must thank my wife for her support and patience.

Bradley A. Wood
Austin, TX
December, 1997

Investigation of Design and Repair Methods for Cantilever Bridge Bents

Publication No. _____

Bradley Allen Wood, PhD.

The University of Texas at Austin, 1997

Supervisor: Michael E. Kreger

Large cantilevered substructures were constructed in San Antonio to support a massive concrete box-girder superstructure. AASHTO Standard Specifications do not integrate design criteria for reinforced concrete, prestressed concrete, corbels, and deep members. Because designers integrated all or most of these criteria in the design of cantilevered substructures, the resulting designs contained highly-congested joint regions.

An experimental program was developed to examine the contributions of reinforcement corresponding with the different design criteria, and to examine the behavior of cantilever-bent specimens designed using an “integrated” approach that incorporated strut-and-tie models to aid in detailing reinforcement. The testing program included a series of large-scale (1:2.75) cantilever-bent specimens with various details. Behavior at service as well as ultimate load levels was evaluated. The experimental program involved construction and testing of five specimens: two San Antonio ‘Y’ prototype models and three integrated design models. The prototype specimens included a reinforced concrete design and a fully-prestressed overhang design. The three integrated design models included a reinforced concrete design with headed reinforcement, a 54 percent prestressed ultimate design, and a 74% prestressed design, where the percentage of prestress indicates the percent of the flexural capacity provided by the prestressed reinforcement.

The design method, service-load performance, and response of specimens to ultimate loads are presented. Results of these tests were used to establish an integrated design method for the design of partially prestressed members.

A strength model that considers details of reinforcement was developed and verified by the experimental study. The strength model was used to evaluate existing cantilever bents. Eight full-scale cantilever substructures with deficient joint details were identified. Reinforcement details and analysis of two of the eight substructures are presented.

One external and two internal post-tensioned repairs were developed to strengthen the (1:2.75) prototype model reinforced concrete and fully-prestressed overhang specimens. The analysis model, design of the repairs, and experimental results are presented.

VITA

Bradley Allen Wood, the son of Phillip and Barbara Wood, was born January 30, 1968, in Summit, New Jersey. He graduated with Honors from New Providence High School in June, 1986. In August, 1986, he began his college studies at Lehigh University. In June, 1990 he graduated with High Honors from Lehigh University with a B.S. degree in Civil Engineering. During the Summer of 1990, he began work on a project studying the residual strength of damaged and/or deteriorated tubular members. His work was supervised by Professor Alexis Ostapenko. He completed the requirements for a Masters of Science Degree in Civil Engineering in May, 1992. In September 1992 he entered the Graduate School of The University of Texas.

Permanent Address: 2222 Westerland Drive #230, Houston, Texas, 77063-2215

This dissertation was typed by the author.

TABLE OF CONTENTS

LIST OF TABLES	xviii
LIST OF FIGURES	xxii
CHAPTER 1 - INTRODUCTION.....	1
1.1 Problem Statement	1
1.2 Scope of Research	3
1.3 Objectives of Research	3
1.4 Organization	4
CHAPTER 2 - BACKGROUND	5
2.1 Introduction	5
2.2 Description of Cantilever Bents in San Antonio	5
2.3 Evaluation of Current Design Practice.....	6
2.3.1 AASHTO Reinforced Concrete Design	7
2.3.1.1 Reinforced Concrete Overhang Design	7
2.3.1.2 Reinforced Concrete Pier Design	8
2.3.1.3 Reinforced Concrete Joint Design.....	9
2.3.2 AASHTO Prestressed Concrete Design	9
2.3.2.1 Fully Prestressed Overhang Design.....	10
2.3.2.2 Fully Prestressed Pier Design	11
2.3.2.3 Fully Prestressed Joint Design	12
2.4 Development of an Integrated Design Method	13
2.4.1 Overview of Related Research	13
2.4.1.1 Strut-and-Tie Modeling.....	14
2.4.1.2 Partial Prestressing	14
2.4.1.3 Deep Beam.....	14

2.4.1.4	<i>Limits on Column Longitudinal Reinforcement</i>	15
2.4.1.5	<i>Design of Headed Reinforcement</i>	15
2.4.1.6	<i>Crack-Width Prediction</i>	16
2.4.1.7	<i>Durability and Maximum Allowable Crack Widths</i>	16
2.4.1.8	<i>Scaling Model Crack Widths and Behavior</i>	17
2.4.1.9	<i>Fatigue Stress Limits</i>	17
2.4.2	Synopsis of Previous Recommendations Used in This Study	18
2.4.2.1	<i>Development of a Strut-and-Tie Model</i>	18
2.4.2.2	<i>Development of FEM for Cantilever Bents</i>	18
2.4.2.3	<i>Tensile Reinforcement Requirements</i>	19
CHAPTER 3	- EXPERIMENTAL PROGRAM	20
3.1	Introduction	20
3.2	Development of the Pier-Overhang-Joint Specimen	21
3.2.1	Selection of Full-Scale Superstructure Loads	21
3.2.2	Full-Scale Prototype Substructure Details	25
3.2.2.1	<i>Reinforced Concrete Prototype Substructure - I4-C</i>	25
3.2.2.2	<i>Substructure with Fully-Prestressed Overhang - C11-C</i>	26
3.2.3	Selection of Scale Factor for Test Specimens	28
3.2.4	Model Loads.....	30
3.2.5	Model Dimensions	30
3.2.5.1	<i>Bar Development Similitude</i>	32
3.3	Design Method for Prototype Pier-Overhang-Joint (POJ) Test Specimens	36
3.3.1	Reinforced Concrete Specimen - POJ-RC-100	36
3.3.1.1	<i>Overhang Design - POJ-RC-100</i>	36
3.3.1.2	<i>Pier Design - POJ-RC-100</i>	42
3.3.1.3	<i>Joint Design - POJ-RC-100</i>	44
3.3.2	Specimen with Fully-Prestressed Concrete Overhang - POJ-PS-100	46
3.3.2.1	<i>Overhang Design - POJ-PS-100</i>	46

3.3.2.2 Pier Design - POJ-PS-100.....	51
3.3.2.3 Joint Design - POJ-PS-100.....	52
3.4 Integrated Design Test Specimens	55
3.4.1 Overview of the Integrated Design Method	55
3.4.1.1 Factored Load Resistance	55
3.4.1.2 Service Load Performance.....	57
3.4.2 Overview of Design Details	59
3.4.3 Design Details for the Reinforced Concrete Specimen with Headed Bars - POJ-RC-100-TH.....	59
3.4.3.1 Finite Element Analysis - POJ-RC-100-TH.....	59
3.4.3.2 Strut-and-Tie Model - POJ-RC-100-TH	63
3.4.3.3 Overhang Design Details - POJ-RC-100-TH	63
3.4.3.4 Pier Details - POJ-RC-100-TH	66
3.4.3.5 Joint Details - POJ-RC-100-TH	68
3.4.4 54% Prestressed Design with T-Headed Bars - POJ-PU-54-TH.....	71
3.4.4.1 Finite Element Analysis - POJ-PU-54-TH.....	71
3.4.4.2 Strut-and-Tie Model - POJ-PU-54-TH.....	76
3.4.4.3 Overhang Details - POJ-PU-54-TH.....	77
3.4.4.4 Pier Details - POJ-PU-54-TH	80
3.4.4.5 Joint Details - POJ-PU-54-TH	83
3.4.5 74% Prestressed Design with T-Head Bars - POJ-PU-74-TH	86
3.4.5.1 Finite Element Analysis - POJ-PU-74-TH.....	86
3.4.5.2 Strut-and-Tie Model - POJ-PU-74-TH.....	90
3.4.5.3 Overhang Details - POJ-PU-74-TH.....	91
3.4.5.4 Pier Design - POJ-PU-74-TH	94
3.4.5.5 Joint Design - POJ-PU-74-TH	97
3.5 Materials.....	100
3.5.1 Concrete	100
3.5.2 Mild Reinforcement	102

3.5.3 Post-Tensioning Steel, Duct, and Anchorage Hardware	104
3.5.4 Grout	106
3.6 Fabrication	108
3.6.1 Reinforcing Cages	108
3.6.2 Placement and Consolidation of Concrete	109
3.6.3 Curing and Form Removal	109
3.7 Test Set-up.....	110
3.7.1 Loading Frame and Rams.....	110
3.7.2 Anchorage of Test Specimen to Floor.....	110
3.7.3 Instrumentation and Data Collection.....	111
3.7.3.1 Data Acquisition System	111
3.7.3.2 Pressure Transducers	111
3.7.3.3 Linear Potentiometers and Displacement Transducers.....	112
3.7.3.4 Strain Gages	113
3.8 Testing Procedure.....	113
3.8.1 Installation of Specimen.....	113
3.8.2 Post-Tensioning Operation.....	116
3.8.3 Static Load Steps.....	119
3.8.4 Crack Identification and Marking Procedure	120
CHAPTER 4 - TEST RESULTS	122
4.1 Introduction	122
4.2 Prototype Model Test Specimens	124
4.2.1 Reinforced Concrete Prototype Specimen - POJ-RC-100.....	127
4.2.1.1 Applied Moment vs. Deflection Behavior - POJ-RC-100.....	134
4.2.1.2 Location and Identification of Strain Gages - POJ-RC-100.....	138
4.2.1.3 Applied Moment vs. Strain Response - POJ-RC-100	143
4.2.1.4 Overhang and Pier Section Strain Profiles:	148
4.2.2 Prestressed Concrete Design - POJ-PS-100	151

4.2.2.1 Applied Moment vs. Deflection Response - POJ-PS-100	160
4.2.2.2 Location and Identification of Strain Gages - POJ-PS-100	164
4.2.2.3 Applied Moment vs. Strain Response - POJ-PS-100	167
4.2.2.4 Strain Profiles for the Pier at Various Cross Sections - POJ-PS-100.....	170
4.3. Integrated Design Method POJ Test Specimens.....	173
4.3.1. Reinforced Concrete Design with T-Headed Bars - POJ-RC-100-TH.....	173
4.3.1.1. Applied Moment vs. Deflection Response - POJ-RC-100-TH	180
4.3.1.2. Location and Identification of Strain Gages - POJ-RC-100-TH.....	184
4.3.1.3. Applied Moment vs. Strain Response - POJ-RC-100-TH	188
4.3.1.4. Overhang and Pier Section Strain Profiles:	193
4.3.2 54% Prestressed Design with T-Headed Reinforcement - POJ-PU-54-TH	196
4.3.2.1 Applied Overhang Moment vs. Deflection Response -POJ-PU-54-TH	203
4.3.2.2 Location and Identification of Strain Gages -POJ-PU-54-TH.....	207
4.3.2.3 Applied Moment vs. Strain Response - POJ-PU-54-TH.....	211
4.3.3 74% Prestressed Design with T-Headed Reinforcement - POJ-PU-74-TH	218
4.3.3.1 Applied Overhang Moment vs. Deflection Response - POJ-PU-74-TH	225
4.3.3.2 Location and Identification of Strain Gages - POJ-PU-74-TH.....	228
4.3.3.3 Overhang Moment vs. Strain Response - POJ-PU-74-TH	232
4.3.3.4 Pier Strain Profiles - POJ-PU-74-TH	237
CHAPTER 5 - ANALYSIS OF TEST RESULTS.....	238
5.1 Introduction	238
5.2 Strength Evaluation	238
5.2.1 Comparison of Overhang Moment vs. Tip Deflection Response.....	239
5.2.2 Comparison of Measured and Predicted Strains	241
5.2.3 Comparison of Computed and Measured Capacities	248
5.3 Serviceability Evaluation	250
5.3.1 Service-Level Tip Deflections.....	250

5.3.2 Comparison of Service Load Cracking Patterns with Tensile Stresses from Finite Element Analyses	251
5.3.3 Evaluation of Crack Widths	258
5.3.3.1 Overhang Crack-Width Envelopes	258
5.3.3.2 Joint Crack-Width Envelopes	259
5.3.3.3 Pier Crack-Width Envelopes.....	261
5.3.4 Crack-Width Frequency and Distribution at Service Loads.....	262
5.3.5 Comparison of Measured vs. Predicted Crack Widths.....	266
5.3.6 Evaluation of Reinforcement Stress Ranges	274
5.4 Constructability and Cost Estimation	276
5.4.1 Constructability	276
5.4.2 Cost Estimation	278
5.5 Summary	286
CHAPTER 6 - PROPOSED DESIGN RECOMMENDATIONS	288
6.1 Introduction	288
6.2 Recommended Modifications to Proposed AASHTO LRFD Bridge Specifications.....	289
6.3 Summary	295
CHAPTER 7 - ANALYSIS OF SAN ANTONIO CANTILEVER BENTS.....	296
7.1 Introduction	296
7.2 Development of the Strength Analysis Model.....	297
7.3 Evaluation of Reinforced Concrete Substructure I4-C.....	301
7.3.1 I4-C Substructure Strength Analysis	304
7.3.2 Finite Element Analysis - I4-C.....	306
7.3.3 Field Inspection of Cracking Pattern - I4-C	311
7.4 Evaluation of Fully-Prestressed Overhang Substructure C11-C.....	312
7.4.1 C11-C Substructure Strength Analysis.....	315
7.4.2 Finite Element Analysis - C11-C	317

7.4.3 Field Inspection Cracking Pattern - C11-C	319
7.5 Summary of Results	320
CHAPTER 8 - DEVELOPMENT AND TESTING OF SELECTED REPAIRS	321
8.1 Introduction	321
8.2 Evaluation of Cantilever Bent Capacity - POJ-RC-100-2 and POJ-PS-100	322
8.2.1 Reinforced Concrete Specimen - POJ-RC-100-2.....	322
8.2.1.1 Reinforcing Details - POJ-RC-100-2.....	323
8.2.1.2 Finite Element Analysis - POJ-RC-100-2.....	325
8.2.1.3 Strut-and-Tie Model - POJ-RC-100-2	326
8.2.1.4 Cantilever Bent Strength Computation - POJ-RC-100-2	327
8.2.1.5 Overhang Moment vs. Tip-Deflection Behavior - POJ-RC-100-2.....	329
8.2.2 Specimen with Fully-Prestressed Overhang - POJ-PS-100.....	331
8.2.2.1 Reinforcement Details - POJ-PS-100.....	331
8.2.2.2 Finite Element Analysis -POJ-PS-100.....	334
8.2.2.3 Strut-and-Tie Model - POJ-PS-100	335
8.2.2.4 Cantilever Bent Strength Computation - POJ-PS-100	336
8.2.2.5 Applied Overhang Moment vs. Tip Deflection - POJ-PS-100	338
8.4 External Post-Tensioned Repair Methods	342
8.4.1 External Vertical Post-Tensioned Repair - Conceptual Design	342
8.4.2 External Diagonal Post-Tensioned Repair - Conceptual Design	344
8.5 Internal Post-Tensioned Repair Methods	346
8.5.1 Internal Vertical Post-Tensioned Repair - Conceptual Design	346
8.5.2 Internal Horizontal Post-Tensioned Repair - Conceptual Design	347
8.5.3 Combined Internal Vertical and Horizontal Post-Tensioning - Conceptual Design.....	348
8.6 Analysis and Behavior of Selected POJ-RC-100 Repairs	350
8.6.1 Diagonal Post-Tensioned Repair (POJ-RC-100-RP1)	350
8.6.1.1 Capacity Analysis (POJ-RC-100-RP1).....	351

8.6.1.2	<i>Finite Element Analysis (POJ-RC-100-RP1)</i>	354
8.6.1.3	<i>Design and Installation Details (POJ-RC-100-RP1)</i>	357
8.6.1.4	<i>Behavior During Testing (POJ-RC-100-RP1)</i>	364
8.6.2.	Internal Vertical Post-Tensioned Repair (POJ-RC-100-RP2).....	366
8.6.2.1.	<i>Capacity Calculation (POJ-RC-100-RP2)</i>	367
8.6.2.2.	<i>Finite Element Analysis (POJ-RC-100-RP2)</i>	370
8.6.2.3.	<i>Design and Installation Details (POJ-RC-100-RP2)</i>	373
8.6.2.4.	<i>Behavior During Testing (POJ-RC-100-RP2)</i>	375
8.7.	Analysis and Behavior of Selected POJ-PS-100 Repairs	377
8.7.1.	External Vertical Post-Tensioned Repairs (POJ-PS-100-RP1 & RP2)	377
8.7.1.1.	<i>Capacity Calculation (POJ-PS-100-RP1 & RP2)</i>	379
8.7.1.2.	<i>Finite Element Analysis (POJ-PS-100-RP1 & RP2)</i>	383
8.7.1.3.	<i>Design and Installation Details (POJ-PS-100-RP1 & RP2)</i>	388
8.7.1.4.	<i>Behavior During Testing (POJ-PS-100-RP1 & RP2)</i>	395
 CHAPTER 9 - ANALYSIS OF TEST RESULTS FROM CANTILEVER BENT STRENGTHENING STUDY.....		398
9.1	Introduction	398
9.2	Comparison of Overhang Moment vs. Tip Deflection Response.....	399
9.2.1	Specimen POJ-RC-100-2 and Repairs RP1 and RP2.....	399
9.2.2	Specimen POJ-PS-100 and Repairs RP1 and RP2	400
9.3	Comparison of Measured Strain Response	401
9.3.1	Reinforced Concrete Design (POJ-RC-100-2) Repairs.....	401
9.3.2	Specimen with Fully-Prestressed Overhang (POJ-PS-100) Repairs	406
9.3.3	Comparison of External Post-Tensioned Repair Strains	411
9.4	Constructability of the Repairs	413
9.4.1	External Diagonal Post-tensioning Repair	413
9.4.2	External Vertical Post-Tensioned Repair	414
9.4.3	Internal Vertical Post-Tensioned Repair	415

9.5 Cost Estimates of Repair Methods.....	416
9.5.1 External Diagonal Post-Tensioning.....	417
9.5.2 External Vertical Post-Tensioning	418
9.5.3 Internal Vertical Post Tensioning.....	419
9.5.4 Repair Cost Comparison	420
9.6 Recommended Repair Method.....	421
CHAPTER 10 - SUMMARY AND CONCLUSIONS.....	423
10.1 Summary	423
10.2 Conclusions and Recommendations.....	427
APPENDIX A - CRACKING PATTERNS AND MAXIMUM CRACK WIDTH MEASUREMENTS	431
Specimen POJ-RC-100.....	431
Specimen POJ-PS-100.....	448
Specimen POJ-RC-100-TH.....	454
Specimen POJ-PU-54-TH	471
Specimen POJ-PU-74-TH	488
APPENDIX B - CANTILEVER BENT DESIGN EXAMPLE	505
Selection of Full-Scale Prototype Superstructure Loads	505
Design of Cantilever Bent using Strut-and-Tie Model Design Procedure.....	508
Selection of Post-Tensioned Reinforcement:.....	508
Overhang Serviceability Provisions:.....	512
Pier Design	515
Joint Design.....	518
REFERENCES-	521
VITA	525

LIST OF TABLES

Table 3.1 Full-Scale Substructure Loads for a 7.9 m (26 ft) Wide Girder	23
Table 3.2 Selection of Scale Factor, Model Bar Diameters and Load	28
Table 3.3 Substructure Design Loads for a 1/2.75 Scale Model.....	29
Table 3.4 Computed Basic Bar Development Length	32
Table 3.5 Comparison of Scaled Development Lengths and Development Lengths for Model Bars	33
Table 3.6 Concrete Mix Design	100
Table 3.7 On-Site Measurements and Mix Modifications.	111
Table 3.8 Concrete Compressive Strength.....	112
Table 3.9 Mild Reinforcement Material Properties	112
Table 3.10 Dimensions of T-Head Plates	113
Table 3.11 Grout Mix Design	117
Table 3.12 Grout Cube Strength.	117
Table 3.13 Events in Load History, Corresponding Load Steps, and Applied Loads	131
Table 4.1 Intended Load History for Pier-Overhang-Joint Specimens.....	123
Table 5.1 Comparison of Computed and Measured Capacities	249
Table 5.2: Computed Overhang Crack Widths at Service Loads	268
Table 5.3 Computed Pier Crack Widths at Service Loads.....	269
Table 5.4 Computed and Experimental Stress Ranges for Overhangs	274
Table 5.5 Computed and Experimental Stress Ranges for Piers.....	275
Table 5.6 Constructability Ratings for Bent Types	277
Table 5.7 Full-Scale POJ-RC-100 - Materials Quantities and Price Estimates	280
Table 5.8 Full-Scale POJ-PS-100 - Material Quantities and Price Estimates.....	281
Table 5.9 Full-Scale POJ-RC-100-TH - Material Quantities and Price Estimates	282
Table 5.10 Full-Scale POJ-PU-54-TH - Material Quantities and Price Estimates	283
Table 5.11 Full-Scale POJ-PU-74-TH - Material Quantities and Price Estimates	284

Table 7.1 Basic Bar Development Lengths for 414 MPa (60 ksi) Reinforcing Bars.....	299
Table 7.2 Computed Superstructure Reactions for Substructure I4-C.....	301
Table 7.3 Computed Superstructure Reactions for Substructure C11-C	313
Table 8.1 Substructure Design Loads for 1/2.75 Scale Models.....	322
Table 9.1 Estimated Cost for the External Diagonal Post-Tensioned Option.....	417
Table 9.2 Estimated Costs for the External Vertical Post-Tensioned Option.....	418
Table 9.3 Estimated Costs for Internal Vertical Post-Tensioned Option.....	419
Table 9.4 Decision Matrix for the Studied Repair Methods	421
Table A.1 POJ-RC-100 - Maximum Crack Widths in mm for North Face of Overhang	437
Table A.2 POJ-RC-100 - Maximum Crack Widths in (in.) for North Face of Overhang.....	437
Table A.3 POJ-RC-100 - Maximum Crack Widths in mm for South Face of Overhang	439
Table A.4 POJ-RC-100 - Maximum Crack Widths in (in.) for South Face of Overhang.....	439
Table A.5 POJ-RC-100 - Maximum Crack Widths in mm for North Face of Joint	441
Table A.6 POJ-RC-100 - Maximum Crack Widths in (in.) for North Face of Joint.....	441
Table A.7 POJ-RC-100 - Maximum Crack Widths in mm for South Face of Joint	443
Table A.8 POJ-RC-100 - Maximum Crack Widths in (in.) for South Face of Joint.....	443
Table A.9 POJ-RC-100 - Maximum Crack Widths in mm for North Face of Pier.....	445
Table A.10 POJ-RC-100 - Maximum Crack Widths in (in.) for North Face of Pier.....	445
Table A.11 POJ-RC-100 - Maximum Crack Widths in mm for South Face of Pier.....	447
Table A.12 POJ-RC-100 - Maximum Crack Widths in (in.) for South Face of Pier.....	447
Table A.13 POJ-PS-100 - Maximum Crack Widths in mm for North Face of Joint	450
Table A.14 POJ-PS-100 - Maximum Crack Widths in (in.) for North Face of Joint	450
Table A.15 POJ-PS-100 - Maximum Crack Widths in mm for South Face of Joint	451
Table A.16 POJ-PS-100 - Maximum Crack Widths in (in.) for South Face of Joint	451
Table A.17 POJ-PS-100 - Maximum Crack Widths in mm for North Face of Pier	452
Table A.18 POJ-PS-100 - Maximum Crack Widths in (in.) for North Face of Pier.....	452
Table A.19 POJ-PS-100 - Maximum Crack Widths in mm for South Face of Pier	453

Table A.20 POJ-PS-100 - Maximum Crack Widths in (in.) for South Face of Pier.....	453
Table A.21 POJ-RC-100-TH Maximum Crack Widths in mm for North Face of Overhang.....	460
Table A.22 POJ-RC-100-TH Maximum Crack Widths in (in.) for North Face of Overhang.....	460
Table A.23 POJ-RC-100-TH Maximum Crack Widths in mm for South Face of Overhang.....	462
Table A.24 POJ-RC-100-TH Maximum Crack Widths in (in.) for South Face of Overhang.....	462
Table A.25 POJ-RC-100-TH Maximum Crack Widths in mm for North Face of Joint	464
Table A.26 POJ-RC-100-TH Maximum Crack Widths in (in.) for North Face of Joint	464
Table A.27 POJ-RC-100-TH Maximum Crack Widths in mm for South Face of Joint	466
Table A.28 POJ-RC-100-TH Maximum Crack Widths in (in.) for South Face of Joint	466
Table A.29 POJ-RC-100-TH Maximum Crack Widths in mm for North Face of Pier	468
Table A.30 POJ-RC-100-TH Maximum Crack Widths in (in.) for North Face of Pier.....	468
Table A.31 POJ-RC-100-TH Maximum Crack Widths in mm for South Face of Pier	470
Table A.32 POJ-RC-100-TH Maximum Crack Widths in (in.) for South Face of Pier.....	470
Table A.33 POJ-PU-54-TH Maximum Crack Widths in mm for North Face of Overhang .	477
Table A.34 POJ-PU-54-TH Maximum Crack Widths in (in.) for North Face of Overhang.	477
Table A.35 POJ-PU-54-TH Maximum Crack Widths in mm for South Face of Overhang .	479
Table A.36 POJ-PU-54-TH Maximum Crack Widths in (in.) for South Face of Overhang	479
Table A.37 POJ-PU-54-TH Maximum Crack Widths in mm for North Face of Joint	481
Table A.38 POJ-PU-54-TH Maximum Crack Widths in (in.) for North Face of Joint	481
Table A.39 POJ-PU-54-TH Maximum Crack Widths in mm for South Face of Joint	483
Table A.40 POJ-PU-54-TH Maximum Crack Widths in (in.) for South Face of Joint	483
Table A.41 POJ-PU-54-TH Maximum Crack Widths in mm for North Face of Pier	485
Table A.42 POJ-PU-54-TH Maximum Crack Widths in (in.) for North Face of Pier.....	485
Table A.43 POJ-PU-54-TH Maximum Crack Widths in mm for South Face of Pier	487
Table A.44 POJ-PU-54-TH Maximum Crack Widths in (in.) for South Face of Pier.....	487
Table A.45 POJ-PU-74-TH Maximum Crack Widths in mm for North Face of Overhang .	494
Table A.46 POJ-PU-74-TH Maximum Crack Widths in (in.) for North Face of Overhang.	494
Table A.47 POJ-PU-74-TH Maximum Crack Widths in mm for South Face of Overhang .	496
Table A.48 POJ-PU-74-TH Maximum Crack Widths in (in.) for South Face of Overhang	496

Table A.49 POJ-PU-74-TH Maximum Crack Widths in mm for North Face of Joint	498
Table A.50 POJ-PU-74-TH Maximum Crack Widths in (in.) for North Face of Joint	498
Table A.51 POJ-PU-74-TH Maximum Crack Widths in mm for South Face of Joint	500
Table A.52 POJ-PU-74-TH Maximum Crack Widths in (in.) for South Face of Joint	500
Table A.53 POJ-PU-74-TH Maximum Crack Widths in mm for North Face of Pier	502
Table A.54 POJ-PU-74-TH Maximum Crack Widths in (in.) for North Face of Pier	502
Table A.55 POJ-PU-74-TH Maximum Crack Widths in mm for South Face of Pier	504
Table A.56 POJ-PU-74-TH Maximum Crack Widths in (in.) for South Face of Pier	504
Table B.1 Full-Scale Substructure Loads for a 7.9 m (26 ft) Wide Girder	508

LIST OF FIGURES

Figure 1.1 Cantilever Bents Supporting Entrance Ramp	2
Figure 2.1 Schematic of Cantilever Bents in San Antonio	6
Figure 2.2 Reinforced Concrete Design.....	8
Figure 2.3 Fully Prestressed Overhang Design with Reinforced Concrete Pier	10
Figure 2.4: Fully Prestressed Substructure with Continuous Post Tensioning	11
Figure 2.5 Schematic of Joint Region for Continuous Post-Tensioning Detail.....	12
Figure 2.6 Schematic of Joint Region For Post-Tensioned Overhang Detail	12
Figure 2.7: Headed Bar Schematic	15
Figure 3.1 Substructure Schematic	22
Figure 3.2 Pier Location and Continuity Factors.....	23
Figure 3.3 Full-Scale Prototype Loads Without Continuity Factors.	24
Figure 3.4 Reinforced Concrete Substructure I4-C Details	25
Figure 3.5 Substructure C11-C Details.....	27
Figure 3.6 Overall Dimensions for POJ Specimens.....	31
Figure 3.7 Top view of POJ Specimen	32
Figure 3.8 Dimensions of the Model Scaled-Up to Full-Scale	35
Figure 3.9 POJ-RC-100 Overhang Reinforcement Cross-Section Details	40
Figure 3.10 POJ-RC-100 Overhang Reinforcement Details.....	42
Figure 3.11 POJ-RC-100 Pier Reinforcement Detail.....	43
Figure 3.12 POJ-RC-100 Joint Reinforcement Details.....	44
Figure 3.13 Elevation of Reinforcement for POJ-RC-100	45
Figure 3.14 PS-100 - Location of Post-Tensioning	46
Figure 3.15 POJ-PS-100 Overhang Cross Section.....	49
Figure 3.16 POJ-PS-100 Overhang Reinforcement Details.....	51
Figure 3.17 POJ-PS-100 Pier Reinforcement Details.....	52
Figure 3.18 POJ-PS-100 Joint Reinforcement Details.....	53

Figure 3.19 Elevation of Reinforcement for POJ-PS-100	54
Figure 3.20 Identification of Crack-Width Control Variables	57
Figure 3.21 Finite Element Model for the POJ-RC-100-TH Specimen.....	60
Figure 3.22 POJ-RC-100-TH - Principal Tensile Stresses and Vectors at Dead Load	61
Figure 3.23 POJ-RC-100-TH - Principal Compressive Stresses and Vectors at Dead Load.	61
Figure 3.24 POJ-RC-100-TH - Principal Tensile Stresses and Vectors at Service Load	62
Figure 3.25 POJ-RC-100-TH - Principal Compressive Stresses and Vectors at Service Load	62
Figure 3.26 POJ-RC-100-TH - Strut-and-Tie Model.....	63
Figure 3.27 POJ-RC-100-TH - Overhang Cross Section Details	64
Figure 3.28 POJ-RC-100-TH - Transverse Reinforcement Details	66
Figure 3.29 POJ-RC-100-TH - Pier Cross Section Details.....	68
Figure 3.30 POJ-RC-100-TH Joint Reinforcement Details	69
Figure 3.31 POJ-RC-100-TH Complete Reinforcement Details	70
Figure 3.32 Finite Element Model for Specimen POJ-PU-54-TH.....	72
Figure 3.33 POJ-PU-54-TH Principal Tensile Stress Contours and Vectors at Dead Load ...	74
Figure 3.34 POJ-PU-54-TH Principal Compressive Stress Contours and Vectors at Dead Load	74
Figure 3.35 POJ-PU-54-TH Principal Tensile Stress Contours and Vectors at Service Load	75
Figure 3.36 POJ-PU-54-TH Principal Compressive Stress Contours and Vectors at Service Load	75
Figure 3.37 POJ-PU-54-TH Strut-and-Tie Model.....	76
Figure 3.38 POJ-PU-54-TH Location of Post-Tensioning Tendons.....	78
Figure 3.39 POJ-PU-54-TH Overhang Cross-Section Details.....	78
Figure 3.40 POJ-PU-54-TH - Transverse Reinforcement Details	80
Figure 3.41 POJ-PU-54-TH Pier Cross-Section Details	82
Figure 3.42 POJ-PU-54-TH Joint Reinforcement Details	84
Figure 3.43 POJ-PU-54-TH Overall Reinforcement Details	85
Figure 3.44 POJ-PU-74-TH Principal Tensile Stress Contours and Vectors at Dead Load ...	88
Figure 3.45 POJ-PU-74-TH Principal Compressive Stress Contours and Vectors at Dead Load	88

Figure 3.46	POJ-PU-74-TH Principal Tensile Stress Contours and Vectors at Service Load	89
Figure 3.47	POJ-PU-74-TH Principal Compressive Stress Contours and Vectors at Service Load	89
Figure 3.48	POJ-PU-74-TH Strut-and-Tie Model	90
Figure 3.49	POJ-PU-74-TH Post-Tensioning Duct Locations	92
Figure 3.50	POJ-PU-74-TH Overhang Cross-Section Details.....	92
Figure 3.51	POJ-PU-74-TH - Overhang Design Details	94
Figure 3.52	POJ-PU-74-TH Pier Reinforcement Details.....	96
Figure 3.53	POJ-PU-74-TH Joint Reinforcement Details	98
Figure 3.54	POJ-PU-74-TH Overall Reinforcement Details	99
Figure 3.55	Anchor Head Dimensions and Weld Locations for a No. 4 Bar	103
Figure 3.56	Stress-Strain Behavior of 13 mm (0.5 in.) Diameter Grade 270 Lo-Lax Strand	104
Figure 3.57	Stress-Strain Behavior of 15 mm (0.6 in.) Diameter Grade 270 Lo-Lax Strand	105
Figure 3.58	Stress-Strain Behavior of 16 mm (5/8 in.) Diameter Grade 150 Dywidag Post Tensioning Bar	106
Figure 3.59	Test Setup and Location of Displacement Transducers	112
Figure 3.60	Top View Of Test Setup.....	114
Figure 3.61	Crack Identification Procedure.....	120
Figure 4.1	Assumed Joint Crack and Method for Computing Forces Developed in Longitudinal Bars.....	125
Figure 4.2	POJ-RC-100 Reinforcing Details	127
Figure 4.3	POJ-RC-100 Free Body and Reinforcement Locations Used in Computing Specimen Capacity.....	128
Figure 4.4	Free Body Used to Compute Capacity of Specimen POJ-RC-100.....	129
Figure 4.5	POJ-RC-100 Principal Tensile Stresses at Dead Load	130
Figure 4.6	Photograph of North Face of Specimen POJ-RC-100 at Service Load.....	131
Figure 4.7	Photograph of North Face of Specimen POJ-RC-100 at Failure.....	133
Figure 4.8	Photograph of Joint Region on North Face of Specimen POJ-RC-100 at Failure	133
Figure 4.9	POJ-RC-100 - Locations of Displacement Transducers.....	134

Figure 4.10 POJ-RC-100 Tip Deflection (LV-75).....	136
Figure 4.11 POJ-RC-100 Top Joint Deflection	136
Figure 4.12 POJ-RC-100 Pier Horizontal Deflections.....	137
Figure 4.13 POJ-RC-100 Bearing Pad Displacements	137
Figure 4.14 POJ-RC-100 Overhang Strain Gage Locations and Labels.....	139
Figure 4.15 Strain Gage Labeling Scheme	140
Figure 4.16 POJ-RC-100 Joint Strain Gage Locations and Labels.....	141
Figure 4.17 POJ-RC-100 Overall Strain Gage Locations and Pier Strain Gage Labels	142
Figure 4.18 POJ-RC-100 Strains in Primary Longitudinal Reinforcement at Layer Z=1 in the Overhang.....	144
Figure 4.19 POJ-RC-100 Strains in Primary Longitudinal Reinforcement at Layer Z=3 in the Overhang.....	144
Figure 4.20 POJ-RC-100 Strains in Primary Longitudinal Reinforcement at Layer Z=10 in the Overhang.....	145
Figure 4.21 POJ-RC-100 Strains in Primary Longitudinal Reinforcement at Layer Z=13 in the Overhang.....	145
Figure 4.22 POJ-RC-100 Strains in Pier Longitudinal Reinforcement at Layer X=1	146
Figure 4.23 POJ-RC-100 Strains in Pier Longitudinal Reinforcement at Layer X=5	146
Figure 4.24 POJ-RC-100 Strains in Pier Longitudinal Reinforcement at Layer X=8	147
Figure 4.25 POJ-RC-100 Strains in Pier Longitudinal Reinforcement at Layer X=11	147
Figure 4.26 POJ-RC-100 Strain Profiles in Overhang at Section X=30.....	148
Figure 4.27 POJ-RC-100 Strain Profiles in Overhang at Section X=35.....	149
Figure 4.28 POJ-RC-100 Strain Profiles in Joint at Section Z=12	149
Figure 4.29 POJ-RC-100 Strain Profiles in Pier at Section Z=24	150
Figure 4.30 POJ-RC-100 Strain Profiles in Pier at Section Z=54	150
Figure 4.31 POJ-PS-100 Reinforcing Details	151
Figure 4.32 POJ-PS-100 Free Body and Reinforcement Locations Used in Strength Model	153
Figure 4.33 POJ-PS-100 Free Body Used to Compute Specimen POJ-PS-100 Capacity	154
Figure 4.34 POJ-PS-100 Overall Principal Tensile Stresses at Dead Load	155
Figure 4.35 POJ-PS-100 Overall Principal Compressive Stresses at Dead Load.....	155
Figure 4.36 Photograph of Specimen POJ-PS-100 Failure Mode Viewed from the North ..	158
Figure 4.37 Photograph of Specimen POJ-PS-100 Bar Anchorage Failure	159

Figure 4.38	Photograph of Joint Crack Opening in Specimen POJ-PS-100.....	159
Figure 4.39	POJ-PS-100 - Location of Displacement Transducers	160
Figure 4.40	POJ-PS-100 Tip Deflection (LV 75).....	162
Figure 4.41	POJ-PS-100 Vertical Displacement of Top of Joint.....	162
Figure 4.42	POJ-PS-100 Pier Horizontal Deflections	163
Figure 4.43	POJ-PS-100 Bearing Pad Shear Displacements	163
Figure 4.44	POJ-PS-100 Joint Strain Gage Locations and Labels	165
Figure 4.45	POJ-PS-100 Overall Strain Gage Locations and Pier Strain Gage Labels	166
Figure 4.46	POJ-PS-100 Strains in Secondary Overhang Reinforcement at Layer Z=9	168
Figure 4.47	POJ-PS-100 Strains in Secondary Overhang Reinforcement at Layer Z=12	168
Figure 4.48	POJ-PS-100 Strains in Secondary Overhang Reinforcement at Layer Z=17	169
Figure 4.49	POJ-PS-100 Strains in Pier Longitudinal Reinforcement at Layer X=8	169
Figure 4.50	POJ-PS-100 Strains in Pier Longitudinal Reinforcement at Layer X=11	170
Figure 4.51	POJ-PS-100 Strain Profiles in Pier at Section Z=12	171
Figure 4.52	POJ-PS-100 Strain Profiles in Pier at Section Z=24	171
Figure 4.53	POJ-PS-100 Strain Profiles in Pier at Section Z=54	172
Figure 4.54	POJ-RC-100-TH Reinforcing Details	173
Figure 4.55	POJ-RC-100-TH Joint Corner Detail	174
Figure 4.56	POJ-RC-100-TH - Photograph of Cracking Pattern on North Face of Specimen at Factored Load.....	177
Figure 4.57	POJ-RC-100-TH - Photograph of Cracking Pattern on North Face of Specimen at Ultimate Load.....	178
Figure 4.58	POJ-RC-100-TH - Photograph of Concrete Spalling in Joint Region at End of Test	178
Figure 4.59	POJ-RC-100-TH - Photograph of Concrete Spalling in Joint Region at End of Test	179
Figure 4.60	POJ-RC-100-TH - Location of Displacement Transducers.....	180
Figure 4.61	POJ-RC-100-TH Tip Deflection (LV 75)	182
Figure 4.62	POJ-RC-100-TH Joint Vertical Displacement	182
Figure 4.63	POJ-RC-100-TH Pier Horizontal Deflection	183
Figure 4.64	POJ-RC-100-TH Bearing Pad Horizontal Displacement	183
Figure 4.65	POJ-RC-100-TH Overhang Strain Gage Locations and Labels	185
Figure 4.66	POJ-RC-100-TH Joint Strain Gage Locations and Labels	186

Figure 4.67	POJ-RC-100-TH Overall Strain Gage Locations and Pier Strain Gage Labels	187
Figure 4.68	POJ-RC-100-TH Strains in Primary Longitudinal Reinforcement at Layer Z=1 in the Overhang	189
Figure 4.69	POJ-RC-100-TH Strains in Primary Longitudinal Reinforcement at Layer Z=3 in the Overhang	190
Figure 4.70	POJ-RC-100-TH Strains in Transverse and Side-face Reinforcement in the Overhang	190
Figure 4.71	POJ-RC-100-TH Strains in Pier Longitudinal Reinforcement at Layer X=1	191
Figure 4.72	POJ-RC-100-TH Strains in Pier Longitudinal Reinforcement at Layer X=5	191
Figure 4.73	POJ-RC-100-TH Strains in Pier Longitudinal Reinforcement at Layer X=8	192
Figure 4.74	POJ-RC-100-TH Strains in Pier Longitudinal Reinforcement at Layer X=11	192
Figure 4.75	POJ-RC-100-TH Overhang Strain Profile at Section X=30	194
Figure 4.76	POJ-RC-100-TH Joint Strain Profile at Section Z=12	194
Figure 4.77	POJ-RC-100-TH Pier Strain Profile at Section Z=24	195
Figure 4.78	POJ-RC-100-TH Pier Strain Profile at Section Z=54	195
Figure 4.79	Reinforcing Details for Specimen POJ-PU-54-TH	196
Figure 4.80	Joint Corner Detail for Specimen POJ-PU-54-TH	197
Figure 4.81	POJ-PU-54-TH Joint Principal Tensile Stresses and Vectors at Service Load	198
Figure 4.82	POJ-PU-54-TH Joint Principal Compressive Stresses and Vectors at Service Load	198
Figure 4.83	Photograph of Cracking Patterns on North Face of Specimen POJ-PU-54-TH at Factored Load	200
Figure 4.84	Photograph of Cracking Pattern on North Face of Specimen POJ-PU-54-TH at Ultimate Load	201
Figure 4.85	Photograph of Concrete Spalling on Underside of Overhang for Specimen POJ PU 54-TH	202
Figure 4.86	Location of Displacement Transducers for Test of Specimen POJ-PU-54-TH	203
Figure 4.87	POJ-PU-54-TH Tip Deflection (LV 75)	205
Figure 4.88	POJ-PU-54-TH Joint Vertical Displacement	205
Figure 4.89	POJ-PU-54-TH Pier Horizontal Deflection	206
Figure 4.90	POJ-PU-54-TH Bearing Pad Shear Displacement	206
Figure 4.91	POJ-PU-54-TH Overhang Strain Gage Locations and Labels	208
Figure 4.92	POJ-PU-54-TH Joint Strain Gage Locations and Labels	209
Figure 4.93	POJ-PU-54-TH Overall Strain Gage Locations and Pier Strain Gage Labels	210

Figure 4.94 POJ-PU-54-TH Strains in Primary Longitudinal Mild Reinforcement at Layer Z=1 in Overhang.....	212
Figure 4.95 POJ-PU-54-TH Strains in Transverse Reinforcement in Overhang.....	212
Figure 4.96 POJ-PU-54-TH Strains in Pier Longitudinal Reinforcement at Layer X=1.....	213
Figure 4.97 POJ-PU-54-TH Strains in Pier Longitudinal Reinforcement at Layer X=5.....	213
Figure 4.98 POJ-PU-54-TH Strains in Pier Longitudinal Reinforcement at Layer X=9.....	214
Figure 4.99 POJ-PU-54-TH Strains in Pier Longitudinal Reinforcement at Layer X=13.....	214
Figure 4.100 POJ-PU-54-TH Strain Profiles in Overhang at Section X=30.....	215
Figure 4.101 POJ-PU-54-TH Strain Profiles in Pier at Section Z=12.....	216
Figure 4.102 POJ-PU-54-TH Strain Profiles in Pier at Section Z=24.....	216
Figure 4.103 POJ-PU-54-TH Strain Profiles in Pier at Section Z=52.....	217
Figure 4.104 Reinforcement Details for Specimen POJ-PU-74-TH.....	218
Figure 4.105 Joint Corner Detail for Specimen POJ-PU-74-TH.....	219
Figure 4.106 POJ-PU-74-TH Joint Principal Tensile Stresses and Vectors at Service Load.....	220
Figure 4.107 POJ-PU-74-TH Joint Principal Compressive Stresses and Vectors at Service Load.....	220
Figure 4.108 Photograph of Cracking Patterns on North Face of Specimen POJ-PU-74-TH at Factored Load.....	223
Figure 4.109 Photograph of Cracking Patterns on North Face of Specimen POJ-PU-74-TH at Maximum Applied Load.....	224
Figure 4.110 POJ-PU-74-TH - Location and Identification of Displacement Gages.....	225
Figure 4.111 POJ-PU-74-TH Tip Deflection (LV 75).....	226
Figure 4.112 POJ-PU-74-TH Vertical Joint Displacement.....	227
Figure 4.113 POJ-PU-74-TH Pier Horizontal Deflection.....	227
Figure 4.114 POJ-PU-74-TH Bearing Pad Displacement.....	228
Figure 4.115 POJ-PU-74-TH Overhang Strain Gage Locations and Labels.....	229
Figure 4.116 POJ-PU-74-TH Joint Strain Gage Locations and Labels.....	230
Figure 4.117 POJ-PU-74-TH Overall Strain Gage Locations and Pier Strain Gage Labels.....	231
Figure 4.118 POJ-PU-74-TH Strains in Primary Longitudinal Mild Reinforcement at Layer Z=1 in Overhang.....	233
Figure 4.119 POJ-PU-74-TH Strains in Side-Face Longitudinal Reinforcement in Overhang.....	234
Figure 4.120 POJ-PU-74-TH Strains in Transverse Reinforcement in Overhang.....	234

Figure 4.121 POJ-PU-74-TH Strains in Pier Longitudinal Reinforcement at Layer X=1	235
Figure 4.122 POJ-PU-74-TH Strains in Pier Longitudinal Reinforcement at Layer X=4	235
Figure 4.123 POJ-PU-74-TH Strains in Pier Longitudinal Reinforcement at Layer X=8	236
Figure 4.124 POJ-PU-74-TH Strain Profiles in Pier at Section Z=55	237
Figure 5.1 Moment vs. Tip Displacement Response for Pier-Overhang-Joint Specimens ...	239
Figure 5.2: Comparison of Moment vs. Tip Displacement Response for Specimens RC-100 and RC-100-TH	240
Figure 5.3 Strain Gage Locations for Specimen RC-100	242
Figure 5.4 POJ-RC-100 - Comparison of Analysis and Test Strain-Profiles for the Overhang at the Face of the Pier	243
Figure 5.5 POJ-RC-100 - Comparison of Analysis and Test Strain-Profiles for a Cross-Section Near Mid-Height of the Pier	243
Figure 5.6 POJ-RC-100-TH Comparison of Analysis and Test Strain-Profiles for a Cross-Section of the Overhang Near the Face of the Pier.....	244
Figure 5.7 POJ-RC-100-TH - Comparison of Analysis and Test Strain-Profiles for a Cross-Section Near Mid-Height of the Pier	245
Figure 5.8 POJ-PU-54 - Comparison of Analysis and Test Strain-Profiles for a Cross-Section of the Overhang Near the Face of the Pier	246
Figure 5.9 POJ-PU-54-TH - Pier Analytical and Experimental Strain-Profiles for a Cross-Section Near Mid-Height of the Pier	247
Figure 5.10 Pier Post-Tensioning Stresses for Specimen POJ-PU-54-TH Estimated from Strain Gage Measurements	248
Figure 5.11 Service-Level Tip Deflections.....	251
Figure 5.12 POJ-RC-100 - Service Load Crack Pattern	253
Figure 5.13 POJ-RC-100 - Principal Tensile Stress Contours at Service Load.....	253
Figure 5.14 POJ-PS-100 - Dead Load Crack Pattern.....	254
Figure 5.15 POJ-PS-100 - Principal Tensile Stress Contours at Dead Load	254
Figure 5.16: POJ-RC-100-TH - Service Load Crack Pattern	255
Figure 5.17 POJ-RC-100-TH - Principal Tensile Stress Contours at Service Load	255
Figure 5.18 POJ-PU-54-TH - Service Load Crack Pattern.....	256
Figure 5.19 POJ-PU-54-TH - Principal Tensile Stress Contours at Service Load	256
Figure 5.20 POJ-PU-74-TH - Service Load Crack Pattern.....	257
Figure 5.21 POJ-PU-74-TH - Principal Tensile Stress Contours at Service Load	257

Figure 5.22 Crack-Width Envelopes for Overhang Region.....	259
Figure 5.23 Crack-Width Envelopes for Joint Region.....	260
Figure 5.24 Crack-Width Envelopes for Pier Region.....	261
Figure 5.25 POJ-RC-100 Crack-Width Frequency and Distribution.....	262
Figure 5.26 POJ-RC-100-TH Crack-Width Frequency and Distribution	263
Figure 5.27 POJ-PU-54-TH Crack-Width Frequency and Distribution	264
Figure 5.28 POJ-PU-74-TH Crack-Width Frequency and Distribution	265
Figure 5.29 Illustration of Crack-Width Equation Variables.....	268
Figure 5.30 POJ-RC-100 Maximum Predicted and Measured Crack Widths	270
Figure 5.31 POJ-RC-100-TH Maximum Predicted and Measured Crack Widths.....	271
Figure 5.32 POJ-PU-54-TH Maximum Predicted and Measured Crack Widths	272
Figure 5.33 POJ-PU-74-TH Maximum Predicted and Measured Crack Widths	273
Figure 5.34 Material Quantities for Full-Scale Bents	285
Figure 5.35 Material Costs for Full-Scale Bents.....	285
Figure 5.36 Bottle-Shaped Compression Field for Joint Corner Detail.....	287
Figure 7.1 Cantilever Substructure Strut-and-Tie Model	297
Figure 7.2 Free Body Used to Compute Bent Capacity.....	298
Figure 7.3 Assumed Joint Crack and Method for Computing Forces Developed in Longitudinal Bars.....	300
Figure 7.4 I4-C - External Dimensions and Points of Superstructure Load Application.....	302
Figure 7.5 I4-C - Pier Reinforcement Details	303
Figure 7.6 I4-C - Overhang Reinforcement Details at Pier Face	303
Figure 7.7 Free Body Used to Compute Substructure I4-C Capacity.....	304
Figure 7.8 I4-C - Free Body and Reinforcement Locations Used in Strength Model	305
Figure 7.9 I4-C - Principal Tensile Stress Contours at Applied Dead Loads	307
Figure 7.10 I4-C - Principal Compressive Stress Contours at Applied Dead Loads	307
Figure 7.11 I4-C - Principal Tensile Stress Contours at Applied Service Loads.....	308
Figure 7.12 I4-C - Principal Compressive Stress Contours at Applied Service Loads.....	308
Figure 7.13 I4-C - Principal Tensile Stress Contours at Applied Dead Load Plus Two Live Loads	309

Figure 7.14 I4-C - Principal Compressive Stress Contours at Applied Dead Load Plus Two Live Loads	309
Figure 7.15 I4-C - Principal Tensile Stress Vectors	310
Figure 7.16 I4-C - Principal Compressive Stress Vectors	310
Figure 7.17 Cracking Pattern and Maximum Crack Widths for I4-C Substructure.....	311
Figure 7.18 C11-C - External Dimensions and Points of Superstructure Load Application.....	313
Figure 7.19 C11-C - Pier Reinforcement Details.....	314
Figure 7.20 C11-C - Overhang Reinforcement Details at Pier Face.....	314
Figure 7.21 Free Body Used to Compute Substructure C11-C Capacity	315
Figure 7.22 C11-C - Free Body and Reinforcement Locations Used in Strength Model	316
Figure 7.23 C11-C - Principal Tensile Stress Contours and Trajectories at Applied Dead Load	318
Figure 7.24 C11-C - Principal Compressive Stress Contours and Trajectories at Applied Dead Load.....	318
Figure 7.25 Cracking Pattern for C11-C Substructure.....	319
Figure 8.1 Elevation of Reinforcement for Specimen POJ-RC-100-2	323
Figure 8.2 POJ-RC-100-2 Pier Reinforcement Details.....	324
Figure 8.3 POJ-RC-100-2 Overhang Reinforcement Details	324
Figure 8.4 POJ-RC-100-2 Principal Tensile Stresses at Service Load	325
Figure 8.5 POJ-RC-100-2 Principal Tensile Stress Vectors at Service Load	326
Figure 8.6 POJ-RC-100-2 Strut-and-Tie Model	327
Figure 8.7 POJ-RC-100-2 Free Body and Reinforcement Locations Used in Strength Model.....	328
Figure 8.8 Free Body Used to Compute Specimen POJ-RC-100-2 Capacity.....	329
Figure 8.9 POJ-RC-100-2 Applied Overhang Moment vs. Tip-Deflection.....	330
Figure 8.10 Elevation of Reinforcement for POJ-PS-100	332
Figure 8.11 POJ-PS-100 Pier Reinforcement Details.....	333
Figure 8.12 POJ-PS-100 Overhang Reinforcement Details.....	333
Figure 8.13 POJ-PS-100 Principal Tensile Stresses at Dead Load.....	334
Figure 8.14 POJ-PS-100 Principal Tensile Stress Vectors	335
Figure 8.15 POJ-PS-100 Strut-and-Tie Model	336

Figure 8.16	POJ-PS-100 - Free Body and Reinforcement Locations Used in Strength Model	337
Figure 8.17	Free Body Used to Compute Strength of Specimen POJ-PS-100	338
Figure 8.18	POJ-PS-100 - Applied Overhang Moment vs. Tip Deflection	339
Figure 8.19	External Vertical PT Repair - Side View	343
Figure 8.20	External Vertical PT Repair - End View	344
Figure 8.21	External Diagonal Post-Tensioned Repair - Side View	345
Figure 8.22	Internal Vertical Post-Tensioned Repair - Conceptual Design.....	347
Figure 8.23	Internal Horizontal Post-Tensioned Repair - Conceptual Design	348
Figure 8.24	Internal Horizontal and Vertical Post-Tensioning - Conceptual Design	349
Figure 8.25	Elevation of External Diagonal Post-Tensioned Repair.....	351
Figure 8.26	POJ-RC-100-RP1 Free Body and Reinforcement Locations Used in Strength Model	352
Figure 8.27	Free Body Used to Determine Post-Tensioning Force for Specimen POJ-RC-100-RP1	353
Figure 8.28	POJ-RC-100-RP1 Overall Principal Tensile Stresses at Service Load	355
Figure 8.29	POJ-RC-100-RP1 Overall Principal Compressive Stresses at Service Load	355
Figure 8.30	POJ-RC-100-RP1 Joint Principal Tensile Stresses and Vectors at Service Load	356
Figure 8.31	POJ-RC-100-RP1 Joint Principal Compressive Stresses and Vectors at Service Load	356
Figure 8.32	POJ-RC-100-RP1 Overall Dimensions - Elevation.....	357
Figure 8.33	POJ-RC-100-RP1 Dimensions - Top View	360
Figure 8.34	POJ-RC-100-RP1 Joint Details	361
Figure 8.35	POJ-RC-100-RP1 Top Plate Dimensions.....	362
Figure 8.36	POJ-RC-100-RP1 Edge Plate Dimensions	363
Figure 8.37	POJ-RC-100-RP1 Overhang Tip Displacement	365
Figure 8.38	POJ-RC-100-RP1 External Post-Tensioning Bar Strains.....	365
Figure 8.39	Elevation of Internal Vertical Post-Tensioned Repair (POJ-RC-100-RP2)	366
Figure 8.40	POJ-RC-100-RP2 Free Body and Reinforcement Locations Used in Strength Model	368
Figure 8.41	Free Body Used to Determine Post-Tensioning Force for Specimen POJ-RC-100-RP2.....	369

Figure 8.42	POJ-RC-100-RP2 - Overall Principal Tensile Stresses and Trajectories at Service Load	371
Figure 8.43	POJ-RC-100-RP2 - Overall Principal Compressive Stresses and Trajectories at Service Load.....	371
Figure 8.44	POJ-RC-100-RP2 - Joint Principal Tensile Stresses and Trajectories at Service Load	372
Figure 8.45	POJ-RC-100-RP2 - Joint Principal Compressive Stresses and Trajectories at Service Load	372
Figure 8.46	POJ-RC-100-RP2 Overall Dimensions - Elevation.....	373
Figure 8.47	POJ-RC-100-RP2 Dimensions - Top View	374
Figure 8.48	POJ-RC-100-RP2 Overhang Tip Displacement	376
Figure 8.49	Elevation of POJ-PS-100-RP1 & RP2 External Vertical PT Repairs	378
Figure 8.50	POJ-PS-100-RP1- Free Body and Reinforcement Locations Used in Capacity Calculation	380
Figure 8.51:	POJ-PS-100-RP2 Free Body and Reinforcement Locations Used in Capacity Calculation	381
Figure 8.52	Free Body Used to Determine Post-Tensioning Force for Specimens POJ-PS-100-RP1 & RP2.....	382
Figure 8.53	POJ-PS-100-RP1 -Overall Principal Tensile Stresses and Trajectories at Service Load	384
Figure 8.54	POJ-PS-100-RP1 - Overall Principal Compressive Stresses and Trajectories at Service Load.....	384
Figure 8.55	POJ-PS-100-RP1 - Joint Principal Tensile Stresses and Trajectories at Service Load	385
Figure 8.56	POJ-PS-100-RP1 - Joint Principal Compressive Stresses and Trajectories at Service Load	385
Figure 8.57	POJ-PS-100-RP2 - Overall Principal Tensile Stresses and Trajectories at Service Loads.....	386
Figure 8.58	POJ-PS-100-RP2 - Overall Principal Compressive Stresses and Trajectories at Service Loads	386
Figure 8.59	POJ-PS-100-RP2 - Joint Principal Tensile Stresses and Trajectories at Service Load	387
Figure 8.60	POJ-PS-100-RP2 - Joint Principal Tensile Stresses and Trajectories at Service Load	387
Figure 8.61	POJ-PS-100 Repair - Elevation	390
Figure 8.62	POJ-PS-100 Repair - End View	391

Figure 8.63 POJ-PS-100 Repair - Top View	392
Figure 8.64 POJ-PS-100 Repair - Side Plate Dimensions and Details	393
Figure 8.65 POJ-PS-100 Repair - Cap Beam Dimensions and Details.....	394
Figure 8.66 POJ-PS-100-RP1 Overhang Moment vs. Tip Deflection Response.....	396
Figure 8.67 POJ-PS-100-RP2- Overhang Moment vs. Tip Deflection Response	396
Figure 8.68 Recorded Strain in External PT Bars for POJ-PS-100-RP1	397
Figure 8.69 Recorded Strain in External PT Bars for POJ-PS-100-RP2	397
Figure 9.1 Comparison of Overhang Tip Displacement Response for Specimen POJ-RC-100-2, and Repairs RP1 and RP2.....	399
Figure 9.2 Comparison of Overhang Tip Displacement Behavior for Specimen POJ-PS-100 and Repairs RP1 and RP2	400
Figure 9.3 POJ-RC-100-2 - Joint Region Strain Gage Locations and Labels	402
Figure 9.4 Comparison of Strain Gage T7Z5A Response for Specimen POJ-RC-100-2 and Repairs RP1 and RP2	403
Figure 9.5 Comparison of Strain Gage F10Z10A Response for Specimen POJ-RC-100-2 and Repairs RP1 and RP2	403
Figure 9.6 Comparison of Strain Gage F17Z13A Response for Specimen POJ-RC-100-2 and Repairs RP1 and RP2	404
Figure 9.7 Comparison of Strain Gage M31Z3A Response for Specimen POJ-RC-100-2 and Repairs RP1 and RP2	404
Figure 9.8 Comparison of Strain Gage C1Z24B Response for Specimen POJ-RC-100-2 and Repairs RP1 and RP2	405
Figure 9.9 Comparison of Strain Gage C11Z12C Response for Specimen POJ-RC-100-2 and Repairs RP1 and RP2	405
Figure 9.10 Comparison of Strain Gage C15Z12A Responses for Specimen POJ-RC-100-2 and Repairs RP1 and RP2.....	406
Figure 9.11 POJ-PS-100 Joint Strain Gage Locations and Labels	408
Figure 9.12 Comparison of Strain Gage T10Z17A Responses for Specimen POJ-PS-100 and Repairs RP1 and RP2	409
Figure 9.13 Comparison of Strain Gage F10Z9B Responses for Specimen POJ-PS-100 and Repairs RP1 and RP2	409
Figure 9.14 Comparison of Strain Gage F10Z12B Response for Specimen POJ-PS-100 and Repairs RP1 and RP2	410
Figure 9.15 Comparison of Strain Gage C8Z12A Responses for Specimen POJ-PS-100 and Repairs RP1 and RP2	410

Figure 9.16 Comparison of Strain Gage C11Z12C Response for Specimen POJ-PS-100 and Repairs RP1 and RP2	411
Figure 9.17 Average Recorded Strains in Post-Tensioned Bars for External Post-Tensioned Repairs	412
Figure 9.18 Cost Comparison of Proposed Repair Methods	420
Figure A.1 POJ-RC-100 - Cracking Pattern on North Face of Specimen at Dead Load	433
Figure A.2 POJ-RC-100 - Cracking Pattern on South Face of Specimen at Dead Load	433
Figure A.3 POJ-RC-100 - Cracking Pattern on North Face of Specimen at Service Load ..	434
Figure A.4 POJ-RC-100 - Cracking Pattern on South Face of Specimen at Service Load ..	434
Figure A.5 POJ-RC-100 - Cracking Pattern on North Face of Specimen at Failure	435
Figure A.6 POJ-RC-100 - Cracking Pattern on South Face of Specimen at Failure	435
Figure A.7 POJ-RC-100 - Cracking Pattern on North Face of Overhang at Dead Load	436
Figure A.8 POJ-RC-100 - Cracking Pattern on North Face of Overhang at Service Load ..	436
Figure A.9 POJ-RC-100 - Cracking Pattern on South Face of Overhang at Dead Load	438
Figure A.10 POJ-RC-100 - Cracking Pattern on South Face of Overhang at Service Load	438
Figure A.11 POJ-RC-100 - Cracking Pattern on North Face of Joint at Dead Load	440
Figure A.12 POJ-RC-100 - Cracking Pattern on North Face of Joint at Service Load	440
Figure A.13 POJ-RC-100 - Cracking Pattern on South Face of Joint at Dead Load	442
Figure A.14 POJ-RC-100 - Cracking Pattern on South Face of Joint at Service Load	442
Figure A.15 POJ-RC-100 - Cracking Pattern for North Face of Pier at Dead Load	444
Figure A.16 POJ-RC-100 - Cracking Pattern for North Face of Pier at Service Load	444
Figure A.17 POJ-RC-100 - Cracking Pattern on South Face of Pier at Dead Load	446
Figure A.18 POJ-RC-100 - Cracking Pattern on South Face of Pier Service Load	446
Figure A.19 POJ-PS-100 - Cracking Pattern on North Face of Specimen at Dead Load	449
Figure A.20 POJ-PS-100 - Cracking Pattern on South Face of Specimen at Dead Load	449
Figure A.21 POJ-PS-100 - Cracking Pattern on North Face of Joint at Dead Load	450
Figure A.22 POJ-PS-100 - Cracking Patterns on South Face of Joint at Dead Load	451
Figure A.23 POJ-PS-100 - Cracking Patterns on North Face of Pier at Dead Load	452
Figure A.24 POJ-PS-100 - Cracking Patterns on South Face of Pier at Dead Load	453
Figure A.25 POJ-RC-100-TH Cracking Pattern on North Face of Specimen at Dead Load	456

Figure A.26 POJ-RC-100-TH Cracking Pattern on South Face of Specimen at Dead Load	456
Figure A.27 POJ-RC-100-TH Cracking Pattern on North Face of Specimen at Service Load	457
Figure A.28 POJ-RC-100-TH Cracking Pattern on South Face of Specimen at Service Load	457
Figure A.29 POJ-RC-100-TH Cracking Pattern on North Face of Specimen at Failure	458
Figure A.30 POJ-RC-100-TH Cracking Pattern on South Face of Specimen at Failure	458
Figure A.31 POJ-RC-100-TH Cracking Pattern on North Face of Overhang at Dead Load	459
Figure A.32 POJ-RC-100-TH Cracking Pattern on North Face of Overhang at Service Load	459
Figure A.33 POJ-RC-100-TH Cracking Pattern on South Face of Overhang at Dead Load	461
Figure A.34 POJ-RC-100-TH Cracking Pattern on South Face of Overhang at Service Load	461
Figure A.35 POJ-RC-100-TH Cracking Pattern on North Face of Joint at Dead Load.....	463
Figure A.36 POJ-RC-100-TH Cracking Pattern on North Face of Joint at Service Load	463
Figure A.37 POJ-RC-100-TH Cracking Pattern on South Face of Joint at Dead Load.....	465
Figure A.38 POJ-RC-100-TH Cracking Pattern on South Face of Joint at Service Load	465
Figure A.39 POJ-RC-100-TH Cracking Pattern on North Face of Pier at Dead Load	467
Figure A.40 POJ-RC-100-TH Cracking Pattern on North Face of Pier at Service Load	467
Figure A.41 POJ-RC-100-TH Cracking Pattern on South Face of Pier at Dead Load.....	469
Figure A.42 POJ-RC-100-TH Cracking Pattern on South Face of Pier at Service Load	469
Figure A.43 Cracking Pattern on North Face of Specimen POJ-PU-54-TH at Dead Load ..	473
Figure A.44 Cracking Pattern on South Face of Specimen POJ-PU-54-TH at Dead Load ..	473
Figure A.45 Cracking Pattern on North Face of Specimen POJ-PU-54-TH at Service Load	474
Figure A.46 Cracking Pattern on South Face of Specimen POJ-PU-54-TH at Service Load	474
Figure A.47 Cracking Pattern on North Face of Specimen POJ-PU-54-TH at Failure	475
Figure A.48 Cracking Pattern on South Face of Specimen POJ-PU-54-TH at Failure	475
Figure A.49 POJ-PU-54-TH Cracking Pattern on North Face of Overhang at Dead Load ..	476
Figure A.50 POJ-PU-54-TH Cracking Pattern on North Face of Overhang at Service Load	476

Figure A.51 POJ-PU-54-TH Cracking Pattern on South Face of Overhang at Dead Load..	478
Figure A.52 POJ-PU-54-TH Cracking Pattern on South Face of Overhang at Service Load	478
Figure A.53 POJ-PU-54-TH Cracking Pattern on North Face of Joint at Dead Load.....	480
Figure A.54 POJ-PU-54-TH Cracking Pattern on North Face of Joint at Service Load	480
Figure A.55 POJ-PU-54-TH Cracking Pattern on South Face of Joint at Dead Load.....	482
Figure A.56 POJ-PU-54-TH Cracking Pattern on South Face of Joint at Service Load	482
Figure A.57 POJ-PU-54-TH Cracking Pattern on North Face of Pier at Dead Load	484
Figure A.58 POJ-PU-54-TH Cracking Pattern on North Face of Pier at Service Load.....	484
Figure A.59 POJ-PU-54-TH Cracking Pattern on South Face of Pier at Dead Load	486
Figure A.60 POJ-PU-54-TH Cracking Pattern on South Face of Pier at Service Load.....	486
Figure A.61 Cracking Patterns on North Face of Specimen POJ-PU-74-TH at Dead Load	490
Figure A.62 Cracking Patterns on South Face of Specimen POJ-PU-74-TH at Dead Load	490
Figure A.63 Cracking Patterns on North Face of Specimen POJ-PU-74-TH at Service Load	491
Figure A.64 Cracking Patterns on South Face of Specimen POJ-PU-74-TH at Service Load	491
Figure A.65 Cracking Patterns on North Face of Specimen POJ-PU-74-TH at End of Test (No Failure).....	492
Figure A.66 Cracking Patterns on South Face of Specimen POJ-PU-74-TH at End of Test (No Failure).....	492
Figure A.67 POJ-PU-74-TH Cracking Patterns on North Face of Overhang at Dead Load	493
Figure A.68 POJ-PU-74-TH Cracking Patterns on North Face of Overhang at Service Load	493
Figure A.69 POJ-PU-74-TH Cracking Patterns on South Face of Overhang at Dead Load	495
Figure A.70 POJ-PU-74-TH Cracking Patterns on South Face of Overhang at Service Load	495
Figure A.71 POJ-PU-74-TH Cracking Patterns on North Face of Joint at Dead Load	497
Figure A.72 POJ-PU-74-TH Cracking Patterns on North Face of Joint at Service Load.....	497
Figure A.73 POJ-PU-74-TH Cracking Patterns on South Face of Joint at Dead Load	499
Figure A.74 POJ-PU-74-TH Cracking Patterns on South Face of Joint at Service Load.....	499

Figure A.75 POJ-PU-74-TH Cracking Patterns on North Face of Pier at Dead Load.....	501
Figure A.76 POJ-PU-74-TH Cracking Patterns on North Face of Pier at Service Loads.....	501
Figure A.77 POJ-PU-74-TH Cracking Patterns on South Face of Pier at Dead Load.....	503
Figure A.78 POJ-PU-74-TH Cracking Patterns on South Face of Pier at Service Load	503
Figure B.1 Substructure Schematic.....	506
Figure B.2 Pier Location and Continuity Factors	507
Figure B.3 Full-Scale Prototype Loads Without Continuity Factors.....	507
Figure B.4 Strut-and-Tie Model	509
Figure B.5 Details for Strut-and-Tie Model of Vertical Tie T2.....	509
Figure B.6 Transverse Reinforcement Details for Example Problem.....	512
Figure B.7 Overhang Cross Section for Example Problem	513
Figure B.8 Identification of Crack-Width Control Variables	514
Figure B.9 Pier Reinforcement Details for Example Problem.....	517
Figure B.10 Joint Reinforcement Details for Example Problem	519
Figure B.11 Overall Reinforcement Details for Example Problem	520

CHAPTER 1

INTRODUCTION

1.1 Problem Statement

An elevated expressway and a series of highway interchanges were constructed in San Antonio to link I-10 and I-35 and reduce traffic congestion. Because right-of-way for the ground level feeder roads and main lanes conflicted with the proposed geometry for on-ramps and off-ramps as well as several portions of the main lane elevated expressway, support piers were designed to cantilever over the existing roadways. These cantilever bents supported large prestressed concrete winged box girders, where dead load of the superstructure comprised approximately four-fifths of the design service load. Loads from the superstructure were transmitted to the substructure through two bearings located beneath the winged box girder. Location of the bearing points on the substructure varied as shown in Figure 1.1. For many of the cantilever bents, both reactions were located on the overhang.

During design of these large bents, some confusion existed because one reaction was often located on the overhang a short distance from the column face, resulting in a small span-to-depth (a/d) ratio less than one, and the second reaction was typically located well out on the overhang (for an a/d ratio greater than one). The 1983 AASHTO Standard Bridge Specifications [1] states that corbel design provisions “shall apply to brackets and corbels with a shear span-to-depth ratio a/d not greater than unity”, where d is measured from the column face. Designers satisfied both corbel and flexural design provisions by providing longitudinal reinforcement in the top of the overhang to resist design moments and longitudinal reinforcement near mid-depth to resist design shear friction. Because the resulting designs were extremely congested, it was believed that the bents were substantially over designed.



Figure 1.1 Cantilever Bents Supporting Entrance Ramp

The separate treatment of reinforced concrete and prestressed concrete members in the AASHTO Standard Bridge Specifications forces engineers to perform either reinforced concrete designs or “fully prestressed” designs which are typically controlled by service-level stresses. This often results in inefficient use of the materials. For example, where the depth of a cantilever is limited by certain factors, such as ground clearance, a fully-prestressed design is often implemented because a reinforced concrete design would be too congested. Cost associated with fully prestressing the cantilever could be reduced if only the prestressing needed to supply the flexural capacity of the member or supplement a portion of the non-prestressed reinforcement is provided instead of fully prestressing the cantilever. In addition, reinforced and prestressed concrete design specifications are contained in separate chapters, resulting in confusion when applying corbel design and shear friction provisions.

A research study (Project 3-5-93-1364) was commissioned by the Texas Department of Transportation and the Federal Highway Administration to develop an alternate design method for design of large structural members utilizing partial prestressing. The primary

objective was to develop a design method whereby a mixture of high-strength prestressed reinforcement and mild reinforcement (often referred to as “partially prestressed concrete” and herein referred to as structural concrete) could be used to provide both strength and adequate serviceability. Previous research conducted at The University of Texas at Austin [2] provided guidelines for structural concrete and use of strut-and-tie models (STM) for design of large concrete members.

1.2 Scope of Research

Research performed as part of Project 3-5-93-1364, was divided into four phases. The first phase investigated the design of the cantilever portion of the substructure. This research was performed by Armstrong [3] and Salas [4], and their studies provided a design method for the cantilever portion of the bent. The second phase, performed by Billington [5], investigated the use of structural concrete for design of large, two-span continuous beams. Results of the study were used to validate the finite element analysis procedure for modeling continuous tendons. The third phase, reported here, investigates the behavior of the cantilever bent as a whole (overhang, pier, and joint) and proposes code language for an integrated design method for structural concrete. In this study, two San Antonio ‘Y’ prototype cantilever bent designs and three integrated design models were constructed and tested. It was determined during this phase that many of the San Antonio ‘Y’ cantilever bents were deficient due to a detailing flaw in the joint region. In order to alleviate this deficiency, the research study was extended to include a fourth phase, reported here and in further detail by Scott [6], in which three strengthening methods were developed, implemented on damaged test specimens, and tested to examine behavior up to design loads.

1.3 Objective of Research

The objective of this research was to evaluate the behavior of large cantilever bents with a/d ratios ranging from less than one to approximately two, evaluate the behavior of the prototype design specimens and behavior of specimens containing different combinations of high-strength prestressed reinforcement and mild reinforcement, and develop a unified design

method for structural concrete. The development, finite element analysis, and evaluation of the three strengthening methods are presented to supplement work performed by Scott [6].

1.4 Organization

This document is organized into ten chapters, as follows:

Chapter 2: Background-----	provides background on design issues involved in the study.
Chapter 3: Experimental Program-----	details the design of each specimen, testing equipment, and material properties.
Chapter 4: Test Results-----	presents moment-deflection response, crack-width measurements, and failure modes.
Chapter 5: Analysis of Test Results-----	compares responses of all specimens, evaluates analysis tools, and provides cost estimates for each design.
Chapter 6: Proposed Design-----	recommends changes to the proposed AASHTO LRFD Specifications based on results of experimental program.
Recommendations	capacity calculation and finite element analysis of a reinforced concrete and a fully prestressed concrete cantilever bent.
Chapter 7: Analysis of San Antonio ‘Y’-----	presents design details for three repair methods, presents finite element analyses and test results.
Cantilever Bents	
Chapter 8: Development and Testing of-----	compares responses of the three repairs, evaluates analysis tools, and provides cost estimates for each repair.
Selected Repairs	
Chapter 9: Analysis of Test Results for-----	summarizes the overall results from the study and gives conclusions reached.
Cantilever Bent Repair Study	
Chapter 10: Summary and Conclusions-----	

1.1 Problem Statement1

1.2 Scope of Research.....3

1.3 Objective of Research.....3

1.4 Organization.....4

Figure 1.1 Cantilever Bents Supporting Entrance Ramp.....2

CHAPTER 2

BACKGROUND

2.1 Introduction

Investigation of the San Antonio bridge substructures was initiated when a preliminary review of the designs revealed substantial congestion in the pier, overhang, and joint regions. Designers admitted that they were baffled by the fragmented provisions for design of reinforced concrete and prestressed concrete contained in the 1986 AASHTO Standard Specifications for Highway Bridges [1] as well as the multiple sections that seemed to simultaneously apply to their particular design case. It was clear that a unified design method, in the form of a specification, would simplify the design process, provide economy, and instill confidence in the users of the design specification.

2.2 Description of Cantilever Bents in San Antonio

The cantilever bents in San Antonio were constructed to support a newly constructed elevated roadway for I-10 and I-35 over the existing ground-level lanes and entrance ramps. The superstructure was a prestressed concrete winged box girder. Loads from the superstructure were transmitted to the substructure through two bearings located beneath the winged box girder. Because the substructure was a cantilevered bent, self weight of the superstructure induced very large dead load reactions and moments on the substructure. Approximately four-fifths of the design service load moment was attributed to the superstructure dead load component. A schematic of the cantilever bent is presented in Figure 2.1.

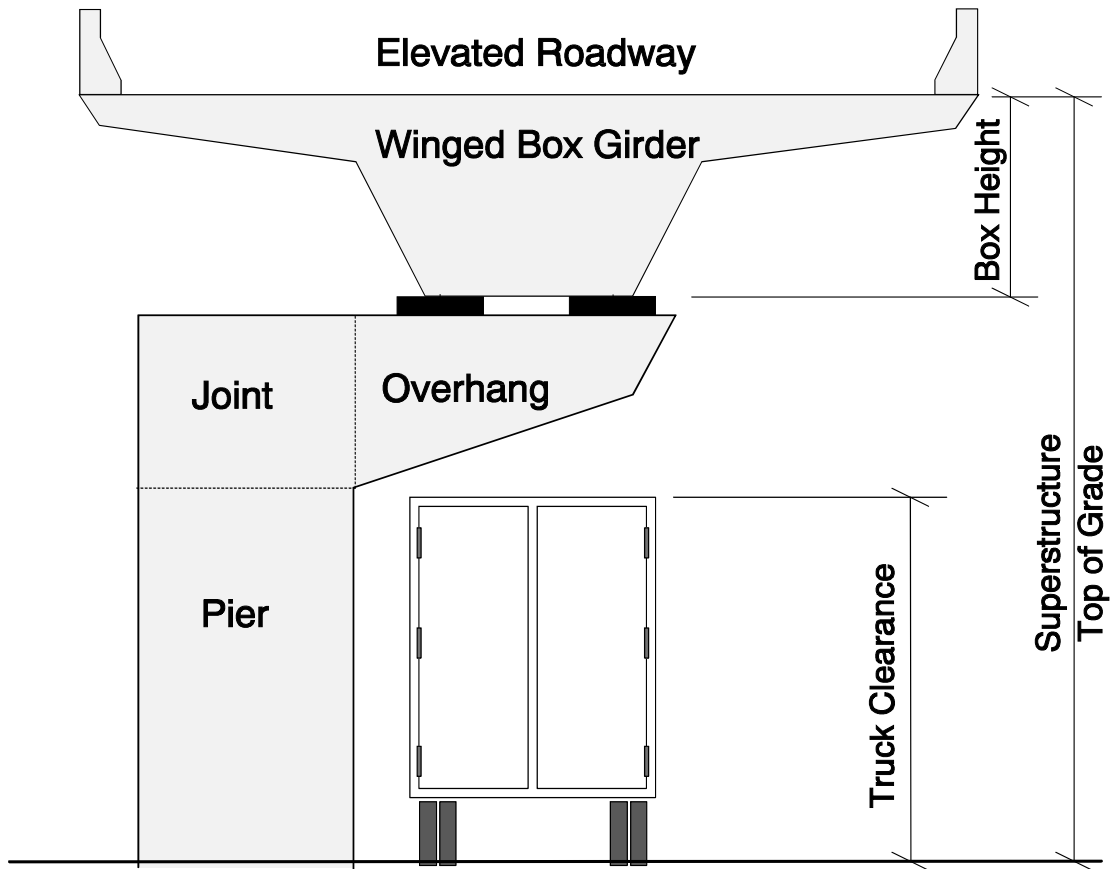


Figure 2.1 Schematic of Cantilever Bents in San Antonio

2.3 Evaluation of Current Design Practice

The 1986 AASHTO Standard Specifications for Highway Bridges [1] was the code standard used for the design of the cantilever bents in the San Antonio and prototype bents tested in the experimental program. An evaluation of strengths and weaknesses of the standard design practice is important in the development of an integrated design method. A more complete explanation of the mechanics and equations in the bridge design specifications is described in Chapter 3. The convention used to describe the different regions of the bent (pier, overhang, and joint regions) are presented in Figure 2.1.

2.3.1 AASHTO Reinforced Concrete Design

The AASHTO Reinforced Concrete Design Specifications are located in Section 8 of the AASHTO Standard Specifications for Highway Bridges. A general overview of the specifications is offered to provide evidence of the confusion inherent in the design requirements for cantilever beams. Because of the confusion, designers of the cantilever bents in San Antonio applied all sections of the specification addressing flexural design, corbel design, deep beam design, shear design, and serviceability requirements to the design of the reinforced concrete cantilever substructures. It was originally thought that their design philosophy was overly conservative, but it is now known that this was not the case.

2.3.1.1 Reinforced Concrete Overhang Design

The flexural design equations were used to determine the amount of flexural steel required to resist factored overhang moments. If the amount of overhang reinforcement exceeded the number of bars that could be placed in two rows of tension reinforcement, a fully-prestressed design was conducted.

In many designs, location of the interior load on the overhang was within the specified shear span-to-depth ratio (a/d) of less than one for corbel design. In Figure 2.2, the interior load is located a distance equal to one half the depth of the beam ($0.5 h$) and the outer load is located one and one-half times the depth of the beam ($1.5 h$) from the column face. Designers provided shear friction reinforcement near mid-depth of the overhang to resist corbel loads associated with the inner reaction. Primary longitudinal reinforcement in the overhang was provided to resist the large moments induced by the outer reaction. Quantity of shear friction reinforcement provided was equal to half of the primary longitudinal reinforcement, but was not considered to contribute to the flexural strength of the section.

The quantity of transverse reinforcement required along the overhang was somewhat ambiguous due to the tapered depth of the overhang. Because the concrete component of the shear strength equation is a function of the depth of the section, a 45° failure plane propagating from the outer reaction was assumed, and the transverse reinforcement necessary

to intersect the diagonal crack and resist the outer reaction was computed. As will be discussed in Chapter 3, geometry of the overhang permitted a force path, by which a portion of the outer reaction flowed directly into the pier. However, the shear design provisions do not consider such force paths. In addition, the shear associated with the inner reaction was addressed through corbel design. As a result, spacing of the transverse reinforcement computed for the outer reaction was used for the entire overhang.

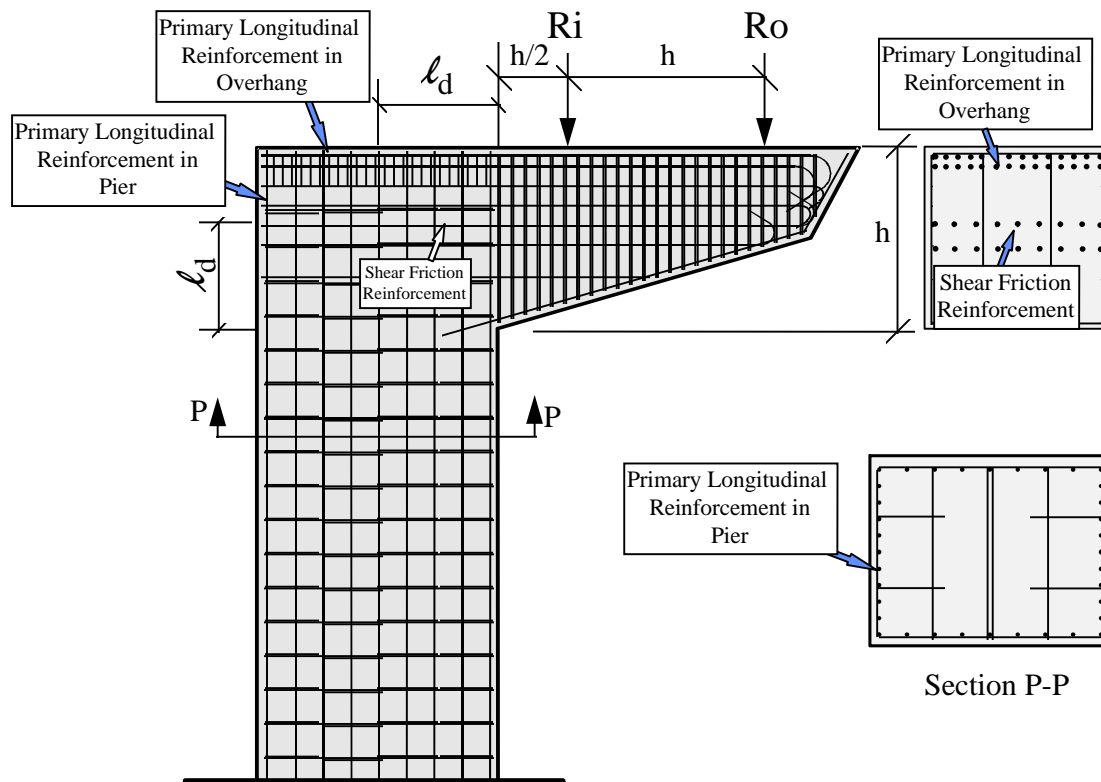


Figure 2.2 Reinforced Concrete Design

Fatigue stress limits in the reinforcement, and distribution of longitudinal reinforcement to control cracking were the serviceability requirements checked for the overhang.

2.3.1.2 Reinforced Concrete Pier Design

The pier design involved the determination of minimum member size and minimum number of longitudinal reinforcing bars to resist axial forces and overturning moments. The pier designs were nearly all controlled by the AASHTO minimum longitudinal reinforcement

ratio requirement of 1 percent ($0.01 A_g$). Serviceability requirements such as fatigue stress limits and limits on cracking for the pier region were not considered by the designers. AASHTO Standard Specifications state in Article 8.16.8.1 that serviceability requirements are applied to “flexural members”. Designers did not consider this to apply because the piers were designed according to Article 8.16.4 titled “Compression Members”, not Article 8.16.3 titled “Flexure”.

2.3.1.3 Reinforced Concrete Joint Design

The joint region for the cantilever substructure was constructed by continuing the longitudinal pier and overhang reinforcement into the joint. Column ties were placed up to the top row of overhang longitudinal reinforcement. Size of the joint was assumed to be sufficient to fully develop the longitudinal reinforcement from the critical sections of the overhang and pier regions into the joint (See Figure 2.2). Joint capacity was not evaluated because it was assumed to be a rigid mass of concrete, not liable to fail under design loads.

2.3.2 AASHTO Prestressed Concrete Design

The Prestressed Concrete Design Specifications are located in Section 9 of the AASHTO Standard Specifications for Highway Bridges. Because the reinforced and prestressed concrete specifications are located in separate sections, there is a distinct split in the design procedures. The prestressed design specifications assume that members are uncracked at service loads. This type of design will be referred to as “fully prestressed” in future discussion. The fully-prestressed design was performed for cantilever bents in San Antonio when it was not possible to fit a sufficient number of mild reinforcing bars into the member to resist factored loads.

In addition to the problem of separate specifications for reinforced concrete and prestressed concrete, the design process is further muddled because many sections of the prestressed specifications make reference to the reinforced concrete specifications. Shear friction design, corbel design, and design of deep beam reinforcement are not addressed in Section 9 of the AASHTO Specifications. For cantilever substructures, the location of the

loads and magnitude of the shear forces on the overhang made these design aspects quite critical for both the reinforced and prestressed concrete designs.

2.3.2.1 Fully Prestressed Overhang Design

The fully prestressed overhang design assumed limiting concrete tensile stresses due to flexure of $3\sqrt{f'_c}$ at service load, and included all the relevant design provisions such as shear friction design, corbel design, and the design of deep beam reinforcement from the AASHTO reinforced concrete design specifications in Section 8. Figure 2.3 shows the fully prestressed overhang design with reinforced concrete pier.

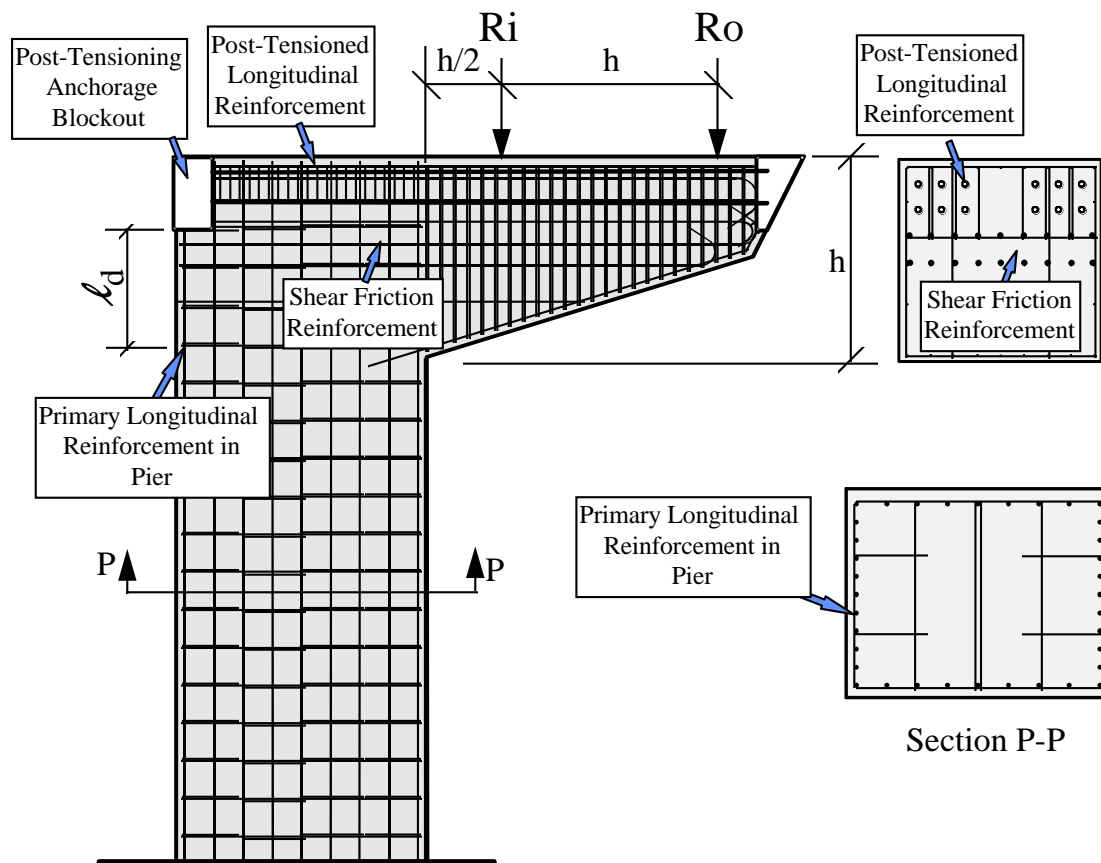


Figure 2.3 Fully Prestressed Overhang Design with Reinforced Concrete Pier

2.3.2.2 Fully Prestressed Pier Design

For cases where the overhang was quite long and the superstructure loading was located well onto the overhang, continuous post tensioning through the overhang, joint, and pier was used (shown in Figure 2.4). The pier longitudinal reinforcement ratio was maintained at 1 percent of the gross concrete area of the pier. Flexural stresses in these piers were limited to the service load tensile stress limit of $3\sqrt{f'_c}$. Due to loss of prestress through the joint region, an additional series of tendons were placed in from the top of the joint and through the pier (shown in Figure 2.4) to provide additional prestressing. As a result, the design strength for the piers was significantly greater than required for design loads.

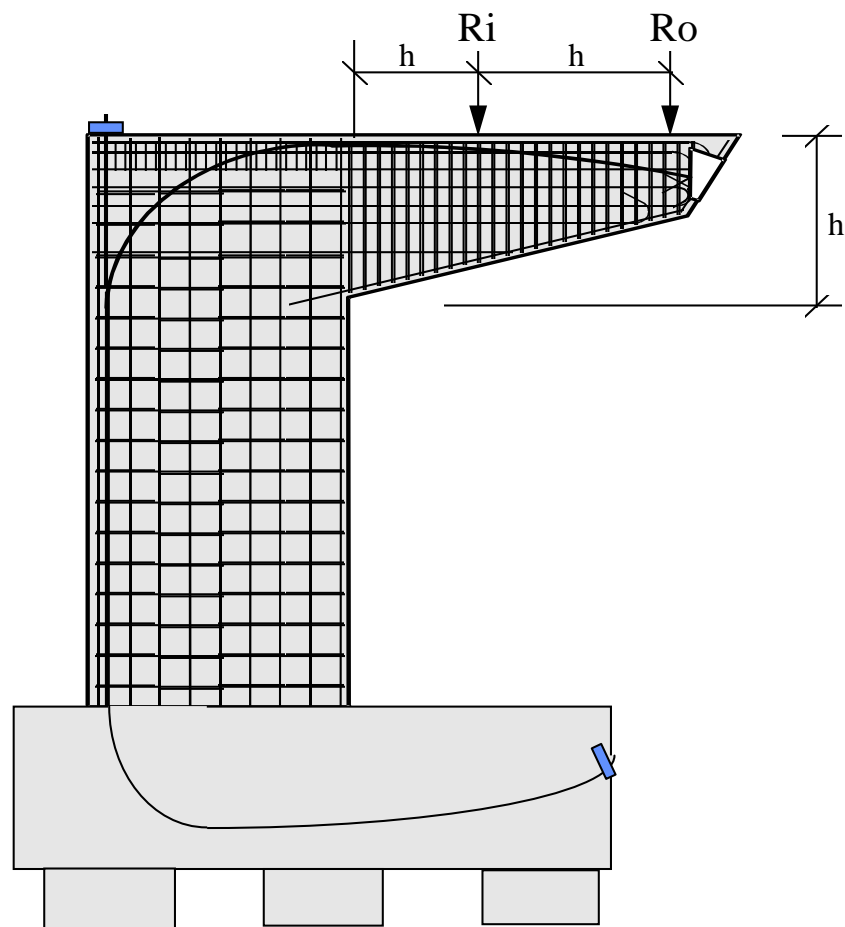


Figure 2.4 Fully Prestressed Substructure with Continuous Post Tensioning

2.3.2.3 Fully Prestressed Joint Design

As in the case of the reinforced concrete joint, overhang and pier longitudinal reinforcement was continued into the joint region and anchored using straight bar development. The continuous post-tensioning through the joint region (shown in Figure 2.5) significantly reduced tensile stresses in the joint region under service loads. For cases where only horizontal post-tensioning was provided through the overhang and the joint (shown in Figure 2.6), the longitudinal bars were terminated in the joint corner.

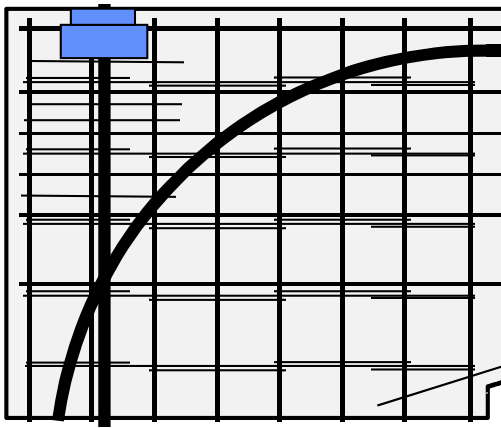


Figure 2.5 Schematic of Joint Region for Continuous Post Tensioning Detail

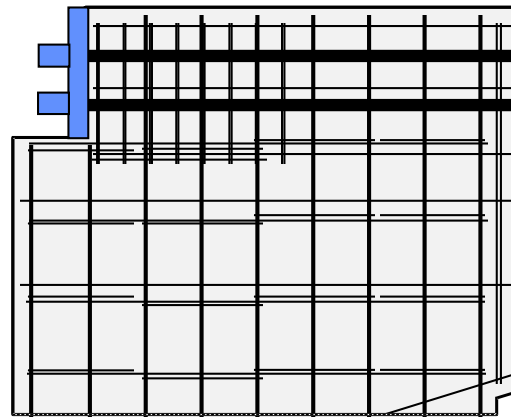


Figure 2.6 Schematic of Joint Region For Post-Tensioned Overhang Detail

2.4 Development of an Integrated Design Method

Development of an integrated design method involved providing a design procedure that would account for any design contingency, be sufficiently clear for easy use by designers, and provide some guidance for use. Design of any structure must involve consideration of strength and serviceability. The newly adopted AASHTO LRFD Bridge Specifications [7] is a specification that has collected the best information on design of structural concrete (reinforced concrete design through to fully prestressed designs) and incorporated it into Section 5 of the specifications. However, the “integrated design method” discussed here refers to the procedure used in this experimental program, and not the AASHTO LRFD Bridge Specifications. There are numerous parallels between the design procedures, and knowledge gained from this study is presented in Chapter 6 in the form of amendments to the AASHTO LRFD Specifications.

The integrated design method allows for use of deformed mild steel and high tensile strength prestressing steel for tension reinforcement. Members are allowed to crack under service loads, but the designer must control crack widths, limit fatigue of the strand and mild reinforcement, and consider factors affecting long-term durability. Design will not be compartmentalized into categories such as shear design, flexural design, etc. but rather the flow of forces through members will be investigated and details provided to yield optimal performance of the structure. Good detailing practices are required and minimum reinforcement limits established to provide sufficient ductility.

2.4.1 Overview of Related Research

An overview of the previous research is presented to illustrate the tools that have been proposed and incorporated into the integrated design procedure used to develop the experimental models.

2.4.1.1 Strut and Tie Modeling

Development of strut-and-tie models for the cantilever bent specimens was greatly assisted by the PCI paper by Schlaich et al. [8]. The behavior and proposed flow of forces for many of the design examples provided insight into the development of the overall flow of forces. The strut-and-tie model for the design of anchorage zones in the prestressed specimens was developed using NCHRP Report No. 356 [9].

2.4.1.2 Partial Prestressing

The history of partial prestressing is discussed in detail in a thesis by Billington [5]. The concept of partial prestressing has been applied in many ways, ranging from allowing extreme concrete tensile fibers to experience minimal tensile stresses (less than cracking) at service loads, to permitting concrete cracking at service loads. Many concepts of partial prestressing generally have been opposed due to concerns about fatigue in the prestressing steel, long-term corrosion durability, and concern about any possibility of large unsightly cracks in members. The use of the following tools to address these concerns should provide some confidence that the issues can be addressed and controlled using good design and detailing practices.

2.4.1.3 Deep Beam

Concerns about concrete deep beam design have historically been related to the fact that plane sections do not remain plane. The majority of deep beam designs are compounded by a lack of understanding about detailing the beam for good serviceability. Although sections might not remain plane in deep beams, the design of the primary longitudinal reinforcement can be achieved by utilizing a strut-and-tie model to compute the area of tension reinforcement required to resist factored loads. Frantz and Breen [10] developed an equation for the design of side-face cracking reinforcement, which was shown to control large cracks near mid-depth of deep members.

2.4.1.4 Limits on Column Longitudinal Reinforcement

The lower limit on column longitudinal reinforcement was developed at the University of Illinois at Urbana-Champaign and Lehigh University during the 1930's and 1940's [11]. The limit was established to preclude creep failure that can occur in concrete columns under sustained compression loads. The researchers conducted over 100 long-term column tests under a range of loads. The 1 percent minimum column reinforcement provision was established to prevent the onset of yielding of 276 MPa (40 ksi) mild longitudinal reinforcement under maximum expected sustained loads. The “load shedding” of the concrete to lesser quantities of mild reinforcement subjected to long-term loading could cause yielding of the column reinforcement, which would result in reduced column strengths.

Research that is currently underway at The University of Texas at Austin is investigating minimum column reinforcement for Grade 60 longitudinal reinforcement [12]. Because preliminary results of the column study were not available at the time specimens were designed and fabricated for this study, a minimum column reinforcement ratio of 0.7 percent was used.

2.4.1.5 Design of Headed Reinforcement

The development and use of headed mild reinforcement (see Figure 2.7) provides for anchorage of reinforcement over very short development lengths (even for large-diameter bars). Headed reinforcement also provides a clearly defined node that can be used when designing strut-and-tie models. The development of nodes is important for redirecting the flow of forces into a more desirable path.

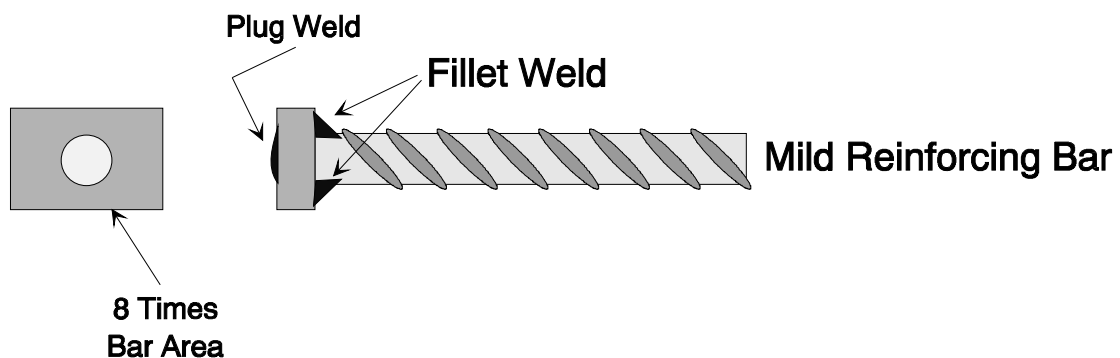


Figure 2.7 Headed Bar Schematic

The minimum area of the head on headed reinforcement has been studied as part of a research program at the University of Texas at Austin [13]. Previous research on headed reinforcement [14] indicated that the area of the welded plate (the head) on the end of the reinforcement should be 6 to 10 times the area of the bar. The use of a smaller plate may allow closer bar spacing and reduced concrete cover requirements for headed bars. Headed bars in this study utilized plate areas equal to 8 times the bar area.

2.4.1.6 Crack-Width Prediction

Many crack-width prediction models have been proposed for control of cracks in the design of structures in North America [15,16,17]. The Building Code Requirements for Reinforced Concrete (ACI 318-93) Eq. (10-4) [18] is generally accepted as the standard for providing a distribution of reinforcement that will control crack widths. However, an all-encompassing, scaleable formula has been sought that considers the effects of prestressing bars and strands, and mild reinforcement in the computation of maximum crack width. Many of the design formulas are discussed in a report by Yip [17].

The crack width equation that was used in this study was similar to the Proposed AASHTO Load and Resistance Factor Design (LRFD) Specifications [19], and was developed to predict the cracking behavior of the overhang specimens studied by Armstrong [3] and Salas [4]. The crack-width formula utilized the steel stress at the tensile reinforcement centroid, the number of mild reinforcing bars, and number of bonded prestressing bars/strands in the tension zone. Crack widths predicted from the equation were in good agreement with the maximum crack widths measured in previous experiments [3,4,5]. Details of the crack-width formula will be discussed in Section 3.4.1.2.

2.4.1.7 Durability and Maximum Allowable Crack Widths

Concern about durability and maximum allowable crack width has existed since the early development of reinforced concrete design. The concern with large crack widths is that chlorides can penetrate into the cracks and initiate corrosion of the reinforcement. Once a corrosion cell is established, the reinforcement oxidizes and loses cross-sectional area. The long-term effects are loss of strength and potential premature failure of a member. Corrosion

of high strength reinforcement is of greatest concern due to the reduced corrosion resistance of small-diameter wire strands. The loss of even a small portion of the prestress can significantly degrade the service load performance and cause premature failure.

Low-permeability, high-alkaline concrete, epoxy-coated bars and strands, galvanized bars and strands, and cathodic protection have all been used to provide durable concrete structures. The long-term behavior of cracked partially-prestressed concrete is being investigated by West [20] to establish guidelines for the development of durable concrete structures. The range of different maximum crack width limits from around the world [21] attests to the lack of a rational limit. If a maximum crack width is identified in West's study or in a subsequent study, it will be possible to use the crack width equation to limit crack widths in members to less than the maximum width.

2.4.1.8 Scaling Model Crack Widths and Behavior

The scaled behavior of crack widths was a concern when test specimens were initially designed. The size of the full-scale prototype necessitated scaling of the specimens to be able to economically construct and test the specimens in the laboratory. The similitude of cracking and deformation behavior for model specimens with a scale factor of 1 (full-scale), 2.5 (2/5th scale), and 4 (1/4 scale) performed by Borges and Lima [22] presented convincing evidence of crack-width similitude. The text on modeling concrete structures by Mirza [23] concluded that crack-width similitude is present for models as small as 1/10th scale.

In order to extrapolate prototype behavior from the scale models, it is important to use mild reinforcement with the same nominal yield as the full-scale prototype, and use scaled aggregate sizes, loads, bar spacing, and concrete cover requirements.

2.4.1.9 Fatigue Stress Limits

Previous research on partial prestressing performed by Abeles [24,25] identified some concerns associated with cracking in prestressed concrete, specifically fatigue of bonded mild and prestressed reinforcement. Based on the research by Wollman [26], the stress range in prestressing tendons should be kept below 100 MPa (14.5 ksi).

2.4.2 Synopsis of Recommendations

A synopsis of the design recommendations from the previous work on the overhang specimens by Armstrong [3] and Salas [4] is presented below.

2.4.2.1 Development of a Strut-and-Tie Model

The strut-and-tie model aids in visualizing the force path through a member from the point of load application, through the specimen, and to the structural supports. The compressive forces indicate where the concrete will direct the forces, and the tension tie forces indicate where steel should be located. By establishing a determinate geometry of compression struts and tension ties, the tension tie forces and compressive stresses can be computed. The overall model is used to design the major regions of the members, but local details such as anchorage zone bursting forces, can also be analyzed and designed. If there is any doubt as to how the forces flow through the member, a finite element model can be developed and executed to analyze the flow of stresses and forces.

2.4.2.2 Development of FEM for Cantilever Bents

Elastic analysis of the reinforced concrete sections provides the principal tensile resultants and compressive resultants which can be used to construct the strut-and-tie model. A plane stress 2D element model with concrete material properties was used throughout the research project to identify the flow of tensile stresses through the section. Once the flow of stresses was identified a strut-and-tie model was fit to the envisioned stress flow to evaluate the force levels and material requirements.

The finite element models (FEM) for the prestressed specimens used external forces to apply the post-tensioning forces and check the tensile stresses at dead load and service loads. It was simple to evaluate the crack-initiation load with the FEM.

2.4.2.3 Tensile Reinforcement Requirements

The amount and approximate location of tensile reinforcement was determined using the STM. Cover requirements and the number of layers of steel often controlled the actual

locations of tensile reinforcement. Once the flow of forces was established, details for the different sections were checked using a linear strain compatibility model.

Design of Longitudinal Reinforcement:

Factored load capacity, crack widths, and tension steel fatigue stress ranges were checked using a strain compatibility design model that assumed a linear variation of strain over the depth of the section. The linear variation of strain over the depth of the section was assumed since the side-face reinforcement was considered to help control non-linear deformation of the deep beam. Only minimum compressive reinforcement was provided to reduce the effects of creep and shrinkage.

Design of Transverse Reinforcement:

Transverse reinforcement was only considered for areas where tension tie forces from the STM were indicated. The amount of tensile reinforcement was reduced by considering the concrete provided a tension force equivalent of $1\sqrt{f'_c} b_w d$. Minimum shear reinforcement was used for the remainder of the overhang.

Design of Anchorage Reinforcement:

The anchorage zone design utilized the design recommendations from NCHRP Report No. 356. This was essentially a STM approach for the design of the anchorage bursting and confinement reinforcing steel.

2.1 Introduction.....	5
2.2 Description of Cantilever Bents in San Antonio	5
2.3 Evaluation of Current Design Practice	6
2.3.1 AASHTO Reinforced Concrete Design.....	7
2.3.2 AASHTO Prestressed Concrete Design	9
2.4 Development of an Integrated Design Method.....	13
2.4.1 Overview of Related Research	13
2.4.2 Synopsis of Recommendations	18
Figure 2.1 Schematic of Cantilever Bents in San Antonio	6
Figure 2.2 Reinforced Concrete Design	8
Figure 2.3 Fully Prestressed Overhang Design with Reinforced Concrete Pier.....	10
Figure 2.4 Fully Prestressed Substructure with Continuous Post Tensioning.....	11
Figure 2.5 Schematic of Joint Region for Continuous Post Tensioning Detail.....	12
Figure 2.6 Schematic of Joint Region For Post-Tensioned Overhang Detail.....	12
Figure 2.7 Headed Bar Schematic	15

CHAPTER 2

BACKGROUND

2.1 Introduction

Investigation of the San Antonio bridge substructures was initiated when a preliminary review of the designs revealed substantial congestion in the pier, overhang, and joint regions. Designers admitted that they were baffled by the fragmented provisions for design of reinforced concrete and prestressed concrete contained in the 1983 AASHTO Standard Specifications for Highway Bridges [1] as well as the multiple sections that seemed to simultaneously apply to their particular design case. It was clear that a unified design method, in the form of a specification, would simplify the design process, provide economy, and instill confidence in the users of the design specification.

2.2 Description of Cantilever Bents in San Antonio

The cantilever bents in San Antonio were constructed to support a newly constructed elevated roadway for I-10 and I-35 over the existing ground-level lanes and entrance ramps. The superstructure was a prestressed concrete winged box girder. Loads from the superstructure were transmitted to the substructure through two bearings located beneath the winged box girder. Because the substructure was a cantilevered bent, self weight of the superstructure induced very large dead load reactions and moments on the substructure. Approximately four-fifths of the design service load moment was attributed to the superstructure dead load component. A schematic of the cantilever bent is presented in Figure 2.1.

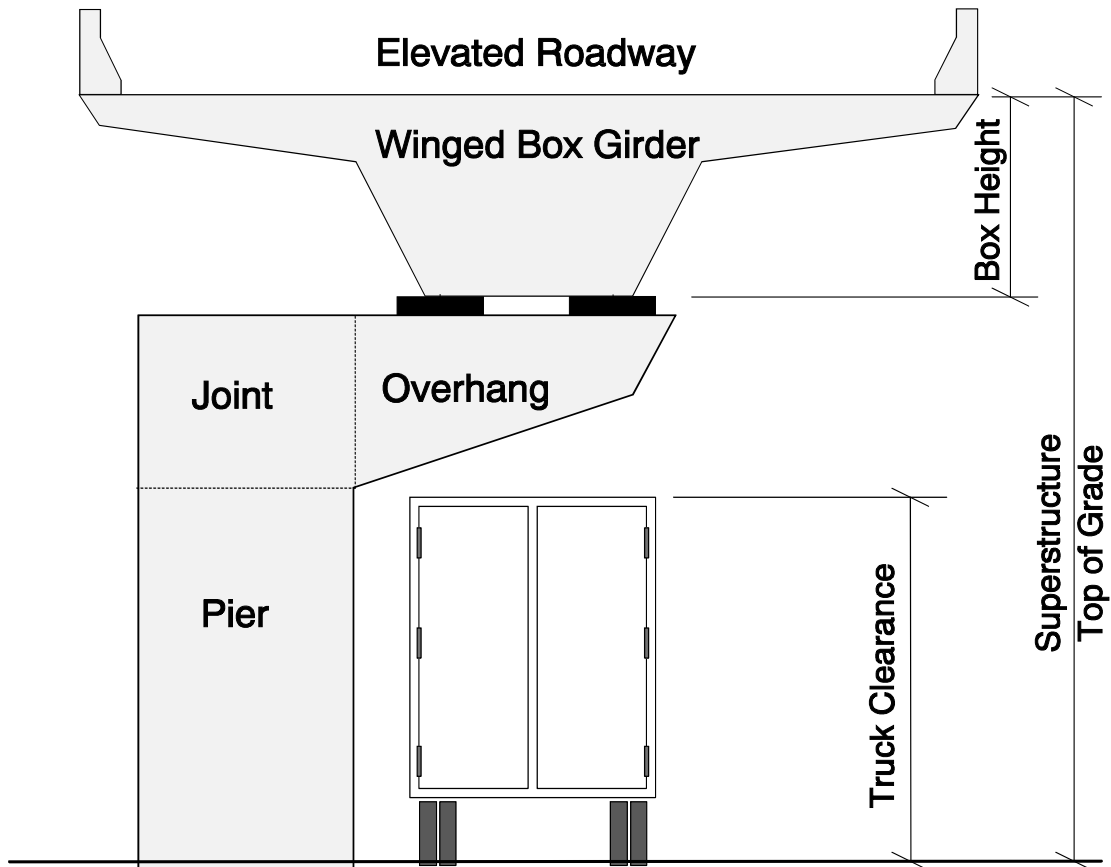


Figure 2.1 Schematic of Cantilever Bents in San Antonio

2.3 Evaluation of Current Design Practice

The 1983 AASHTO Standard Specifications for Highway Bridges [1] was the code standard used for the design of the cantilever bents in the San Antonio and prototype bents tested in the experimental program. An evaluation of strengths and weaknesses of the standard design practice is important in the development of an integrated design method. A more complete explanation of the mechanics and equations in the bridge design specifications is described in Chapter 3. The convention used to describe the different regions of the bent (pier, overhang, and joint regions) is presented in Figure 2.1.

2.3.1 AASHTO Reinforced Concrete Design

The AASHTO Reinforced Concrete Design Specifications are located in Section 8 of the AASHTO Standard Specifications for Highway Bridges. A general overview of the specifications is offered to provide evidence of the confusion inherent in the design requirements for cantilever beams. Because of the confusion, designers of the cantilever bents in San Antonio applied all sections of the specification addressing flexural design, corbel design, deep beam design, shear design, and serviceability requirements to the design of the reinforced concrete cantilever substructures. It was originally thought that their design philosophy was overly conservative, but it is now known that this was not the case.

2.3.1.1 Reinforced Concrete Overhang Design

The flexural design equations were used to determine the amount of flexural steel required to resist factored overhang moments. If the amount of overhang reinforcement exceeded the number of bars that could be placed in two rows of tension reinforcement, a fully-prestressed design was conducted.

In many designs, location of the interior load on the overhang was within the specified shear span-to-depth ratio (a/d) of less than one for corbel design. In Figure 2.2, the interior load is located a distance equal to one half the depth of the beam ($0.5 h$) and the outer load is located one and one-half times the depth of the beam ($1.5 h$) from the column face. Designers provided shear friction reinforcement near mid-depth of the overhang to resist corbel loads associated with the inner reaction. Primary longitudinal reinforcement in the overhang was provided to resist the large moments induced by the outer reaction. Quantity of shear friction reinforcement provided was equal to half of the primary longitudinal reinforcement, but was not considered to contribute to the flexural strength of the section.

The quantity of transverse reinforcement required along the overhang was somewhat ambiguous due to the tapered depth of the overhang. Because the concrete component of the shear strength equation is a function of the depth of the section, a 45° failure plane propagating from the outer reaction was assumed, and the transverse reinforcement necessary to intersect the diagonal crack and resist the outer reaction was computed. As will be

discussed in Chapter 3, geometry of the overhang permitted a force path, by which a portion of the outer reaction flowed directly into the pier. However, the shear design provisions in the Standard Specifications do not consider such force paths. In addition, the shear associated with the inner reaction was addressed through corbel design. As a result, spacing of the transverse reinforcement computed for the outer reaction was used for the entire overhang.

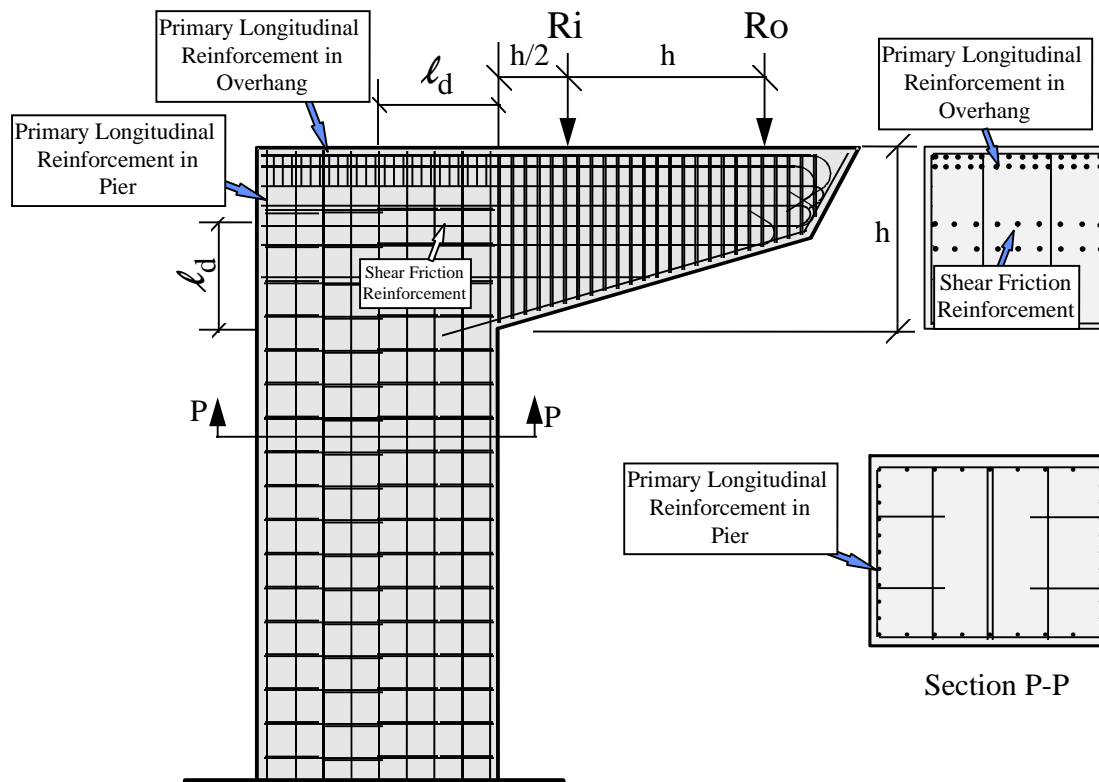


Figure 2.2 Reinforced Concrete Design

Fatigue stress limits in the reinforcement, and distribution of longitudinal reinforcement to control cracking were the serviceability requirements checked for the overhang.

2.3.1.2 Reinforced Concrete Pier Design

The pier design involved the determination of minimum member size and minimum number of longitudinal reinforcing bars to resist axial forces and overturning moments. The pier designs were nearly all controlled by the AASHTO minimum longitudinal reinforcement

ratio requirement of 1 percent ($0.01 A_g$). Serviceability requirements such as fatigue stress limits and limits on cracking for the pier region were not considered by the designers. AASHTO Standard Specifications state in Article 8.16.8.1 that serviceability requirements are applied to “flexural members”. Designers did not consider this to apply because the piers were designed according to Article 8.16.4 titled “Compression Members”, not Article 8.16.3 titled “Flexure”.

2.3.1.3 Reinforced Concrete Joint Design

The joint region for the cantilever substructure was constructed by continuing the longitudinal pier and overhang reinforcement into the joint. Column ties were placed up to the top row of overhang longitudinal reinforcement. Size of the joint was assumed to be sufficient to fully develop the longitudinal reinforcement from the critical sections of the overhang and pier regions into the joint (See Figure 2.2). Joint capacity was not evaluated because it was assumed to be a rigid mass of concrete, not liable to fail under design loads.

2.3.2 AASHTO Prestressed Concrete Design

The Prestressed Concrete Design Specifications are located in Section 9 of the AASHTO Standard Specifications for Highway Bridges. Because the reinforced and prestressed concrete specifications are located in separate sections, there is a distinct split in the design procedures. The prestressed design specifications assume that members are uncracked at service loads. This type of design will be referred to as “fully prestressed” in future discussion. The fully-prestressed design was performed for cantilever bents in San Antonio when it was not possible to fit a sufficient number of mild reinforcing bars into the member to resist factored loads.

In addition to the problem of separate specifications for reinforced concrete and prestressed concrete, the design process is further muddled because many sections of the prestressed specifications make reference to the reinforced concrete specifications. Shear friction design, corbel design, and design of deep beam reinforcement are not addressed in Section 9 of the AASHTO Specifications. For the cantilever substructures in the San Antonio Y Project, the location of the loads and magnitude of the shear forces on the

overhang made these design aspects quite critical for both the reinforced and prestressed concrete designs.

2.3.2.1 Fully Prestressed Overhang Design

The fully prestressed overhang design (Figure 2.3) was based on limiting concrete tensile stresses due to flexure of $3\sqrt{f'_c}$ at service load, and included all the design provisions assumed to be relevant, such as shear friction design, corbel design, and the design of deep beam reinforcement from the AASHTO reinforced concrete design specifications in Section 8. Figure 2.3 shows the fully prestressed overhang design with reinforced concrete pier.

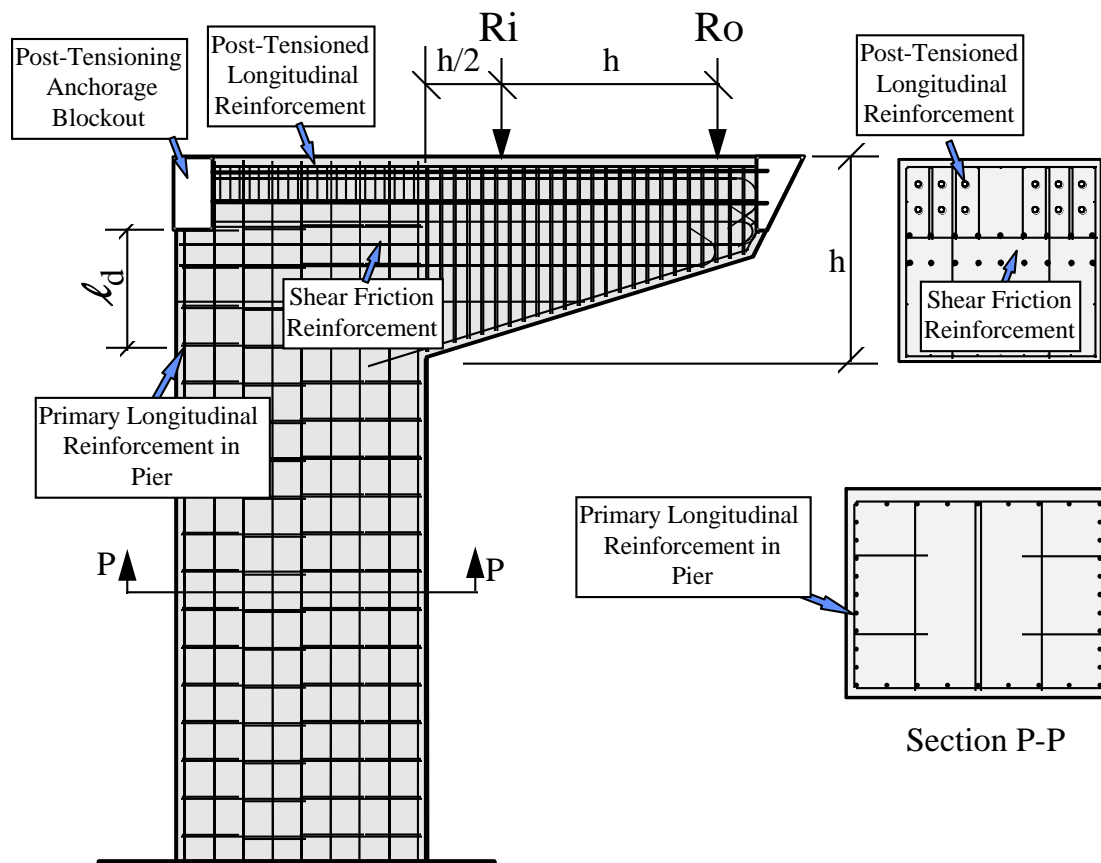


Figure 2.3 Fully Prestressed Overhang Design with Reinforced Concrete Pier

2.3.2.2 Fully Prestressed Pier Design

For cases where the overhang was quite long and the superstructure loading was located well onto the overhang, continuous post tensioning through the overhang, joint, and pier was used (shown in Figure 2.4). The pier longitudinal reinforcement ratio was maintained at 1 percent of the gross concrete area of the pier. Flexural stresses in these piers were limited to the service load tensile stress limit of $3\sqrt{f'_c}$. Due to loss of prestress through the joint region, an additional series of tendons were placed in from the top of the joint and through the pier (shown in Figure 2.4) to provide additional prestressing. As a result, the design strength of the piers was significantly greater than required for design loads.

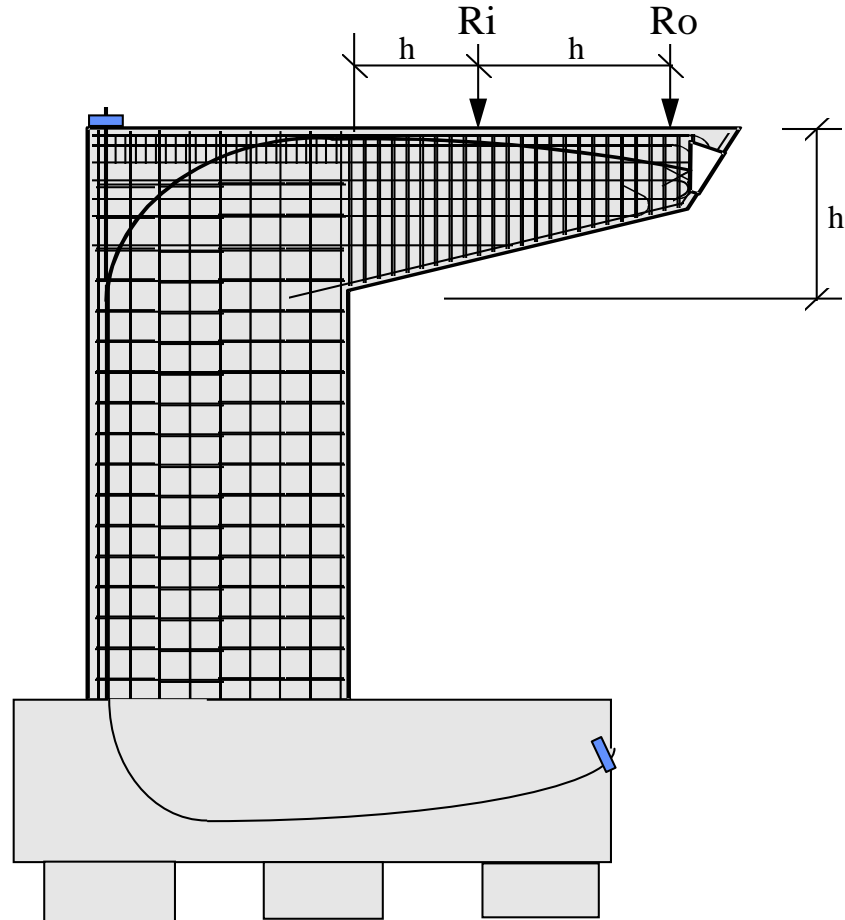


Figure 2.4 Fully Prestressed Substructure with Continuous Post Tensioning

2.3.2.3 Fully Prestressed Joint Design

As in the case of the reinforced concrete joint, overhang and pier longitudinal reinforcement was continued into the joint region and anchored using straight bar development. The continuous post-tensioning through the joint region (shown in Figure 2.5) significantly reduced tensile stresses in the joint region under service loads. For cases where only horizontal post-tensioning was provided through the overhang and the joint (shown in Figure 2.6), the longitudinal bars were terminated in the joint corner.

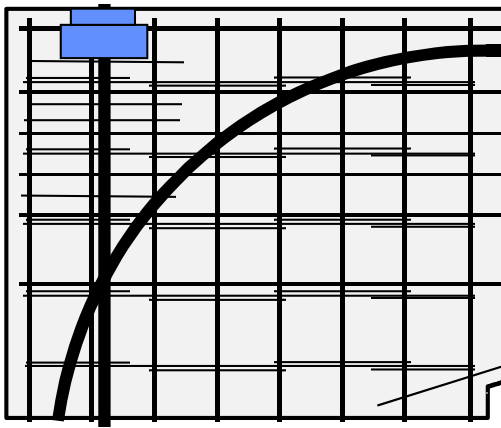


Figure 2.5 Schematic of Joint Region for Continuous Post-Tensioning Detail

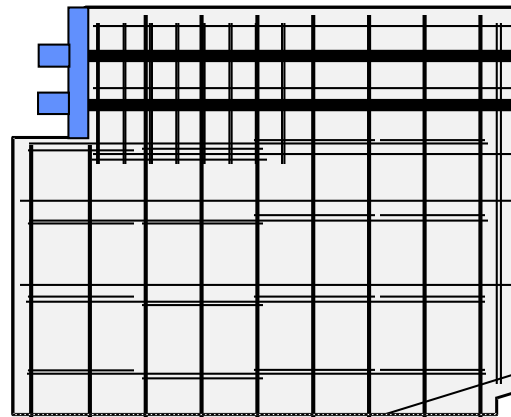


Figure 2.6 Schematic of Joint Region For Post-Tensioned Overhang Detail

2.4 Development of an Integrated Design Method

Development of an integrated design method involved providing a design procedure that would account for any design contingency, be sufficiently clear for easy use by designers, and provide some guidance for use. Design of any structure must involve consideration of strength and serviceability. Section 5 of the recently adopted 1996 AASHTO Load and Resistance Factored Design (LRFD) Bridge Specifications [7] contains design methods for structural concrete (reinforced concrete through to fully-prestressed concrete designs). However, the “integrated design method” refers to the procedure used in this experimental program, and not the AASHTO LRFD Bridge Specifications. Knowledge gained from this study is presented in Chapter 6 in the form of an amendment to the AASHTO LRFD Specifications.

The integrated design method allows use of both deformed mild steel and high-strength prestressing steel for tension reinforcement. Members are allowed to crack under service loads, but the designer must control crack widths, limit fatigue of the strand and mild reinforcement, and consider factors affecting long-term durability. Design will not be compartmentalized into categories such as shear design, flexural design, etc. but rather the flow of forces through members will be investigated and details provided to yield optimal performance of the structure. Good detailing practices are required and minimum reinforcement limits established to provide sufficient ductility.

2.4.1 Overview of Related Research

An overview of the previous research is presented to illustrate the tools that have been proposed and incorporated into the integrated design procedure used to develop the experimental models tested as part of this study.

2.4.1.1 *Strut-and-Tie Modeling*

Development of strut-and-tie models for the cantilever bent specimens was greatly assisted by the PCI paper by Schlaich et al. [8]. The behavior and proposed flow of forces for

many of the design examples provided insight into the development of the overall flow of forces. The strut-and-tie model used in the design of anchorage zones in the prestressed specimens was developed using NCHRP Report No. 356 [9].

2.4.1.2 Partial Prestressing

The history of partial prestressing is discussed in detail in a thesis by Billington [5]. The concept of partial prestressing has been applied in many ways, ranging from allowing extreme concrete tensile fibers to experience minimal tensile stresses (less than cracking) at service loads, to permitting concrete cracking at service loads. Many concepts of partial prestressing generally have been opposed due to concerns about fatigue in the prestressing steel, long-term corrosion durability, and concern about any possibility of large unsightly cracks in members. The use of the following tools to address these concerns should provide some confidence that the issues can be addressed and controlled using good design and detailing practices.

2.4.1.3 Deep Beam

Concerns about concrete deep beam design have historically been related to the fact that plane sections do not remain plane. The majority of deep beam designs are compounded by a lack of understanding about detailing the beam for good serviceability. Although sections might not remain plane in deep beams, the design of the primary longitudinal reinforcement can be achieved by utilizing a strut-and-tie model to compute the area of tension reinforcement required to resist factored loads. Frantz and Breen [10] developed an equation for the design of side-face cracking reinforcement, which was shown to control large cracks near mid-depth of deep members.

2.4.1.4 Limits on Column Longitudinal Reinforcement

The lower limit on column longitudinal reinforcement was developed at The University of Illinois at Urbana-Champaign and Lehigh University during the 1930's and 1940's [11]. The limit was established to preclude creep failure that can occur in concrete columns under sustained compression loads. The researchers conducted over 100 long-term column tests under a range of loads. The 1 percent minimum column reinforcement

provision was established to prevent the onset of yielding of 276 MPa (40 ksi) mild longitudinal reinforcement under maximum expected sustained loads. The “load shedding” of the concrete to lesser quantities of mild reinforcement subjected to long-term loading could cause yielding of the column reinforcement.

Research that is currently underway at The University of Texas at Austin is investigating minimum column reinforcement for Grade 60 longitudinal reinforcement [12]. Because preliminary results of the column study were not available at the time specimens were designed and fabricated for this study, a lower limit of 0.7 percent for the column reinforcement was used.

2.4.1.5 Design of Headed Reinforcement

The development and use of headed mild reinforcement (see Figure 2.7) provides for anchorage of reinforcement over very short embedment lengths (even for large-diameter bars). Headed reinforcement also provides a clearly defined node that can be used when designing strut-and-tie models. The development of nodes is important for redirecting the flow of forces into the desired path.

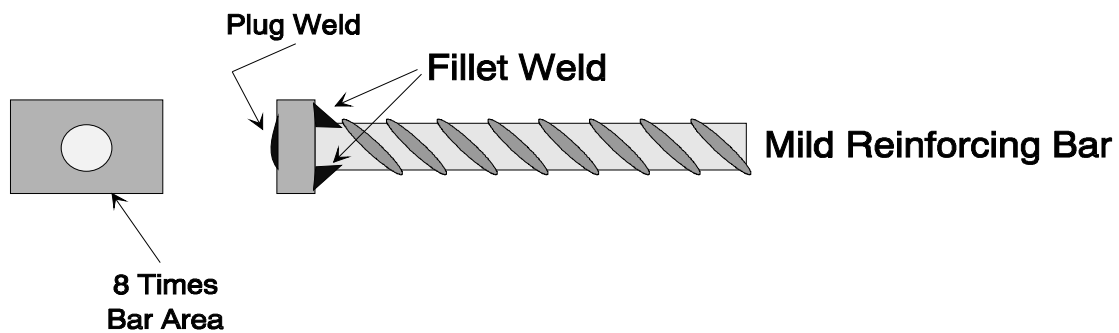


Figure 2.7 Headed Bar Schematic

The minimum area of the head on headed reinforcement has been studied as part of a research program at The University of Texas at Austin [13]. Previous research on headed reinforcement [14] indicated that the area of the welded plate (the head) on the end of the reinforcement should be 6 to 10 times the area of the bar. The use of a smaller plate may allow closer bar spacing and reduced concrete cover requirements for headed bars. Headed bars used in this study utilized plate areas equal to 8 times the bar area.

2.4.1.6 Crack-Width Prediction

Many crack-width prediction models have been proposed for control of cracks in the design of structures in North America [15,16,17]. The Building Code Requirements for Reinforced Concrete (ACI 318-93) Eq. (10-4) [18] are generally accepted as the standard for providing a distribution of reinforcement that will control crack widths. However, an all-encompassing, scaleable formula has been sought that considers the effects of prestressing bars and strands, and mild reinforcement in the computation of maximum crack width. Many of the design formulas are discussed in a report by Yip [17].

The crack-width equation that was used in this study was similar to the AASHTO LRFD Bridge Specifications [7], and was developed to predict the cracking behavior of the overhang specimens studied by Armstrong [3] and Salas [4]. The crack-width formula utilized the steel stress at the tensile reinforcement centroid, the number of mild reinforcing bars, and number of bonded prestressing bars/strands in the tension zone. Crack widths predicted from the equation were in good agreement with the maximum crack widths measured in previous experiments [3,4,5]. Details of the crack-width formula will be discussed in Section 3.4.1.2.

2.4.1.7 Durability and Maximum Allowable Crack Widths

Concern about durability and maximum allowable crack width has existed since the early development of reinforced concrete design. The concern with large crack widths is that chlorides can penetrate into the cracks and initiate corrosion of the reinforcement. Once a corrosion cell is established, the reinforcement oxidizes and loses cross-sectional area. The long-term effects are loss of strength and potential premature failure of a member. Corrosion of high-strength reinforcement is of greatest concern due to the reduced corrosion resistance of small-diameter wire strands. The loss of even a small portion of the prestress can significantly degrade the service load performance and cause premature failure.

Low-permeability, high-alkaline concrete, epoxy-coated bars and strands, galvanized bars and strands, and cathodic protection have all been used to provide durable concrete structures. The long-term behavior of cracked partially-prestressed concrete is being investigated by West [19] to establish guidelines for the development of durable concrete

structures. The range of different maximum crack-width limits from around the world [20] attests to the lack of a rational limit. If a maximum crack width is identified in West's study or in a subsequent study, it will be possible to use the crack-width equation to limit crack widths in members to less than the maximum width.

2.4.1.8 Scaling Model Crack Widths and Behavior

The scaled behavior of crack widths was a concern when test specimens were initially designed. The size of the full-scale prototype necessitated scaling of the test specimens to be able to economically construct and test the specimens in the laboratory. The similitude of cracking and deformation behavior for model specimens with a scale factor of 1 (full-scale), 2.5 (2/5th scale), and 4 (1/4 scale) performed by Borges and Lima [21] presented convincing evidence of crack-width similitude. The text on modeling concrete structures by Sabnis, et al [22] concluded that crack-width similitude is present for models as small as 1/10th scale.

In order to extrapolate full-scale behavior from the scale models, it was important to use mild reinforcement with the same nominal yield as used in the full-scale bents, and use scaled aggregate sizes, loads, bar spacing, and concrete cover requirements.

2.4.1.9 Fatigue Stress Limits

Previous research on partial prestressing performed by Abeles [23,24] identified some concerns associated with cracking in prestressed concrete; specifically, fatigue of bonded mild and prestressed reinforcement. Based on the research by Wollman [25], the stress range in prestressing tendons should be kept below 100 MPa (14.5 ksi).

2.4.2 Synopsis of Previous Recommendations Used in This Study

A synopsis of the design recommendations, from the previous work on the overhang specimens by Armstrong [3] and Salas [4] is presented below.

2.4.2.1 Development of a Strut-and-Tie Model

The strut-and-tie model (STM) aids in visualizing the force path through a member from the point of load application, through the specimen, and to the structural supports. The compressive forces indicate where the concrete will direct the forces, and the tension tie forces indicate where steel should be located. By establishing a determinate geometry of compression struts and tension ties, the tension tie forces and compressive stresses can be computed. The overall model is used to design the major regions of the members, but local details such as anchorage zone bursting forces, can also be analyzed and designed. If there is any doubt as to how the forces flow through the member, a finite element model can be developed and executed to analyze the flow of stresses and forces.

2.4.2.2 Development of FEM for Cantilever Bents

Elastic analysis of the reinforced concrete sections provides the principal tensile resultants and compressive resultants which can be used to construct the strut-and-tie model. A plane stress 2D element model with concrete material properties was used throughout the research project to identify the flow of tensile stresses through the section. Once the flow of stresses was identified, a strut-and-tie model was fit to the envisioned stress flow to evaluate the force levels and material requirements.

The finite element models (FEM) for the prestressed specimens used external forces to apply the post-tensioning forces. It was simple to check tensile stresses at dead and service loads and to evaluate the crack-initiation load with the FEM.

2.4.2.3 Tensile Reinforcement Requirements

The amount and approximate location of tensile reinforcement was determined using the STM. Cover requirements and the number of layers of steel often controlled the actual locations of tensile reinforcement. Once the flow of forces was established, details for the different sections were checked using a cracked section analysis assuming a linear strain profile.

Design of Longitudinal Reinforcement:

Factored load capacity, crack widths, and tension steel fatigue stress ranges were checked using a strain compatibility design model that assumed a linear variation of strain over the depth of the section. A linear variation of strain was assumed because the side-face reinforcement was considered to help control non-linear deformation of the deep beam. Only minimum compressive reinforcement was provided to reduce the effects of creep and shrinkage.

Design of Transverse Reinforcement:

Transverse reinforcement was considered only for areas where tension tie forces from the STM were indicated. The amount of tensile reinforcement was reduced by considering a concrete contribution equal to $1\sqrt{f'_c} b_w d$. Minimum shear reinforcement was used for the remainder of the overhang.

Design of Anchorage Reinforcement:

The anchorage zone design utilized the design recommendations from NCHRP Report No. 356 [9]. This was essentially a STM approach for the design of the anchorage bursting and confinement reinforcing steel.

2.1 Introduction.....	5
2.2 Description of Cantilever Bents in San Antonio	5
2.3 Evaluation of Current Design Practice	6
2.3.1 AASHTO Reinforced Concrete Design.....	7
2.3.1.1 Reinforced Concrete Overhang Design	7
2.3.1.2 Reinforced Concrete Pier Design	8
2.3.1.3 Reinforced Concrete Joint Design	9
2.3.2 AASHTO Prestressed Concrete Design	9
2.3.2.1 Fully Prestressed Overhang Design.....	10
2.3.2.2 Fully Prestressed Pier Design	11
2.3.2.3 Fully Prestressed Joint Design.....	12
2.4 Development of an Integrated Design Method.....	13
2.4.1 Overview of Related Research	13
2.4.1.1 Strut-and-Tie Modeling	13
2.4.1.2 Partial Prestressing.....	14
2.4.1.3 Deep Beam.....	14
2.4.1.4 Limits on Column Longitudinal Reinforcement.....	14
2.4.1.5 Design of Headed Reinforcement.....	15
2.4.1.6 Crack-Width Prediction	16
2.4.1.7 Durability and Maximum Allowable Crack Widths.....	16
2.4.1.8 Scaling Model Crack Widths and Behavior	17
2.4.1.9 Fatigue Stress Limits	17
2.4.2 Synopsis of Previous Recommendations Used in This Study	17
2.4.2.1 Development of a Strut-and-Tie Model.....	18
2.4.2.2 Development of FEM for Cantilever Bents	18
2.4.2.3 Tensile Reinforcement Requirements.....	18

Figure 2.1 Schematic of Cantilever Bents in San Antonio	6
Figure 2.2 Reinforced Concrete Design	8
Figure 2.3 Fully Prestressed Overhang Design with Reinforced Concrete Pier.....	10
Figure 2.4 Fully Prestressed Substructure with Continuous Post Tensioning.....	11
Figure 2.5 Schematic of Joint Region for Continuous Post-Tensioning Detail.....	12
Figure 2.6 Schematic of Joint Region For Post-Tensioned Overhang Detail.....	12
Figure 2.7 Headed Bar Schematic	15

CHAPTER 3

EXPERIMENTAL PROGRAM

3.1 Introduction

Tools for the integrated design method were developed during an earlier phase of the sponsored research study investigating partially-prestressed large substructure members. Armstrong [3] and Salas [4] tested eight-1/5.5 scale-models of overhang elements with geometry similar to the cantilevers used in the San Antonio ‘Y’ project. A portion of their study was intended to test the efficiency of a strut-and-tie model for the design of primary tensile reinforcement and transverse reinforcement. A series of four partially-prestressed specimens with 54 to 100 percent of the flexural capacity provided by prestressed reinforcement, and models of two prototype cantilever bents were tested. Service-load performance and ultimate strength were evaluated for each specimen. During this investigation, a strain-compatibility model and crack-width prediction model for partially-prestressed concrete members were developed and evaluated. The overhang study indicated the strut-and-tie model, crack prediction model, and strain compatibility model provided reasonable prediction of specimen behavior. The same tools and similar design methodology were used to design the test specimens for this study.

Specimens investigated in this testing program were intended to study not only the behavior of the overhang, but also the behavior of the connection between the overhang and column elements. The resulting cantilever bent specimen contains a pier (column), overhang (cantilever), and joint (connection region), and will henceforth be referred to as the Pier-Overhang-Joint (POJ) specimen (see Figure 3.1 for an example of this substructure system). The study involved the construction and testing of five specimens: two models of cantilever bents designed using the same process used for the San Antonio ‘Y’ full-scale bents (hereafter referred to as the ‘prototype models’) and three integrated design models. The two prototype models included a reinforced concrete model and a fully-prestressed overhang with a reinforced concrete pier (discussed in Chapter 2). The three integrated design models

included: a reinforced concrete design with headed reinforcement, a 54% prestressed design, and a 74% prestressed design, where the percentage indicated the percent of the flexural capacity provided by the prestressed reinforcement.

The Pier-Overhang-Joint experimental program was initiated to verify the experimental results from the overhang study as well as expand the use of the integrated design method to include the design of the joint and pier regions. Several studies that may impact the final recommendations of this study are currently underway at The University of Texas at Austin. Included in this group are: minimum longitudinal column reinforcement [12], maximum crack width for durability [19], and design recommendations for headed reinforcement [13]. Final recommendations from this study should be reviewed once these related studies are completed.

3.2 Development of the Pier-Overhang-Joint Specimen

3.2.1 Selection of Full-Scale Superstructure Loads

The San Antonio ‘Y’ substructures supported a variety of box girder superstructures that included: a 17.7 m (58 ft) wide main lane box girder, a 14.6 m (48 ft) wide transition girder, or a 7.9 m (26 ft) wide entrance-ramp girder (shown in Figure 3.1).

A review of the substructures supporting the 17.7 m (58 ft) wide main lane girder indicated that when both superstructure reactions were positioned on the overhang, a fully-prestressed design was always used. A reinforced concrete substructure design was not possible given the maximum depth and width of the overhang, and the number of mild reinforcing bars that were required to resist the factored moment. As a rule, if more than two rows of closely spaced No. 11 bars were required to resist factored loads in the overhang, a fully-prestressed design was implemented. A partially-prestressed design was a viable alternative for some cases, but because a reinforced concrete design was not possible, the 17.7 m (58 ft) wide superstructure was not modeled in this study.

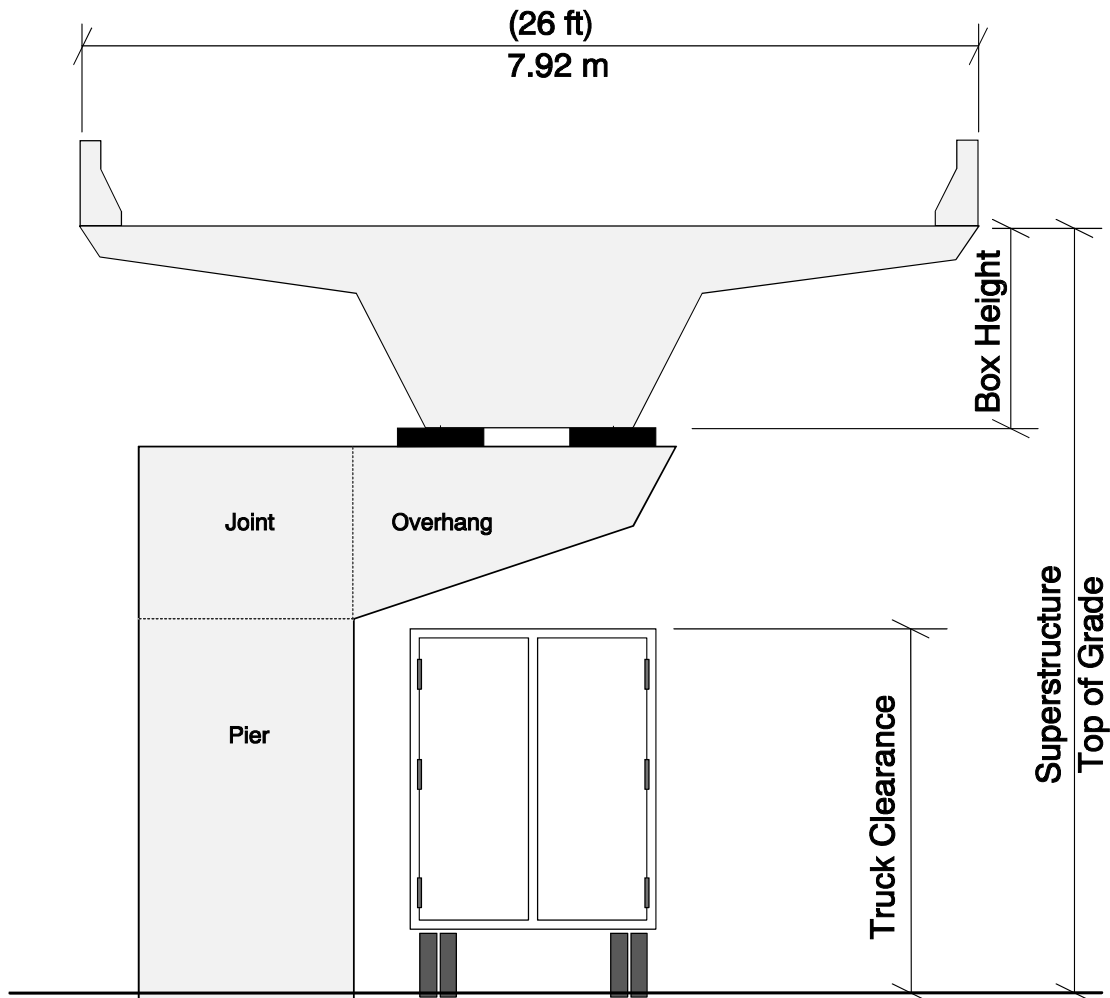


Figure 3.1 Substructure Schematic

A review of the substructures supporting the 7.9 m (26 ft) wide entrance-ramp girder indicated that both reinforced concrete and fully-prestressed concrete designs were possible designs. In most cases, if the two superstructure loads were positioned on the overhang, and truck clearance beneath the overhang was not a concern, designers used a reinforced concrete design. In areas where the maximum depth of the overhang was restricted, a fully-prestressed design was used. It was clear that only a small difference in the design flexural capacity of the members drove the design away from a reinforced concrete design to the more conservative fully-prestressed design. For these cases, a mixture of high-strength prestressing steel and mild reinforcing steel (partial prestressing) could be used to reduce steel congestion, provide supplemental tensile reinforcement to resist factored loads, and provide good

serviceability. Based on these factors, it was decided to model the bents supporting the 7.9 m (26 ft) wide box girder superstructure.

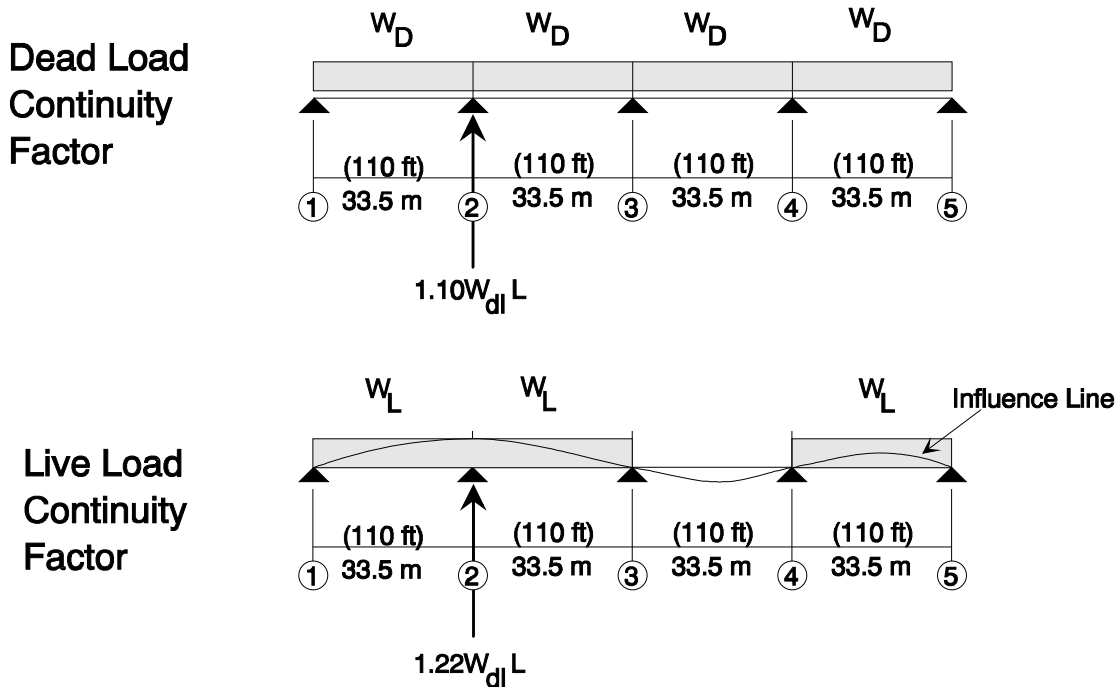


Figure 3.2 Pier Location and Continuity Factors

The design loads shown in Table 3.1 were computed for a four span continuous 7.9 m (26 ft) box girder superstructure with spans of 33.5 m (110 ft). The substructure under consideration in this study was the second pier. Because the superstructure was continuous, the support reactions based on a tributary span length were amplified by a 1.10 dead load continuity multiplier and a 1.22 live load continuity multiplier. The multipliers were computed for the lane loading on the bridge superstructure shown in Figure 3.2. Lane loads were applied on the box girder cross section as shown in Figure 3.3. Inside reactions (nearest the column), R_i , and outside reactions (nearest the overhang tip), R_o , for dead load (DL) and live load plus impact (LL) are listed in Figure 3.3. These reactions do not include the continuity multipliers, and were computed using the typical span length of 33.5 m (110 ft). The reactions including continuity multipliers, are listed in Table 3.1 for five load cases.

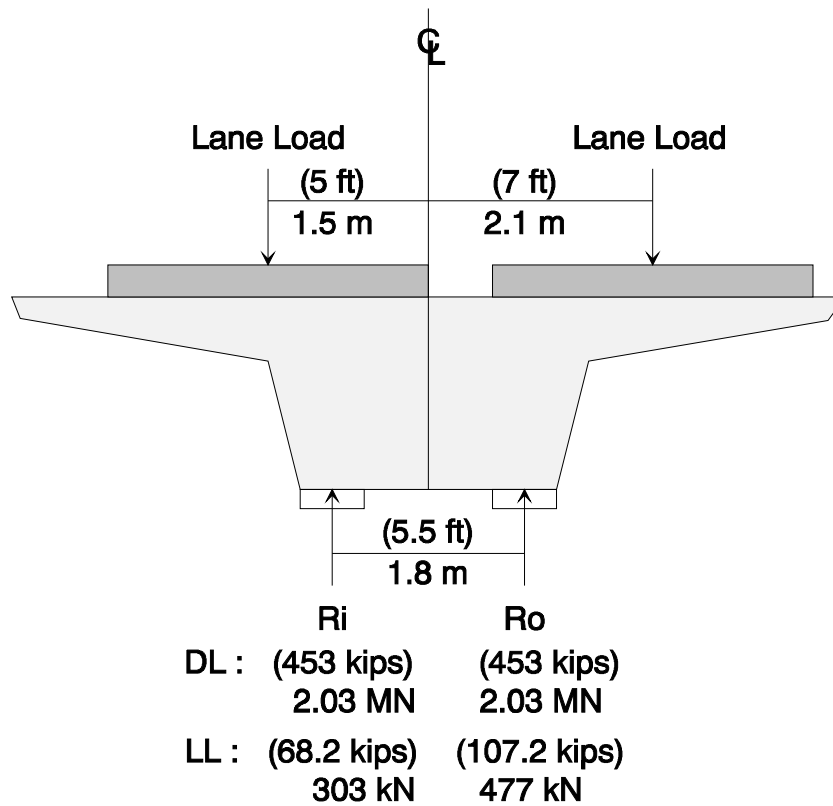


Figure 3.3 Full-Scale Prototype Loads Without Continuity Factors

Table 3.1 Full-Scale Substructure Loads for a 7.9 m (26 ft) Wide Girder

Load Description	Load Abbreviation	Ri		Ro	
		kN	(kips)	kN	(kips)
Dead Load	DL	2217	498.3	2217	498.3
Dead Load + 1/2 Live Load	(DL + 1/2 LL)	2362	531.1	2616	588.1
Service Load	(DL+LL)	2589	582.0	3015	677.8
Dead Load + 2 Live Load	(DL+2LL)	2961	665.7	3813	857.3
Factored Load	(1.3DL + 2.17LL)	3690	829.5	4614	1037.2
Factored Load / Φ	(1.3DL + 2.17LL)/ Φ	4100	921.7	5126	1152.4

3.2.2 Full-Scale Prototype Substructure Details

3.2.2.1 Reinforced Concrete Prototype Substructure - I4-C

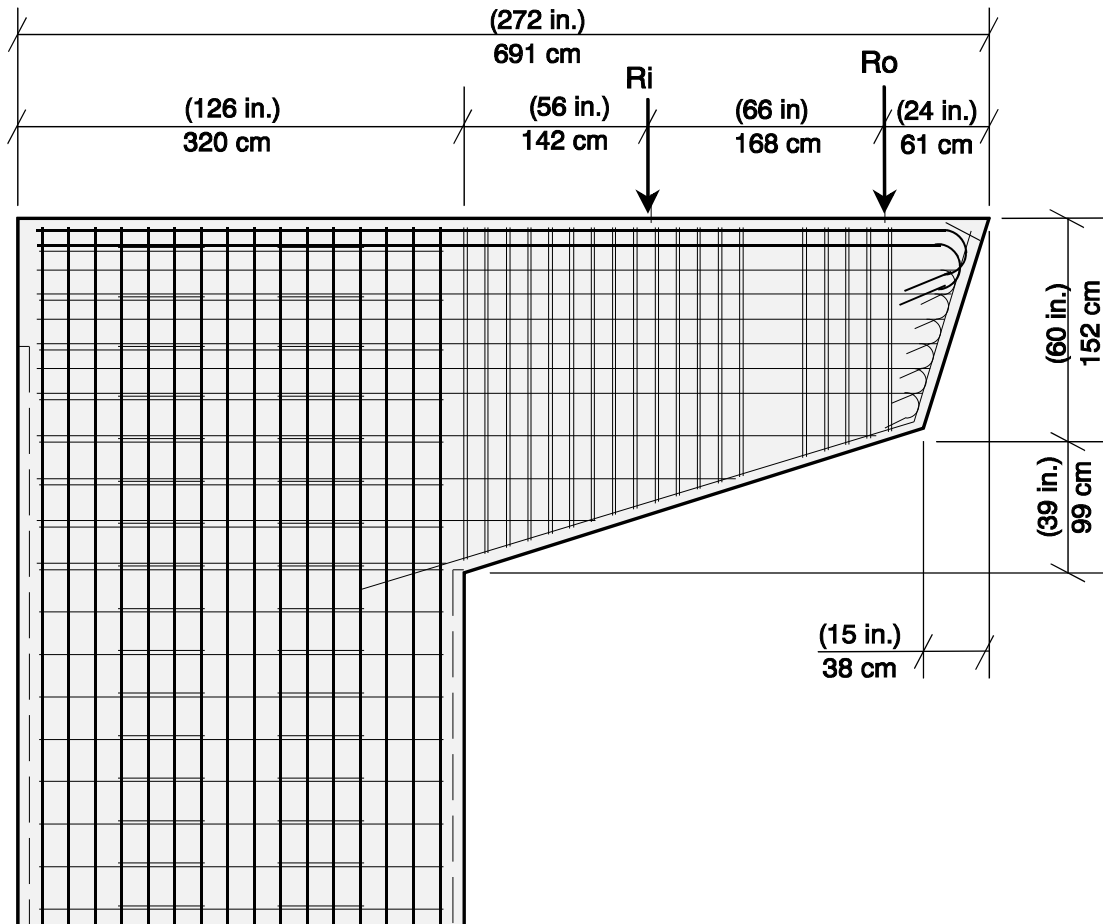


Figure 3.4 Reinforced Concrete Substructure I4-C Details

Details for a typical reinforced concrete San Antonio 'Y' cantilever bent (Substructure I4-C) are shown in Figure 3.4. The top two layers of longitudinal reinforcement in the overhang were closely spaced No. 11 bars. The side face reinforcement consisted of No. 8 bars spaced at 30 cm (12 in.). The double No. 6 bar transverse reinforcement was spaced at 10 cm (4 in.).

Longitudinal pier reinforcement incorporated closely spaced No. 11 bars near extreme tension and compression fibers and No. 11 side face bars spaced at 40 cm (16 in.). The pier reinforcement ratio (area of longitudinal reinforcement / gross section area of pier) was equal to the minimum 1 percent required by the AASHTO Standard Specifications.

Pier and overhang longitudinal reinforcement were anchored in the joint using straight-bar anchorage instead of hooked bars. After an investigation of the bent strength (discussed in Chapter 7), field inspection of the I4-C substructure element revealed several diagonal cracks in the joint region which resulted in closure of the on-ramp until repairs were completed [26,27].

3.2.2.2 Substructure with Fully-Prestressed Overhang - C11-C

The C11-C substructure presented in Figure 3.5 was designed utilizing a fully-prestressed overhang because the maximum available depth of the overhang at the column face was only 150 cm (60 in.) to provide adequate truck clearance beneath the cantilever bent. For the limited depth, more than two rows of mild longitudinal reinforcement would have been necessary to resist factored loads. To provide sufficient strength, the design of the overhang was changed from a reinforced concrete load-factor design to a fully-prestressed design.

The post-tensioning in the overhang consisted of two rows of eight - 3.49 cm (1-3/8 in.) diameter deformed high-strength post-tensioning bars. The side-face reinforcement consisted of No. 8 bars spaced at 30 cm (12 in.). The double No. 6 bar transverse reinforcement was spaced at 10 cm (4 in.). The gap in the transverse reinforcement in the overhang provided a space for a drainage pipe that passed from the superstructure into the substructure.

Pier longitudinal reinforcement was closely spaced No. 11 bars on the extreme tensile and compressive fibers and No. 11 side face bars at 20 cm (8 in.) spacing. The pier reinforcement ratio was equal to the minimum 1 percent required by the AASHTO Standard Specifications.

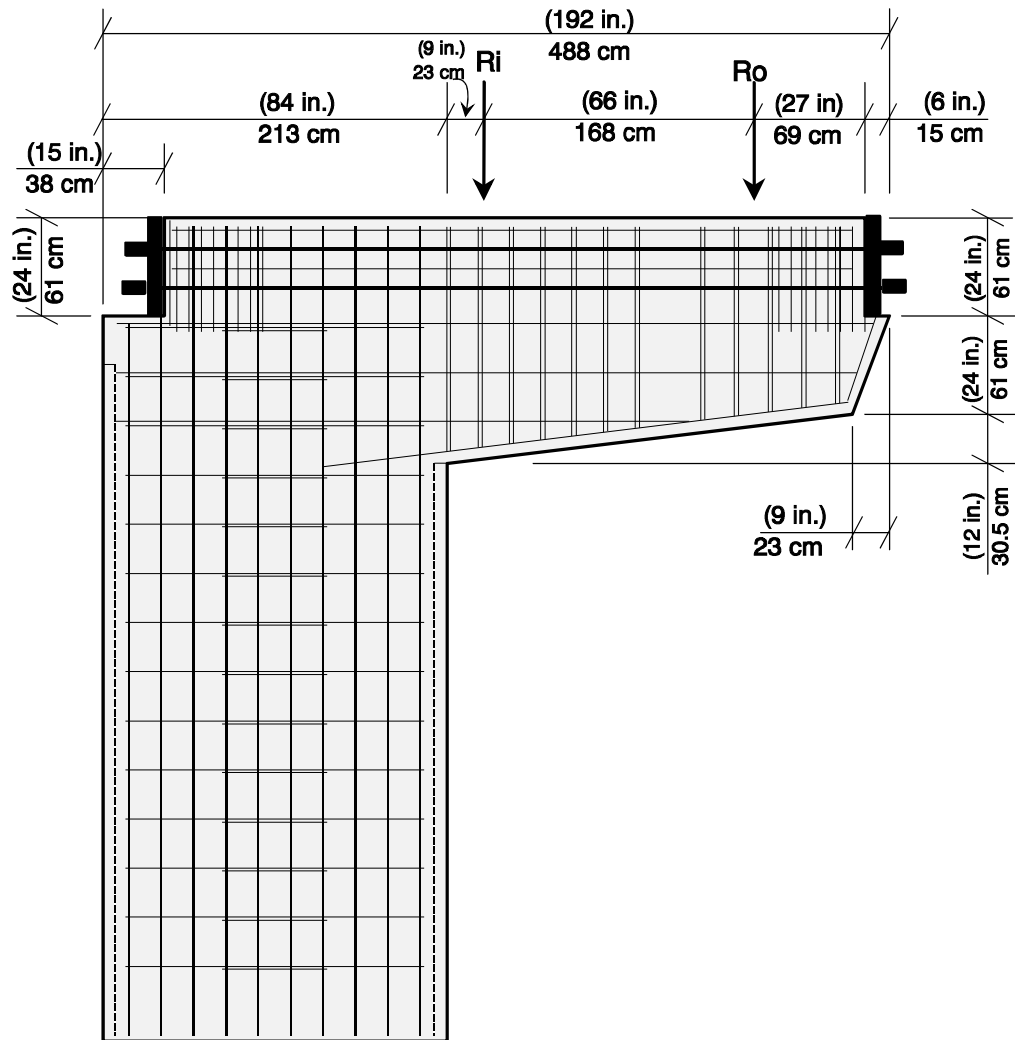


Figure 3.5 Substructure C11-C Details

The overhang post-tensioning bars were anchored in the joint corner. As depicted in Figure 3.5, a block-out was cast into the corner to conceal the post-tensioning anchorage hardware. The pier longitudinal reinforcement on the exterior face (furthest from the overhang) was cut short to accommodate the corner block-out. No hooks were used to anchor longitudinal reinforcement in the joint region. During construction of the San Antonio ‘Y’ Project, as the entrance-ramp girder was placed on the C11-C substructure overhang, a large diagonal crack developed in the joint region and gradually extended until the load from the superstructure was removed. As will be explained later in Chapter 7, the

shortened pier longitudinal bars and lack of reinforcement continuity in the joint were major factors influencing the bent strength. A significant improvement in the design could have been achieved by utilizing an integrated design method that would have identified detailing problems in the joint during the design phase.

3.2.3 Selection of Scale Factor for Test Specimens

The overhang experimental study conducted by Armstrong [3] and Salas [4] utilized an interior load located at a distance of one half the beam depth (0.5 h) from the column face and an outer load at one and one-half times the beam depth (1.5 h) from the column face. The location of these loads was a critical part of the original Overhang Specimen investigation. The proximity of the interior load to the column face required the design to satisfy the corbel provisions, while the outer load was within a 1.5 span-to-depth ratio which required consideration of the deep beam provisions and also induced large moments. The array of different design provisions that applied due to the load positions is one of the items that can be eliminated by utilizing an integrated design method. It was determined that the use of these load points in the present study would provide additional data on overhang behavior. Based on a review of full-scale substructures located in San Antonio, the load positions used in this study were as severe as any identified for the cantilever bents in San Antonio.

The model dimensions were determined as follows:

$$\text{Model Length} = \frac{\text{Prototype Length}}{\text{Scale Factor}}$$

$$\text{Model Area} = \frac{\text{Prototype Area}}{(\text{Scale Factor})^2}$$

$$\text{Model Force} = \frac{\text{Prototype Force}}{(\text{Scale Factor})^2}$$

Selection of the scale factor for the Pier-Overhang-Joint study (presented in Table 3.2) was made by identifying a scale factor that would allow standard size bars to be used in

models while limiting scaled loads to less than 667 kN (150 kips). It was decided to limit each maximum design reaction to 667 kN (150 kips) to provide sufficient reserve capacity in the 889 kN (200 kip) rams used in the testing program to fail the specimen. Based on the combination of these factors, it was determined that a 2.75 scale factor was the smallest scale factor that satisfied both requirements. It should be noted that the selected scale factor for the test specimens was one-half the 5.5 scale factor used in the overhang study conducted by Armstrong [3] and Salas [4].

Table 3.2 Selection of Scale Factor, Model Bar Diameters and Load

Prototype Bar Size		Model Bar Size SF=2.25		Model Bar Size SF=2.75		Model Bar Size SF=3.75		Model Bar Size SF=5.5	
No. 14		No. 6		No. 5		~No. 4		~No. 3	
No. 11		No. 5		No. 4		No. 3		No. 2	
No. 8		~No. 4		No. 3		No. 2		7 ga. wire	
No. 6		~No. 3		No. 2		7 ga. wire		10 ga. wire	

Prototype Load		SF=2.25		SF=2.75		SF=3.75		SF=5.5	
(kN)	(kips)	kN	(kips)	kN	kips	kN	(kips)	kN	(kips)
5126	1152	1012	227	677	153	365	82	169	38

The reasons for using a 2.75 scale factor were that standard, 414 MPa (60 ksi) nominal yield deformed bars could be used, anchorage of the bars in the joint region was reasonably realistic, and 889 kN (200 kip) rams were readily available.

3.2.4 Model Loads

The 7.9 m (26 ft) wide box-girder superstructure loads (presented in Table 3.1) were divided by the square of the scale factor $[(2.75)^2]$ to determine the loads for the model specimens (presented in Table 3.3). Load steps used during testing are discussed in Section

3.8.3. The effect of the self weight of the overhang was not considered in this experimental program.

Table 3.3 Substructure Design Loads for a 1/2.75 Scale Model

Load Description	Load Abbreviation	Ri		Ro	
		kN	(kips)	kN	(kips)
Dead Load	DL	293	65.9	293	65.9
Dead Load + 1/2 Live Load	(DL + 1/2 LL)	318	71.4	344	77.4
Service Load	(DL+LL)	343	77.0	399	89.6
Dead Load + 2 Live Load	(DL+2LL)	409	92.0	496	111.4
Factored Load	(1.3DL + 2.17LL)	488	109.7	610	137.2
Factored Load / Φ	(1.3DL + 2.17LL)/ Φ	543	122.1	679	152.7

3.2.5 Model Dimensions

The model dimensions shown in Figure 3.6 and Figure 3.7 were determined by scaling the 1.67 m (5.5 ft) distance between the reactions for the 7.92 m (26 ft) winged superstructure by the 2.75 scale factor. The distance between the model loads was 61 cm (24 in.). The interior load was positioned (0.5h) or 30.5 cm (12 in.) from the column face, and the outer load was positioned (1.5h) or 91.5 cm (36 in.) from the column face. The size of the joint was determined by multiplying the ratio of the I4-C pier-to-overhang dimensions by the depth of the model overhang, resulting in a pier depth of 76 cm (30 in.). The minimum width of the section was 61 cm (24 in.) because two rows of fourteen No. 4 reinforcing bars with a minimum bar spacing of 4.3 cm (1.7 in.) were required to resist the factored moment. The slope of the bottom face of the overhang, 12/39, and the overall dimensions of the overhang were quite similar to the overhangs tested by Armstrong [3] and Salas[4].

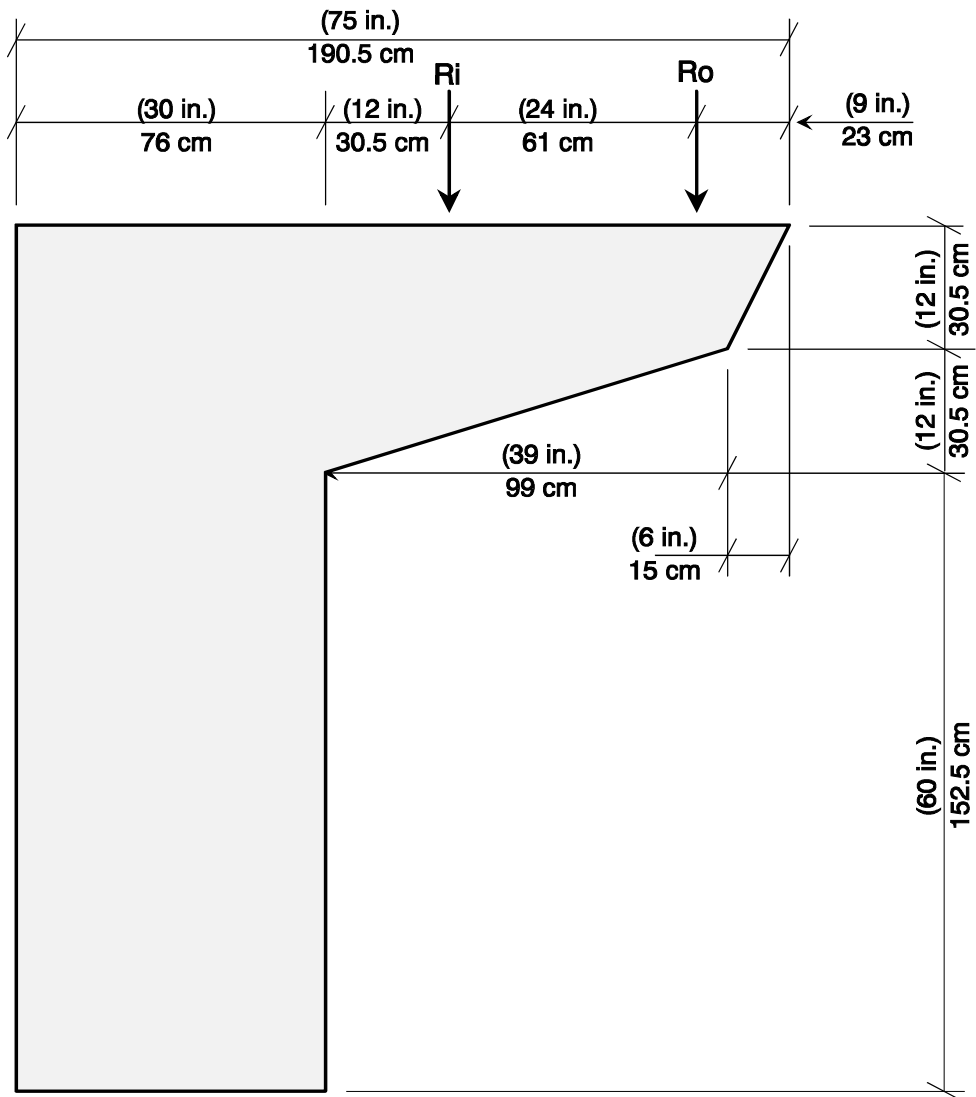


Figure 3.6 Overall Dimensions for POJ Specimens

For No. 14 and Larger $u_u = 6\sqrt{f'_c} \leq (800 \text{ psi}) 5.5 \text{ MPa}$ [3-3]

$f'_c =$ Specified Compressive Strength of the Concrete (psi)
= (5,000 psi) 34 MPa.

The computed basic bar development lengths are tabulated in Table 3.4 for a variety of bar sizes, assuming f_y is 414 MPa (60 ksi) and a concrete compressive strength of 34 MPa (5000 psi).

Table 3.4 Computed Basic Bar Development Lengths

	Bar Diameter		Bar Area		ACI-318 (1963) Bond Stress		Development Length	
	mm	(in.)	mm ²	(in.) ²	MPa	(psi)	cm	(in.)
No. 2	6	0.25	30	0.048	5.5	800	12	4.7
No. 3	10	0.375	70	0.11	5.5	800	18	7.0
No. 4	13	0.50	130	0.20	5.5	800	24	9.4
No. 5	16	0.625	200	0.31	5.5	800	30	11.7
No. 6	19	0.75	280	0.44	5.5	800	36	14
No. 8	25	1.00	510	0.79	4.6	671	57	22.4
No. 11	36	1.41	1010	1.56	2.9	424	127	49.9
No. 14	43	1.693	1450	2.25	2.9	424	152	59.9

A comparison of the scaled-bar basic development lengths and the model bar basic development lengths for several bar sizes with 414 MPa (60 ksi) nominal yield in 34.4 MPa (5000 psi) concrete is shown in Table 3.5.

Table 3.5 Comparison of Scaled Development Lengths and Development Lengths for Model Bars

Prototype Bar Size	Straight Bar Development ACI-318 -63		Scaled Bar Development SF=2.75		Model Bar Size SF=2.75	Model Bar Development ACI-318 - 63		% Diff.
	cm	(in.)	cm	(in.)		cm	(in.)	
No. 14	152	59.9	55	21.8	No. 5	30	11.7	86 %
No. 11	127	49.9	46	18.1	No. 4	24	9.4	92 %
No. 8	57	22.4	21	8.1	No. 3	18	7.0	16 %
No. 6	36	14	13	5.0	No. 2	12	4.7	6 %

Development lengths scaled from the computed development lengths for prototype bar sizes were 6 to 92 % longer than development lengths for model bars. Although the bar development lengths did not scale directly, the reduced size of the joint in the model provided a similar ratio of joint dimension to development length for bars as for the I4-C joint. Using a horizontal joint dimension of 76 cm (30 in.) and a vertical joint dimension of 61 cm (24 in.) for the model, the following ratios were computed.

$$\frac{\text{Model Joint Horizontal Dimension}}{(\ell_d \text{ for No. 4})} \approx \left[\frac{\text{I4 - C Pier Depth}}{\ell_d \text{ for No. 11}} \right]$$

$$3.2 \cong 2.5$$

$$\frac{\text{Model Joint Vertical Dimension}}{(\ell_d \text{ for No. 5})} \approx \left[\frac{\text{I4 - C Overhang Depth}}{\ell_d \text{ for No. 11}} \right]$$

$$2.1 \cong 2.0$$

The ratios imply that the model dimensions for the joint (and thus, the pier and overhang depths) provide an acceptable representation of the I4-C prototype joint. In addition, when the dimensions of the model are scaled-up to full-scale, as shown in Figure 3.8, they are very similar to the substructure C11-C dimensions shown in Figure 3.5.

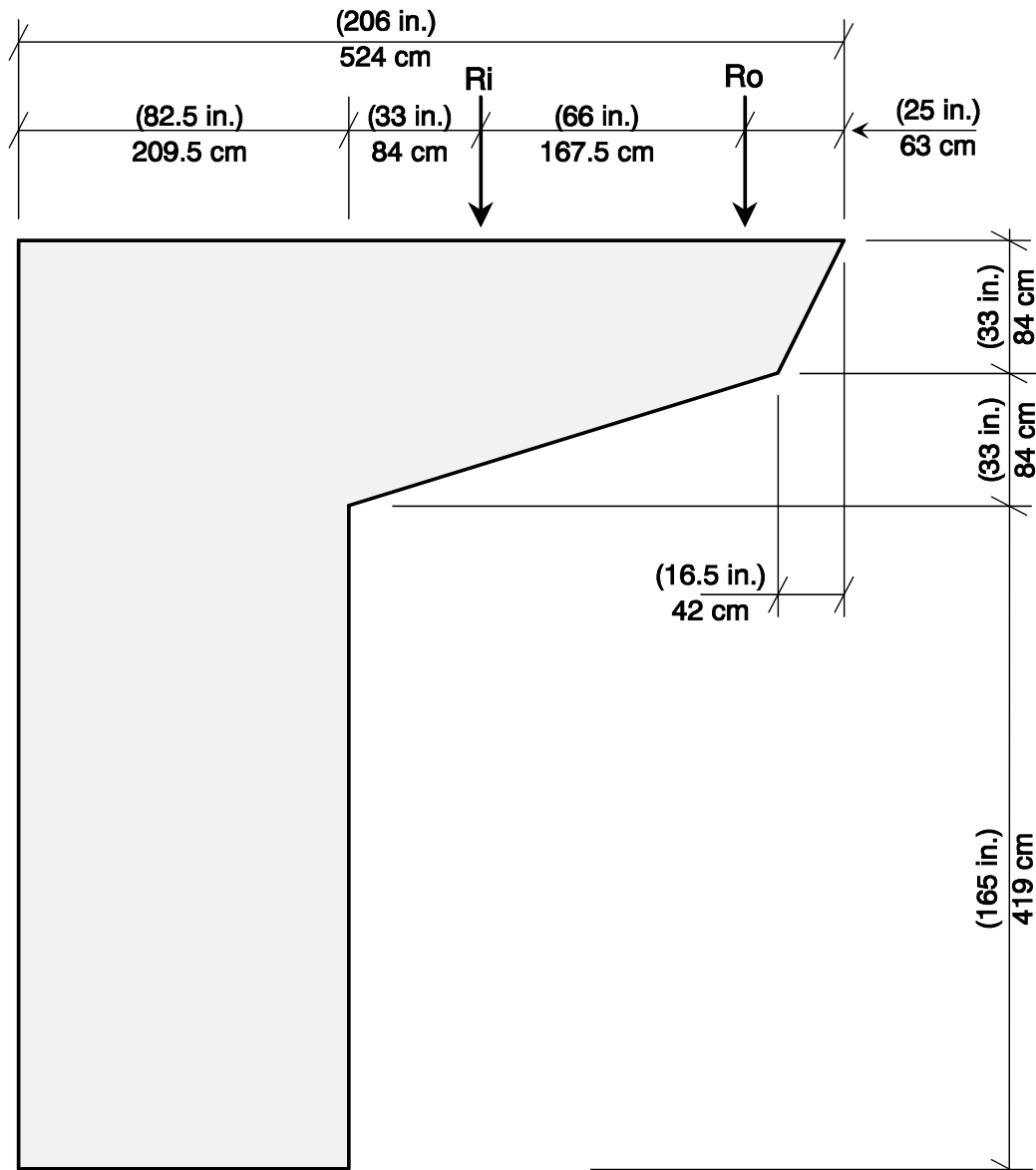


Figure 3.8 Dimensions of the Model Scaled-Up to Full-Scale

3	20
3.1 Introduction	20
3.2 Development of the Pier-Overhang-Joint Specimen	21
3.2.1 Selection of Full-Scale Superstructure Loads	21
3.2.2 Full-Scale Prototype Substructure Details	25
3.2.2.1 Reinforced Concrete Prototype Substructure - I4-C	25
3.2.2.2 Substructure with Fully-Prestressed Overhang - C11-C	26
3.2.3 Selection of Scale Factor for Test Specimens	28
3.2.4 Model Loads	29
3.2.5 Model Dimensions	30
3.2.5.1 Bar Development Similitude	32
Figure 3.1 Substructure Schematic	22
Figure 3.2 Pier Location and Continuity Factors	23
Figure 3.3 Full-Scale Prototype Loads Without Continuity Factors	24
Figure 3.4 Reinforced Concrete Substructure I4-C Details	25
Figure 3.5 Substructure C11-C Details	27
Figure 3.6 Overall Dimensions for POJ Specimens	31
Figure 3.7 Top view of POJ Specimen	32
Figure 3.8 Dimensions of the Model Scaled-Up to Full-Scale	35
Table 3.1 Full-Scale Substructure Loads for a 7.9 m (26 ft) Wide Girder	24
Table 3.2 Selection of Scale Factor, Model Bar Diameters and Load	29
Table 3.3 Substructure Design Loads for a 1/2.75 Scale Model	30
Table 3.4 Computed Basic Bar Development Lengths	33
Table 3.5 Comparison of Scaled Development Lengths and Development Lengths for Model Bars	34

3.3 Design Method for Prototype Pier-Overhang-Joint (POJ) Test Specimens

In the experimental study, a prototype design is defined as a specimen designed using the same design procedures used for the San Antonio ‘Y’ substructures. Specimens tested are not scaled replicas of particular bents. The reinforced concrete and fully-prestressed concrete prototype designs considered the shear friction and corbel design provisions, side-face cracking provisions, and minimum longitudinal column reinforcement provisions.

3.3.1 Reinforced Concrete Specimen - POJ-RC-100

The POJ-RC-100 prototype reinforced concrete specimen was designed according to the 1983 AASHTO Standard Specifications using the same considerations assumed by designers of the San Antonio ‘Y’.

3.3.1.1 Overhang Design - POJ-RC-100

Flexural Reinforcement for Strength :

The primary flexural reinforcement was computed by AASHTO Article 8.16.3.2, Rectangular Sections with Tension Reinforcement Only (Equation 8-15):

$$M_u \leq \Phi M_n = \Phi \left[A_s f_y d \left(1 - \frac{0.6 \rho f_y}{f_c'} \right) \right] \quad [3-4]$$

where:

M_u	=	Factored Moment = 1.3DL+2.17LL = 706.6 kN-m (6253 k-in.)
Φ	=	Phi Factor for flexural members = 0.9
M_n	=	Nominal moment capacity = 806 kN-m (7140 k-in.)
A_s	=	Area of mild reinforcement = 36 cm ² (5.6 in. ²)
f_y	=	Nominal yield stress of mild steel = 414 MPa (60 ksi)
ρ	=	Reinforcement ratio $A_s / b_w d = 0.0106$
b_w	=	Member width = 61 cm (24 in.)
d	=	Distance from extreme compression fiber to centroid of tension reinforcement = 56 cm (22 in.)
f_c'	=	Specified compressive strength of the concrete
	=	34 MPa (5 ksi).

Shear Friction Reinforcement:

The amount of shear friction reinforcement was specified by Article 8.16.6.4.4, Shear-Friction Design Method. The nominal shear capacity across a potential cracking plane at the column face was calculated by computing the required amount of longitudinal reinforcement placed perpendicular to the potential shear plane and applying AASHTO Equation 8-56:

$$V_u \leq \Phi V_n = \Phi (A_{vf} F_y \mu) \quad [3- 5]$$

where:

V_u	=	Applied Factored Shear from both reactions = 1098 kN (246.9 kips)
V_n	=	Nominal shear friction capacity = 1292 kN (291 kips)
Φ	=	Phi Factor = 0.85
A_{vf}	=	Area of mild steel perpendicular to potential shear crack
	=	22.3 cm ² (3.46 in ²)
μ	=	Coefficient of friction = 1.4.

Additionally, in Article 8.16.6.8.4, Special Provisions for Brackets and Corbels, an area of mild steel, A_h , shall be “uniformly distributed within two-thirds of the effective depth adjacent to A_s ” where the larger of

$$A_h = \left(\frac{A_{vf}}{3} \right) = 7.4 \text{ cm}^2 (1.15 \text{ in}^2) \quad [3- 6]$$

or

$$A_h = 0.5(A_s) = 18 \text{ cm}^2 (2.8 \text{ in}^2) \quad [3- 7]$$

determined the required area of shear friction steel.

The amount of shear friction reinforcement, 18 cm² (2.8 in²), was controlled by Equation 3-7. The quantity of side-face reinforcement was considered as part of the required shear friction reinforcement. As a result, four of the side-face bars near mid-depth were changed to No. 3 bars. Two rows of twelve - No. 3 reinforcing bars distributed near mid-depth of the section were used to satisfy the required area of shear friction steel.

Detailing of Side-Face Reinforcement:

The distribution and quantity of longitudinal skin reinforcement were determined using the equations developed by Frantz and Breen [10]. The reinforcement ratio was based on dimensions of the full-scale prototype, and the required area of reinforcement was computed using that reinforcement ratio. The reinforcement ratio was computed using:

$$\rho_{sk} \geq 0.00024(d - 30) \quad \text{For } d \leq (100 \text{ in.}) \quad [3- 8]$$

where:

$$\begin{aligned} d &= \text{Full Scale distance from extreme compression fiber to main} \\ &\text{tensile reinforcement in (in.)} \\ &= 56 \text{ cm (22.1 in.)} * 2.75 = 154 \text{ cm (60.8 in.)} \end{aligned}$$

and :

$$\rho_{sk} = \frac{A_{sk}}{2 [d/2 \cdot 2d_c]} \quad [3- 9]$$

where:

$$\begin{aligned} \rho_{sk} &= \text{Skin reinforcement ratio} = 0.007409 \\ A_{sk} &= \text{Area of skin reinforcement} = 2.4 \text{ cm}^2 (0.374 \text{ in}^2) \\ d &= \text{Distance from extreme compression fiber to main tensile} \\ &\text{reinforcement of the model} = 56 \text{ cm (22.1 in.)} \\ d_c &= \text{Distance from skin steel centroid to nearest outside face of} \\ &\text{the concrete of the model} = 2.9 \text{ cm (1.14 in.)} \end{aligned}$$

The side-face reinforcement consisted of four- No. 2 reinforcing bars equally spaced at 6 cm (2.6 in.) on each outer face of the specimen. The lower two rows of side-face reinforcement were replaced by No. 3 bars as described in the section for shear friction.

Serviceability Criteria:

Distribution of the main flexural reinforcement was checked using Article 8.16.8.4, Distribution of Flexural Reinforcement, (Equation 8-61):

$$f_s = \frac{z}{(d_c A)^{1/3}} \leq 0.6 f_y \quad [3-10]$$

where:

f_s	=	Limiting steel stress in the reinforcement at service loads in (ksi) = 278 MPa (40.4 ksi)
z	=	Scaled crack distribution factor for moderate exposure conditions (170/2.75) = 62
d_c	=	Thickness of concrete cover from extreme tension fiber to centroid of tension reinforcement in inches 4.7 cm (1.85 in.)
A	=	Effective Tension Area in (in ²) surrounding the flexural tension reinforcement divided by the number of bars (in ² / # Bars) 573 cm ² (88.8 in ² / 28 bars).

The computed steel stress at service load using the strain compatibility analysis was [236 MPa (34.3 ksi)], which satisfied the limiting service load stress, f_s , of [278 MPa (40.4 ksi)] computed from Equation 3-10 and the limiting value of $0.6 f_y$ [248 MPa (36 ksi)].

Fatigue stress limits were considered by determining the steel stresses at dead load and service load using a strain compatibility analysis considering all the flexural reinforcement. The limit stated in AASHTO Equation 8-60 is:

$$f_s < f_f = 21 - 0.33 f_{\min} + 2.4 \quad [3-11]$$

where:

f_s	=	Computed Stress Range in specimen = 58 MPa (8.5 ksi)
f_f	=	Maximum Allowable Stress range in (ksi) for primary flexural reinforcement $f_f \leq f_{(DL+LL+I)} - f_{(DL)} = 99 \text{ MPa (14.4 ksi)}$
f_{\min}	=	Stress level (at dead loads) in (ksi) 188 MPa (27.3 ksi).

The computed stress range in the specimen of 58 MPa (8.5 ksi) was within the acceptable range computed by Equation 3-11. The resulting longitudinal reinforcement details are shown in Figure 3.9.

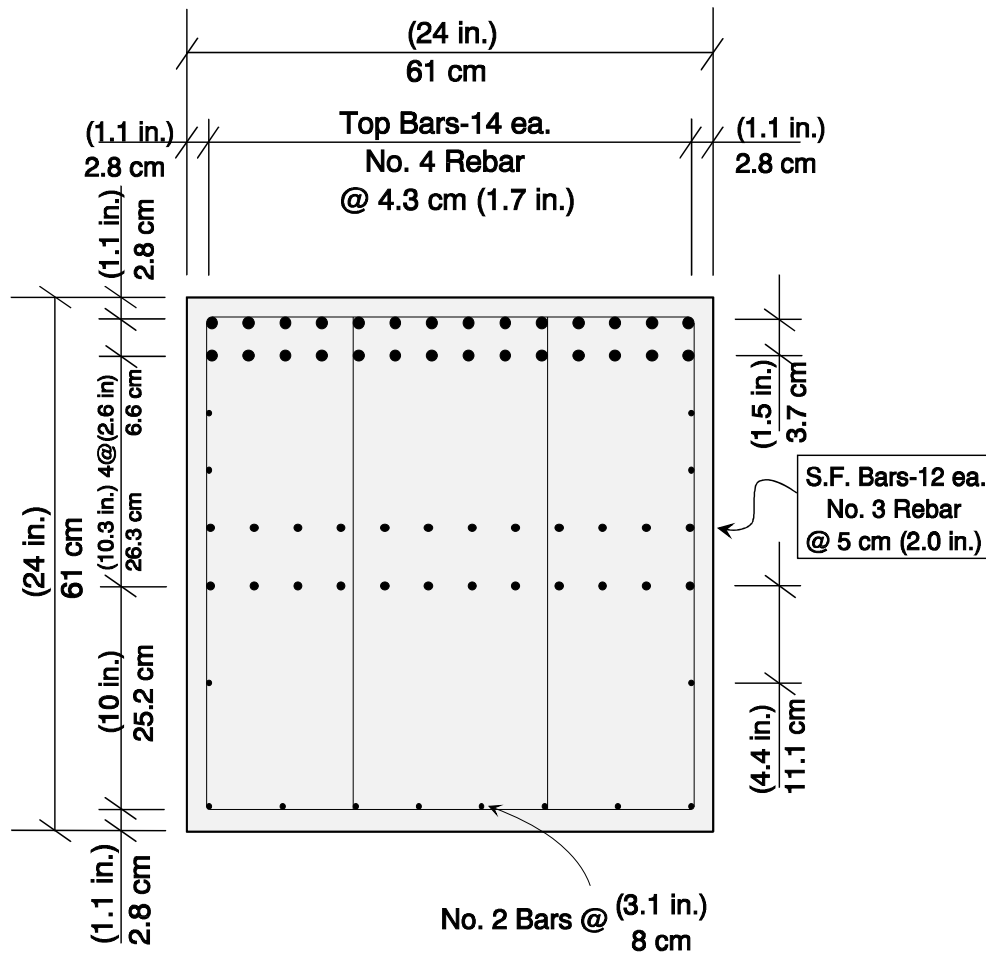


Figure 3.9 POJ-RC-100 Overhang Reinforcement Cross-Section Details

Transverse Reinforcement:

The amount of transverse reinforcement was determined using AASHTO Article 8.16.6.1, Shear Strength (Equations 8-46 and 8-47):

$$V_u \leq \Phi V_n = \Phi (V_c + V_s) \quad [3- 12]$$

where:

V_u	=	Factored Shear = 610 kN (137.2 kips)
Φ	=	Phi factor for Shear = 0.85
V_n	=	Nominal Shear Capacity = 717 kN (161.3 kips).

The nominal concrete contribution to shear strength, V_c , is defined by Equation 8-49:

$$V_c = 2\sqrt{f'_c} b_w d \quad [3- 13]$$

where:

V_c	=	Nominal concrete contribution to shear strength = 233 kN (52.5 kips)
f'_c	=	Specified compressive strength of the concrete in (psi) 34 MPa (5000 psi)
b_w	=	Beam width = 61 cm (24 in.)
d	=	Beam depth at 45° angle from load point = 40 cm (15.5 in.).

The shear strength provided by stirrups, V_s was quantified by Equation 8-53:

$$V_s = \frac{A_s f_y d}{s} \quad [3- 14]$$

where:

V_s	=	Nominal shear strength = 484 kN (108.8 kips)
A_s	=	Area of stirrups = 1.2 cm ² (0.192 in. ²)
f_y	=	Nominal yield stress of the mild steel = 414 MPa (60 ksi)
s	=	Spacing of the transverse reinforcement = 4 cm (1.6 in.).

The designers assumed the factored shear loading, V_u , was equal to the factored outside superstructure reaction, R_o . The depth, d , was determined at the section defined by the intersection of the extreme compression fiber and a 45° line drawn from the outer load point. This critical section was assumed to resist the entire shear force from the outer reaction. The stirrups were double No. 2 hoops with a total area of 1.2 cm² (0.192 in²). The stirrup spacing, s , was determined using Equation 3-11 after subtracting the concrete contribution (Equation 3-10) from the applied factored shear. The stirrup spacing, s , of 4.2 cm (1.6 in.) was used over the entire overhang (see Figure 3.10).

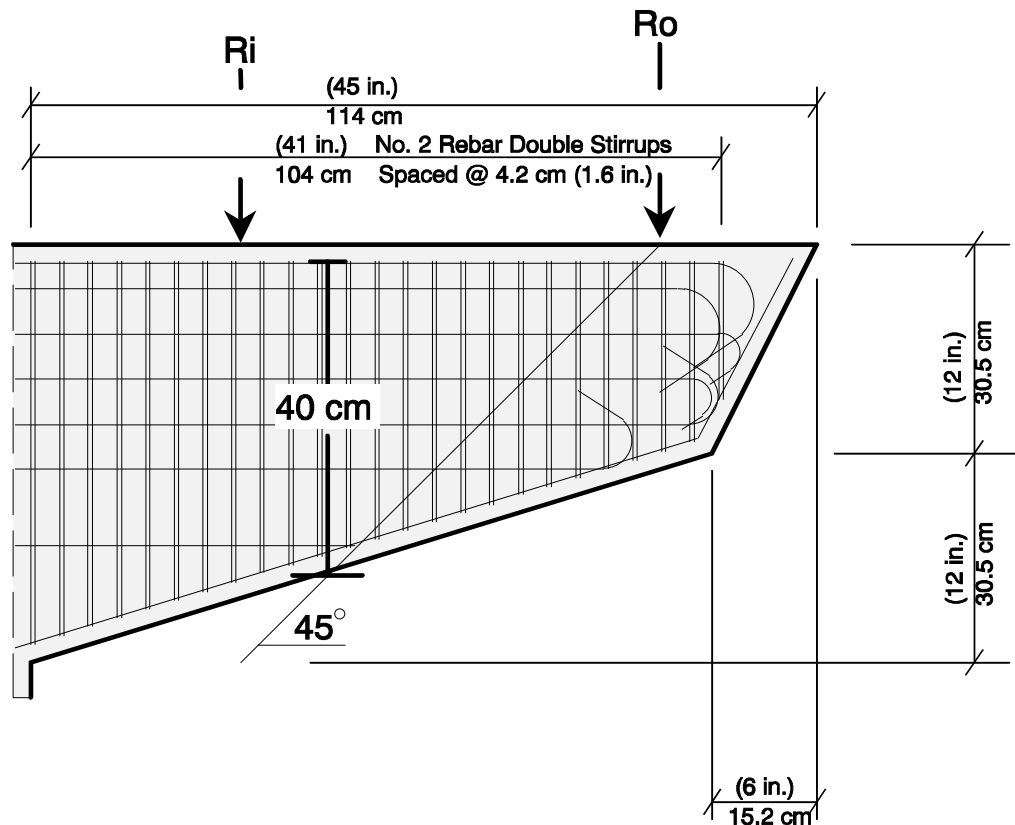


Figure 3.10 POJ-RC-100 Overhang Reinforcement Details

3.3.1.2 Pier Design - POJ-RC-100

Flexural Reinforcement:

The amount of longitudinal reinforcement in the pier was determined using a strain compatibility analysis, allowed by Article 8.16.3.4.2, which was similar to the procedure used by the designers of the San Antonio 'Y'. The computed nominal flexural strength (M_n) was multiplied by a Φ factor and compared with the factored moment, $\Phi M_n \geq M_u$. The Φ factor increases linearly from 0.7 to 0.9 as the design axial load decreases from $0.10 f_c' A_g$ to zero, based on the provisions in Article 8.16.1.1.2.

The required minimum percentage of longitudinal reinforcement often controlled the amount of pier reinforcement used for the San Antonio 'Y' substructures. Article 8.18.1.2 states the minimum area of longitudinal reinforcement must be greater than $0.01 A_g$. In the

model, the percentage of pier reinforcement was $0.0155 A_g$ due to the high flexural forces. The distribution of longitudinal reinforcement in the pier is shown in Figure 3.11.

Transverse Reinforcement:

Transverse reinforcement was detailed using Article 8.18.2.3. Tie spacing and bar size requirements were scaled by the 2.75 scale factor. The No. 4 ties required by AASHTO were modeled using 7 ga. wire. The minimum longitudinal spacing in the pier of 30 cm (12 in.) was divided by the 2.75 scale factor resulting in a tie spacing of 11 cm (4.4 in.). The maximum distance to a restrained bar of 61 cm (2 ft) was divided by the 2.75 scale factor resulting in a distance of 22 cm (8.7 in.) (see Figure 3.11).

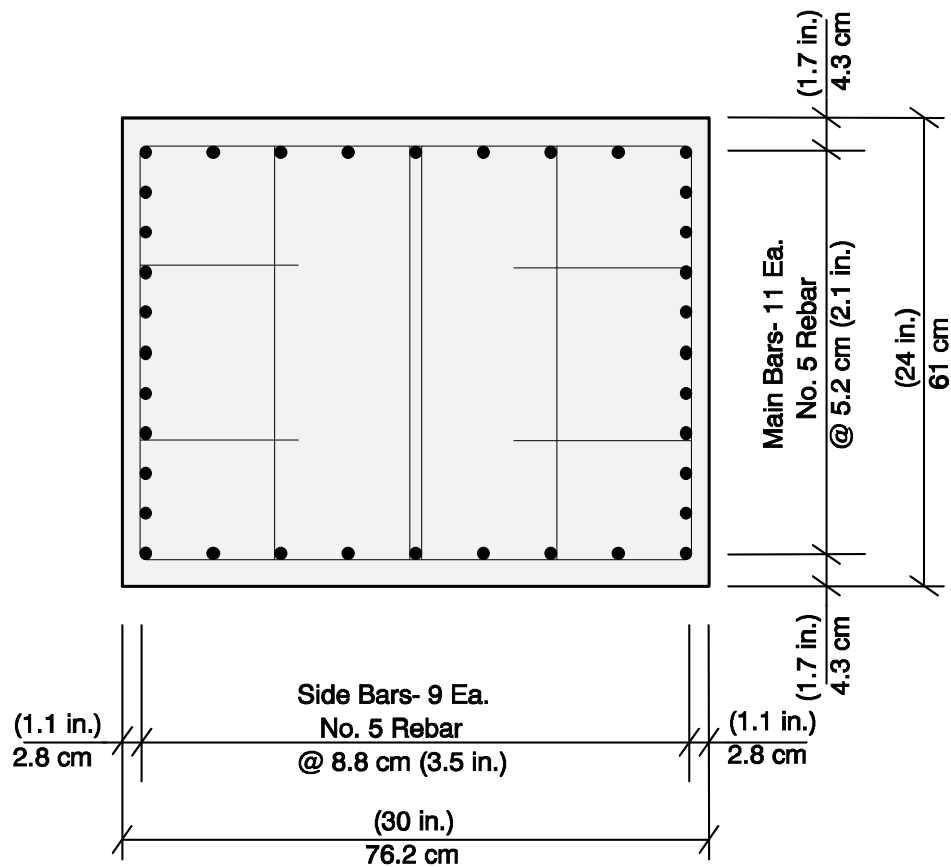


Figure 3.11 POJ-RC-100 Pier Reinforcement Detail

3.3.1.3 Joint Design - POJ-RC-100

Bar Anchorage:

Anchorage of the pier and overhang reinforcement in the joint was assumed to be based on straight bar development. Bar development length was compared with the available embedment from the critical moment sections of the overhang and pier to the back and top of the joint, as had been done for the San Antonio 'Y' bents. Because bars used in the model have more than twice the straight bar development required by the specifications, hooks, welded plates, and other methods of positive anchorage were not provided. An enlarged view of the reinforcement in the joint is shown in Figure 3.12, and an elevation of the reinforcement details used in Specimen POJ-RC-100 is presented in Figure 3.13.

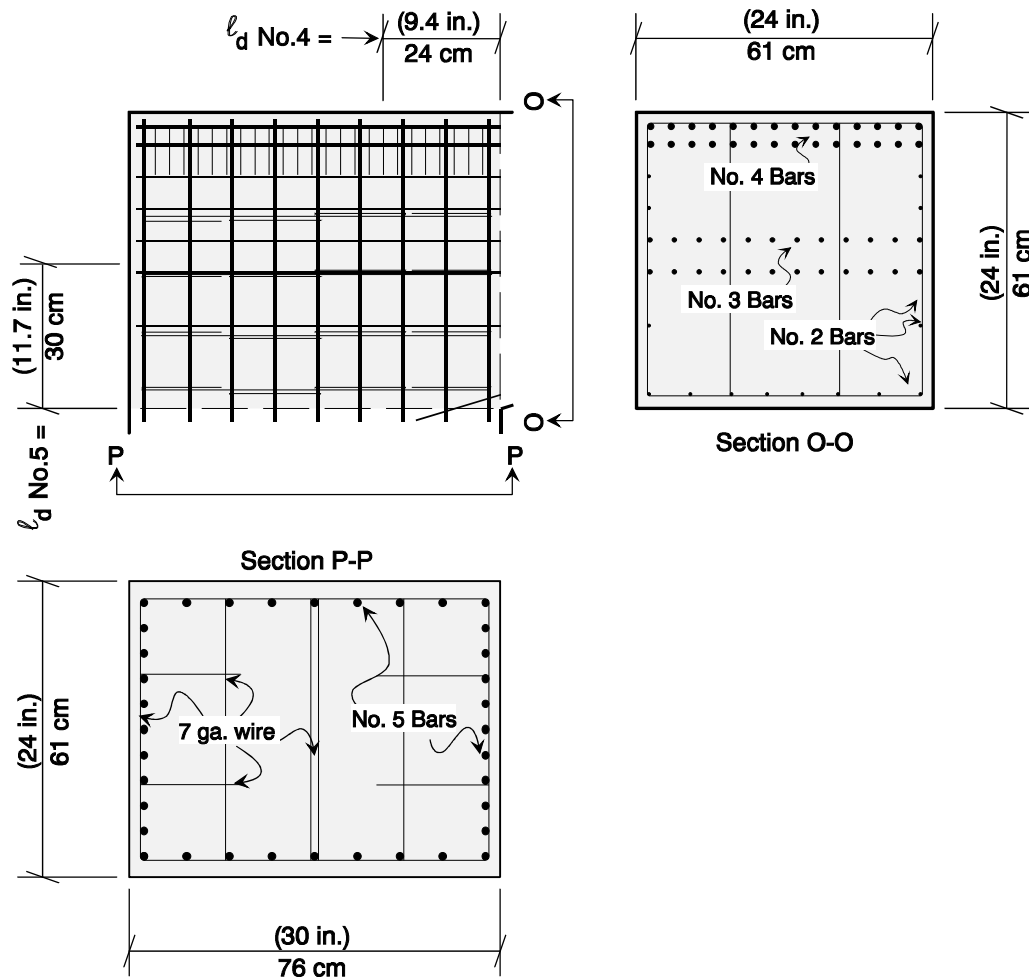


Figure 3.12 POJ-RC-100 Joint Reinforcement Details

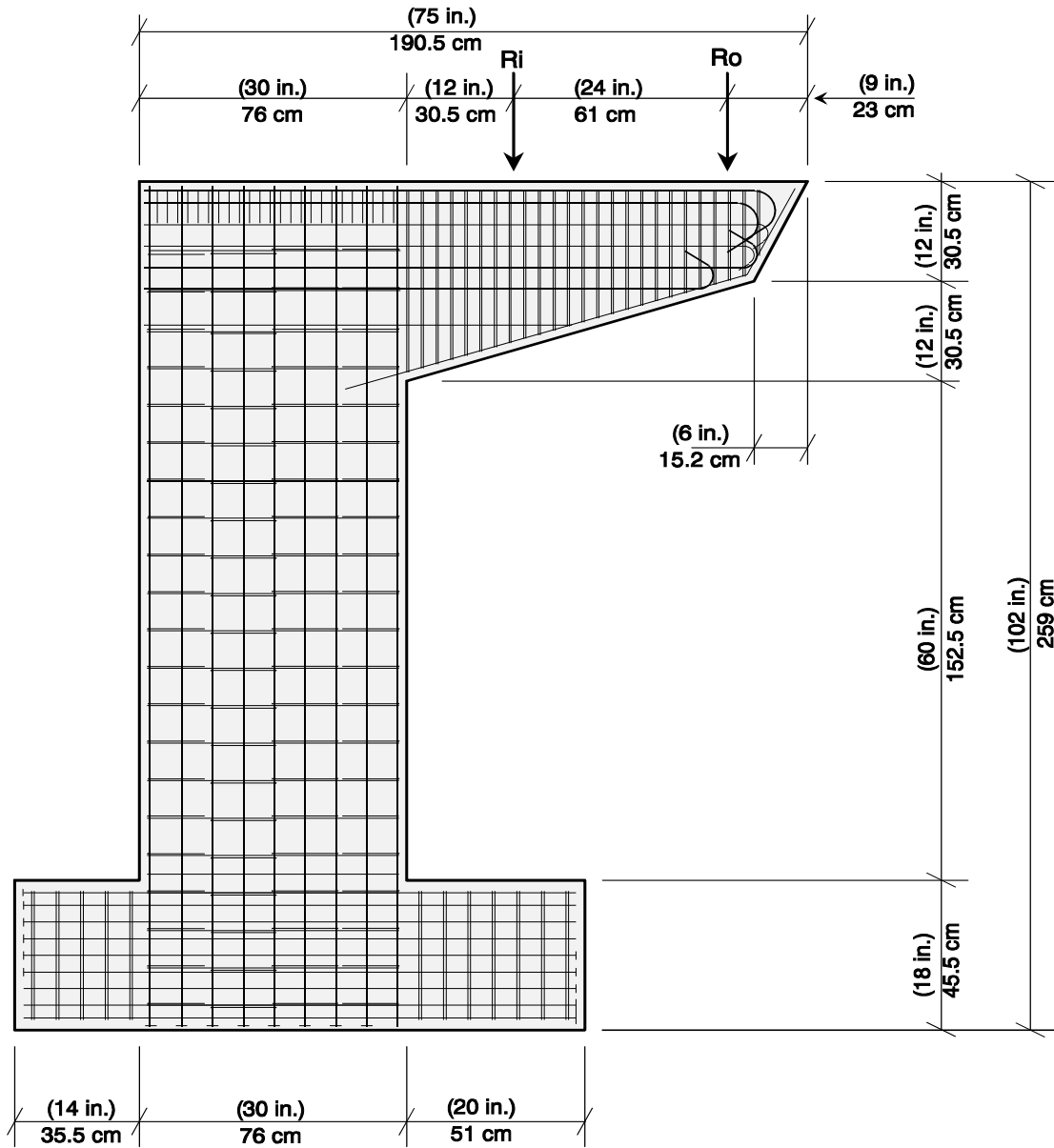


Figure 3.13 Elevation of Reinforcement for POJ-RC-100

3.3 Design Method for Prototype Pier-Overhang-Joint (POJ) Test Specimens	36
3.3.1 Reinforced Concrete Specimen - POJ-RC-100	36
3.3.1.1 Overhang Design - POJ-RC-100	36
3.3.1.2 Pier Design - POJ-RC-100.....	42
3.3.1.3 Joint Design - POJ-RC-100	44
Figure 3.9 POJ-RC-100 Overhang Reinforcement Cross-Section Details	40
Figure 3.10 POJ-RC-100 Overhang Reinforcement Details.....	42
Figure 3.11 POJ-RC-100 Pier Reinforcement Detail.....	43
Figure 3.12 POJ-RC-100 Joint Reinforcement Details.....	44
Figure 3.13 Elevation of Reinforcement for POJ-RC-100	45

3.3.2 Specimen with Fully-Prestressed Concrete Overhang - POJ-PS-100

The pier-overhang-joint specimen with the fully-prestressed concrete overhang (Specimen POJ-PS-100) was designed according to the 1983 AASHTO Standard Specifications using the same considerations assumed by designers of the San Antonio 'Y'.

3.3.2.1 Overhang Design - POJ-PS-100

Flexural Reinforcement:

The AASHTO prestressed concrete design provisions state in Article 9.17.1 that a member may be assumed to remain uncracked at service load. The design procedure is limited by Article 9.15.2.2 which specifies a maximum allowable extreme tensile fiber stress computed by:

$$-\frac{P}{A} - \frac{Pe y}{I_g} + \frac{M_{(DL+LL)} y}{I_g} \leq 3\sqrt{f'_c} \quad [3-15]$$

where:

- P = Applied post-tensioning force = 1345 kN (302.4 kips)
- A = Area of concrete = $b_w h = (576 \text{ in}^2) 0.371 \text{ m}^2$
- e = Eccentricity of post-tensioning strand above beam centroid
= 19 cm (7.5 in.).
- y = Distance to extreme tensile fiber from beam centroid
= 30 cm (12 in.)
- I_g = Gross moment of inertia = $1/12 (b_w)(h)^3 = 0.453 \text{ m}^3 (27,648 \text{ in}^3)$
- $M_{(DL+LL)}$ = Applied service load moment = 469 kN-m (4150 k-in.).

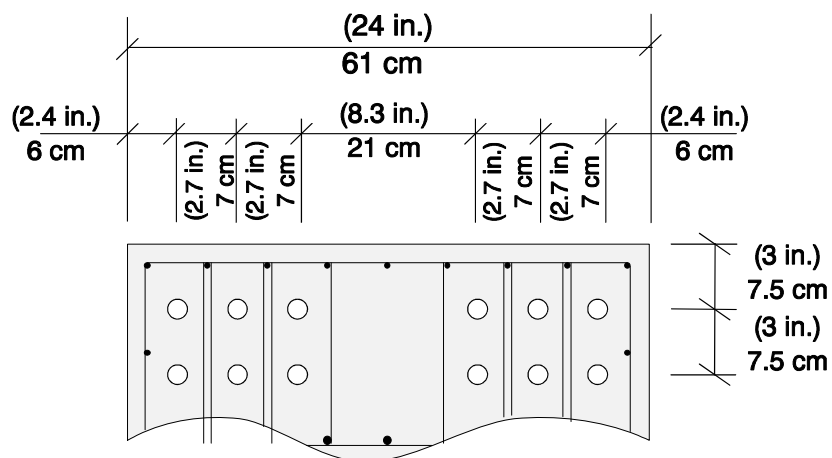


Figure 3.14 PS-100 - Location of Post-Tensioning

The post-tensioning stress (P/A_{pt}) was set equal to $0.6 f_{pu} = 620 \text{ MPa}$ (90 ksi) based on long-term losses. Twelve - 16 mm (5/8 in.) diameter Dywidag bars with an area of 1.84 cm^2 (0.28 in.^2) were required to satisfy Equation 3-15. The location and spacing of the post-tensioning ducts are shown in Figure 3.14.

Shear Friction Steel:

The concern about corbel-type shear friction behavior forced the designers to use the shear friction design method specified in Article 8.16.6.4.4. The amount of shear friction reinforcement was reduced from that specified by Article 8.16.6.4.4 to utilize the excess post-tensioning reinforcement beyond that required for flexural strength.

The area of post-tensioning required for ultimate strength design was computed using AASHTO Equation 9-13:

$$M_u \leq \Phi M_n = \Phi \left[A_s^* f_{su}^* d \left(1 - 0.6 \frac{\rho^* f_{su}^*}{f'_c} \right) \right] \quad [3-16]$$

and Equation 9-17:

$$f_{su}^* = f'_s \left[1 - \left(\gamma^* / B_1 \right) \left(\rho^* f'_s / f'_c \right) \right] \quad [3-17]$$

where:

M_u	=	Factored moment = 706.7 kN-m (6254 k-in.)
Φ	=	Phi factor for flexural design of prestressed concrete = 0.95
M_n	=	Nominal flexural strength = 877 kN-m (7758.3 k-in.)
A_s^*	=	Area of prestressing steel = 22 cm^2 (3.36 in^2)
f_{su}^*	=	Average prestressing steel stress at ultimate load
	=	923 MPa (133.8 ksi)
d	=	Distance from extreme compression fiber to prestressing centroid = 50 cm (19.5 in.)
ρ^*	=	Prestressing reinforcement ratio = $(A_s^* / b_w d) = 0.007179$
f'_c	=	Nominal concrete strength (ksi) = 34.5 MPa (5 ksi)
γ^*	=	Prestressing steel factor = 0.55 for prestressing bars
β_1	=	Concrete factor = 0.8 for 34.5 MPa (5000 psi) concrete.

The computed capacity, ΦM_n , for the fully-prestressed overhang was 833 kN-m (7370 k-in.) which was 126 kN-m (1116 k-in.) in excess of the factored moment M_u . The excess area of post-tensioning, 2.5 cm^2 (0.392 in^2), was converted into an equivalent area of

mild steel by multiplying by $\left[\frac{150 \text{ ksi}}{60 \text{ ksi}} \right]$. This area of steel, 6.3 cm^2 (0.98 in^2), was considered to contribute to the shear friction steel requirement.

The amount of shear friction reinforcement was specified by Article 8.16.6.4.4, the Shear Friction Design Method. The nominal shear capacity across a potential cracking plane at the column face was calculated by considering the required amount of longitudinal reinforcement placed perpendicular to the potential shear plane and applying AASHTO Equation 8-56:

$$V_u \leq \Phi V_n = \Phi (A_{vf} f_y \mu) \quad [3-18]$$

where:

V_u	=	Applied factored shear from both reactions = 1098 kN (246.9 kips)
V_n	=	Nominal shear friction capacity = 1292 kN (291 kips)
Φ	=	Phi Factor = 0.85
A_{vf}	=	Required area of mild steel perpendicular to potential shear crack = 22 cm^2 (3.46 in^2)
μ	=	Coefficient of friction = 1.4.

Additionally, in Article 8.16.6.8.4, Special Provisions for Brackets and Corbels, an area of mild steel, A_h , shall be “uniformly distributed within two-thirds of the effective depth adjacent to A_s ” where the larger of

$$A_h = \left(\frac{A_{vf}}{3} \right) = 7.4 \text{ cm}^2 (1.15 \text{ in}^2) \quad [3-19]$$

or

$$A_h = 0.5(A_s) = 18 \text{ cm}^2 (2.8 \text{ in}^2) \quad [3-20]$$

determined the required area of shear friction steel.

The amount of shear friction reinforcement, 18 cm^2 (2.8 in^2), was reduced by the 2.4 cm^2 (0.38 in^2) area of side-face reinforcement that was located near mid-depth of the section, and by the 6.3 cm^2 (0.98 in^2) equivalent area of mild steel from the excess post-tensioning. Two rows of nine no. 2 bars were needed to form a portion of the confinement cages for the post-tensioning anchorage in the overhang and the joint. The lowest row was replaced by nine No. 3 bars to provide the top row of shear friction reinforcement (see Figure 3.15).

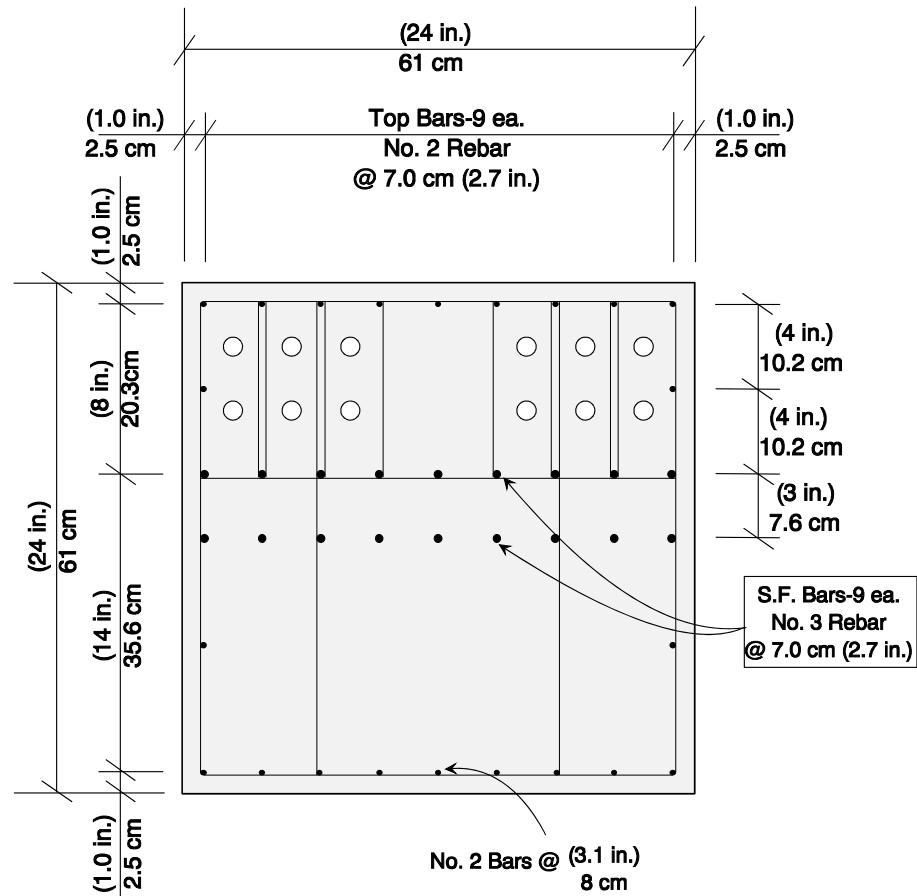


Figure 3.15 POJ-PS-100 Overhang Cross Section

Transverse Reinforcement in the Overhang:

The design procedure used for the San Antonio ‘Y’ Project did not consider any beneficial effects from the post-tensioning when computing the required area of transverse reinforcement in the overhang. The amount of transverse reinforcement in the overhang was computed using the same procedure as for the POJ-RC-100 test specimen.

Post-Tensioning Anchorage Reinforcement:

The amount of anchorage reinforcement was computed using the Guyon bursting stress equation:

$$T_b = \frac{P}{3}(1 - \gamma) \quad [3- 21]$$

and the Guyon spalling stress equation:

$$T_s = \frac{P}{4} \quad [3- 22]$$

where:

T_b	=	Tensile bursting stress = 23 kN (5.2 kips)
P	=	Maximum post-tensioning force = 310 kN (69.8 kips)
γ	=	Ratio of anchorage plate height to concrete cone limit (3.5 in. x 2)/(4.5 in. x 2) = 0.778
T_s	=	Maximum Tensile spalling stress = 78 kN (17.4 kips).

The area of required anchorage reinforcement was then computed by:

$$A_v = \frac{T_b}{f_s} + \frac{T_s}{f_s} \quad [3- 23]$$

where:

A_v	=	Area of anchorage reinforcement = 4.9 cm ² (0.75 in ²)
f_s	=	Allowable tensile stress = 166 MPa (24 ksi).

The anchorage reinforcement consisted of eight sets of interlocked No. 2 ties. The anchorage ties were threaded over the No. 2 longitudinal reinforcement and spaced at 4 cm (1.6 in.) to provide reinforcement that extended beyond the limits of a 45° crack that may form from the base of the anchorage plate to the top surface of the overhang (see Figure 3.16). The same amount of anchorage reinforcement was used for both the end of the overhang as well as the joint corner.

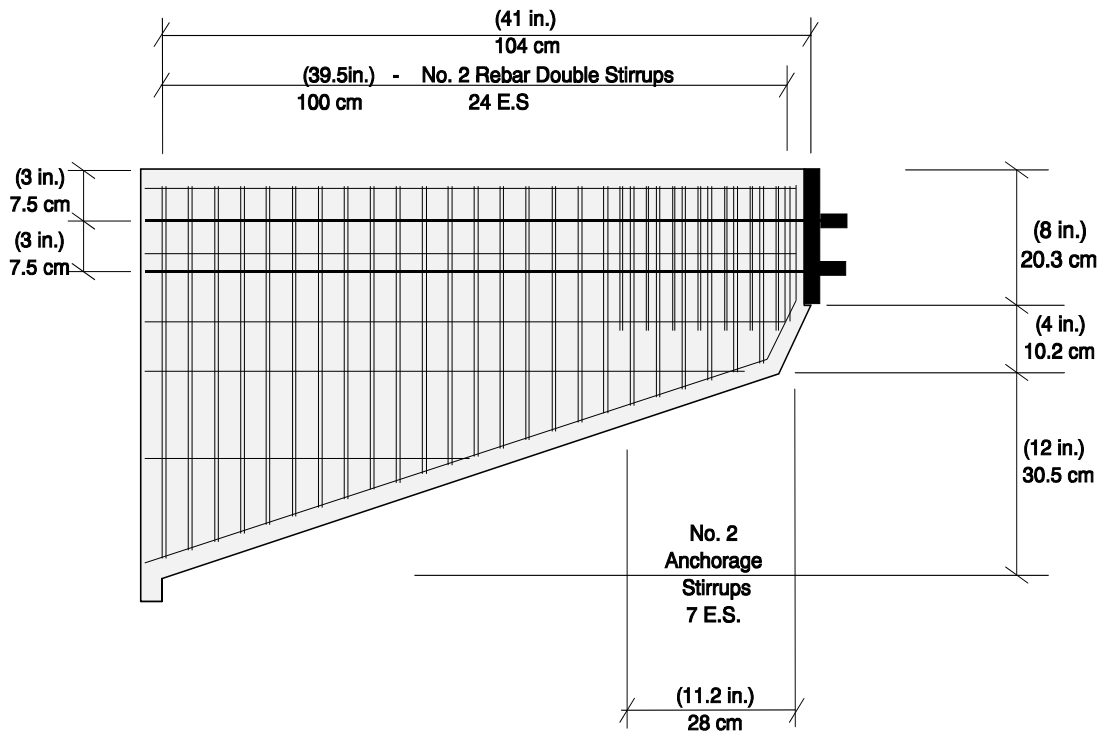


Figure 3.16 POJ-PS-100 Overhang Reinforcement Details

3.3.2.2 Pier Design - POJ-PS-100

Flexural Reinforcement:

The amount of flexural reinforcement in the pier (see Figure 3.17) was identical to that used for the POJ-RC-100 test specimen. The percentage of pier longitudinal reinforcement, which was $0.0155 A_g$, satisfied the minimum longitudinal column reinforcement ratio of $0.01 A_g$.

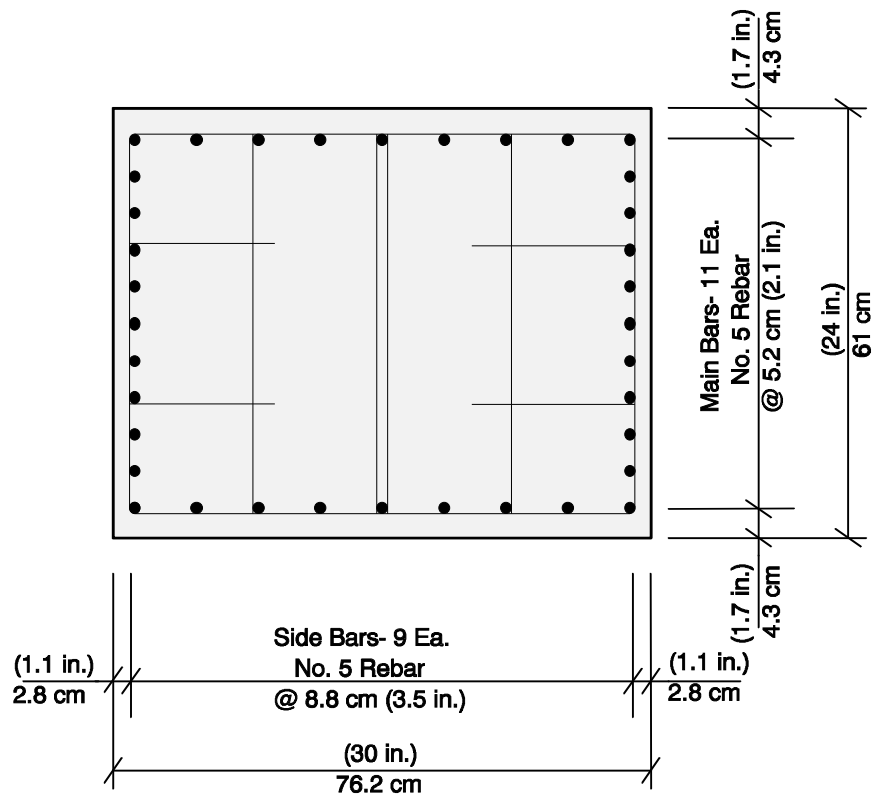


Figure 3.17 POJ-PS-100 Pier Reinforcement Details

3.3.2.3 Joint Design - POJ-PS-100

Bar Anchorage:

Anchorage of the pier and overhang reinforcement in the joint was assumed to be based on straight bar development. The bar development length was compared with the available embedment from the critical moment sections of the overhang and pier to the back and top of the joint. Because the bars used in the model have more than twice the straight bar development required by the specifications, hooks, welded plates, and other methods of positive anchorage were not provided.

Post-tensioning bars from the overhang provided a positive anchorage for the transfer of forces into the joint region. Although the shear friction reinforcement was not hooked in the joint region, it was placed deep into the joint where it could provide some contribution to the bent capacity. A majority of pier longitudinal reinforcement (all bars on the back face and some side-face bars) was cut short to provide space for the joint corner block-out that was used to conceal the post-tensioning hardware (see Figure 3.18). An elevation of the reinforcement used in Specimen POJ-PS-100 is presented in Figure 3.19.

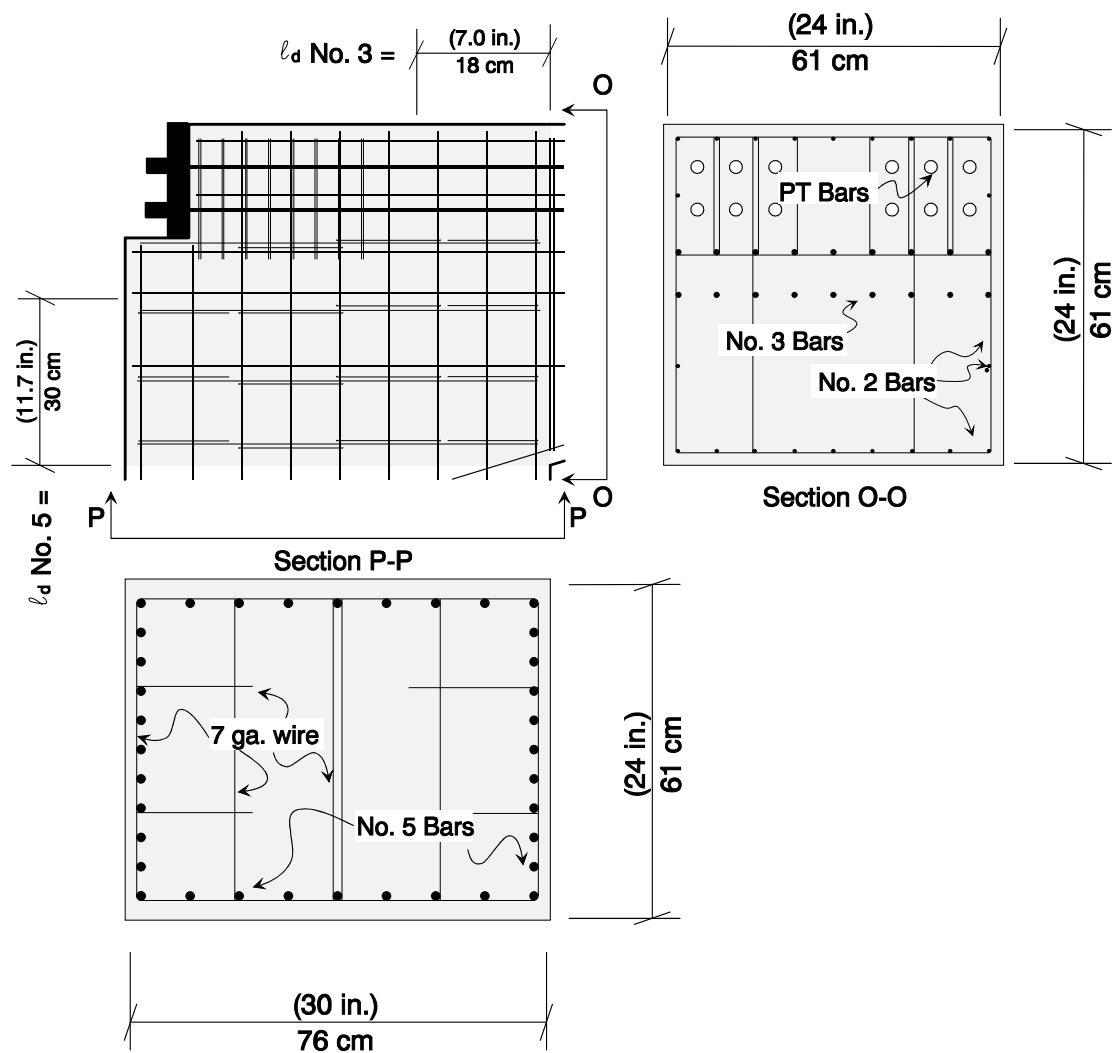


Figure 3.18 POJ-PS-100 Joint Reinforcement Details

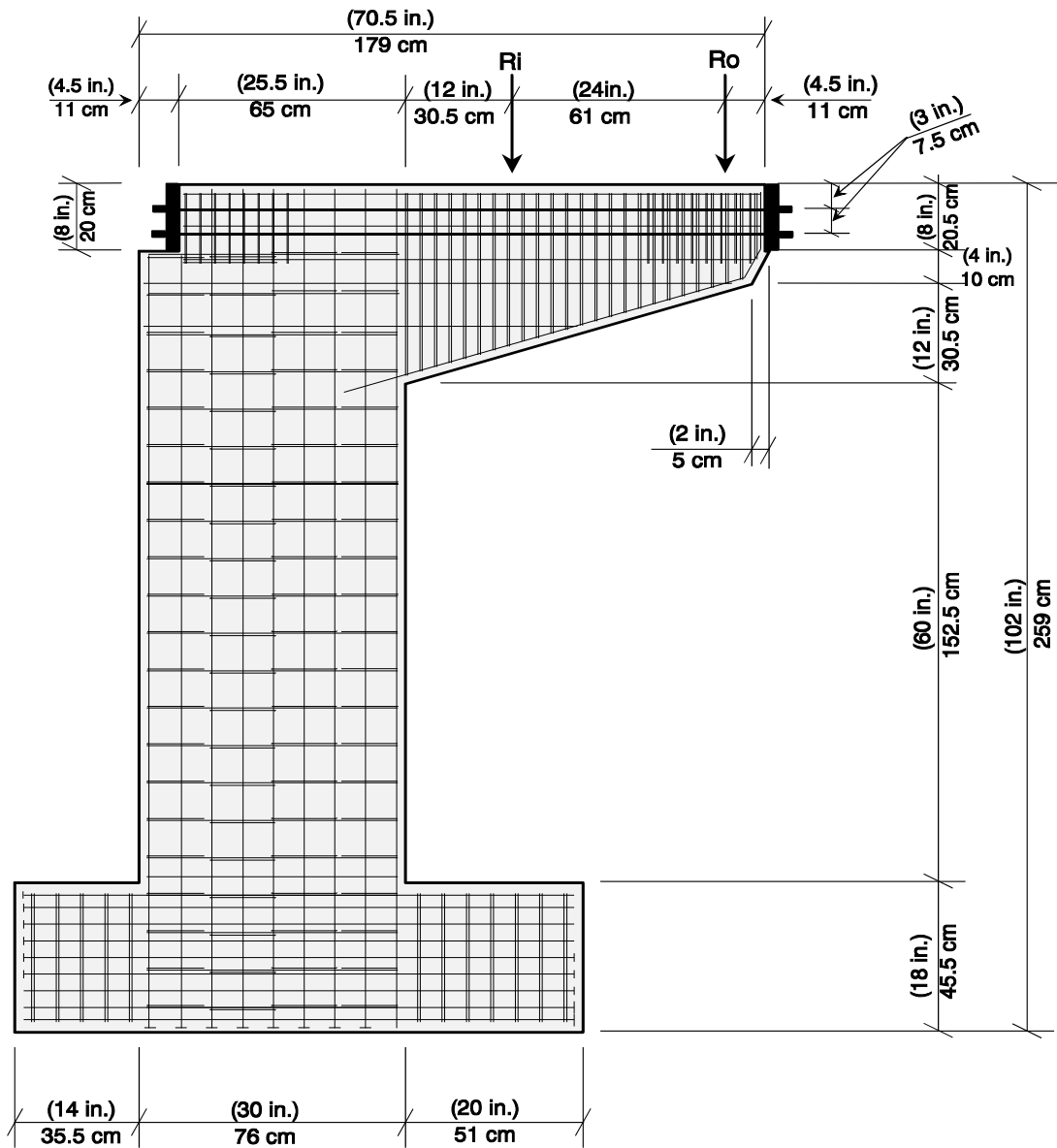


Figure 3.19 Elevation of Reinforcement for POJ-PS-100

3.3.2 Specimen with Fully-Prestressed Concrete Overhang - POJ-PS-100	46
3.3.2.1 Overhang Design - POJ-PS-100	46
3.3.2.2 Pier Design - POJ-PS-100.....	51
3.3.2.3 Joint Design - POJ-PS-100	52
Figure 3.14 PS-100 - Location of Post-Tensioning	46
Figure 3.15 POJ-PS-100 Overhang Cross Section.....	49
Figure 3.16 POJ-PS-100 Overhang Reinforcement Details.....	51
Figure 3.17 POJ-PS-100 Pier Reinforcement Details	52
Figure 3.18 POJ-PS-100 Joint Reinforcement Details.....	53
Figure 3.19 Elevation of Reinforcement for POJ-PS-100	54

3.4 Integrated Design Test Specimens

The remaining three Pier-Overhang-Joint test specimens were designed with combinations of prestressed and non-prestressed (mild) reinforcement. The approach used was based on the results and recommendations of the overhang study reported by Armstrong [3] and Salas [4]. Details of the design process are reported here.

3.4.1 Overview of the Integrated Design Method

The integrated design method utilized a strut-and-tie model to visualize a determinate path for transfer of forces through each specimen at factored loads. Combinations of high-strength prestressed reinforcement and mild steel were used to resist the tension tie forces. The amount and distribution of reinforcement were examined to limit steel stresses and control crack widths under service loads. A planar 2D finite element analysis model was used to compute the principal tensile and compressive stresses and aid in formulation of a determinate strut-and-tie model. Once geometry of the model was established, strut-and-tie forces were computed for applied factored loads.

3.4.1.1 Factored Load Resistance

Tie forces were used to compute required quantities of tensile reinforcement, and stresses in compression struts were compared with allowable stresses. Factored resistance of struts and ties was taken as the nominal resistance (T_n) times the appropriate resistance factor or phi factor. Phi factors for flexure and shear were 0.9 and 0.85, respectively.

Strength of Tension Ties:

Tie forces (primary flexural reinforcement) were provided by combinations of prestressed steel and longitudinal mild steel. The total resistance is

$$T_n = A_{ms} f_y + A_{ps} f_{su} \quad [3- 24]$$

where:

T_n	=	STM longitudinal tension tie force
A_{ms}	=	Area of mild steel primary flexural reinforcement
f_y	=	Nominal yield stress of mild reinforcement
A_{ps}	=	Area of prestressed primary flexural reinforcement
f_{su}	=	Prestressing steel stress at Ultimate Load.

Transverse tie reinforcement quantities were computed using:

$$T_n = A_{vs} f_y + 1\sqrt{f_c'} b_w d \quad [3- 25]$$

where:

T_n	=	STM tie force
A_{vs}	=	Total area of required shear reinforcement
f_y	=	Nominal yield stress of shear reinforcement
f_c'	=	Nominal concrete compressive stress (psi)
b_w	=	Beam width (in.)
d	=	Distance from extreme compression fiber to centroid of primary tension reinforcement at the location of the tension tie (in.).

Compression Strut Limits:

The compression stress limit at factored loads, $f_{c \max}$, was taken to be:

$$f_{c \max} = 0.85 f_c' \quad [3- 26]$$

where:

f_c'	=	Nominal concrete compressive stress.
--------	---	--------------------------------------

Reinforcement Detailing:

The area of skin reinforcement, A_{sk} , per foot of height for each side face of the overhang was based on the relationship established by Frantz and Breen [10] for control of side-face cracking:

$$A_{sk} = 0.0012 (d - 30) \text{ for } d > 36 \text{ in.} \quad [3- 27]$$

where:

A_{sk}	=	Area of side face reinforcement (in ²)
d	=	Distance from extreme compression fiber to centroid of primary tension reinforcement at maximum depth of the member (in.).

The minimum transverse reinforcement was designed in accordance with:

$$s_{\max} = \frac{A_v(f_y)}{50b_w} \leq d/2 \text{ and } \frac{24(in.)}{2.75} \quad [3- 28]$$

where:

s_{\max}	=	Maximum allowable transverse reinforcement spacing (in.)
A_v	=	Area of transverse reinforcement (in ²)
f_y	=	Nominal yield stress of transverse reinforcement (ksi)
b_w	=	Beam width in (in.).

The force flow indicated by the strut-and-tie model for each pier-overhang-joint specimen illustrates the need for positive anchorage of mild reinforcement in the joint region. These models will be presented later in Sections 3.4.3.2, 3.4.4.2, and 3.4.5.2. Interlocked headed mild reinforcing bars were used to provide positive anchorage in the joint region for all of the integrated design specimens.

3.4.1.2 Service Load Performance

A finite element analysis was used to compute the concrete principal tensile stresses to determine if and where cracking would occur. If the member was predicted to crack, tensile stresses were computed at dead load and service load using a cracked-section analysis to evaluate crack widths and fatigue stress ranges.

Distribution of Tension Reinforcement in Flexural Members:

The tensile stress was limited (by adjusting the amount and distribution of reinforcement) to control the width of cracks ($170 / \text{Scale Factor} = 62$).

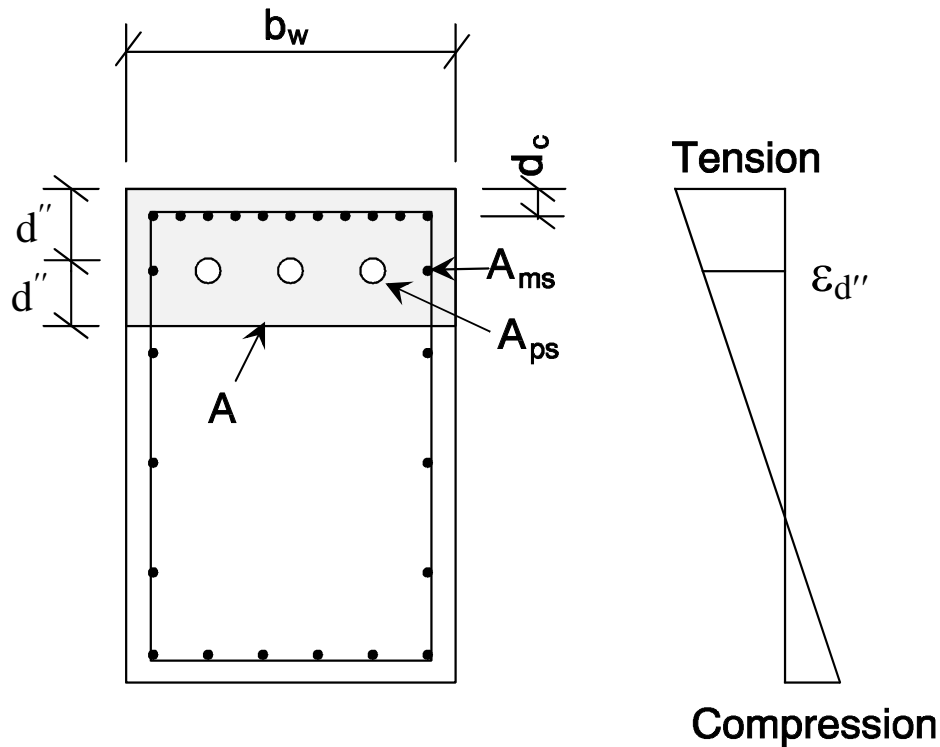


Figure 3.20 Identification of Crack-Width Control Variables

Variables used for the following equation are depicted in Figure 3.20, and are defined as follows:

$$f_{sa} \leq f_{sl} = \frac{Crk}{(d_c A)^{1/3}} \quad [3-29]$$

- f_{sa} = Steel tensile stress at a distance d'' from the extreme tensile fiber = $\epsilon_{d''}$ (29,000 ksi)
- $\epsilon_{d''}$ = Strain a distance d'' from the extreme tensile fiber based on a linear strain profile
- f_{sl} = Computed Limiting steel stress (ksi)
- Crk = Crack width limiting factor based on exposure criteria
= $(170 / 2.75) = 62$
- d_c = Distance from the extreme tension fiber to the centroid of the closest layer of primary tension reinforcement (in.)
- A = Area of tension block ($2 \times d'' \times b_w$) divided by the number of Prestressing strands and/or mild reinforcing bars located within the tension block [$\text{in}^2/\#$ bars]
- d'' = Distance from extreme tensile fiber to centroid of tensile reinforcement. (Areas of prestressed reinforcement, A_{ps} , located a distance, d_{ps} , from the extreme tensile fiber and/or areas of mild reinforcement, A_{ms} , located a distance, d_{ms} , from the extreme tensile fiber are considered in the equation.).

$$d'' = \frac{\left[\sum (A_{ps} f_{su}) d_{ps} + \sum (A_{ms} f_y) d_{ms} \right]}{\left[\sum A_{ps} f_{su} + \sum A_{ms} f_y \right]} \quad [3-30]$$

The value of f_{sa} was computed using a cracked-section analysis. Bonded prestressing steel (including estimates of long-term losses) was included in the calculation of f_{sa} . The value of f_{sa} was computed at the centroid of the primary tensile reinforcement, at a distance d'' from the extreme tension fiber. The value of f_{sa} determined from analysis should not exceed the value of f_{sl} from Eq. 3-29.

In order to avoid fatigue of reinforcement under service-level loads, the following stress ranges were checked for non-prestressed and prestressed reinforcement. Obviously, fatigue was not a concern during testing, but these service-level limits had the potential to change the quantity or distribution of reinforcement in each specimen.

Fatigue Stress Range:

The assumed fatigue stress range for the mild reinforcement was determined using AASHTO Equation 8-60:

$$f_f = 21 - 0.33f_{\min} + 2.4 \quad [3- 31]$$

where:

f_f = Maximum stress range (ksi) in mild steel reinforcement
 f_{\min} = Minimum stress level (at dead load) in (ksi).

The allowable stress range for the post-tensioning steel was 100 MPa (14.5 ksi) based on the recommendations of Wollman, et al [25].

3.4.2 Overview of Design Details

This section reviews the steps involved in the design of the three integrated design specimens: POJ-RC-100-TH, POJ-PU-54-TH, and POJ-PU-74-TH. Finite element analyses at dead-load and service-load levels were used to visualize the flow of forces through each specimen as well as estimate the level of tensile and compressive stresses that would develop at service-load levels in each specimen. The strut-and-tie models were produced so that the struts and ties were centered on the principal stress vectors predicted by the finite element method. The detailed design utilized the strut-and-tie model forces to proportion and locate the primary tensile reinforcement. Cross sections and side views of each specimen are presented to document bar sizes and bar locations for each specimen.

3.4.3 Design Details for the Reinforced Concrete Specimen with Headed Bars - POJ-RC-100-TH

The reinforced concrete specimen with headed bars (POJ-RC-100-TH) utilized interlocked headed reinforcement in the joint corner to provide a tensile force path through the joint.

3.4.3.1 Finite Element Analysis - POJ-RC-100-TH

An elastic finite element analysis of the reinforced concrete specimen with headed bars was used to visualize the flow of forces from the load points into the pier. Because the analysis did not consider non-linear material properties, the level of tensile stresses in some

areas was unrealistic. If the level of tensile stresses was above $7\sqrt{f'_c}$ (psi) [3.44 MPa (500 psi)], the region was considered to be cracked. Although the POJ-RC-100-TH specimen was computed to crack under dead load, the service load finite element analysis is included here to illustrate the increase in tensile stresses in the joint region. The test specimen was modeled using eight-node isoparametric elements. The finite element mesh is illustrated in Figure 3.21. Computed principal tensile and compressive stresses for dead-load and service-load levels are presented in the form of stress contours and principal tensile vectors in Figure 3.22 through Figure 3.25. The principal tensile stress contours at dead load indicated tensile stresses in the joint were nearly $7\sqrt{f'_c}$ (psi) [3.44 MPa (500 psi)]. It was clear from Figure 3.22 that cracking in the joint would occur at loads slightly above dead load. Plots of principal tensile and compressive stress vectors aided the development of a strut-and-tie model.

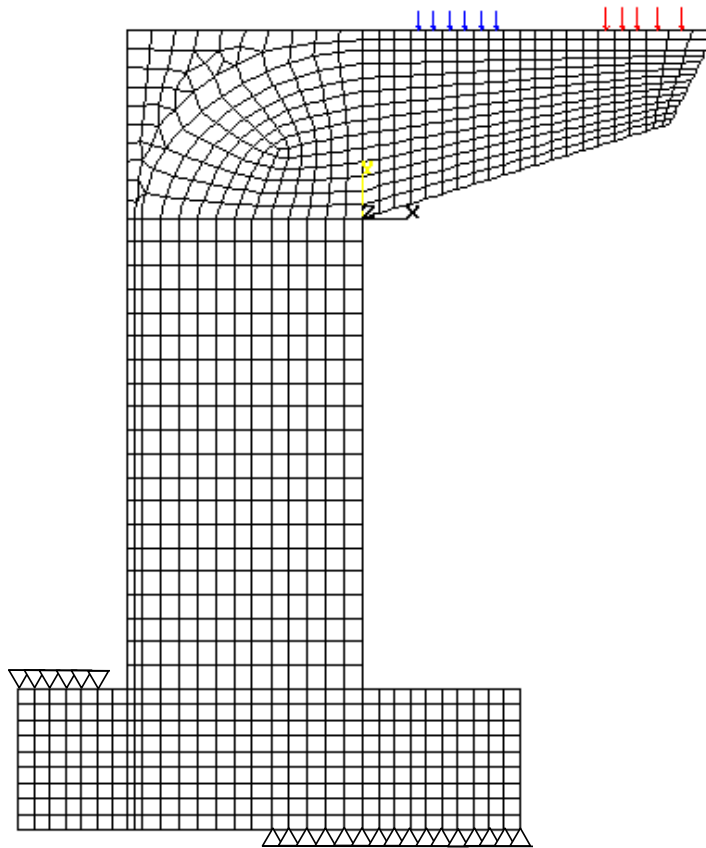


Figure 3.21 Finite Element Model for the POJ-RC-100-TH Specimen

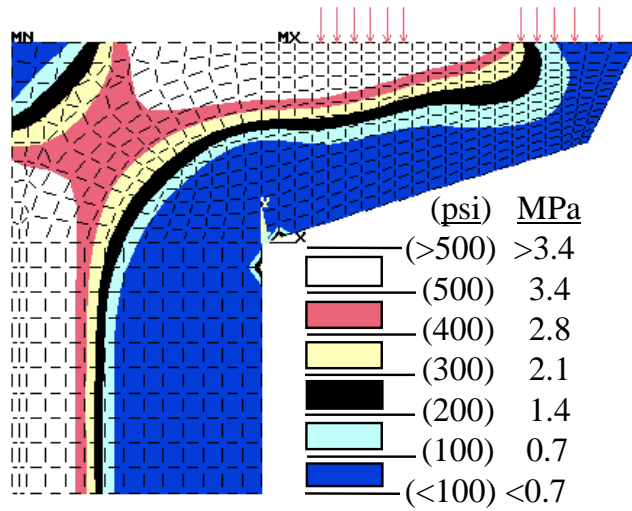


Figure 3.22 POJ-RC-100-TH - Principal Tensile Stresses and Vectors at Dead Load

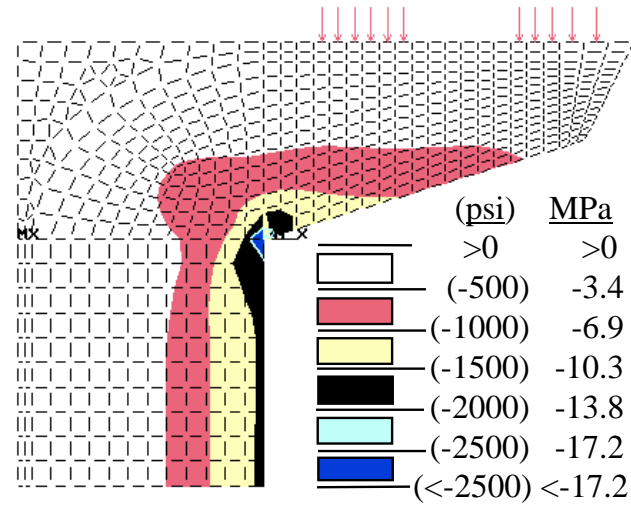
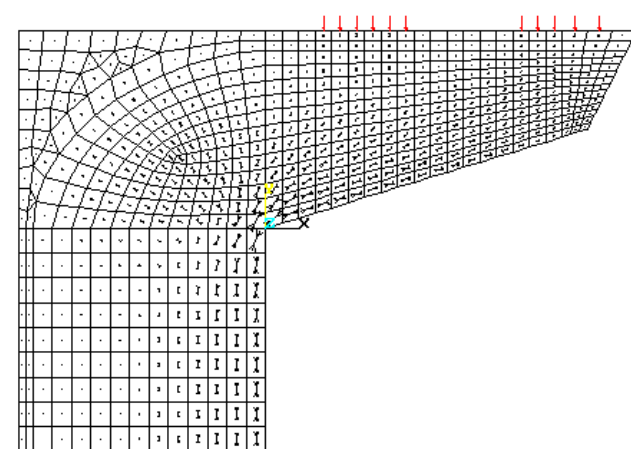
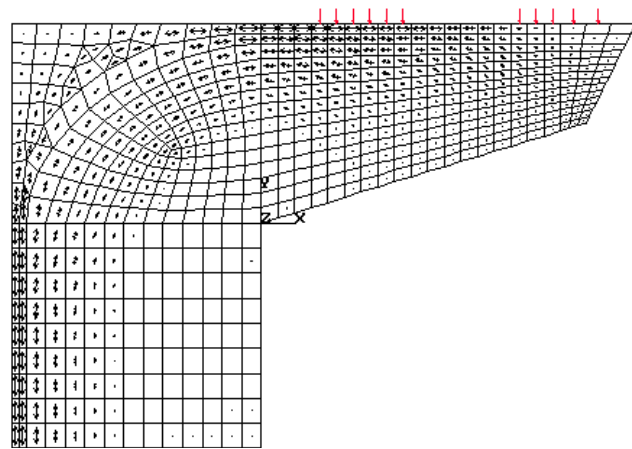


Figure 3.23 POJ-RC-100-TH - Principal Compressive Stresses and Vectors at Dead Load.



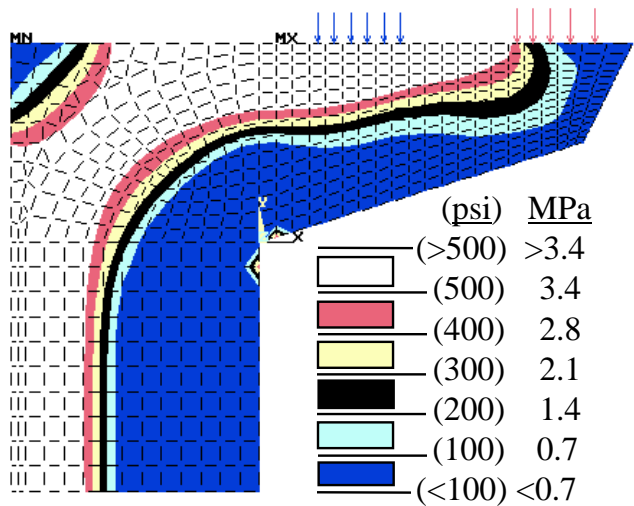


Figure 3.24 POJ-RC-100-TH - Principal Tensile Stresses and Vectors at Service Load

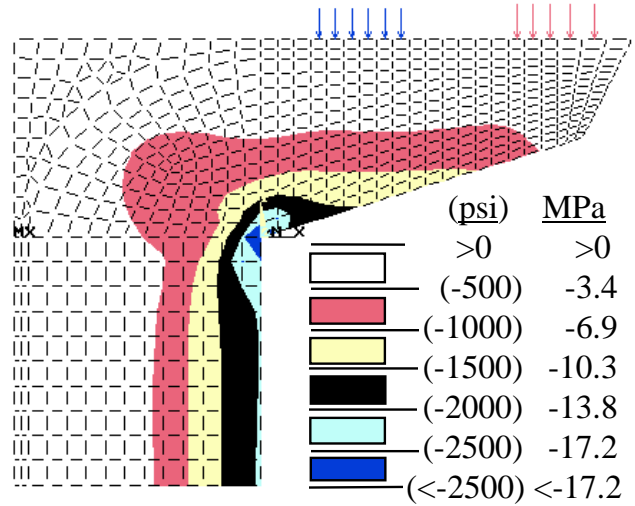
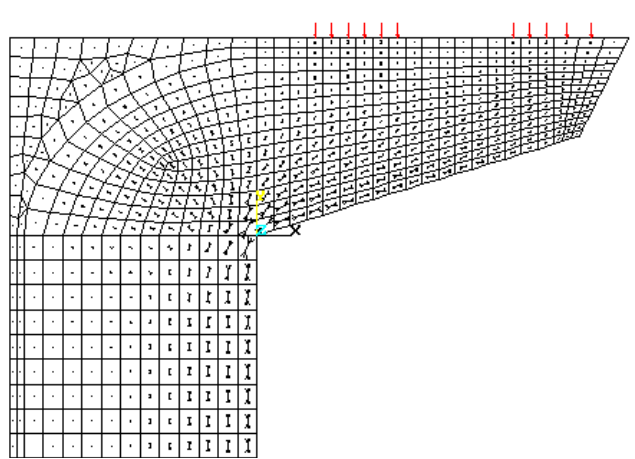
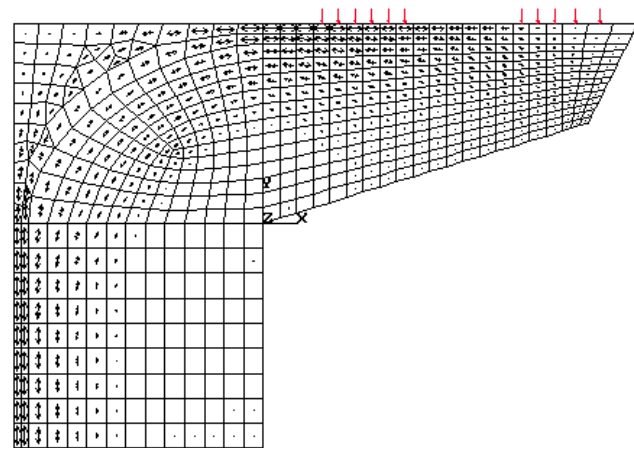


Figure 3.25 POJ-RC-100-TH - Principal Compressive Stresses and Vectors at Service Load



3.4.3.2 Strut-and-Tie Model - POJ-RC-100-TH

The strut-and-tie model shown in Figure 3.26 was based loosely on the principal stress vectors presented in Figure 3.24 and Figure 3.25. Details about the computation of reinforcement corresponding with the tension ties shown in Figure 3.26 are presented in the following subsections.

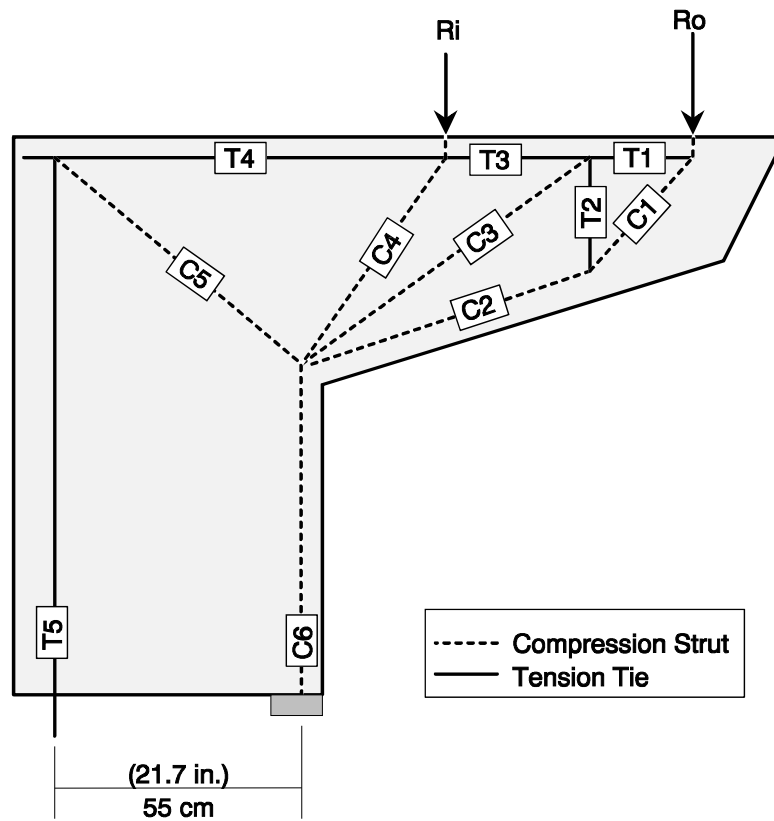


Figure 3.26 POJ-RC-100-TH - Strut-and-Tie Model

3.4.3.3 Overhang Design Details - POJ-RC-100-TH

Longitudinal Reinforcement:

The amount of longitudinal reinforcement in the overhang was determined using the maximum force in the top cord (Tension Tie T4) of the strut-and-tie model (STM). The amount of reinforcement required to resist the model factored loads was computed by:

$$T_4 \leq \Phi(A_s f_y) \quad [3-32]$$

where:

T_4	=	STM tension tie force = 1368 kN (307.5 kips)
Φ	=	Phi factor = 0.9
A_s	=	Area of primary flexural reinforcement = 36 cm ² (5.6 in ²)
f_y	=	Nominal yield stress of mild reinforcement = 414 MPa (60 ksi).

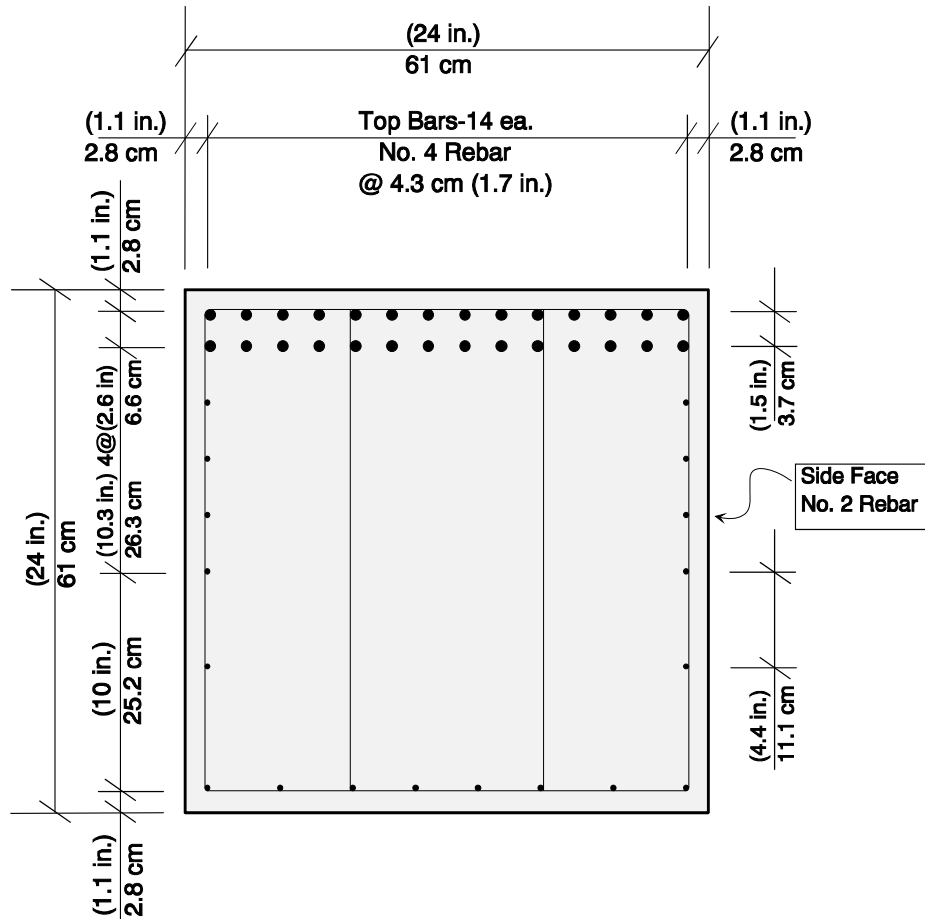


Figure 3.27 POJ-RC-100-TH - Overhang Cross Section Details

The area of mild steel required by the equation was equal to that computed using AASHTO Equation 8-15. Based on the STM, no shear friction reinforcement was provided. Side-face reinforcement was determined using the Frantz and Breen relationship presented in Eq. 3-27. The quantity of side face reinforcement was computed to be 1.3 cm² (0.19 in²) per face. Details of the longitudinal reinforcement in the overhang at a cross section adjacent to the pier are shown in Figure 3.27. Once the amount of side-face reinforcement was computed, a

cracked-section analysis (considering all longitudinal reinforcement) was conducted to determine the steel stresses at service and dead loads. Steel stresses were used to check crack-widths and determine the maximum stress range.

Serviceability Provisions:

Crack widths were intended to be controlled by the relationship presented in Eq. 3-29. The average steel stress due to service loads was computed to be 252 MPa (36.5 ksi), and was less than the stress, f_{sl} , of 278 MPa (40.3 ksi) associated with the limiting crack width.

The fatigue stress range was determined by computing the difference in steel stresses in the top-most reinforcing bars resulting from service loads and dead loads. Stress in the top reinforcing bars was 200 MPa (29.1 ksi) for dead loads and 264 MPa (38.3 ksi) due to service loads. The resulting 63 MPa (9.2 ksi) stress range was within the allowable fatigue stress range of 95 MPa (13.8 ksi) computed by Eq. 3-28. The peak stress in the reinforcement was greater than $0.6f_y = 248$ MPa (36 ksi).

Transverse Reinforcement:

Only one vertical tie (Tension Tie T2) was considered in the STM. The quantity of transverse reinforcement required to resist the tension tie force (T2) of 367 kN (82.6 kips) was computed using Eq. 3-25. The resulting quantity of transverse reinforcement, A_{vs} , was 7.9 cm^2 (1.22 in^2). The $1\sqrt{f'_c} b_w d$ contribution was included to account for a concrete contribution to shear strength, which reduced the required amount of transverse reinforcement. Results from the overhang study performed by Armstrong [3] and Salas [4] indicated the strut-and-tie analysis overestimated the required amount of transverse reinforcement. The inclusion of a concrete contribution significantly reduced congestion of transverse reinforcement located in the region of the T2 tension tie, and provided a more economical design with sufficient strength to resist factored loads. The tension tie reinforcement was uniformly spaced over a distance equal to the effective depth, d , of the section at the tension tie.

Minimum transverse reinforcement was provided over the remainder of the overhang according to the equation for maximum spacing (Eq. 3-28). This maximum spacing was

18 cm (7 in.), and was determined for an effective depth, d , of 36 cm (14 in.). Transverse reinforcement details are presented in Figure 3.28.

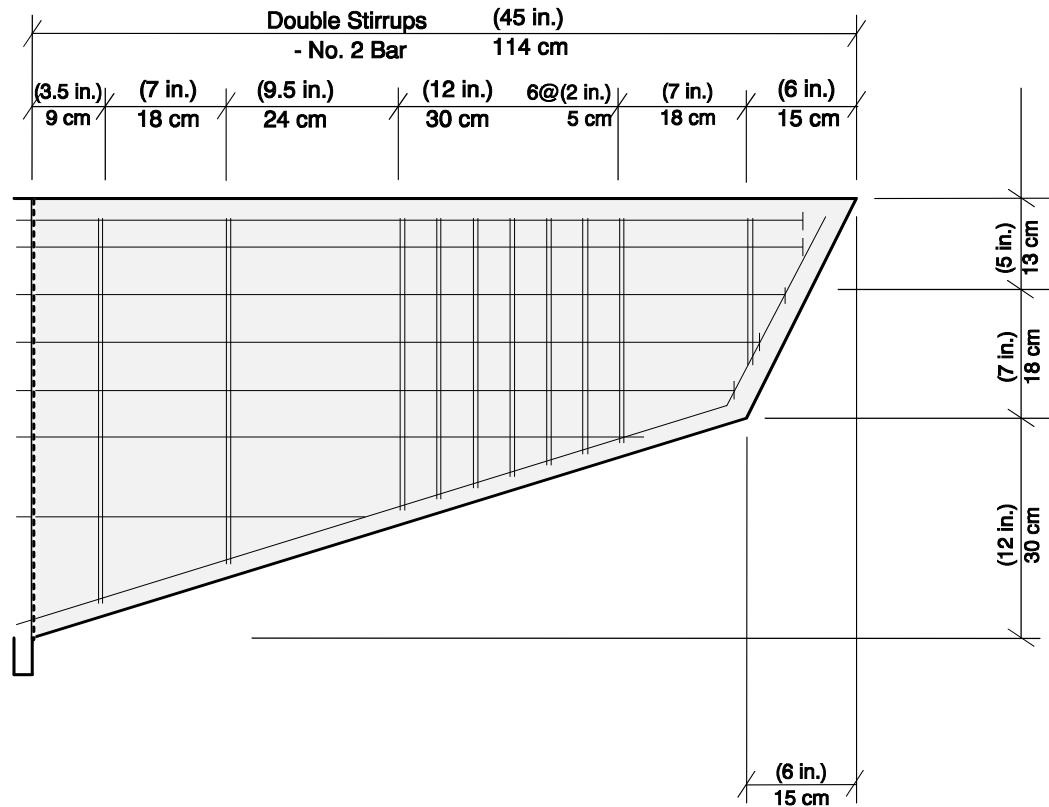


Figure 3.28 POJ-RC-100-TH - Transverse Reinforcement Details

3.4.3.4 Pier Details - POJ-RC-100-TH

Pier longitudinal reinforcement was determined using a strut-and-tie model and cracked-section analysis. The total area of longitudinal pier reinforcement for Specimen POJ-RC-100-TH was identical to that for Specimen POJ-RC-100. The distribution of longitudinal pier reinforcement was also the same to determine the effect headed reinforcement had on specimen capacity. However, it should be noted that the distribution of longitudinal reinforcement in the pier did not satisfy serviceability requirements.

Longitudinal Reinforcement:

The quantity of longitudinal reinforcement was based on the tie force, T_5 , of the STM illustrated in Figure 3.26. The amount of reinforcement required to resist factored loads was computed by:

$$T_5 \leq \Phi(A_s f_y) \tag{3- 33}$$

where:

- T_5 = STM tension tie force = 1420 kN (319 kips)
- Φ = Phi factor = 0.8 based on the level of axial load
- A_s = Area of primary flexural reinforcement = 43.3 cm² (6.72 in²)
- f_y = Nominal yield stress of mild reinforcement = 414 MPa (60 ksi).

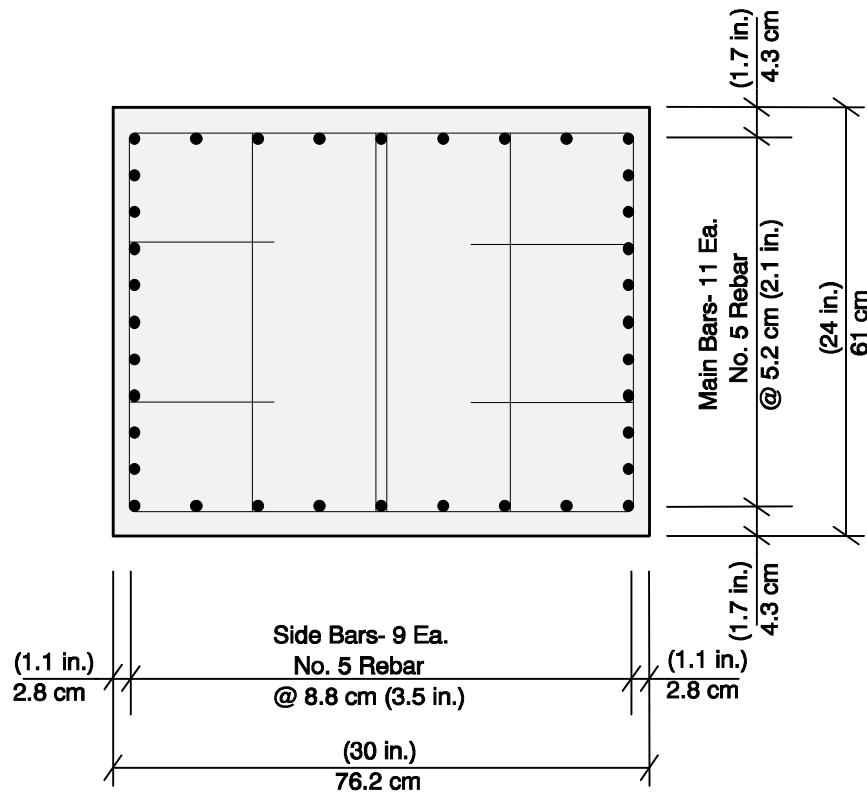


Figure 3.29 POJ-RC-100-TH - Pier Cross Section Details

Transverse Reinforcement:

Transverse reinforcement was detailed using AASHTO Article 8.18.2.3. The transverse tie-spacing and bar-size requirements were divided by the 2.75 scale factor. The No. 4 minimum bar size specified in AASHTO was modeled using 7 ga. wire. The specified

minimum longitudinal tie spacing of 30 cm (12 in.) was divided by the 2.75 scale factor, resulting in a tie spacing of 11 cm (4.4 in.). The specified maximum distance to a restrained bar of 61 cm (2 ft) was divided by the 2.75 scale factor resulting in a distance of 22 cm (8.7 in.). Detailing of the transverse reinforcement and the distribution of longitudinal reinforcement in the pier is illustrated in Figure 3.29. A cracked-section analysis was conducted to determine steel stresses due to service loads and dead loads to check crack-widths and determine the maximum stress range.

Serviceability Provisions:

Crack widths were checked using the relationship presented in Eq. 3-29. The average steel stress due to service loads was computed to be 203 MPa (29.4 ksi), which was greater than the stress, f_{st} , of 165 MPa (23.9 ksi) associated with the limiting crack width. Although the equation was not satisfied, the bar distribution in the pier was not modified in order to evaluate the performance of the headed reinforcement (see Sections 3.3.1.3 and 3.4.3.5).

The fatigue stress range was determined by computing the difference in steel stresses in the extreme tensile reinforcing bars resulting from service loads and dead loads. Stress in the reinforcing bars was 213 MPa (30.9 ksi) due to dead loads and 278 MPa (40.3 ksi) due to service loads. The resulting stress range of 65 MPa (9.4 ksi) was within the allowable fatigue stress range of 112 MPa (13.2 ksi) computed by Eq. 3-28. Peak stress in the reinforcement at service load was 278 MPa (40.3 ksi), which was greater than $0.6f_y = 248$ MPa (36 ksi).

3.4.3.5 Joint Details - POJ-RC-100-TH

Bar Anchorage:

The use of headed reinforcement in the joint region assured development of the longitudinal reinforcement beginning at the face of the steel plate. This facilitated the formation of tension ties through the joint region and a diagonal compression strut between the interlocking heads and the opposite (compression) corner of the joint (see Figure 3.30).

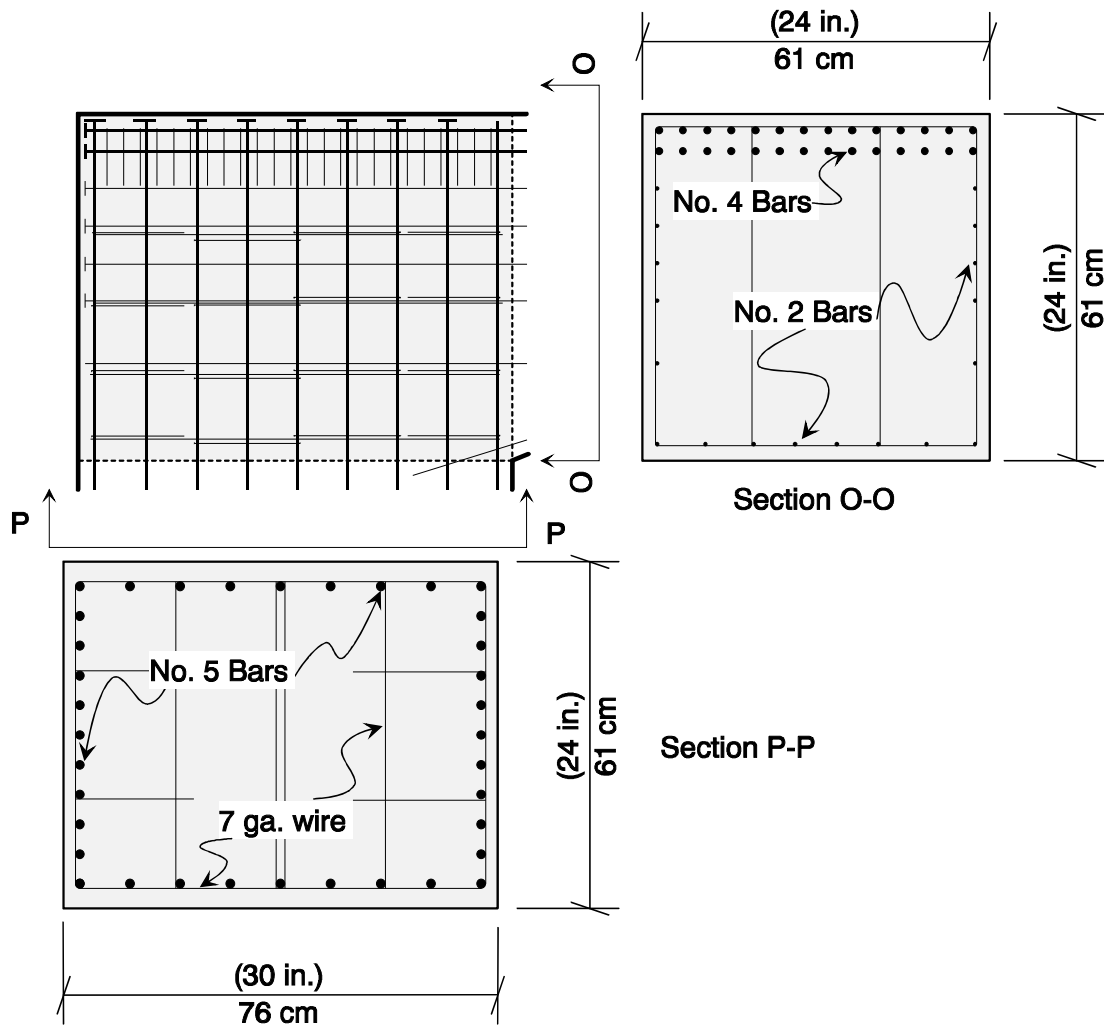


Figure 3.30 POJ-RC-100-TH Joint Reinforcement Details

Specimen strength was computed using the model that will be presented in Section 7.2. Because all of the primary tensile reinforcement in the overhang and pier were fully developed at the anchor head, the computed capacity was 1.26 times the strength required to resist applied factored loads. Reinforcement details for the joint and complete specimen are illustrated in Figure 3.30 and Figure 3.31, respectively.

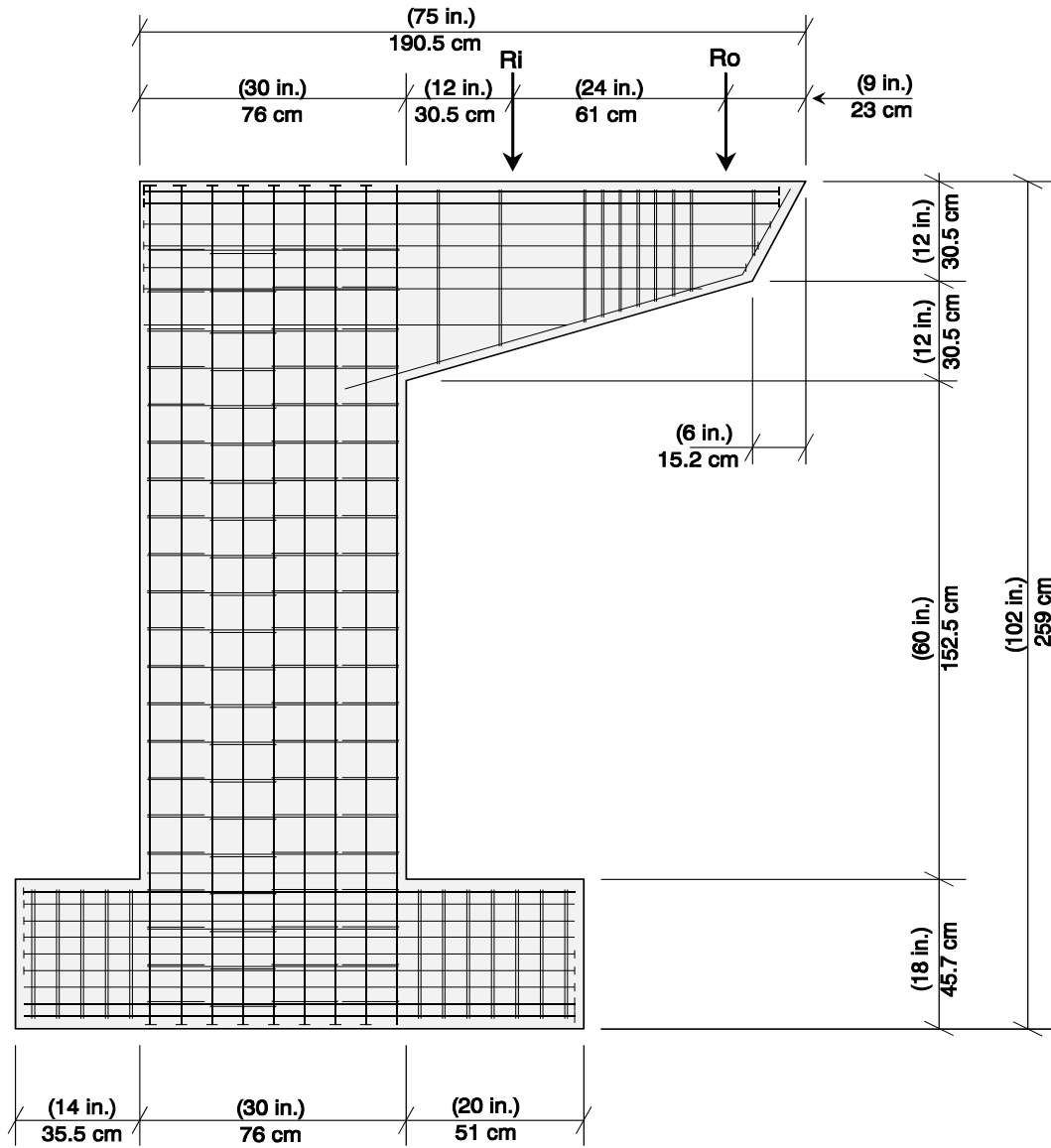


Figure 3.31 POJ-RC-100-TH Complete Reinforcement Details

3.4 Integrated Design Test Specimens.....	55
3.4.1 Overview of the Integrated Design Method.....	55
3.4.1.1 Factored Load Resistance	55
3.4.1.2 Service Load Performance	57
3.4.2 Overview of Design Details	59
3.4.3 Design Details for the Reinforced Concrete Specimen with Headed Bars - POJ-RC-100-TH	59
3.4.3.1 Finite Element Analysis - POJ-RC-100-TH	59
3.4.3.2 Strut-and-Tie Model - POJ-RC-100-TH.....	63
3.4.3.3 Overhang Design Details - POJ-RC-100-TH.....	63
3.4.3.4 Pier Details - POJ-RC-100-TH	66
3.4.3.5 Joint Details - POJ-RC-100-TH.....	68
Figure 3.20 Identification of Crack-Width Control Variables	57
Figure 3.21 Finite Element Model for the POJ-RC-100-TH Specimen.....	60
Figure 3.22 POJ-RC-100-TH - Principal Tensile Stresses and Vectors at Dead Load.....	61
Figure 3.23 POJ-RC-100-TH - Principal Compressive Stresses and Vectors at Dead Load...61	
Figure 3.24 POJ-RC-100-TH - Principal Tensile Stresses and Vectors at Service Load	62
Figure 3.25 POJ-RC-100-TH - Principal Compressive Stresses and Vectors at Service Load62	
Figure 3.26 POJ-RC-100-TH - Strut-and-Tie Model.....	63
Figure 3.27 POJ-RC-100-TH - Overhang Cross Section Details	64
Figure 3.28 POJ-RC-100-TH - Transverse Reinforcement Details	66
Figure 3.29 POJ-RC-100-TH - Pier Cross Section Details.....	67
Figure 3.30 POJ-RC-100-TH Joint Reinforcement Details	69
Figure 3.31 POJ-RC-100-TH Complete Reinforcement Details	70

3.4.4 54% Prestressed Design with T-Headed Bars - POJ-PU-54-TH

The 54% prestressed specimen contained three post-tensioned tendons that were continuous through the overhang, joint, and pier. The percentage (54%) indicates the portion of tie force in the overhang that was provided by tendons.

3.4.4.1 *Finite Element Analysis - POJ-PU-54-TH*

Finite element analysis of the 54 percent prestressed specimen utilized a more complex ANSYS 5.0 [32] model than was used for the reinforced concrete specimen. The finite element model was developed by generating separate meshes for the post-tensioning tendon (one tendon in the FE model represented all tendons in the actual specimen) and concrete members, then introducing displacement compatibility links between the tendon nodes and concrete nodes. Tendon nodes were free to displace along the concrete mesh, but concrete and tendon nodal displacements were linked normal to the tendon path. Friction losses were not included in the finite element analysis.

Mesh boundaries were established by generating a continuous line that passed through the overhang, joint, and pier. A spline curve was used in the joint region to produce the arc. Once straight portions of the tendon path in the overhang and pier were generated, the spline arc was generated in the joint to connect the end points of the overhang and pier sections of the tendon. Ends of the spline were required to have the same slope as the connecting segments. Once tendon geometry was established, the concrete model was generated using the tendon profile as a boundary for the concrete elements.

Once the eight-node isoparametric plane-stress elements were generated, the two-node link elements were generated on a set of coincident nodes. Compatibility between the tendon and concrete was established by linking the X or Y deformations of concrete-element nodes and nodes for the tendon elements. Local-coordinate nodes on the concrete elements and tendon elements were rotated tangent to the tendon path. The tangent rotation angle was determined using an EXCEL spreadsheet [33]. If the rotation angle for the X axis was greater than 0.785 Radians (45°), the Y-axis was rotated. Once the nodes were rotated, local X or Y

displacements of the coincident nodes were linked, depending on which axis was rotated and the orientation of the tendon path (See Figure 3.32).

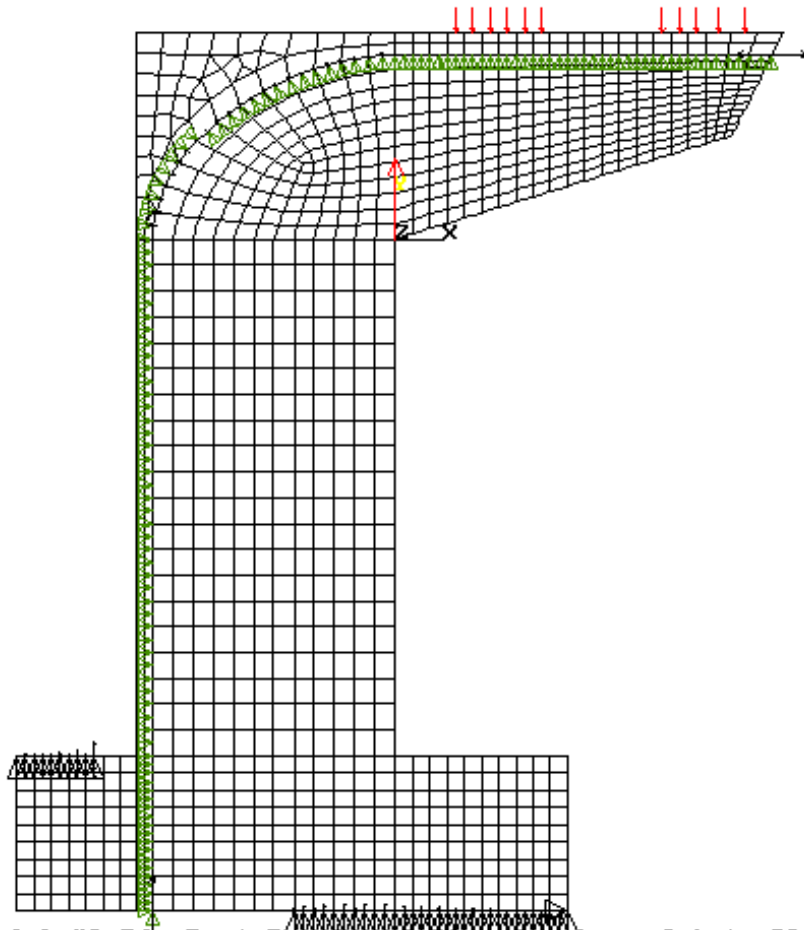


Figure 3.32 Finite Element Model for Specimen POJ-PU-54-TH

Tendon elements in the model were “stressed” by applying a concentrated load on the tendon at the tip of the overhang and an equal and opposite concentrated load on the specimen. Because the points on the tip of the overhang were coincident, there was no eccentricity created at the point of load application. The other end of the tendon was fixed at a point in the base of the model. The hold-down member at the base of the specimen (on the left side of Figure 3.32) was fixed against vertical displacement at the top. The base of the specimen (from a point near the center of the pier and extending to the tip of the stub on the right side of Figure 3.32) was fixed from vertical displacement at the bottom. A single point

at the tip of the base member was fixed from horizontal displacement to stop rigid-body displacements.

Finite element analyses were performed for service loads and dead loads. Because the analyses did not consider non-linear material properties, tensile stresses in some areas may be over-estimated. If tensile stresses were above $7\sqrt{f_c'}$ (psi) [3.44 MPa (500 psi)], the region was considered cracked. Although the POJ-PU-54-TH specimen was computed to crack under dead loads, finite element analysis was also performed at service loads to illustrate the increase in tensile stresses in the joint. Computed principal tensile and compressive stresses for dead-load and service-load levels are presented as stress contours and vectors in Figure 3.33 through Figure 3.36. Principal tensile contours at dead load indicated stresses in the overhang and pier were greater than the $7\sqrt{f_c'}$ (psi) [3.44 MPa (500 psi)] concrete cracking stress. However, principal tensile stresses across the joint diagonal were less than $2.8\sqrt{f_c'}$ (psi) [1.38 MPa (200 psi)] at dead load, and less than $5.6\sqrt{f_c'}$ (psi) [2.76 MPa (400 psi)] at service load. This was a significant improvement over principal tensile stresses plotted for Specimens POJ-RC-100 and POJ-RC-100-TH. As before, principal tensile and compressive stress vectors were used to aid in development of a strut-and-tie model.

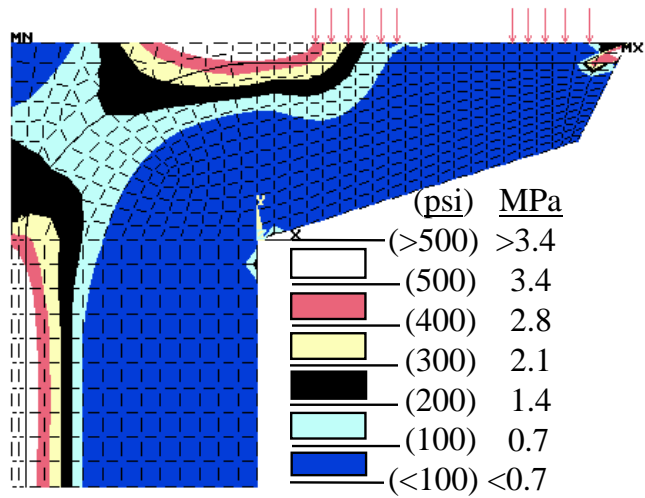


Figure 3.33 POJ-PU-54-TH Principal Tensile Stress Contours and Vectors at Dead Load

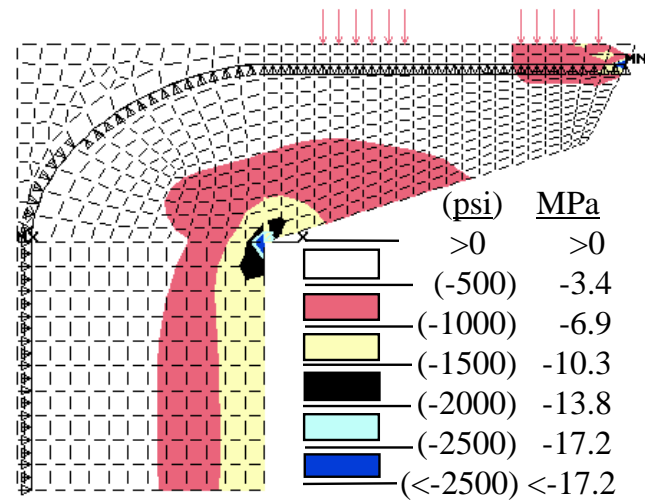
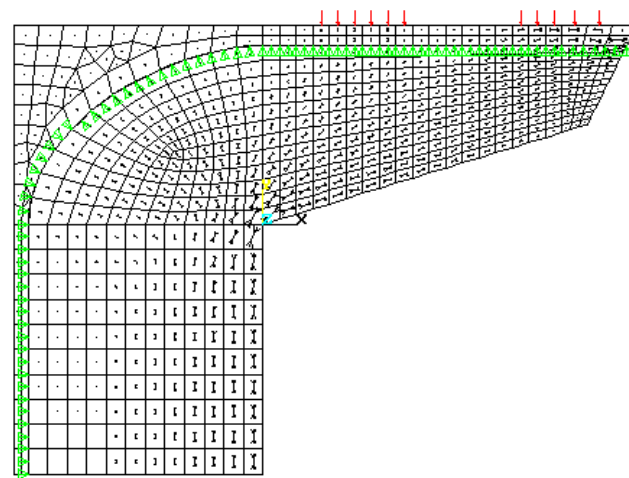
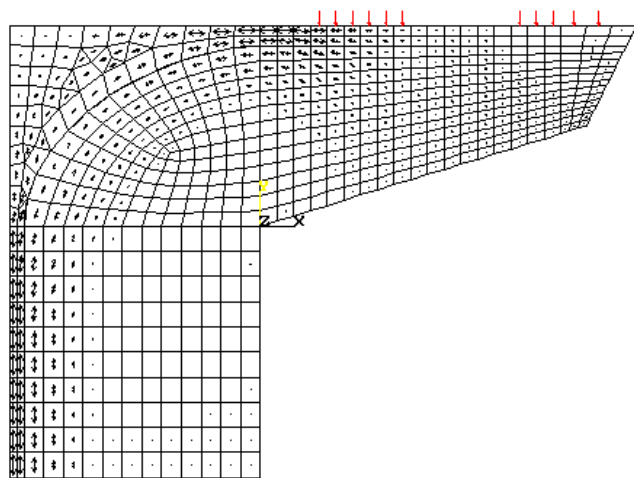


Figure 3.34 POJ-PU-54-TH Principal Compressive Stress Contours and Vectors at Dead Load



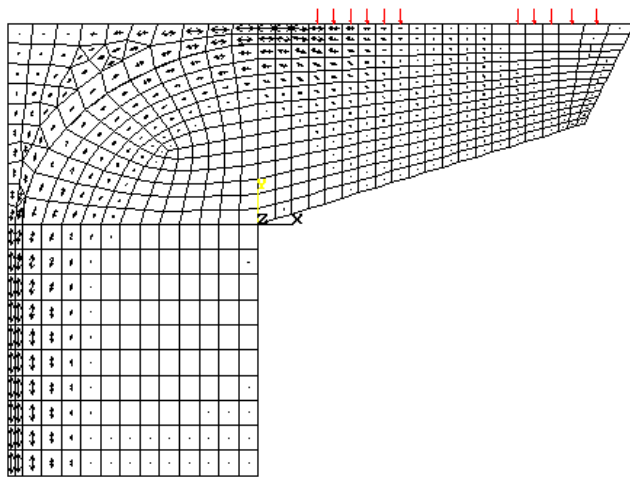
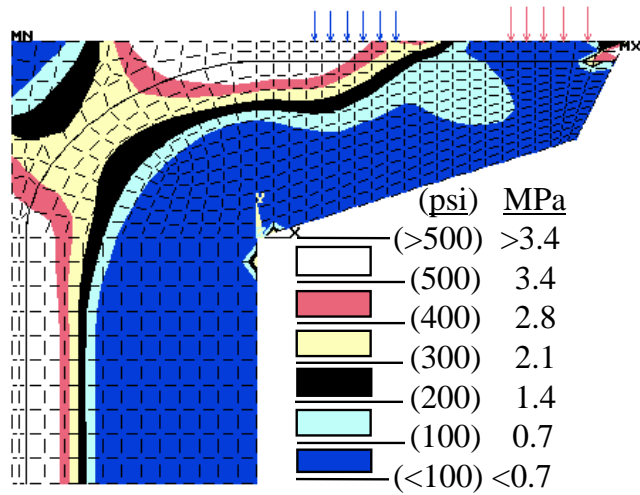


Figure 3.35 POJ-PU-54-TH Principal Tensile Stress Contours and Vectors at Service Load

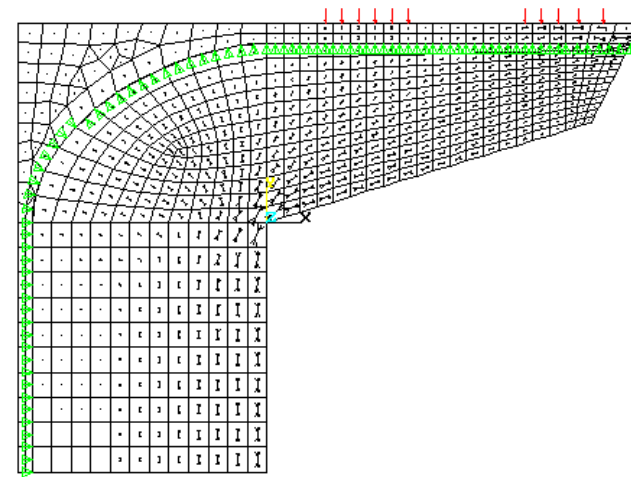
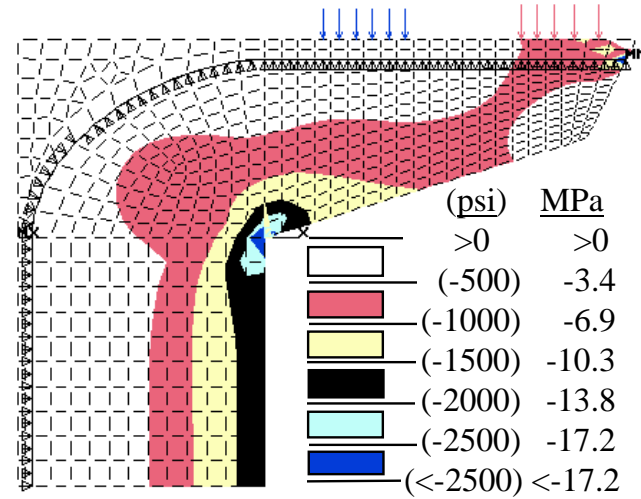


Figure 3.36 POJ-PU-54-TH Principal Compressive Stress Contours and Vectors at Service Load

3.4.4.2 Strut-and-Tie Model - POJ-PU-54-TH

The strut-and-tie model is intended to represent the flow of forces implied by the principal stress vectors presented in Figure 3.35 and Figure 3.36. Principal tensile and compressive stress vectors were used to aid in positioning tension ties and compression struts, respectively. Details about the computation of reinforcement corresponding with the tension ties shown in Figure 3.37 are presented in the following subsections.

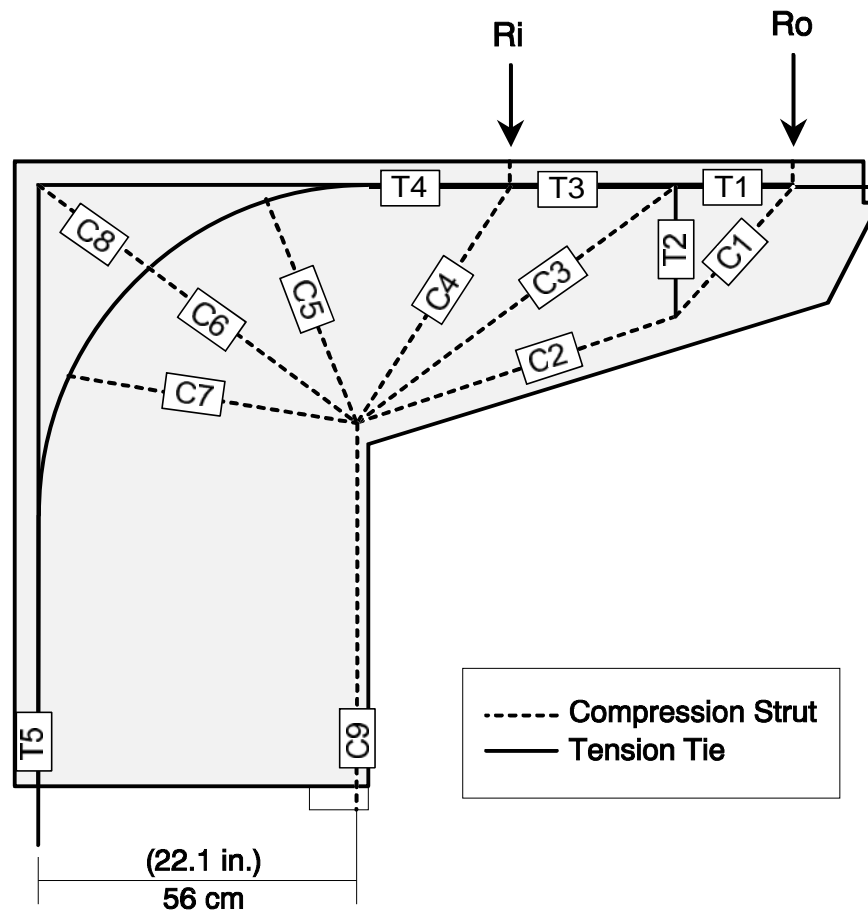


Figure 3.37 POJ-PU-54-TH Strut-and-Tie Model

3.4.4.3 Overhang Details - POJ-PU-54-TH

Longitudinal Reinforcement:

The amount of longitudinal reinforcement in the overhang was determined using the maximum force in the top cord (Tension Tie T4) of the strut-and-tie model. The amount of reinforcement required to resist the model factored loads was computed by:

$$T_4 \leq \Phi (A_{ms} f_y + A_{ps} f_{pu}) \quad [3-34]$$

where:

T4	=	STM tension tie force = 1414 kN (318 kips).
Φ	=	Phi factor = 0.9
A_{ms}	=	Area of mild steel primary flexural reinforcement
	=	15.4 cm ² (2.4 in ²)
f_y	=	Nominal yield stress of mild reinforcement = 414 MPa (60 ksi)
A_{ps}	=	Area of prestressed primary flexural reinforcement
	=	4.16 cm ² (0.645 in ²)
f_{pu}	=	Prestressing steel stress at Ultimate Load = 1860 MPa (270 ksi).

The quantity of mild steel provided was 46 % of the tension tie force (T4), and the quantity of prestressing steel provided was 54% of the tension tie force. Based on the strut-and-tie model, there was no need to provide shear-friction reinforcement. Side-face reinforcement was determined using the Frantz and Breen [10] relationship presented in Eq. 3-27. The quantity of side face reinforcement was computed to be 1.3 cm² (0.19 in²) per face. Details of the longitudinal overhang reinforcement at the cross section adjacent to the pier are shown in Figure 3.39.

Selection of Post-Tensioning Reinforcement:

The quantity of post-tensioned steel was provided by three -15 mm (0.6 in.) diameter strands, located 4.8 cm (1.9 in.) from the extreme tension fiber. The location and spacing of the post-tensioned steel is presented in Figure 3.38.

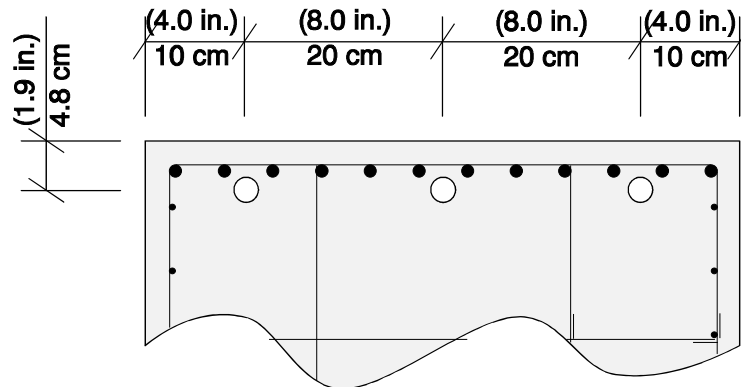


Figure 3.38 POJ-PU-54-TH Location of Post-Tensioning Tendons

Once the amount of side-face reinforcement was computed, a cracked-section analysis (considering all longitudinal reinforcement) was conducted to determine the steel stresses at service and dead loads. Steel stresses were used to check crack widths and determine the maximum stress range.

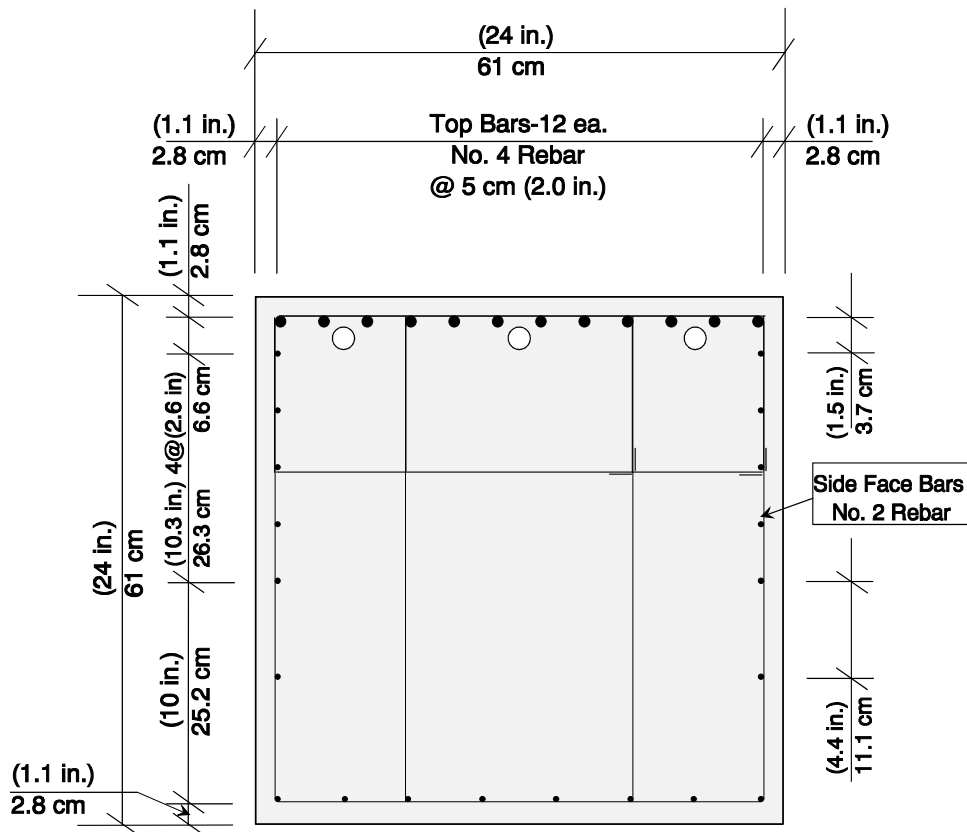


Figure 3.39 POJ-PU-54-TH Overhang Cross-Section Details

Serviceability Provisions:

Flexural crack widths were intended to be controlled by the relationship presented in Eq. 3-29. The average steel stress due to service loads was computed to be 241 MPa (34.9 ksi), and was less than the stress, f_{sl} , associated with the limiting crack width.

The fatigue stress range was determined by computing the difference in steel stresses in the top-most reinforcing bars resulting from service loads and dead loads. Stress in the top reinforcing bars was 148 MPa (21.4 ksi) due to dead loads and 247 MPa (35.8 ksi) due to service loads. The resulting 99 MPa (14.4 ksi) stress range was within the allowable fatigue stress range of 122 MPa (16.3 ksi) determined by Eq. 3-31. The peak stress in reinforcement was less than the $0.6 f_y = 248$ MPa (36 ksi) limiting steel stress.

Stress in the prestressing tendons was 1123 MPa (162.8 ksi) due to dead loads and 1214 MPa (176.1 ksi) due to service loads. The resulting 92 MPa (13.3 ksi) stress range was within the allowable fatigue stress range of 100 MPa (14.5 ksi).

Transverse Reinforcement:

As in the POJ-RC-100-TH design, only one vertical tie was considered in the STM for the POJ-PU-54-TH overhang. The quantity of transverse reinforcement required to resist the tension tie force (T2) of 367 kN (82.6 kips) was computed using Eq. 3-25. The resulting quantity of transverse reinforcement, A_{vs} , was 7.9 cm^2 (1.22 in^2). The location and quantity of transverse reinforcement was identical to that used for the POJ-RC-100-TH specimen because the post-tensioning force did not reduce the tension tie force, based on the results of the strut-and-tie model. The finite element analysis indicated tensile stresses in the overhang were reduced, but the flow of forces was the same as the STM for the POJ-RC-100-TH specimen. Tension tie T2 reinforcement was uniformly spaced over a distance equal to the effective depth, d , of the section at the tension tie.

Minimum transverse reinforcement was provided over the remainder of the overhang according to the equation for maximum spacing (Eq. 3-28). This maximum spacing was 18 cm (7 in.), and was determined for an effective depth, d , of 36 cm (14 in.). Transverse reinforcement details are presented in Figure 3.40.

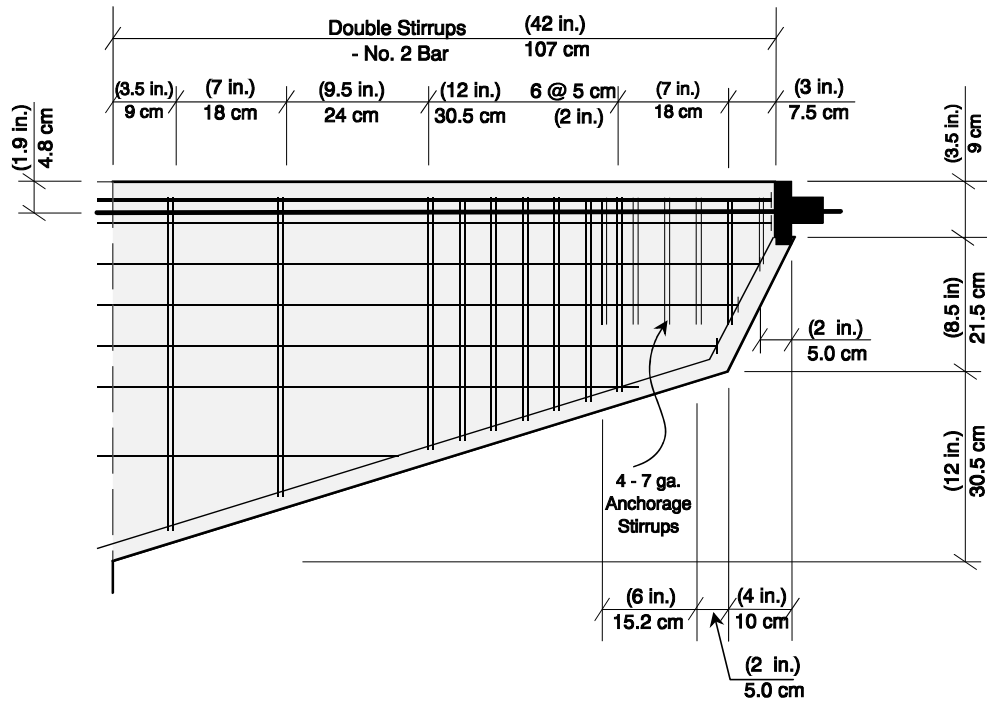


Figure 3.40 POJ-PU-54-TH - Transverse Reinforcement Details

3.4.4.4 Pier Details - POJ-PU-54-TH

Pier longitudinal reinforcement was determined using a strut-and-tie model and a cracked-section analysis. The quantity of post-tensioned steel, determined from the overhang design, was three 15 mm (0.6 in.) diameter strands. Because the prestressing tendons were continuous through the specimen, the amount of prestress in the pier accounted for less than 54% of the total tension tie force.

Longitudinal Reinforcement:

The quantity of longitudinal reinforcement was based on the tie force, T_5 , of the STM illustrated in Figure 3.37. The amount of reinforcement required to resist factored loads was computed by:

$$T_5 \leq \Phi (A_{ms} f_y + A_{ps} f_{pu}) \quad [3-35]$$

where:

- | | | |
|----------|---|---|
| T_5 | = | STM tension tie force = 1393 kN (313.3 kips). |
| Φ | = | Phi factor = 0.8 |
| A_{ms} | = | Area of mild steel primary flexural reinforcement |

	=	24 cm ² (3.72 in ²)
f_y	=	Nominal yield stress of mild reinforcement = 414 MPa (60 ksi)
A_{ps}	=	Area of prestressed primary flexural reinforcement
	=	4.16 cm ² (0.645 in ²)
f_{pu}	=	Prestressing steel stress at Ultimate Load = 1860 MPa (270 ksi).

The quantity of mild steel used provided 56 % of the tension tie force (T4) and the quantity of prestressing steel provided 44 % of the (T5) tension tie force. A cracked-section analysis was conducted to determine steel stresses due to service and dead loads to estimate crack widths and the maximum stress range. The cracked-section analysis was conducted using the reduced tendon force, T_x , at the pier-joint cross section. The total area of longitudinal mild reinforcement in the pier, 46 cm² (7.13 in²), was set equal to the minimum 1 % specified by the AASHTO column design provisions.

Transverse Reinforcement:

Transverse reinforcement was detailed using AASHTO Article 8.18.2.3. Transverse tie-spacing and bar-size requirements were divided by the 2.75 scale factor. The No. 4 minimum bar size specified in AASHTO was modeled using 7 ga. wire. The specified minimum longitudinal tie spacing of 30 cm (12 in.) was divided by the 2.75 scale factor, resulting in a tie spacing of 11 cm (4.4 in.). The specified maximum distance to a restrained bar of 61 cm (2 ft) was divided by the 2.75 scale factor resulting in a distance of 22 cm (8.7 in.). Positioning of the transverse reinforcement and distribution of longitudinal reinforcement in the pier is shown in Figure 3.41.

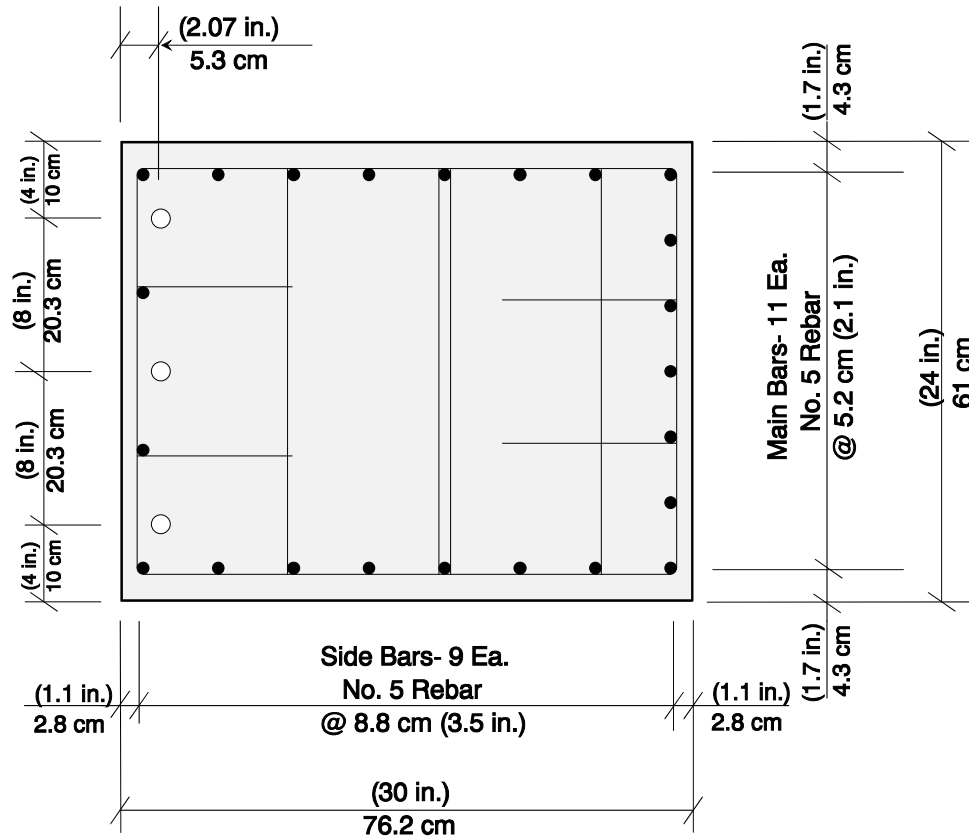


Figure 3.41 POJ-PU-54-TH Pier Cross-Section Details

Serviceability Provisions:

The post-tensioning tendon stress in the pier, after friction losses, was computed using AASHTO Equation 9-1:

$$T_x = \frac{T_o}{e^{(KL + \mu\alpha)}} \quad [3- 36]$$

where:

- | | | |
|----------|---|--|
| T_x | = | Prestressing force at distance (x=12 ft.) from jacking end |
| | = | 850 MPa (123.4 ksi) |
| T_o | = | Prestressing force at jacking end in (ksi) = 1396 kN (202.5 ksi) |
| K | = | Friction wobble coefficient = 0.002 |
| μ | = | Coefficient of friction = 0.3 |
| α | = | Total change of angle in radians = 1.5708 Rad. |
| L | = | Length (x) in (ft) = 3.7 m (12 ft). |

Crack widths in the pier were checked using the relationship presented in Eq. 3-29. The average steel stress due to service loads was computed to be 243 MPa (35.2 ksi), which was greater than the limiting stress, f_{sl} , of 161 MPa (23.3 ksi) associated with the limiting crack width. The equation was not satisfied because of a miscalculation during design of the specimen. To satisfy the equation, a larger number of small-diameter reinforcing bars should have been used for the pier longitudinal reinforcement.

The fatigue stress range was determined by computing the difference in steel stresses in the extreme tensile reinforcing bars resulting from service loads and dead loads. Stress in the reinforcing bars was 205 MPa (29.8 ksi) due to dead loads and 307 MPa (44.6 ksi) due to service loads. The resulting stress range of 101 MPa (14.8 ksi) was within the allowable fatigue stress range of 103 MPa (15 ksi) computed using Eq. 3-31. Peak stress in the reinforcement at service loads was 307 MPa (44.6 ksi), which was greater than $0.6f_y = 248$ MPa (36 ksi).

Stress in the prestressing tendons was 851 MPa (123 ksi) due to dead loads and 994 MPa (137 ksi) due to service loads. The resulting stress range in the prestressing of 93 MPa (13.6 ksi) was within the allowable fatigue stress range of 100 MPa (14.5 ksi).

3.4.4.5 Joint Details - POJ-PU-54-TH

Bar Anchorage:

The use of headed reinforcement in the joint region assured development of longitudinal reinforcement beginning at the face of the steel plate. This facilitated the formation of tension ties through the joint region, and a diagonal compression strut between the interlocking heads and the opposite (compression) corner of the joint (see Figure 3.42).

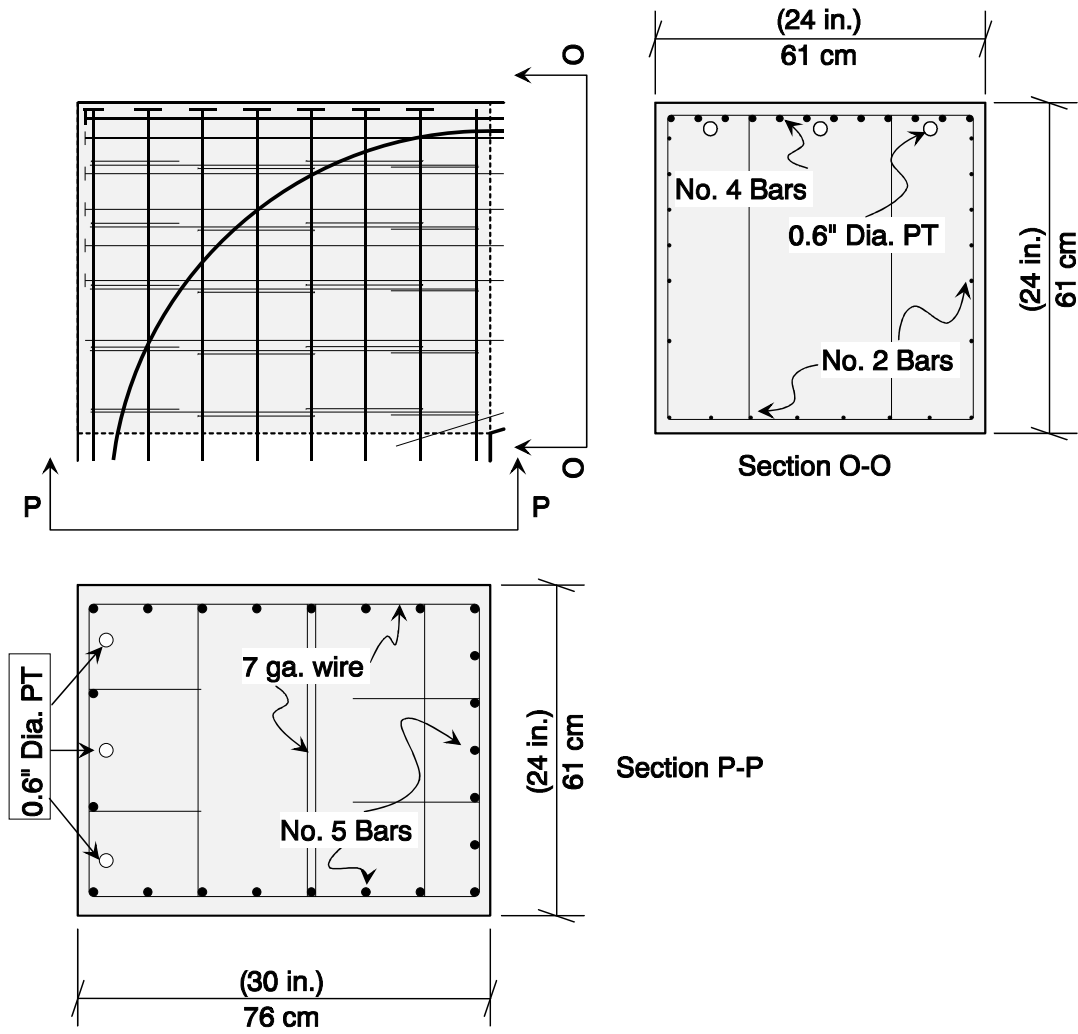


Figure 3.42 POJ-PU-54-TH Joint Reinforcement Details

The continuous prestressing through the joint significantly reduced tensile stresses in the joint. In addition to reducing the tensile stresses, the prestressing steel provided a high-strength tensile tie across any potential diagonal joint crack. The computed specimen capacity using the model described in Section 7.2 was 1.28 times the strength required to resist applied factored loads. Reinforcement details for the joint and complete specimen are illustrated in Figure 3.42 and Figure 3.43, respectively.

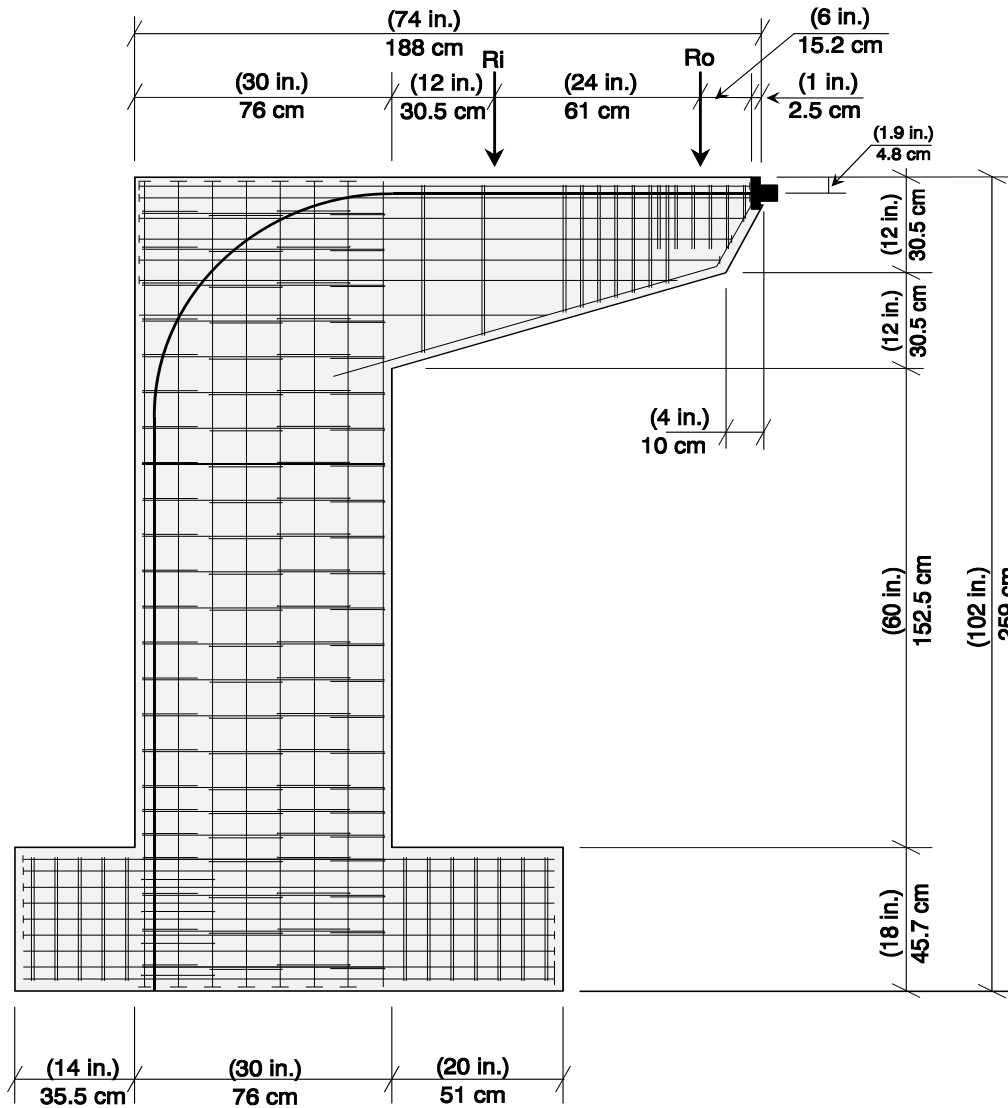


Figure 3.43 POJ-PU-54-TH Overall Reinforcement Details

3.4.4 54% Prestressed Design with T-Headed Bars - POJ-PU-54-TH.....	71
3.4.4.1 Finite Element Analysis - POJ-PU-54-TH.....	71
3.4.4.2 Strut-and-Tie Model - POJ-PU-54-TH.....	76
3.4.4.3 Overhang Details - POJ-PU-54-TH.....	77
3.4.4.4 Pier Details - POJ-PU-54-TH.....	80
3.4.4.5 Joint Details - POJ-PU-54-TH.....	83
Figure 3.32 Finite Element Model for Specimen POJ-PU-54-TH.....	72
Figure 3.33 POJ-PU-54-TH Principal Tensile Stress Contours and Vectors at Dead Load ...	74
Figure 3.34 POJ-PU-54-TH Principal Compressive Stress Contours and Vectors at Dead Load	74
Figure 3.35 POJ-PU-54-TH Principal Tensile Stress Contours and Vectors at Service Load	75
Figure 3.36 POJ-PU-54-TH Principal Compressive Stress Contours and Vectors at Service Load	75
Figure 3.37 POJ-PU-54-TH Strut-and-Tie Model.....	76
Figure 3.38 POJ-PU-54-TH Location of Post-Tensioning Tendons.....	78
Figure 3.39 POJ-PU-54-TH Overhang Cross-Section Details.....	78
Figure 3.40 POJ-PU-54-TH - Transverse Reinforcement Details	80
Figure 3.41 POJ-PU-54-TH Pier Cross-Section Details.....	82
Figure 3.42 POJ-PU-54-TH Joint Reinforcement Details	84
Figure 3.43 POJ-PU-54-TH Overall Reinforcement Details	85

3.4.5 74% Prestressed Design with T-Head Bars - POJ-PU-74-TH

The 74% prestressed specimen (Specimen POJ-PU-74-TH) contained five post-tensioned tendons that were continuous through the overhang, joint, and pier. The percentage (74%) indicates the portion of tie force in the overhang that was provided by the tendon.

3.4.5.1 Finite Element Analysis - POJ-PU-74-TH

The finite element analysis of Specimen POJ-PU-74-TH utilized the same procedure used for the 54 percent prestressed specimen. The finite element model was developed by generating separate meshes for the post-tensioning tendon (modeled using two-node truss elements) and concrete elements (modeled using 8-node isoparametric plate elements), then introducing displacement compatibility links between the tendon nodes and concrete nodes. Nodal displacements for the concrete and tendon elements were coupled for displacements normal to the tendon axis, but were free to displace along the tendon axis. Friction losses were not included in the finite element analysis.

Tendon elements in the model were “stressed” by applying a concentrated load on the tendon at the tip of the overhang and an equal and opposite concentrated load on the specimen. Because the points on the tip of the overhang were coincident, there was no eccentricity created at the point of load application. The other end of the tendon was fixed at a point in the base of the model. The base of the specimen was fixed from vertical displacement at the top and bottom at the locations indicated in Figure 3.32.

Finite element analyses were performed for service loads and dead loads. Because the analyses did not consider non-linear material properties, tensile stresses in some areas may be over-estimated. If tensile stresses were above $7\sqrt{f'_c}$ (psi) [3.44 MPa (500 psi)], the region was considered to be cracked. Although some regions of the POJ-PU-74-TH specimen were computed to be cracked under dead loads, finite element analysis was also performed at service loads to illustrate the increase in tensile stresses in the joint. Computed principal tensile and compressive stresses for dead-load and service-load levels are presented as stress contours and principal tensile stress vectors in Figure 3.44 through Figure 3.47.

Maximum computed principal tensile stresses for the specimen at dead load (shown in Figure 3.44) occurred in the overhang and pier, and stresses were slightly greater than the assumed concrete cracking tensile stress of $7\sqrt{f'_c}$ (psi) [3.44 MPa (500 psi)], indicating cracking would initiate at dead load. Maximum principal tensile stresses in the overhang and pier regions for Specimen POJ-PU-74-TH at dead load were slightly greater than the assumed concrete cracking tensile stress. However, principal tensile stresses in the joint region at dead load (where a critical diagonal crack could develop) were less than $1.4\sqrt{f'_c}$ (psi) [0.69 MPa (100 psi)], indicating cracking would not initiate at dead load. Additionally, principal tensile stresses in the joint region at service loads (shown in Figure 3.44) were slightly greater than $4.3\sqrt{f'_c}$ (psi) [2.07 MPa (300 psi)], indicating a critical diagonal crack would not initiate at service loads. Increased tensile stresses in the pier and overhang regions at service loads (shown in Figure 3.44) indicate that cracks initiated at dead load would extend further under the increased applied load.

As discussed previously, the principal tensile and compressive stress vectors (presented in Figure 3.44 through Figure 3.47) were used to aid in development of the strut-and-tie model presented in Figure 3.48.

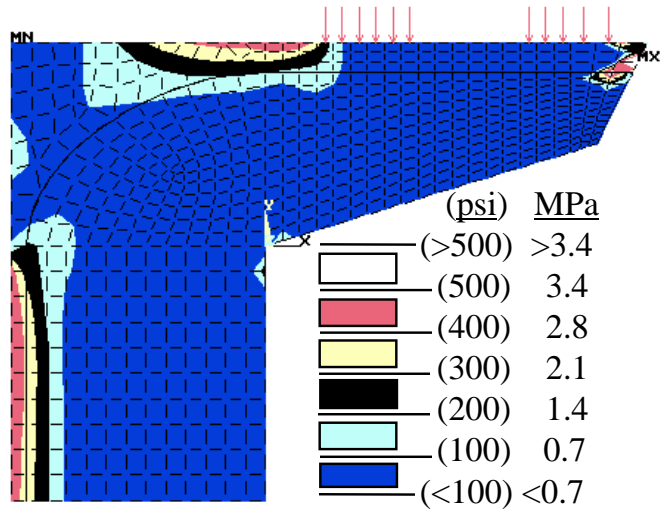


Figure 3.44 POJ-PU-74-TH Principal Tensile Stress Contours and Vectors at Dead Load

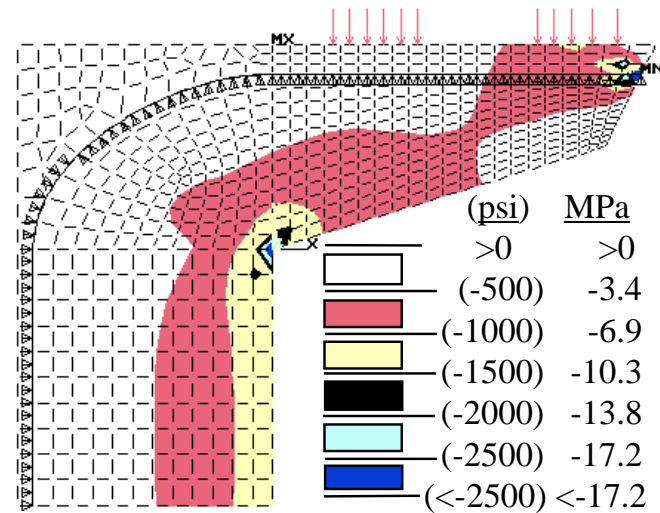
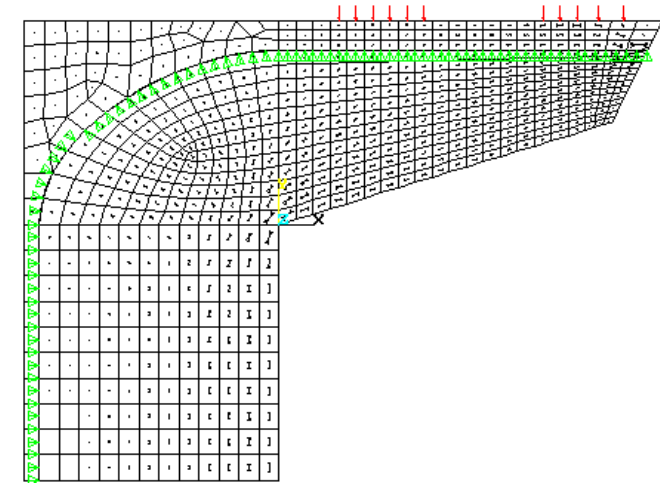
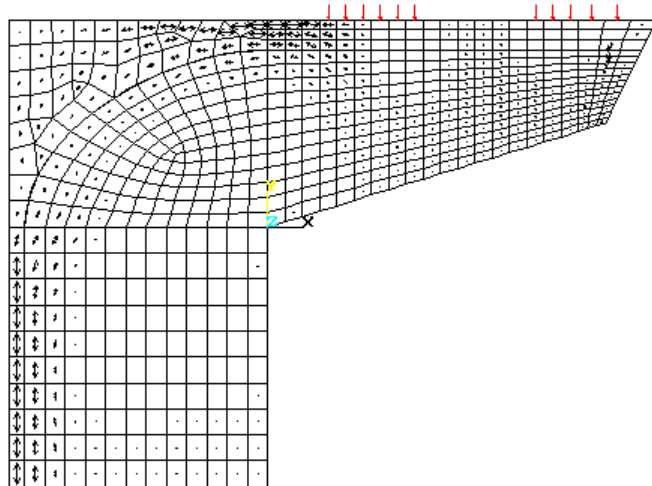


Figure 3.45 POJ-PU-74-TH Principal Compressive Stress Contours and Vectors at Dead Load



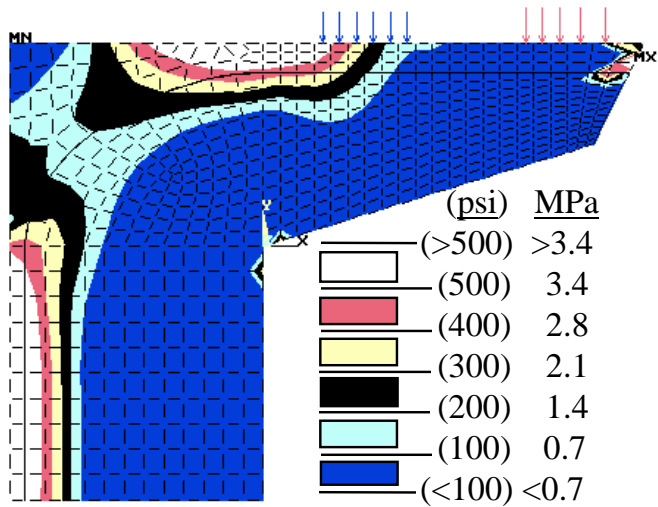


Figure 3.46 POJ-PU-74-TH Principal Tensile Stress Contours and Vectors at Service Load

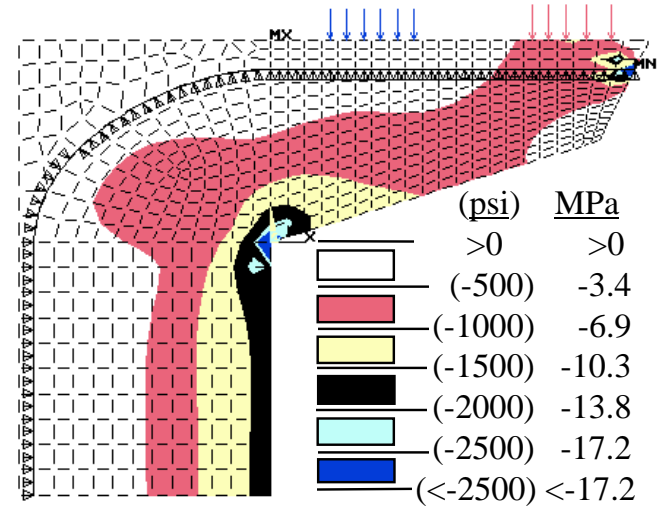
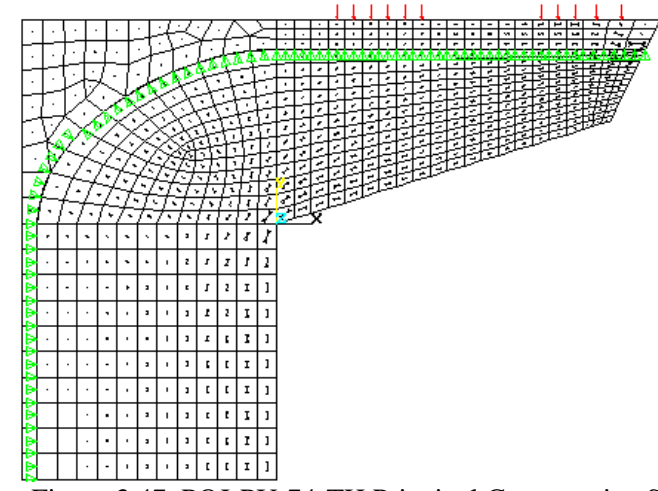
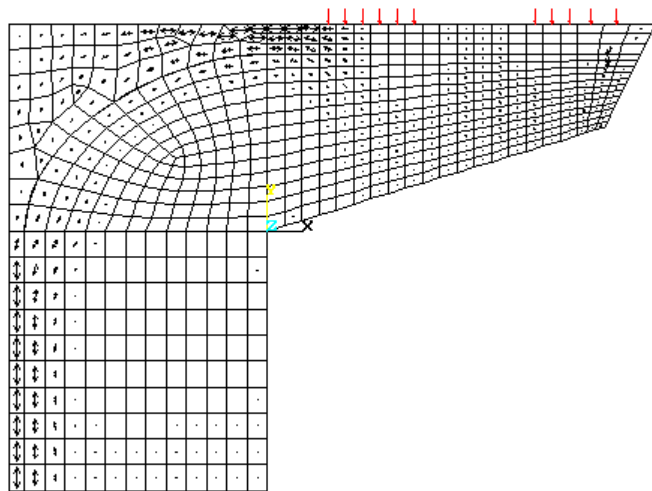


Figure 3.47 POJ-PU-74-TH Principal Compressive Stress Contours and Vectors at Service Load



3.4.5.2 Strut-and-Tie Model - POJ-PU-74-TH

The strut-and-tie model was intended to represent the flow of stresses indicated by the principal stress vectors presented in Figure 3.46 and Figure 3.47. Principal tensile and compressive stress vectors were used to aid in positioning the tension ties and compression struts, respectively. Details about the computation of reinforcement corresponding with the tension ties shown in Figure 3.48 are presented in the following subsections.

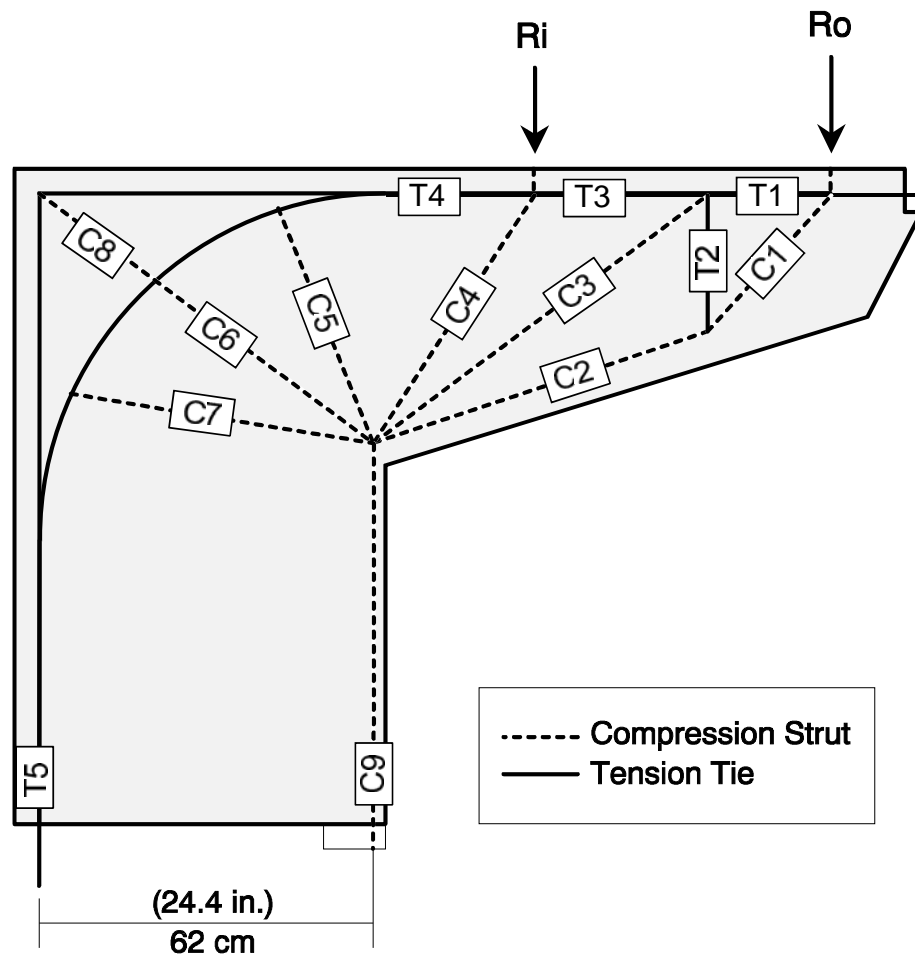


Figure 3.48 POJ-PU-74-TH Strut-and-Tie Model

3.4.5.3 Overhang Details - POJ-PU-74-TH

Longitudinal Reinforcement:

The amount of longitudinal reinforcement in the overhang was determined using the maximum force in the top cord (Tension Tie T4) of the strut-and-tie model (shown in Figure 3.48). The amount of reinforcement required to resist the model factored loads was computed by:

$$T4 \leq \Phi (A_{ms} f_y + A_{ps} f_{pu}) \quad [3-37]$$

where:

T4	=	STM tension tie force = 1439 kN (323.5 kips).
Φ	=	Phi factor = 0.9
A_{ms}	=	Area of mild steel primary flexural reinforcement
	=	10.3 cm ² (1.6 in ²)
f_y	=	Nominal yield stress of mild reinforcement = 414 MPa (60 ksi)
A_{ps}	=	Area of prestressed primary flexural reinforcement
	=	6.13 cm ² (0.951 in ²)
f_{pu}	=	Prestressing steel stress at Ultimate Load = 1860 MPa (270 ksi).

The quantity of mild steel provided 26% of the tension tie force (T4), and the quantity of prestressing steel provided 74% of the tension tie force. Based on the strut-and-tie model, there was no need to provide shear-friction reinforcement. Side-face reinforcement was determined using the Frantz and Breen [10] relationship presented in Eq. 3-27. The quantity of side-face reinforcement was computed to be 1.3 cm² (0.19 in²) per face. Details of the longitudinal overhang reinforcement at the cross section adjacent to the pier are shown in Figure 3.50.

Selection of Post-Tensioned Reinforcement:

The quantity of post-tensioned steel was provided by three-15 mm (0.6 in.) diameter strands and two -13 mm (1/2 in.) diameter strands located 9 cm (3.5 in.) from the extreme tension fiber. The location and spacing of the post-tensioning ducts is presented in Figure 3.49.

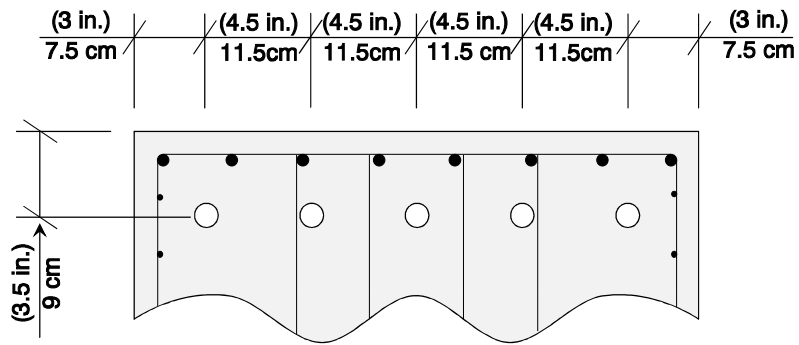


Figure 3.49 POJ-PU-74-TH Post-Tensioning Duct Locations

Once the amount of side face reinforcement was computed, a cracked-section analysis (considering all longitudinal reinforcement) was conducted to determine steel stresses at service and dead loads. Steel stresses were used to check crack widths and determine the maximum stress range.

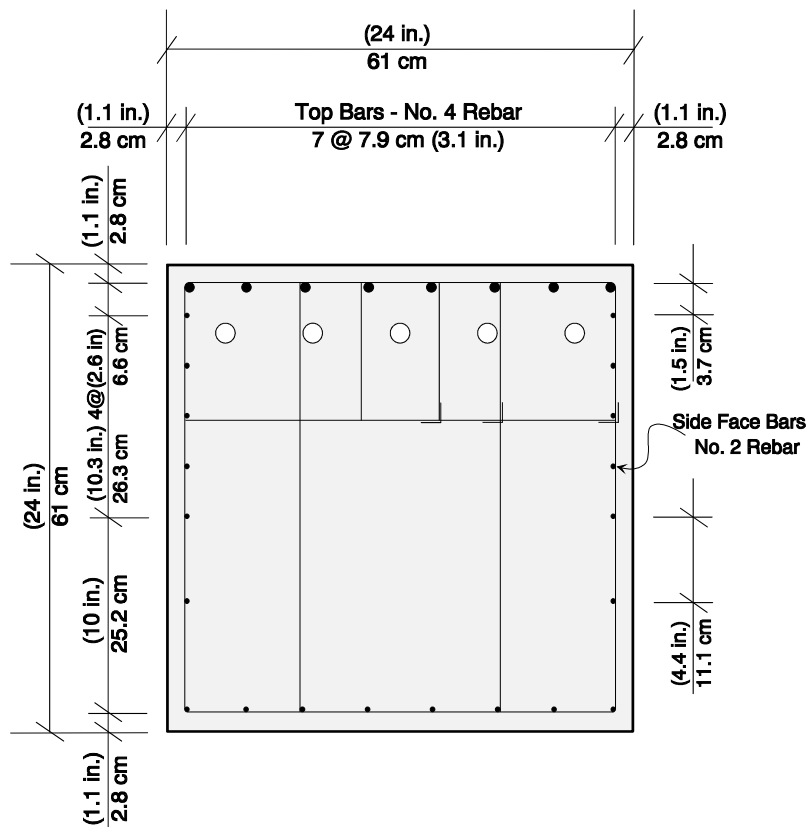


Figure 3.50 POJ-PU-74-TH Overhang Cross-Section Details

Serviceability Provisions:

Size of crack widths was intended to be controlled by the relationship presented in Eq. 3-29. The average steel stress due to service loads was computed to be 197 MPa (28.6 ksi), and was slightly greater than the stress, f_{sl} , of 196 MPa (28.4 ksi) associated with the limiting crack width.

The fatigue stress range was determined by computing the difference in steel stresses in the top-most reinforcing bars resulting from service loads and dead loads. Stress in the top reinforcing bars was 103 MPa (15 ksi) due to dead loads and 223 MPa (32.3 ksi) due to service loads. The resulting 119 MPa (17.3 ksi) stress range was within the allowable fatigue stress range of 134 MPa (19.4 ksi) determined by Eq. 3-31. Peak stress in the reinforcement of 223 MPa (32.3 ksi) due to service loads was less than the $0.6 f_y = 248$ MPa (36 ksi) limiting steel stress.

Stress in the prestressing strands was 1100 MPa (160 ksi) due to dead loads and 1200 MPa (174.5 ksi) due to service loads. The resulting 100 MPa (14.5 ksi) stress range was equal to the allowable fatigue stress range of 100 MPa (14.5 ksi).

Transverse Reinforcement:

As for the POJ-PU-54-TH design, only one vertical tie was considered in the STM for the POJ-PU-74-TH overhang. The quantity of transverse reinforcement required to resist the tension tie force (T2) of 367 kN (82.6 kips) was computed using Eq. 3-25. The resulting quantity of transverse reinforcement, A_{vs} , was 7.9 cm^2 (1.22 in^2). The location and quantity of transverse reinforcement was identical to that used for the POJ-PU-54-TH specimen because the different amount of post-tensioning did not reduce the tension tie force, based on the results of the strut-and-tie model. Finite element analysis indicated tensile stresses in the overhang were reduced, but the flow of forces from the STM were the same as for Specimen POJ-RC-100-TH. The tension tie reinforcement was uniformly spaced over a distance equal to the effective depth, d , of the section at the tension tie.

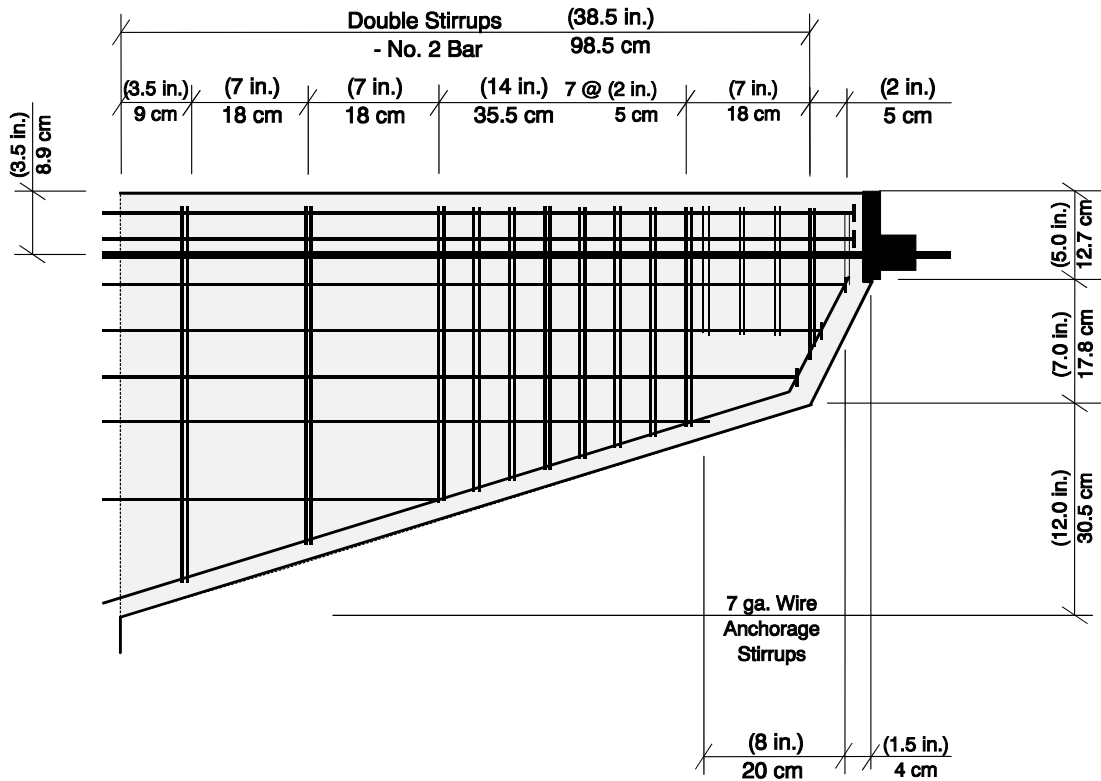


Figure 3.51 POJ-PU-74-TH - Overhang Design Details

Minimum transverse reinforcement, according to the equation for maximum spacing (Eq. 3-28), was provided over the remainder of the overhang. This maximum spacing was 18 cm (7 in.), and was determined for an effective depth, d , of 36 cm (14 in.). Transverse reinforcement details are presented in Figure 3.51.

3.4.5.4 Pier Design - POJ-PU-74-TH

Pier longitudinal reinforcement was determined using a strut-and-tie model and cracked-section analysis. The quantity of post-tensioned steel, determined from the overhang design, was three-15 mm (0.6 in.) diameter strands and two -13 mm (1/2 in.) diameter strands. Because the prestressing strands were continuous through the specimen, the percentage of prestress in the pier was less than 74% of the total tension tie force.

Longitudinal Reinforcement:

The quantity of longitudinal reinforcement in the pier was based on the tie force, T5 , of the STM illustrated in Figure 3.48. The amount of reinforcement required to resist factored loads was computed by:

$$T5 \leq \Phi (A_{ms} f_y + A_{ps} f_{pu}) \quad [3-38]$$

where:

T5	=	STM tension tie force =1267 kN (285.0 kips).
Φ	=	Phi factor = 0.8
A_{ms}	=	Area of mild steel primary flexural reinforcement 15.5 cm ² (2.40 in ²)
f_y	=	Nominal yield stress of mild reinforcement = 414 MPa (60 ksi)
A_{ps}	=	Area of prestressed primary flexural reinforcement 6.1 cm ² (0.951 in ²)
f_{pu}	=	Prestressing steel stress at Ultimate Load =1860 MPa (270 ksi).

The quantity of mild steel used provided 36% of the tension tie force (T5) and the quantity of prestressing steel provided 64 % of the (T5) tension tie force. A cracked-section analysis was conducted to determine steel stresses due to service and dead loads to check crack widths and maximum stress range. The cracked-section analysis was conducted using the reduced tendon force, $T_x = 850$ MPa (123.4 ksi), computed using Eq. 3-42 in Section 3.4.4.4.

The total area of longitudinal mild reinforcement in the pier, 33.5 cm² (5.2 in²), provided a column reinforcement ratio of 0.72 %. The design provided a realistic combination of mild reinforcement, based on a potential relaxation of the 1% minimum column reinforcement provision, and prestressing steel, based on strength design.

Transverse Reinforcement:

Transverse reinforcement was detailed using AASHTO Article 8.18.2.3. Transverse tie spacing and bar requirements were divided by the 2.75 scale factor. A 7 ga. undeformed wire was used to model the ties. Tie longitudinal spacing was 11.5 cm (4.5 in.). Detailing of transverse reinforcement and the distribution of longitudinal reinforcement are shown in Figure 3.52.

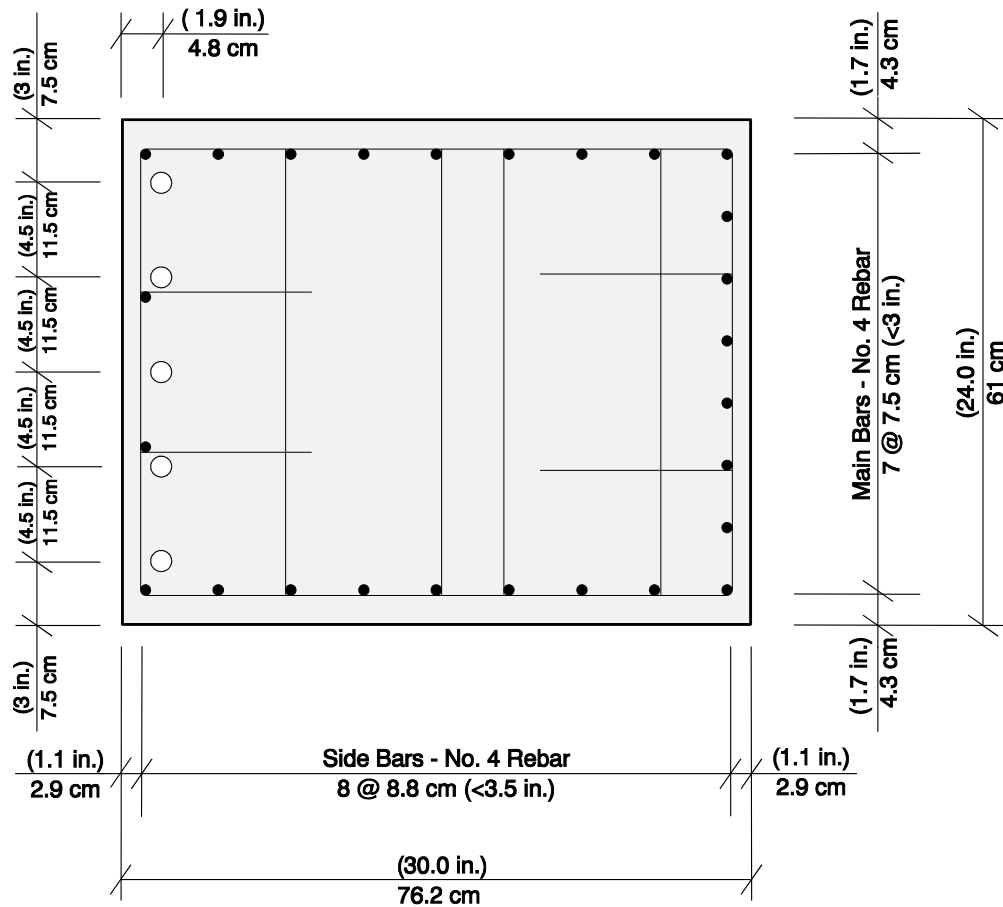


Figure 3.52 POJ-PU-74-TH Pier Reinforcement Details

Serviceability Provisions:

Crack widths in the pier were controlled by the relationship presented in Eq. 3-29. The average steel stress due to service loads was computed to be 231 MPa (33.5 ksi), which was greater than the limiting stress, f_{sl} , of 170 MPa (24.7 ksi) associated with the limiting crack width. The equation was not satisfied because of a miscalculation during design of the specimen. To satisfy the equation, a larger number of small-diameter longitudinal bars should have been used in the pier.

The fatigue stress range was determined by computing the difference in steel stresses in the extreme tensile reinforcing bars resulting from service loads and dead loads. Stress in the reinforcing bars was 149 MPa (21.6 ksi) due to dead loads and 261 MPa (37.8 ksi) due to

service loads. The resulting stress range of 112 MPa (16.2 ksi) was within the allowable fatigue stress range of 126 MPa (18.3 ksi) computed using Eq. 3-31. Peak stress in the reinforcement at service loads was 261 MPa (37.8 ksi), which was greater than $0.6f_y = 248$ MPa (36 ksi).

Stress in the prestressing tendons was 854 MPa (123.8 ksi) due to dead loads and 958 MPa (138.9 ksi) due to service loads. The resulting stress range in the prestressing of 104 MPa (15.1 ksi) was above the allowable fatigue stress range of 100 MPa (14.5 ksi). This limit was not satisfied because of a miscalculation that occurred during design of the specimen. To satisfy this requirement, tendons should be located further from the extreme tension fiber.

3.4.5.5 Joint Design - POJ-PU-74-TH

Bar Anchorage:

Use of headed reinforcement in the joint region assured development of longitudinal reinforcement beginning at the face of the steel plate. This facilitated the formation of tension ties through the joint region and a diagonal compression strut between the interlocking heads and opposite (compression) corner of the joint. Continuous post-tensioning through the joint reduced tensile stresses in the joint significantly. In addition to reducing tensile stresses, the post-tensioning steel provided a high-strength tensile tie across any potential diagonal joint crack. The computed specimen strength, using the analysis model described in Section 7.2, was 1.35 times the strength required to resist applied factored loads. Reinforcement details for the joint and complete specimen are illustrated in Figure 3.53 and Figure 3.54, respectively.

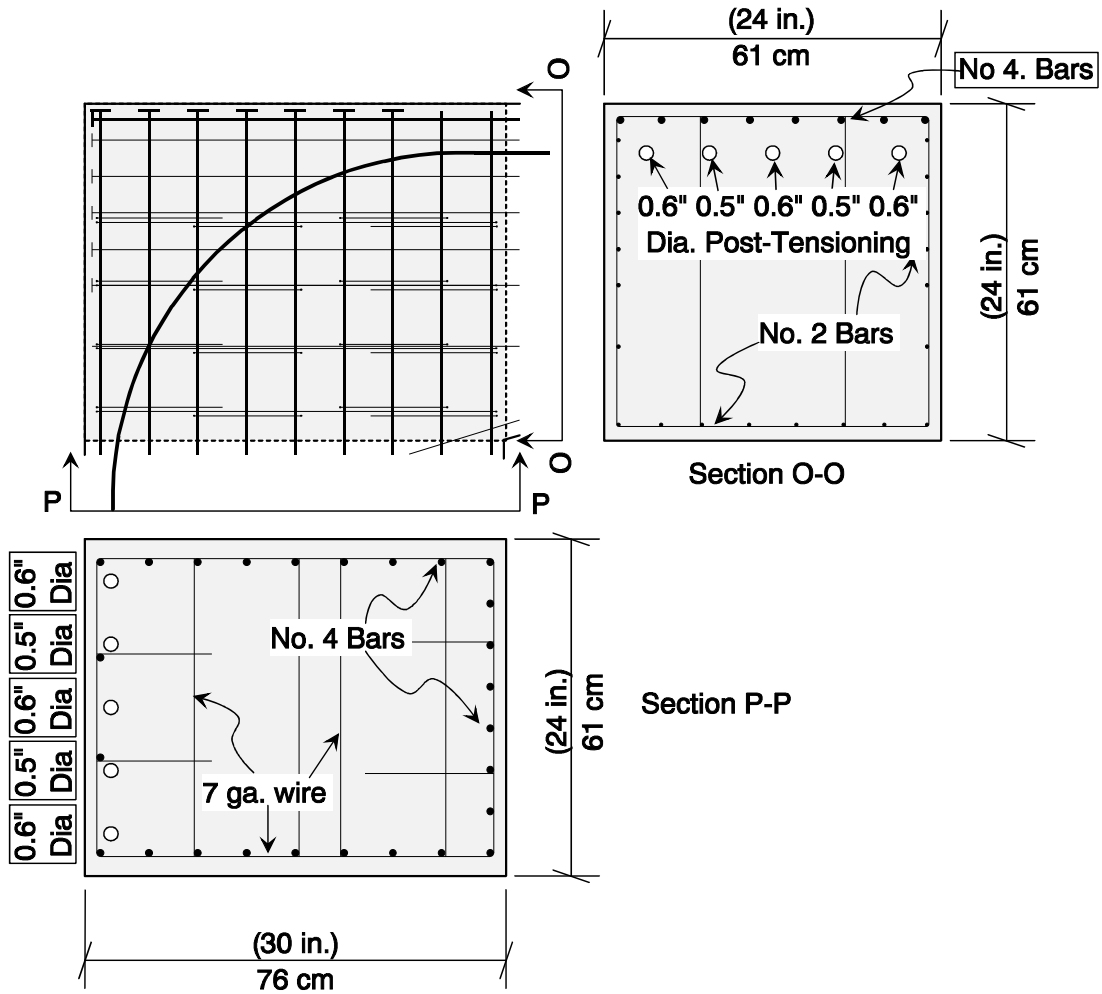


Figure 3.53 POJ-PU-74-TH Joint Reinforcement Details

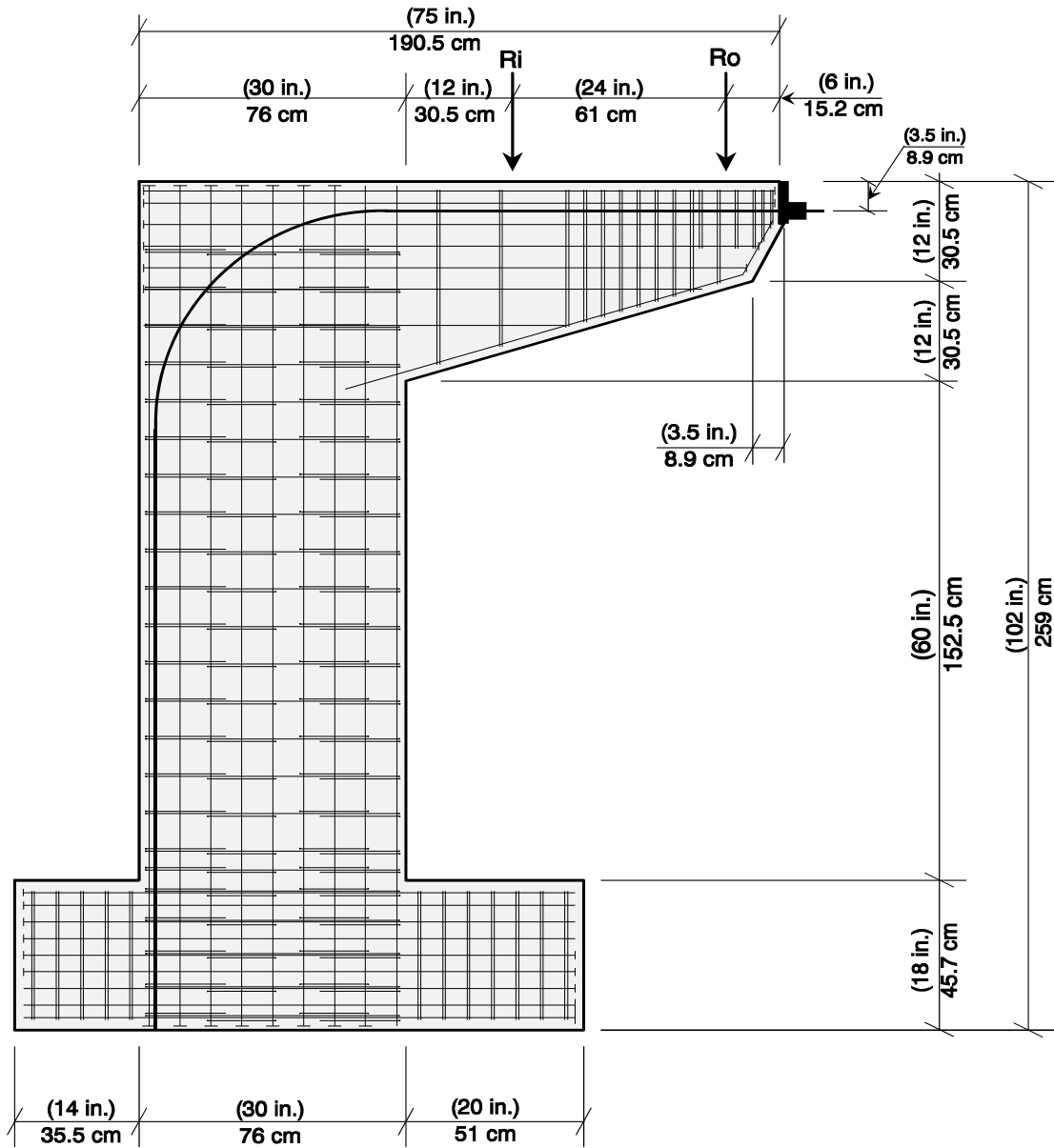


Figure 3.54 POJ-PU-74-TH Overall Reinforcement Details

3.4.5 74% Prestressed Design with T-Head Bars - POJ-PU-74-TH	86
3.4.5.1 Finite Element Analysis - POJ-PU-74-TH.....	86
3.4.5.2 Strut-and-Tie Model - POJ-PU-74-TH	90
3.4.5.3 Overhang Details - POJ-PU-74-TH.....	91
3.4.5.4 Pier Design - POJ-PU-74-TH	94
3.4.5.5 Joint Design - POJ-PU-74-TH.....	97
Figure 3.44 POJ-PU-74-TH Principal Tensile Stress Contours and Vectors at Dead Load ...	88
Figure 3.45 POJ-PU-74-TH Principal Compressive Stress Contours and Vectors at Dead Load	88
Figure 3.46 POJ-PU-74-TH Principal Tensile Stress Contours and Vectors at Service Load	89
Figure 3.47 POJ-PU-74-TH Principal Compressive Stress Contours and Vectors at Service Load	89
Figure 3.48 POJ-PU-74-TH Strut-and-Tie Model	90
Figure 3.49 POJ-PU-74-TH Post-Tensioning Duct Locations	92
Figure 3.50 POJ-PU-74-TH Overhang Cross-Section Details.....	92
Figure 3.51 POJ-PU-74-TH - Overhang Design Details	94
Figure 3.52 POJ-PU-74-TH Pier Reinforcement Details.....	96
Figure 3.53 POJ-PU-74-TH Joint Reinforcement Details	98
Figure 3.54 POJ-PU-74-TH Overall Reinforcement Details	99

3.5 Materials

3.5.1 Concrete

The concrete mix design used for the POJ specimens (shown in Table 3.6) was the same concrete design used in the overhang study conducted by Armstrong [3] and Salas [4]. The concrete mix design used a 1 cm (3/8 in) aggregate to model 4.45 cm (1.75 in) aggregate used in the full-scale prototype bents.

Table 3.6 Concrete Mix Design

Material	Quantity	
	SI per 1 m ³	Customary per 1 yd ³
Type I Cement	335 Kg	564 lb
Aggregate	867 Kg	1463 lb
Sand	968 Kg	1631 lb
Water	119 Kg	200 lb
Retarder	967 ml	25 oz.
HRWR*	1741 ml	45 oz.

* High-range water reducer (super-plasticizer)

Concrete compressive strength was anticipated to be 34.4 MPa (5000 psi) at 14 days, and a maximum of 44.8 MPa (6500 psi) at 28 days. The mix design included instructions for water to be added at the concrete batching plant if the initial slump (at the plant) was less than 13 cm (5 in.). Because the quantity of water added at the batching plant was not always measured (in violation of instructions), calculations for water-cement ratio are not presented.

The on-site slump was measured using the standard ASTM slump test procedure. A 25 cm (10 in.) high slump cone was filled in three lifts and each lift was tamped twenty-five times with a smooth metal rod, then the top was struck smooth. The cone was then removed slowly and the slump was measured.

If the initial slump was less than 10 centimeters (4 inches), water was added to increase the slump to 13 cm (5 inches). Once a slump of at least 13 centimeters (5 inches)

was achieved, Rheobuild super-plasticizer was added to the concrete and mixed for five minutes. The resulting slump was typically between 18 and 20 centimeters (7 to 8 inches). Measured slumps and mix modifications completed at the laboratory are reported in Table 3.7.

Table 3.7 On-Site Measurements and Mix Modifications.

Specimen	Initial Slump		Water Added		Slump		HRWR*		Final Slump	
	cm	(in.)	L	(gal)	cm	(in.)	L	(oz)	cm	(in)
POJ-RC-100	22	8.5	-	-	-	-	-	-	22	8.5
POJ-PS-100	11	4.5	-	-	-	-	1.9	64	19	7.5
POJ-RC-100-TH	5	2	38	10	9	3.5	3.8	128	22	8.5
POJ-PU-54-TH	11	4.5	-	-	-	-	3.8	128	23	9
POJ-PU-74-TH	11	4.5	-	-	-	-	3.8	128	22	8.5

* High-range water reducer (super-plasticizer)

During casting of each specimen, 24, 15.2 cm x 30.5 cm (6.0 in. x 12.0 in.) concrete cylinders were cast. These cylinders were used to measure concrete compressive strength at 1, 3, 7, 14, 21, 28 days, at the start of testing, and when the specimen failed. Only two cylinders were tested on each specified day unless a significant deviation in strength was measured. If this occurred, a third cylinder was tested. Concrete compressive strength at time of testing, at 28 days, and at completion of the test are shown Table 3.8.

Table 3.8 Concrete Compressive Strengths

Specimen	7 Day		@ Completion of Test			28 Day	
	MPa	(ksi)	Age	MPa	(ksi)	MPa	(ksi)
POJ-RC-100	28.3	4.11	23	31.7	4.60	31.7	4.60
POJ-PS-100	43.1	6.26	22	48.4	7.02	50.7	7.36
POJ-RC-100-TH	35.0	5.08	13	37.6	5.46	41.7	6.05
POJ-PU-54-TH	35.2	5.11	15	38.7	5.62	40.8	5.92
POJ-PU-74-TH	41.6	6.04	26	47.9	6.95	49.4	7.17

3.5.2 Mild Reinforcement

The mild reinforcing bars used included standard bars, deformed small-scale bars, and undeformed wire. The standard bars included: No. 3's, 4's, and 5's, and were used for primary longitudinal tension reinforcement in the pier and overhang. The No. 2 deformed small-scale bars were used for side-face reinforcement, overhang stirrups, and overhang compressive reinforcement. Undeformed 7 ga. wire was used for column ties and anchorage zone reinforcement. Material properties of the reinforcement are presented in Table 3.9.

Table 3.9 Mild Reinforcement Material Properties

Mild Steel Size	Diameter		Area		Yield		Yield Strain	Ultimate	
	cm	(in.)	cm ²	(in ²)	MPa	(ksi)		MPa	(ksi)
No. 5 Bar	1.58	0.625	2.0	0.31	413	59.9	0.00203	683	99.1
No. 4 Bar	1.27	0.500	1.3	0.20	416	60.3	0.00204	766	111.1
No. 3 Bar	0.95	0.375	0.71	0.11	427	62.0	0.00210	637	92.4
No. 2 Bar	0.63	0.247	0.31	0.048	512	74.2	0.00252	619	89.8
7 ga. wire	0.45	0.177	0.15	0.024	567	82.2	0.00279	596	86.4

Area of the anchor heads for headed bars was determined by using eight times the bar area. Plate sizes for the different bars are given in Table 3.10. Holes were drilled through the center of each plate, bar deformations on the tip of the reinforcing bar were ground-off, and the bar was pressed into the hole until the tip of the bar was nearly flush with the backside of the plate. A fillet weld on the front side of the plate and a button of weld material on the back side were used to attach the anchor plate to the bar (See Figure 3.55). When two T-heads were required on the same bar, the heads on the two ends were carefully aligned and welded so their orientations matched. It should be noted that T-head reinforcing bars are commercially available, but they were fabricated in the laboratory because some non-standard small-scale bars were required for the study.

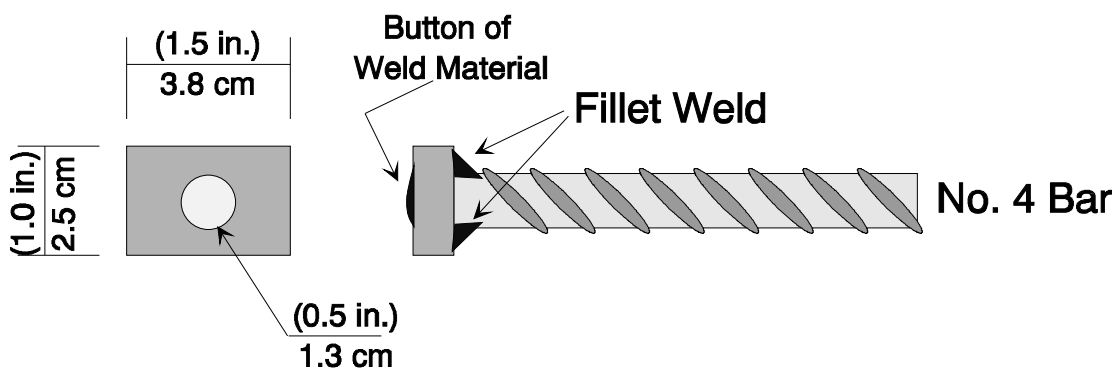


Figure 3.55 Anchor Head Dimensions and Weld Locations for a No. 4 Bar

Table 3.10 Dimensions of T-Head Plates

Reinforcing Bar Size	T-Head Dimensions	
	SI cm x cm x cm	Customary (in.)x(in.)x(in.)
No. 2	2.5 x 2.5 x 1.3	1 x 1 x 0.5
No. 3	2.5 x 2.5 x 1.3	1 x 1 x 0.5
No. 4	3.8 x 2.5 x 1.3	1.5 x 1 x 0.5
No. 5	4.8 x 3.8 x 1.9	1.88 x 1.5 x 0.75

3.5.3 Post-Tensioning Steel, Duct, and Anchorage Hardware

Grade 270 Lo-Lax prestressing strands were used to prestress the integrated prestressed designs (POJ-PU-54-TH & POJ-PU-74-TH). Grade 150 Dywidag post-tensioning bars were used for the fully-prestressed specimen (POJ-PS-100).

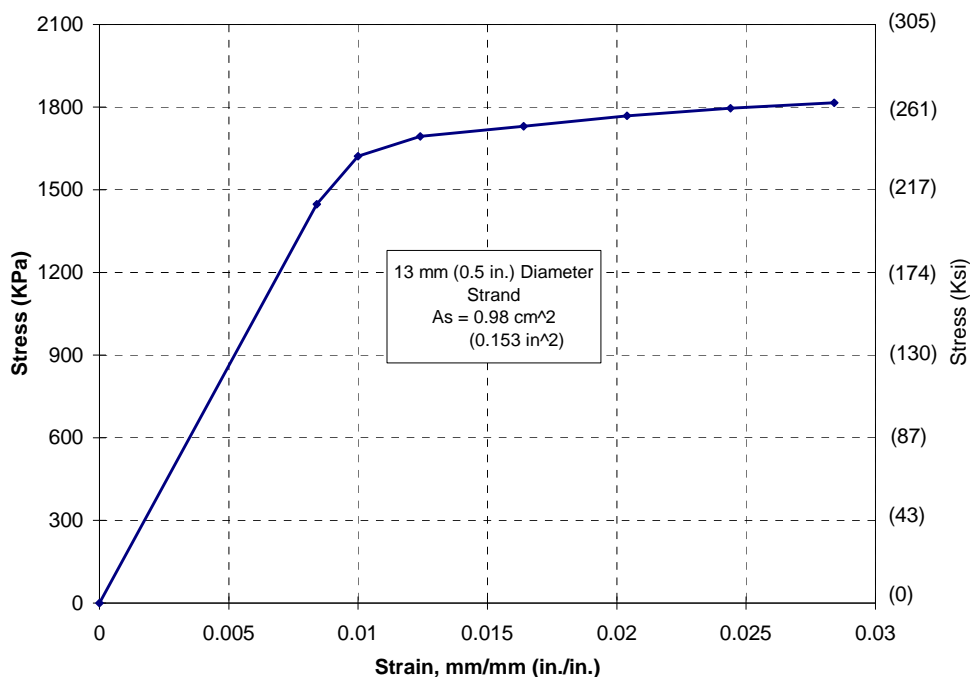


Figure 3.56 Stress-Strain Behavior of 13 mm (0.5 in.) Diameter Grade 270 Lo-Lax Strand

The stress vs. strain behavior of the 13 mm (0.5 in.) and 15 mm (0.6 in.) diameter, Grade 270, seven wire strands are shown in Figure 3.56 and Figure 3.57, respectively. Anchorage hardware for the prestressing strand consisted of standard chucks and special adjustable chucks with threads for a 5.7 cm (2.25 in.) diameter nut on the live end. This made it possible to stress the strand and make fine adjustments to the final position of the anchor without having to re-seat the chucks on the strand each time an adjustment was made.

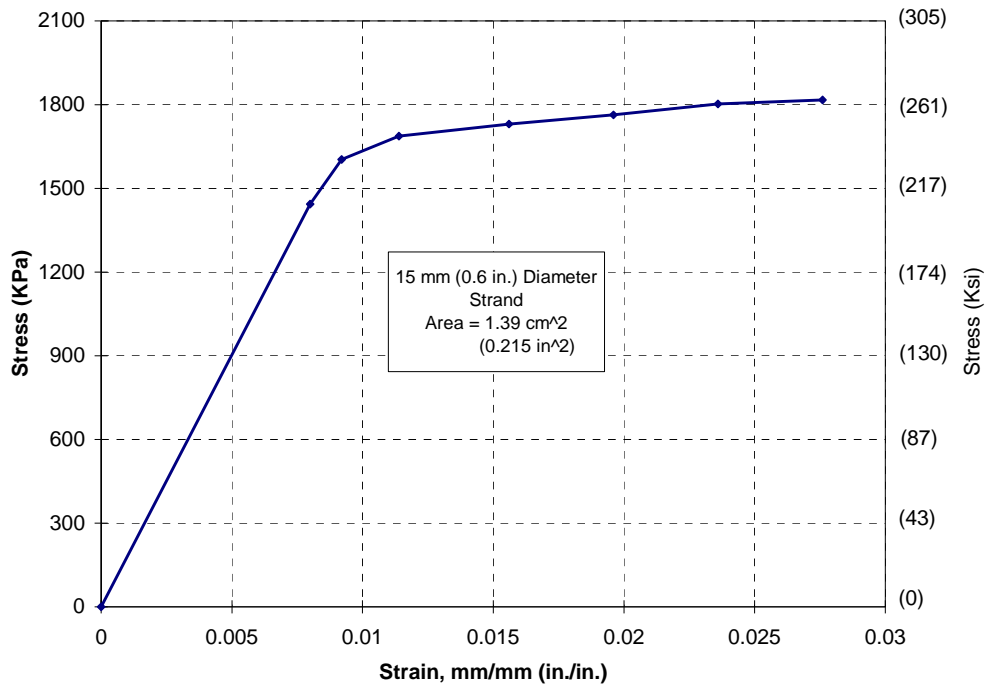


Figure 3.57 Stress-Strain Behavior of 15 mm (0.6 in.) Diameter Grade 270 Lo-Lax Strand

The stress-strain response for 16 mm (5/8 in.) diameter post-tensioning bars is shown in Figure 3.58. The Dywidag post-tensioning bar system uses a special threaded nut to anchor the bars. The nut allowed for adjustments during the stressing process, which meant that the post-tensioning force could be closely controlled.

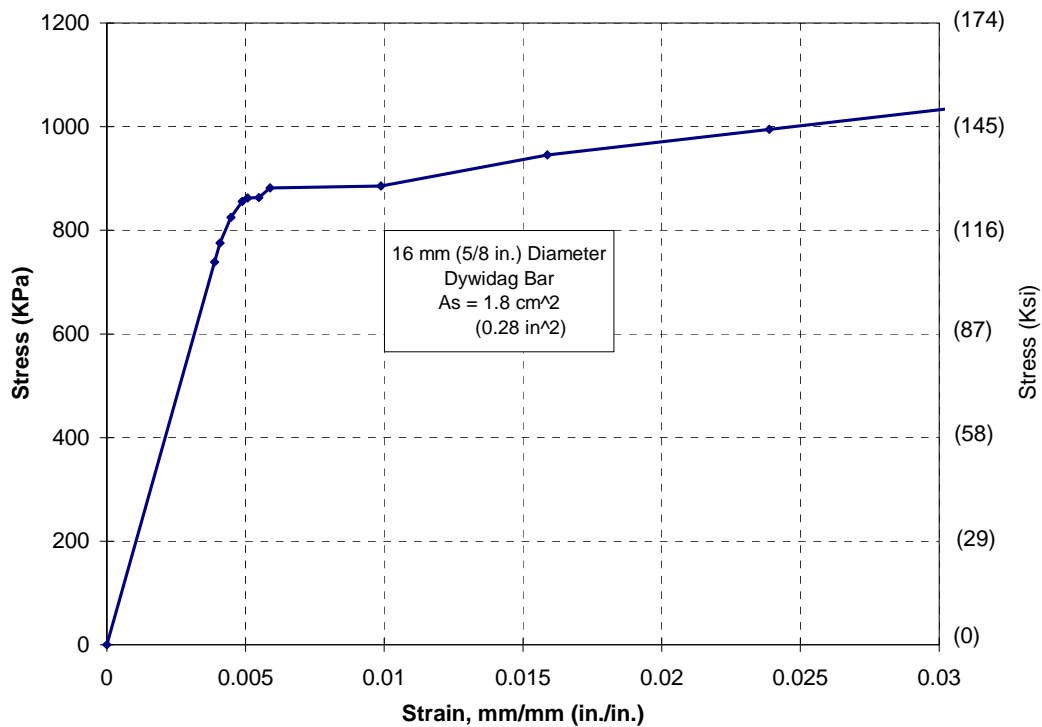


Figure 3.58 Stress-Strain Behavior of 16 mm (5/8 in.) Diameter Grade 150 Dywidag Post-Tensioning Bar

3.5.4 Grout

The grout mix design used throughout the project required Type I portland cement, water, and Interplast N. Interplast N is an expansive water-reducing agent that was added to offset grout shrinkage in the duct and provide a more fluid mixture that was easily injected into the ducts. Quantities used in the grout mix design, listed in Table 3.11, yielded 0.022 m³ (0.8 ft³) of grout.

Table 3.11 Grout Mix Design

Material	Amount	
	kg	(lbs)
Cement	27.2	60.0
Water	13.2	29.2
Interplast N	0.27	0.6

Grout was pumped into the post-tensioning ducts through 13 mm diameter Dywidag grout ports that were cast into the specimen. After the grout was pumped, samples were placed in standard 5.1 x 5.1 x 5.1 cm (2x2x2 in.) cube forms. Grout cube strengths are presented in Table 3.12.

Table 3.12 Grout Cube Strengths

Specimen	1st Measurement			2nd Measurement			3rd Measurement			Age
	Age	MPa	(ksi)	Age	MPa	(ksi)	Age	MPa	(ksi)	CT*
POJ-PS-100	2	9.5	1.38	7	17.9	2.59	14	24.7	3.59	8
POJ-PU-54-TH	3	21.5	3.12	6	36.2	5.25				6
POJ-PU-74-TH	2	8.1	1.18	5	16.3	2.36	7	15.4	2.23	12

* Age of Grout (in Days) at Completion of Test

3.6 Fabrication

Specimens were fabricated in the horizontal position. This simplified assembly of the reinforcement cage, facilitated placement of concrete, and assured that positioning of the bars would be as accurate as possible.

3.6.1 Reinforcing Cages

Components of the cages were carefully measured and bent to the dimensions specified in the designs. The 7 ga. wire column ties and anchorage reinforcement were bent on a template to assure uniformity. Stirrups were bent using a bar bending machine. Final assembly of the cage went quickly once all reinforcing bars were cut to size and stirrups and ties were bent. The T-headed bars were fabricated by drilling a hole in the steel anchor plate, welding around the bar with a 6 mm (1/4 in.) fillet weld, then filling in the annulus between the bar and plate with a “button” of weld material (See Figure 3.55). Size of the anchor plates was given in Section 3.5.2.

Every effort was made to keep locations of bars in each model as close as possible to the design locations. A combination of metal wire ties and plastic ties were used to keep bars fixed firmly in position.

For prestressed specimens, the 2.5 cm (1 in.) diameter galvanized electrical conduit (used as post-tensioning duct) was placed in the cage after the majority of overhang and pier reinforcement was tied in place. Strands were instrumented with 2mm electrical strain gages, water-proofed, and carefully threaded into the galvanized duct. Once the strand was in the duct, the duct was positioned inside the cage. In the joint region, the inner radius of the duct was tied in place so that the strand, when pulled tight against the duct during stressing, would be in the specified location. The ducts were held in place by short pieces of No. 2 reinforcing bar tied to the reinforcing cage at closely-spaced intervals.

Once a cage was assembled, the forms were oiled with form-release compound, and eight to ten - 1.9 cm (0.75 in.) diameter PVC spacers were placed on the bottom of the form to support the weight of the cage and provide the specified clear cover.

Prestressed specimens had holes drilled in the forms to allow prestressing strands to pass through the formwork. Special plywood components were constructed to provide the stressing shelf and anchorage plate lip. Silicon caulk was placed around the holes in the formwork and galvanized conduit to prevent water and paste seepage.

3.6.2 Placement and Consolidation of Concrete

Concrete was designed with a high slump to ensure good consolidation and workability. After the desired slump was achieved, a large hopper, lifted by the overhead crane, was used to transport concrete to the forms. Each specimen was cast in three layers and consolidated using two hand-held pencil vibrators and two formwork vibrators. Concrete cylinders were filled in three layers and each layer was tamped 25 times with a smooth steel rod. Excess concrete was removed by rolling the steel rod over the top of the cylinder.

Once water bleeding stopped, tops of cylinders were finished and covered with a thin plastic sheet. The specimens often took four to five hours to reach an initial set. At this time the surface of the concrete was finished with a trowel. Several short wood poles were nailed to the formwork and used to “tent” the plastic sheet covering the specimen. Three hours after initial set, water was pooled on the specimen. The top surface was wetted several times a day until concrete temperature decreased.

3.6.3 Curing and Form Removal

After three days of wetting the top surface of the specimen and checking the surface temperature, the forms were removed and the specimen was prepared for installation in the testing frame.

3.7 Test Set-up

The test set-up consisted of two frames, a stiff load beam with two - 890 kN (200 kip) capacity hydraulic rams, and two restraining beams for fixing the base of the specimen.

3.7.1 Loading Frame and Rams

The loading frame with a test specimen in place is shown in Figure 3.59. Columns for each frame were spaced 2.4 m (8 ft) apart, and the frames were spaced 1.2 m (4 ft) apart. Distances were dictated by the 1.2 m x 1.2 m (4 ft x 4 ft) spacing of the testing floor anchor locations. Four- 2.5 cm (1.0 in.) diameter high-strength threaded rods were used to secure each W12 x 65 steel column to the testing floor. The base of each column was not tensioned to the floor to allow some lateral motion to occur, thus reducing any restraining forces caused by deflection of the member. The 3.9 m (13 ft) long W30 x 108 steel cross beams were bolted to each column with twelve - 2.4 cm (1.0 in.) diameter ASTM 325 bolts. The W12 X 145 longitudinal load beam with the attached rams was fastened into place with steel clamps.

Each of the rams on the longitudinal load beam was held in position by four-2.5 cm (1 in.) diameter threaded rods that were threaded into nuts welded to the bottom flange of the beam. The outside of the ram casing was held tight against the bottom flange of the beam by tightening nuts against the outer-face of a 10 mm (3/8 in.) thick steel plate with a 10 cm (4 in.) hole located in the center (for the ram piston).

Both the inside ram and outside ram had a capacity of 890 kN (200 kips) with an effective ram area of 137 cm² (21.3 in²).

3.7.2 Anchorage of Test Specimen to Floor

Each test specimen was anchored to the floor with a 3.96 m (13 ft) long W12 x 145 steel beam on the back side of the specimen and a 2.28 m (9 ft) long W12 x 145 steel beam on the front side of the specimen. The beams had a nominal yield stress of 344 MPa (50 ksi). The longer beam on the back side of the specimen was tied down using 12 - 2.5 cm (1.0 in.)

diameter high-strength threaded rods. This side of the specimen was clamped to the test floor with a total of 1495 kN (336 kips). The shorter tie-down beam was tied to the floor by wrench-tightening the anchor bolts. The high-strength rods were threaded into floor anchors that were embedded approximately 120 cm (4 ft) inside the reaction floor. Placement of the beams is shown in Figure 3.59 and Figure 3.60.

3.7.3 Instrumentation and Data Collection

3.7.3.1 *Data Acquisition System*

The data acquisition system was a 140 channel Hewlett Packard 3497A scanner controlled by an IBM compatible Hewlett Packard XT personal computer. Software to control the scanner and record the data was a Ferguson Laboratory computer program (HPDAS2). The system allowed different types of gages to be identified and read by the scanner. Pressure transducers, linear potentiometers, and displacement transducers were connected using a full-bridge circuit having a 10 volt excitation which were, in turn, connected to the scanner to measure output voltage. Strain gages were connected to quarter-bridge circuits having a 2 volt excitation.

3.7.3.2 *Pressure Transducers*

The two pressure transducers used for measuring applied ram loads had a 10 V/mV accuracy with a maximum range of 69 MPa (10,000 psi).

3.7.3.3 Linear Potentiometers and Displacement Transducers

The position and designations for the displacement-measuring devices are shown in Figure 3.59. The first test (POJ-RC-100) used a combination of 15 cm (6.0 in.) and 5 cm (2 in.) linear potentiometers to measure pier and joint deformations, and a combination of 13 cm (5 in.) and 38 cm (15 in.) displacement transducers to measure overhang displacements. Because the long wires for the LV1 and LV29 displacement transducers were disturbed during crack readings, only 5 cm (2 in.) linear potentiometers with an accuracy of 0.03 mm (± 0.001 in.) were used to measure pier and joint displacements for subsequent tests. In addition, overhang displacements were measured using 13 cm (5 in.) displacement transducers with an accuracy of 0.03 mm (± 0.001 in.).

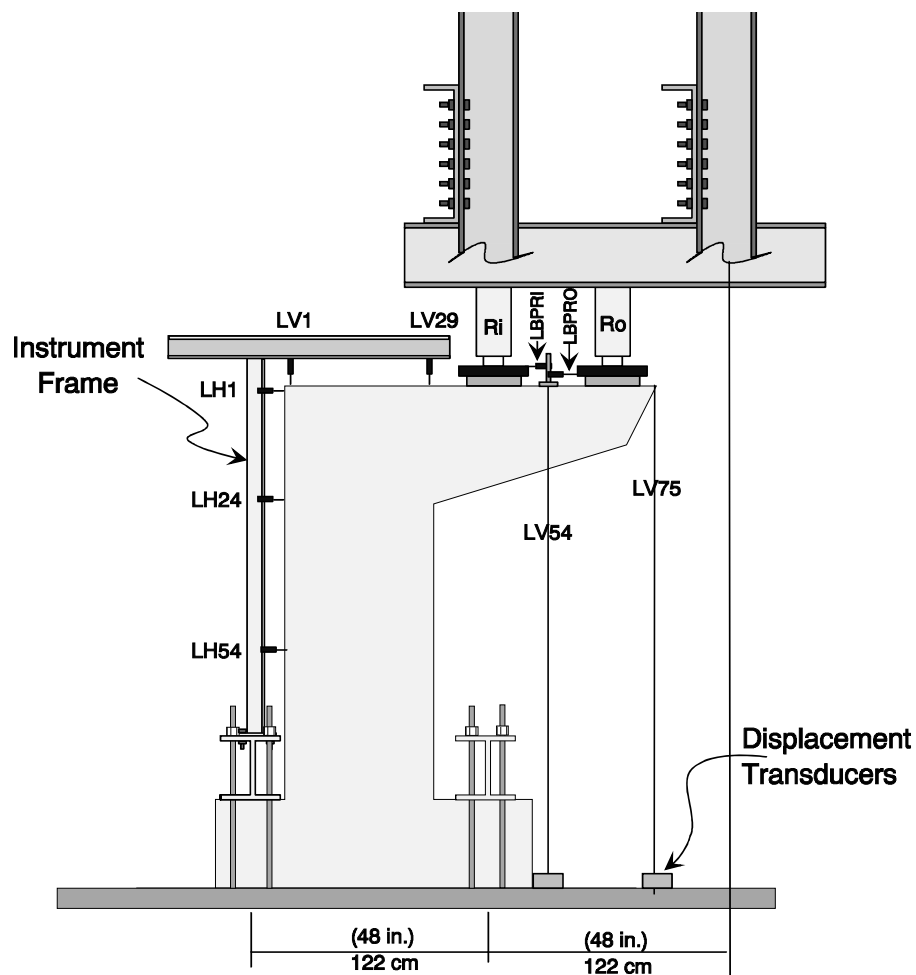


Figure 3.59 Test Setup and Location of Displacement Transducers

3.7.3.4 Strain Gages

Two sizes of electrical-resistance strain gages were used to measure steel strains in specimens. Five-mm-wide strain gages with pre-soldered two wire, 5 m leads were used to measure strains in the No. 5, No. 4, and No. 3 bars and 5/8" dia. Dywidag bars. Two-mm-wide strain gages with pre-soldered two wire, 5 m leads were used to measure strains in the No. 2 bars and prestressing strand.

3.8 Testing Procedure

3.8.1 Installation of Specimen

Each specimen had four lifting inserts cast into the top of the specimen and one lifting insert in the side of the pier. The four top lifting inserts were positioned to enable lifting through the center of gravity of the specimen. To install the specimen, the model was lifted off the form using the top lifting hooks and the 178 kN (20 ton) overhead crane. Before the specimen was lifted off the floor, the centerline of the pier was marked on the top, bottom, and mid-thickness of the base member at the front and back end of the member. Because the prestressing chucks at the base of the POJ-PU-54-TH and POJ-PU-74-TH specimens were not accessible once the specimens were placed in the test setup, strain-gage leads exiting from the base of each specimen had to be protected, and a minimal stress had to be applied to the post-tensioning strands to seat the post-tensioning anchorages. For the POJ-PU-74-TH and POJ-PU-54-TH specimens, grooves were ground into the anchorage plates to provide a path for the strand strain gage wires to pass. Ends of the ducts were sealed with silicon caulk, and anchorage plates were also sealed to the specimen to prevent grout seepage. Once the ducts were sealed, strands were stressed to $0.05 f_{pu}$ to seat the post-tensioning chucks.

Once the specimen was fully prepared, lifting cleavises were attached to the lifting inserts, and the specimen was transported from the casting site to the testing area. The east loading frame cross beam (see Figure 3.60) was removed for the installation procedure. The specimen was centered over the testing area and hydrostone was pooled into a form slightly larger than the base of the specimen. Ten cm (4 in.) thick steel plates with small gaps to accommodate the post-tensioning chucks were placed under the specimen. The steel plates were not necessary for the POJ-RC-100 and POJ-RC-100-TH specimens.

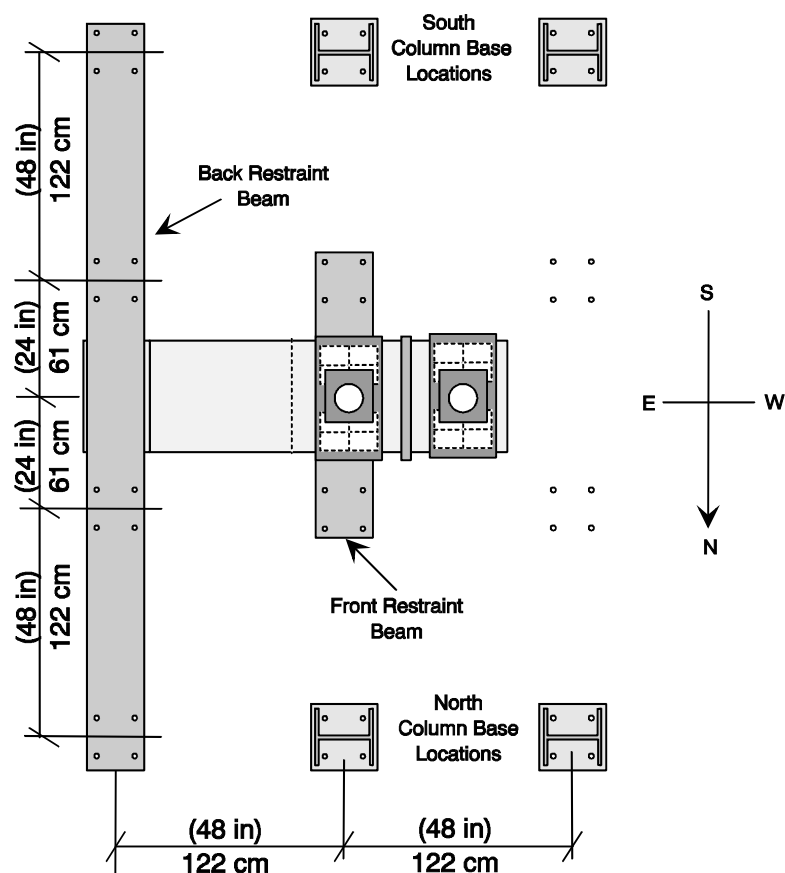


Figure 3.60 Top View of Test Setup

The specimen was then guided into position by four people as it was lowered into the hydrostone. Marks on the floor and specimen centerlines on the N,S,E,and W sides were used to position the specimen relative to the testing frame. Minor adjustments to ram locations were often made to correct for small misalignments.

Once the hydrostone hardened, the restraint beams were installed. First, a ring of silicon was placed on top of the east end of the base member of the specimen, and hydrostone was pooled in the ring. The east restraint beam was lowered slowly into position using the crane, then was leveled using the threaded floor anchor rods. The west beam used the same procedure except it was lowered into position using an electric forklift. The west beam was not stressed; the four anchor rods were hand-tightened using a wrench. After a day, the east restraint beam was stressed against the specimen. Twelve floor anchor rods were each stressed to 125 kN (28 kips) to provide the required resistance.

After the specimen was anchored to the floor, the load bearings, which consisted of four- 28 cm x 20 cm (11 in. x 8 in.) steel laminated elastomeric bearings, were positioned on the specimen. Two bearings were located at 30.5 cm (12 in.) from the face of the pier for the interior load, R_i , and two bearings were located at 91.5 cm (36 in.) from the face of the pier for the outside load, R_o . A stiffened steel plate was centered on top of the bearings to transfer ram forces equally to the two bearing pads. Torsional loads were not applied to the specimen.

Load plates on top of the specimen were used to center the load beam and rams over the specimen. The beam was lowered into position using the crane and adjusted using hammers until the rams and load beam were positioned directly over the two load plates. Once the position was correct, the load beam and ram assembly was clamped to the loading frame with four heavy steel clamps.

Linear potentiometers for the pier and east face of the joint were attached to a vertical steel section that was bolted to the prestressed restraint beam. Linear potentiometers for the top of the joint were attached to a horizontal channel section connected to the vertical steel section, and a steel structural column in the laboratory (column not depicted in Figure 3.59). Displacement transducers were attached to the floor and connected by piano wire to the specimen. Two displacement transducers were used to measure overhang deformations at the two locations shown in Figure 3.59. At each location, one transducer was located on the north side and the south side. The POJ-RC-100 test specimen utilized steel-wire displacement transducers to measure all vertical displacements. This approach was

discontinued for subsequent specimens because the piano wires in the joint region were disturbed many times while measuring crack widths.

Pressure transducers were connected to the hydraulic lines of two independent pumps. One pump was used to control the inside load (Ri) and another controlled the outside load (Ro). Multimeters were connected to the pressure transducers so the individual applying load to the specimen could accurately control the load steps. An X-Y plotter was used to monitor the tip deflection and outside ram pressure transducer (and thus, Ro). The X-Y plot was used to monitor the load and tip deflection, and control displacement steps after ultimate load was reached.

3.8.2 Post-Tensioning Operation

Post-tensioning was carried out on Specimens POJ-PS-100, POJ-PU-54, and POJ-PU-74. The procedure involved the use of a 267 kN (60 kip) ram, a 69.0 MPa (10,000 psi) pressure transducer, and a 5 cm (2 in.) linear potentiometer. Once the specimen was in place, the design stressing sequence was used to safely stress the specimen. The stressing sequence was different for each specimen, but the main objective was to stress all tendons to $0.6 f_{pu}$ [1.10 GPa (160 ksi)] while keeping maximum flexural tension stresses below $3\sqrt{f'_c}$ [1.46 MPa (212 psi)]. Flexural tensile stresses were computed using the following equation:

$$-\frac{P_{tx}}{A} - \frac{P_{tx} e y}{I_g} + \frac{M_{(applied)x} y}{I_g} \leq 3\sqrt{f'_c} \quad [3- 39]$$

where:

P_{tx}	=	Total applied post-tensioning force at stage of stressing
A	=	Area of concrete = $b_w h$
e	=	Eccentricity of post-tensioning strand above beam centroid
y	=	Distance to extreme tensile fiber from beam centroid
I_g	=	Gross moment of inertia = $1/12 (b_w)(h)^3$
$M_{(applied)x}$	=	Applied overhang moment at stage of stressing.

Both the top and bottom-fiber tensile stresses were evaluated along the length of the member at all stages of post-tensioning.

All post-tensioning strands were “overstressed” to $0.9 f_y$ to overcome friction losses in each tendon. The prestressing operation was carried out at the overhang tip because the chuck on the bottom of the specimen was not accessible, and it would not be possible to stress tendons in the pier region of a full-scale bent to $0.6 f_{pu}$ because of losses that would occur in the curved portion of the tendon. As stated earlier, the computed post-tensioning losses in the pier region were considered in design of the pier.

Once tendons were initially stressed, a lift-off test was conducted to verify tendon tension. A lift-off test is conducted by monitoring movement of an anchorage device while pulling against the tendon (strand). Lift-off (a sudden increase in movement) of the tendon anchor occurs when load in the ram used to perform the lift-off test reaches a load exceeding the initial tendon force. The sudden increase in deformation at lift off occurs because the length of tendon that elongates changes suddenly from the length inside the ram and anchor device to the free (unbonded) length of the tendon.

Lift-off tests performed on tendons in Specimens POJ-PU-54-TH and POJ-PU-74-TH did not yield definitive information about tendon forces. Because a portion of the post-tensioning ducts was curved, tendons were in contact with the curved portion of the ducts as well as some portion of the straight duct leading into the curved portion. After lift off, the free length of tendon changed incrementally as contact friction along the tendon was gradually overcome. Gradual elongation of tendons instead of a sudden increase in elongation made it difficult to discern the lift-off force for each tendon. Because accuracy of the lift-off procedure was in question, a simpler procedure for determining lift-off was developed.

The adjustable chucks for anchoring the post-tensioned strands had a large nut that was used to make fine adjustments in the chuck position without having to re-seat the chuck. After the initial lift-off test was performed, each tendon was slowly stressed again and the adjusting nut was tapped with a hammer while the ram load was monitored. When the nut turned, the lift-off load was determined. If the tendon force was too low, the strand was fully stressed to $0.9 f_y$, the nut was tightened, and the ram load was released. The strand was then stressed again, and the nut was again tapped to determine the lift off load.

Once the tendons were stressed, holes in the anchorage plates were filled with silicon caulk. After the caulk set, cement, water, and Interplast N were weighed, divided in half, and placed in separate five gallon buckets. Grout was mixed using a hand-held electric drill and mixing bit. The mixer was started in the bucket containing water, then cement was slowly added. After cement and water were mixed, Interplast N was added. Consistency of the mixture was noticeably more fluid with Interplast N. The bucket of grout was poured into the electric grout pump, and the grout hose was attached to the bottom grout port. The grout pump was switched on and off in spurts to keep the grout pressure below 0.28 MPa (40 psi) to avoid rupture or separation of the hose connections.

During the grouting procedure, flow of grout from the port in the tip of the overhang was monitored. The pump was switched off and grout ports closed when grout flowing from the port in the tip of the overhang was free of air bubbles. The procedure was repeated until all ducts were grouted. The grouting procedure had to be completed quickly, and small quantities were mixed because the grout was noticeably less fluid after only 10 minutes.

Three grout cubes were made from each grout mix. Cube compressive strengths were tested four days and six days after grouting the specimen, and on the day testing was completed. Once the grout reached a compressive strength of 10.3 MPa (1500 psi), each specimen was tested.

3.8.3 Static Load Steps

The testing procedure was similar to the procedure used in the overhang study by Armstrong [3] and Salas [4]. Major events in the loading history and number of load steps corresponding with each event are listed in Table 3.13.

Table 3.13 Events in Load History, Corresponding Load Steps, and Applied Loads

Load Step	Load Event	Load Abbreviation	R _i		R _o	
			kN	(kips)	kN	(kips)
20	Dead Load	DL	293	65.9	293	65.9
27	Dead Load + 1/2 Live Load	(DL + 1/2 LL)	318	71.4	344	77.4
34	Service Load	(DL+LL)	343	77.0	399	89.6
35	Dead Load	(DL)	318	65.9	293	65.9
49	Service Load	(DL+LL)	343	77.0	344	89.6
60	Dead Load + 2 Live Loads	(DL+2LL)	409	92.0	496	111.4
73	Factored Load	(1.3DL + 2.17LL)	488	109.7	610	137.2
80	Factored Load / Φ	(1.3DL + 2.17LL)/ Φ	543	122.1	679	152.7
100	Maximum Applied Load	1.44 x Factored Load	701	157.7	877	197.1

The load steps started with 0 (no load), and equal-size steps were applied between each load event. After every two load steps, the specimen was examined for new cracks. During initial load steps, once a crack was observed in the pier, overhang, or joint, it was marked on the specimen, the width was measured using a 0.013 mm (± 0.0005 in.) optical crack-width comparator, and photographs were taken. Crack widths were measured at the outer fibers and at grid locations shown in Figure 3.61. Loads and crack widths corresponding with first cracking were recorded for the pier, overhang, and joint sections. Once first cracking occurred in a region, cracks were examined every two load steps to identify new cracks or crack extensions. Cracks were marked with a magic-marker on the surface of the specimen, numbered according to the load step, and recorded on a map of the north and south side of the specimen.

Photographs were taken and all visible cracks in the overhang, joint, and pier were numbered and measured separately at the major load events listed in Table 3.13. Crack widths were not measured after load step 60 (DL+2LL) was reached, but cracks were still identified and marked on the specimen.

Loads steps were continued beyond Factored Load / Φ in the same increments applied between load steps 73 to 80. Reinforcement strains, deflections, and pressure transducer readings were scanned by the data acquisition system at every load step. After ultimate load was reached, the X-Y plotter was used to monitor displacement increments in the post-ultimate range. Cracks were no longer marked on the specimen because of safety concerns.

All specimens were loaded as far as possible into the post-ultimate range without damaging the test setup or rams. Once a test was concluded, any new cracks that formed were marked and photographs were taken to record the final state of the specimen.

3.8.4 Crack Identification and Marking Procedure

A crack identification and marking procedure was developed to keep a record of cracks as they formed. All marked cracks have a unique identification number that was used to identify respective crack widths. Figure 3.61 illustrates the rules used to identify each crack.

As stated in the previous section, cracks were measured at specific load steps. The object of this was to keep the test progressing because, on average, it required two hours to measure all the crack widths. Cracks were associated with different specimen regions to facilitate evaluation of the cracking performance. Each crack was always associated with the region in which it initiated, regardless of where it propagated later in the test.

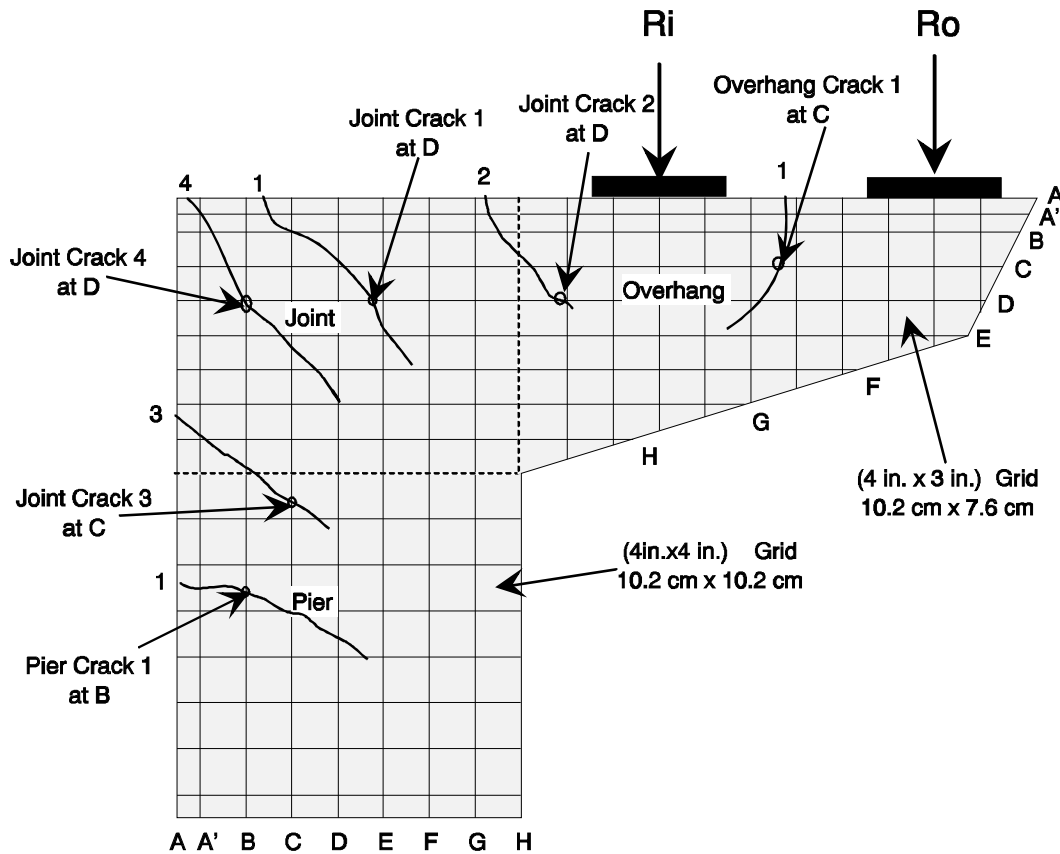


Figure 3.61 Crack Identification Procedure

All crack identifications incorporated a load step number, but the letter portion of the crack width depended on the orientation of the crack. If the crack initiated on the horizontal top face of the overhang or joint, the horizontal grid lines and corresponding letter labels applied. If the crack initiated on the outside face of the pier or joint, the vertical grid lines and corresponding letter labels applied. This convention was used regardless of the final orientation of the crack. Cracking patterns and crack widths for all the specimens are presented in Appendix A.

3.5 Materials	100
3.5.1 Concrete	100
3.5.2 Mild Reinforcement	102
3.5.3 Post-Tensioning Steel, Duct, and Anchorage Hardware	104
3.5.4 Grout	106
3.6 Fabrication	108
3.6.1 Reinforcing Cages	108
3.6.2 Placement and Consolidation of Concrete	109
3.6.3 Curing and Form Removal	109
3.7 Test Set-up	110
3.7.1 Loading Frame and Rams	110
3.7.2 Anchorage of Test Specimen to Floor	110
3.7.3 Instrumentation and Data Collection	111
3.7.3.1 Data Acquisition System	111
3.7.3.2 Pressure Transducers	111
3.7.3.3 Linear Potentiometers and Displacement Transducers	112
3.7.3.4 Strain Gages	113
3.8 Testing Procedure	113
3.8.1 Installation of Specimen	113
3.8.2 Post-Tensioning Operation	116
3.8.3 Static Load Steps	119
3.8.4 Crack Identification and Marking Procedure	120
Figure 3.55 Anchor Head Dimensions and Weld Locations for a No. 4 Bar	103
Figure 3.56 Stress-Strain Behavior of 13 mm (0.5 in.) Diameter Grade 270 Lo-Lax Strand	104
Figure 3.57 Stress-Strain Behavior of 15 mm (0.6 in.) Diameter Grade 270 Lo-Lax Strand	105
Figure 3.58 Stress-Strain Behavior of 16 mm (5/8 in.) Diameter Grade 150 Dywidag Post-Tensioning Bar	106
Figure 3.59 Test Setup and Location of Displacement Transducers	112

Figure 3.60 Top View of Test Setup.....	114
Figure 3.61 Crack Identification Procedure.....	121
Table 3.6 Concrete Mix Design.....	100
Table 3.7 On-Site Measurements and Mix Modifications.....	101
Table 3.8 Concrete Compressive Strengths.....	102
Table 3.9 Mild Reinforcement Material Properties.....	102
Table 3.10 Dimensions of T-Head Plates.....	103
Table 3.11 Grout Mix Design.....	107
Table 3.12 Grout Cube Strengths.....	107
Table 3.13 Events in Load History, Corresponding Load Steps, and Applied Loads.....	119

CHAPTER 5

ANALYSIS OF TEST RESULTS

5.1 Introduction

Two prototype design specimens (POJ-RC-100 and POJ-PS-100) and three integrated design specimens (POJ-RC-100-TH, POJ-PU-54-TH, and POJ-PU-74-TH) were evaluated using the following criteria: strength, serviceability, constructability, and estimated cost. The strength criterion was evaluated using the plots of experimental moment-deflection behavior and measured vs. predicted moment-strain profiles for each specimen. The service load evaluation included service load tip deflections, specimen cracking patterns and maximum crack-widths, and reinforcement tensile stress ranges. Ease of constructing the model specimens provided the basis for evaluating constructability of full-scale bents. Estimated costs for full-scale bents were based on material quantities used for the model specimens multiplied by the appropriate scale factor and material unit costs.

5.2 Strength Evaluation

Experimental results for the prototype and integrated design specimens clearly illustrate the strength deficiency of the prototype designs and increased strength obtained from the integrated design specimens. Each specimen was evaluated for strength and ductility by examining the moment-deflection response for applied loads above the factored load level, and by evaluating the observed failure mode. The predicted failure load and measured capacity were compared to evaluate the accuracy of the analytical models. Recorded and predicted strain-profiles for pier and overhang cross-sections were compared to evaluate the suitability of the assumed linear strain profile used in section analyses.

5.2.1 Comparison of Overhang Moment vs. Tip Deflection Response

The graph of the overhang moment versus tip displacement response, shown in Figure 5.1, illustrates the poor performance of the two prototype model specimens and the improved behavior of the three integrated design specimens. The maximum applied load for the model of the prototype reinforced concrete bent (POJ-RC-100) was slightly larger than $DL + 1.6LL$, which was equivalent to 0.76 times factored loads. The specimen with the fully-prestressed overhang (POJ-PS-100) failed at a load equivalent to $DL + 0.5LL$ (0.58 times factored loads). Both prototype model bents failed in the joint region because anchorage of overhang and pier longitudinal reinforcement in the joint was insufficient after a diagonal crack developed in the joint.

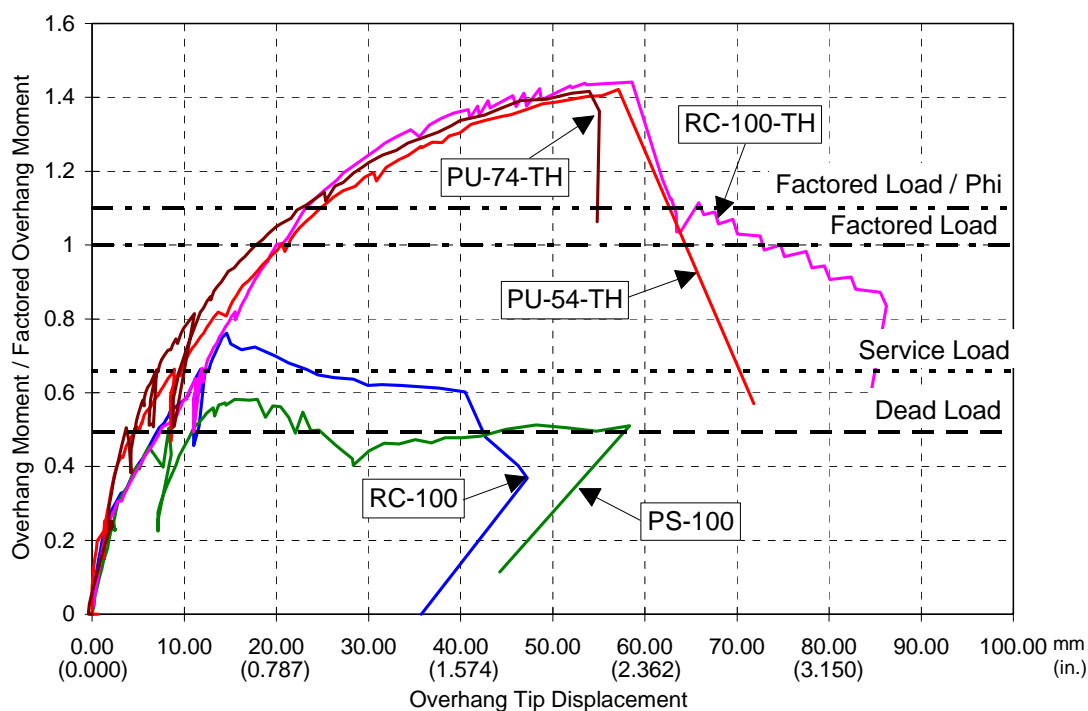


Figure 5.1 Moment vs. Tip Displacement Response for Pier-Overhang-Joint Specimens

The reinforced concrete design with headed reinforcement (POJ-RC-100-TH) resisted an ultimate load of $DL + 5.9 LL$, which was equivalent to 1.44 times factored loads. The improved performance of the integrated design reinforced concrete specimen (POJ-RC-100-TH) over the prototype model reinforced concrete bent (POJ-RC-100) (shown in Figure 5.2) was attributed to the interlocked headed mild reinforcement used in the joint corner. Specimen POJ-RC-100-TH was constructed with 24.8 percent less steel than Specimen POJ-RC-100 because the design provided tensile reinforcement only in tensile regions identified by a strut-and-tie model.

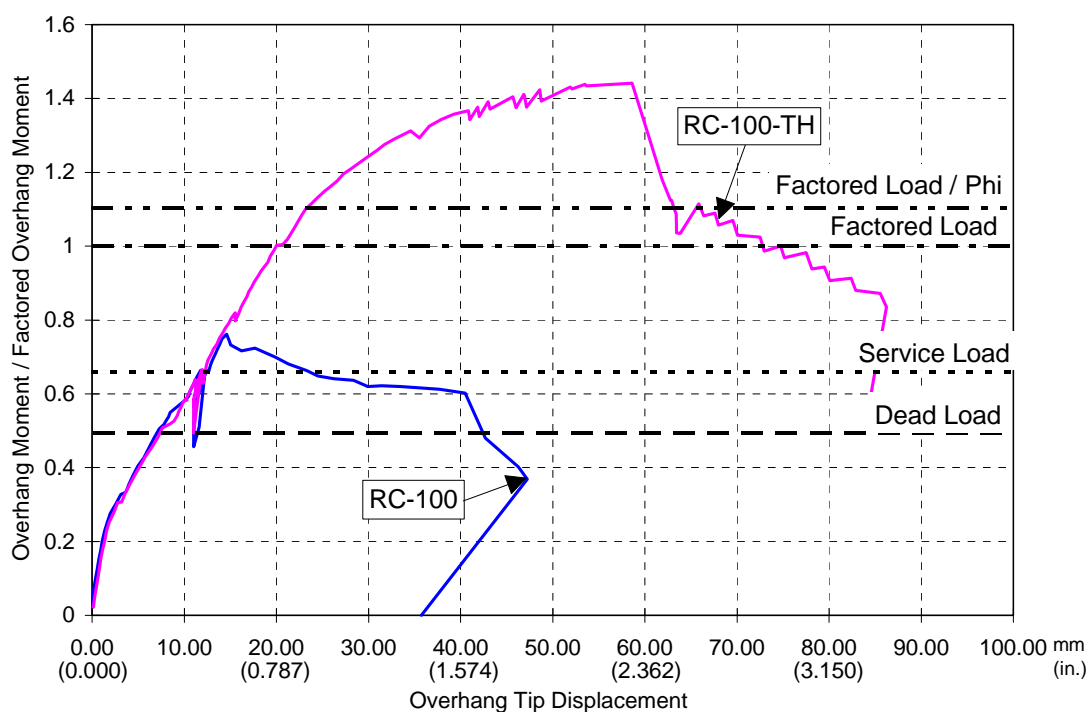


Figure 5.2: Comparison of Moment vs. Tip Displacement Response for Specimens RC-100 and RC-100-TH

The partially-prestressed specimens (POJ-PU-54-TH and POJ-PU-74-TH) utilized headed mild reinforcement and continuous high-strength prestressed reinforcement to resist factored loads. Specimen POJ-PU-54-TH utilized a combination of prestressed reinforcement that provided 54 percent of the total tensile tie force in the overhang and mild reinforcement to resist factored loads. At ultimate, $DL+5.8 LL$ or 1.42 times factored loads, the underside of the overhang for Specimen POJ-PU-54-TH spalled at the face of the column,

resulting in a brittle failure of the overhang. Specimen POJ-PU-74-TH utilized a larger fraction of prestressed reinforcement and also had a capacity well above factored loads. The specimen capacity was not determined because it exceeded the capacity of the testing frame (DL + 6LL).

The three integrated design specimens had similar moment-deflection responses. These specimens were designed using a strut-and-tie model and a strain compatibility-based strength analysis (where plane sections were assumed to remain plane), resulting in nearly identical capacities. All model bents were proportioned for design loads (factored loads / ϕ) to permit realistic capacity and serviceability comparisons with full-scale bents. A portion of the overstrength for the integrated designs is attributed to ϕ factors used in the design.

5.2.2 Comparison of Measured and Predicted Strains

Recorded reinforcement strains were compared with predicted reinforcement strains at the column-overhang cross-section ($X = 30$) and pier mid-height cross-section ($Z = 54$), to evaluate the suitability of a linear strain-gradient used in analysis. Strain gage locations are depicted in Figure 5.3.

Cross-section strain profiles at dead load (DL), service load (DL + LL), dead plus two live loads (DL + 2LL), and factored load (FL) are presented in each graph. The experimental strains presented in each plot were determined by computing the arithmetic average of strain gage readings at the section (i.e. C1 determined from average of strain gage readings for gages A, B, and C). Predicted strains were computed using a spreadsheet-based strain-compatibility analysis. Cross-section strain profiles for Specimen POJ-PS-100 were not plotted due to the early failure of the specimen. Profiles for Specimen POJ-PU-74-TH were not plotted because strain gages malfunctioned.

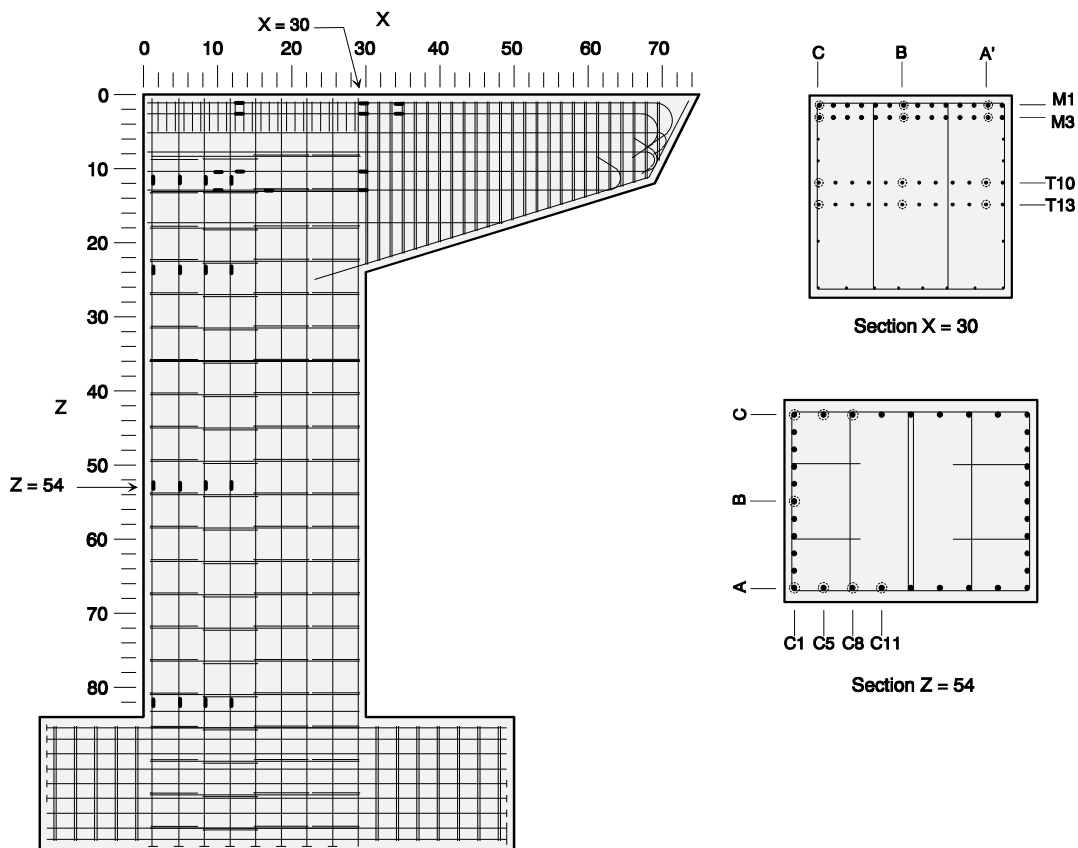


Figure 5.3 Strain Gage Locations for Specimen RC-100

Measured strain profiles for Specimen POJ-RC-100 (prototype model of reinforced concrete bent), shown in Figure 5.4 and Figure 5.5, correlated reasonably well with the analytical model. Due to the early failure in the joint region, the largest recorded applied load was only DL+1.6 LL.

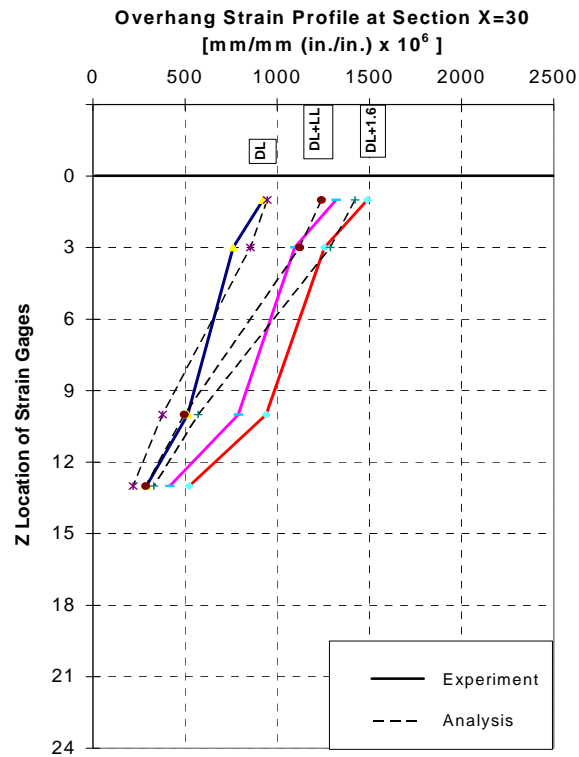


Figure 5.4 POJ-RC-100 - Comparison of Analysis and Test Strain-Profiles for the Overhang at the Face of the Pier

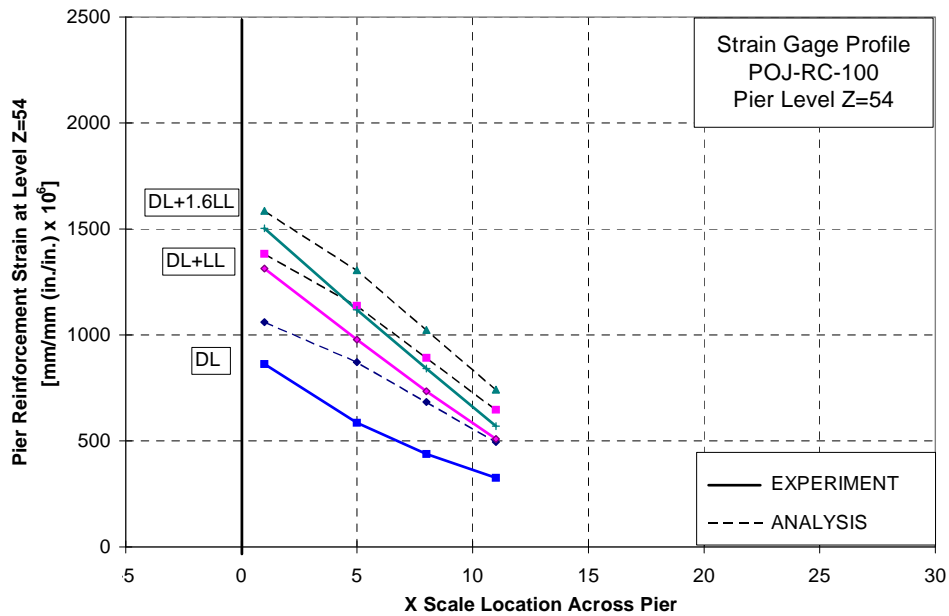


Figure 5.5 POJ-RC-100 - Comparison of Analysis and Test Strain-Profiles for a Cross-Section Near Mid-Height of the Pier

Experimental and predicted strains for Specimen POJ-RC-100-TH (integrated design reinforced concrete specimen with headed reinforcement), shown in Figure 5.6 and Figure 5.7, were in good agreement for the pier cross-section (Figure 5.7), but not for the overhang cross-section (Figure 5.6). The experimental results indicated strains in the side face reinforcement 33 cm (13 in.) from the top surface of the overhang were nearly twice what would be expected from a linear strain profile assumption. However, computed tensile stresses near the top fiber were in close agreement with computed values. The strain-profile for the cross-section of the overhang near the face of the pier Figure 5.6 is similar to the profiles present in the report by Frantz and Breen [10]. The side-face reinforcement controlled strains near mid-depth of the overhang, thus controlling side-face crack widths, but it did not linearize the strain profiles.

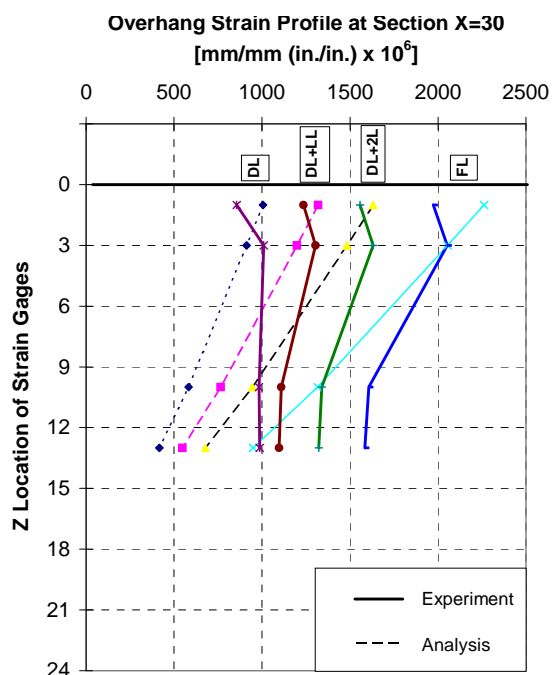


Figure 5.6 POJ-RC-100-TH Comparison of Analysis and Test Strain-Profiles for a Cross-Section of the Overhang Near the Face of the Pier

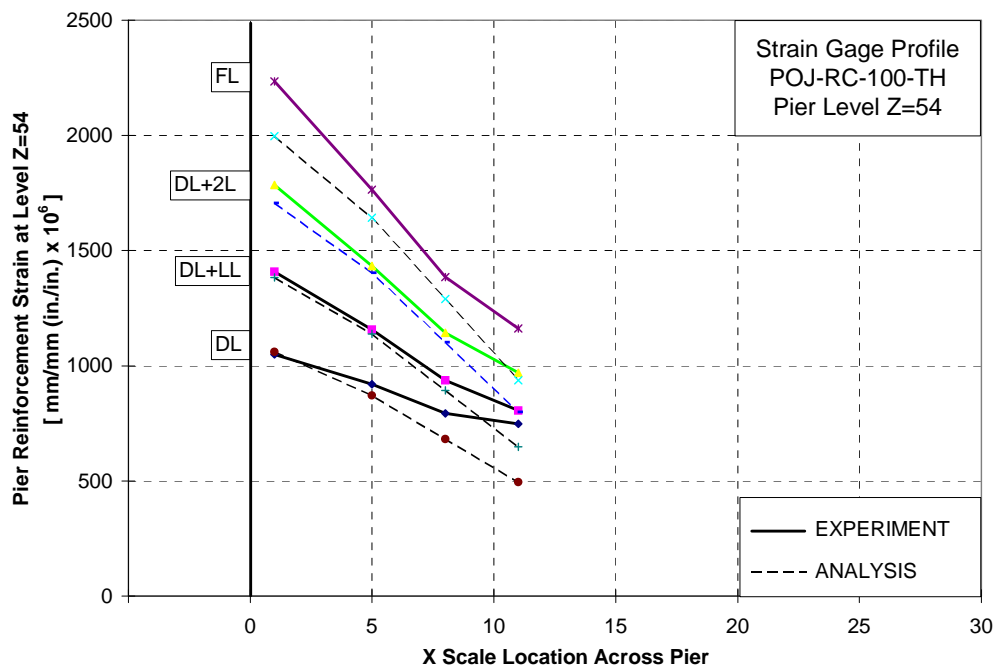


Figure 5.7 POJ-RC-100-TH - Comparison of Analysis and Test Strain-Profiles for a Cross-Section Near Mid-Height of the Pier

The recorded and predicted steel-strains for the overhang cross-section for Specimen POJ-PU-54-TH (Figure 5.8) were in good agreement near the top fibers, but the strain-profiles differed significantly. The strain-profiles at the overhang cross-section, shown in Figure 5.8, were computed assuming the prestress was 1100 MPa (160 ksi) in the overhang. The recorded strain profile indicated reinforcement strains 25 cm (10 in.) from the top of the overhang were nearly twice what would be expected using a linear strain profile.

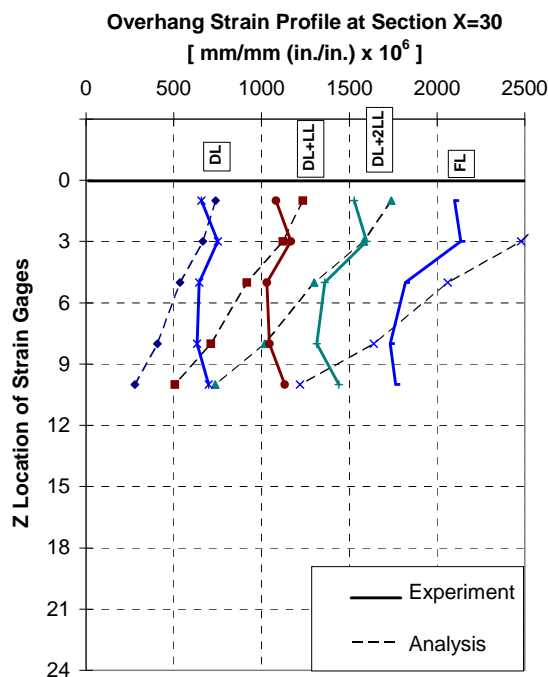


Figure 5.8 POJ-PU-54 - Comparison of Analysis and Test Strain-Profiles for a Cross-Section of the Overhang Near the Face of the Pier

Predicted strain profiles for the pier shown in Figure 5.9 were computed assuming a prestress of 850 MPa (123 ksi) in the pier region after losses occurred in the joint. The assumed pier post-tensioning corresponded with dead load on the bent. The predicted strain-profiles for the cross-section near mid-height of the pier (cross-section Z=54) did not agree with results from the strain gages. Predicted strains in the pier, using a post-tensioning stress of 850 MPa (123 ksi), over-estimated strains in the extreme tensile reinforcement by more than 500 $\mu\epsilon$ (which corresponds to a stress of 100 MPa (14.5 ksi)). The disparity in computed and measured results was attributed to smaller-than-expected post-tensioning losses.

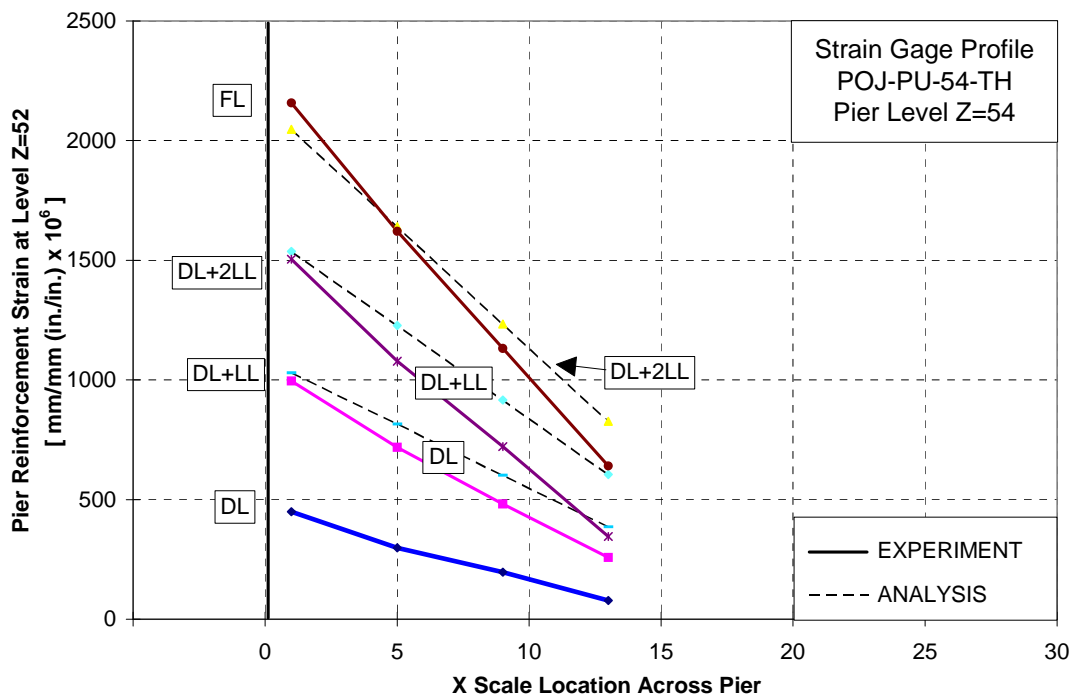


Figure 5.9 POJ-PU-54-TH - Pier Analytical and Experimental Strain-Profiles for a Cross-Section Near Mid-Height of the Pier

The plot of moment vs. measured post-tensioning stress at the base of the pier (shown in Figure 5.10) indicated the average post-tensioning stress was 926 MPa (134 ksi) at dead load [assuming a post-tensioning steel modulus of 193 GPa (28,000 ksi)]. The effective post-tensioning stress at dead load was estimated to be 1030 MPa (150 ksi) using recorded mild steel strains and a strain-compatibility analysis. This indicates the effective post-tensioning stress was larger than the post-tensioning stress assumed during design [850 MPa (123 ksi)]. The increased effective post-tensioning stress in the pier would have resulted in smaller-than-expected crack-widths. Crack-widths are discussed in Section 5.3.3.

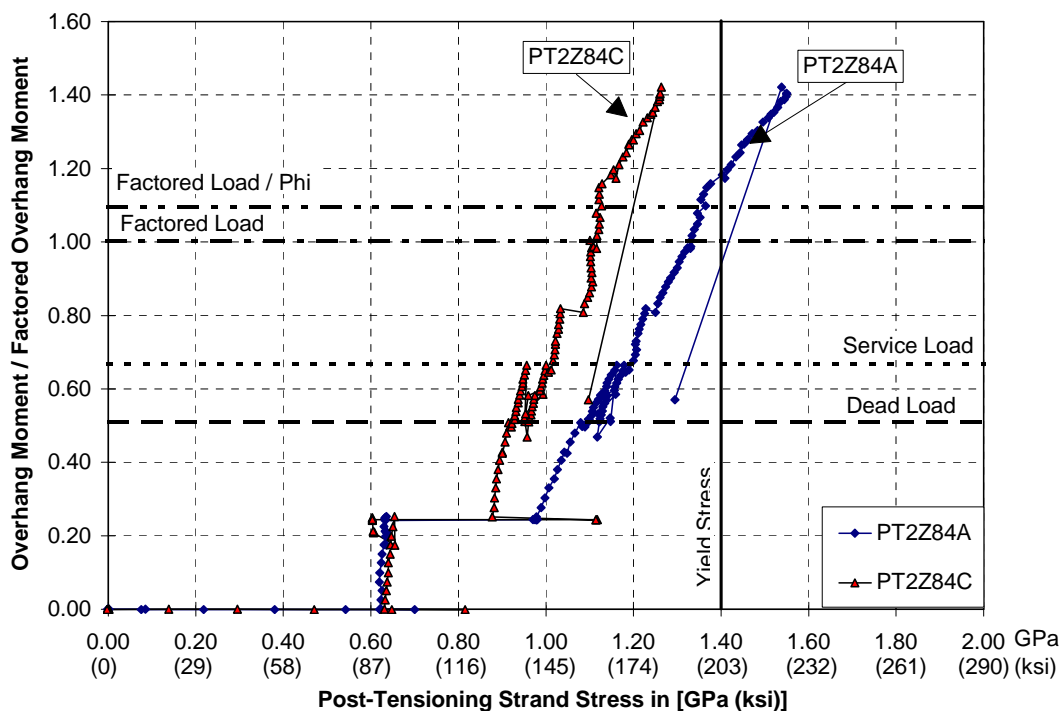


Figure 5.10 Pier Post-Tensioning Stresses for Specimen POJ-PU-54-TH Estimated from Strain Gage Measurements

5.2.3 Comparison of Computed and Measured Capacities

The capacity for each specimen was calculated using both a cracked-section analysis (for flexural strength) and a joint bond-strength model. Nominal yield stress of the mild reinforcement [413 MPa (60 ksi)] was used for computing nominal flexural capacity of the overhang and pier, and the experimentally obtained stress-strain behavior of the mild reinforcement was used to estimate the ultimate flexural capacity of the same members. Nominal capacities are presented to illustrate the difference between ultimate capacities and nominal capacities used in design of the bents. The joint bond-strength model utilized a uniform bond-stress model, nominal yield of the mild reinforcement, and tensile strength of the bonded prestressing strands to determine the bent capacity (as discussed in Chapter 4).

Table 5.1 lists the computed overhang, pier, and “joint” capacities as a fraction of the moment developed at the joint face at factored loads. The ratio of measured-to-predicted capacity was determined by dividing the measured capacity by the computed capacity associated with the observed failure mode. These computed capacities are highlighted in Table 5.1. The proximity of these ratios to unity indicates that both the joint bond-strength model and analysis model for flexural strength provide reasonable strength predictions.

The joint bond-strength model performed best for the prototype model bents, and had an accuracy of $\pm 10\%$. The joint bond-strength model predicted much lower capacities for the integrated designs with headed reinforcement because it did not account for strain hardening of the mild reinforcement. Predicted flexural strength of the overhang and pier were computed using nominal yield of the mild reinforcement (Nominal Capacity) and using the measured stress-strain response the reinforcement (Ultimate Capacity).

Flexural capacity of the integrated design specimens was more than 15% greater than the predicted ultimate capacity. Specimen PU-74-TH was proof-tested to 1.41 times factored loads, so the ratio of measured-to-predicted capacity listed in Table 5.1 is a lower-bound estimate based on the computed ultimate capacity of the overhang. Moment deflection response of Specimen PU-74-TH indicated that it was near the maximum applied load when the test was discontinued.

Table 5.1 Comparison of Computed and Measured Capacities

	OVERHANG		PIER		JOINT	Measured Capacity	Measured/Predicted Capacity	Failure Location
	Nominal Capacity	Ultimate Capacity	Nominal Capacity	Ultimate Capacity	Computed Capacity			
RC-100	1.36	1.49	1.27	1.39	0.69	0.76	1.10	Joint
PS-100	1.63	1.65	1.27	1.39	0.57	0.58	1.02	Joint
RC-100-TH	1.17	1.38	1.27	1.39	1.21	1.44	1.19	Joint
PU-54-TH	1.12	1.24	1.25	1.30	1.23	1.42	1.15	Overhang
PU-74-TH	1.13	1.21	1.31	1.35	1.19	>1.41	>1.17	N/A

5.3 Serviceability Evaluation

Three serviceability conditions were evaluated for each of the specimens: service load deflection, maximum crack-width at service load, and steel stress range. In addition, cracking patterns and crack-width frequency were also examined. Serviceability of the fully-prestressed overhang (POJ-PS-100) was not considered due to early failure of the specimen at DL + 1/2 LL.

5.3.1 Service-Level Tip Deflections

Service-level tip deflections for the models were compared with the L/300 displacement limit stated in AASHTO Section 8.9.3.2 for cantilever members (shown in Fig. 5.11). The allowable service-load deflection was 3.8 mm (0.15 in.) based on an overhang length of 114 cm (45 in.). The prototype reinforced concrete specimen (POJ-RC-100) and reinforced concrete specimen with headed bars (POJ-RC-100-TH) had unacceptable service-level tip deflections that were equivalent to L/229 and L/266 respectively. The partially-prestressed specimens, POJ-PU-54-TH and POJ-PU-74-TH, had acceptable service-level deflections of L/306 and L/497, respectively.

The service-level tip deflections (deflections after initial loading to dead load, referred to as “virgin dead load”) shown in Figure 5.11 demonstrate the reduced deflections associated with increasing percentages of prestressed reinforcement. Dead load deflections following unloading from DL+LL were as much as 66 percent greater than the deflections resulting from first application of dead load. This may have been due to internal friction in the rams during unloading. Deflections resulting from reloading Specimen POJ-PU-54-TH to DL+LL resulted in unacceptable service-level tip deflections, equivalent to L/265. This was a 6 percent increase in deflection. Specimen POJ-PU-74-TH had an acceptable service level tip deflection equivalent to L/465.

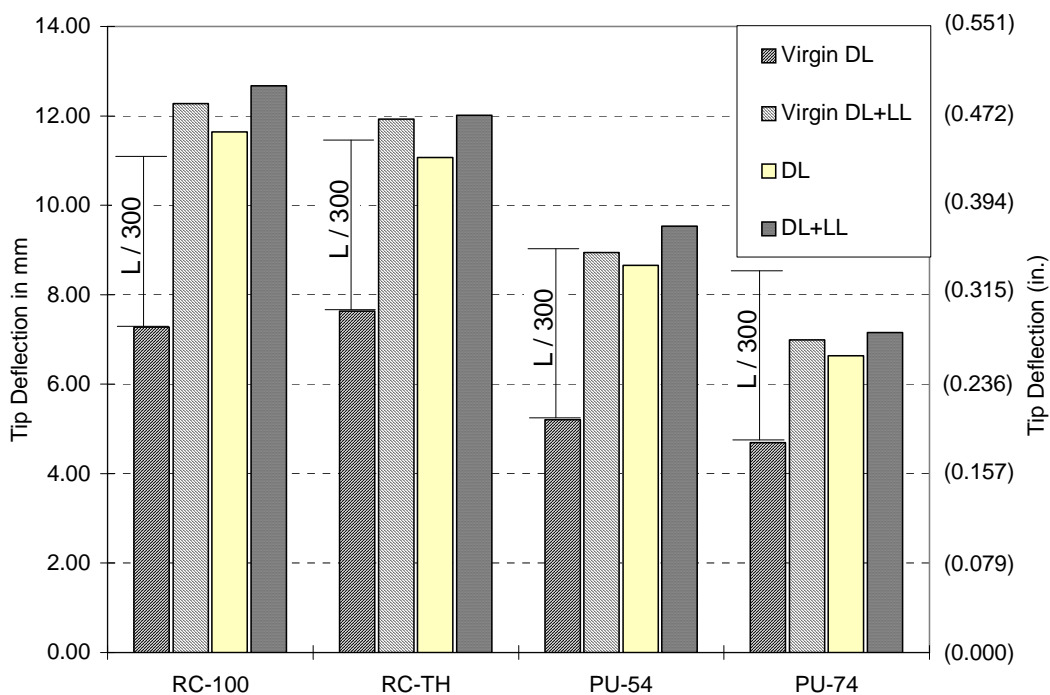


Figure 5.11 Service-Level Tip Deflections

5.3.2 Comparison of Service Load Cracking Patterns with Tensile Stresses from Finite Element Analyses

The service load crack patterns are shown with principal tensile stress contours computed by finite element analyses in Figure 5.12 through Figure 5.21. Elastic finite element analyses confirmed the large principal tensile stresses that existed at service load and dead load, respectively, in the joint regions of the model of the prototype reinforced concrete design (POJ-RC-100) and the model of the prototype fully-prestressed overhang design (POJ-PS-100) (Figs. 5.13 and 5.15, respectively). Due to poor detailing of the joint region in the prototype designs, large tensile stresses resulted in formation of critical diagonal joint cracks (heavier-weighted lines in Figure 5.12 and Figure 5.14) and premature failure of anchorage in the joint.

The finite element analysis for Specimen POJ-RC-100-TH at service-loads (Figure 5.17) indicated the principal tensile stresses in the overhang, joint, and pier regions were above the assumed concrete cracking stress of $7\sqrt{f'_c}$ (psi) [34.4 MPa (500 psi)]. During testing, the specimen developed 28 cracks (shown in Fig. 5.16) located within high tensile regions indicated by the finite element analysis. Cracks in the specimen were well-distributed throughout the tensile regions. Headed reinforcement in the joint corner prevented the diagonal crack (number 9 in Figure 5.16) from propagating to the exterior of the specimen. The pattern of joint cracking suggests additional side-face reinforcement should have been provided for adequate crack control (as shown in Figure 5.36).

The introduction of partial-prestressing had two benefits: it reduced the number of cracks observed at service-loads, and it reduced computed principal tensile stresses in the specimens. Specimen POJ-PU-54-TH had 14 cracks at service loads (Figure 5.18) and computed peak principal tensile stresses across the joint diagonal of 3.8 MPa (400 psi) at service loads (Figure 5.19). As expected, cracks were concentrated in the regions where computed principal tensile stresses were largest. Cracks were well-spaced in the overhang and pier regions, and very few cracks formed in the joint region. Specimen POJ-PU-74-TH had eight cracks at service loads (Figure 5.20) and peak computed principal tensile stresses across the joint diagonal of 1.7 MPa (200 psi) at service loads (Figure 5.21). Cracks in the overhang and pier regions formed in areas where computed principal tensile stresses exceeded the assumed cracking stress of $7\sqrt{f'_c}$ (psi) [34.4 MPa (500 psi)].

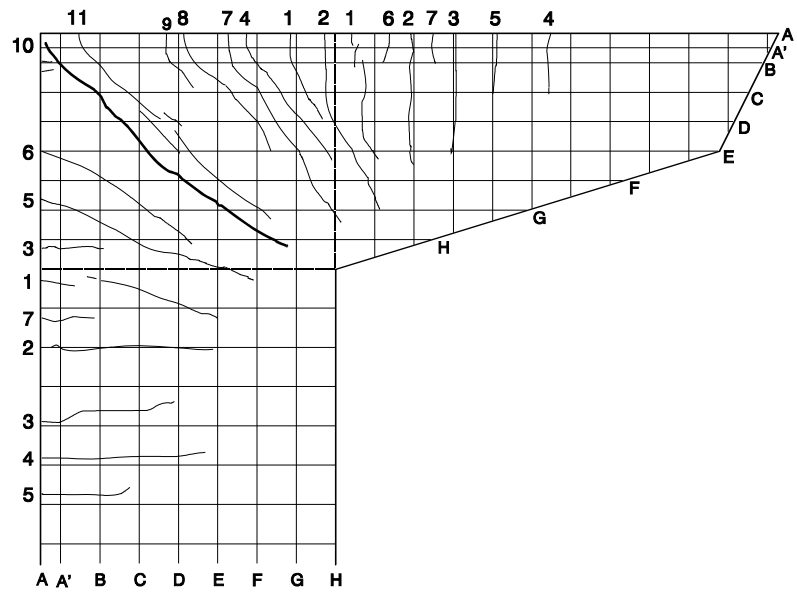


Figure 5.12 POJ-RC-100 - Service Load Crack Pattern

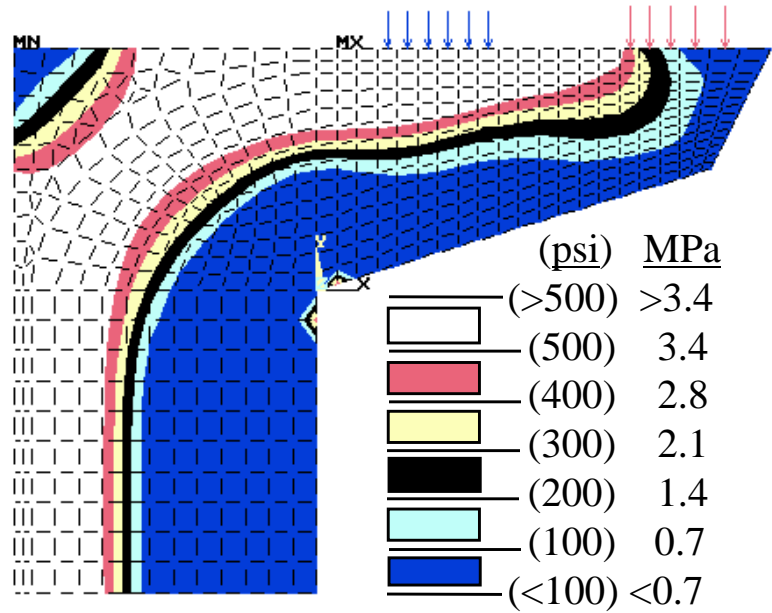


Figure 5.13 POJ-RC-100 - Principal Tensile Stress Contours at Service Load

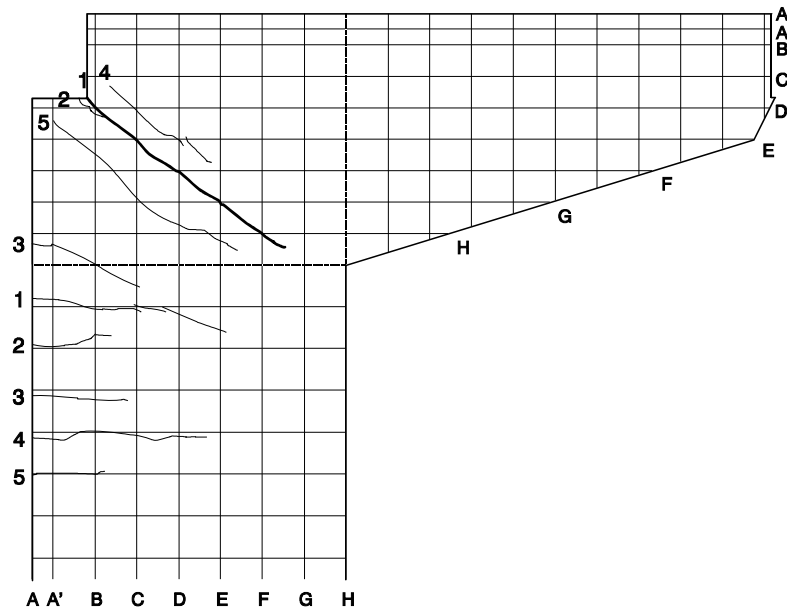


Figure 5.14 POJ-PS-100 - Dead Load Crack Pattern

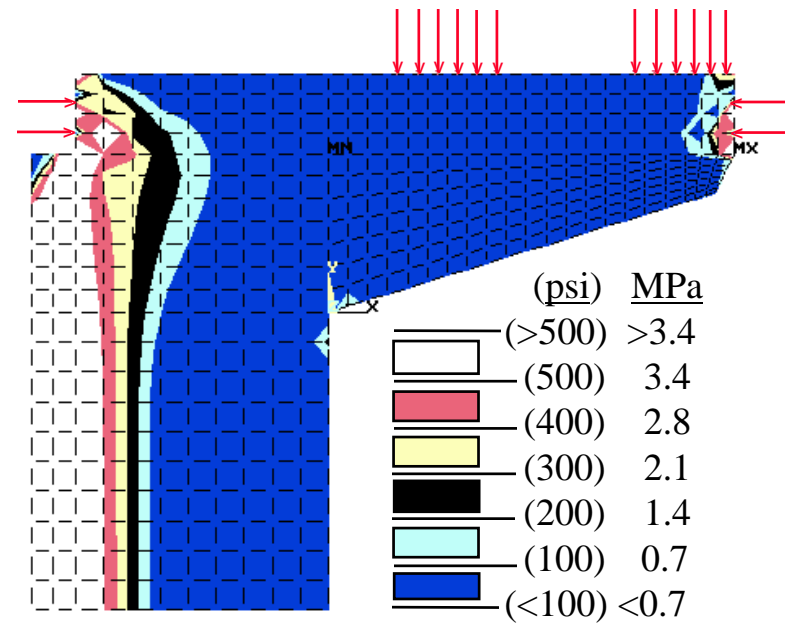


Figure 5.15 POJ-PS-100 - Principal Tensile Stress Contours at Dead Load

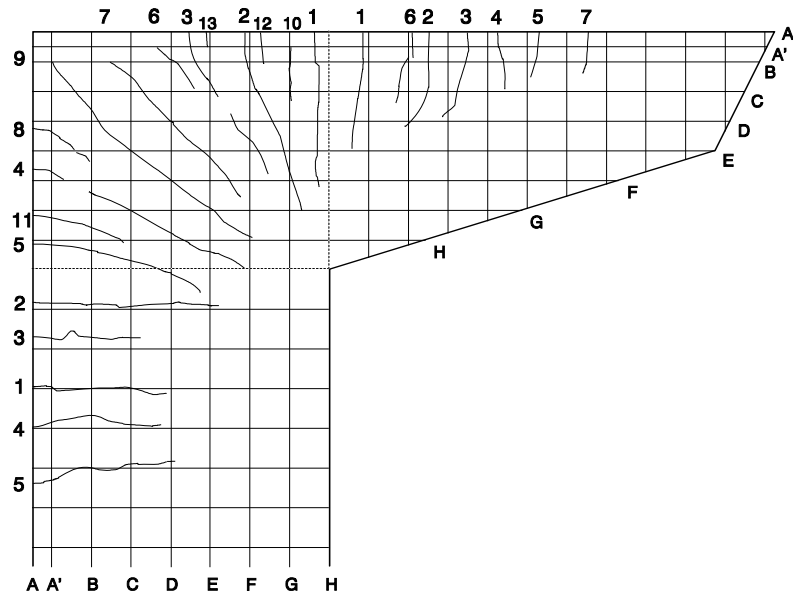


Figure 5.16: POJ-RC-100-TH - Service Load Crack Pattern

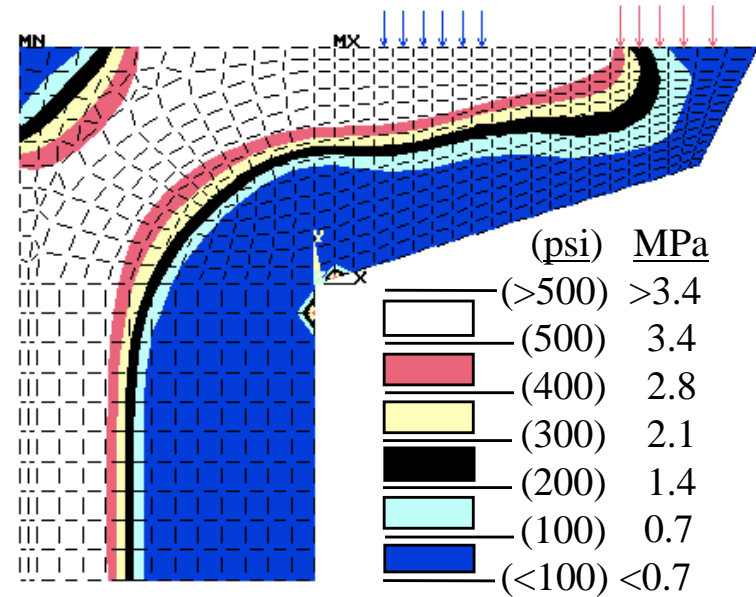


Figure 5.17 POJ-RC-100-TH - Principal Tensile Stress Contours at Service Load

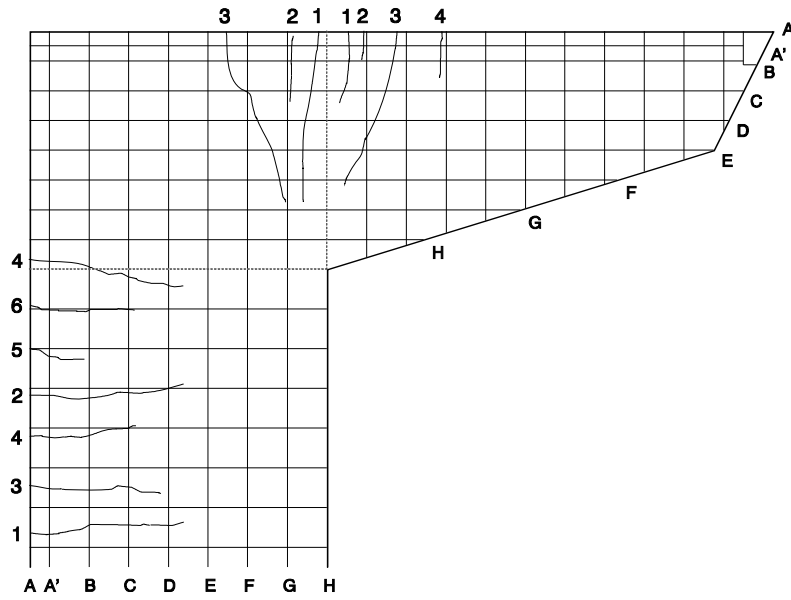


Figure 5.18 POJ-PU-54-TH - Service Load Crack Pattern

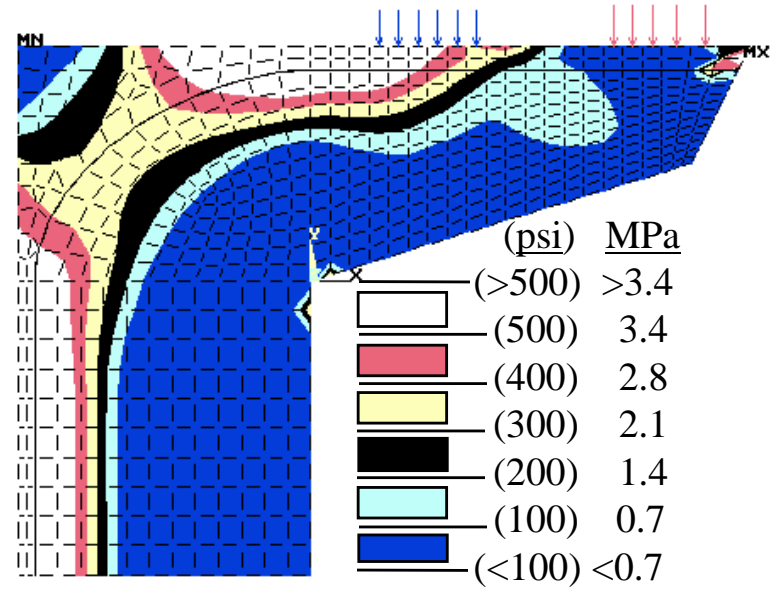


Figure 5.19 POJ-PU-54-TH - Principal Tensile Stress Contours at Service Load

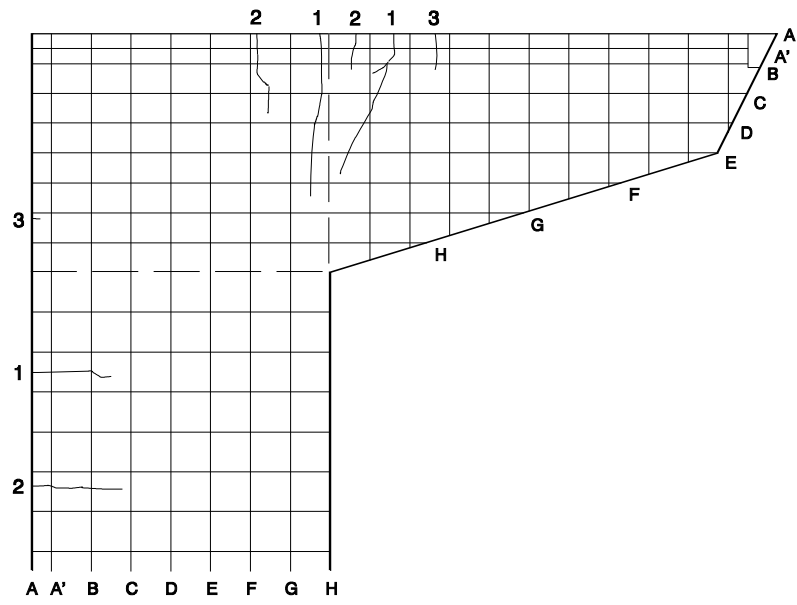


Figure 5.20 POJ-PU-74-TH - Service Load Crack Pattern

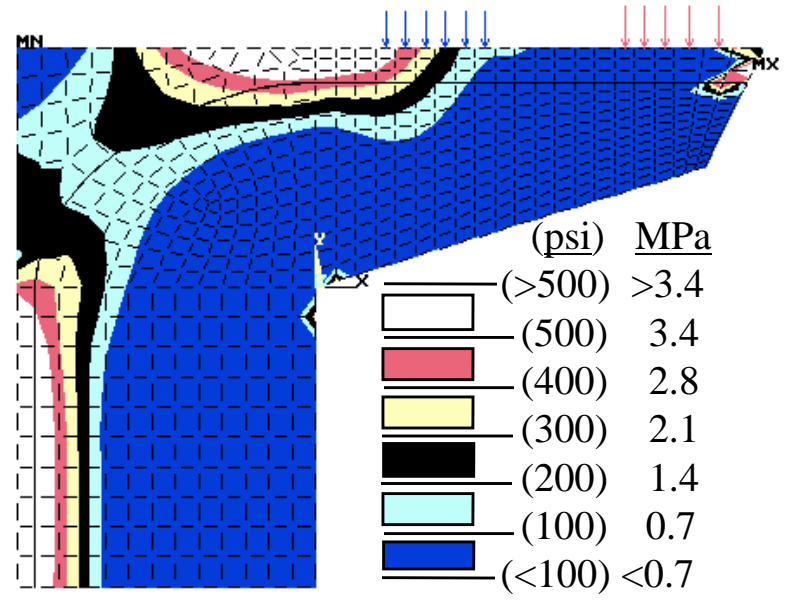


Figure 5.21 POJ-PU-74-TH - Principal Tensile Stress Contours at Service Load

5.3.3 Evaluation of Crack Widths

Crack widths were measured at first cracking, dead load (DL), service load (DL+LL), and dead load plus two live loads (DL + 2LL). Cracks in the overhang, joint, and pier were considered to be of an acceptable width if they were 0.14 mm (0.0055 in.) or smaller. The limiting crack width of 0.14 mm (0.0055 in.) was computed by dividing the 1983 AASHTO Standard Specifications [1] Z factor of 170 (which corresponds to a crack width of 0.039 mm (0.0155 in.)) by the 2.75 scale-factor used in the model. Crack widths were measured in inches using an optical crack-width comparator with an accuracy of ± 0.013 mm (± 0.0005 in.).

The maximum crack widths in the overhang, pier, and joint regions at the loads listed above were used to develop the maximum crack-width envelopes for these regions. Plots of moment versus maximum measured crack width for the three regions are shown in Figure 5.22 through Figure 5.24. Applied moment in the figures is non-dimensionalized using the factored moment, and the measured crack width is non-dimensionalized using the maximum allowable crack width of 0.14 mm (0.0055 in.).

5.3.3.1 Overhang Crack-Width Envelopes

The crack-width envelope for the overhang region of each specimen is shown in Figure 5.22. The plot indicates the integrated design reinforced concrete specimen (POJ-RC-100-TH) and the 54 % prestressed specimen (POJ-PU-54-TH) had maximum measured crack widths at loads at or below DL+LL that exceeded the maximum allowable crack width of 0.14 mm (0.0055 in.). Specimens POJ-RC-100-TH and POJ-PU-54-TH had maximum overhang crack-widths of 0.18 mm (0.007 in.) and 0.15 mm (0.006 in.), respectively, at service load. Both cracks were located at the extreme tensile fiber of the overhang (Level (A)). Frequency distribution plots, shown in Figure 5.26 and Figure 5.27, indicate that only 0.4 percent and 1.1 percent of measured crack widths for Specimens POJ-RC-100-TH and POJ-PU-54-TH, respectively, were greater than the maximum allowable crack width.

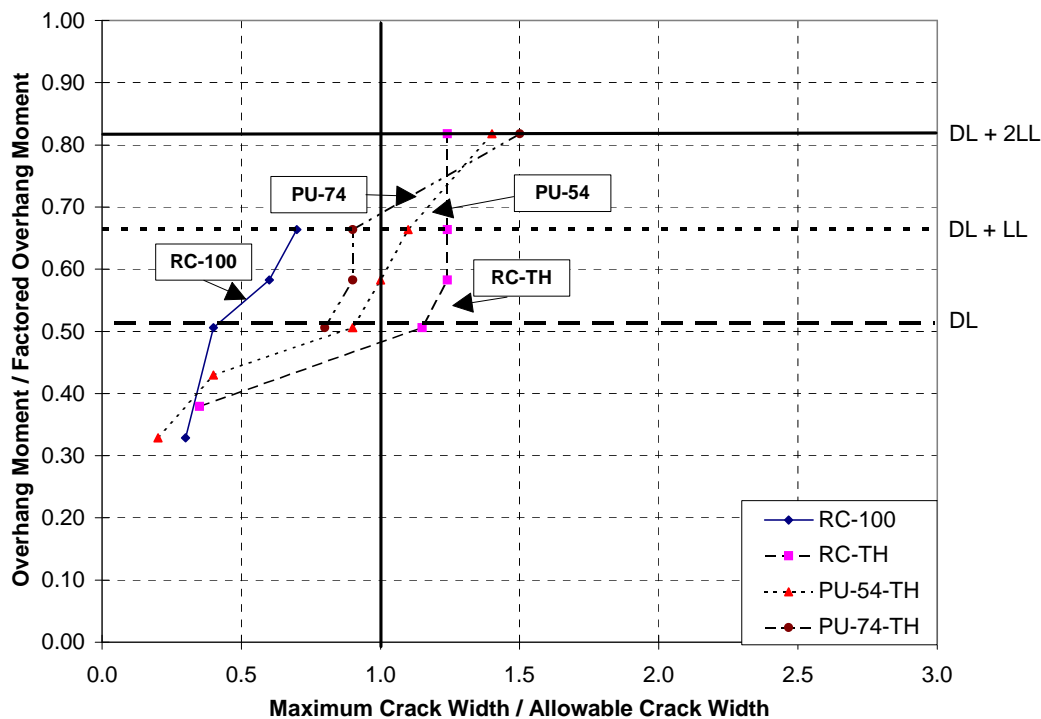


Figure 5.22 Crack-Width Envelopes for Overhang Region

5.3.3.2 Joint Crack-Width Envelopes

The joint crack-width envelopes, shown in Figure 5.23, indicate the prototype reinforced concrete model (POJ-RC-100), integrated reinforced concrete (POJ-RC-100-TH), and 54% prestressed (POJ-PU-54-TH) specimens had joint crack widths greater than the limiting crack width of 0.14 mm (0.0055 in.). Specimens POJ-RC-100 and POJ-RC-100-TH had 31 and 42 crack measurements, respectively, that exceeded the maximum allowable crack-width (which corresponds to 14.8 % and 9.4 % of all measured cracks, respectively). The maximum joint crack width in Specimen POJ-PU-54-TH [0.17 mm (0.0065 in.)] was measured in one location on the north side and two locations on the south side after loading to service load a second time. The crack-width frequency plots for Specimen POJ-PU-54-TH, shown in Figure 5.27, indicate only 1.8 percent of the measured joint crack widths exceeded the maximum allowable crack width.

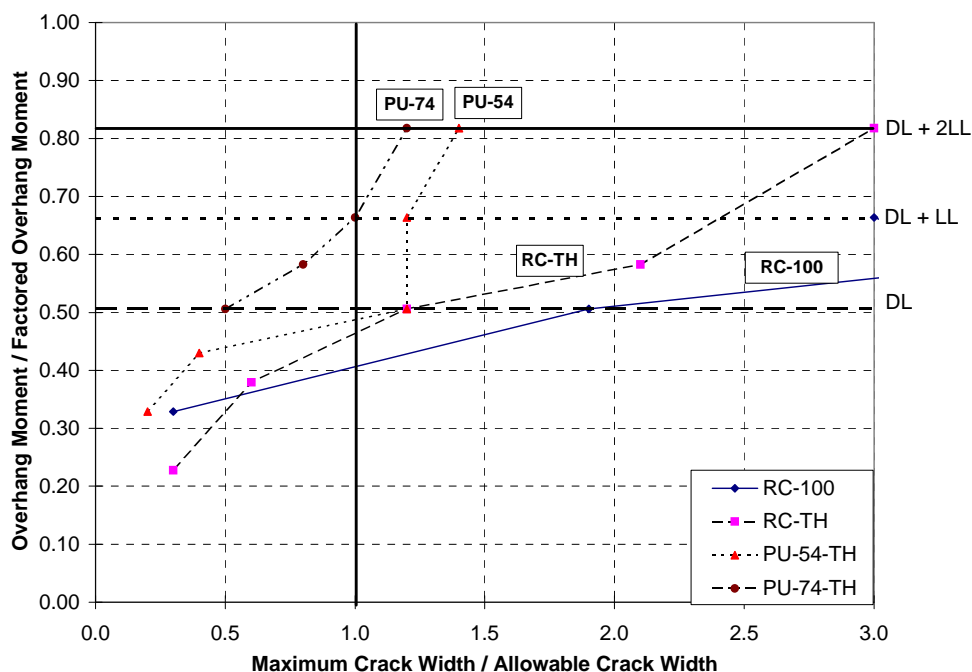


Figure 5.23 Crack-Width Envelopes for Joint Region

At service load, both Specimens POJ-RC-100 and POJ-RC-100-TH had numerous cracks in the joint region with widths that exceeded the maximum allowable crack width. Joint cracks in Specimen POJ-RC-100 were indicative of the imminent bond failure that ultimately resulted due to the lack of adequate bar anchorage in the joint region. Joint cracks in Specimen POJ-RC-100-TH indicated the need for additional side-face reinforcement to improve serviceability. It was known prior to construction of this specimen that additional transverse reinforcement was needed in the joint (as shown in Figure 5.36). However, additional detailing reinforcement was not provided in order to isolate and evaluate the effect of headed mild reinforcement on the behavior of the specimen.

5.3.3.3 Pier Crack-Width Envelopes

Crack-width envelopes for the pier region, shown in Figure 5.24, indicate the reinforced concrete specimens (POJ-RC-100 and POJ-RC-100-TH) had crack widths that exceeded the maximum allowable crack width at service loads. The reinforced concrete piers had identical designs, and envelopes of the maximum crack widths were similar. Pier crack widths could have been reduced by replacing the longitudinal bars used in the piers with a greater number of smaller-diameter bars. Crack-width envelopes for the partially-prestressed specimens, POJ-PU-54-TH and POJ-PU-74-TH, indicated crack-widths were acceptable.

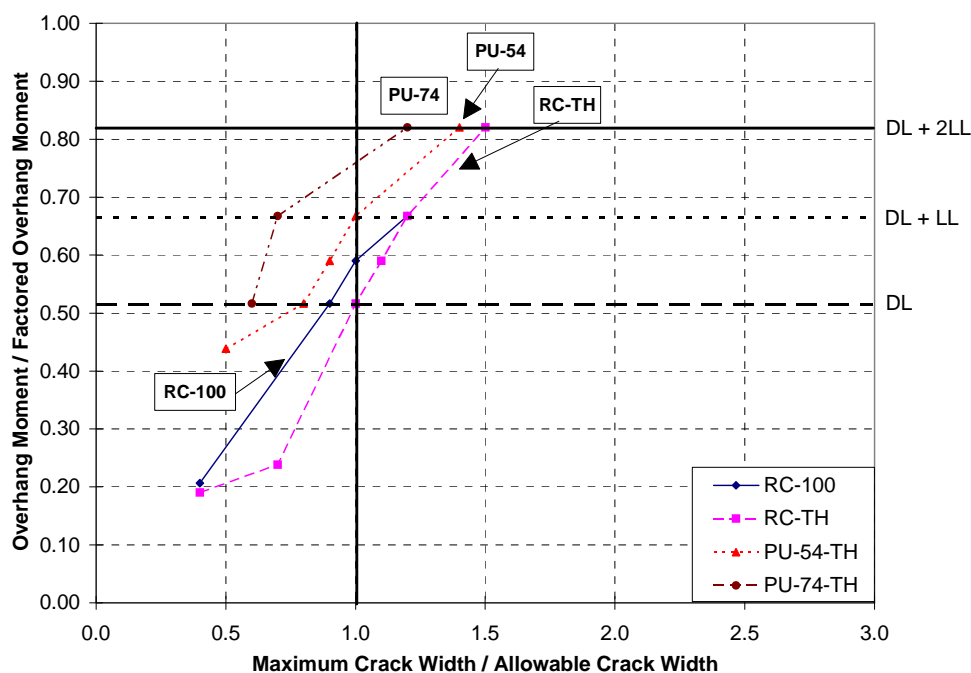


Figure 5.24 Crack-Width Envelopes for Pier Region

5.1 Introduction	238
5.2 Strength Evaluation	238
5.2.1 Comparison of Overhang Moment vs. Tip Deflection Response.....	239
5.2.2 Comparison of Measured and Predicted Strains	241
5.2.3 Comparison of Computed and Measured Capacities	248
5.3 Serviceability Evaluation.....	250
5.3.1 Service-Level Tip Deflections	250
5.3.2 Comparison of Service Load Cracking Patterns with Tensile Stresses from Finite Element Analyses.....	251
5.3.3 Evaluation of Crack Widths	258
5.3.3.1 Overhang Crack-Width Envelopes	258
5.3.3.2 Joint Crack-Width Envelopes	259
5.3.3.3 Pier Crack-Width Envelopes.....	261
 Figure 5.1 Moment vs. Tip Displacement Response for Pier-Overhang-Joint Specimens ...	239
Figure 5.2: Comparison of Moment vs. Tip Displacement Response for Specimens RC-100 and RC-100-TH.....	240
Figure 5.3 Strain Gage Locations for Specimen RC-100	242
Figure 5.4 POJ-RC-100 - Comparison of Analysis and Test Strain-Profiles for the Overhang at the Face of the Pier.....	243
Figure 5.5 POJ-RC-100 - Comparison of Analysis and Test Strain-Profiles for a Cross- Section Near Mid-Height of the Pier.....	243
Figure 5.6 POJ-RC-100-TH Comparison of Analysis and Test Strain-Profiles for a Cross- Section of the Overhang Near the Face of the Pier	244
Figure 5.7 POJ-RC-100-TH - Comparison of Analysis and Test Strain-Profiles for a Cross- Section Near Mid-Height of the Pier.....	245
Figure 5.8 POJ-PU-54 - Comparison of Analysis and Test Strain-Profiles for a Cross-Section of the Overhang Near the Face of the Pier	246

Figure 5.9 POJ-PU-54-TH - Pier Analytical and Experimental Strain-Profiles for a Cross- Section Near Mid-Height of the Pier.....	247
Figure 5.10 Pier Post-Tensioning Stresses for Specimen POJ-PU-54-TH Estimated from Strain Gage Measurements.....	248
Figure 5.11 Service-Level Tip Deflections.....	251
Figure 5.12 POJ-RC-100 - Service Load Crack Pattern	253
Figure 5.13 POJ-RC-100 - Principal Tensile Stress Contours at Service Load.....	253
Figure 5.14 POJ-PS-100 - Dead Load Crack Pattern.....	254
Figure 5.15 POJ-PS-100 - Principal Tensile Stress Contours at Dead Load	254
Figure 5.16: POJ-RC-100-TH - Service Load Crack Pattern	255
Figure 5.17 POJ-RC-100-TH - Principal Tensile Stress Contours at Service Load	255
Figure 5.18 POJ-PU-54-TH - Service Load Crack Pattern.....	256
Figure 5.19 POJ-PU-54-TH - Principal Tensile Stress Contours at Service Load	256
Figure 5.20 POJ-PU-74-TH - Service Load Crack Pattern.....	257
Figure 5.21 POJ-PU-74-TH - Principal Tensile Stress Contours at Service Load	257
Figure 5.22 Crack-Width Envelopes for Overhang Region.....	259
Figure 5.23 Crack-Width Envelopes for Joint Region.....	260
Figure 5.24 Crack-Width Envelopes for Pier Region.....	261
 Table 5.1 Comparison of Computed and Measured Capacities.....	 249

5.3.4 Crack-Width Frequency and Distribution at Service Loads

The crack-width frequency and distribution plots, shown in Figure 5.25 through Figure 5.28, indicate which regions of each specimen contained the widest cracks and/or the largest number of cracks. The plots depict the number of crack measurements (of a particular width) that occurred in the pier, overhang, and joint regions as a percentage of all crack-width measurements taken at service loads. The plots were typically developed using the crack-width readings taken at "virgin" service loads and after reloading each specimen to service loads (the POJ-RC-100 specimen used only the readings taken at "virgin" service-loads). Crack-widths were measured in inches with 0.013 mm (0.0005 in.) increments.

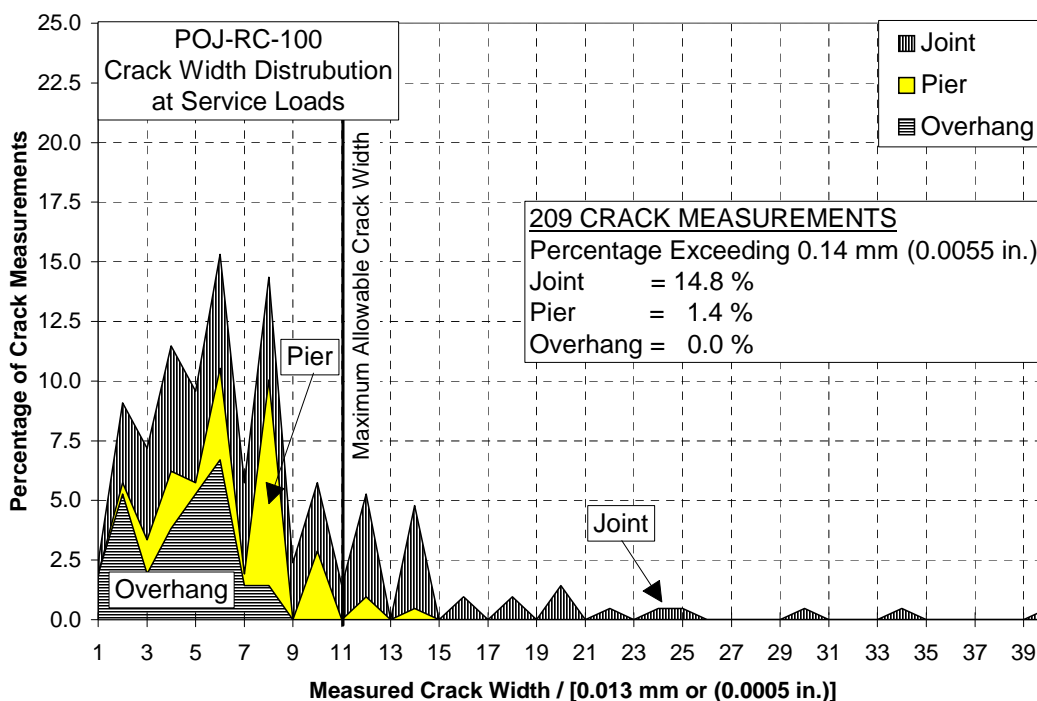


Figure 5.25 POJ-RC-100 Crack-Width Frequency and Distribution

The crack-width frequency and distribution for the prototype reinforced concrete specimen (POJ-RC-100), shown in Figure 5.25, was developed using one set of service load crack-width readings. At service loads, 209 crack widths were measured (112 on the north side and 97 on the south side of the specimen). Over 16 percent of all crack measurements

for the specimen exceeded the maximum allowable crack width; 14.8 percent and 1.4 percent of the crack measurements at service load were in the joint and pier regions, respectively.

The frequency and distribution of crack widths within the different regions for the reinforced concrete specimen with T-headed bars (POJ-RC-100-TH) is shown in Figure 5.26. The north side had 231 crack-width measurements and the south side had 223 measurements at service-loads. The pier, overhang, and joint regions of the specimen all had crack widths that exceeded the maximum allowable crack width of 0.14 mm (0.0055 in.). In the joint region, 42 crack measurements (9.4 percent of all measured cracks) exceeded the maximum allowable crack width. Only seven crack measurements in the pier and two in the overhang (1.5 percent and 0.4 percent of the measured crack-widths, respectively) exceeded the maximum allowable crack width at service loads.

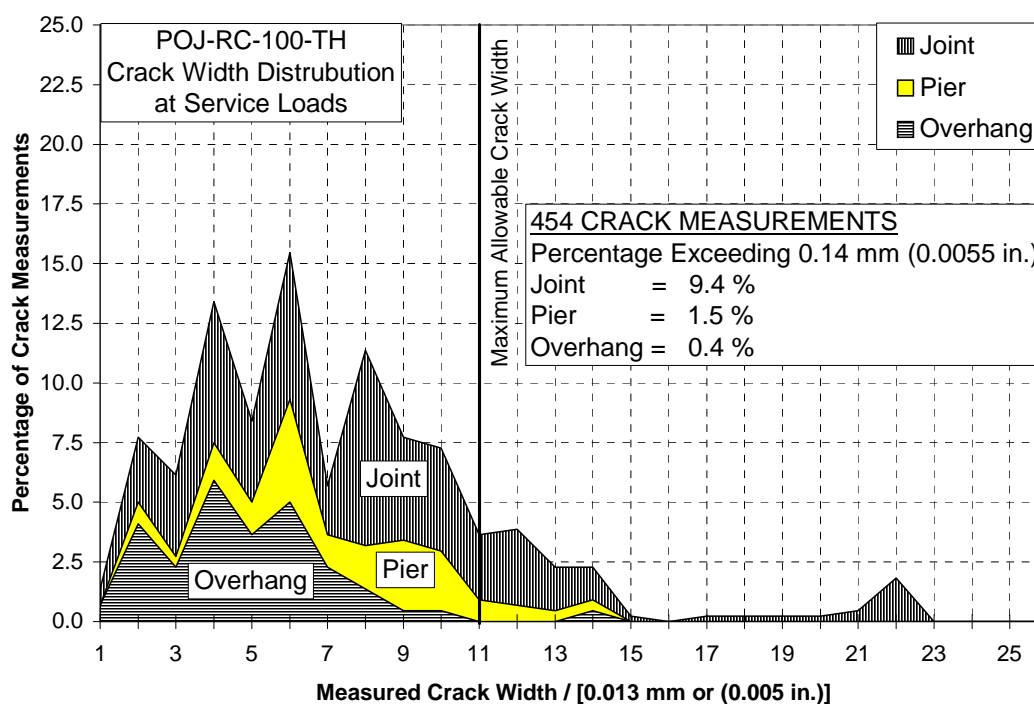


Figure 5.26 POJ-RC-100-TH Crack-Width Frequency and Distribution

The crack-width frequency and distribution plot for the specimen with a 54 percent prestressed overhang and headed bars (POJ-PU-54-TH) is shown in Figure 5.27. The north side had 130 crack-width measurements and the south-side had 142 crack-width

measurements. Only 2.9 percent of the 272 crack widths measured exceeded the maximum allowable crack width at service load. The crack widths that exceeded the maximum allowable crack width were located in the joint region (five crack measurements or 1.8 percent of all measurements) and the overhang region (three crack measurements or 1.1 percent).

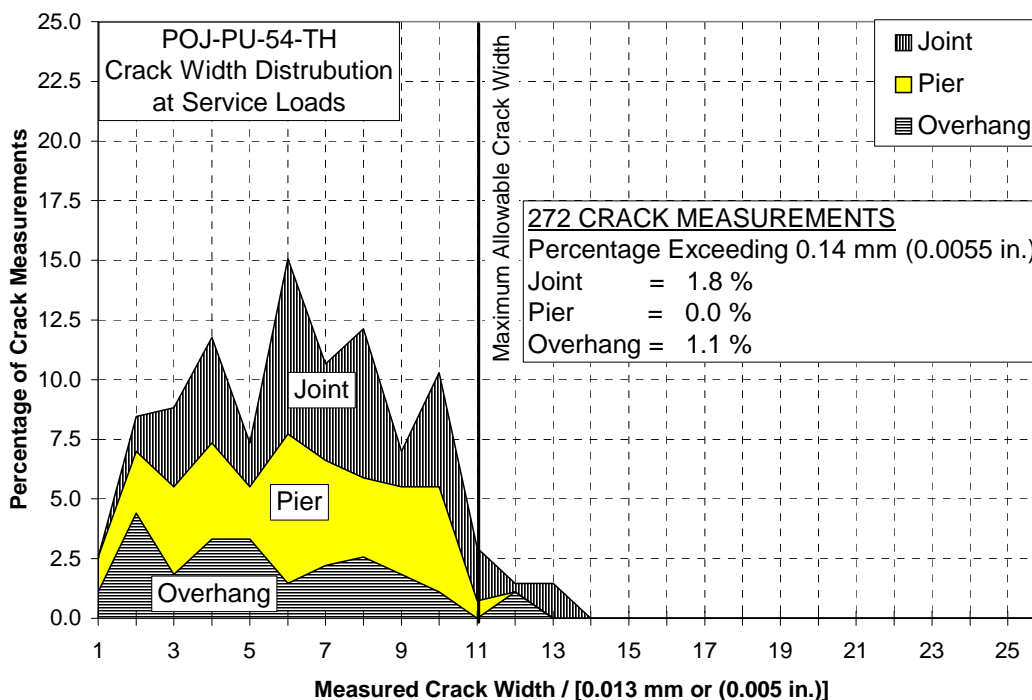


Figure 5.27 POJ-PU-54-TH Crack-Width Frequency and Distribution

The crack-width frequency and distribution for the specimen with a 74 percent prestressed overhang and T-headed bars (POJ-PU-74-TH), shown in Figure 5.28, indicated all measured crack widths were less than the crack-width limit. The 128 crack-width measurements taken at service loads included 54 crack-width measurements on the north side and 74 crack-width measurements on the south side of the specimen. Crack widths on the north side of the specimen were fairly well distributed, while crack widths on the south side were small (typically less than 0.6 mm (0.025 in.)).

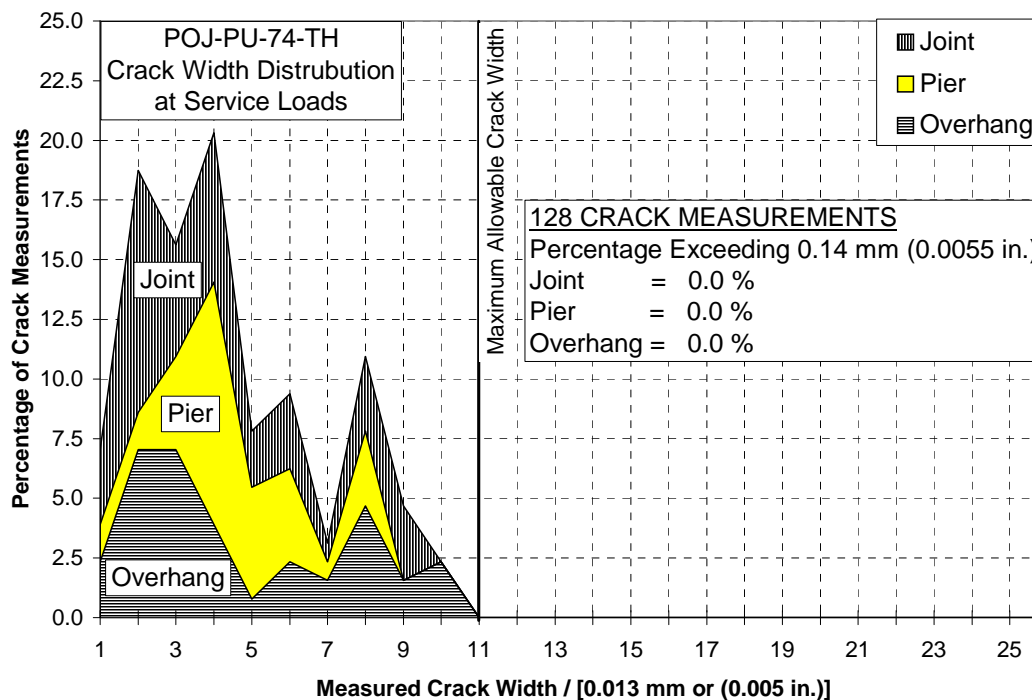


Figure 5.28 POJ-PU-74-TH Crack-Width Frequency and Distribution

5.3.5 Comparison of Measured vs. Predicted Crack Widths

Values for the maximum measured crack widths and maximum predicted crack widths, shown in Figure 5.30 through Figure 5.33, are plotted at dead load (DL), service load (DL+LL), and DL+2 LL for the overhang and pier regions. Predicted crack-widths were computed using the proposed crack width model (which will be presented shortly) and a strain compatibility analysis.

The accuracy of crack-width equations has been historically limited to an accuracy of ± 50 percent [16]. The rough appearance of the crack width on the surface, the distribution of cracks, and lack of repeatable experimental crack-width results make it difficult to accurately predict crack widths. Crack-width equations, used in design, determine the distribution of reinforcement in members. This serviceability check should produce members with controlled crack widths, resulting in aesthetically pleasing and durable structures.

The maximum allowable crack width of 0.14 mm (0.0055 in.) and the corresponding Z factor of 62 used for the study, were determined by dividing the full-scale maximum allowable crack width of 0.39 mm (0.0155 in.) and corresponding Z factor of 170 by the 2.75 scale factor. A Z factor of 170 provides protection for moderate exposure conditions and ensures cracks are not visible from a reasonable distance. If a more stringent limiting crack width for durability is specified for partially-prestressed members, the crack-width equation can be used to further limit crack widths.

Distribution of Tension Reinforcement:

The crack-width equation used in this study was similar to the formula in the 1992 AASHTO LRFD (Eq. 5.7.3.4.2-1) [19] and was developed to predict maximum crack widths for the overhang specimens studied by Armstrong [3] and Salas [4]. The important variables in the equation are: steel tension stress, size of the tension block, and number of bars in the tension block. Steel tensile stress is determined using a cracked-section model. Size of the tension block is computed by determining the effective steel centroid of the mild and prestressed reinforcement. The number of steel reinforcing bars in the tension block as well as the number of bonded prestressing strands or grouted post-tensioning ducts were considered to help control crack widths.

Crack-Width Equation:

The crack-control equation used for the integrated design procedure, presented in Eq. 3-29, is reformulated in Eq. 5-1 to compute crack widths for direct comparison with maximum-measured crack widths. Variables for the crack-width equation (Eq. 5-1) are illustrated in Figure 5.30 and are defined below:

$$w = 0.000076\beta f_{sa} (d_c A)^{\frac{1}{3}} \quad [5- 1]$$

where:

- | | | |
|----------|---|---|
| w | = | Maximum Crack-Width (in.) |
| β | = | Value of 1.2 |
| f_{sa} | = | Average steel tensile stress (ksi) at a distance d'' from the extreme |
| | | tensile fiber = $\epsilon_{d''}$ (29,000 ksi) , where $\epsilon_{d''}$ is the tensile strain at the effective steel centroid, d'' |
| d_c | = | Distance from the extreme tension fiber to the centroid of the closest |

layer of primary tension reinforcement (in.)

A = Area of tension block ($2 \times d'' \times b_w$) (in^2) divided by the total number of mild reinforcing bars, bonded prestressing strands, and/or grouted post-tensioning ducts located within the tension block

$$d'' = \frac{[\sum A_{ps} d_{ps} f_{su} + \sum A_{ms} d_{ms} f_y]}{[\sum A_{ps} f_{su} + \sum A_{ms} f_y]} \quad [5-2]$$

where:

d_{ps} = Distance from the extreme tension fiber to centroid of each layer of prestressed reinforcement in the tension zone

A_{ps} = Area of prestressed reinforcement at a layer

d_{ms} = Distance from extreme tension fiber to centroid of each layer of mild reinforcement in the tension zone

A_{ms} = Area of mild reinforcement at a layer.

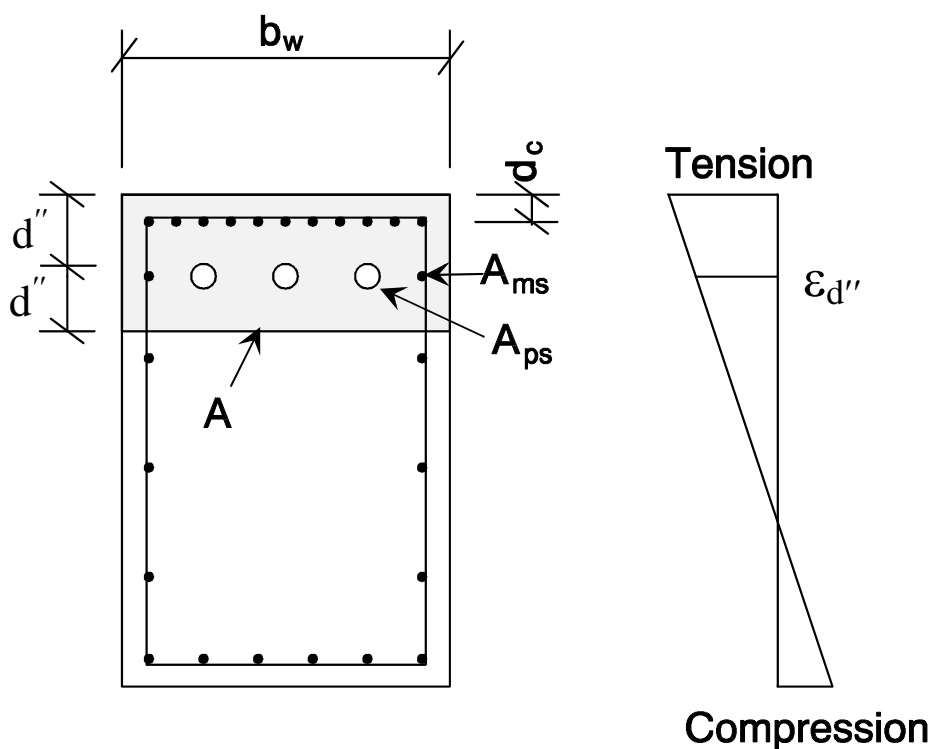


Figure 5.29 Illustration of Crack-Width Equation Variables

The average steel tensile stress, f_{sa} , was computed by multiplying the strain, $\epsilon_{d''}$, at the effective steel centroid by 29,000 ksi. Strain at the effective steel centroid, $\epsilon_{d''}$, was determined using a strain compatibility analysis where stress in the bonded prestressed

reinforcement was reduced to account for long-term losses. Computed crack widths in the overhang and pier for service loads, using Eq. 5-1, are shown in Table 5.2 and Table 5.3, respectively.

Table 5.2: Computed Overhang Crack Widths at Service Loads

	d	d''	A	fsa	w	w
	(in.)	(in.)	(in²/#)	(ksi)	(in.)	mm
RC-100	1.14	5.00	7.50	26.9	0.0050	0.13
RC-100-TH	1.14	1.86	3.19	36.5	0.0051	0.13
PU-54-TH	1.14	1.55	4.37	34.9	0.0054	0.14
PU-74-TH	1.14	2.85	8.05	28.6	0.0055	0.14

Table 5.3 Computed Pier Crack Widths at Service Loads

	d	d''	A	fsa	w	w
	(in.)	(in.)	(in²/#)	(ksi)	(in.)	mm
RC-100	1.13	4.76	15.23	32.8	0.0077	0.196
RC-100-TH	1.13	4.76	15.23	32.8	0.0077	0.196
PU-54-TH	1.13	5.24	22.86	35.4	0.0095	0.241
PU-74-TH	1.11	3.29	14.36	33.5	0.0077	0.196

Maximum measured and predicted crack widths for the pier and overhang, shown in Figure 5.30 through Figure 5.33, are compared at dead load (DL), dead load plus one-half live load (DL+1/2 LL), service load (DL+LL), and dead-load plus two live loads (DL+ 2 LL). The maximum crack widths were non-dimensionalized by dividing by the maximum allowable crack width of 0.14 mm (0.00055 in.), which corresponds with a Z factor of 62 ($Z=170 / 2.75$ scale factor).

For the prototype reinforced concrete specimen (POJ-RC-100), maximum measured crack-widths in the overhang were slightly less than crack-widths predicted by Eq. 5-1, as shown in Figure 5.30. Measured crack widths in the pier were in good agreement with predicted crack widths.

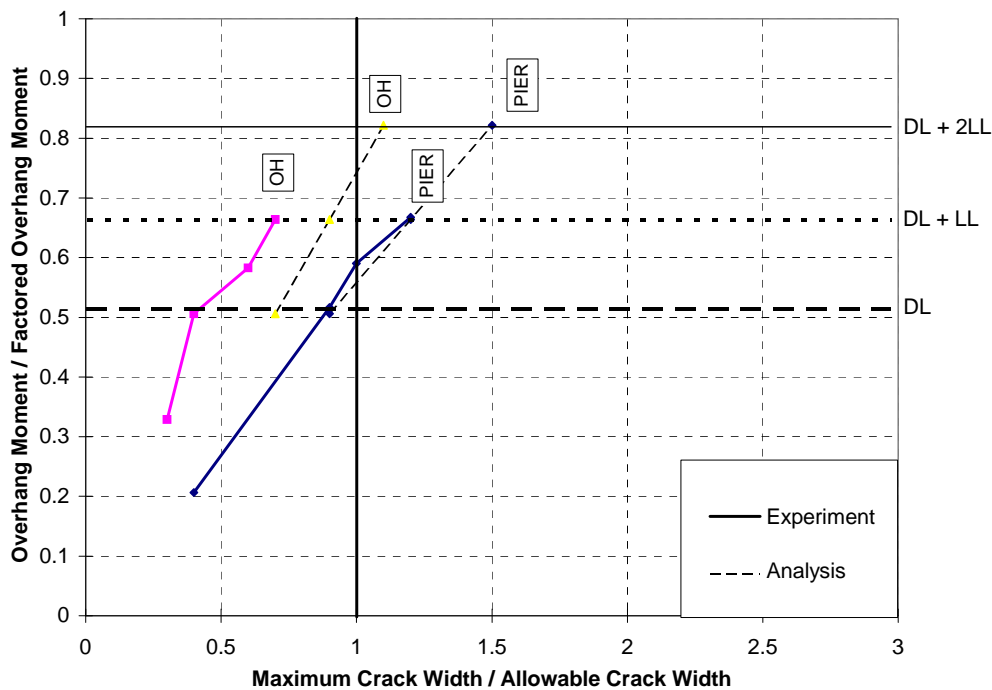


Figure 5.30 POJ-RC-100 Maximum Predicted and Measured Crack Widths

For the reinforced concrete specimen with headed reinforcement (POJ-RC-100-TH), the maximum measured crack widths in the pier closely matched the crack-widths predicted by Eq. 5-1. The maximum measured crack width in the overhang at service load was nearly 50 percent larger than the value predicted using Eq. 5-1, but the maximum predicted and measured crack widths were in good agreement at DL+2LL. Figure 5.31 indicates a large crack developed at DL, but the crack width did not significantly increase with increased load to DL + 2LL.

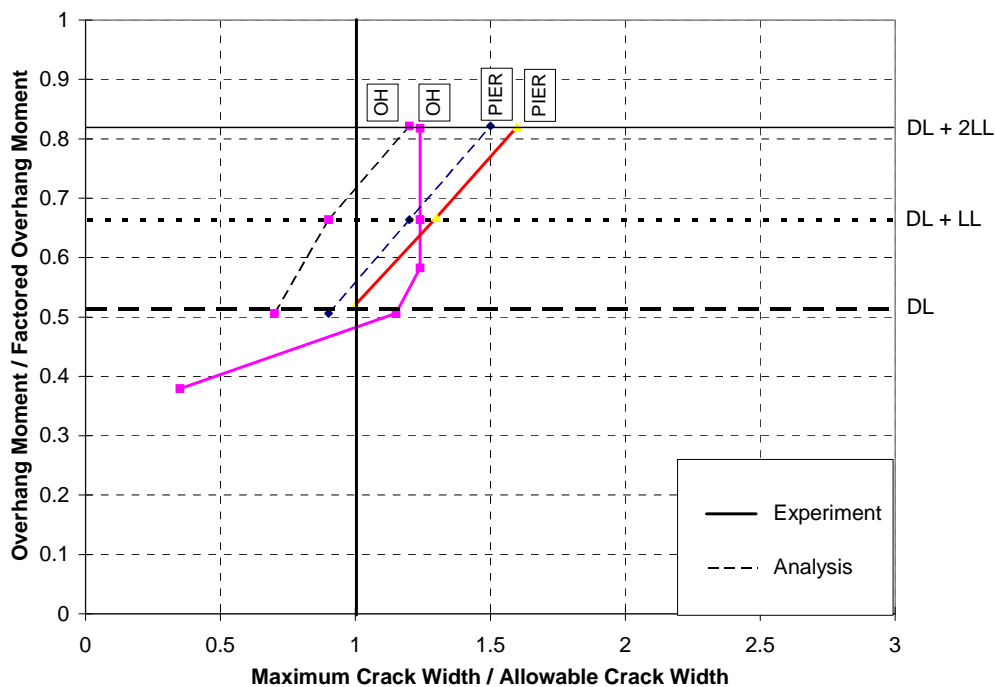


Figure 5.31 POJ-RC-100-TH Maximum Predicted and Measured Crack Widths

The comparison of maximum measured and predicted crack widths for Specimen POJ-PU-54-TH are shown in Figure 5.32. The proposed crack-width equation over-estimated the pier region maximum measured crack width at service loads by 50 percent. The over-estimation was attributed to smaller-than-expected post-tensioning losses in the pier. The maximum crack width in the overhang was only 9 % larger than the crack width predicted by Eq. 5-1. Only three out of 66 crack measurements in the overhang exceeded the predicted maximum crack width at service loads.

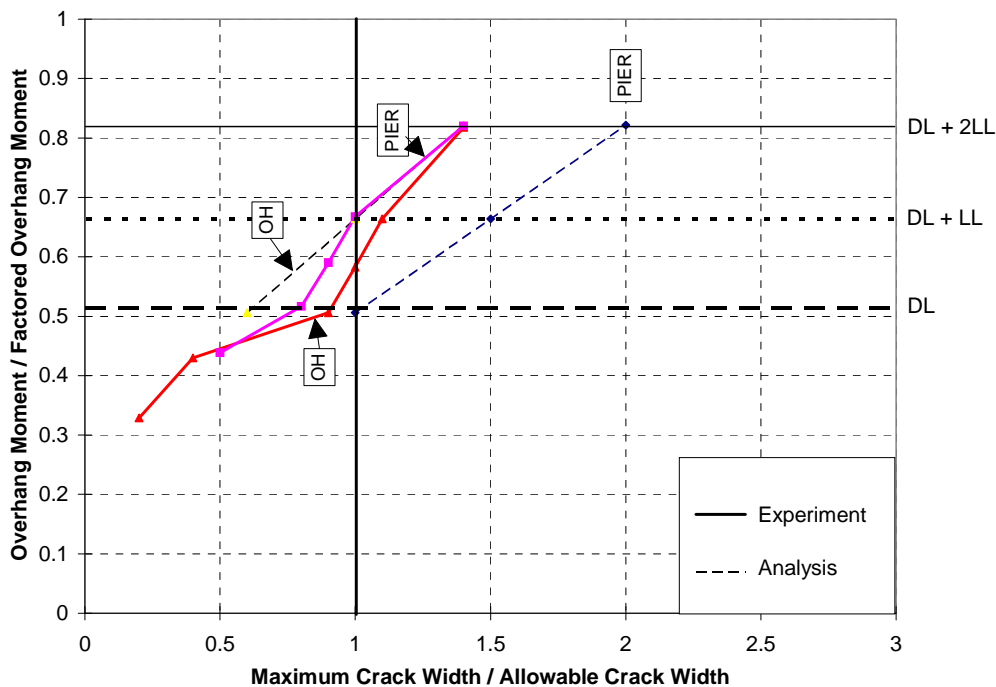


Figure 5.32 POJ-PU-54-TH Maximum Predicted and Measured Crack Widths

The comparison of maximum measured and predicted crack widths for Specimen POJ-PU-74-TH is shown in Figure 5.33. Maximum measured crack-widths in the overhang region were similar to the maximum crack widths predicted by Eq. 5-1. However, at service loads, the maximum measured crack width in the pier was 35 percent smaller than the predicted crack width. Once again, this was attributed to smaller-than-predicted losses in the post-tensioning.

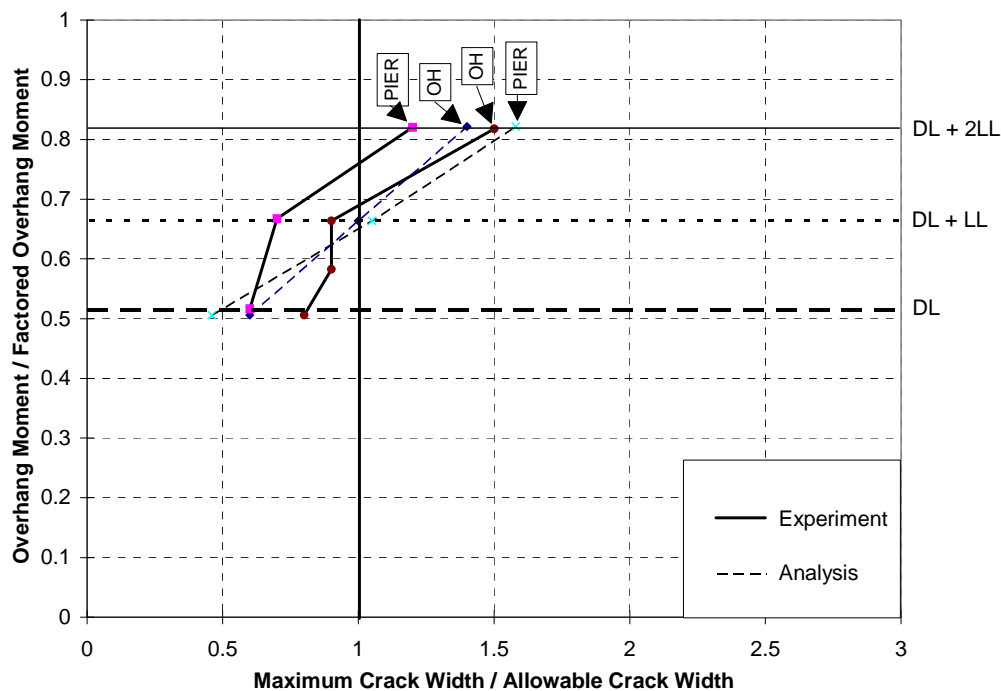


Figure 5.33 POJ-PU-74-TH Maximum Predicted and Measured Crack Widths

In summary, maximum measured crack widths in the overhangs were in good agreement with crack widths predicted by Eq. 5-1. The crack-width equation over-estimated pier crack widths for Specimens POJ-PU-54-TH and POJ-PU-74-TH by as much as 50 percent. This conservatism was attributed to the difficulty in determining the actual post-tensioning stress at dead load. The equation provided acceptable predictions of maximum crack widths; predicted crack widths were within the historically-accepted range of plus-or-minus 50 percent.

5.3.6 Evaluation of Reinforcement Stress Ranges

Calculated and measured stress ranges for the mild reinforcement and prestressed reinforcement are shown in Table 5.4 and Table 5.5. The calculated steel stress range was determined using a strain-compatibility analysis. The experimental stress range was computed by multiplying measured steel strains by 200 MPa (29,000 ksi).

Calculated stress ranges for mild reinforcement in the overhang were between 59 MPa (8.5 ksi) and 119 MPa (17.3 ksi), and were within the allowable limits stated in AASHTO Equation (8-60), as detailed in Table 5.4. The experimentally-obtained stress ranges were also smaller than the limiting mild reinforcement stress range. Calculated stress ranges for post-tensioning steel in the overhang of Specimens POJ-PU-54-TH and POJ-PU-74-TH were smaller than the limiting stress range of 100 MPa (14.5 ksi). Measured strains for the post-tensioning are not provided for Specimens POJ-PU-54-TH and POJ-PU-74-TH because strain gages were damaged during installation of the post tensioning.

Table 5.4 Computed and Experimental Stress Ranges for Overhangs

	Overhang Mild Steel Reinforcement						Post Tensioning	
	Allowable S_r		Calculated S_r		Experimental S_r		Calculated S_r	
	MPa	(ksi)	MPa	(ksi)	MPa	(ksi)	MPa	(ksi)
RC-100	99	14.4	59	8.5	90	13.1	N/A	N/A
PS-100	N/A	N/A	N/A	N/A	N/A	N/A	N/A	N/A
RC-100-TH	95	13.8	63	9.2	73	10.6	N/A	N/A
PU-54-TH	122	16.3	100	14.5	91	13.2	92	13.4
PU-74-TH	134	19.4	119	17.3	**	**	100	14.5

** Faulty gages

Calculated stress ranges for mild reinforcement in the pier were between 65 MPa (9.4 ksi) and 112 MPa (16.2 ksi), and were within the allowable limits stated in AASHTO Equation (8-60), as detailed in Table 5.5. The experimentally-obtained stress ranges were also smaller than the limiting mild reinforcement stress range, except for Specimen POJ-PU-54-TH, where the experimental reinforcement stress range was 8% greater than the limiting

mild reinforcement stress range. Calculated stress ranges for post-tensioning steel in the pier of Specimens POJ-PU-54-TH was smaller than the limiting stress range of 100 MPa (14.5 ksi). As stated in Chapter 3, Specimen POJ-PU-74-TH had a stress range that was 3.5 % larger than the limiting stress range. Measured strains for the post-tensioning are not provided for Specimens POJ-PU-54-TH and POJ-PU-74-TH because strain gages were damaged during installation of the post-tensioning.

Table 5.5 Computed and Experimental Stress Ranges for Piers

	Pier Mild Steel Reinforcement						Post-Tensioning	
	Allowable S_r		Calculated S_r		Experimental S_r		Calculated S_r	
	MPa	(ksi)	MPa	(ksi)	MPa	(ksi)	MPa	(ksi)
RC-100	112	13.2	65	9.4	90	13.1	N/A	N/A
PS-100	112	13.2	65	9.4	N/A	N/A	N/A	N/A
RC-100-TH	112	13.2	65	9.4	73	10.6	N/A	N/A
PU-54-TH	103	15.0	102	14.8	112	16.2	92	13.4
PU-74-TH	126	18.3	112	16.2	**	**	103	15.0

** Faulty gages

5.3.4 Crack-Width Frequency and Distribution at Service Loads	330
5.3.5 Comparison of Measured vs. Predicted Crack Widths.....	333
5.3.6 Evaluation of Reinforcement Stress Ranges	341
Figure 5.25 POJ-RC-100 Crack-Width Frequency and Distribution.....	330
Figure 5.26 POJ-RC-100-TH Crack-Width Frequency and Distribution	331
Figure 5.27 POJ-PU-54-TH Crack-Width Frequency and Distribution	332
Figure 5.28 POJ-PU-74-TH Crack-Width Frequency and Distribution	333
Figure 5.29 Illustration of Crack-Width Equation Variables.....	335
Figure 5.30 POJ-RC-100 Maximum Predicted and Measured Crack Widths	337
Figure 5.31 POJ-RC-100-TH Maximum Predicted and Measured Crack Widths.....	338
Figure 5.32 POJ-PU-54-TH Maximum Predicted and Measured Crack Widths	339
Figure 5.33 POJ-PU-74-TH Maximum Predicted and Measured Crack Widths	340
Table 5.2: Computed Overhang Crack Widths at Service Loads	336
Table 5.3 Computed Pier Crack Widths at Service Loads.....	336
Table 5.4 Computed and Experimental Stress Ranges for Overhangs	341
Table 5.5 Computed and Experimental Stress Ranges for Piers.....	342

5.3.4 Crack-Width Frequency and Distribution at Service Loads

The crack-width frequency and distribution plots, shown in Figure 5.25 through Figure 5.28, indicate which regions of each specimen contained the widest cracks and/or the largest number of cracks. The plots depict the number of crack measurements (of a particular width) that occurred in the pier, overhang, and joint regions as a percentage of all crack-width measurements taken at service loads. Recall from Section 4.1 that crack widths were measured at (4 in. x 3 in.) 10.2 cm x 7.5 cm grid lines on both sides of the overhang and joint and (4 in. x 4 in.) 10.2 cm x 10.2 cm grid lines on the side-faces of the pier. The plots were typically developed using the crack-width readings taken at "virgin" service loads and after reloading each specimen to service loads (the POJ-RC-100 specimen used only the readings taken at "virgin" service-loads). Crack-widths were measured in inches with 0.013 mm (0.0005 in.) accuracy.

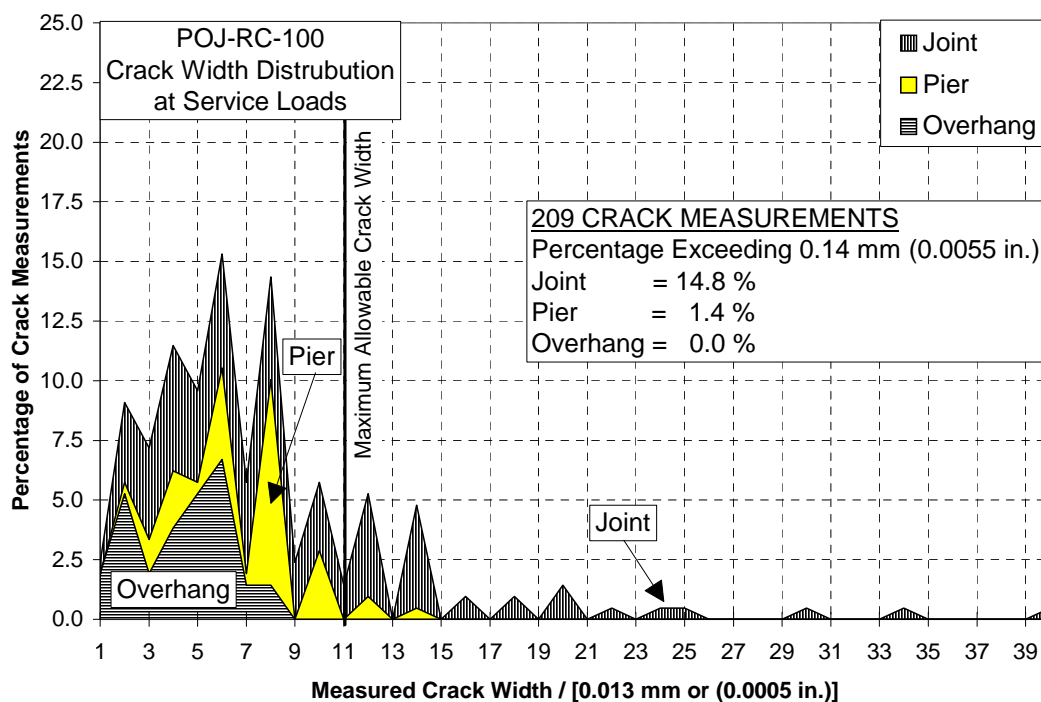


Figure 5.25 POJ-RC-100 Crack-Width Frequency and Distribution

The crack-width frequency and distribution for the prototype model reinforced concrete specimen (POJ-RC-100), shown in Figure 5.25, was developed using one set of

service load crack-width readings. At service loads, 209 crack widths were measured (112 on the north side and 97 on the south side of the specimen). Over 16 percent of all crack measurements for the specimen exceeded the maximum allowable crack width; 14.8 percent and 1.4 percent of the crack measurements at service load were in the joint and pier regions, respectively.

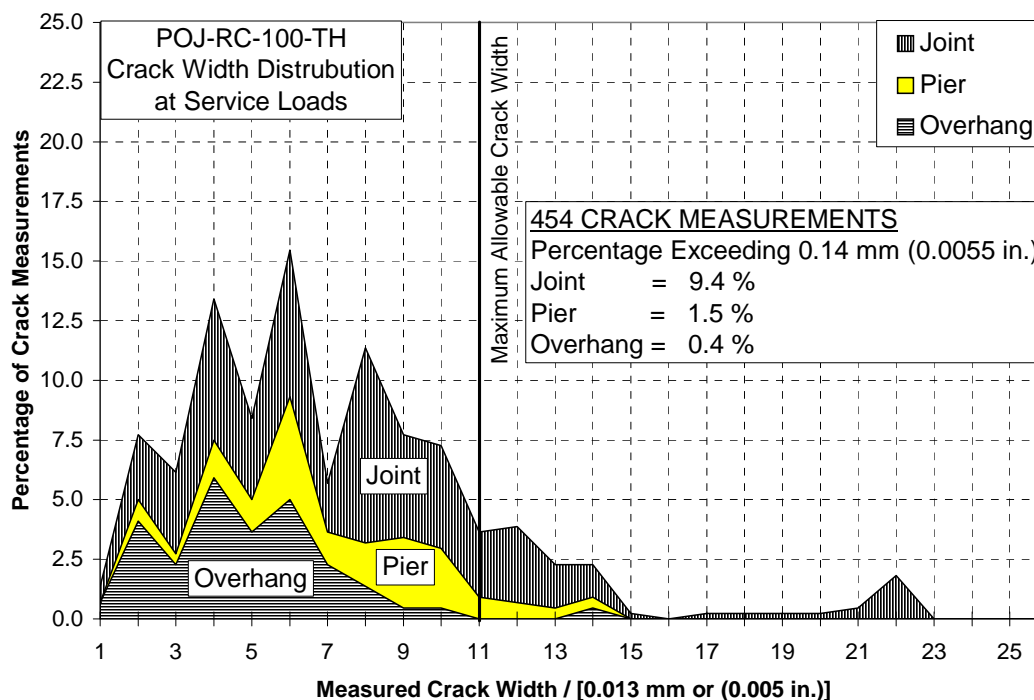


Figure 5.26 POJ-RC-100-TH Crack-Width Frequency and Distribution

The frequency and distribution of crack widths within the different regions for the reinforced concrete specimen with T-headed bars (POJ-RC-100-TH) is shown in Figure 5.26. The north side had 231 crack-width measurements and the south side had 223 measurements at service-loads. The pier, overhang, and joint regions of the specimen all had crack widths that exceeded the maximum allowable crack width of 0.14 mm (0.0055 in.). In the joint region, 42 crack measurements (9.4 percent of all measured cracks) exceeded the maximum allowable crack width. Only seven crack measurements in the pier and two in the overhang (1.5 percent and 0.4 percent of the measured crack-widths, respectively) exceeded the maximum allowable crack width at service loads.

The crack-width frequency and distribution plot for the specimen with a 54 percent prestressed overhang and headed bars (POJ-PU-54-TH) is shown in Figure 5.27. The north side had 130 crack-width measurements and the south-side had 142 crack-width measurements. Only 2.9 percent of the 272 crack widths measured exceeded the maximum allowable crack width at service load. The crack widths that exceeded the maximum allowable crack width were located in the joint region (five crack measurements or 1.8 percent of all measurements) and the overhang region (three crack measurements or 1.1 percent).

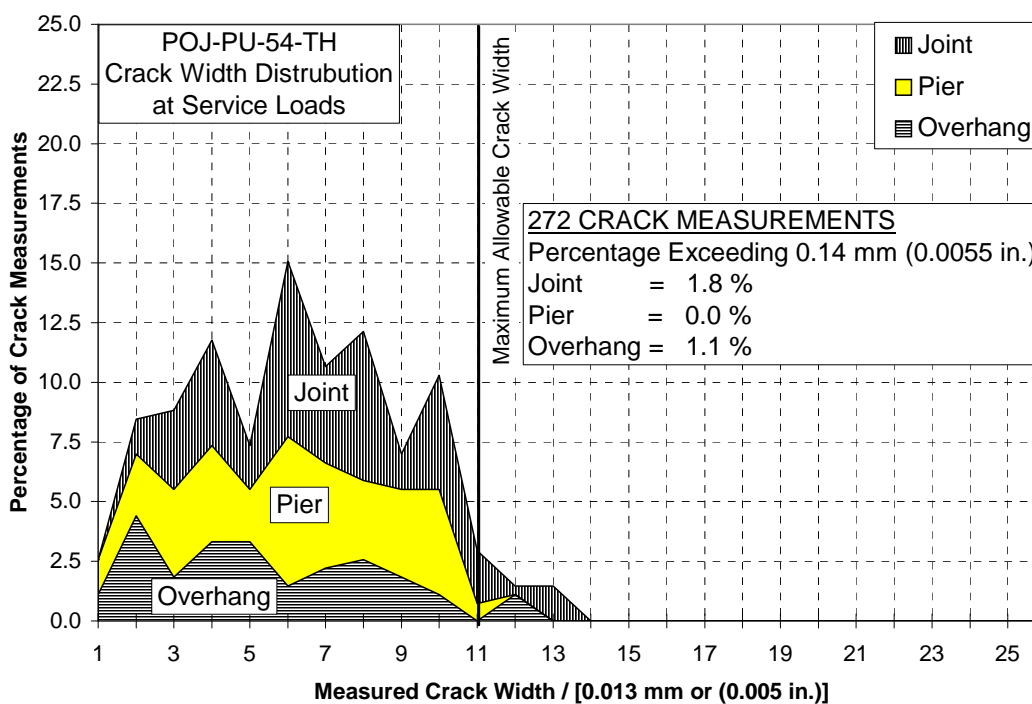


Figure 5.27 POJ-PU-54-TH Crack-Width Frequency and Distribution

The crack-width frequency and distribution for the specimen with a 74 percent prestressed overhang and T-headed bars (POJ-PU-74-TH), shown in Figure 5.28, indicated all measured crack widths were less than the crack-width limit. The 128 crack-width measurements taken at service loads included 54 crack-width measurements on the north side and 74 crack-width measurements on the south side of the specimen. Crack widths on the north side of the specimen were fairly well distributed, while crack widths on the south side were small (typically less than 0.6 mm (0.025 in.)).

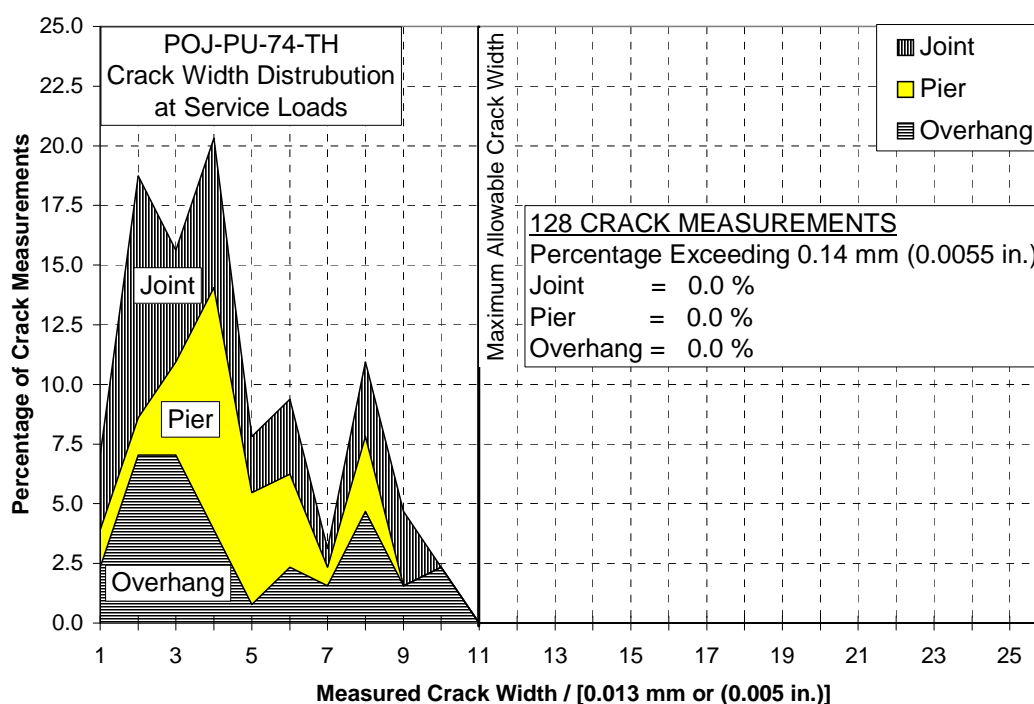


Figure 5.28 POJ-PU-74-TH Crack-Width Frequency and Distribution

5.3.5 Comparison of Measured vs. Predicted Crack Widths

Values for the maximum measured crack widths and maximum predicted crack widths, shown in Figure 5.30 through Figure 5.33, are plotted at dead load (DL), service load (DL+LL), and DL+2LL for the overhang and pier regions. Predicted crack-widths were computed using the proposed crack width model (which will be presented shortly) and a strain compatibility analysis.

The accuracy of crack-width equations has been historically limited to an accuracy of ± 50 percent [16]. The rough appearance of the crack width on the surface, the distribution of cracks, and lack of repeatable experimental crack-width results make it difficult to accurately predict crack widths. Crack-width equations, used in design, determine the distribution of reinforcement in members. This serviceability check should produce members with controlled crack widths, resulting in aesthetically pleasing and durable structures.

The maximum allowable crack width of 0.14 mm (0.0055 in.) and the corresponding Z factor of 62 used for the study, were determined by dividing the full-scale maximum allowable crack width of 0.39 mm (0.0155 in.) and corresponding Z factor of 170 by the 2.75 scale factor. A Z factor of 170 provides protection for moderate exposure conditions and ensures cracks are not visible from a reasonable distance. If a more stringent limiting crack width for durability is specified for partially-prestressed members, the crack-width equation can be used to further limit crack widths.

Distribution of Tension Reinforcement:

The crack-width equation used in this study was similar to the formula in the 1992 AASHTO LRFD Specifications (Eq. 5.7.3.4.2-1) [7] and was developed to predict maximum crack widths for the overhang specimens studied by Armstrong [3] and Salas [4]. The important variables in the equation are: steel tension stress, size of the tension block, and number of bars in the tension block. Steel tensile stress is determined using a cracked-section model. Size of the tension block is computed by determining the effective steel centroid of the mild and prestressed reinforcement. The number of steel reinforcing bars in the tension

block as well as the number of bonded prestressing strands or grouted post-tensioning ducts were considered to help control crack widths.

Crack-Width Equation:

The crack-control equation used for the integrated design procedure, presented in Eq. 3-29, is reformulated in Eq. 5-1 to compute crack widths for direct comparison with maximum-measured crack widths. Variables for the crack-width equation (Eq. 5-1) are illustrated in Figure 5.30 and are defined below:

$$w = 0.000076\beta f_{sa} (d_c A)^{1/3} \quad [5-1]$$

where:

w = Maximum Crack-Width (in.)
 β = Value of 1.2
 f_{sa} = Average steel tensile stress (ksi) at a distance d'' from the extreme

tensile fiber = $\epsilon_{d'}$ (29,000 ksi), where $\epsilon_{d'}$ is the tensile strain at the effective steel centroid, d''

d_c = Distance from the extreme tension fiber to the centroid of the closest layer of primary tension reinforcement (in.)

A = Area of tension block ($2 \times d'' \times b_w$) (in^2) divided by the total number of mild reinforcing bars, bonded prestressing strands, and/or grouted post-tensioning ducts located within the tension block

$$d'' = \frac{\left[\sum A_{ps} d_{ps} f_{su} + \sum A_{ms} d_{ms} f_y \right]}{\left[\sum A_{ps} f_{su} + \sum A_{ms} f_y \right]} \quad [5-2]$$

where:

d_{ps} = Distance from the extreme tension fiber to centroid of each layer of prestressed reinforcement in the tension zone

A_{ps} = Area of prestressed reinforcement at a layer

d_{ms} = Distance from extreme tension fiber to centroid of each layer of mild reinforcement in the tension zone

A_{ms} = Area of mild reinforcement at a layer.

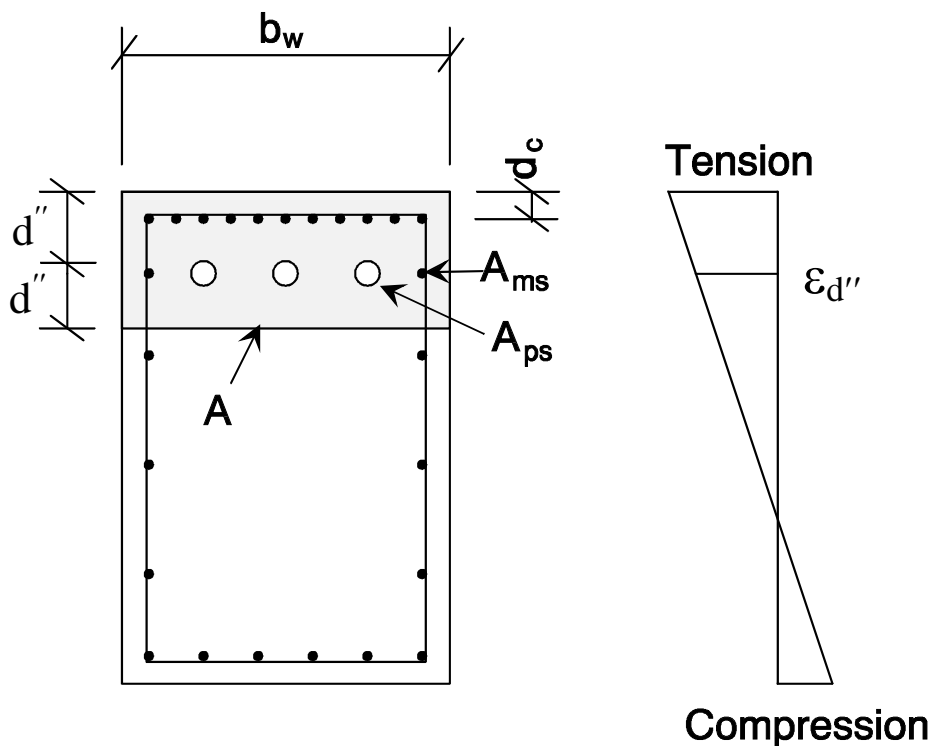


Figure 5.29 Illustration of Crack-Width Equation Variables

The average steel tensile stress, f_{sa} , was computed by multiplying the strain, $\epsilon_{d''}$, at the effective steel centroid by 29,000 ksi. Strain at the effective steel centroid, $\epsilon_{d''}$, was determined using a strain compatibility analysis where stress in the bonded prestressed reinforcement was reduced to account for long-term losses. Computed crack widths in the overhang and pier for service loads, using Eq. 5-1, are shown in Table 5.2 and Table 5.3, respectively.

Table 5.2: Computed Overhang Crack Widths at Service Loads

	d (in.)	d'' (in.)	A (in ² /#)	f_{sa} (ksi)	w (in.)	w mm
RC-100	1.14	5.00	7.50	26.9	0.0050	0.13
RC-100-TH	1.14	1.86	3.19	36.5	0.0051	0.13
PU-54-TH	1.14	1.55	4.37	34.9	0.0054	0.14
PU-74-TH	1.14	2.85	8.05	28.6	0.0055	0.14

Table 5.3 Computed Pier Crack Widths at Service Loads

	d (in.)	d'' (in.)	A (in ² /#)	fsa (ksi)	w (in.)	w mm
RC-100	1.13	4.76	15.23	32.8	0.0077	0.20
RC-100-TH	1.13	4.76	15.23	32.8	0.0077	0.20
PU-54-TH	1.13	5.24	22.86	35.4	0.0095	0.24
PU-74-TH	1.11	3.29	14.36	33.5	0.0077	0.20

Maximum measured and predicted crack widths for the pier and overhang, shown in Figure 5.30 through Figure 5.33, are compared at dead load (DL), dead load plus one-half live load (DL+1/2 LL), service load (DL+LL), and dead-load plus two live loads (DL+ 2 LL). The maximum crack widths were non-dimensionalized by dividing by the maximum allowable crack width of 0.14 mm (0.00055 in.), which corresponds with a Z factor of 62 ($Z=170 / 2.75$ scale factor).

For the prototype model reinforced concrete specimen (POJ-RC-100), maximum measured crack-widths in the overhang were slightly less than crack-widths predicted by Eq. 5-1, as shown in Figure 5.30. Measured crack widths in the pier were in good agreement with predicted crack widths.

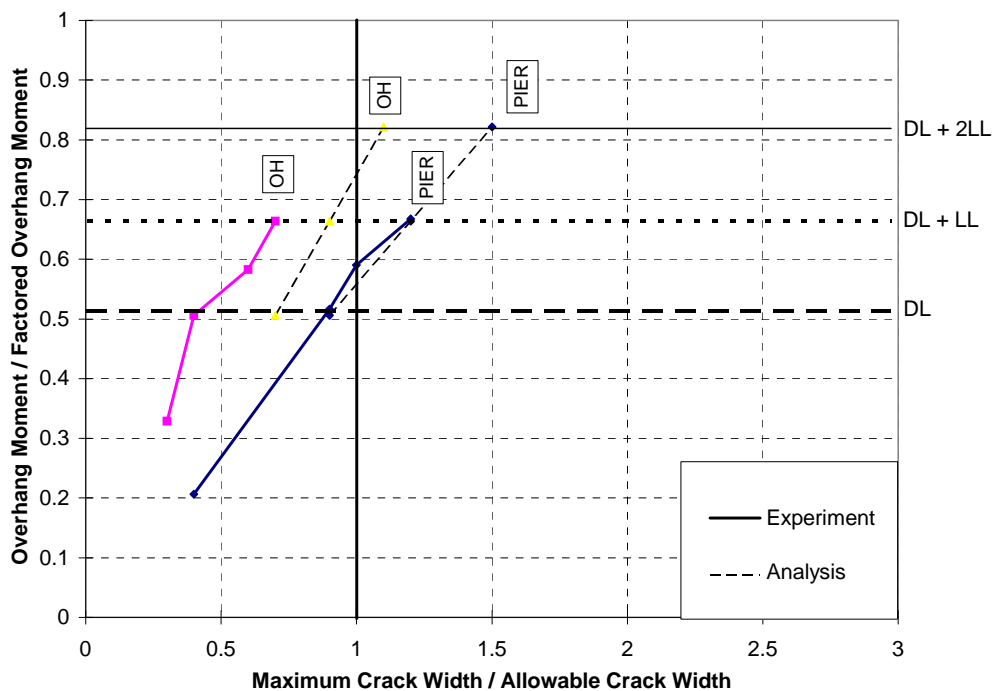


Figure 5.30 POJ-RC-100 Maximum Predicted and Measured Crack Widths

For the reinforced concrete specimen with headed reinforcement (POJ-RC-100-TH), the maximum measured crack widths in the pier closely matched the crack-widths predicted by Eq. 5-1. The maximum measured crack width in the overhang at service load was nearly 50 percent larger than the value predicted using Eq. 5-1, but the maximum predicted and measured crack widths were in good agreement at DL+2LL. Figure 5.31 indicates a large crack developed at DL, but the crack width did not increase significantly with increased load to DL + 2LL.

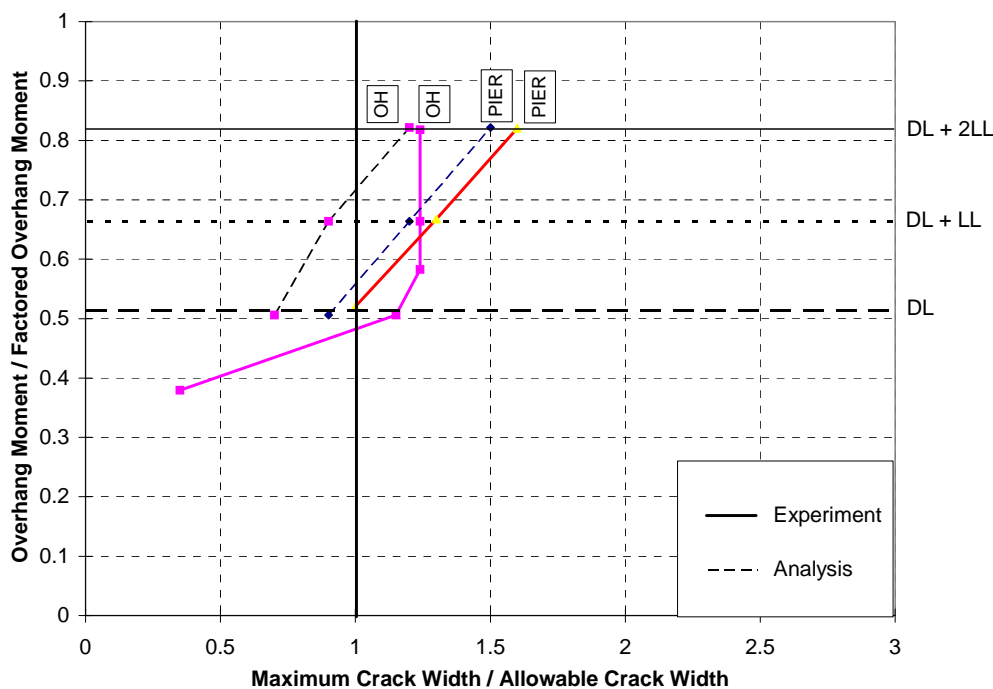


Figure 5.31 POJ-RC-100-TH Maximum Predicted and Measured Crack Widths

The comparison of maximum measured and predicted crack widths for Specimen POJ-PU-54-TH are shown in Figure 5.32. The proposed crack-width equation over-estimated the pier region maximum measured crack width at service loads by 50 percent. The over-estimation was attributed to smaller-than-expected post-tensioning losses in the pier. The maximum crack width in the overhang was only 9% larger than the crack width predicted by

Eq. 5-1. Only three out of 66 crack measurements in the overhang exceeded the predicted maximum crack width at service loads.

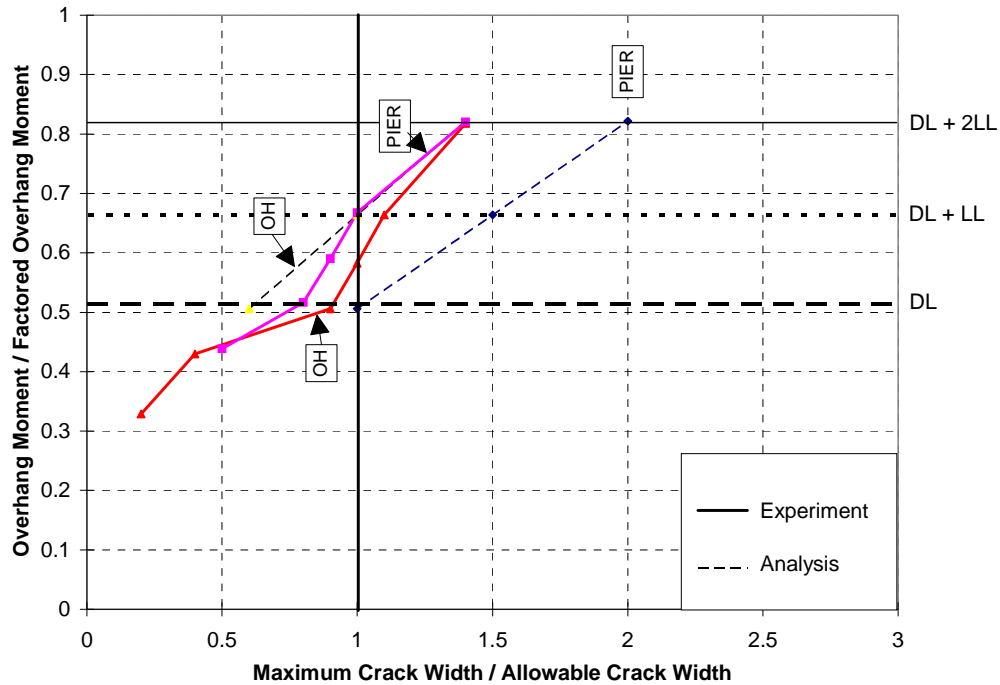


Figure 5.32 POJ-PU-54-TH Maximum Predicted and Measured Crack Widths

The comparison of maximum measured and predicted crack widths for Specimen POJ-PU-74-TH is shown in Figure 5.33. Maximum measured crack-widths in the overhang region were similar to the maximum crack widths predicted by Eq. 5-1. However, at service loads, the maximum measured crack width in the pier was 35 percent smaller than the predicted crack width. Once again, this was attributed to smaller-than-predicted losses in the post-tensioning.

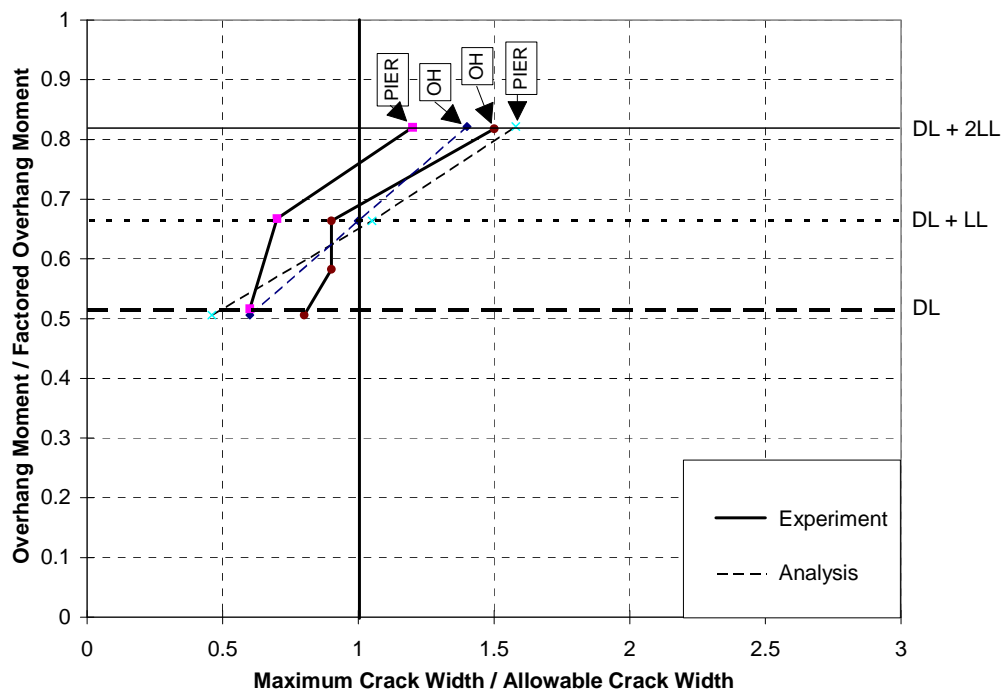


Figure 5.33 POJ-PU-74-TH Maximum Predicted and Measured Crack Widths

In summary, maximum measured crack widths in the overhangs were in good agreement with crack widths predicted by Eq. 5-1. The crack-width equation over-estimated pier crack widths for Specimens POJ-PU-54-TH and POJ-PU-74-TH by as much as 50 percent. This conservatism was attributed to the difficulty in determining the actual post-tensioning stress at dead load. The equation provided acceptable predictions of maximum crack widths; predicted crack widths were within the historically-accepted range of plus-or-minus 50 percent.

5.3.6 Evaluation of Reinforcement Stress Ranges

Calculated and measured stress ranges for the mild reinforcement and prestressed reinforcement are shown in Table 5.4 and Table 5.5. The calculated steel stress range was determined using a strain-compatibility analysis. The experimental stress range was computed by multiplying measured steel strains by 200 MPa (29,000 ksi).

Calculated stress ranges for mild reinforcement in the overhang were between 59 MPa (8.5 ksi) and 119 MPa (17.3 ksi), and were within the allowable limits stated in AASHTO Standard Specifications Equation (8-60), as detailed in Table 5.4. The experimentally-obtained stress ranges were also smaller than the limiting mild reinforcement stress range. Calculated stress ranges for post-tensioning steel in the overhang of Specimens POJ-PU-54-TH and POJ-PU-74-TH were smaller than the limiting stress range of 100 MPa (14.5 ksi). Measured strains for the post-tensioning are not provided for Specimens POJ-PU-54-TH and POJ-PU-74-TH because strain gages were damaged during installation and/or stressing of the post tensioning.

Table 5.4 Computed and Experimental Stress Ranges for Overhangs

	Overhang Mild Steel Reinforcement						Post Tensioning	
	Allowable S_r		Calculated S_r		Experimental S_r		Calculated S_r	
	MPa	(ksi)	MPa	(ksi)	MPa	(ksi)	MPa	(ksi)
RC-100	99	14.4	59	8.5	90	13.1	N/A	N/A
PS-100	N/A	N/A	N/A	N/A	N/A	N/A	N/A	N/A
RC-100-TH	95	13.8	63	9.2	73	10.6	N/A	N/A
PU-54-TH	122	16.3	100	14.5	91	13.2	92	13.4
PU-74-TH	134	19.4	119	17.3	**	**	100	14.5

** Faulty gages

Calculated stress ranges for mild reinforcement in the pier were between 65 MPa (9.4 ksi) and 112 MPa (16.2 ksi), and were within the allowable limits stated in AASHTO Standard Specifications Equation (8-60), as detailed in Table 5.5. The experimentally-obtained stress ranges were also smaller than the limiting mild reinforcement stress range, except for Specimen POJ-PU-54-TH, where the experimental reinforcement stress range was 8% greater than the limiting mild reinforcement stress range. The Calculated stress range for post-tensioning steel in the pier of Specimen POJ-PU-54-TH was smaller than the limiting stress range of 100 MPa (14.5 ksi). As stated in Chapter 3, Specimen POJ-PU-74-TH had a stress range that was 3.5 % larger than the limiting stress range. Measured strains for the post-tensioning are not provided for Specimens POJ-PU-54-TH and POJ-PU-74-TH because strain gages were damaged during installation and/or stressing of the post-tensioning.

Table 5.5 Computed and Experimental Stress Ranges for Piers

	Pier Mild Steel Reinforcement						Post-Tensioning	
	Allowable S_r		Calculated S_r		Experimental S_r		Calculated S_r	
	MPa	(ksi)	MPa	(ksi)	MPa	(ksi)	MPa	(ksi)
RC-100	112	13.2	65	9.4	90	13.1	N/A	N/A
PS-100	112	13.2	65	9.4	N/A	N/A	N/A	N/A
RC-100-TH	112	13.2	65	9.4	73	10.6	N/A	N/A
PU-54-TH	103	15.0	102	14.8	112	16.2	92	13.4
PU-74-TH	126	18.3	112	16.2	**	**	103	15.0

** Faulty gages

5.3.4 Crack-Width Frequency and Distribution at Service Loads	262
5.3.5 Comparison of Measured vs. Predicted Crack Widths.....	266
5.3.6 Evaluation of Reinforcement Stress Ranges	273
Figure 5.25 POJ-RC-100 Crack-Width Frequency and Distribution.....	262
Figure 5.26 POJ-RC-100-TH Crack-Width Frequency and Distribution	263
Figure 5.27 POJ-PU-54-TH Crack-Width Frequency and Distribution	264
Figure 5.28 POJ-PU-74-TH Crack-Width Frequency and Distribution	265
Figure 5.29 Illustration of Crack-Width Equation Variables.....	268
Figure 5.30 POJ-RC-100 Maximum Predicted and Measured Crack Widths	270
Figure 5.31 POJ-RC-100-TH Maximum Predicted and Measured Crack Widths.....	270
Figure 5.32 POJ-PU-54-TH Maximum Predicted and Measured Crack Widths	271
Figure 5.33 POJ-PU-74-TH Maximum Predicted and Measured Crack Widths	272
Table 5.2: Computed Overhang Crack Widths at Service Loads	268
Table 5.3 Computed Pier Crack Widths at Service Loads.....	269
Table 5.4 Computed and Experimental Stress Ranges for Overhangs	273
Table 5.5 Computed and Experimental Stress Ranges for Piers.....	274

5.4 Constructability and Cost Estimation

5.4.1 Constructability

Constructability of the full-scale prototype and integrated-design bents was extrapolated from the scale-model specimens by considering the time and effort required to construct the model specimens. The ease of construction was graded on a scale of 1 to 10, where a rating of 1 corresponded with the highest degree of difficulty.

The prototype model reinforced concrete bent (POJ-RC-100) had closely-spaced longitudinal bars and numerous closed stirrups in the overhang, as well as a congested joint region. Congestion in the joint region was due to the maze of overlapping pier and overhang bars that were anchored in the joint region. The separate design of the overhang and pier cross sections meant that bars often had to be forced into place. Hooked longitudinal bars, located at the tip of the overhang, were difficult to place and tie together. Transverse reinforcement in the overhang was closely spaced and required substantial time to install. The difficult placement and overall number of bars that had to be placed and tied in Specimen POJ-RC-100 resulted in a rating of 4.

The prototype model prestressed overhang design (POJ-PS-100) was congested in the overhang and joint regions due to the number of shear friction bars, stirrups, and confinement reinforcement for the post-tensioning anchorages. The most difficult operation was the installation of the closely-spaced confinement reinforcement. After the specimen was cast, the Dywidag bars were stressed and the twelve ducts were grouted. The stressing and grouting operations were time-consuming and required many steps to complete. Because the construction of the reinforcing cage and post-tensioning operation were difficult, the specimen was given a constructability rating of 3.

Headed mild reinforcement used for the integrated reinforced concrete T-head design (POJ-RC-100-TH) reduced assembly time and simplified placement of longitudinal reinforcement. The joint region was not congested because a reduced number of longitudinal bars were used. The well-spaced closed stirrups in the overhang were easy to install, and headed longitudinal reinforcement reduced congestion at the tip of the overhang. The ease of constructing this resulted in a constructability rating of 9.

The integrated 54% prestressed specimen with headed mild reinforcement (POJ-PU-54-TH) did not require many reinforcing bars in the overhang and pier region, resulting in a rapid initial assembly of the cage. It took time to place the anchorage reinforcement and thread the three post-tensioning tendons through the cage and tie them into position. The post-tensioning operation went quickly, because only three strands were stressed and grouted. The additional time required to stress the specimen reduced the constructability ranking to an 8.

The integrated 74% prestressed specimen with headed mild reinforcement (POJ-PU-74-TH) did not require many reinforcing bars, resulting in the quickest initial assembly of the mild reinforcement cage. Installation of the five post-tensioning ducts and tendons required some time, but placement of the anchorage reinforcement and grout ports went efficiently. The post-tensioning operation required more time than for the 54% prestressed specimen, and the additional grouting operations resulted in a ranking of 7.

A summary of constructability ratings for the different bent types is presented in Table 5.6.

Table 5.6 Constructability Ratings for Bent Types

	Specimen	Rating
Prototype Designs	POJ-RC-100	4
	POJ-PS-100	3
Integrated Designs	POJ-RC-100-TH	9
	POJ-PU-54-TH	8
	POJ-PU-74-TH	7

5.4.2 Cost Estimation

Estimated costs for different bent types were calculated for full-scale bents. Material quantities for full-scale bents were determined by scaling up quantities for the scale models using the 2.75 scale factor. Concrete material and placement costs were not included in the cost estimates.

Material costs were estimated using the unit costs listed below. The prototype specimens were included to provide a base-line price comparison for the integrated design specimens. It should be noted that the prototype specimens did not provide factored-load resistance and were unacceptable design options.

The integrated design options utilized interlocking headed reinforcement in the joint corner to provide anchorage for the longitudinal reinforcement. Additional costs for steel plates used for the headed bars were included in a separate unit-cost item. The cost of friction welding the plates onto the ends of bars was included in the plate unit cost.

The unit costs used are as follows:

Mild Reinforcement-

Closed Ties and Stirrups:	\$0.50 / lb.
All Other:	\$0.36 / lb.

Headed Reinforcement [34] -

5.5 in x 4.125 in. x 1.375 in. Plate:	\$8.85 ea.
4.125 in. x 2.75 in. x 1.0 in. Plate:	\$3.22 ea.
2.75 in. x 2.75 in. x 1.0 in. Plate:	\$2.14 ea.

Strand Post-Tensioning Systems-

Strand:	\$1.00 / lb.
Multi-Strand Anchors:	\$100 ea.
Plates:	\$30 ea.

Bar Post-Tensioning Systems [35] -

Dywidag Bar:	\$1.50 / lb.
Threaded Nuts:	\$9.25 ea.
Plates:	\$22.85 ea.

The estimated costs for the five full-scale bents are computed in Table 5.7 through Table 5.10. The bar chart of steel weights, shown in Figure 5.34, indicates the full-scale PU-74-TH bent would require the least steel [2091 kg (4610 lb.)]. The RC-100 bent would require the most steel [3476 kg (7665 lb.)].

The estimated costs for the full-scale specimens, shown in Figure 5.35, indicate the prototype reinforced concrete bent (RC-100) and reinforced concrete bent with headed bars were almost identical in price (\$3043 and \$3009, respectively). The premium price of \$1 / pound (\$ 2.20 / Kg) used to estimate the post-tensioning costs plus the cost of multi-strand anchors, resulted in higher estimated costs for the 54 percent and 74 percent prestressed specimens. However, it must be noted that the RC-100 design would not support factored loads, and consideration of the additional costs associated with concrete placement in congested reinforcement cages would likely reduce or offset these cost differences. A fully-prestressed bent utilizing continuous post-tensioning, and designed to satisfy the AASHTO Standard Specifications, would be significantly more expensive than any of the options listed (from 1.16 to 1.5 times more).

In considering serviceability and durability aspects, specimens with fewer well-controlled cracks were considered to be superior to specimens with numerous well-controlled cracks. The 74 percent prestressed option exhibited only eight small cracks at service loads. The 54 percent prestressed option had 14 long cracks, and the reinforced concrete specimen with headed bars had 25 cracks. Although all of the integrated-design specimens would contain cracks at service loads, the 74 percent prestressed specimen limited the number and length of cracks that formed.

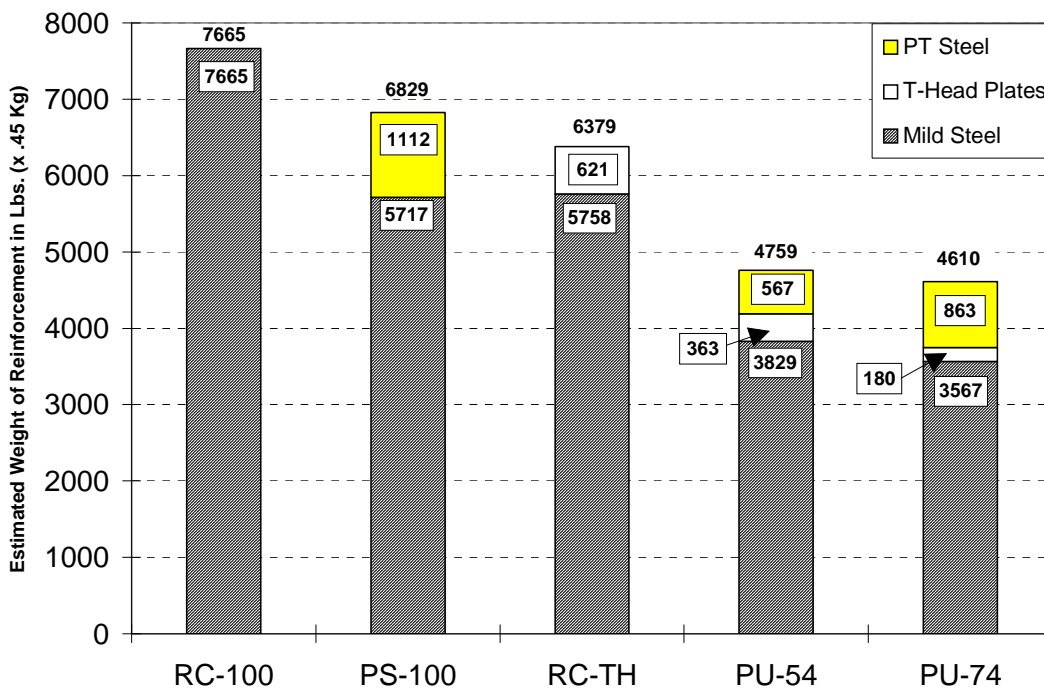


Figure 5.34 Material Quantities for Full-Scale Bents

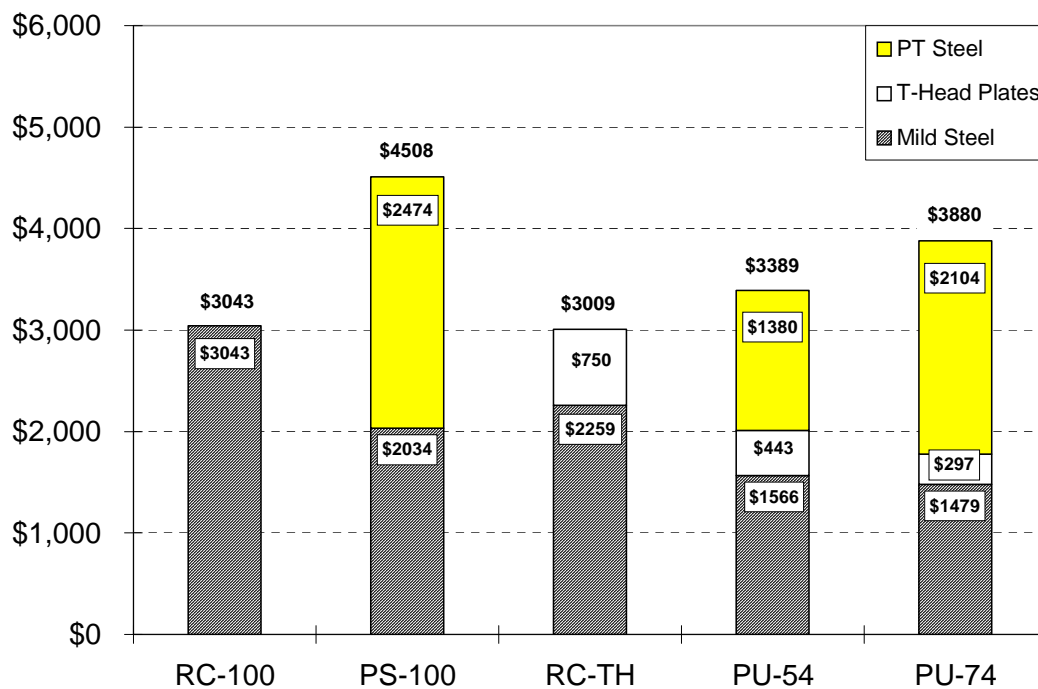


Figure 5.35 Material Costs for Full-Scale Bents

5.5 Summary

The analytical and experimental results from the pier-overhang-joint study indicated the prototype model reinforced concrete and prototype model fully-prestressed overhang designs did not provide sufficient anchorage of longitudinal reinforcement in the joint region. Further discussion and recommendations for repairing these structures are discussed in Chapters 7 through 9.

All integrated-design specimens provided sufficient strength to resist factored loads. Anchorage of reinforcement in the joint, and ultimately, integrity of the joint was assured by interlocking the headed mild reinforcement in the joint corner and by reducing the joint principal tensile stresses by providing continuous post-tensioning through the bent. Sufficient longitudinal and transverse reinforcement was provided in zones of high tensile stresses to resist factored loads.

The POJ-RC-100-TH specimen failed in the joint after the longitudinal reinforcement yielded and load on the specimen was above the predicted capacity. A transverse headed bar in the joint corner may have provided lateral joint confinement, but is not recommended because it would also cause unwanted congestion in the joint corner.

Spalling of the underside of the overhang that occurred for all the integrated design specimens suggested a larger amount of reinforcement should be provided in the compression zone. It was recognized that the overhang compression node was part of the critical force path that supported the outer superstructure reaction. Additional compressive reinforcement would provide added ductility to the specimens.

Service-load performance of the integrated design specimens was evaluated by measuring service-load crack widths. The partially-prestressed designs (POJ-PU-54-TH and POJ-PU-74-TH) provided adequate crack control in the different regions of the specimen, and reduced the number of cracks that formed. The integrated reinforced concrete design (POJ-RC-100-TH) had unacceptable crack-widths in the joint region at service load. It is recommended that a quantity of mild reinforcement be added to the joint region, based on

detailing for a “bottle-shaped” compression field, shown in Figure 5.36 [8]. Additional detailing steel would provide additional strength and improve serviceability of the joint.

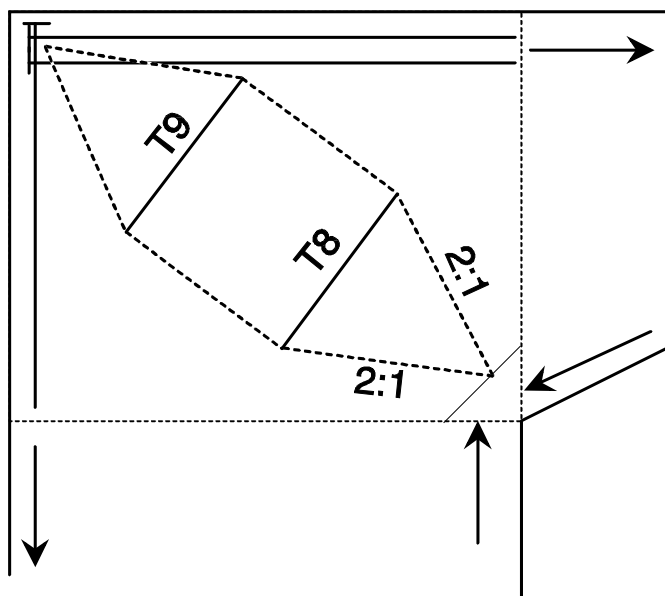


Figure 5.36 Bottle-Shaped Compression Field for Joint Corner Detail

Constructability and construction costs of specimens indicated all integrated design models were economically feasible and practical design options. The prestressed options (POJ-PU-54-TH and POJ-PU-74-TH) had fewer visible cracks than the reinforced concrete option (POJ-RC-100-TH). The slight increase in cost for the additional post-tensioned reinforcement in the 74% prestressed bent is more than offset by the improved serviceability. If costs associated with concrete placement and formwork had been considered, the percentage increase in cost for Specimens POJ-PU-54-TH and POJ-PU-74-TH would have been very small. Reduced cage congestion of the partially prestressed bents may even offset the cost associated with post tensioning the bent. Specimen POJ-PU-74-TH is clearly the best design option given the excellent serviceability performance and overall strength of the bent.

5.4 Constructability and Cost Estimation	276
5.4.1 Constructability	276
5.4.2 Cost Estimation	278
5.5 Summary	286
Figure 5.34 Material Quantities for Full-Scale Bents	285
Figure 5.35 Material Costs for Full-Scale Bents.....	285
Figure 5.36 Bottle-Shaped Compression Field for Joint Corner Detail.....	287
Table 5.6 Constructability Ratings for Bent Types	277
Table 5.7 Full-Scale POJ-RC-100 - Materials Quantities and Price Estimates	280
Table 5.8 Full-Scale POJ-PS-100 - Material Quantities and Price Estimates.....	281
Table 5.9 Full-Scale POJ-RC-100-TH - Material Quantities and Price Estimates	282
Table 5.10 Full-Scale POJ-PU-54-TH - Material Quantities and Price Estimates	283
Table 5.11 Full-Scale POJ-PU-74-TH - Material Quantities and Price Estimates	284

Recommended Modifications to Proposed AASHTO LRFD Bridge Specifications

Recommended modifications to Section 5 of the Proposed AASHTO LRFD Specifications are presented in this section. The modified subsections are presented in a format similar to that used in the April 16, 1992 draft of the specifications. Subsections related to research that is underway in other studies at The University of Texas at Austin will be noted. Recommendations for these subsections will be presented based on information that is available at this time and may be modified as more information becomes available.

5.6 DESIGN CONSIDERATIONS

·
·
·

5.6.3 Strut-and-Tie Model

5.6.3.1 GENERAL

Strut-and-tie models may be used to proportion reinforcement and concrete in member regions where nonlinear distributions of strain are expected at strength and extreme event limit states. The strut-and-tie model should be considered for the design of members in which the distance between applied loads and the supporting reactions is less than about twice the member thickness.

C5.6.3.1

Where the conventional methods of strength of materials are not adequate due to nonlinear strain distribution, strut-and-tie modeling can provide a useful tool for approximating the flow of stresses through these member regions. Examples of such regions include connections between members, brackets and corbels, locations where reactions exist or concentrated loads are introduced, and members in which the distance

between applied loads and supporting reactions is less than approximately twice the member depth. An elastic finite element analysis can be used to identify the flow of forces in a member, simplifying the development of the strut-and-tie model.

5.6.3.2 STRUCTURAL IDEALIZATION

⋮

5.6.3.4 PROPORTIONING OF TENSION TIES

5.6.3.4.1 Strength of Tie

Tension tie reinforcement shall be anchored to the nodal zones by specified embedment lengths, hooks, or mechanical anchorages. The tension force shall be developed at the interface of the nodal zone.

The nominal resistance of a tension tie shall be taken as:

$$P_n = A_{st} f_y + A_{ps} f_{pu} \quad (5.6.3.4.1-1)$$

where:

A_{st} = total area of longitudinal mild steel reinforcement in the tie (IN²)

A_{ps} = area of prestressing steel (IN²)

f_y = yield strength of mild steel reinforcement (KSI)

f_{pu} = specified tensile strength of prestressed reinforcement (KSI).

For transverse reinforcement:

$$P_n = A_{vs} f_y + 1\sqrt{f'_c} b_w d \quad (5.6.3.4.1-2)$$

where:

P_n = STM tie force (KIP)

A_{vs}	=	Total area of required shear reinforcement (IN ²)
f_y	=	Nominal yield stress of shear reinforcement (KSI)
f'_c	=	Nominal concrete compressive stress (PSI)
b_w	=	Beam width (IN)
d	=	Distance from extreme compression fiber to centroid of primary tension reinforcement at the location of the tension tie (IN).

The transverse reinforcement A_{vs} should be distributed over a distance d in the region of the transverse tension tie.

C5.6.3.4.1

Equation 5.6.3.4.1-1 is intended to represent the strength of the combined mild steel/prestressed longitudinal steel tension tie. Studies have shown that the equation is a good approximation of the strength for a tension tie in deep beams.

The quantity of transverse reinforcement in beams can be computed using Equation 5.6.3.4.1-2. A term $[1\sqrt{f'_c} b_w d]$ is included to account for the concrete contribution to the shear strength, which resulted in conservative, but more realistic estimates of strength.

5.6.3.6 CRACK CONTROL REINFORCEMENT

Provisions of Section 5.7.3.4.2 shall be satisfied.

5.7 DESIGN FOR FLEXURAL AND AXIAL FORCES

⋮

5.7.3.4 CONTROL OF CRACKING

5.7.3.4.1 Scope

The provisions specified, herein, shall apply to all concrete components in which service loads cause tension in the gross section in excess of $0.22\sqrt{f'_c}$. Components subject to flexure and compressive axial load for which there is no tension exceeding $0.22\sqrt{f'_c}$ in the gross section of the concrete at service limit states shall be considered exempt from the provisions herein specified.

C5.7.3.4.1

All concrete members are subject to cracking under any load condition which produces tension in the gross section in excess of the cracking strength of the concrete. It is important to remember that not all potential sources of tensile stress are considered in the normal design calculations. Sources of tensile stress not normally directly considered include abrupt changes of section, intermediate anchorage of post-tension tendons, thermal effects and restraint of deformations. Where there is concern about cracking in these locations at service limit states, a finite element analysis shall be performed.

5.7.3.4.2 Distribution of Tension Reinforcement in Flexural Members

Provisions specified, herein, shall be used for the distribution of tension reinforcement to control flexural cracking in members. For structures subject to very aggressive exposure, special investigations and precautions, not specified, herein, shall be applied.

The distribution of reinforcement required in one-way slabs may be considered as exempt from the provisions specified herein.

When the specified yield strength, f_y , for tension reinforcement exceeds 40.0 KSI, components shall be so proportioned that the tensile stress in the reinforcement at service loads, f_{sa} (KSI), does not exceed:

$$f_{sa} = \frac{C_{rk}}{(d_c A)^{1/3}} \quad (5.7.3.4.2-1)$$

d	=	Distance from extreme compression fiber to centroid of primary tension reinforcement at the location of the tension tie (IN).
f_{sa}	=	Steel tensile stress at a distance d'' from the extreme tensile fiber = $\epsilon_{d''}$ (29,000 KSI)
$\epsilon_{d''}$	=	Strain a distance d'' from the extreme tensile fiber based on a linear strain profile
C_{rk}	=	Limiting crack-width factor determined from exposure criteria. Values for C_{rk} from Table 5.7.3.4.2-1 shall be based on clear cover requirements specified in Table 5.12.3-1

Table 5.7.3.4.2-1 - Values for C_{rk} for Unprotected Reinforcing Steel (K/IN)

Exposure Conditions	Cover (IN)	C_{rk} (K/IN)
Moderate	≤ 2 IN	0.170
Moderate	> 2 IN	$0.170 + 0.02(\text{Cover} - 2.0)$
Moderate to Severe	≤ 2 IN	0.130
Moderate to Severe	> 2 IN	$0.130 + 0.02(\text{Cover} - 2.0)$

For very severe exposure conditions, additional protection shall be furnished to provide additional corrosion resistance, in addition to satisfying Equation 5.7.3.4.2-1.

d_c = Distance from the extreme tension fiber to the centroid of the closest layer of primary tension reinforcement (IN)

A = Area of tension block ($2 \times d'' \times b_w$) divided by the number of mild reinforcing bars, bonded strands, and/or grouted tendons located within the tension block [$\text{IN}^2/\# \text{ BARS}$]

d'' = Distance from extreme tensile fiber to centroid of tensile reinforcement (IN)

$$d'' = \frac{\left[\sum (A_{ps} f_{su}) d_{ps} + \sum (A_{ms} f_y) d_{ms} \right]}{\left[\sum A_{ps} f_{su} + \sum A_{ms} f_y \right]} \quad (5.7.3.4.2-2)$$

where:

d_{ps} = Distance from extreme tension fiber to centroid of layer of prestressed reinforcement in the tension zone

A_{ps} = Area of prestressed reinforcement in a layer

d_{ms} = Distance from extreme tension fiber to centroid of longitudinal mild reinforcement

A_{ms} = Area of mild reinforcement in a layer.

The stress, f_{sa} , shall be computed using a cracked-section analysis. Bonded prestressing steel may be included in the calculation of

f_{sa} . Prestressing stress should be reduced to account for long-term losses as specified in Section 5.9.5. The steel stress, f_{sa} , shall be determined at a distance d'' from the extreme tension fiber and shall not exceed the limiting stress computed using Equation 5.7.3.4.2-1.

C5.7.3.4.2

In applying Equation 5.7.3.4.2-1, the actual cover, d_c , shall be used. Thicker or additional cover, exceeding 2.0 IN, provides additional corrosion protection. Values for C_{rk} provide a gradual transition in cover requirements from severe to moderate exposure conditions without a penalty for using more concrete cover.

Figure C5.7.3.4.2-1 illustrates the variables used for Equation 5.7.3.4.2-1.

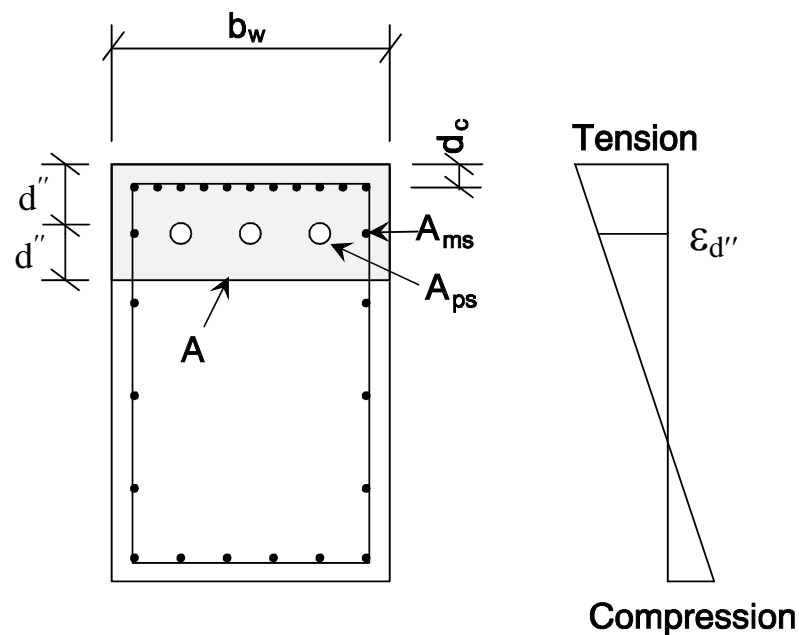


Figure C5.7.3.4.2-1 Identification of Crack-Width Variables

Summary

The proposed changes to the AASHTO LRFD Bridge Specifications incorporate many of the design criteria that were used in development of specimens tested in the cantilever-bent study. Shear friction provisions and design equations for deep beams, brackets, and corbels were retained but should be phased out as the strut-and-tie method becomes the design standard. Strut-and-tie models used in the study provided a thorough understanding of the flow of forces in disturbed regions, and resulted in concise requirements for designing reinforcement and checking concrete compressive stresses. Tests also demonstrated good behavior for specimens designed using STM.

Use of the proposed and modified design provisions is demonstrated through a cantilever bent design example presented in Appendix B.

6.1 Introduction.....	Error! Bookmark not defined.
6.2 Recommended Modifications to Proposed AASHTO LRFD Bridge Specifications.....	1
6.3 Summary	7

CHAPTER 7

ANALYSIS OF SAN ANTONIO CANTILEVER BENTS

7.1 Introduction

Design reviews, strength analyses, and field inspections were performed on eight cantilever bents located in San Antonio after the model prototype reinforced concrete specimen (POJ-RC-100) failed prematurely. A review of the joint details revealed that the pier and overhang longitudinal reinforcement were anchored in the joint using straight-bar anchorage. It was concluded that if a diagonal crack developed in the joint region, the anchorage length of many of the longitudinal bars would be reduced, resulting in reduced bent capacity. A model that considers bar anchorage of longitudinal reinforcement in the joint (strength analysis model) was developed to compute strength of the bent after a diagonal crack formed in the joint.

The joint bond-model assumed a crack develops in the joint between the compression resultant and the joint corner opposite the compression resultant (Figure 7.1 and Figure 7.2). The peak force developed by each bar that crosses the assumed diagonal crack was computed by utilizing the ratio of embedment length to development length in a uniform bond-stress model. After computing the individual bar forces, the maximum applied load on the cantilever bent was computed by balancing the moments about the joint compression resultant.

Two of the eight suspected deficient substructures are presented in the following sections. The reinforcement details, strength calculations, finite element analyses, and field inspection results for a reinforced concrete cantilever substructure (I4-C) and a fully-prestressed cantilever substructure (C11-C) are presented in Sections 7.3 and 7.4, respectively.

7.2 Development of the Strength Analysis Model

The strut-and-tie model, shown in Figure 7.1, is intended to represent the flow of forces produced when the reactions (R_i and R_o) from the superstructure are positioned on the overhang of the substructure. Tensile force in the top cord of the overhang and outer cord of the pier are represented by tension ties T4 and T5, respectively. The strut-and-tie model indicates that both the overhang and pier longitudinal tensile reinforcement need to be fully anchored in the joint corner to produce a viable tensile force path. Because straight bar anchorage was used for the primary longitudinal reinforcement in the pier and overhang, the majority of the pier and overhang longitudinal reinforcement was ineffective because of insufficient bar anchorage beyond a potential diagonal joint crack.

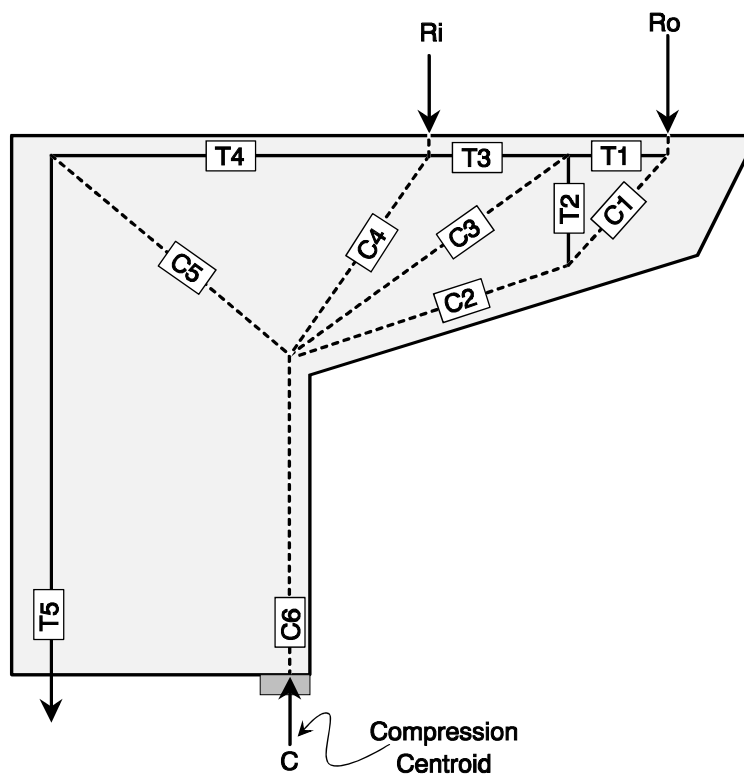
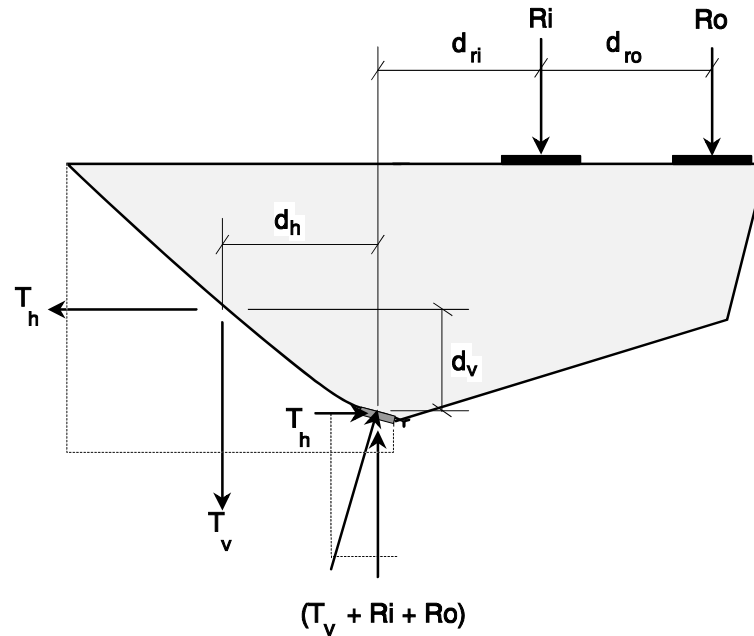


Figure 7.1 Cantilever Substructure Strut-and-Tie Model

The effective tension forces produced in the longitudinal overhang and pier reinforcement crossing the joint failure plane were labeled T_h and T_v , respectively. Distances from the compression centroid (in the lower corner of the joint) to the centroid of the

horizontal and vertical forces were labeled (d_v) and (d_h), respectively. The labeling scheme and assumed failure mechanism is shown in Figure 7.2.



Joint Resistance = Applied Moment

$$T_h (d_v) + T_v (d_h) = Ri(d_{ri}) + Ro(d_{ro} + d_{ri})$$

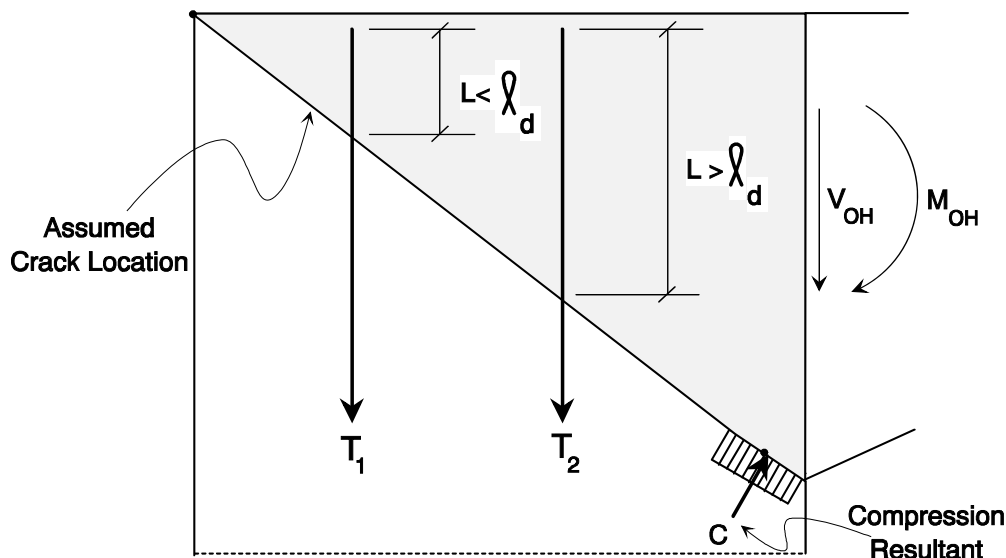
Figure 7.2 Free Body Used to Compute Bent Capacity.

The basic bar development length, l_d , was computed using the ACI 318 (1963) development length equation (Eq 3-1 from Section 3.2.5.1). A nominal yield stress, f_y , of 414 MPa (60 ksi) and a nominal concrete compressive strength, f'_c , of 34.5 MPa (5000 psi) were assumed. Development lengths shown in Table 7.1 were computed using Eq. 3-1 from Section 3.2.5.1.

Table 7.1 Basic Bar Development Lengths for 414 MPa (60 ksi) Reinforcing Bars

	Bar Diameter		Bar Area		ACI-318 (1963) Bond Stress		Development Length (l_d)	
	mm	(in.)	mm ²	(in.) ²	MPa	(psi)	cm	(in.)
No. 2	6	0.25	30	0.048	5.5	800	12	4.7
No. 3	10	0.375	70	0.11	5.5	800	18	7.0
No. 4	13	0.50	130	0.2	5.5	800	24	9.4
No. 5	16	0.625	200	0.31	5.5	800	30	11.7
No. 6	19	0.75	280	0.44	5.5	800	36	14.0
No. 8	25	1.00	510	0.79	4.6	671	57	22.4
No. 11	36	1.41	1010	1.56	2.7	424	127	49.9
No. 14	43	1.69	1450	2.25	2.9	424	152	59.9

The force developed by each bar that crosses the diagonal crack assumed to propagate through the joint was computed by multiplying the nominal yield strength of the bar by the ratio of the embedment length beyond the crack, L , to the computed development length, l_d (See Figure 7.3). If the available anchorage length, L , was less than l_d , the maximum stress in the bar was computed as the fraction of the available anchorage length, L , divided by l_d , multiplied by the nominal yield stress, f_y . It was assumed that all reinforcing bars reached their respective computed maximum forces simultaneously (ie. when anchorage in the joint failed).



$$T_1 = \frac{L}{l_d} f_y A_s \text{ for } L < l_d$$

or

$$T_2 = f_y A_s \text{ for } L > l_d$$

Figure 7.3 Assumed Joint Crack and Method for Computing Forces Developed in Longitudinal Bars

At failure, shown in Figure 7.2, the overhang and a portion of the joint were assumed to act as a rigid-body. The maximum applied moment was determined by varying the applied load until equilibrium was achieved for the free body shown in Figure 7.2. Moments were summed about the compression centroid in the joint corner. The compression centroid (determined from the summation of the horizontal and vertical forces) was recomputed as the applied loads were varied, resulting in a change in the location of the compression centroid. The applied load that corresponded with joint failure was that which resulted in equilibrium of the free body.

The strength model was capable of computing the nominal moment capacities for a range of failure mechanisms including: overhang-flexural failure, failures involving a diagonal crack in the joint, and pier flexural failure. The location of the crack on the exterior face of the pier or top face of the joint was varied in the strength model to identify the lowest

failure load. For this study, it was determined that a crack propagating through the corner, shown in Figure 7.3, resulted in the least capacity.

Joint cracks were assumed to form if the computed concrete principal tensile stresses exceeded an assumed concrete tensile stress of $7\sqrt{f'_c}$ [3.4 MPa (500 psi)] in the joint region. Elastic finite element models were used to compute tensile stresses in the joint for the different specimens at applied dead load and service load.

7.3 Evaluation of Reinforced Concrete Substructure I4-C

The reinforced concrete substructure (I4-C) was one of the supports for a four-span continuous 7.92m (26 ft) wide entrance ramp box superstructure with spans of 33.5 m (110 ft). The I4-C substructure was the second pier. The computed superstructure reactions are shown in Table 7.2, and details of the superstructure are presented in Section 3.2.1.

Table 7.2 Computed Superstructure Reactions for Substructure I4-C

Load Description	Load Abbreviation	Ri		Ro	
		kN	(kips)	kN	(kips)
Dead Load	DL	2217	498.3	2217	498.3
Dead Load + 1/2 Live Load	(DL + 1/2 LL)	2403	540.1	2616	588.1
Service Load	(DL+LL)	2589	582.0	3015	677.8
Dead Load + 2 Live Load	(DL+2LL)	2961	665.7	3813	857.3
Factored Load	(1.3DL + 2.17LL)	3690	829.5	4614	1037
Factored Load / Φ	(1.3DL + 2.17LL)/ Φ	4100	921.7	5126	1152

Locations of the superstructure reactions and overall dimensions are shown in Figure 7.4. The interior reaction was located 135 cm (53 in.) from the inner face of the pier. The outer load was 168 cm (66 in.) from the interior load.

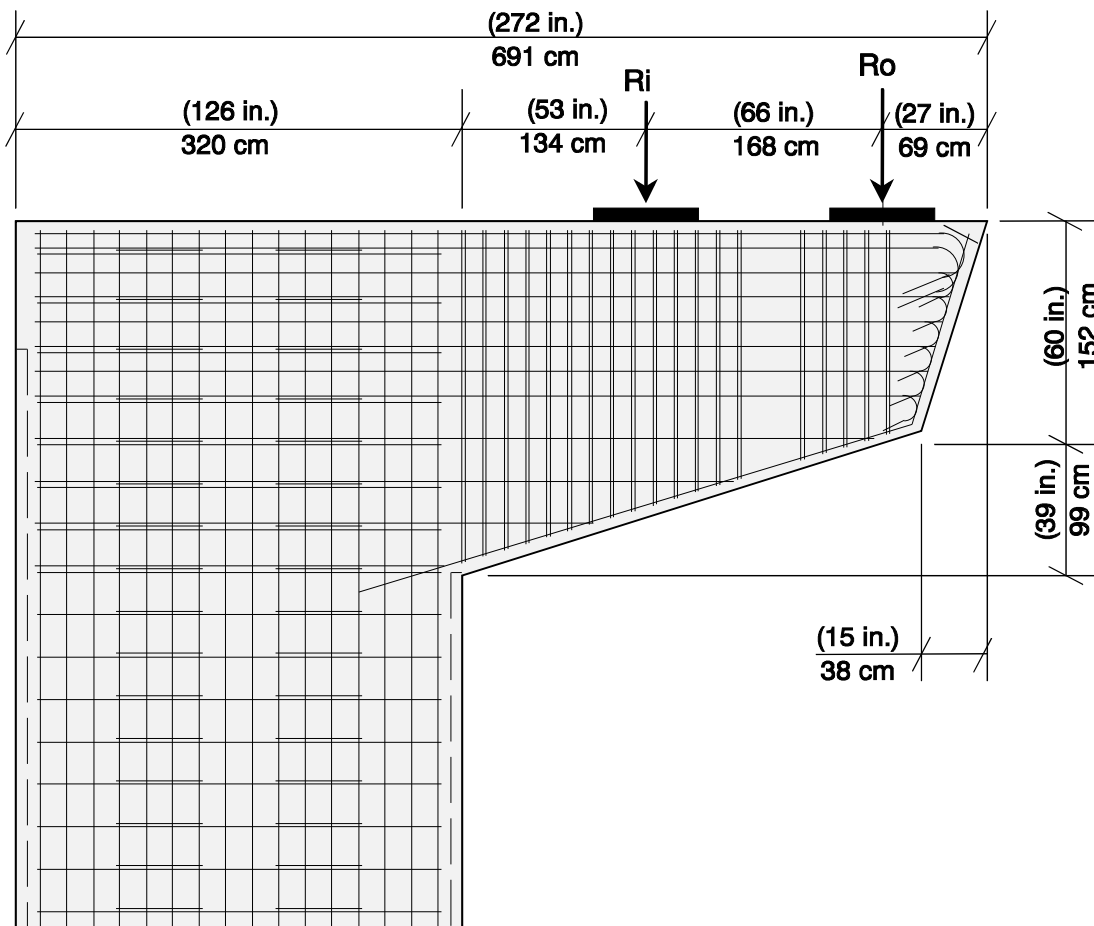


Figure 7.4 I4-C - External Dimensions and Points of Superstructure Load Application

Longitudinal reinforcement details for a pier cross-section and overhang cross-section (adjacent to the column face) are shown in Figure 7.5 and Figure 7.6, respectively. Field inspection of the pier indicated the 7.5 cm (3 in.) recessed architectural detail (shown in the design drawings) was not present in the as-built structure. The 2.5 cm (1 in.) recess on the side faces of the pier was included in the as-built structure. Field measurements confirmed that the overall pier dimensions were maintained. It was assumed that a larger concrete cover was used for the pier longitudinal bars because changing the core dimensions would require changes in the pier transverse reinforcement dimensions.

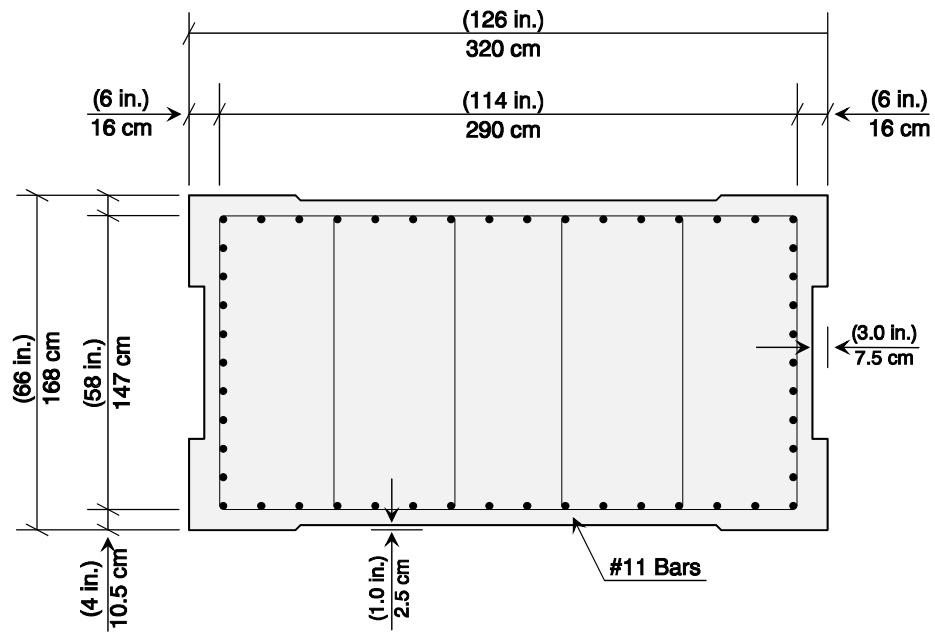


Figure 7.5 I4-C - Pier Reinforcement Details

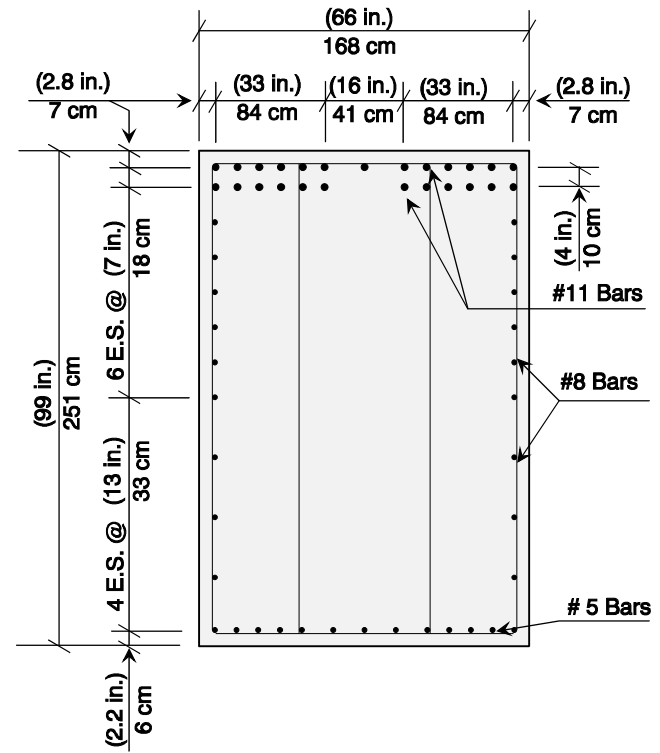
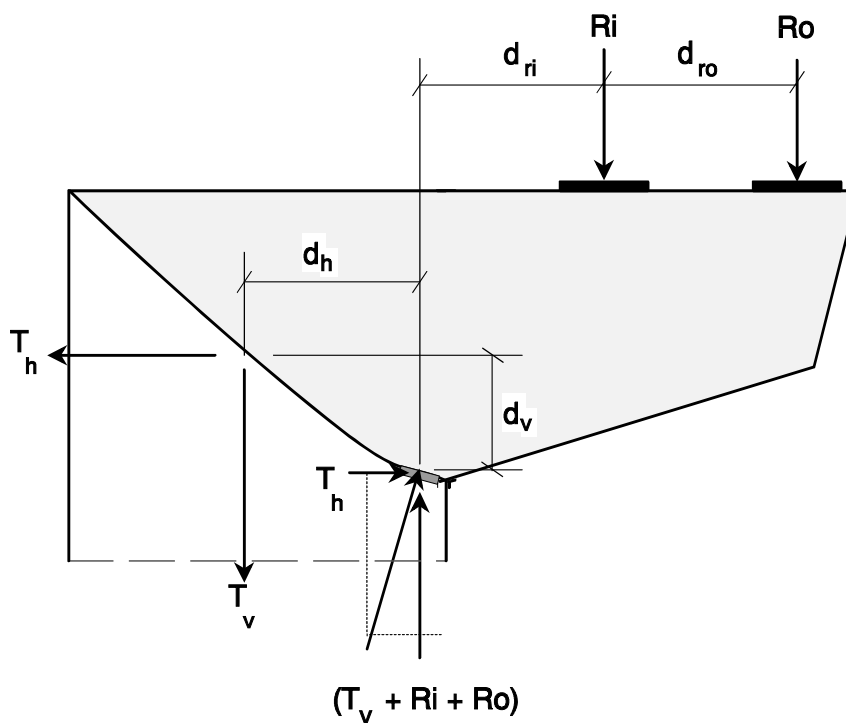


Figure 7.6 I4-C - Overhang Reinforcement Details at Pier Face

7.3.1 I4-C Substructure Strength Analysis

Strength of the reinforced concrete substructure (I4-C) was computed utilizing the reinforcing bar sizes and bar locations shown in Figure 7.5 and Figure 7.6. As stated earlier, anchorage of the overhang and pier longitudinal reinforcement would be significantly reduced in the event a diagonal crack formed in the joint. The computed bent strength and applied loads at failure are shown in Figure 7.7. A detailed drawing of the joint, including dimensions and bar sizes, is presented in Figure 7.8.



$$\text{Joint Resistance} = \text{Applied Moment}$$

$$T_h(d_v) + T_v(d_h) = R_i(d_{ri}) + R_o(d_{ro} + d_{ri})$$

$$(1105 \text{ Kips})(53.9 \text{ in.}) + (1982 \text{ Kips})(42.7 \text{ in.}) = (637 \text{ Kips})(59 \text{ in.}) + (820 \text{ Kips})(125 \text{ in.})$$

$$4915 \text{ kN}(137 \text{ cm}) + 8816 \text{ kN}(108 \text{ cm}) = 2833 \text{ kN}(150 \text{ cm}) + 3647 \text{ kN}(318 \text{ cm})$$

Figure 7.7 Free Body Used to Compute Substructure I4-C Capacity

The applied loads, R_i and R_o , that would induce bond failure in a cracked joint were computed to be 2833 kN (637 kips) and 3647 kN (820 kips), respectively. These loads correspond to 96 percent of applied dead load plus two live loads $[0.96(DL+2LL)]$ or 69 percent of applied factored loads / ϕ .

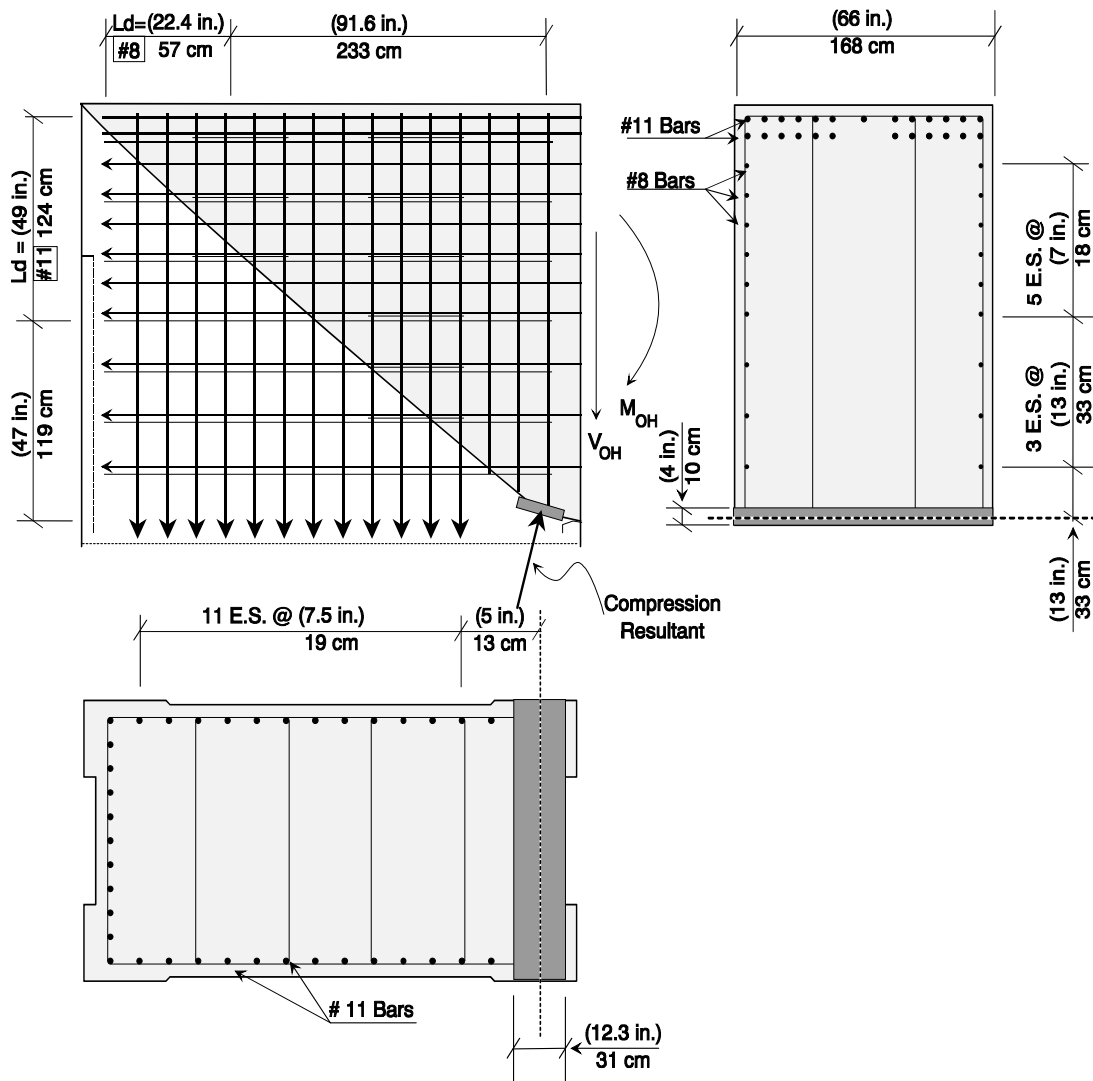


Figure 7.8 I4-C - Free Body and Reinforcement Locations Used in Strength Model

7.3.2 Finite Element Analysis - I4-C

An elastic finite element analysis of the reinforced concrete substructure (I4-C) was performed to determine the level of principal tensile stresses in the joint region. The substructure was modeled using eight-node isoparametric elements. Computed principal tensile and compressive stresses for dead-load, service-load, and DL + 2LL are presented as stress contours in Figure 7.9 through Figure 7.14. Principal tensile and compressive stress vectors are presented in Figure 7.15 and Figure 7.16, respectively.

If the level of tensile stresses exceeded $7\sqrt{f'_c}$ (psi) [3.44 MPa (500 psi)], the region was considered to be cracked. Principal tensile stresses in the joint region due to applied dead loads, shown in Figure 7.9, were less than 2.1 MPa (300 psi), indicating the joint was not cracked. At applied service-level loads, principal tensile stresses (shown in Figure 7.11) were less than 2.8 MPa (400 psi), indicating a diagonal crack would only develop under an applied load than larger than DL + LL. Principal tensile stresses for applied dead load plus two live loads were nearly 2.8 MPa (400 psi), as shown in Figure 7.13.

Results from the finite element analyses indicate principal tensile stresses may not be large enough to form the diagonal crack in the joint at the predicted failure load. It is clear that the joint failure would occur at a slightly larger load, but little or no warning in the form of a well-developed crack pattern would precede failure. This mode of failure is unacceptable from both a strength and ductility stand-point, and immediate action was required to strengthen the joint region.

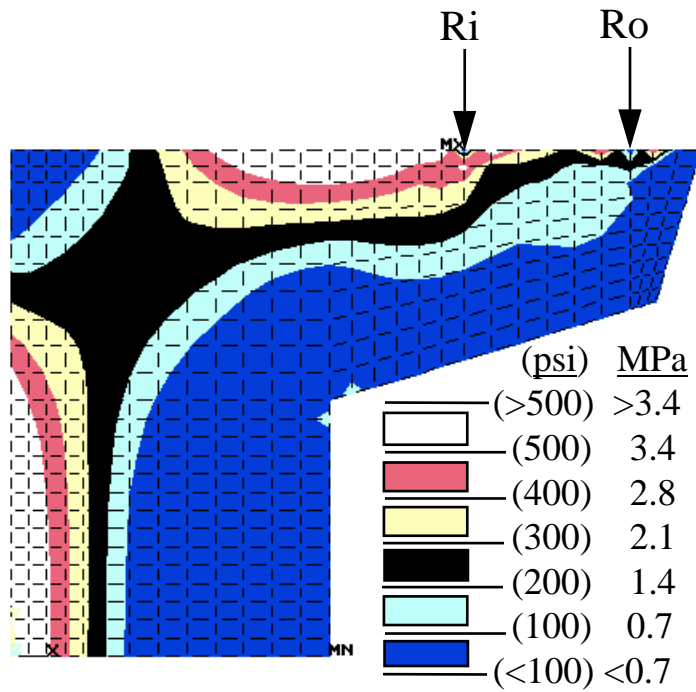


Figure 7.9 I4-C - Principal Tensile Stress Contours at Applied Dead Loads

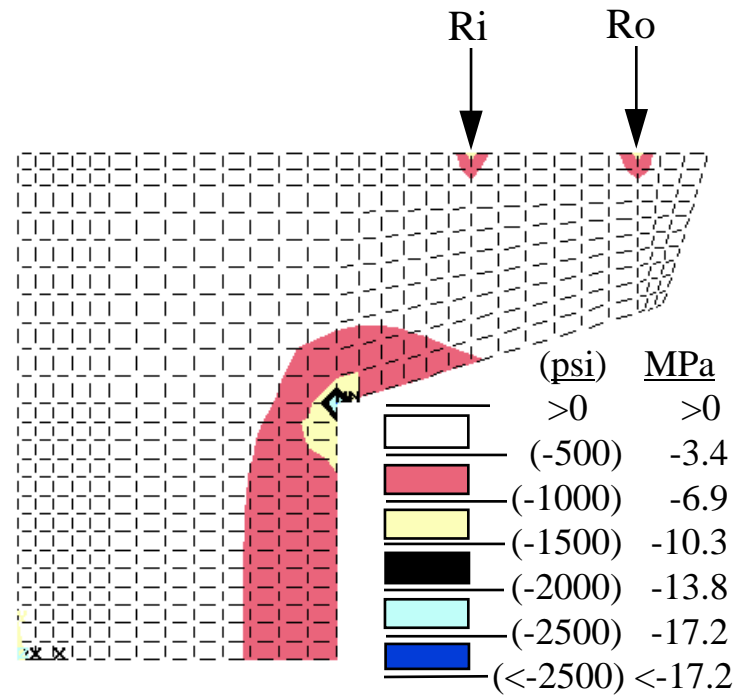


Figure 7.10 I4-C - Principal Compressive Stress Contours at Applied Dead Loads

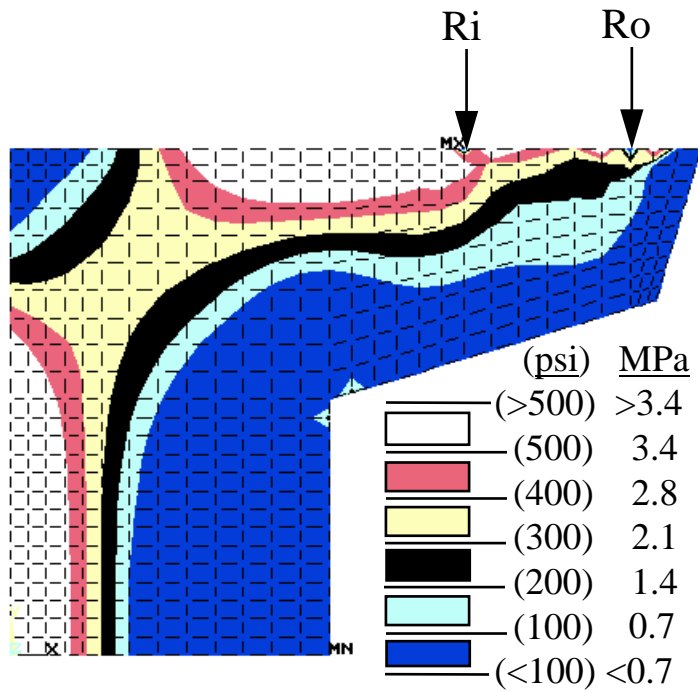


Figure 7.11 I4-C - Principal Tensile Stress Contours at Applied Service Loads

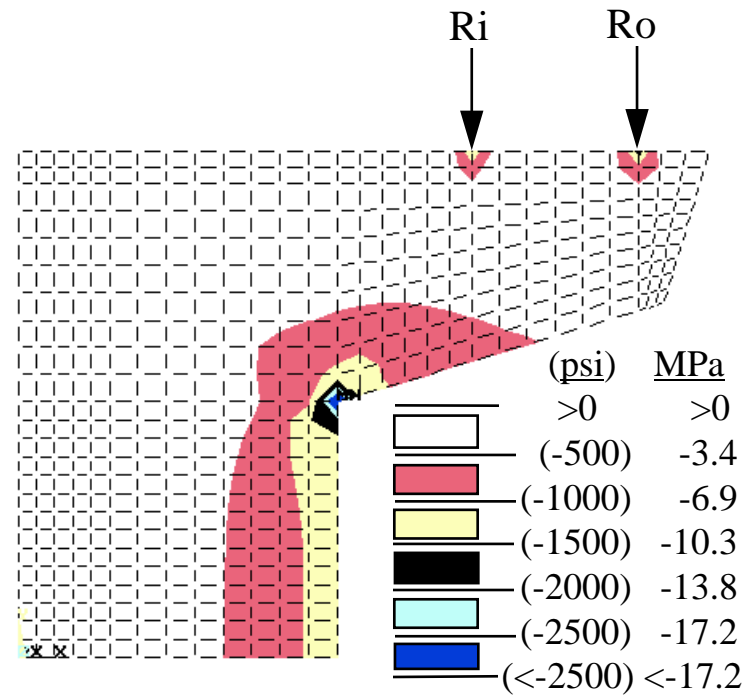


Figure 7.12 I4-C - Principal Compressive Stress Contours at Applied Service Loads

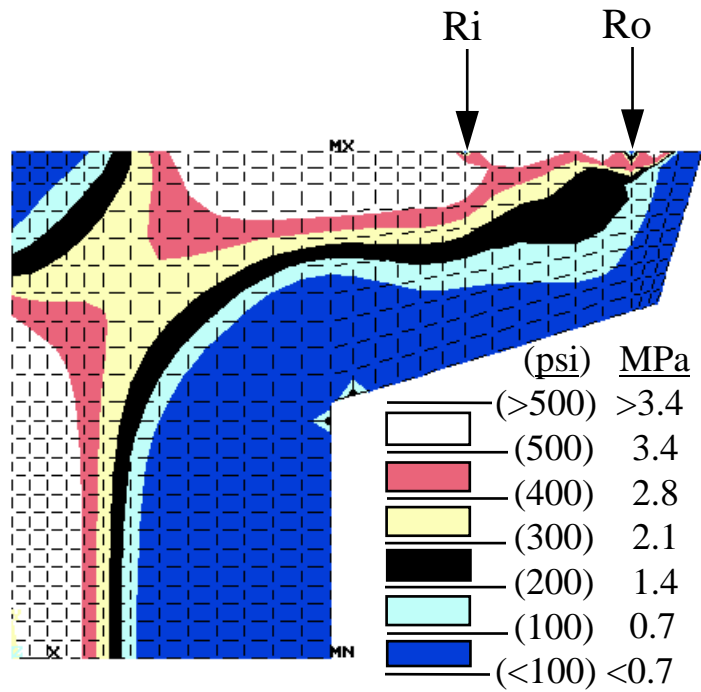


Figure 7.13 I4-C - Principal Tensile Stress Contours at Applied Dead Load Plus Two Live Loads

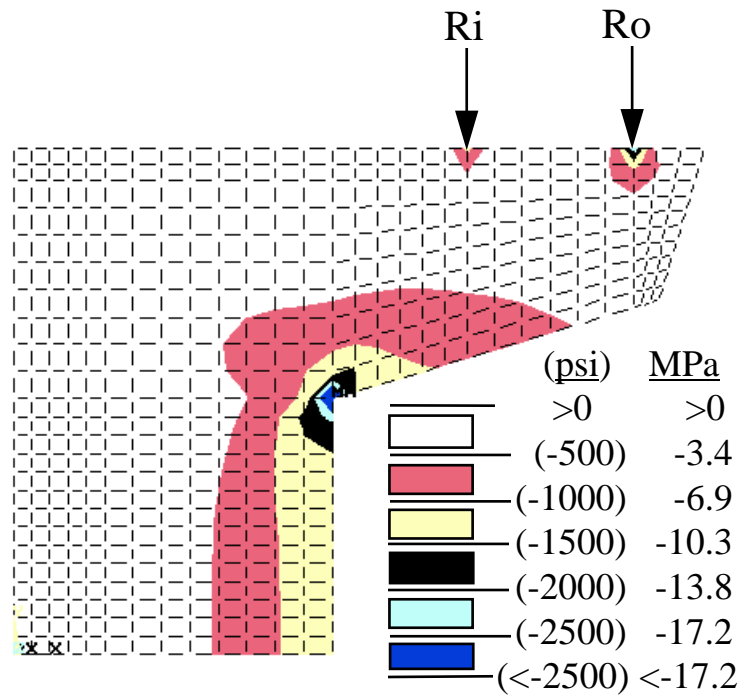


Figure 7.14 I4-C - Principal Compressive Stress Contours at Applied Dead Load Plus Two Live Loads

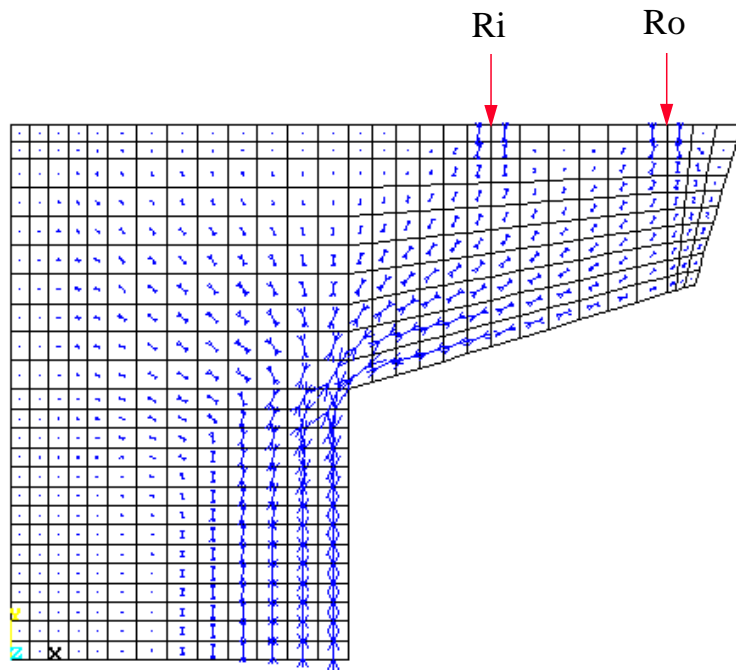


Figure 7.15 I4-C - Principal Tensile Stress Vectors

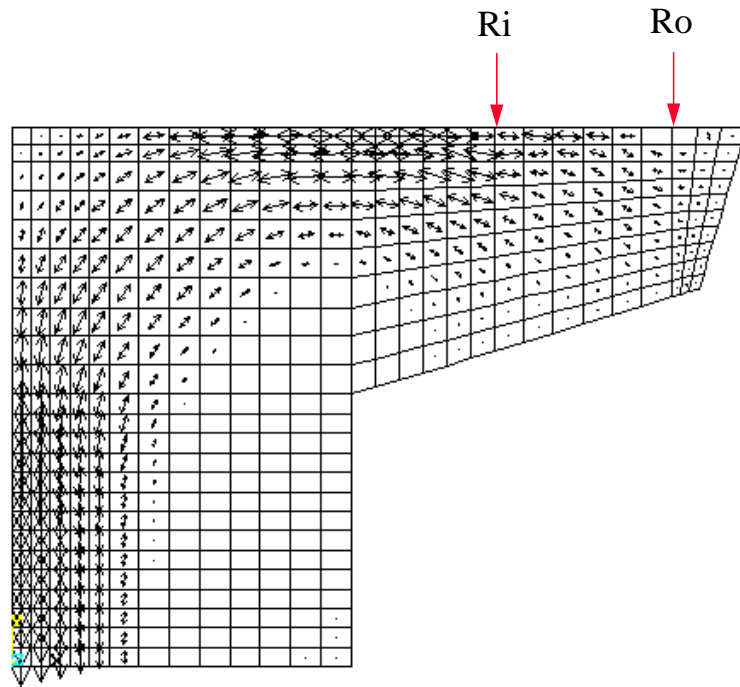


Figure 7.16 I4-C - Principal Compressive Stress Vectors

7.3.3 Field Inspection of Cracking Pattern - I4-C

Field inspection of the I4-C substructure revealed three cracks in the joint region and a long (almost full-depth) crack in the overhang. The locations and measured crack widths are shown in Figure 7.17. Two joint cracks were close to the $7\sqrt{f'_c}$ (psi) [3.44 MPa (500 psi)] contour line in Figure 7.11, indicating the substructure may have experienced loads equivalent to applied dead load plus two live loads or that cracking occurred at a lower stress than assumed.

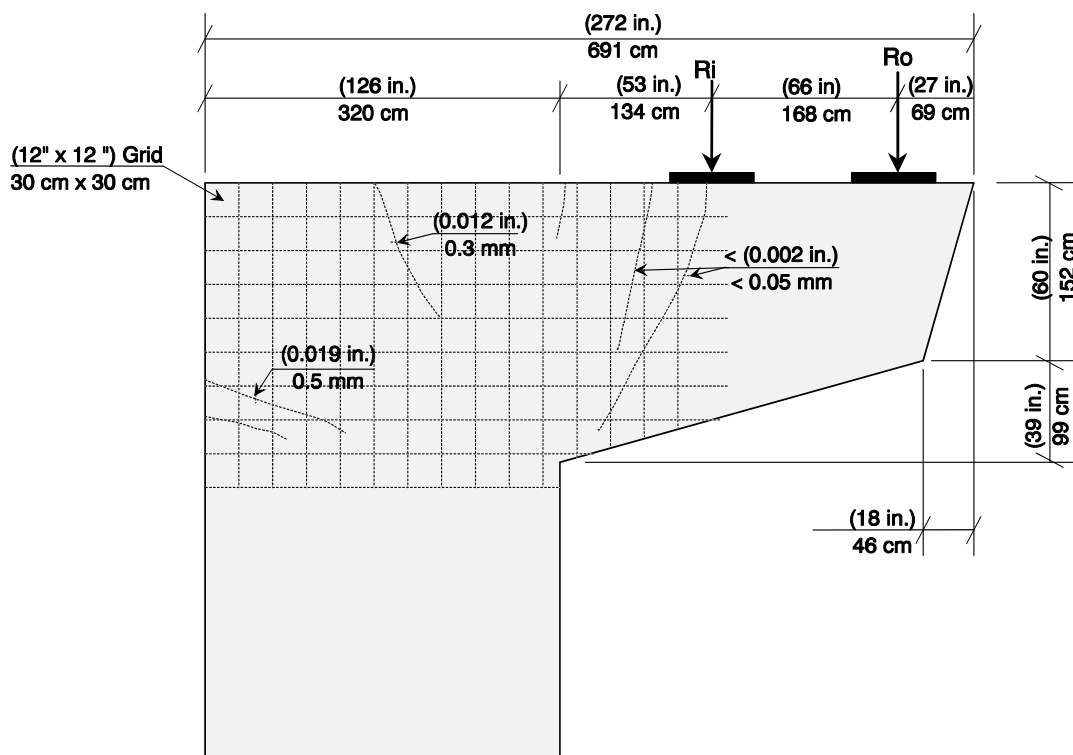


Figure 7.17 Cracking Pattern and Maximum Crack Widths for I4-C Substructure

Dirt and dust that outlined the nearly full-depth crack in the overhang made it visible from the ground, but under closer inspection, the crack was too small to measure with a crack-width comparator. TxDOT engineers expressed concern that because shear friction reinforcement was not provided near mid-depth of the overhang, a shear-friction failure might occur. Load tests performed on the POJ-RC-100-2 model (after shear friction steel was cut

with a core drill), indicated a narrow, nearly full-depth crack developed when dead loads were applied, but an applied load of 2.02 MN (455 kips) was required to fail the specimen (equivalent to 1.6 times the strength required to resist applied factored loads). It was concluded that the crack in the overhang of the I4-C substructure was not an indication of imminent shear-friction failure.

7.4 Evaluation of Fully-Prestressed Overhang Substructure C11-C

The fully-prestressed overhang substructure C11-C was designed utilizing post-tensioned bars anchored in the exterior corner of the joint and tip of the overhang. A block-out was cast into the corner and overhang to conceal the post-tensioning anchorage hardware. The pier longitudinal reinforcement on the exterior face (furthest from the overhang) was cut short to accommodate the corner block-out. Hooks or other forms of mechanical anchorage were not used to anchor the pier or overhang longitudinal reinforcement in the joint.

During construction of the San Antonio ‘Y’ Project, placement of the entrance-ramp girder onto the C11-C cantilever caused a large diagonal crack to develop in the joint region (see Figure 7.25). It will be demonstrated shortly that the substructure was deficient and on the verge of failure because of a lack of a viable tensile force path through the joint.

The substructure reactions, shown in Table 7.3, were computed for a four-span continuous 7.9 m (26 ft) wide box-girder superstructure with spans of 33.5 m (110 ft). Calculation of the superstructure reactions was presented in Section 3.2.1. The position of the reactions on the substructures is illustrated in Figure 7.18.

Post-tensioning in the overhang consisted of sixteen - 3.5 cm (1-3/8 in.) diameter Dywidag post-tensioning bars with a tensile capacity of 1.0 GPa (150 ksi). Details of the longitudinal reinforcement for the pier cross-section and overhang cross-section (adjacent to the column face) are shown in Figure 7.19 and Figure 7.20, respectively.

Table 7.3 Computed Superstructure Reactions for Substructure C11-C

Load Description	Load Abbreviation	Ri		Ro	
		kN	(kips)	kN	(kips)
Dead Load	DL	2217	498.3	2217	498.3
Dead Load + 1/2 Live Load	(DL + 1/2 LL)	2402	540.1	2616	588.1
Service Load	(DL+LL)	2589	582.0	3015	677.8
Dead Load + 2 Live Loads	(DL+2LL)	2961	665.7	3813	857.3
Factored Load	(1.3DL + 2.17LL)	3690	829.5	4614	1037
Factored Load / Φ	(1.3DL + 2.17LL)/Φ	4100	921.7	5126	1152

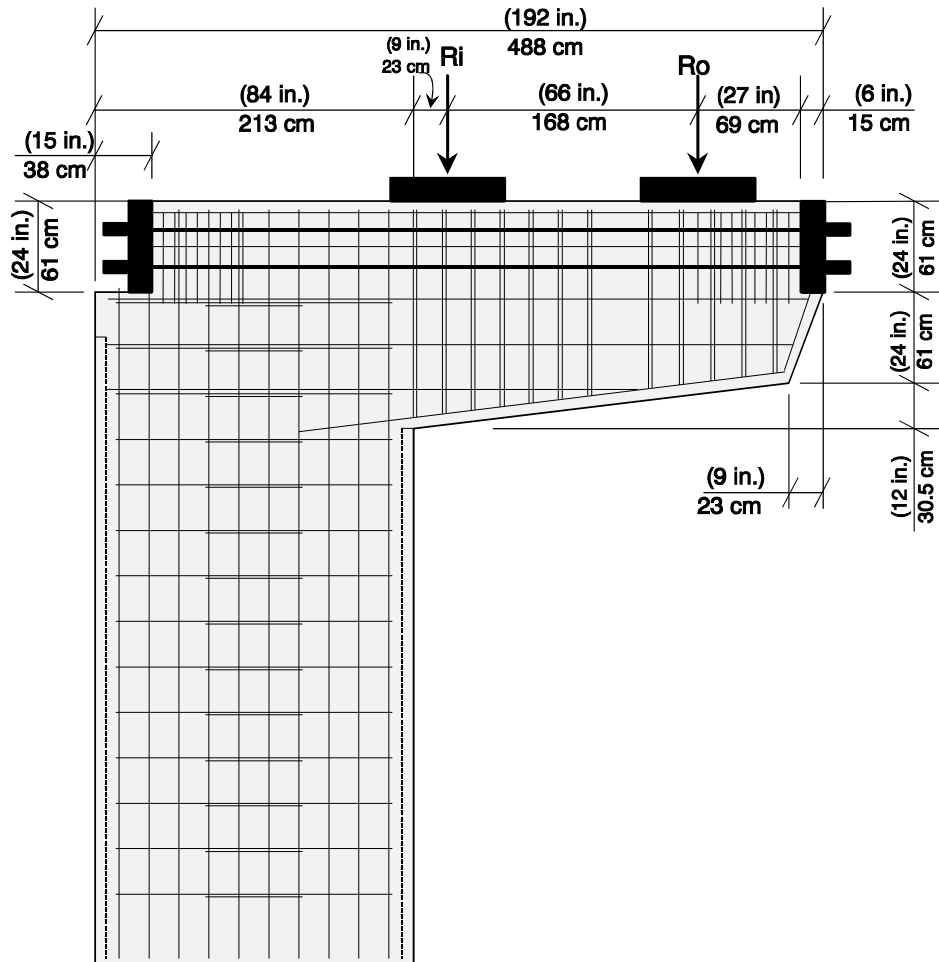


Figure 7.18 C11-C - External Dimensions and Points of Superstructure Load Application

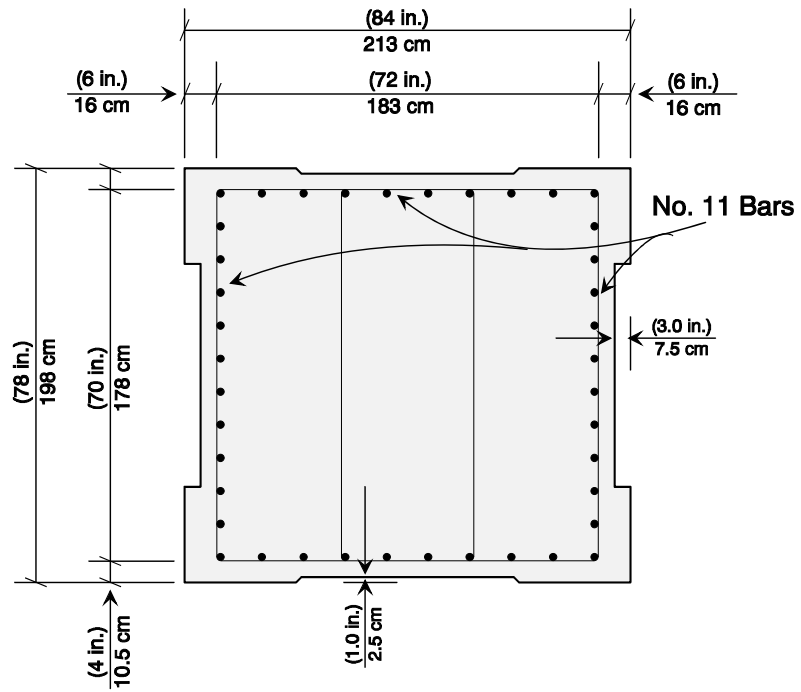


Figure 7.19 C11-C - Pier Reinforcement Details

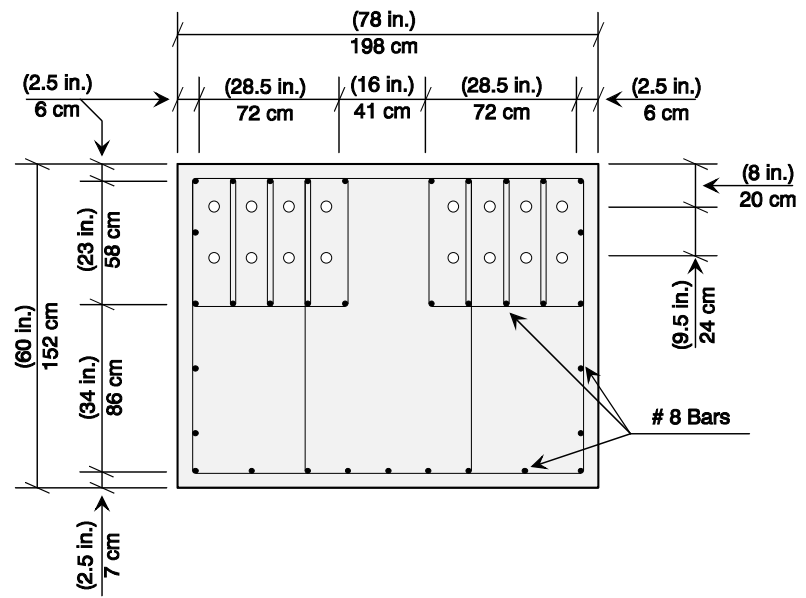
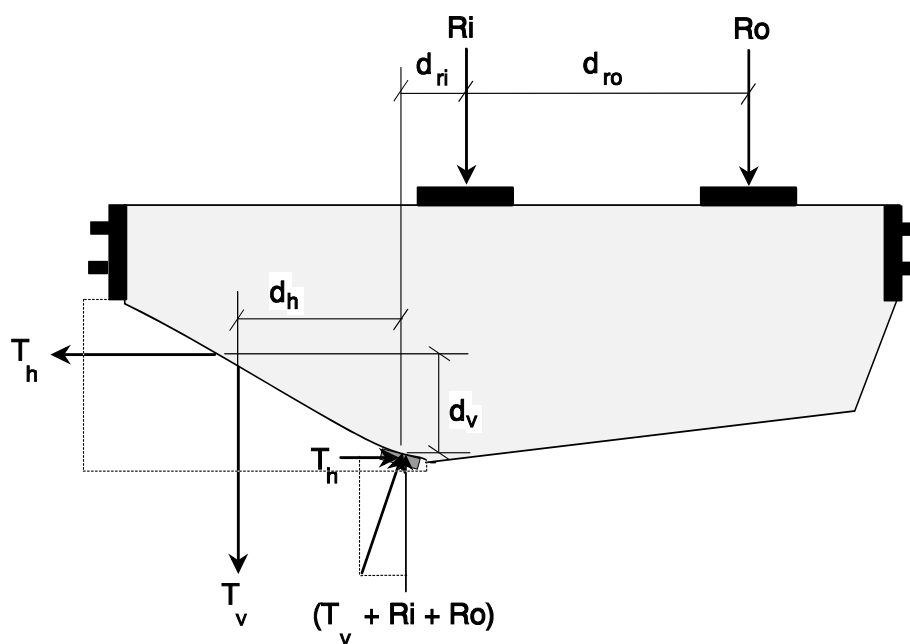


Figure 7.20 C11-C - Overhang Reinforcement Details at Pier Face

7.4.1 C11-C Substructure Strength Analysis

Strength of the C11-C substructure was computed utilizing the reinforcing bar sizes and locations shown in Figure 7.19 and Figure 7.20. The post-tensioned overhang bars reduced principal tensile stresses in the overhang, but the primary pier flexural reinforcement (located near the exterior face of the pier) was cut short to accommodate the post-tensioning anchorage block-out. Because the pier longitudinal reinforcement (located near the exterior face) did not intercept the potential diagonal joint crack (shown in Figure 7.21), it could not contribute to strength of the bent. The longitudinal overhang reinforcement that passed under the anchorage block-out, and the pairs of side reinforcement in the pier (located outside the joint block-out region) crossed the joint crack and were included in the strength calculation.



$$\text{Joint Resistance} = \text{Applied Moment}$$

$$T_h(d_v) + T_v(d_h) = R_i(d_{ri}) + R_o(d_{ro} + d_{ri})$$

$$(671 \text{ Kips})(27 \text{ in.}) + (740 \text{ Kips})(33 \text{ in.}) = (448 \text{ Kips})(11.5 \text{ in.}) + (448 \text{ Kips})(77.5 \text{ in.})$$

$$2985 \text{ kN} (69 \text{ cm}) + 3291 \text{ kN} (84 \text{ cm}) = 1993 \text{ kN} (29 \text{ cm}) + 1993 \text{ kN} (197 \text{ cm})$$

Figure 7.21 Free Body Used to Compute Substructure C11-C Capacity

The failure mechanism and predicted capacity are presented in Figure 7.21. A detailed drawing of the joint, including dimensions and bar locations, is illustrated in Figure 7.22.

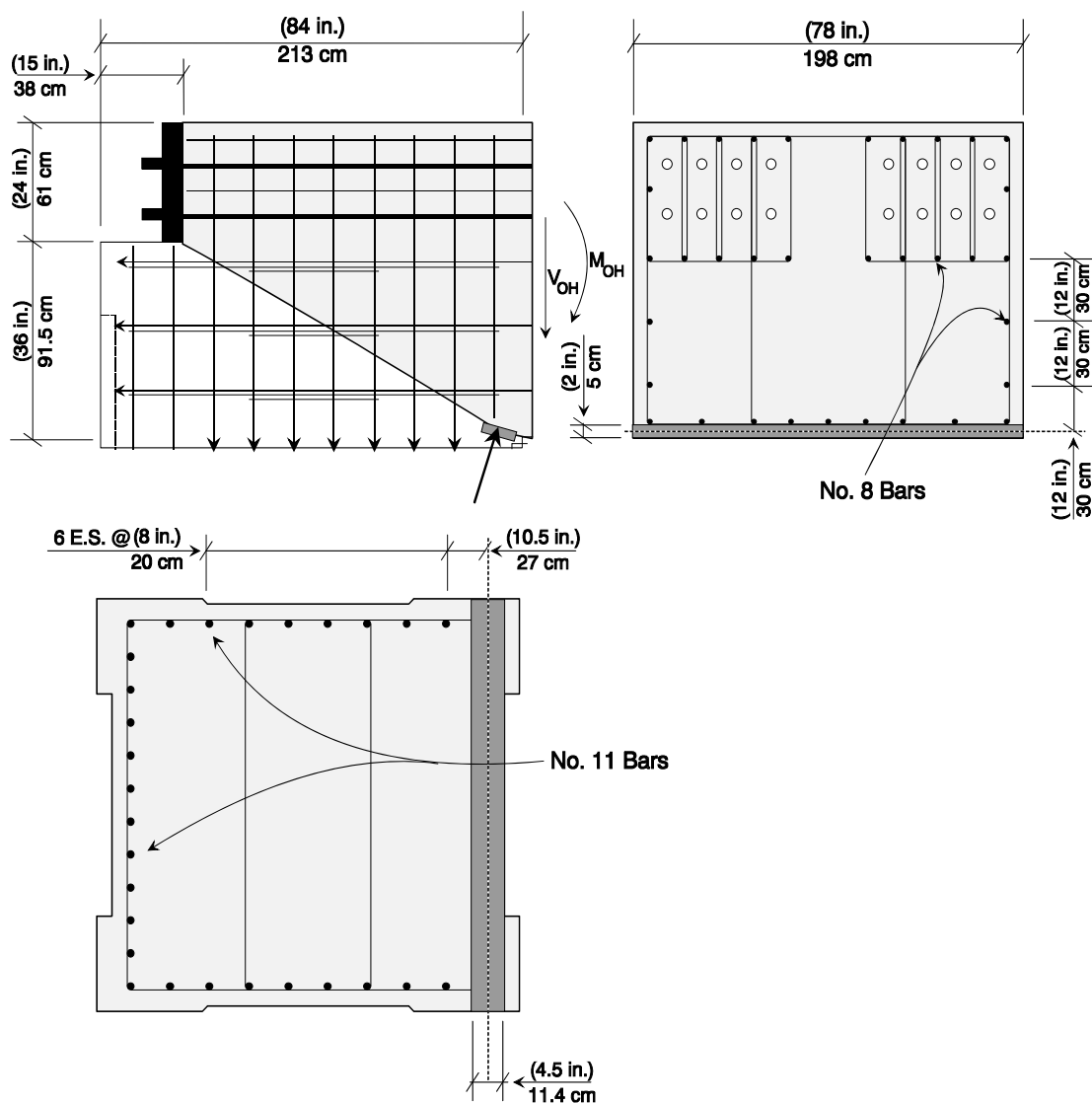


Figure 7.22 C11-C - Free Body and Reinforcement Locations Used in Strength Model

The applied loads, R_i and R_o , that were computed to cause failure were computed to be 1993 kN (448 kips) each. These loads correspond to 90 percent of applied dead load (0.90 DL), and are equal to 50 percent of applied factored loads / ϕ . Because the C11-C

substructure cracked after the superstructure dead load was applied, the computed failure load was considered to be a reasonably accurate estimate of the full-scale substructure strength.

7.4.2 Finite Element Analysis - C11-C

An elastic finite element analysis model of the C11-C substructure was performed to determine the level of principal tensile stresses in the joint region. The substructure was modeled using eight-node isoparametric elements. Post-tensioning forces were modeled as point loads in the overhang and joint.

The block-out in the joint corner significantly increased principal tensile stresses in the joint region. Principal tensile and compressive stresses are plotted as contours and vectors for applied dead load in Figure 7.23 and Figure 7.24, respectively. Principal tensile stresses in the joint, shown in Figure 7.23, exceeded the concrete cracking stress of $7\sqrt{f'_c}$ [3.4 MPa (500 psi)] , indicating a diagonal crack would have formed in the joint at applied dead load.

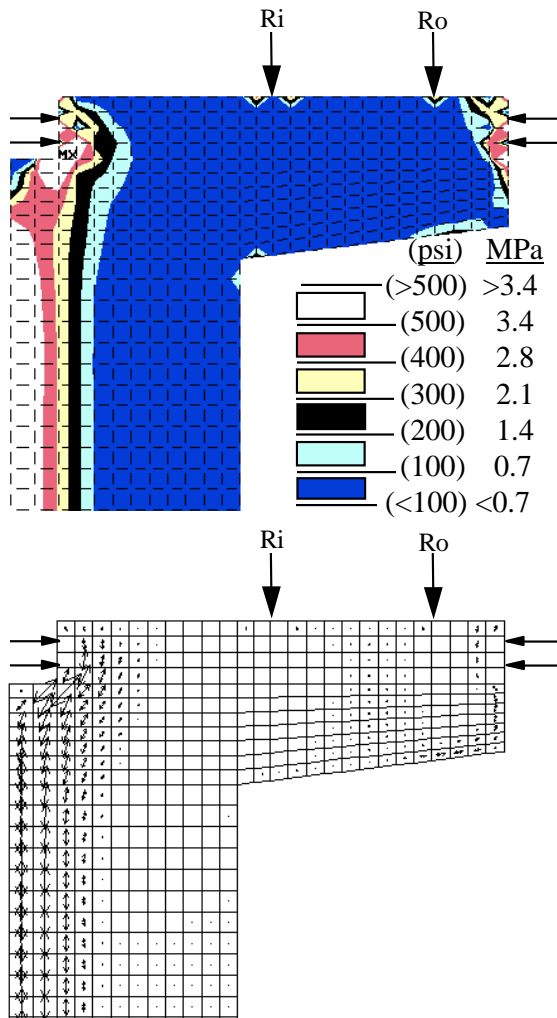


Figure 7.23 C11-C - Principal Tensile Stress Contours and Trajectories at Applied Dead Load

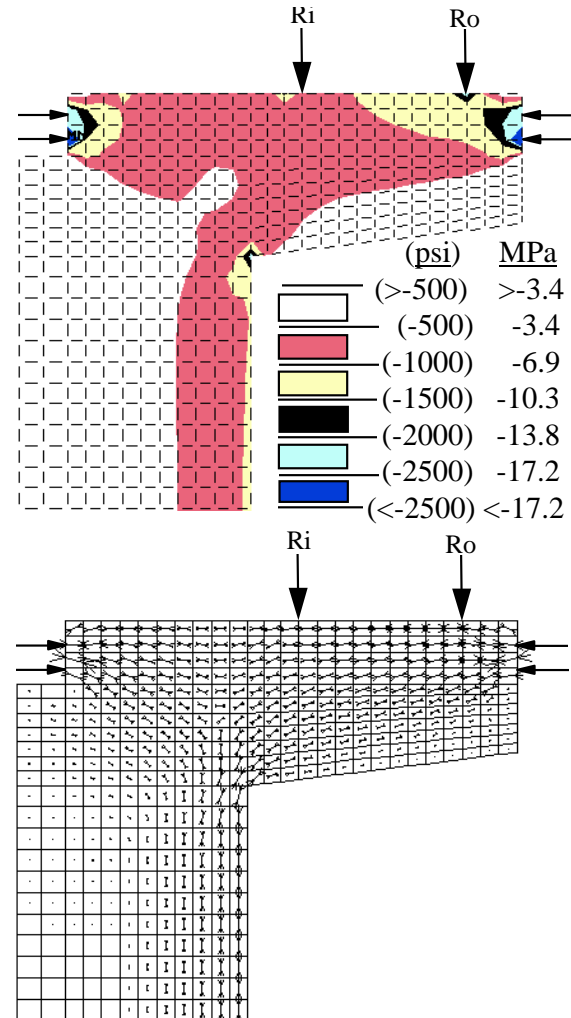


Figure 7.24 C11-C - Principal Compressive Stress Contours and Trajectories at Applied Dead Load

7.4.3 Field Inspection Cracking Pattern - C11-C

After the C11-C substructure failed, the superstructure was supported and internal vertical post tensioning was installed to increase the capacity of the bent. Cracks were epoxy injected after the repair was installed, and the location and orientation of the major joint crack was still visible and is shown in Figure 7.25. Specimen POJ-PS-100 tested in the laboratory experienced a similar failure. It was concluded that the substructures with similar joint details needed to be inspected, evaluated, and repaired (if they were found to be deficient).

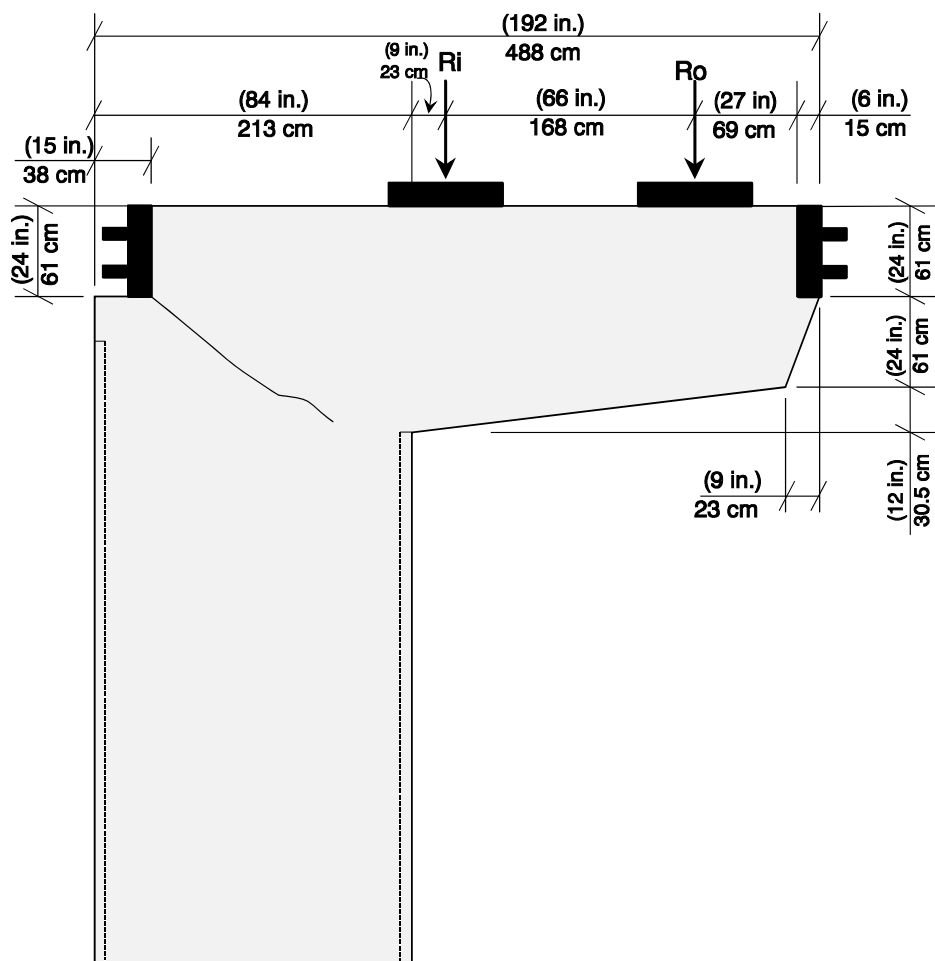


Figure 7.25 Cracking Pattern for C11-C Substructure

7.5 Summary of Results

Results from substructure analyses and field inspections provided sufficient evidence to warrant closing three entrance ramps on Interstate Highway 10 in San Antonio, Texas on April 6, 1995. The research project on “Design of Large Structural Members Utilizing Partial Prestressing”, CTR Project No. 1364, at The University of Texas at Austin was extended to develop and evaluate three repair/strengthening methods for the substructures. The repairs were installed on 1/2.75-scale model specimens then were tested. Results of the tests are presented in Chapter 8.

7.1 Introduction	296
7.2 Development of the Strength Analysis Model.....	297
7.3 Evaluation of Reinforced Concrete Substructure I4-C.....	301
7.3.1 I4-C Substructure Strength Analysis.....	304
7.3.2 Finite Element Analysis - I4-C.....	306
7.3.3 Field Inspection of Cracking Pattern - I4-C.....	311
7.4 Evaluation of Fully-Prestressed Overhang Substructure C11-C	312
7.4.1 C11-C Substructure Strength Analysis	315
7.4.2 Finite Element Analysis - C11-C	317
7.4.3 Field Inspection Cracking Pattern - C11-C	319
7.5 Summary of Results.....	320
Figure 7.1 Cantilever Substructure Strut-and-Tie Model	297
Figure 7.2 Free Body Used to Compute Bent Capacity.....	298
Figure 7.3 Assumed Joint Crack and Method for Computing Forces Developed in Longitudinal Bars.....	300
Figure 7.4 I4-C - External Dimensions and Points of Superstructure Load Application.....	302
Figure 7.5 I4-C - Pier Reinforcement Details	303
Figure 7.6 I4-C - Overhang Reinforcement Details at Pier Face	303
Figure 7.7 Free Body Used to Compute Substructure I4-C Capacity.....	304
Figure 7.8 I4-C - Free Body and Reinforcement Locations Used in Strength Model	305
Figure 7.9 I4-C - Principal Tensile Stress Contours at Applied Dead Loads	307
Figure 7.10 I4-C - Principal Compressive Stress Contours at Applied Dead Loads	307
Figure 7.11 I4-C - Principal Tensile Stress Contours at Applied Service Loads.....	308
Figure 7.12 I4-C - Principal Compressive Stress Contours at Applied Service Loads.....	308
Figure 7.13 I4-C - Principal Tensile Stress Contours at Applied Dead Load Plus Two Live Loads.....	309

Figure 7.14 I4-C - Principal Compressive Stress Contours at Applied Dead Load Plus Two Live Loads.....	309
Figure 7.15 I4-C - Principal Tensile Stress Vectors	310
Figure 7.16 I4-C - Principal Compressive Stress Vectors	310
Figure 7.17 Cracking Pattern and Maximum Crack Widths for I4-C Substructure.....	311
Figure 7.18 C11-C - External Dimensions and Points of Superstructure Load Application	313
Figure 7.19 C11-C - Pier Reinforcement Details.....	314
Figure 7.20 C11-C - Overhang Reinforcement Details at Pier Face.....	314
Figure 7.21 Free Body Used to Compute Substructure C11-C Capacity	315
Figure 7.22 C11-C - Free Body and Reinforcement Locations Used in Strength Model	316
Figure 7.23 C11-C - Principal Tensile Stress Contours and Trajectories at Applied Dead Load	318
Figure 7.24 C11-C - Principal Compressive Stress Contours and Trajectories at Applied Dead Load	318
Figure 7.25 Cracking Pattern for C11-C Substructure.....	319
Table 7.1 Basic Bar Development Lengths for 414 MPa (60 ksi) Reinforcing Bars.....	299
Table 7.2 Computed Superstructure Reactions for Substructure I4-C.....	301
Table 7.3 Computed Superstructure Reactions for Substructure C11-C	313

CHAPTER 8

DEVELOPMENT AND TESTING OF SELECTED REPAIRS

8.1 Introduction

A review of San Antonio 'Y' substructures I4-C (reinforced concrete) and C11-C (fully-prestressed overhang), described in Chapter 7, indicated longitudinal overhang and pier reinforcing bars were not adequately anchored in the joint, and predicted capacities for both substructures were less than design factored loads. Two prototype specimens were constructed at 1/2.75 scale: a reinforced concrete specimen (POJ-RC-100-2) and a fully-prestressed overhang specimen (POJ-PS-100). Each specimen failed at applied loads less than design factored loads, and recorded maximum applied loads were consistent with capacities computed using the method described in Chapter 7. Six other substructures were identified as being potentially deficient.

The following sections present strength calculations and experimental results for Specimens POJ-RC-100-2 and POJ-PS-100. Several repair methods are discussed, and three particular repair methods were selected for further development and testing. Each prototype specimen was repaired twice and repairs were proof loaded to design factored loads / ϕ , where ϕ equals 0.9. Capacity calculations, design drawings, and experimental results are presented for two external repair methods and one internal repair method.

8.2 Evaluation of Cantilever Bent Capacity - POJ-RC-100-2 and POJ-PS-100

Capacities for the scaled prototype bents were determined utilizing the procedure presented in Section 7.2. Reinforcing details and predicted capacity for Specimens POJ-RC-100-2 and POJ-PS-100 are presented in Sections 8.2.1 and 8.2.2, respectively. The applied load sequence for the model study was based on the loads presented in Table 8.1. Loads were determined from calculations presented in Section 3.2.1.

Table 8.1 Substructure Design Loads for 1/2.75 Scale Models

Load Description	Load Abbreviation	Ri		Ro	
		kN	(Kips)	kN	(Kips)
Dead Load	DL	293	65.9	293	65.9
Dead Load + 1/2 Live Load	(DL + 1/2 LL)	318	71.5	346	77.8
Service Load	(DL+LL)	343	77.0	398	89.6
Dead Load + 2 Live Loads	(DL+2LL)	409	92.0	496	111.4
Factored Load	(1.3DL + 2.17LL)	488	109.7	610	137.2
Factored Load / Φ	(1.3DL + 2.17LL)/ Φ	543	122.1	679	152.7

8.2.1 Reinforced Concrete Specimen - POJ-RC-100-2

Reinforced concrete Specimen POJ-RC-100-2 was designed according to the 1983 AASHTO Standard Specifications using the same considerations assumed by the designers of the San Antonio 'Y' Project. Specimen POJ-RC-100-2 was constructed after specimen POJ-RC-100 was tested to failure (reported in Section 4.2.1). Reinforcing details, presented in Section 3.3.1 were used to construct Specimen POJ-RC-100-2 with the following modifications: repositioned lift inserts away from the joint-failure plane, no U-bar reinforcement over the top layer of overhang-longitudinal reinforcement, and an increased number of strain gages located in the joint.

8.2.1.1 Reinforcing Details - POJ-RC-100-2

An elevation of the reinforcement for Specimen POJ-RC-100-2 is presented in Figure 8.1. Distribution of longitudinal reinforcement in the pier and the overhang cross-section adjacent to the column face are shown in Figure 8.2 and Figure 8.3, respectively. Because bars used in the model had more than twice the straight-bar development required by the specifications, hooks, welded plates, and other methods of positive anchorage were not provided.

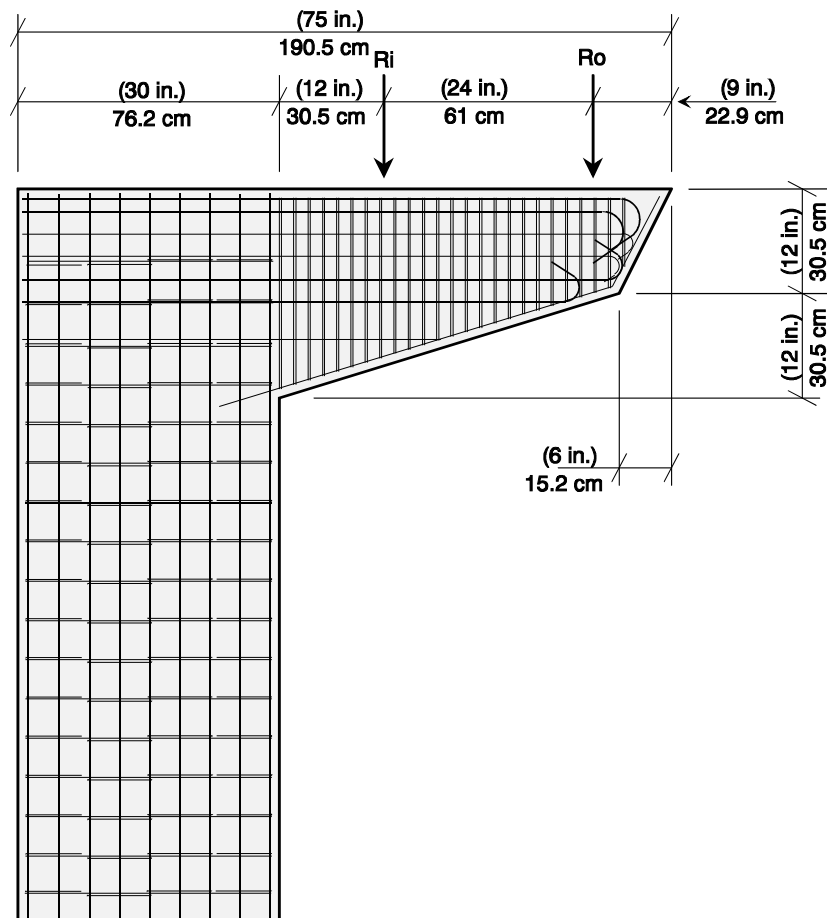


Figure 8.1 Elevation of Reinforcement for Specimen POJ-RC-100-2

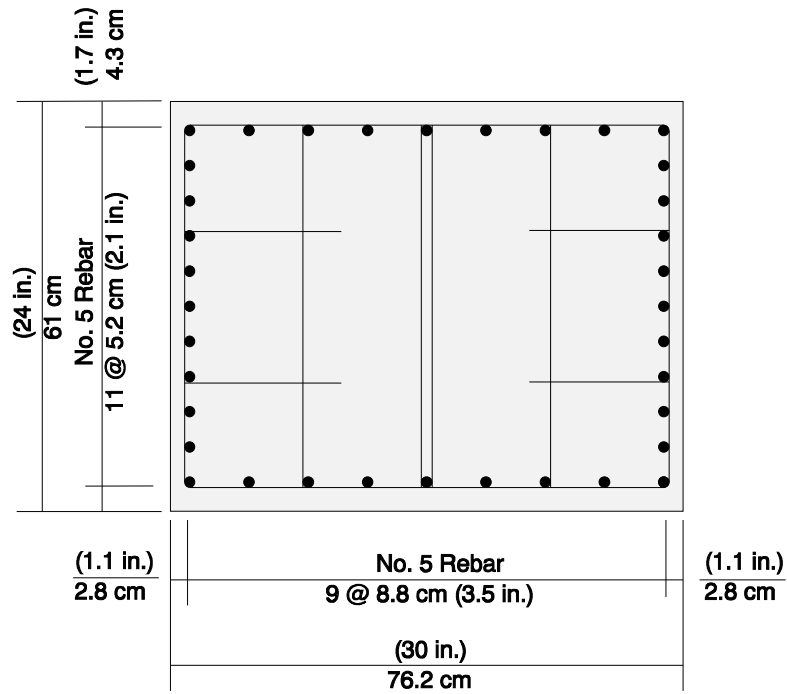


Figure 8.2 POJ-RC-100-2 Pier Reinforcement Details

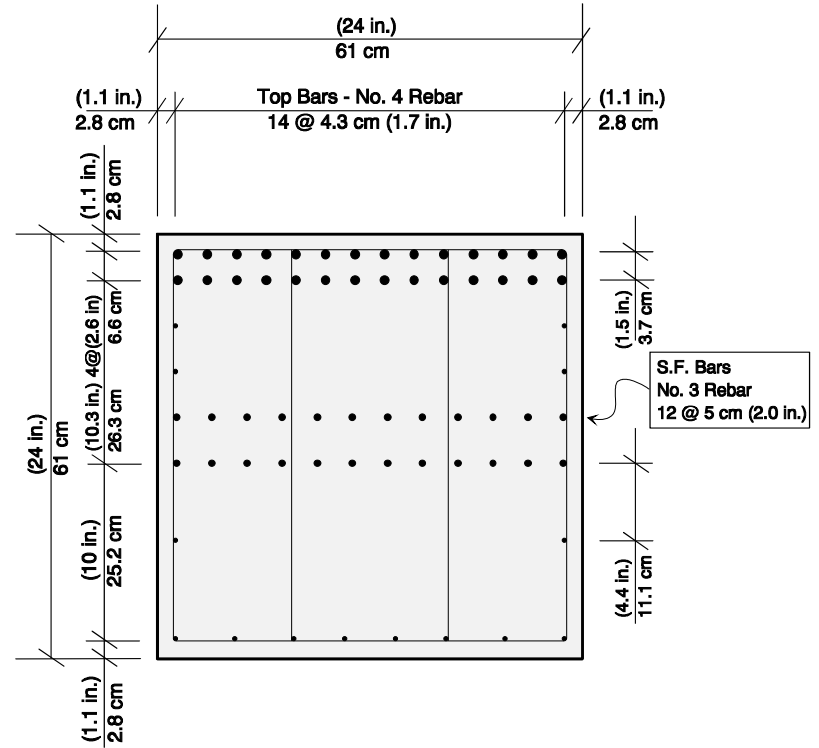


Figure 8.3 POJ-RC-100-2 Overhang Reinforcement Details

8.2.1.2 Finite Element Analysis - POJ-RC-100-2

An elastic finite element analysis of Specimen POJ-RC-100-2 was performed to determine the level of principal tensile stresses in the joint region under applied service loads. Computed principal tensile stresses at applied service loads are presented in the form of stress contours in Figure 8.4.

Computed principal tensile stresses in the joint region were greater than the assumed concrete cracking tensile strength of $7\sqrt{f'_c}$ [3.4 MPa (500 psi)], which indicated the critical diagonal crack would develop in the joint before applied service loads were reached. Principal tensile stress vectors, shown in Figure 8.5, illustrate the predicted flow of tensile stresses through the overhang and joint regions.

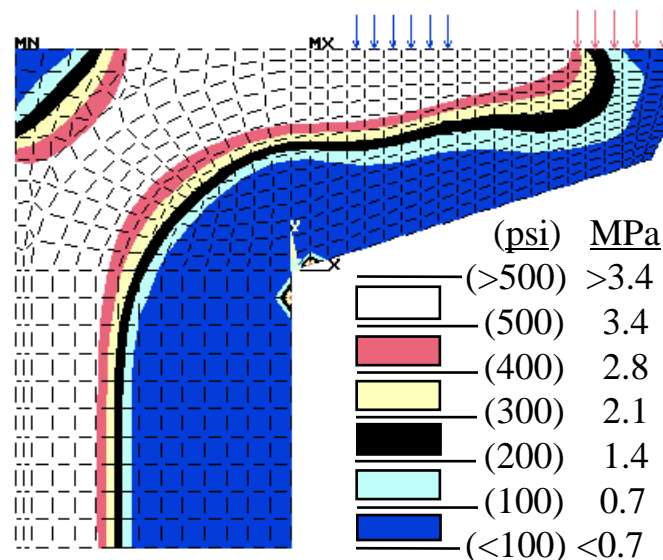


Figure 8.4 POJ-RC-100-2 Principal Tensile Stresses at Service Load

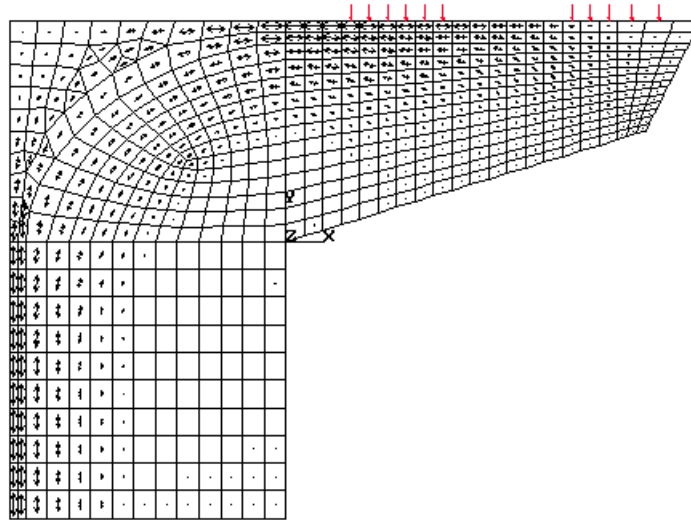


Figure 8.5 POJ-RC-100-2 Principal Tensile Stress Vectors at Service Load

8.2.1.3 Strut-and-Tie Model - POJ-RC-100-2

The strut-and-tie model, shown in Figure 8.6, is intended to represent the flow of forces produced after applied loads (R_i and R_o) produce a diagonal crack in the joint. It is clear, from Figure 8.6, that maximum applied loads (R_i and R_o) are limited by the maximum tensile forces (T_h and T_v), developed by straight bar anchorage of the longitudinal overhang and pier reinforcement, respectively. Maximum force at failure for each longitudinal bar was computed utilizing the ACI-318 (1963) basic development length equation [28] and the bond-stress model, presented in Section 7.2. The bent capacity, using this model, is computed in Section 8.2.1.4.

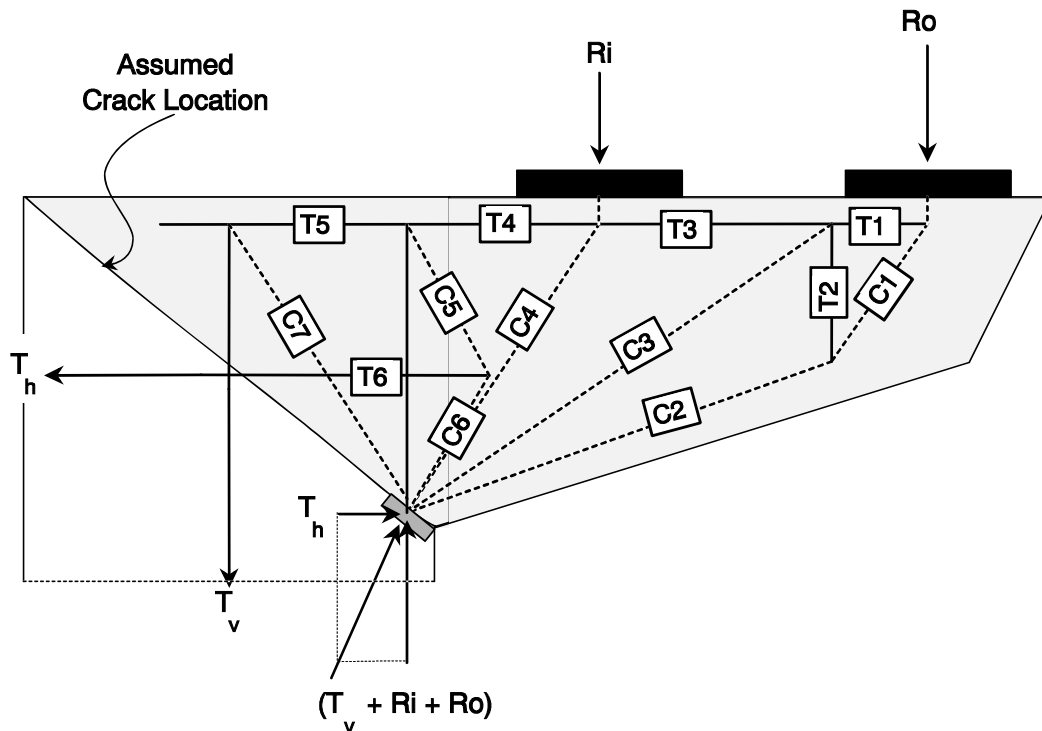


Figure 8.6 POJ-RC-100-2 Strut-and-Tie Model

8.2.1.4 Cantilever Bent Strength Computation - POJ-RC-100-2

A portion of the free body used to compute the specimen capacity is shown in Figure 8.7. Capacities of bars crossing the assumed critical diagonal crack in the joint were determined as outlined previously, after determining the development length, l_d , and the embedment length, L , of each bar. Computed bar forces and moment arms are detailed in Figure 8.7. Computed maximum applied loads, R_i and R_o , were 338 kN (75.9 kips) and 386 kN (86.8 kips), respectively. These loads are nearly equivalent to applied service loads (DL+0.9LL) and are 66 percent of applied factored loads. A simple free-body diagram of the capacity calculation, presented in Figure 8.8, illustrates the balance of forces.

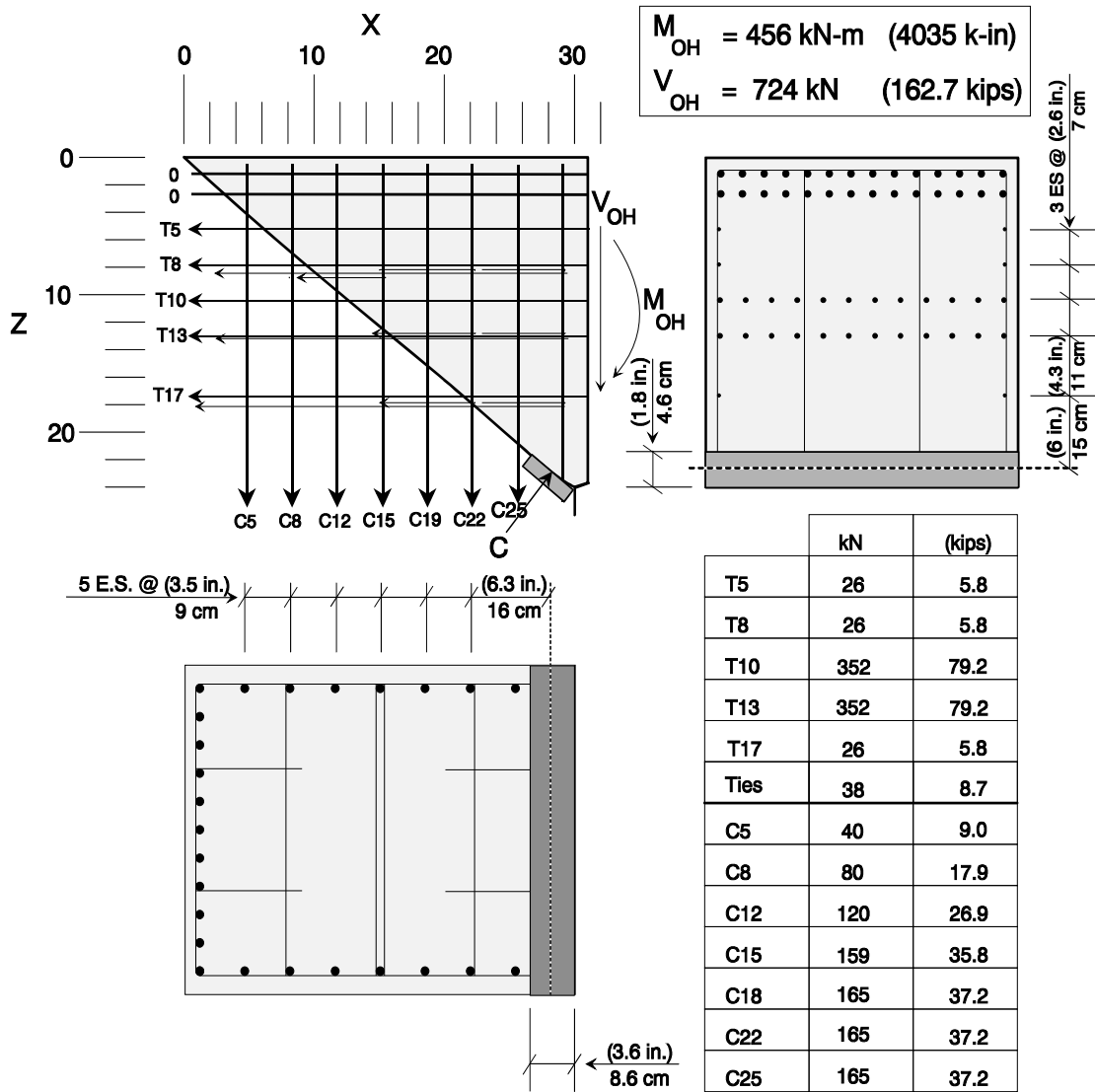
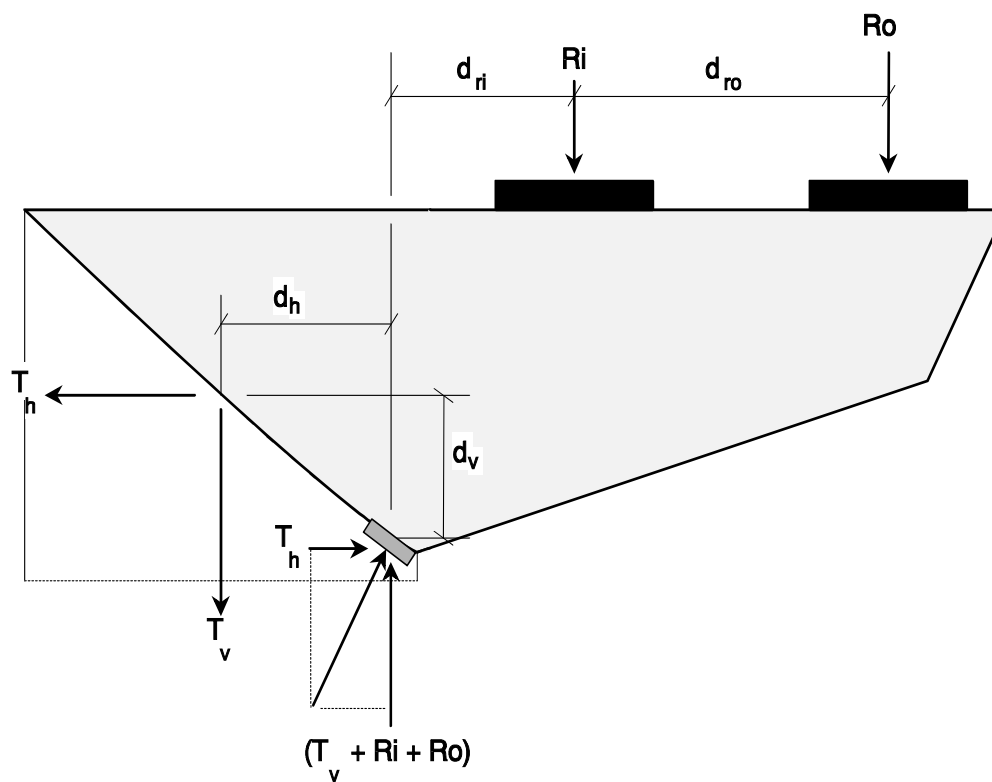


Figure 8.7 POJ-RC-100-2 Free Body and Reinforcement Locations Used in Strength Model



Joint Resistance = Applied Moment

$$T_h(d_v) + T_v(d_h) = Ri(d_{ri}) + Ro(d_{ro} + d_{ri})$$

$$(184.3 \text{ kips})(11.6 \text{ in.}) + (201.1 \text{ kips})(10.9 \text{ in.}) = (76.0 \text{ kips})(13.8 \text{ in.}) + (86.8 \text{ kips})(37.8 \text{ in.})$$

$$820 \text{ kN} (29.5 \text{ cm}) + 895 \text{ kN} (27.7 \text{ cm}) = 338 \text{ kN} (35.0 \text{ cm}) + 386 \text{ kN} (96.0 \text{ cm})$$

Figure 8.8 Free Body Used to Compute Specimen POJ-RC-100-2 Capacity

8.2.1.5 Overhang Moment vs. Tip-Deflection Behavior - POJ-RC-100-2

Loads were applied according to the load sequence presented in Table 8.1. During testing, crack widths were measured at DL and DL + 1/2 LL using a crack microscope. At both load levels, a reduction in applied load was recorded after crack measurements were completed, as shown in the moment-deflection plot (Figure 8.9). The reduction in load was caused by a slight increase in tip deflection over a period of 2 hours (the length of time required to measure crack widths). Because the load was applied using hydraulic rams, any

increase in ram displacement resulted in a decrease in hydraulic pressure, and thus applied load. After cracks widths were measured at $DL + 1/2LL$, the applied load was increased back to $DL + 1/2LL$. Subsequent load steps resulted in a significant increase in the overhang tip-deflection, and a large crack developed across the joint diagonal. Maximum recorded applied loads (R_i and R_o) were 340 kN (76.4 kips) and 388 kN (87.3 kips), respectively. These loads correspond to 65 percent of applied factored loads / ϕ . The specimen was displaced further, resulting in growth of the diagonal joint crack and reduction of specimen resistance. Displacements in the recorded applied moment vs. tip deflection response, shown in Figure 8.9, remained constant during unloading, which indicated the joint crack remained open as POJ-RC-100-2 was unloaded. Crack-width measurements and additional results from the test are presented in a thesis by Scott [6].

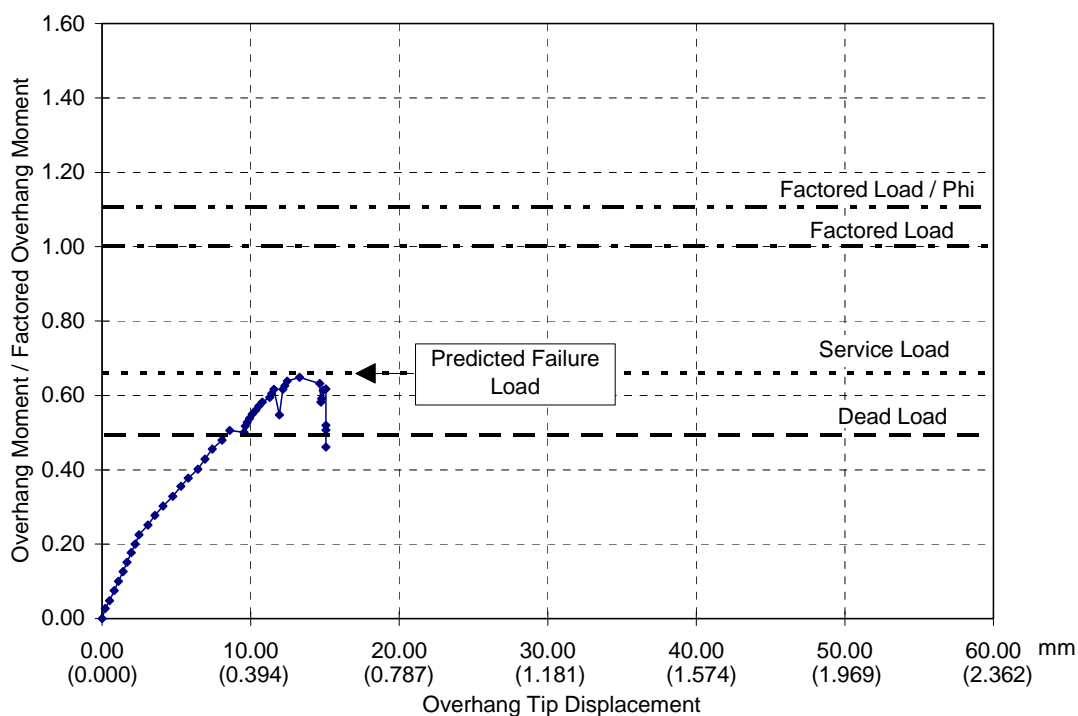


Figure 8.9 POJ-RC-100-2 Applied Overhang Moment vs. Tip-Deflection

8.2.2 Specimen with Fully-Prestressed Overhang - POJ-PS-100

Specimen POJ-PS-100 (a prototype cantilever bent with fully-prestressed overhang) was designed according to the AASHTO 1983 Design Provisions using the same considerations assumed by designers of the San Antonio 'Y'. Design calculations for Specimen POJ-PS-100 are presented in Section 3.3.2, and a complete report of the experimental results is presented in Section 4.2.2.

8.2.2.1 Reinforcement Details - POJ-PS-100

An elevation of the reinforcing details and overall dimensions for the POJ-PS-100 specimen are shown in Figure 8.10. Distribution of longitudinal reinforcement in the pier, and the overhang cross-section adjacent to the column face are shown in Figure 8.11 and Figure 8.12, respectively. Because bars used in the model have more than twice the straight bar development required by design specifications, hooks, welded plates, and other methods of positive anchorage were not provided. Overhang post-tensioning consisted of two rows of six - 1.6 cm (5/8 in.) diameter, 1034 MPa (150 ksi) Dywidag post-tensioning bars. Top and bottom rows of post-tensioning were located 7.6 cm (3 in.) and 15.2 cm (6 in.) from the top surface of the overhang, respectively.

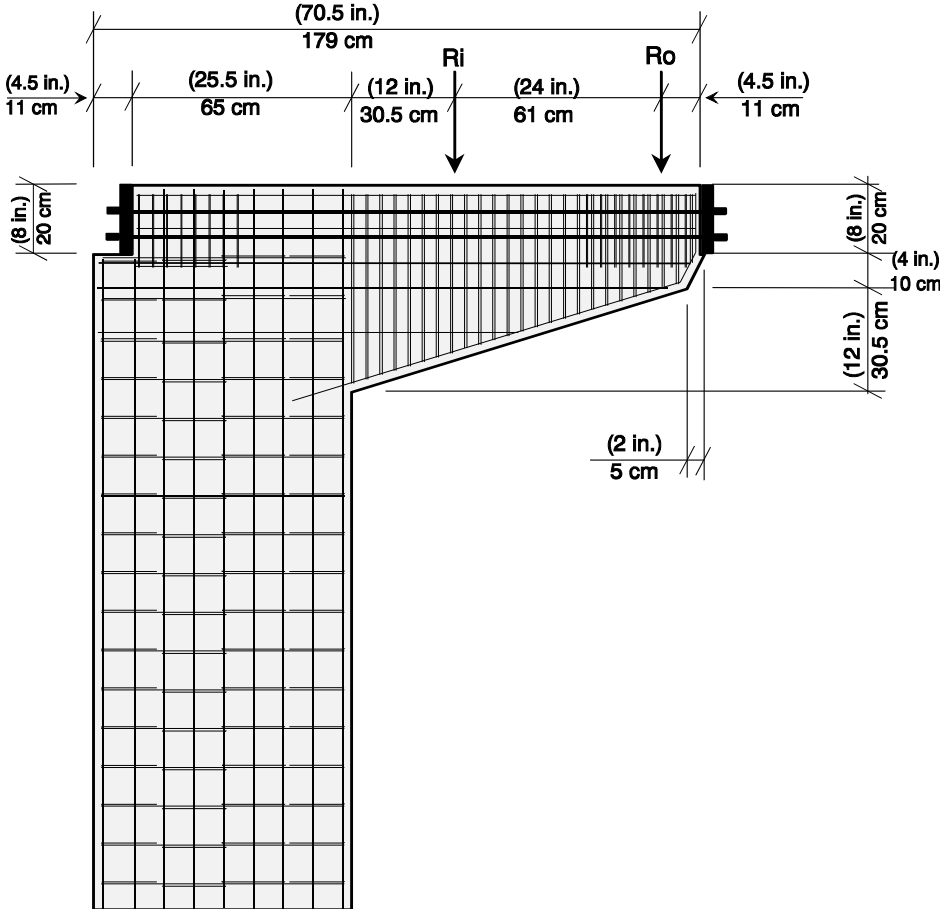


Figure 8.10 Elevation of Reinforcement for POJ-PS-100

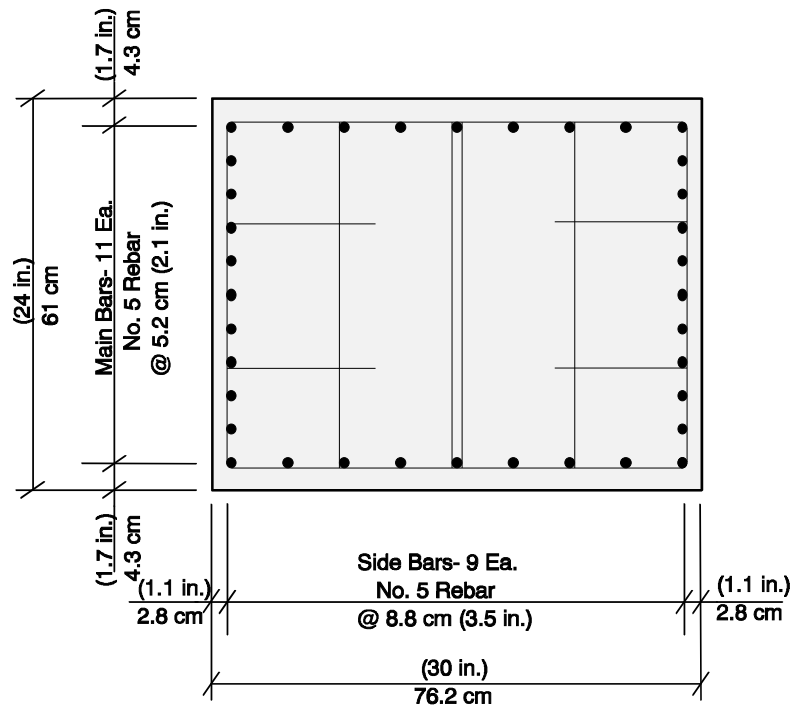


Figure 8.11 POJ-PS-100 Pier Reinforcement Details

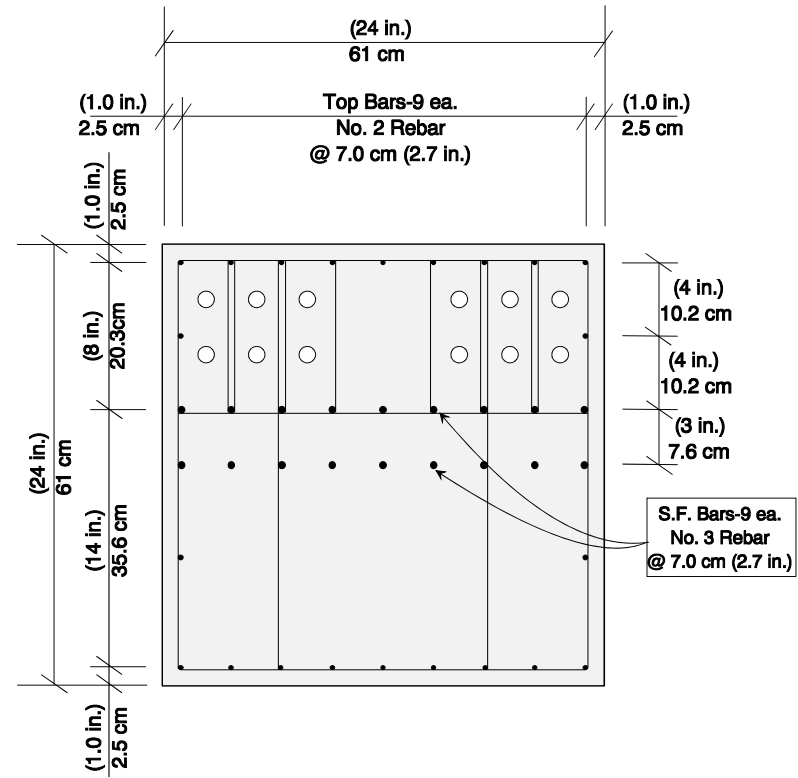


Figure 8.12 POJ-PS-100 Overhang Reinforcement Details

8.2.2.2 Finite Element Analysis -POJ-PS-100

An elastic finite element analysis of Specimen POJ-PS-100 was performed to determine the level of principal tensile stresses in the joint region at dead loads. Computed principal tensile stresses at applied dead loads are presented in the form of stress contours in Figure 8.13. The level of tensile stresses in the joint region were above $7\sqrt{f'_c}$ (psi) [3.4 MPa (500 psi)], indicating it was likely a diagonal joint crack would develop when dead loads were applied. Principal tensile vectors, shown in Figure 8.14, illustrate the flow of tensile stresses through the overhang and joint regions. Both figures reveal the discontinuity produced by the breakout for the bar anchorages (in the joint corner), resulting in a localized region of high principal tensile stresses.

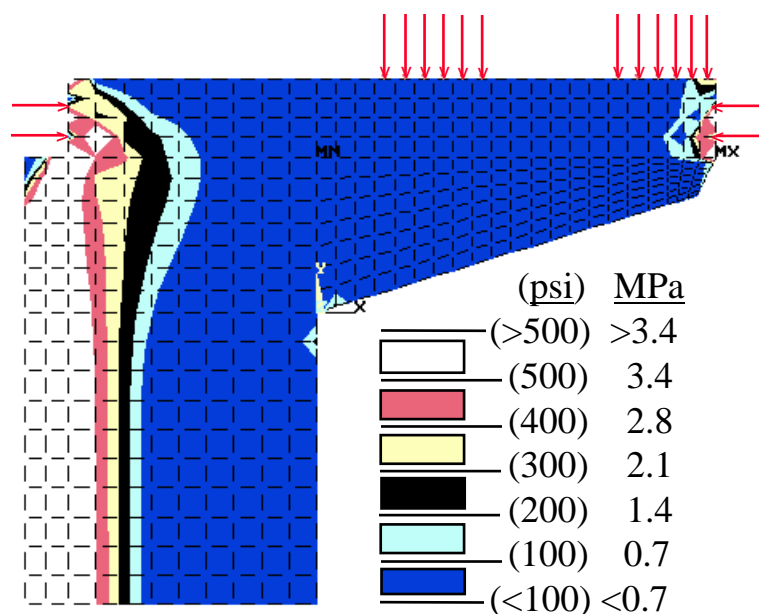


Figure 8.13 POJ-PS-100 Principal Tensile Stresses at Dead Load

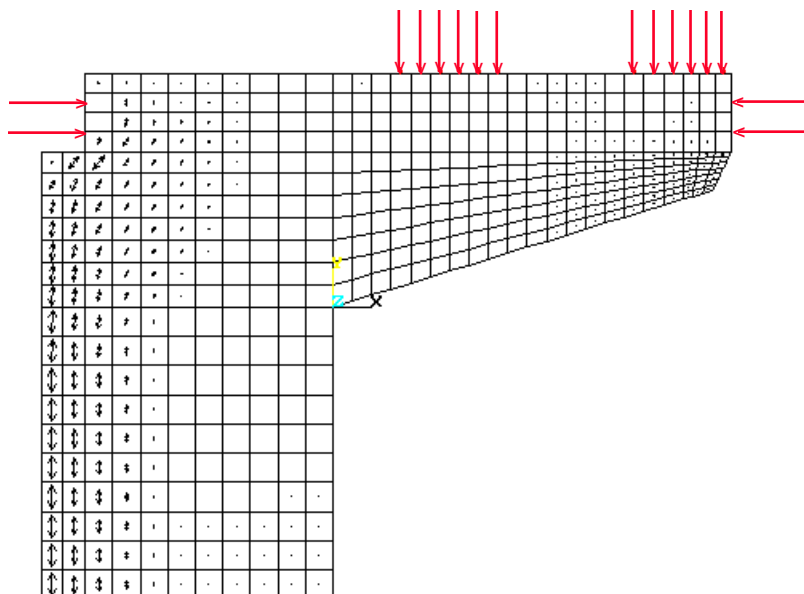


Figure 8.14 POJ-PS-100 Principal Tensile Stress Vectors

8.2.2.3 *Strut-and-Tie Model - POJ-PS-100*

The strut-and-tie model for Specimen POJ-PS-100, shown in Figure 8.15, is intended to represent the flow of forces produced after applied loads (R_i and R_o) induced a crack in the joint. It is clear from Figure 8.15, that the maximum applied loads (R_i and R_o) are limited by the maximum tensile forces (T_h and T_v), defined by the anchorage capacity of the longitudinal overhang and pier reinforcing bars, respectively. After determining the maximum tensile forces (T_h and T_v), utilizing the ACI-318 (1963) basic development length equation [28] and a uniform-bond stress model, it was possible to compute the applied loads (R_i and R_o) that resulted in failure. Specimen capacity calculations are presented in Section 8.2.2.4.

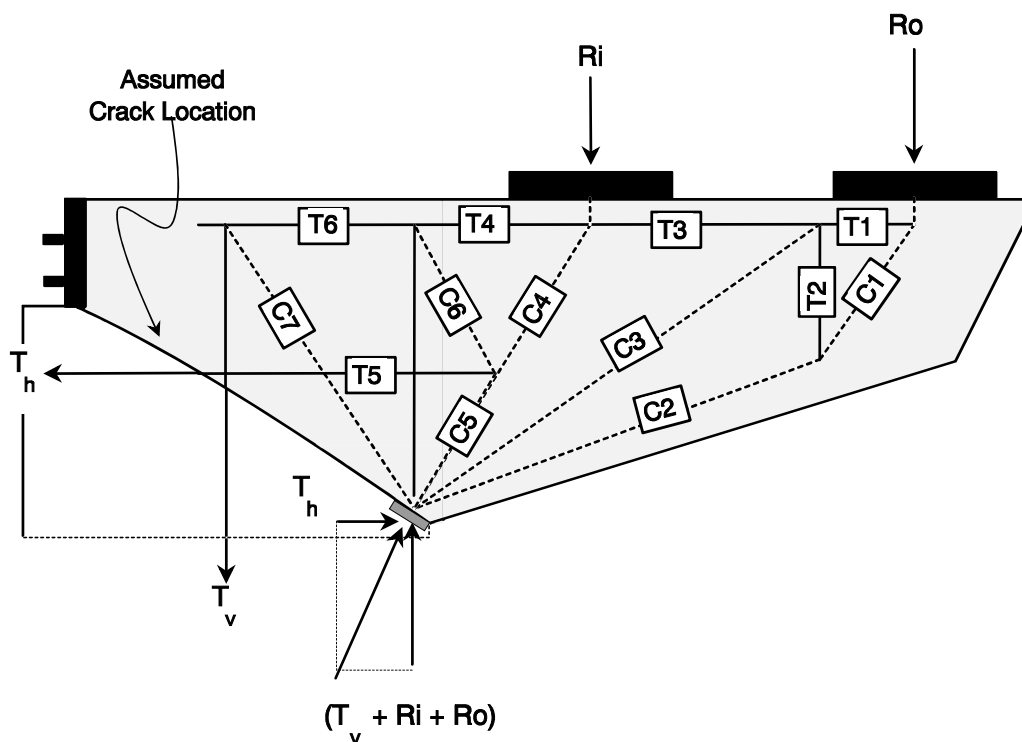


Figure 8.15 POJ-PS-100 Strut-and-Tie Model

8.2.2.4 Cantilever Bent Strength Computation - POJ-PS-100

A portion of the free body used to compute specimen capacity is shown in Figure 8.16. Capacities of bars crossing the diagonal crack in the joint were determined as outlined previously after determining the development length, l_d , and the embedment length, L , of each bar. Computed bar forces and moment arms are detailed in Figure 8.16.

Computed maximum applied loads, R_i and R_o , were determined to be 316 kN (71.1 kips) and 338 kN (75.9 kips), respectively. These loads are equivalent to $DL+0.45LL$ and are 60 percent of applied factored loads. A simple free-body diagram for the capacity calculation, presented in Figure 8.17, illustrates the balance of forces.

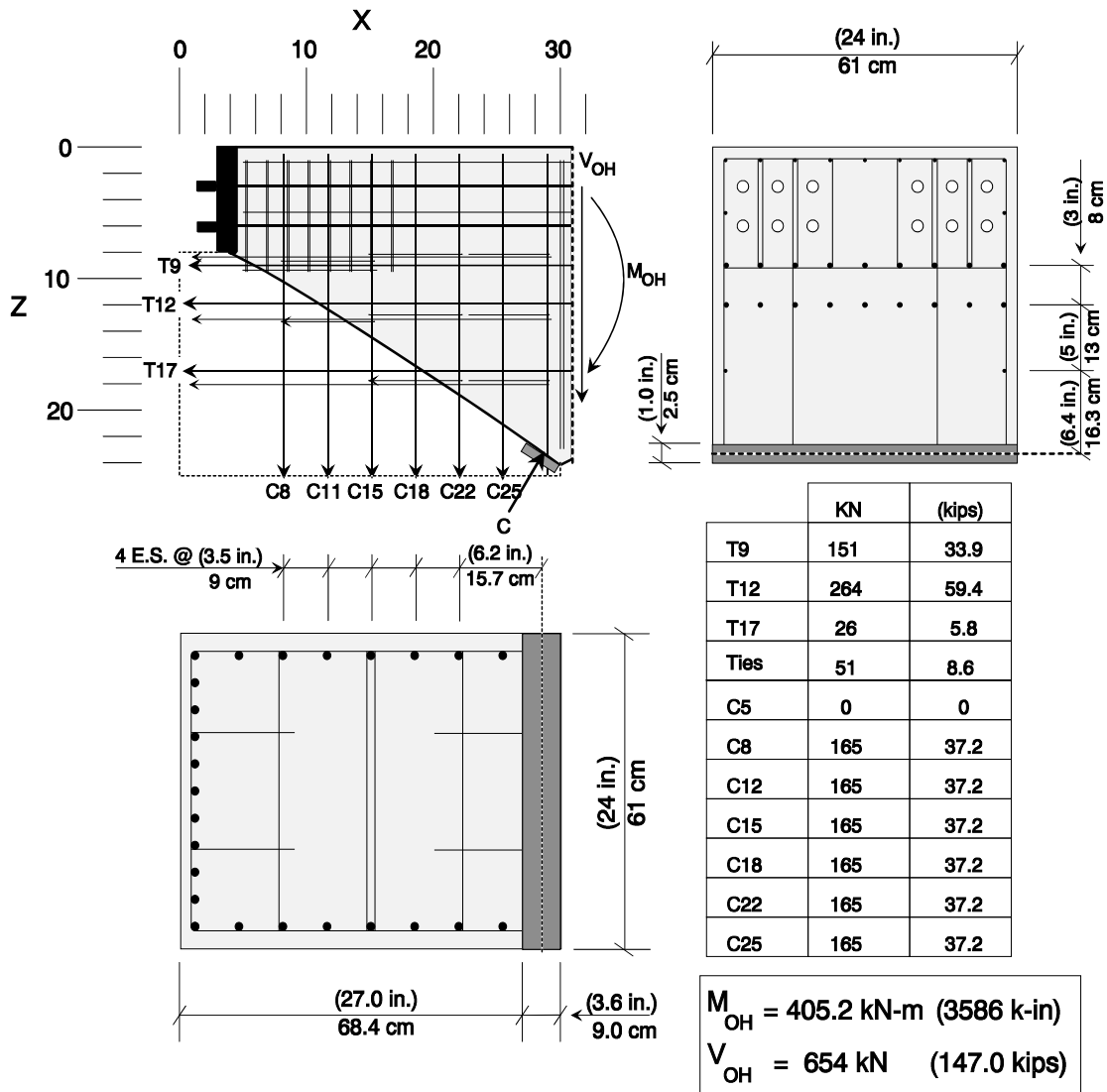
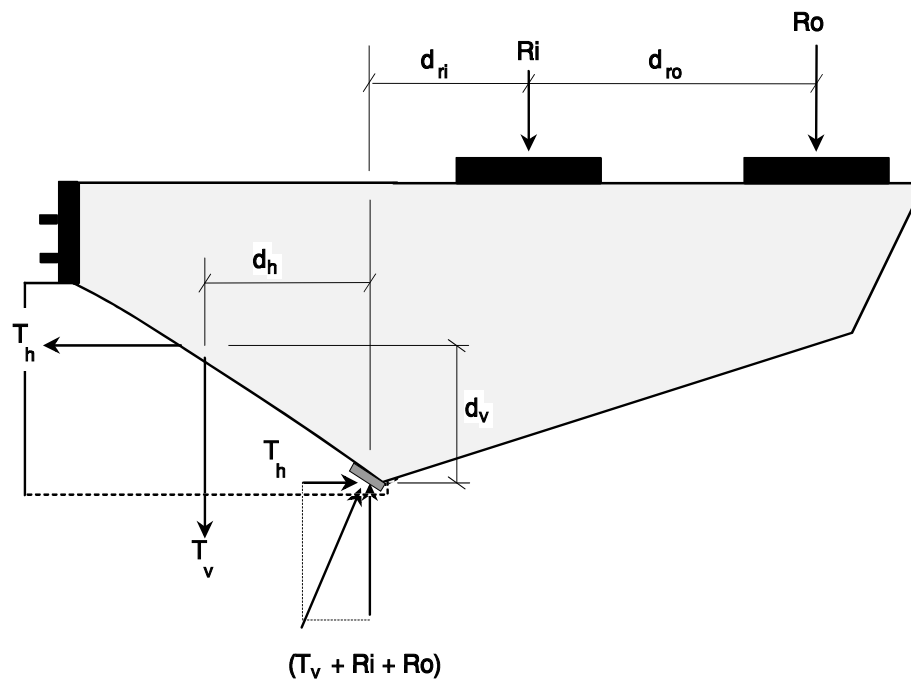


Figure 8.16 POJ-PS-100 - Free Body and Reinforcement Locations Used in Strength Model



Joint Resistance = Applied Moment

$$T_h(d_v) + T_v(d_h) = R_i(d_{ri}) + R_o(d_{ri} + d_{ro})$$

$$(107.7 \text{ kips})(12.0 \text{ in.}) + (223.2 \text{ kips})(11.5 \text{ in.}) = (71.1 \text{ kips})(13.8 \text{ in.}) + (75.9 \text{ kips})(37.8 \text{ in.})$$

$$479 \text{ kN} (30.5 \text{ cm}) + 993 \text{ kN} (29.2 \text{ cm}) = 316 \text{ kN} (35 \text{ cm}) + 338 \text{ kN} (96 \text{ cm})$$

Figure 8.17 Free Body Used to Compute Strength of Specimen POJ-PS-100

8.2.2.5 Applied Overhang Moment vs. Tip Deflection - POJ-PS-100

Measured applied moment vs. tip deflection behavior for Specimen POJ-PS-100 is presented in Figure 8.18. Load was applied to the specimen incrementally according to the sequence presented in Table 8.1. During testing, a diagonal crack was observed in the joint region of the specimen at an applied load equal to one-half dead load. Under applied dead load, large diagonal cracks were observed in the joint. The specimen did not sustain applied dead load, and at this point applied load was reduced to preserve the specimen for the repair study.

After the repair study was completed, Specimen POJ-PS-100 was loaded to failure. Maximum applied loads were 58 percent of design factored loads. Additional tip

displacement resulted in increased joint-crack widths and a decrease in total applied load. Testing was discontinued once the tip of the specimen was displaced more than 60 mm (2.4 in). The specimen maintained applied loads equal to design dead load after extreme overhang displacements were imposed. Applied overhang moment vs. tip deflection for the specimen, shown in Figure 8.18, illustrates the closeness of the predicted failure load to the experimental value.

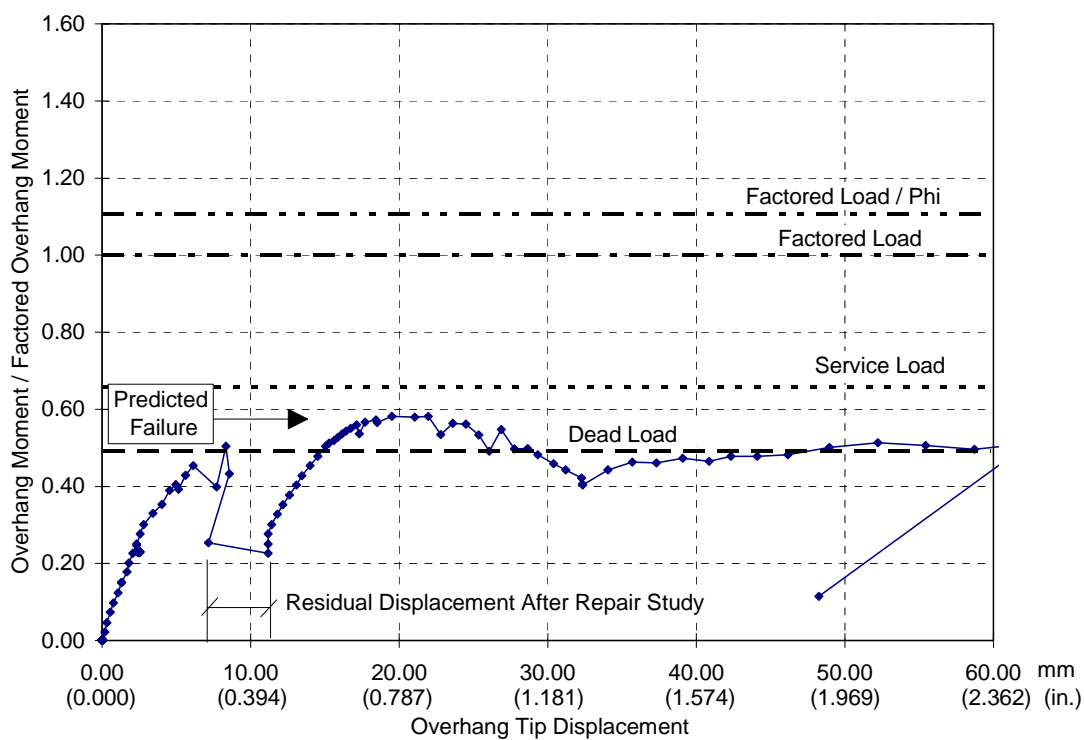


Figure 8.18 POJ-PS-100 - Applied Overhang Moment vs. Tip Deflection

8.3 Augmenting the Tensile Force Path in the Joint

It is clear from the analyses performed in Sections 8.2.1.4 and 8.2.2.4 that the reduced capacity of the reinforced concrete and fully-prestressed concrete prototypes was caused by inadequate anchorage of the overhang and pier longitudinal reinforcement. Augmenting the existing tensile force path through the joint by introducing an alternate tensile force path that crossed the diagonal joint crack was considered the most direct approach to rehabilitating the bents. Supplemental tensile reinforcement in the joint region was intended to increase the capacity of the bent above design factored loads / ϕ (where ϕ is 0.9). Tensile force in the overhang tension tie (Tie T6 shown in Figure 8.6 and Figure 8.15) could be transferred across the joint crack via either a prestressed or non-prestressed tension tie.

A non-prestressed tension tie, such as bonded external plates, was considered but rejected because large deformations in the joint would be required to develop the supplemental tensile forces. The resulting deformations could cause significant damage to the superstructure and substructure.

A prestressed tension tie, such as prestressing strands or bars located internally or externally, was preferred because post-tensioning forces reduce tensile stresses in the joint region, and ensure external hardware bears fully against the specimen (eliminating slack and gaps that result during fabrication and installation of the repair hardware). During an extreme loading event (where the joint crack re-opens), elastic straining of the post-tensioning provides an additional restorative force. For these reasons, only prestressed external or internal repairs were investigated in this experimental program.

The required post-tensioning force was computed by balancing the joint moment resulting from applied factored loads/ ϕ with the resisting moment provided by the combination of the supplementary post-tensioning and the residual moment capacity of the joint-overhang assembly (see Figure 8.17).

Repairs utilizing grouted internal post-tensioning bars were assumed to achieve guaranteed ultimate tensile strength, f_{pu} [1.03 GPa (150 ksi)], at failure loads. External post-

tensioning bars were assumed to achieve a stress of $0.75 f_{pu}$ [0.775 GPa (112.5 ksi)] at failure because large elongations were required to fail the post-tensioning bars. Minimum free lengths of post-tensioned bars were used so that a seating loss of 0.2 mm (0.01 in.) would result in no more than 10 percent loss [62 MPa (9 ksi)] of initial post-tensioning stress ($0.6 f_{pu}$) [620 MPa (90 ksi)]. Lengths of external post-tensioned bars were also limited to twice the minimum post-tensioned bar length to ensure bars achieved yield stress at inception of joint failure.

Two retrofit designs utilizing external post-tensioning and one design utilizing internal post-tensioning were developed and tested. The designs and test results are described in the following sections.

8.1 Introduction	321
8.2 Evaluation of Cantilever Bent Capacity - POJ-RC-100-2 and POJ-PS-100	322
8.2.1 Reinforced Concrete Specimen - POJ-RC-100-2.....	322
8.2.1.1 Reinforcing Details - POJ-RC-100-2.....	323
8.2.1.2 Finite Element Analysis - POJ-RC-100-2.....	325
8.2.1.3 Strut-and-Tie Model - POJ-RC-100-2	326
8.2.1.4 Cantilever Bent Strength Computation - POJ-RC-100-2.....	327
8.2.1.5 Overhang Moment vs. Tip-Deflection Behavior - POJ-RC-100-2	329
8.2.2 Specimen with Fully-Prestressed Overhang - POJ-PS-100	331
8.2.2.1 Reinforcement Details - POJ-PS-100	331
8.2.2.2 Finite Element Analysis -POJ-PS-100.....	334
8.2.2.3 Strut-and-Tie Model - POJ-PS-100	335
8.2.2.4 Cantilever Bent Strength Computation - POJ-PS-100.....	336
8.2.2.5 Applied Overhang Moment vs. Tip Deflection - POJ-PS-100	338
8.3 Augmenting the Tensile Force Path in the Joint.....	340
Figure 8.1 Elevation of Reinforcement for Specimen POJ-RC-100-2	323
Figure 8.2 POJ-RC-100-2 Pier Reinforcement Details.....	324
Figure 8.3 POJ-RC-100-2 Overhang Reinforcement Details	324
Figure 8.4 POJ-RC-100-2 Principal Tensile Stresses at Service Load	325
Figure 8.5 POJ-RC-100-2 Principal Tensile Stress Vectors at Service Load	326
Figure 8.6 POJ-RC-100-2 Strut-and-Tie Model	327
Figure 8.7 POJ-RC-100-2 Free Body and Reinforcement Locations Used in Strength Model.....	328
Figure 8.8 Free Body Used to Compute Specimen POJ-RC-100-2 Capacity.....	329
Figure 8.9 POJ-RC-100-2 Applied Overhang Moment vs. Tip-Deflection.....	330
Figure 8.10 Elevation of Reinforcement for POJ-PS-100	332
Figure 8.11 POJ-PS-100 Pier Reinforcement Details.....	333

Figure 8.12 POJ-PS-100 Overhang Reinforcement Details.....	333
Figure 8.13 POJ-PS-100 Principal Tensile Stresses at Dead Load.....	334
Figure 8.14 POJ-PS-100 Principal Tensile Stress Vectors	335
Figure 8.15 POJ-PS-100 Strut-and-Tie Model	336
Figure 8.16 POJ-PS-100 - Free Body and Reinforcement Locations Used in Strength Model.....	337
Figure 8.17 Free Body Used to Compute Strength of Specimen POJ-PS-100	338
Figure 8.18 POJ-PS-100 - Applied Overhang Moment vs. Tip Deflection	339
Table 8.1 Substructure Design Loads for 1/2.75 Scale Models.....	322

8.6 Analysis and Behavior of Selected POJ-RC-100 Repairs

The prototype reinforced concrete specimen (POJ-RC-100-2) was strengthened first using a diagonal post-tensioned repair (POJ-RC-100-RP1), and then an internal vertical post-tensioned repair (POJ-RC-100-RP2). Each repaired specimen was proof-loaded to design factored loads/ ϕ to evaluate strength. Ultimate strength of the repaired specimens was not determined experimentally in order to perform multiple tests using the same prototype specimen. Analysis and design details, as well as plots of moment vs. deflection behavior and moment vs. post-tensioning strain are presented in the following sections. Additional details are presented by Scott [6].

8.6.1 Diagonal Post-Tensioned Repair (POJ-RC-100-RP1)

The diagonal post-tensioned repair provided a clamping force normal to the joint failure plane (54 degrees with respect to horizontal), acting a short distance from the edge of the specimen (see Figure 8.25). Post-tensioning bars were located externally because diagonally coring through the joint would likely damage many longitudinal overhang and pier mild-reinforcing bars. A large, effective moment arm (measured from the joint compression centroid to the line of action of the post-tensioning force) minimized the post-tensioning force required to resist design factored loads / ϕ .

Stiffened steel plates, located on the top surface and outer vertical surface of the specimen, distributed post-tensioning forces (acting normal to the surface) across the width of the joint. Anchor bolts resisted shear forces parallel to each surface produced by the post-tensioning force. Steel quantities required in fabrication of the built-up plates were minimized because a small post-tensioning force was used for this repair.

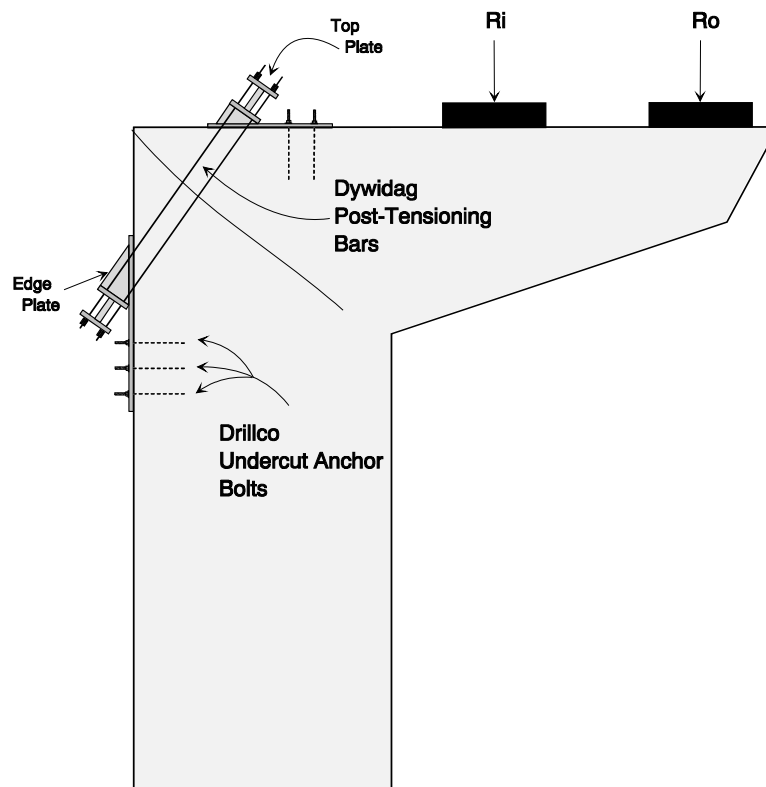


Figure 8.25 Elevation of External Diagonal Post-Tensioned Repair

8.6.1.1 Capacity Analysis (POJ-RC-100-RP1)

The repair was intended to provide sufficient strength to resist applied loads equal to design factored loads / ϕ and remain uncracked under applied service-level loads. In order to calculate the capacity of the repaired specimen, it was assumed that the external post-tensioning would achieve nominal yield stress ($0.75 f_{pu}$ [776 MPa (112.5 ksi)]) at inception of joint failure. A portion of the free body used to compute the specimen capacity is shown in Figure 8.26. Capacities of bars crossing the diagonal crack in the joint, and respective moment arms are detailed in Figure 8.26. Vertical and horizontal force components and moments calculated about the joint compression centroid are shown in Figure 8.27. Computed maximum applied loads, R_i and R_o , were 519 kN (116.7 kips) and 649 kN (146.0 kips). These loads are equivalent to DL + 3.5LL and are slightly less than factored loads / ϕ (1.06 times applied factored loads). Forty-eight percent of the total bent capacity was provided by the diagonal post-tensioning.

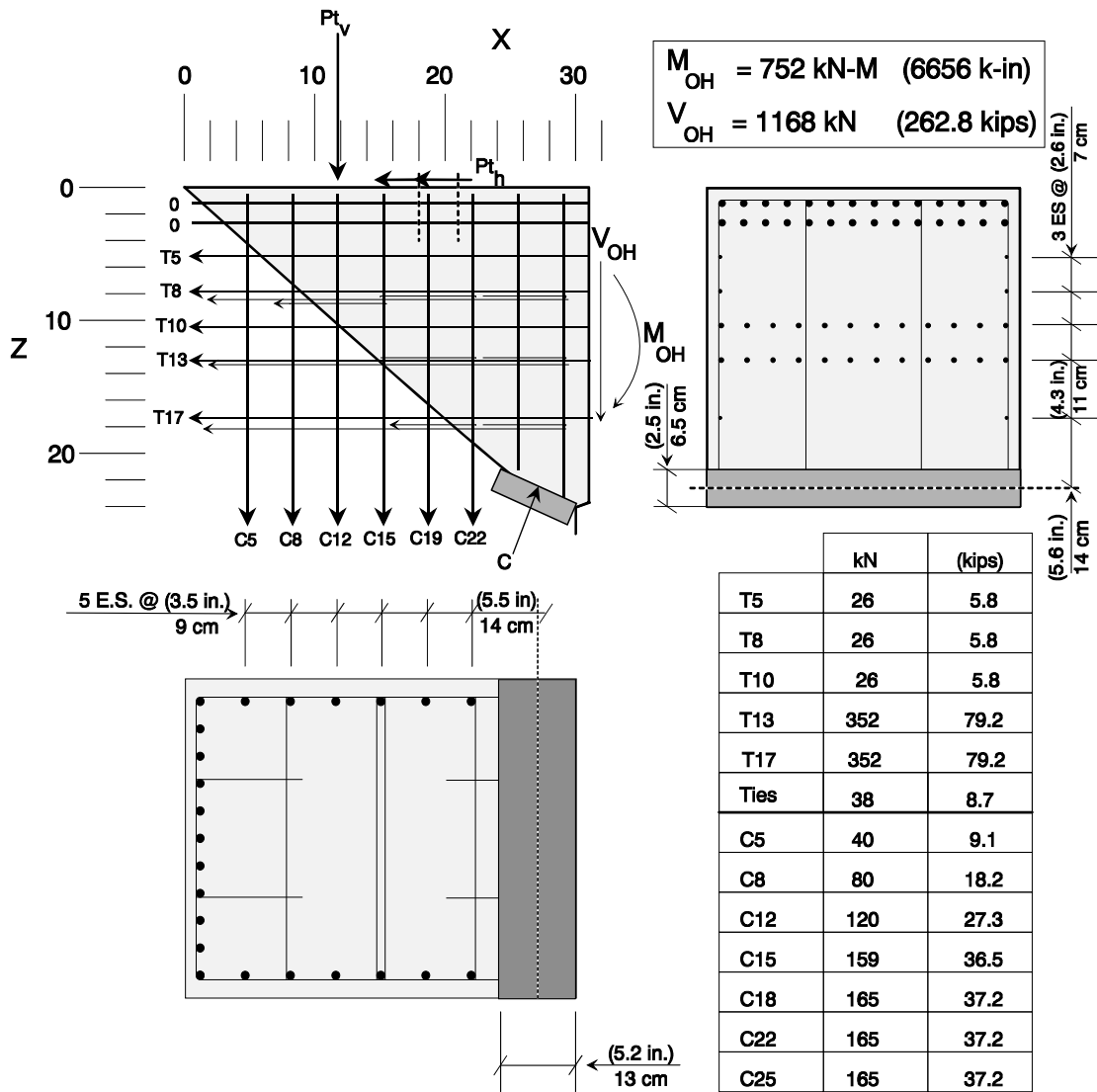
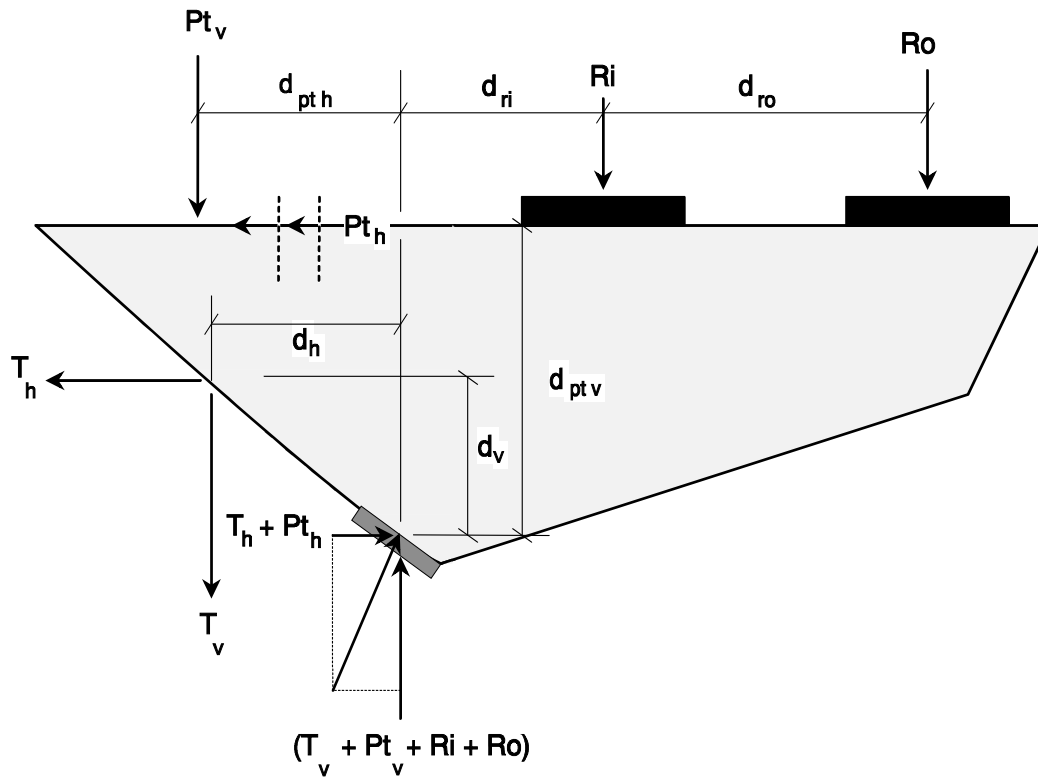


Figure 8.26 POJ-RC-100-RP1 Free Body and Reinforcement Locations Used in Strength Model



Joint Resistance = Applied Moment

$$T_h(d_v) + T_v(d_h) + Pt_v(d_h) + Pt_h(d_v) = Ri(d_{ri}) + Ro(d_{ro})$$

$$(184.3 \text{ kips})(11.3 \text{ in}) + (165.5 \text{ kips})(12 \text{ in}) + (102 \text{ kips})(15.7 \text{ in}) + (74 \text{ kips})(22.7 \text{ in}) = (116.7 \text{ k})(14.6 \text{ in}) + (146 \text{ k})(38.6 \text{ in.})$$

$$820 \text{ kN}(28.7 \text{ cm}) + 736 \text{ kN}(30.5 \text{ cm}) + 454 \text{ kN}(40 \text{ cm}) + 329 \text{ kN}(58 \text{ cm}) = 519 \text{ kN}(37 \text{ cm}) + 649 \text{ kN}(98 \text{ cm})$$

Figure 8.27 Free Body Used to Determine Post-Tensioning Force for Specimen POJ-RC-100-RP1

8.6.1.2 Finite Element Analysis (POJ-RC-100-RP1)

As stated earlier, the externally post-tensioned bent was intended to remain uncracked under applied service-level loads. Principal tensile stresses under service loads were computed using finite element analysis. Stresses across the joint diagonal were maintained below $7\sqrt{f'_c}$ [6.9 MPa (500 psi)] (the assumed concrete tensile strength) to prevent the critical diagonal crack from developing in the joint. Horizontal and vertical components of the applied post-tensioning force [448 kN (100.8 kips)] were modeled as applied concentrated loads. Forces acting normal to the surface of the specimen were applied at the point of intersection between the force vector and the surface. Shearing forces were applied at the element nodes corresponding to anchor bolt positions and were distributed equally among the nodes.

Principal tensile stresses are plotted as contours and vectors for applied service loads in Figure 8.28, and principal compressive stress contours and vectors are shown in Figure 8.29. Principal tensile and compressive stresses in the joint are presented as stress contour plots and vector plots in Figure 8.30 and Figure 8.31, respectively. Principal compressive stress contours in Figure 8.31 are presented over a smaller range of compressive stresses than depicted in Figure 8.29.

Principal tensile stresses in the joint region (specifically across the path of the diagonal joint crack) were slightly greater than $4.2\sqrt{f'_c}$ [2.1 MPa (300 psi)] at applied service load. This indicated that the critical diagonal joint crack would not develop under applied service loads if the main diagonal joint crack was epoxy injected. Cracks were not epoxy injected for the experimental study because strength of the post-tensioned repairs could not be evaluated if the diagonal joint crack remained closed at factored load / phi.

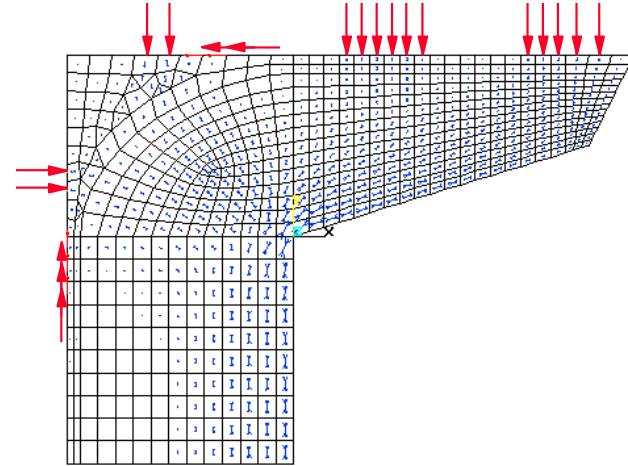
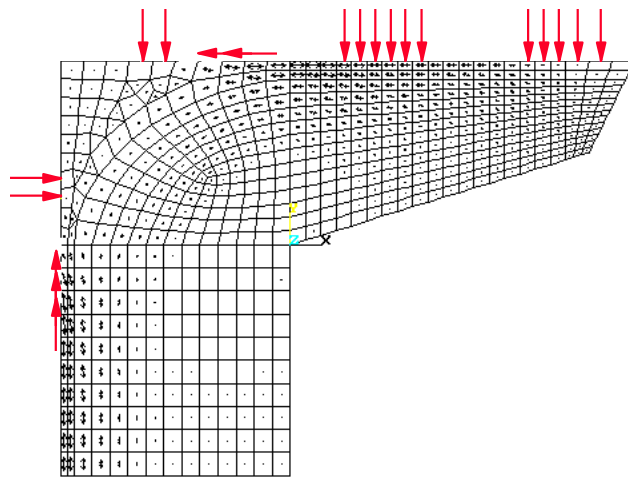
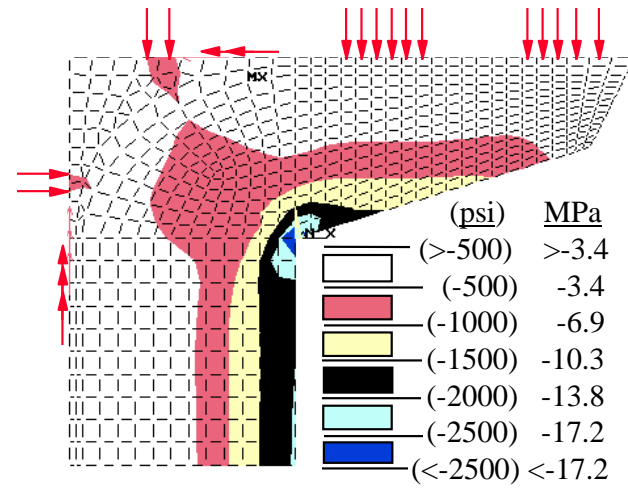
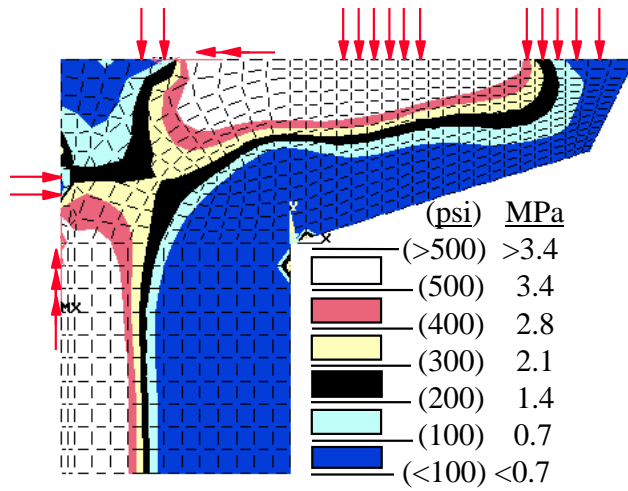


Figure 8.28 POJ-RC-100-RP1 Overall Principal Tensile Stresses at Service Load

Figure 8.29 POJ-RC-100-RP1 Overall Principal Compressive Stresses at Service Load

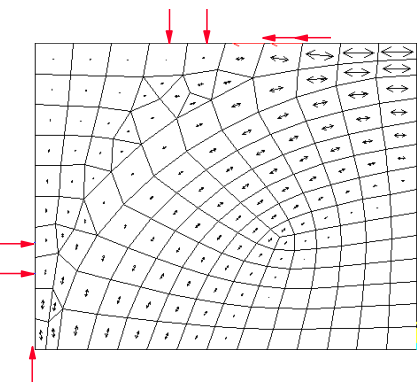
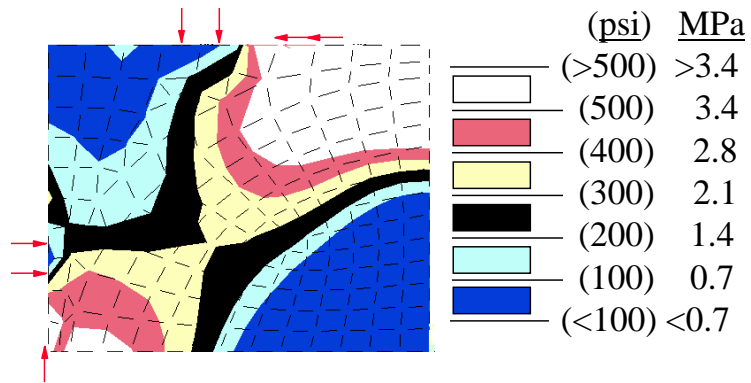


Figure 8.30 POJ-RC-100-RP1 Joint Principal Tensile Stresses and Vectors at Service Load

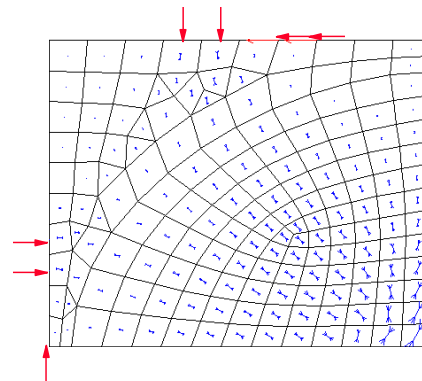
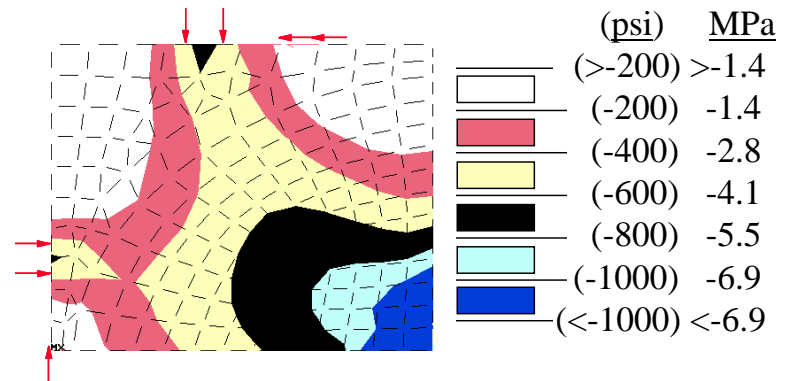


Figure 8.31 POJ-RC-100-RP1 Joint Principal Compressive Stresses and Vectors at Service Load

8.6.1.3 Design and Installation Details (POJ-RC-100-RP1)

Design details for the diagonal externally post-tensioned repair (POJ-RC-100-RP1) are presented in Figure 8.32 through Figure 8.36. The repair was designed to rehabilitate the 1/2.75 scale prototype reinforced concrete substructure model (POJ-RC-100-2). As shown in Figure 8.32, the first row of anchor bolts for the top plate was located 46 cm (18 in.) away from the joint corner, and the first row of anchor bolts for the vertical edge plate was located 64 cm (25 in.) from the joint corner, which was equivalent to 1.9 and 2.1 times the basic bar development length for the overhang and pier longitudinal reinforcement, respectively.

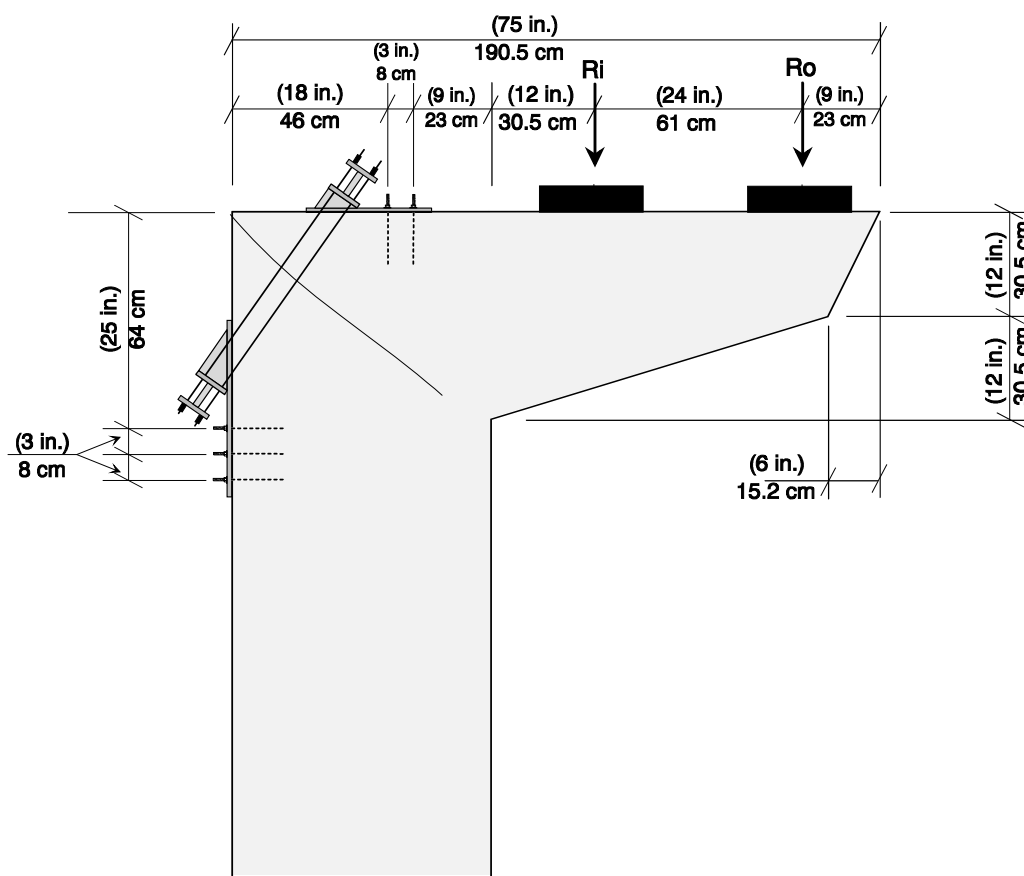


Figure 8.32 POJ-RC-100-RP1 Overall Dimensions - Elevation

Post-tensioning was designed to act at a 54-degree angle with respect to the horizontal. The top plate was anchored to the top surface of the joint with six- 1.3 cm (1/2 in.) diameter Drillco undercut anchors with a 15 cm (6 in.) concrete embedment. The edge plate (located on the outside vertical face of the pier) was attached using eight - 1.3 cm (1/2 in.) diameter Drillco undercut anchors.

The minimum number of anchor bolts required was determined by computing the total connection shear with the post-tensioning at an ultimate stress of 1.0 GPa (150 ksi).

$$V_u \leq \Phi V_n = \Phi V_f + \Phi V_s$$

where:

V_u	=	Shear Force at Ultimate Loads
Φ	=	Phi Factor = 0.65
V_n	=	Nominal Shear Resistance
V_f	=	Friction Force = $0.4 \times$ (Normal Force)
V_s	=	Anchor Ultimate Shear Capacity = 82.3 kN (18.5 kips)/ Anchor

The outer sleeve and threaded portions of the anchor bolts were designed to bear against the 1.3 cm (1/2 in.) thick steel plate, thus providing maximum shear resistance using a minimum number of anchors. Based on four shear tests performed on the 13 mm (1/2 in.) diameter Drillco undercut anchors, once the initial slip occurred, the load-displacement relationship for the anchor bolts was linear to a load of 53 kN (12 kips). All anchors tested failed by shearing through both the high strength steel sleeve (nominal ultimate stress of 590 MPa (80 ksi)) and threaded shaft (nominal ultimate steel stress of 860 MPa (125 ksi)). Average ultimate capacity of the anchor bolts tested was 82.3 kN (18.5 kips).

Holes were drilled into the top surface and outside vertical face of the specimen at points located between the longitudinal reinforcing bars. Because drilling was performed using a carbide drill bit (not a coring bit), reinforcing bars were not cut during the drilling process. After each hole was drilled and vacuumed, the bottom of the hole was flared using an undercutting tool. Flaring the base of the hole allowed the expansive portion of the undercut anchors to bear against the sides of the hole, improving the pull-out resistance of the anchor in cracked concrete. The undercutting tool was set at the specified concrete embedment depth of 15 cm (6 in.) to ensure the 16.5 cm (6.5 in.) sleeve length of the anchor extended 1.3 cm (0.5 in.) outside the specimen. Undercut anchors were installed and

expanded in the hole using a hand bolt setter. A 1.3 cm (0.5 in.) thick steel plate was placed between the bolt setter and surface of the specimen to ensure the sleeve did not retract into the hole as the anchor bolt expanded.

Due to the tight spacing of overhang longitudinal reinforcing bars, regular hole spacing on the top surface of the specimen was not possible. After the anchors were installed, a template of the anchor locations was created to transfer hole locations to the steel plates.

The 2.1 cm (0.81 in.) diameter of the holes in the top and edge steel plates (shown in Figure 8.35 and Figure 8.36, respectively) were 0.2 mm (1/16 in.) larger than the 1.9 cm (0.75 in.) diameter of the outer sleeve of the anchor bolt. Close tolerances between the outside diameter of the anchor bolt and hole minimized slippage and modeled the close tolerances that could be achieved at full scale.

Welds in the built-up steel plates had a minimum throat thickness of 0.6 cm (1/4 in.). Hydrostone was placed between each plate and the surface of the specimen to assure a uniform bearing pressure between the heat-affected surface of the welded plates and the uneven surface of the specimen. Each anchor bolt was torqued to 81 N-m (60 ft-lbs.) before hydrostone was pooled under the built-up steel plate.

Once both plates were bolted to the specimen, two- 16 mm (5/8 in.) diameter, 1.0 GPa (150 ksi) Dywidag bars were installed on each side of the specimen, and each bar was stressed to $0.6 F_{pu}$ [112 kN (25.2 kips)]. Two -267 kN (60 kip) rams were utilized to stress each pair of bars. Steel stressing chairs were placed between the welded I-beams on the stiffened plates and the rams to provide a gap to adjust the anchor nuts on the post-tensioning bars. Two rams were alternated between the diagonal pairs of bars until an average stress of $0.60 f_{pu}$ [620 MPa (90 ksi)] was achieved. Strain gages on the post-tensioning bars were monitored and lift-off tests were performed to verify the final stress level.

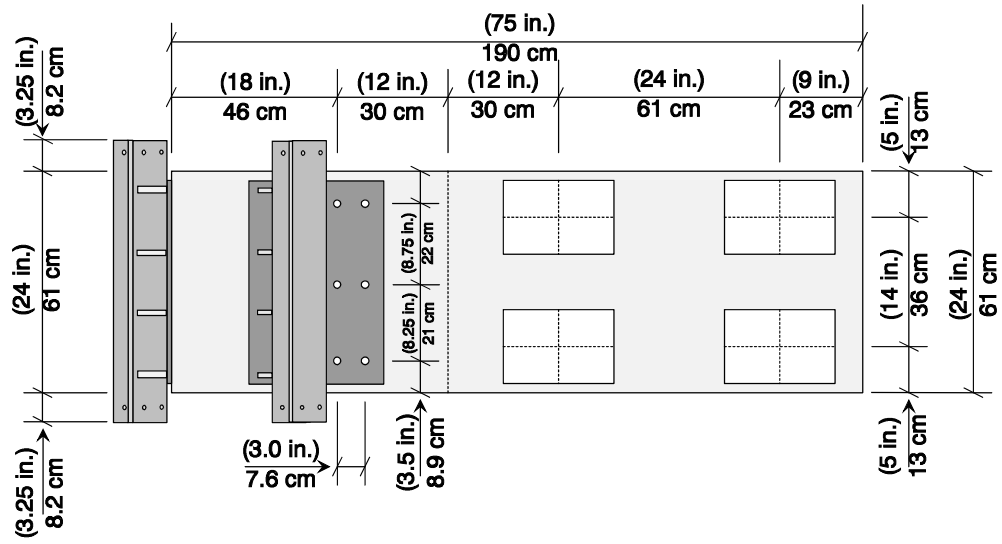


Figure 8.33 POJ-RC-100-RP1 Dimensions - Top View

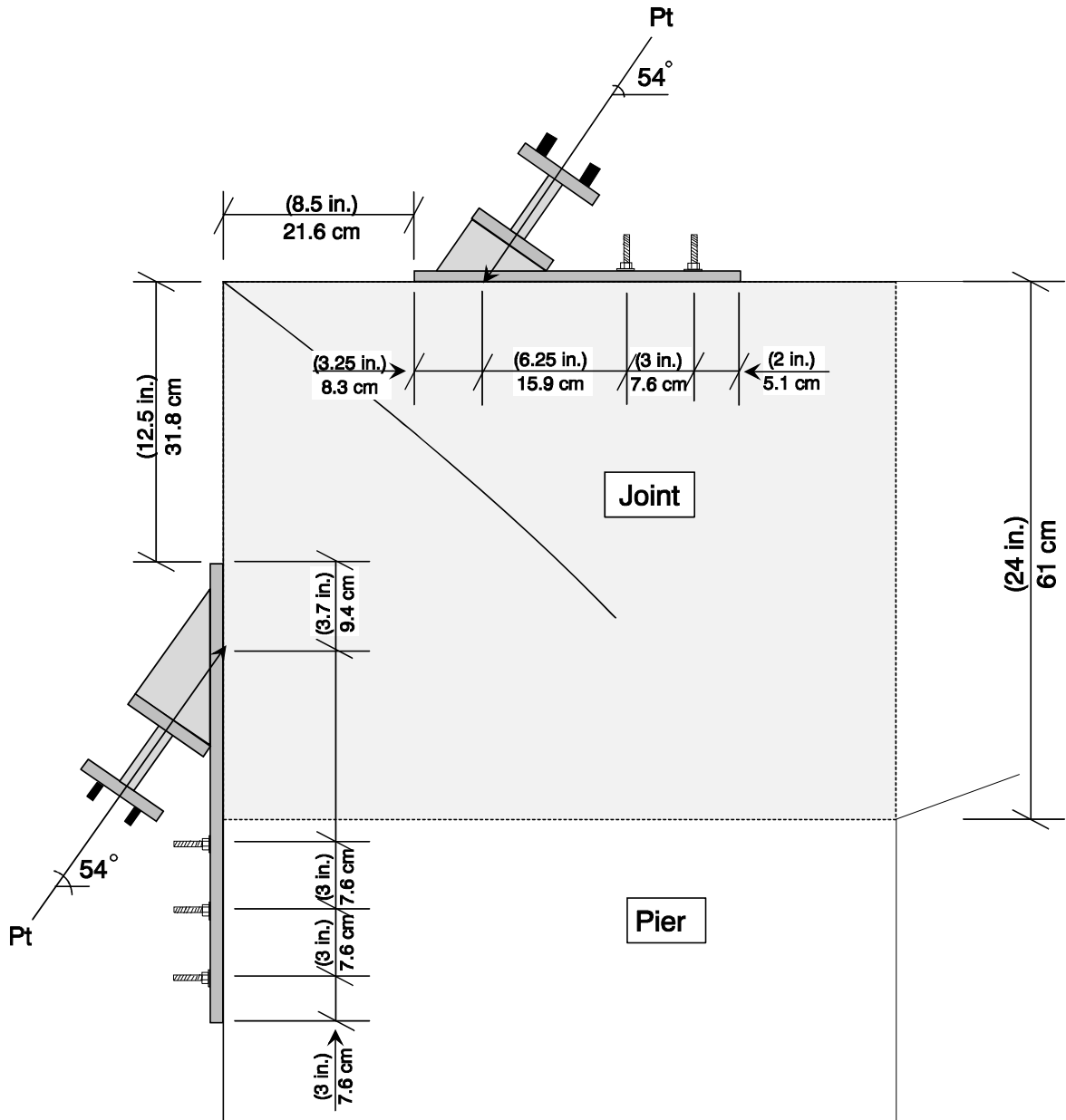


Figure 8.34 POJ-RC-100-RP1 Joint Details

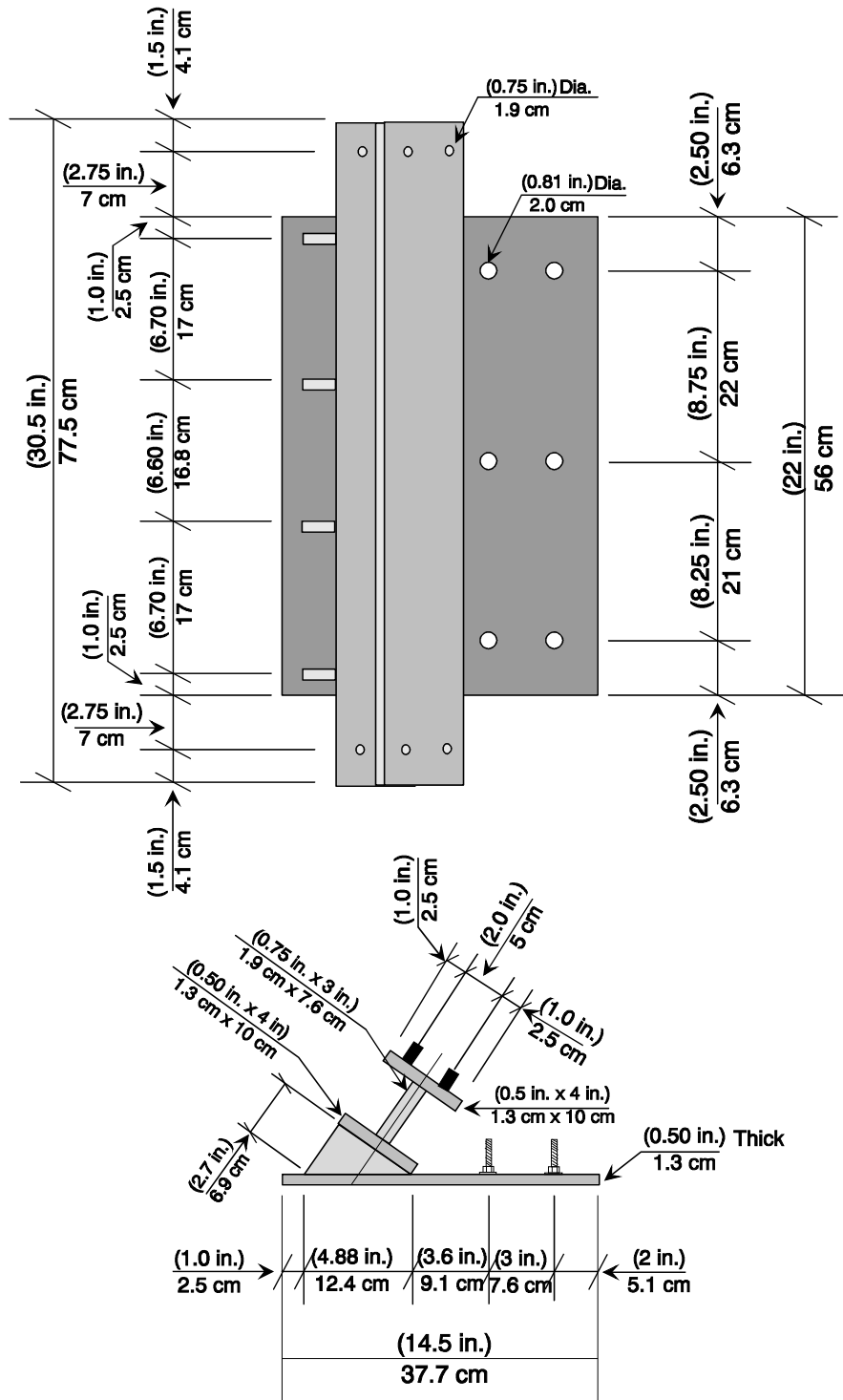


Figure 8.35 POJ-RC-100-RP1 Top Plate Dimensions

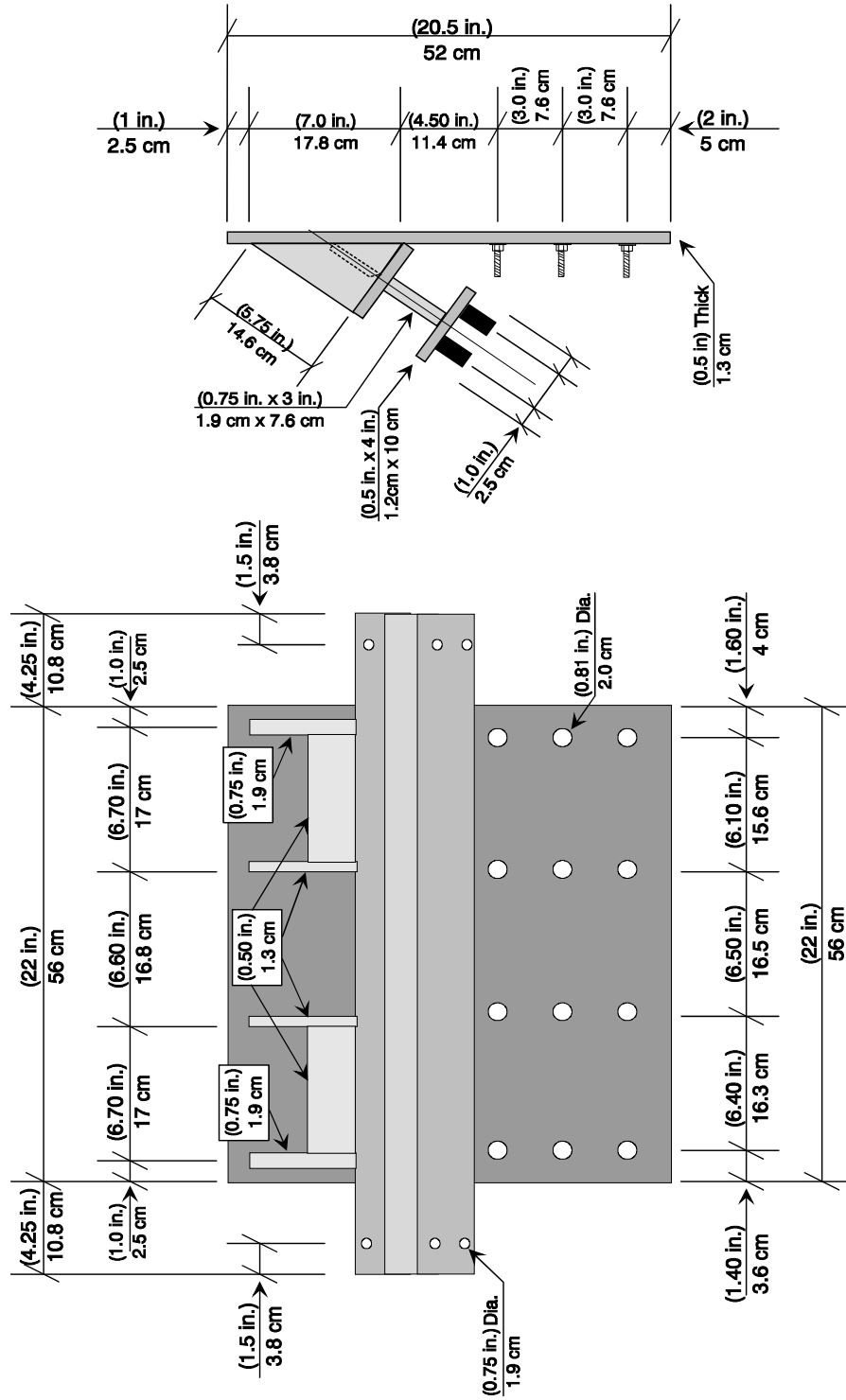


Figure 8.36 POJ-RC-100-RP1 Edge Plate Dimensions

8.6.1.4 Behavior During Testing (POJ-RC-100-RP1)

The unrepaired POJ-RC-100-2 specimen was loaded incrementally to one-half dead load. The repair was installed while one-half dead load remained applied to the two reaction points on the overhang (specimen now renamed POJ-RC-100-RP1). Post-tensioning bars were stressed to $0.6 f_{pu}$ before additional load was applied to the specimen, simulating an initial level of loading expected for a full-scale repair. A total of four - 16 mm (5/8 in.) diameter post-tensioning bars were stressed to 620 kPa (90 ksi) to complete the repair. After the bars were stressed, the specimen was loaded incrementally to dead load. Because the existing cracks were not epoxy injected before testing, cracks were marked and measured to evaluate crack control and crack growth. Crack widths were measured at applied dead load, DL + 1/2 LL, DL + LL, and DL + 2 LL. A detailed report of crack locations and crack-width measurements is presented by Scott [6].

During testing, two displacement transducers were located at the overhang tip to ensure accurate readings for the moment vs. overhang tip displacement response (shown in Figure 8.37). Post-tensioning strain (measured utilizing a portable strain indicator and the data acquisition system) began increasing after service level loads were applied (see Figure 8.38). The increase in post-tensioning strain was attributed to growth of the joint crack, which occurred early because the crack was not epoxy injected before testing. The recorded applied moment vs. overhang tip displacement response for Specimen POJ-RC-100-RP1 (shown in Figure 8.37) was nearly linear to an applied load equal to design factored flexure / ϕ , indicating the repair provided adequate additional capacity. Additional load was not applied beyond factored flexure / ϕ to preserve the specimen for later testing utilizing a second repair method.

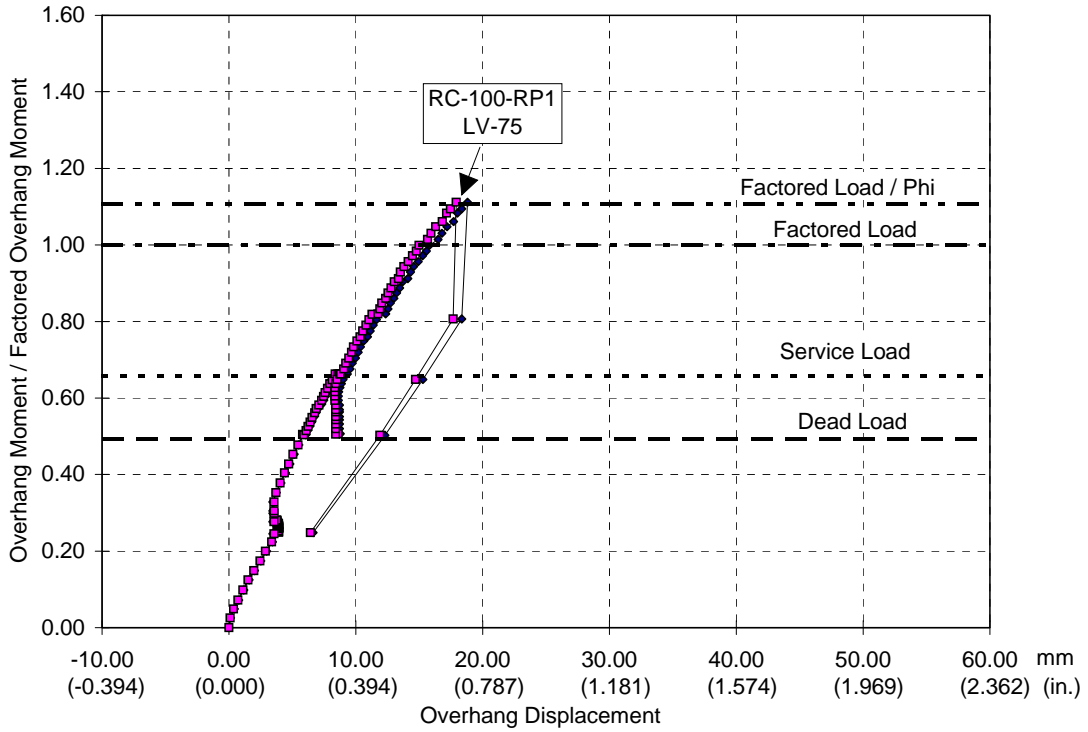


Figure 8.37 POJ-RC-100-RP1 Overhang Tip Displacement

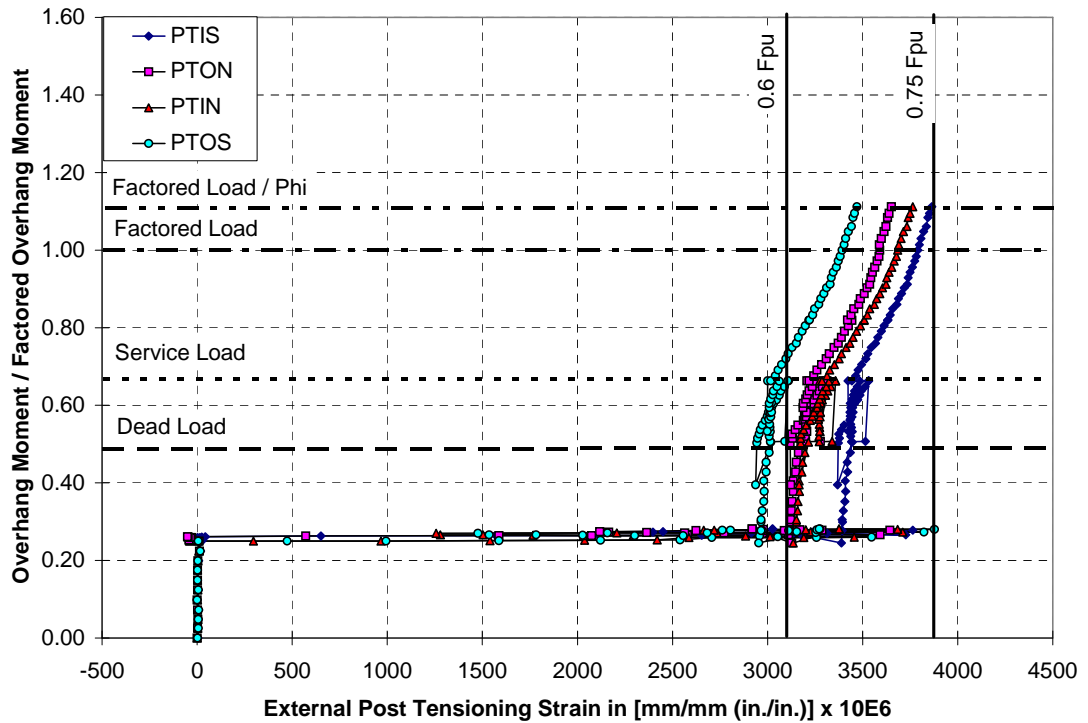


Figure 8.38 POJ-RC-100-RP1 External Post-Tensioning Bar Strains

8	350
8.6 Analysis and Behavior of Selected POJ-RC-100 Repairs	350
8.6.1 <i>Diagonal Post-Tensioned Repair (POJ-RC-100-RP1)</i>	350
8.6.1.1 Capacity Analysis (POJ-RC-100-RP1).....	351
8.6.1.2 Finite Element Analysis (POJ-RC-100-RP1)	354
8.6.1.3 Design and Installation Details (POJ-RC-100-RP1).....	357
8.6.1.4 Behavior During Testing (POJ-RC-100-RP1)	364
Figure 8.25 Elevation of External Diagonal Post-Tensioned Repair	351
Figure 8.26 POJ-RC-100-RP1 Free Body and Reinforcement Locations Used in Strength Model....	352
Figure 8.27 Free Body Used to Determine Post-Tensioning Force for Specimen POJ-RC-100-RP1	353
Figure 8.28 POJ-RC-100-RP1 Overall Principal Tensile Stresses at Service Load.....	355
Figure 8.29 POJ-RC-100-RP1 Overall Principal Compressive Stresses at Service Load.....	355
Figure 8.30 POJ-RC-100-RP1 Joint Principal Tensile Stresses and Vectors at Service Load.....	356
Figure 8.31 POJ-RC-100-RP1 Joint Principal Compressive Stresses and Vectors at Service Load...	356
Figure 8.32 POJ-RC-100-RP1 Overall Dimensions - Elevation	357
Figure 8.33 POJ-RC-100-RP1 Dimensions - Top View	360
Figure 8.34 POJ-RC-100-RP1 Joint Details	361
Figure 8.35 POJ-RC-100-RP1 Top Plate Dimensions	362
Figure 8.36 POJ-RC-100-RP1 Edge Plate Dimensions	363
Figure 8.37 POJ-RC-100-RP1 Overhang Tip Displacement	365
Figure 8.38 POJ-RC-100-RP1 External Post-Tensioning Bar Strains	365

8.4 External Post-Tensioned Repair Methods

External post-tensioned repairs were investigated because they could be applied in a variety of orientations and locations without coring into the joint region. Coring or sawing in the joint region was avoided because it could be quite costly and damage the joint reinforcement, resulting in reduced residual bent capacity.

Repairs were positioned away from the exterior corner of the joint (specifically more than 1.5 times the straight-bar development length) to prevent major cracks from forming outside the stressed zone, resulting in loss of bar anchorage and reduced capacity. An example of placing vertical post-tensioning too close to the joint corner is shown in Figure 8.19. In this scenario, it is likely a major crack will form to the right of the external post-tensioning. Development length of the longitudinal reinforcing bars is increased, but the post-tensioning no longer contributes to the joint capacity, resulting in reduced total capacity.

8.4.1 External Vertical Post-Tensioned Repair - Conceptual Design

External vertical post-tensioning, shown in Figure 8.19, was developed during a meeting with TxDOT design engineers. Vertical internal post-tensioning was used to repair San Antonio 'Y' substructure C11-C (a fully-prestressed overhang). It was believed, by the researchers, that locating the post-tensioning bars externally would reduce concrete coring costs and reduce construction time.

The vertical external post-tensioned repair incorporates a steel cap beam (a stiffened, steel member positioned across the top of the joint), post-tensioned bars located on each side of the bent, and two steel side plates attached near the base of the pier. The cap beam extends over the joint sides in order to attach the external post-tensioned bars and provide space for stressing the bars. Horizontal holes are cored through the pier a distance away from the joint region to install high-strength anchors through the pier. Stiffened side plates bolted against the pier (see Figure 8.20) transfer vertical post-tensioning forces into the pier. In essence, the assembly provides a substantial clamping force between the steel cap assembly and side plates, sufficient in combination with the residual bent capacity, to resist applied factored

loads / ϕ . A substantial vertical post-tensioning force is required to resist factored loads/ ϕ because the moment arm for the post-tensioning, about the compression centroid, is small compared to the moment arm for the applied forces, as shown in Figure 8.19.

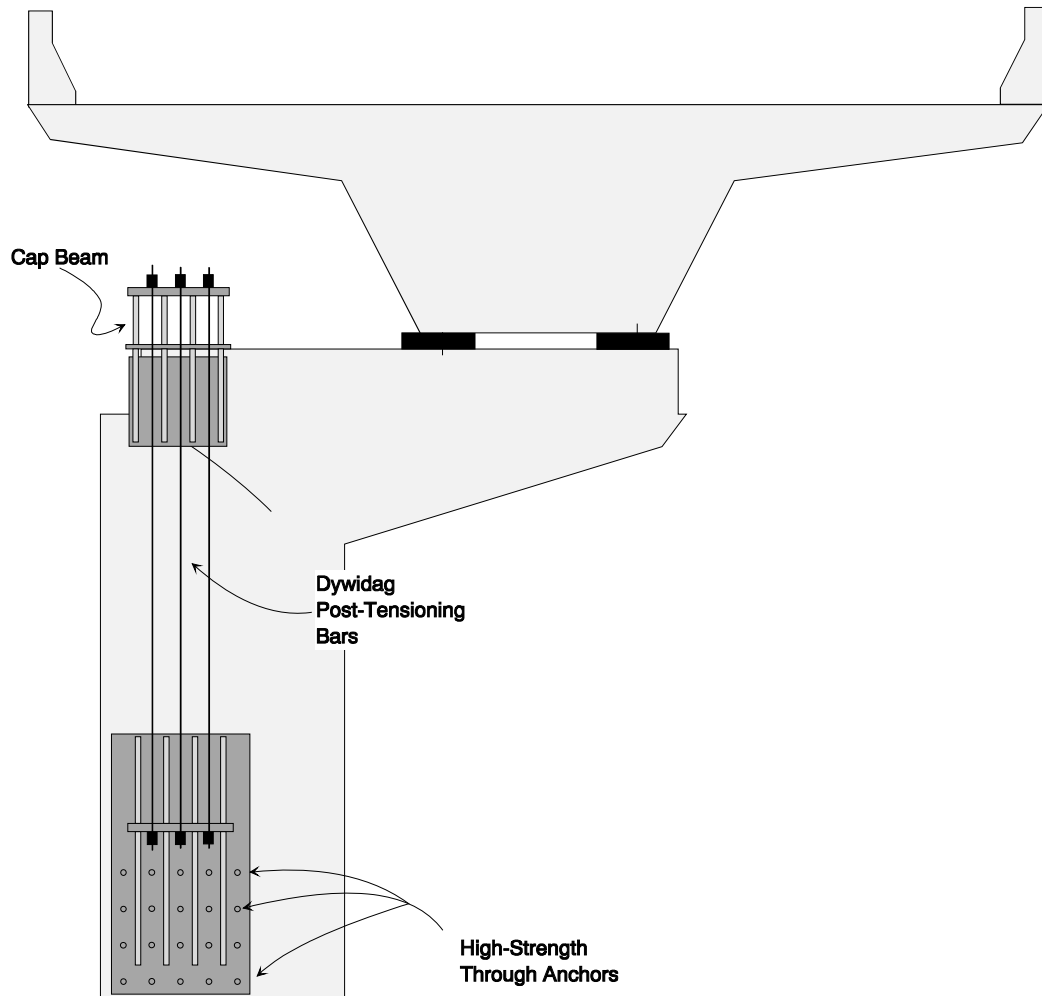


Figure 8.19 External Vertical PT Repair - Side View

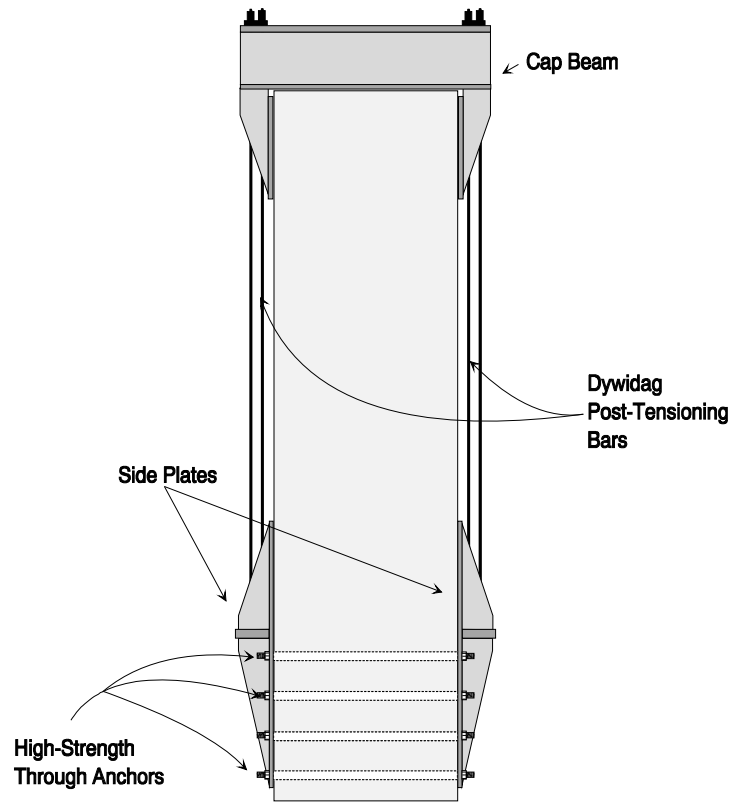


Figure 8.20 External Vertical PT Repair - End View

8.4.2 External Diagonal Post-Tensioned Repair - Conceptual Design

The external diagonal post-tensioned repair, shown in Figure 8.21, provides a clamping force normal to the assumed failure plane in the joint. A diagonal post-tensioned repair can be compact, reducing visibility of the repair, because it has a large, effective moment arm and will not require as large a post-tensioning force to achieve the desired bent strength.

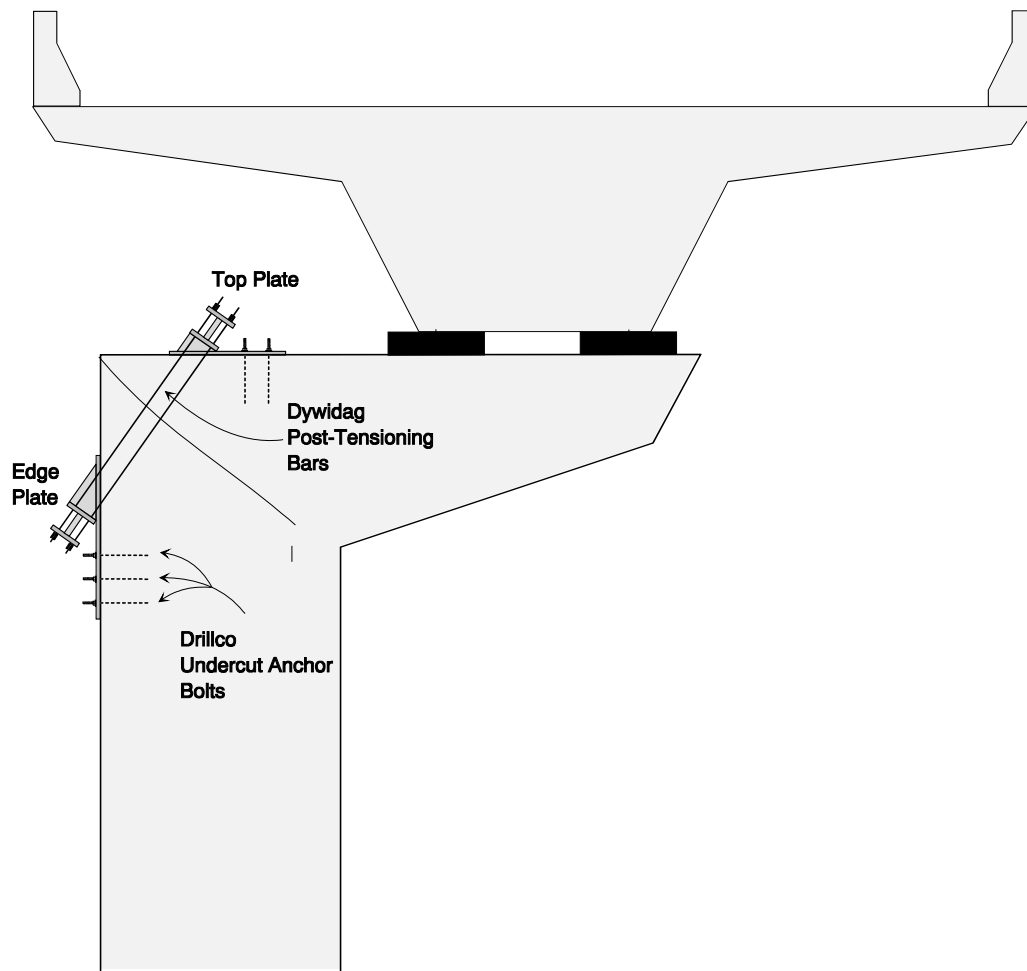


Figure 8.21 External Diagonal Post-Tensioned Repair - Side View

Large-diameter undercut anchors transfer shear forces from the top and edge connection plates into the specimen. Undercut anchors are envisioned because they provide large shear and pull-out resistance in cracked concrete. Anchor bolts would be designed to resist a shear force equivalent to ultimate tensile strength of the diagonal post-tensioning bars.

8.5 Internal Post-Tensioned Repair Methods

Internal post-tensioned repair options were appealing to TxDOT engineers because they would be protected from corrosion and be concealed from view of the public. Many internal joint repairs were considered, including: an internal vertical PT repair, a horizontal PT repair, and a combined horizontal and vertical PT repair. As stated earlier, post-tensioning needed to be positioned away from the exterior corner of the joint (specifically more than 1.5 times the straight-bar development length) to prevent a critical diagonal crack from forming outside the clamped region of the joint.

The general construction procedure for internal post-tensioning involved coring or drilling holes in the structure, inserting quick-setting epoxy cartridges at the bottom of each core to anchor the post-tensioning, installing Dywidag post-tensioning bars, and stressing the bars.

8.5.1 Internal Vertical Post-Tensioned Repair - Conceptual Design

An internal vertical post-tensioned repair, similar to that depicted in Figure 8.22, was completed on the C11-C substructure during the construction phase of the San Antonio Downtown 'Y' project after cracks were observed in the joint region. Because TxDOT design engineers were familiar with the procedure and pleased with the final results, the internal vertical post-tensioned repair was a preferred repair option. Coring was accomplished by operating a truck-mounted coring drill from the superstructure.

For cases where the superstructure extends over the top of the joint (as shown in Figure 8.22), drilling from the superstructure may be restricted to prevent damage to the bridge deck. If coring is performed from the top of the substructure, the limited clearance between the bottom of the superstructure and top surface of the joint complicates the coring operation and installation of the post-tensioning bars. Both the core bits and post-tensioning bars need to be coupled, in relatively short segments, to access the cored holes. This would hamper the coring operation and lengthen the time required to complete the repair.

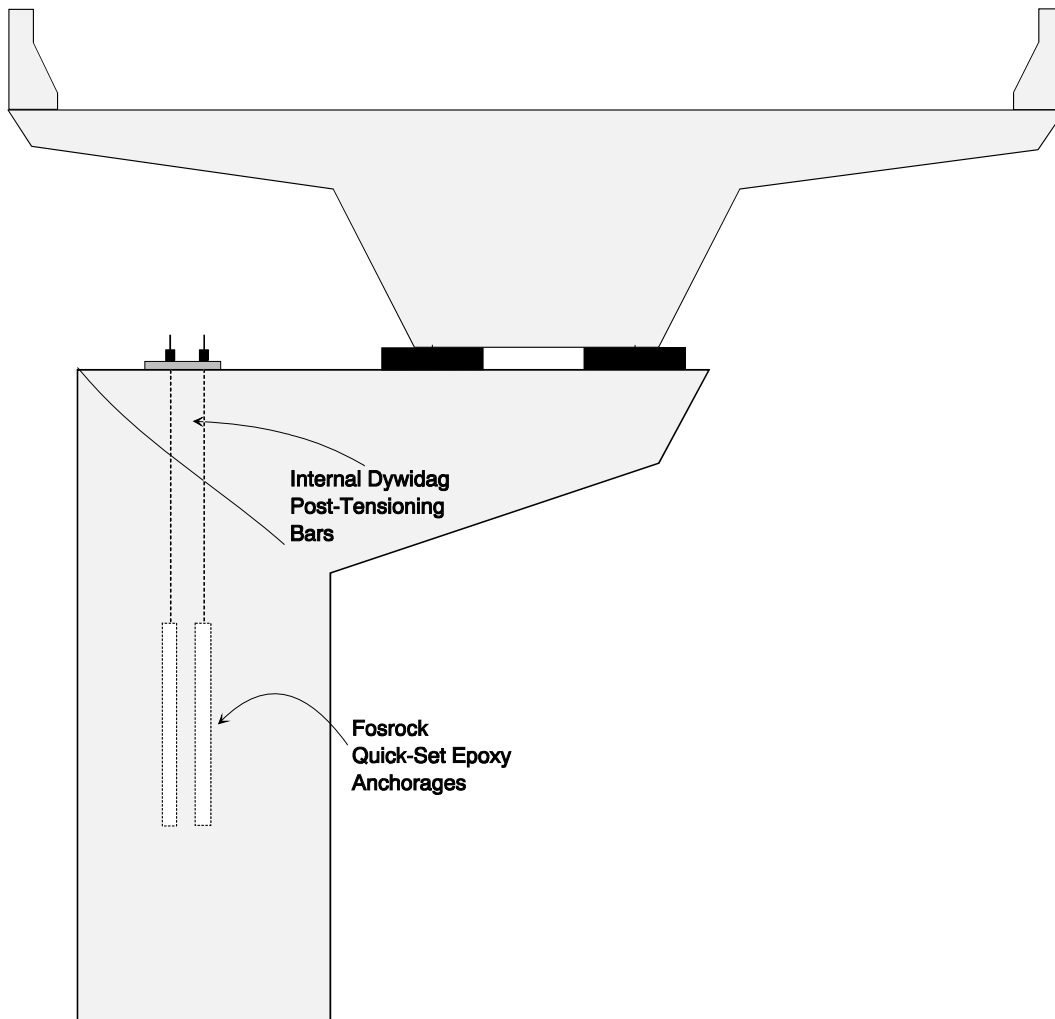


Figure 8.22 Internal Vertical Post-Tensioned Repair - Conceptual Design

8.5.2 Internal Horizontal Post-Tensioned Repair - Conceptual Design

A horizontal internal post-tensioned repair, shown in Figure 8.23, can be effective when access to the top of the joint is restricted or the quality of the concrete on the top surface of the joint is poor.

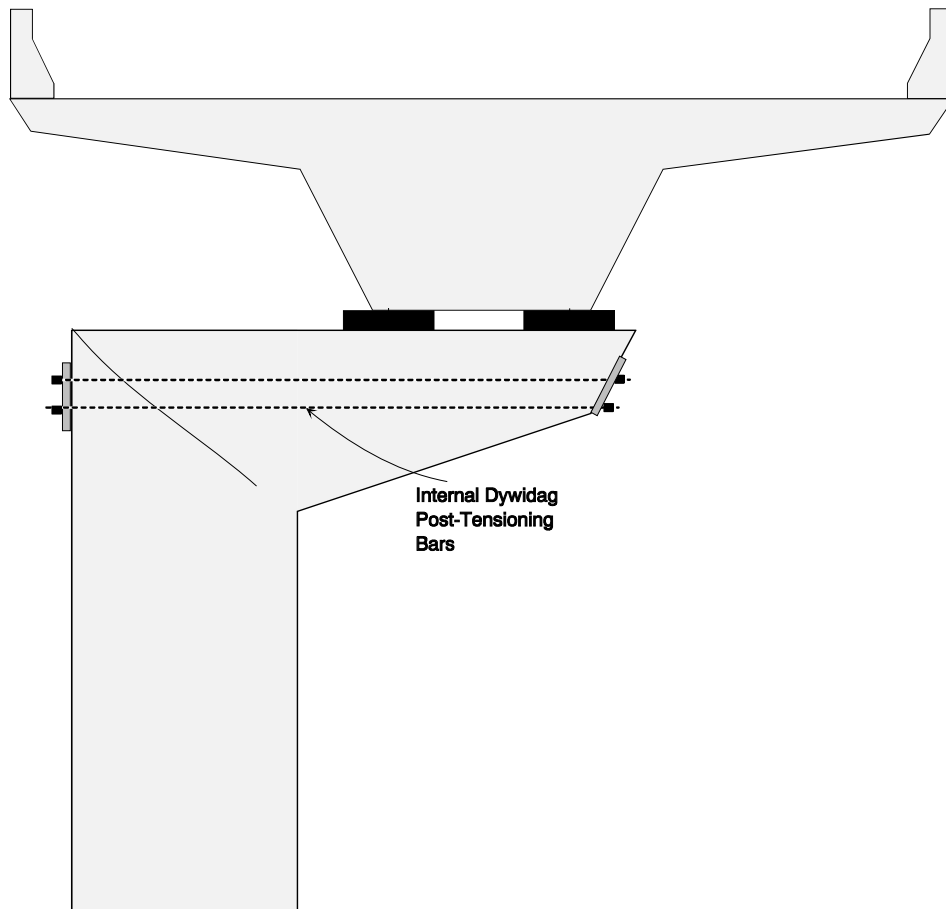


Figure 8.23 Internal Horizontal Post-Tensioned Repair - Conceptual Design

A disadvantage of horizontal internal PT is controlling the core trajectory; ensuring the core passes through the overhang, without damaging the transverse reinforcement located in the overhang. Compressive stresses at the tip of the overhang must be evaluated to prevent anchorage zone failure. Bursting and spalling forces must be checked for this design.

8.5.3 Combined Internal Vertical and Horizontal Post-Tensioning - Conceptual Design

Combined vertical and horizontal post-tensioning, illustrated in Figure 8.24, provides the optimum resistance of the three internal strengthening options discussed. Post-tensioning can be positioned near the extreme tensile fibers of the overhang and pier regions because it forms a continuous tensile force path through the joint, and an alternate failure plane cannot

develop. Increased effective moment arms for the horizontal and vertical post-tensioning bars reduces the number of bars required to resist applied factored loads/ ϕ .

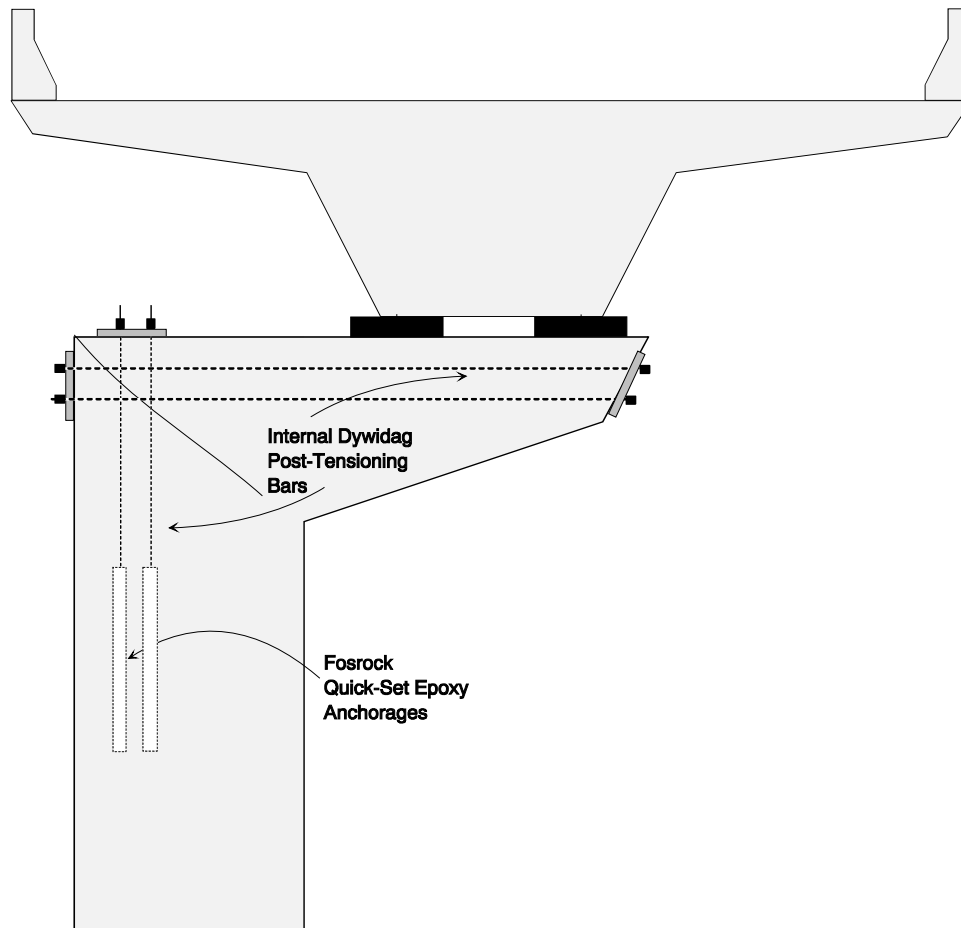


Figure 8.24 Internal Horizontal and Vertical Post-Tensioning - Conceptual Design

8	342
8.4 External Post-Tensioned Repair Methods	342
8.4.1 External Vertical Post-Tensioned Repair - Conceptual Design.....	342
8.4.2 External Diagonal Post-Tensioned Repair - Conceptual Design.....	344
8.5 Internal Post-Tensioned Repair Methods	346
8.5.1 Internal Vertical Post-Tensioned Repair - Conceptual Design.....	346
8.5.2 Internal Horizontal Post-Tensioned Repair - Conceptual Design	347
8.5.3 Combined Internal Vertical and Horizontal Post-Tensioning - Conceptual Design.....	348
Figure 8.19 External Vertical PT Repair - Side View.....	343
Figure 8.20 External Vertical PT Repair - End View	344
Figure 8.21 External Diagonal Post-Tensioned Repair - Side View.....	345
Figure 8.22 Internal Vertical Post-Tensioned Repair - Conceptual Design.....	347
Figure 8.23 Internal Horizontal Post-Tensioned Repair - Conceptual Design.....	348
Figure 8.24 Internal Horizontal and Vertical Post-Tensioning - Conceptual Design	349

8.6.2. Internal Vertical Post-Tensioned Repair (POJ-RC-100-RP2)

Reinforced concrete Specimen POJ-RC-100-2 was repaired with internal vertical post-tensioning after the diagonal post-tensioned repair (POJ-RC-100-RP1) was removed. Vertical post-tensioning bars were positioned away from the outside joint corner to prevent anchorage failure of the longitudinal overhang reinforcement. Consequently, the effective moment arm for the post-tensioning (measured from the joint compression centroid to the post-tensioning) was small, resulting in a larger post-tensioning force than that required for the POJ-RC-100-RP1 repair. An elevation of the POJ-RC-100-RP1 repair is presented in Figure 8.39.

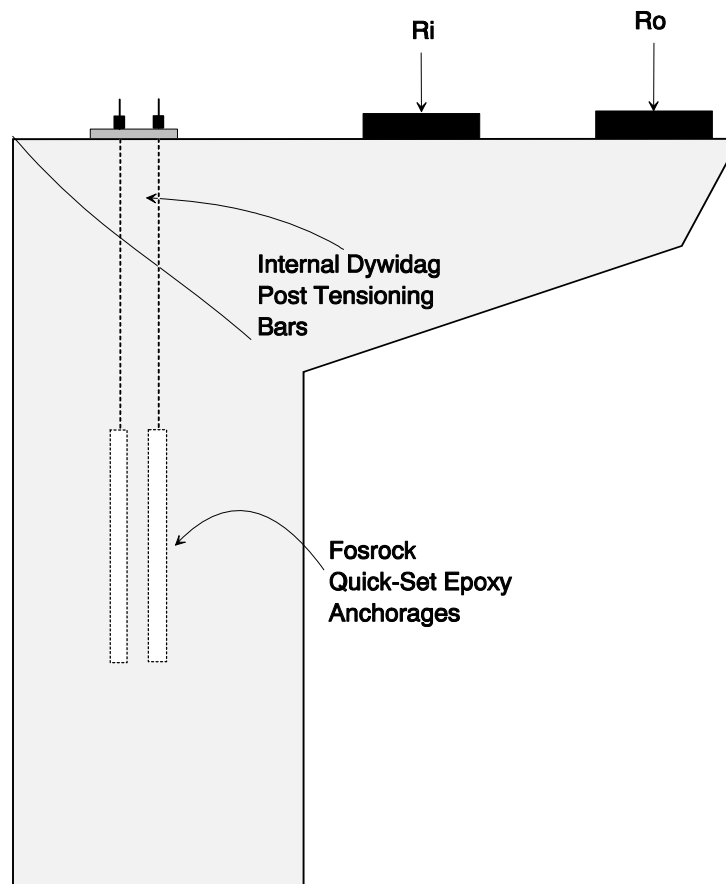


Figure 8.39 Elevation of Internal Vertical Post-Tensioned Repair (POJ-RC-100-RP2)

8.6.2.1. Capacity Calculation (POJ-RC-100-RP2)

Repaired specimen POJ-RC-100-RP2 was designed to resist applied factored loads / ϕ . Vertical post tensioning was located 33 cm (13.0 in.) from the joint corner, providing sufficient length (equal to 1.4 times straight-bar development length) to anchor the No. 4 longitudinal overhang reinforcement. In order to calculate the capacity of the repaired specimen, it was assumed that grouted, internal post-tensioning would achieve guaranteed ultimate stress (f_{pu} [1.03 GPa (150 ksi)]) at inception of joint failure.

A portion of the free body used to compute the specimen capacity is shown in Figure 8.40. Tensile capacities of bars crossing the critical diagonal crack in the joint were determined as described in Section 7.2. Vertical and horizontal force components and moments calculated about the joint compression centroid are detailed in Figure 8.40. Computed maximum applied loads, R_i and R_o , were 519 kN (116.7 kips) and 649 kN (146.0 kips), respectively. A simplified free-body diagram used to compute specimen capacity (where individual bar forces along the crack interface were replaced by vertical and horizontal resultants) is presented in Figure 8.41. Computed moment capacity of the repaired specimen was equivalent to DL+4.4 LL and greater than factored load / ϕ (1.15 times applied factored loads).

Eight-16 mm (5/8 in.) diameter post-tensioning bars (with a specified tensile capacity of 1.03 GPa (150 ksi)) provided a vertical clamping force equal to $0.6 F_{pu}$ [0.90 MN (202 kips)] at applied service loads and F_{pu} [1.50 MN (336 kips)] at failure loads. Post-tensioning forces contributed 52 percent of the specimen capacity at failure.

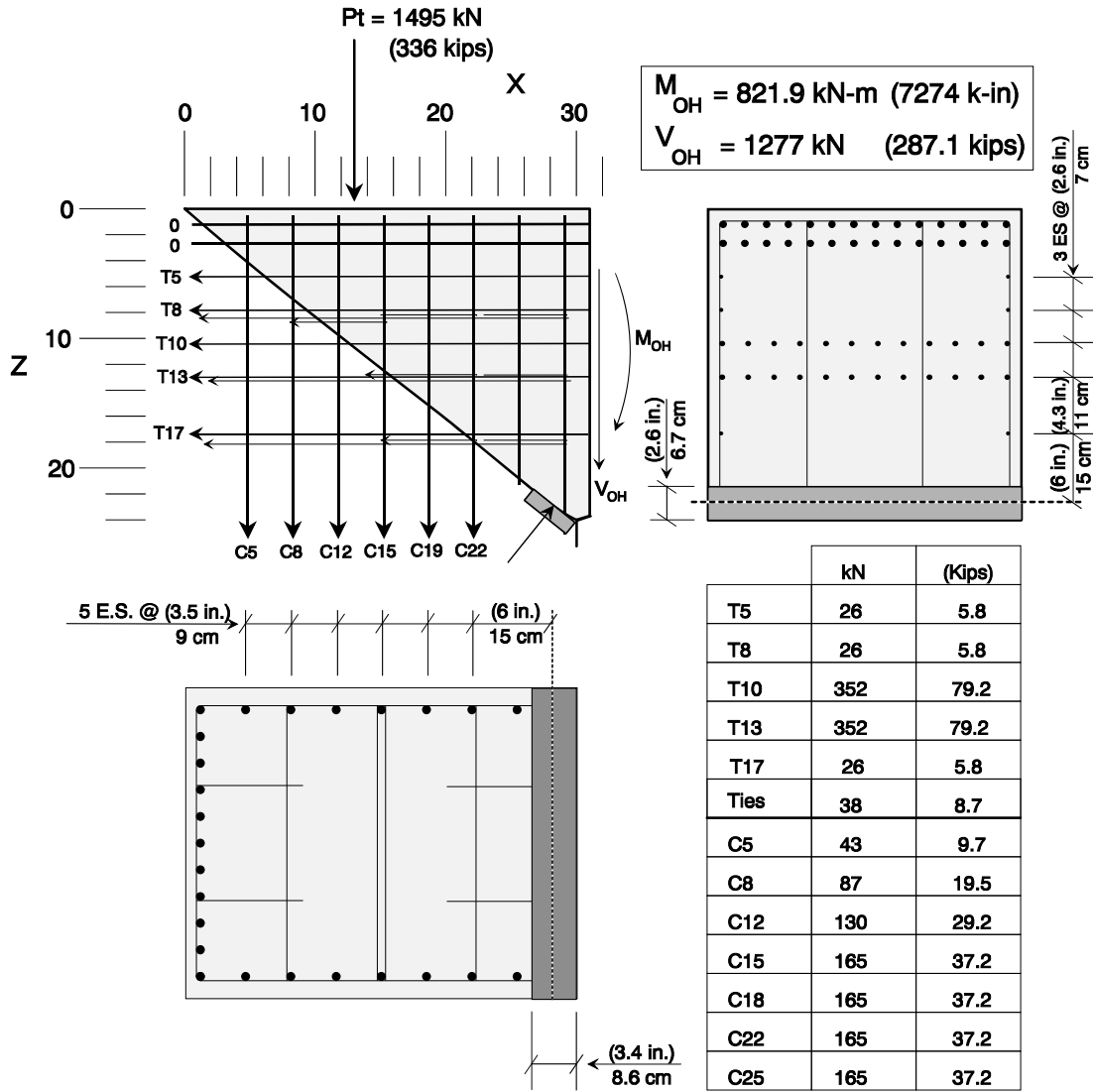
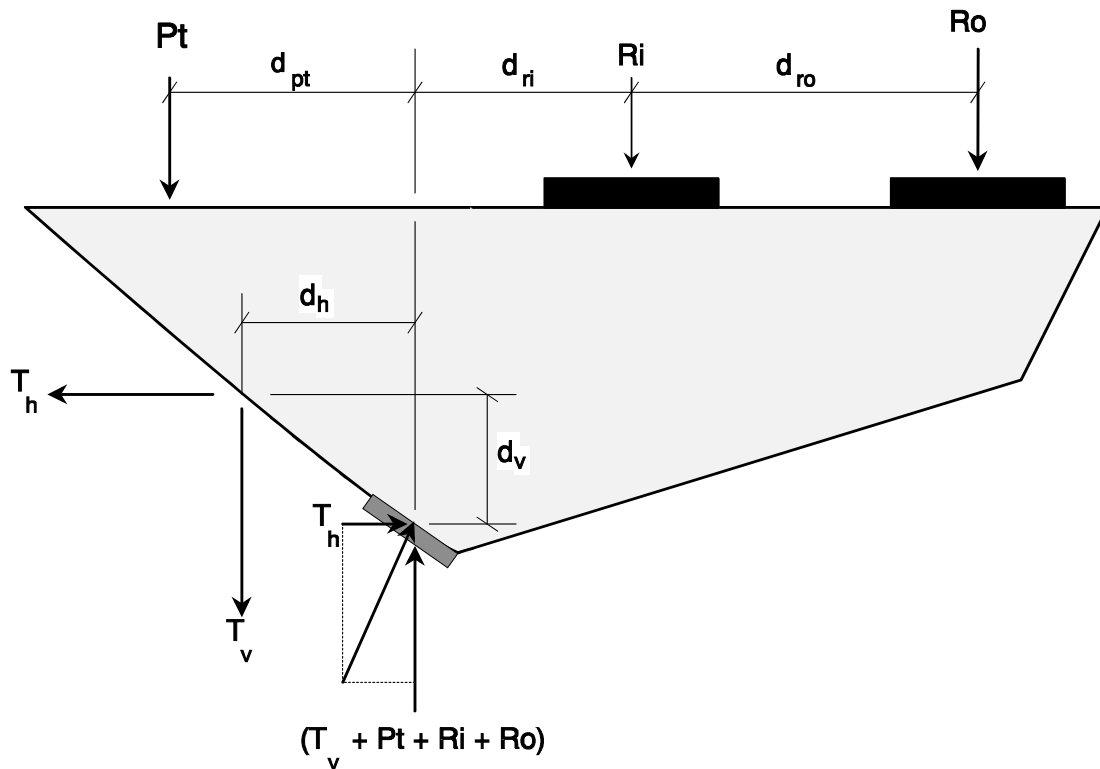


Figure 8.40 POJ-RC-100-RP2 Free Body and Reinforcement Locations Used in Strength Model



Joint Resistance = Applied Moment

$$T_h(d_v) + T_v(d_h) + Pt(d_{pt}) = Ri(d_{ri}) + Ro(d_{ro})$$

$$(184 \text{ kips})(11.6 \text{ in}) + (170 \text{ kips})(10.8 \text{ in}) + (336 \text{ kips})(13.1 \text{ in}) = (123.3 \text{ kips})(16 \text{ in.}) + (154.3 \text{ kips})(40 \text{ in.})$$

$$818 \text{ KN}(29.5 \text{ cm}) + 756 \text{ KN}(27.5 \text{ cm}) + 1495 \text{ KN}(33 \text{ cm}) = 548 \text{ KN}(40 \text{ cm}) + 686 \text{ KN}(102 \text{ cm})$$

Figure 8.41 Free Body Used to Determine Post-Tensioning Force for Specimen POJ-RC-100-RP2

8.6.2.2. Finite Element Analysis (POJ-RC-100-RP2)

Specimen POJ-RC-100-RP2 was designed to remain uncracked under applied service-level loads. Principal tensile stresses at applied service loads were computed using a finite element analysis. Principal tensile stresses near the diagonal joint crack were maintained below $7\sqrt{f'_c}$ (the assumed concrete cracking stress). Vertical post-tensioning forces, equal to $0.6 F_{pu}$ [0.90 MN (202 kips)], were applied as a uniform distributed load perpendicular to the top surface of the specimen.

Principal tensile and compressive stresses are plotted as contours and vectors for applied service loads in Figure 8.42 and Figure 8.43, respectively. Joint principal tensile and compressive stresses are plotted as contours and vectors in Figure 8.44 and Figure 8.45, respectively. Principal compressive stress contours in Figure 8.45 are presented using a smaller range of compressive stresses than depicted in Figure 8.43 to highlight the flow of compressive stresses.

Principal tensile stresses in the joint region (specifically across the path of the diagonal joint crack) were $5.6\sqrt{f'_c}$ [2.8 MPa (400 psi)], indicating the specimen would remain uncracked at applied service loads if the joint cracks were epoxy injected before testing.

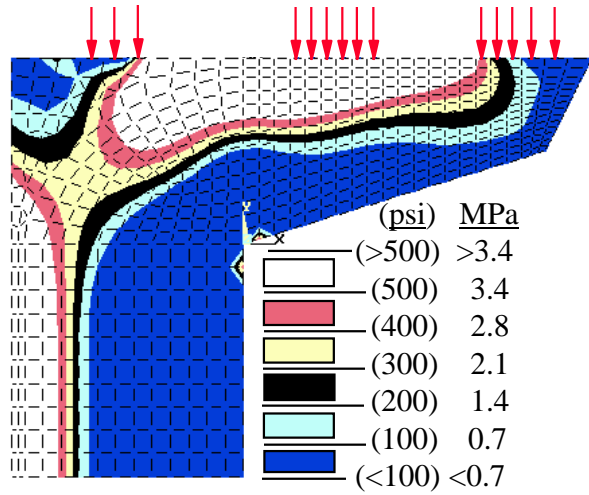


Figure 8.42 POJ-RC-100-RP2 - Overall Principal Tensile Stresses and Trajectories at Service Load

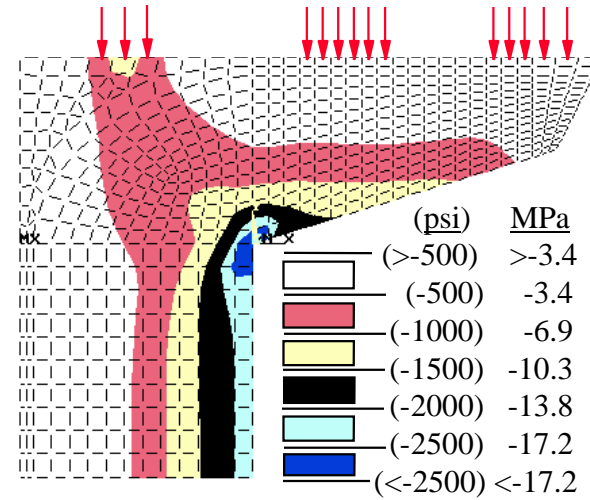
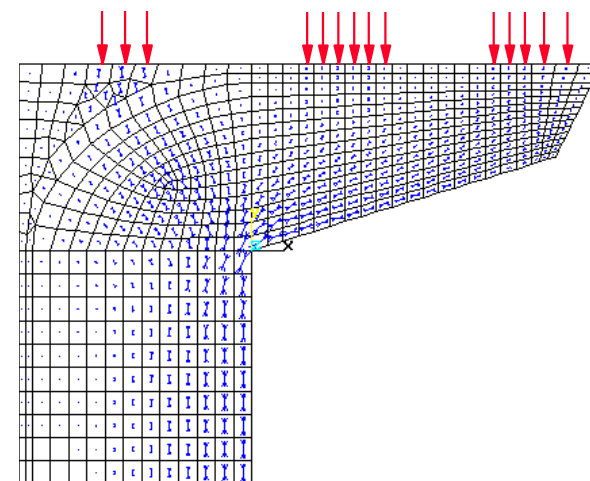
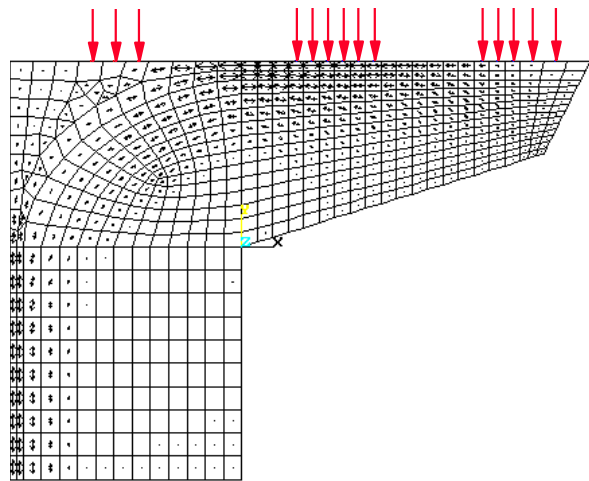


Figure 8.43 POJ-RC-100-RP2 - Overall Principal Compressive Stresses and Trajectories at Service Load



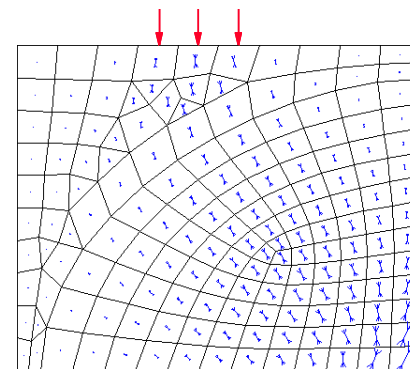
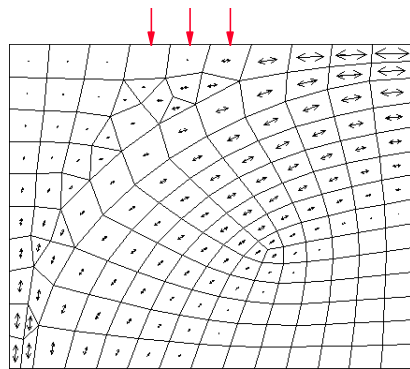
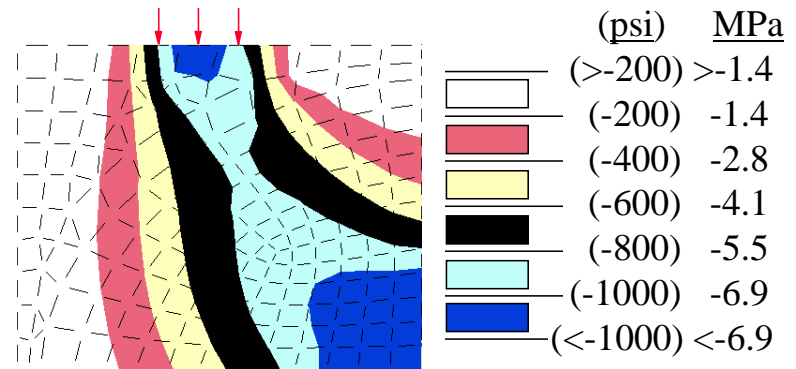
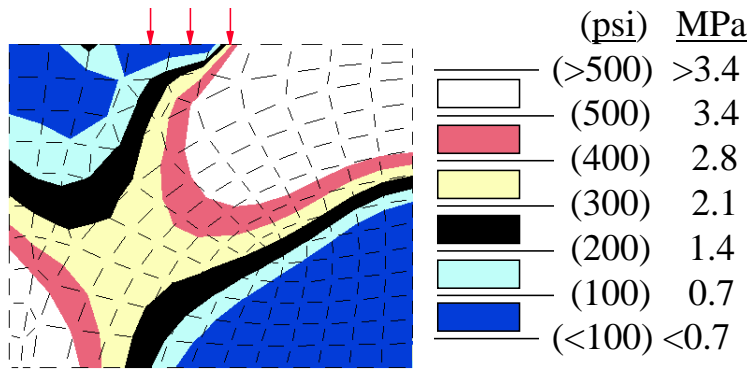


Figure 8.44 POJ-RC-100-RP2 - Joint Principal Tensile Stresses and Trajectories at Service Load

Figure 8.45 POJ-RC-100-RP2 - Joint Principal Compressive Stresses and Trajectories at Service Load

8.6.2.3. Design and Installation Details (POJ-RC-100-RP2)

Design details for the internal vertical post-tensioned repair (POJ-RC-100-RP2) are presented in Figure 8.46 and Figure 8.47. The location of the resultant of the vertical post-tensioning, shown in Figure 8.46, was located 33 cm (13 in.) from the joint edge. This provided sufficient anchorage to yield the longitudinal overhang reinforcement, and prevented an alternative failure path from forming that excluded the post-tensioned repair. If sufficient distance from the joint corner was not provided, an alternate failure plane (specifically, a diagonal crack located to the right of the post-tensioning shown in Figure 8.46) could develop, resulting in reduced capacity.

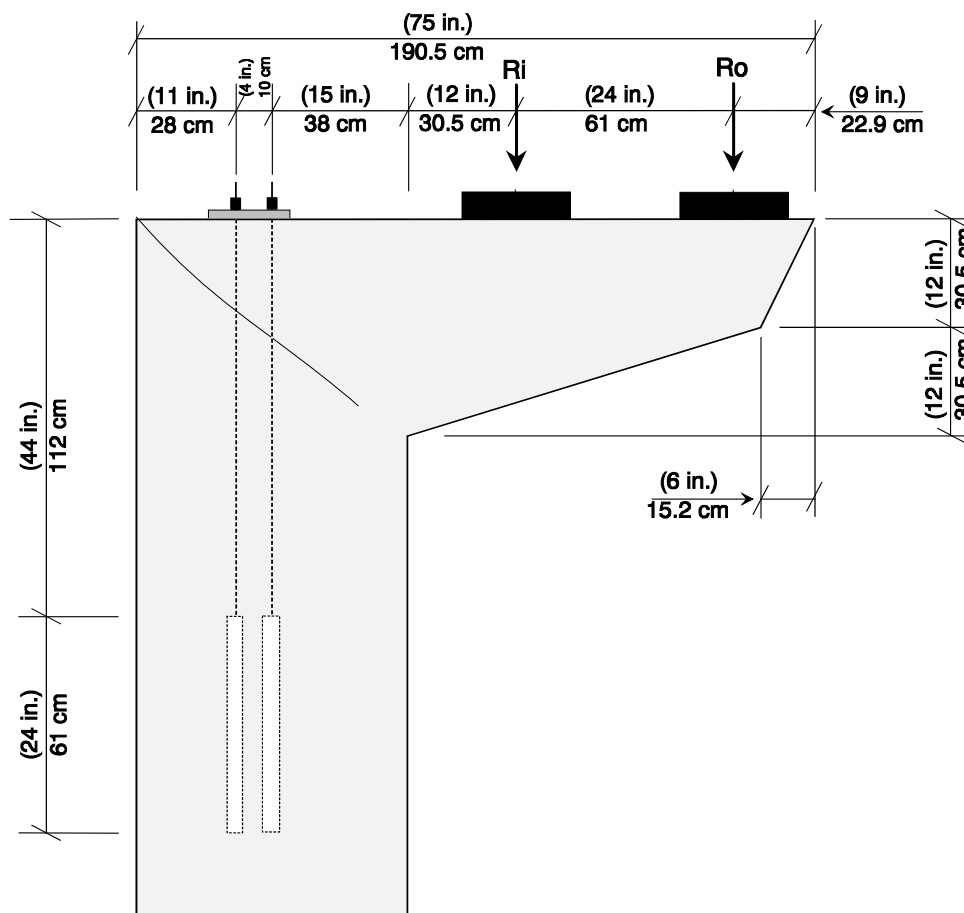


Figure 8.46 POJ-RC-100-RP2 Overall Dimensions - Elevation

Coring was not required for this specimen because eight- 2.5 cm (1.0 in.) diameter galvanized electrical conduits were placed in the reinforcing cage before Specimen POJ-RC-

100-2 was cast to “create” the core holes. Two rows of four holes, shown in Figure 8.47, extended a total depth of 173 cm (68 in.) into the specimen. The galvanized conduit was removed three days after casting the specimen.

Before post-tensioning bars were installed, each hole was flushed with water, vacuumed, and dried with pressurized air. Once all holes were dry, two packets of quick-set epoxy (set time of 90 seconds and a material yield of 30 cm (12 in.) depth of the “core”) were lowered to the bottom of each hole. This provided a 60 cm (24 in.) length to anchor each 16 mm (5/8 in.) diameter Dywidag post-tensioning bar. Three and one-half packets of slow setting epoxy (set time of 23 minutes) were stacked in the remaining voided space at the top of the hole. An industrial strength air wrench was used to spin each Dywidag bar through the epoxy matrix packages at a speed of 100 RPM. As the bar continued down the hole, it penetrated and blended the contents of the two-part epoxy packets. The air wrench turned the bar 4 seconds once it reached the bottom of the hole [38]. After waiting 2 minutes, a center-hole hydraulic ram was used to tension the bar to a stress of $0.60 f_{pu}$ [0.620 GPa (90 ksi)]. The relatively low post-tensioning stress was used to simulate long-term post-tensioning losses. Cracks were not epoxy injected after the specimen was stressed.

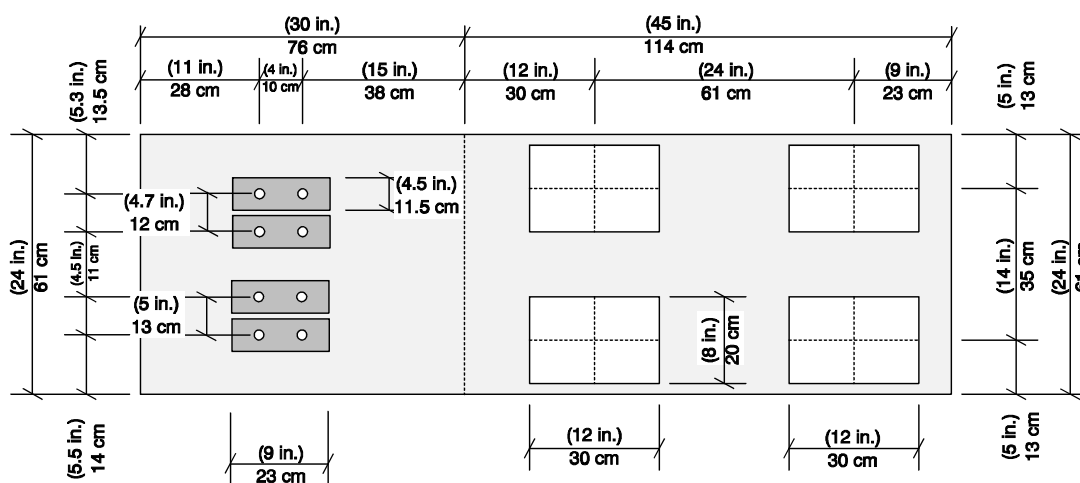


Figure 8.47 POJ-RC-100-RP2 Dimensions - Top View

8.6.2.4. Behavior During Testing (POJ-RC-100-RP2)

Vertical post-tensioning bars were installed with 1/2 dead load applied to the specimen. This was the load maintained on the specimen after the POJ-RC-100-RP1 test was completed. Strain gages were re-zeroed before testing commenced.

The specimen was loaded in the sequence specified in Table 8.1. Crack growth was monitored by measuring crack widths at dead load, DL + 1/2 LL, service load, and DL + 2LL using a crack microscope. Cracks would not have been expected to form in the joint had the specimen been epoxy injected after post-tensioning was installed. Crack locations and crack-width measurements are reported by Scott [6].

Applied overhang moment vs. tip displacement response for Specimen POJ-RC-100-RP2 (shown in Figure 8.48) was nearly linear from DL to applied factored load / phi. The test indicated that the quantity of installed post-tensioning provided sufficient strength to resist design factored loads / phi.

After the first test was completed, further testing was conducted to investigate the strength of the specimen after several of the overhang longitudinal reinforcing bars were intentionally damaged by coring into the top surface of the specimen. This test is discussed by Scott [6].

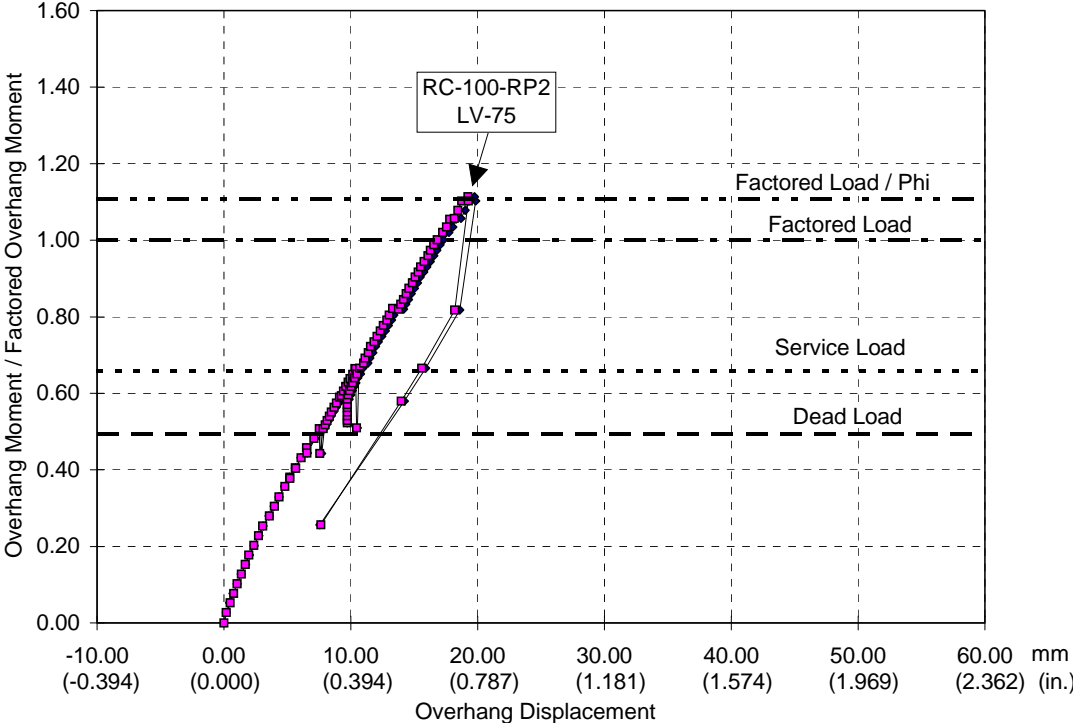


Figure 8.48 POJ-RC-100-RP2 Overhang Tip Displacement

8.	366
8.6.2. <i>Internal Vertical Post-Tensioned Repair (POJ-RC-100-RP2)</i>	366
8.6.2.1. Capacity Calculation (POJ-RC-100-RP2)	367
8.6.2.2. Finite Element Analysis (POJ-RC-100-RP2)	370
8.6.2.3. Design and Installation Details (POJ-RC-100-RP2)	373
8.6.2.4. Behavior During Testing (POJ-RC-100-RP2)	375
Figure 8.39 Elevation of Internal Vertical Post-Tensioned Repair (POJ-RC-100-RP2)	366
Figure 8.40 POJ-RC-100-RP2 Free Body and Reinforcement Locations Used in Strength Model	368
Figure 8.41 Free Body Used to Determine Post-Tensioning Force for Specimen POJ-RC-100-RP2	369
Figure 8.42 POJ-RC-100-RP2 - Overall Principal Tensile Stresses and Trajectories at Service Load	371
Figure 8.43 POJ-RC-100-RP2 - Overall Principal Compressive Stresses and Trajectories at Service Load	371
Figure 8.44 POJ-RC-100-RP2 - Joint Principal Tensile Stresses and Trajectories at Service Load	372
Figure 8.45 POJ-RC-100-RP2 - Joint Principal Compressive Stresses and Trajectories at Service Load	372
Figure 8.46 POJ-RC-100-RP2 Overall Dimensions - Elevation	373
Figure 8.47 POJ-RC-100-RP2 Dimensions - Top View	374
Figure 8.48 POJ-RC-100-RP2 Overhang Tip Displacement	376

8.7. Analysis and Behavior of Selected POJ-PS-100 Repairs

The prototype fully prestressed concrete specimen (POJ-PS-100) was strengthened with an external vertical post-tensioned repair, developed in cooperation with TxDOT design engineers. Two tests were performed to evaluate the post-tensioning force required to resist design factored load / ϕ . Repair POJ-PS-100-RP1 utilized a prestress force 1.5 times greater than the force used for POJ-PS-100-RP2. Each repaired specimen was proof-loaded to design factored load / ϕ to evaluate strength. Ultimate strength of Specimen POJ-PS-100-RP1 was not determined experimentally in order to perform multiple tests using the same prototype specimen. Analysis and design details, as well as plots of moment vs. deflection response and moment vs. post-tensioning strain are presented in the following sections. Additional details for these tests are presented by Scott [6].

8.7.1. External Vertical Post-Tensioned Repairs (POJ-PS-100-RP1 & RP2)

A vertical clamping force was applied normal to the top surface of the joint, reducing tensile stresses and resisting the moments tending to open the diagonal joint crack. A vertical post-tensioned repair (similar to that used to repair Specimen POJ-RC-100-RP2, shown in Figure 8.39) was applied to the San Antonio ‘Y’ substructure C11-C, but it was an expensive and time-consuming repair. Locating post-tensioning bars externally would simplify installation of the repair on substructures with small clearance between the superstructure and the top surface of the substructure (as shown in Figure 8.19).

For the external vertical repair, a stiffened steel beam (cantilevered over the edges of the joint) was post-tensioned vertically, distributing vertical compressive forces across the width of the joint. Post-tensioning bars extended down the sides of the substructure (as shown in Figure 8.49) and were attached to stiffened plates anchored to the sides of the pier. A pair of stiffened plates (one on each side of the pier) were attached to the pier by anchor-bolts which extended through the thickness of the pier. These through-anchors were designed to resist shear forces produced at ultimate tensile capacity of the post-tensioning bars. Perceived advantages of the repair scheme included: pre-fabrication of steel shapes, ease of

installation, and limited coring in the pier. Disadvantages included aesthetics, questionable durability, and quantity of plate steel and welding required to form the stiffened sections.

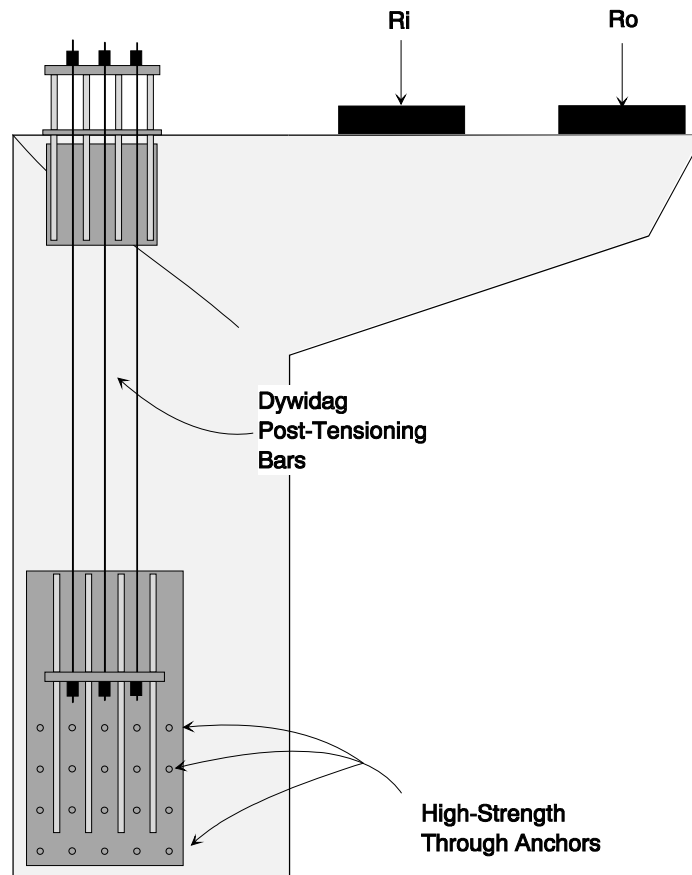


Figure 8.49 Elevation of POJ-PS-100-RP1 & RP2 External Vertical PT Repairs

8.7.1.1. Capacity Calculation (POJ-PS-100-RP1 & RP2)

Repairs were intended to increase capacity of the specimen above design factored loads / ϕ . Capacity was calculated by summing moments about the compression resultant. Capacities of bars crossing the critical diagonal crack were determined as described in Section 7.2. The resultant of the vertical post-tensioning was located 24.5 cm (10.0 in.) from the outer edge of the specimen, providing an area to distribute compressive stresses (less than $0.45 f_c'$) across the width of the specimen. It was assumed that ungrouted, external post-tensioned bars would achieve nominal yield stress ($0.75f_{pu}$ [776 MPa (112.5 ksi)]) at inception of failure.

Repaired Specimen POJ-PS-100-RP1 was designed assuming longitudinal shear friction reinforcement (T9 & T12) did not contribute to specimen capacity. Based on this assumption, the required post-tensioning force was 1.68 MN (378 kips), as calculated using the free-body diagram shown in Figure 8.50.

Repaired Specimen POJ-PS-100-RP2 was designed assuming shear friction reinforcement (T9 & T12) was partially effective, based on the bar capacity calculation described in Section 7.2. The post-tensioning force, P_t , was computed to be 1.21 MN (252 kips). A portion of the free-body diagram used to compute specimen capacity is shown in Figure 8.51.

A simplified free-body diagram (where individual bar forces across the crack interface were replaced by vertical and horizontal resultants) is presented for both repairs in Figure 8.52. Computed maximum applied loads, R_i and R_o , for Specimen POJ-PS-100-RP1 were 616 kN (138.6 kips) and 771 kN (173.3 kips), respectively. These loads are equivalent to DL+4.8LL and are greater than factored loads/ ϕ (1.26 times applied factored loads). Computed maximum applied loads, R_i and R_o , for Specimen POJ-PS-100-RP2 were 523 kN (117.7 kips) and 655 kN (147.1 kips), respectively. These loads are equivalent to DL+3.6LL and are slightly less than factored loads/ ϕ (1.07 times applied factored loads).

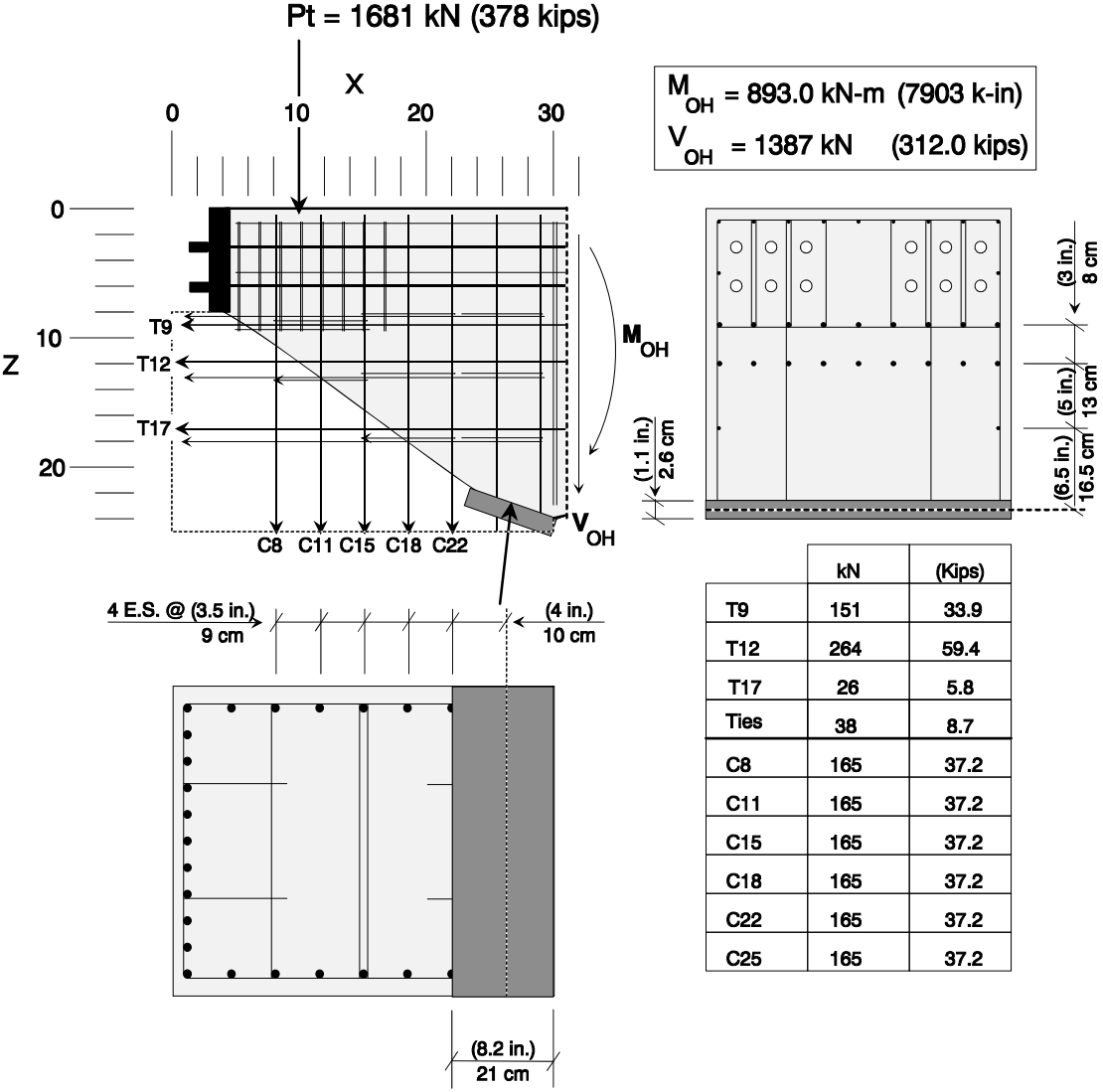


Figure 8.50 POJ-PS-100-RP1- Free Body and Reinforcement Locations Used in Capacity Calculation

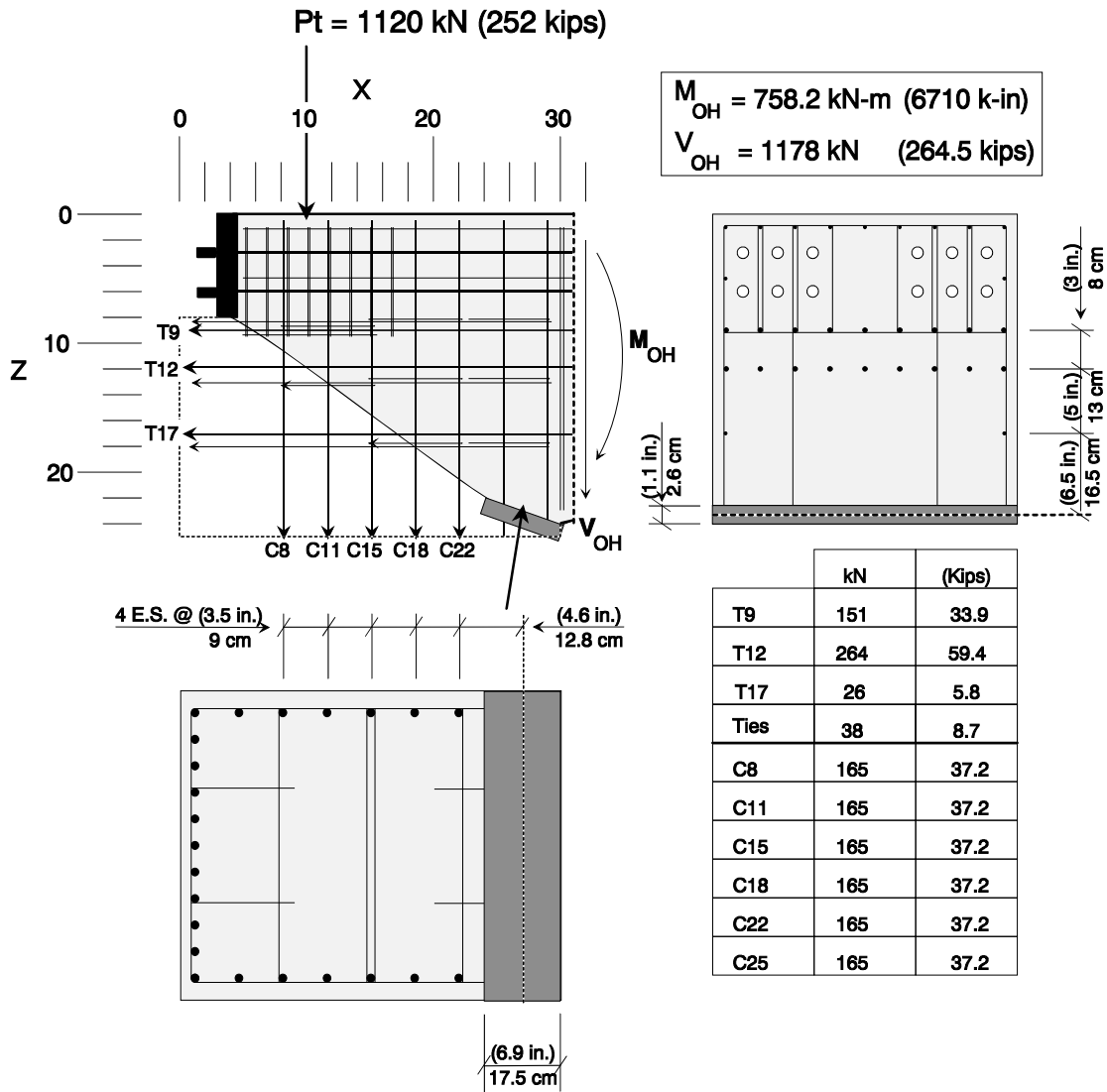
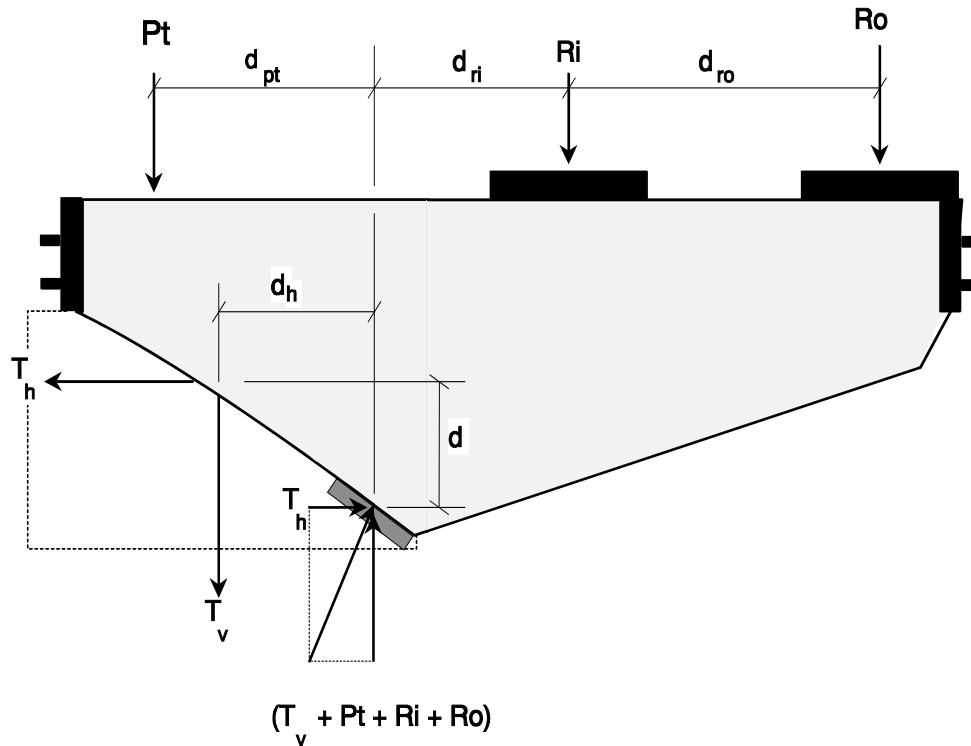


Figure 8.51: POJ-PS-100-RP2 Free Body and Reinforcement Locations Used in Capacity Calculation



Joint Resistance = Applied Moment

$$T_h (d_v) + T_v (d_h) + Pt(d_{pt}) = Ri(d_{ri}) + Ro(d_{ro})$$

POJ-PS-100-RP1

$$(107.7 \text{ kips})(12.1 \text{ in}) + (148.8 \text{ kips})(12.6 \text{ in}) + (378 \text{ kips})(15.9 \text{ in}) = (138.6 \text{ kips})(16.1 \text{ in}) + (173.3 \text{ kips})(40.1 \text{ in})$$

$$479 \text{ KN}(31 \text{ cm}) + 662 \text{ KN}(32 \text{ cm}) + 1681 \text{ KN}(40 \text{ cm}) = 617 \text{ KN}(41 \text{ cm}) + 771 \text{ KN}(102 \text{ cm})$$

POJ-PS-100-RP2

$$(107.7 \text{ kips})(12.1 \text{ in}) + (186 \text{ kips})(11.5 \text{ in}) + (252 \text{ kips})(16.6 \text{ in}) = (117.7 \text{ kips})(15.4 \text{ in}) + (147.1 \text{ kips})(39.4 \text{ in})$$

$$579 \text{ KN}(31 \text{ cm}) + 752 \text{ KN}(21 \text{ cm}) + 1121 \text{ KN}(42 \text{ cm}) = 524 \text{ KN}(39 \text{ cm}) + 654 \text{ KN}(100 \text{ cm})$$

Figure 8.52 Free Body Used to Determine Post-Tensioning Force for Specimens POJ-PS-100-RP1 & RP2

8.7.1.2. Finite Element Analysis (POJ-PS-100-RP1 & RP2)

Repaired Specimens POJ-PS-100-RP1 and RP2 were designed to remain uncracked under applied service-level loads. Principal tensile stresses at applied service loads were computed using finite element analyses. Principal tensile stresses near the diagonal crack were maintained below $7\sqrt{f'_c}$ [3.4 MPa (500 psi)] (the assumed concrete cracking stress) to prevent the critical diagonal crack from forming. Post-tensioning forces were modeled as a uniformly distributed load over a length corresponding to the position of the steel cap.

Principal tensile and compressive stresses are plotted as contours and vectors for applied service loads in Figure 8.53 and Figure 8.54, respectively. Joint principal tensile and compressive stresses are plotted as contours and vectors in Figure 8.55 and Figure 8.56, respectively. Principal tensile stresses for Specimen PS-100-RP1 were less than $2.8\sqrt{f'_c}$ [1.4 MPa (200 psi)] due to the overhang post-tensioning and large vertical post-tensioning force. Maximum principal tensile stresses for Specimen PS-100-RP2 (shown in Figure 8.57) were $4.2\sqrt{f'_c}$ [2.1 MPa (300 psi)]. Stresses of 1.4 MPa (200 psi) were calculated in a larger zone for Specimen POJ-PS-100-RP2 than for Specimen POJ-PS-100-RP1. Principal compressive stress contours and vectors for Specimen POJ-PS-100-RP2 are plotted in Figure 8.58. Joint principal tensile and compressive stresses are plotted as contours and vectors in Figure 8.59 and Figure 8.60, respectively. It was concluded that both repairs would remain uncracked under applied service loads if joint cracks were epoxy injected before testing.

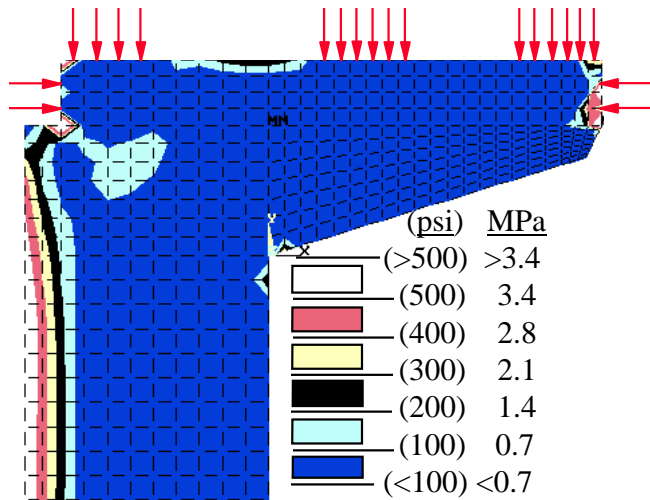


Figure 8.53 POJ-PS-100-RP1 -Overall Principal Tensile Stresses and Trajectories at Service Load

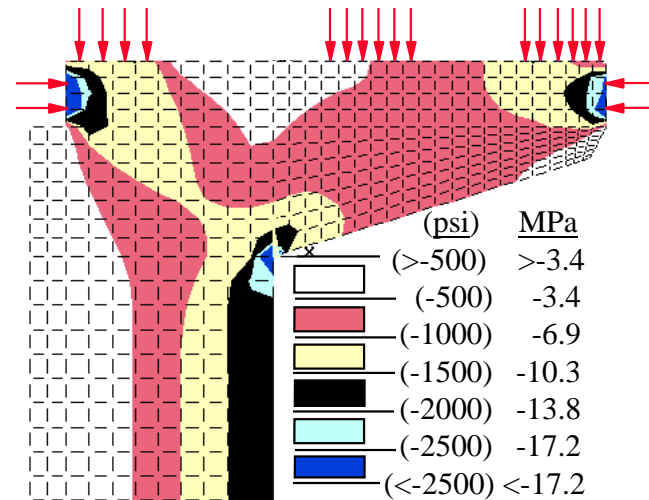


Figure 8.54 POJ-PS-100-RP1 - Overall Principal Compressive Stresses and Trajectories at Service Load

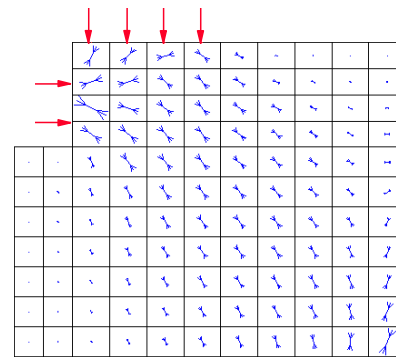
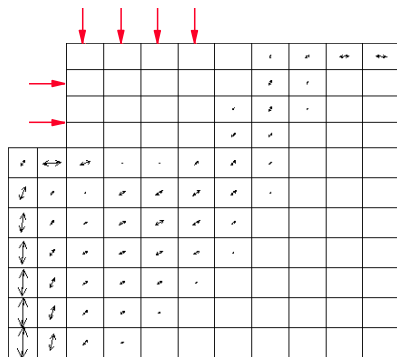
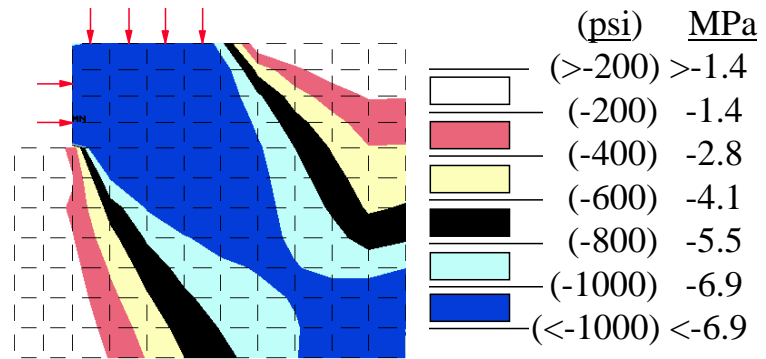
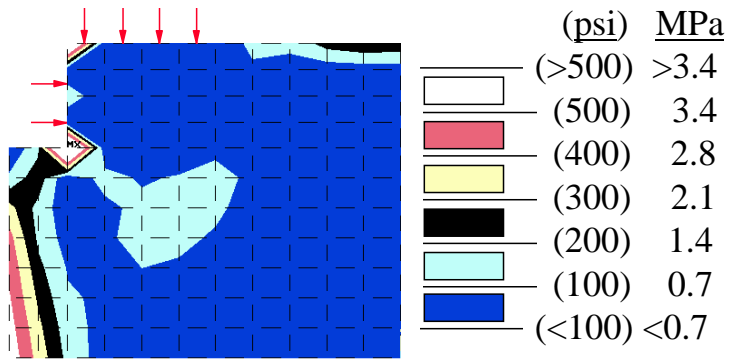


Figure 8.55 POJ-PS-100-RP1 - Joint Principal Tensile Stresses and Trajectories at Service Load

Figure 8.56 POJ-PS-100-RP1 - Joint Principal Compressive Stresses and Trajectories at Service Load

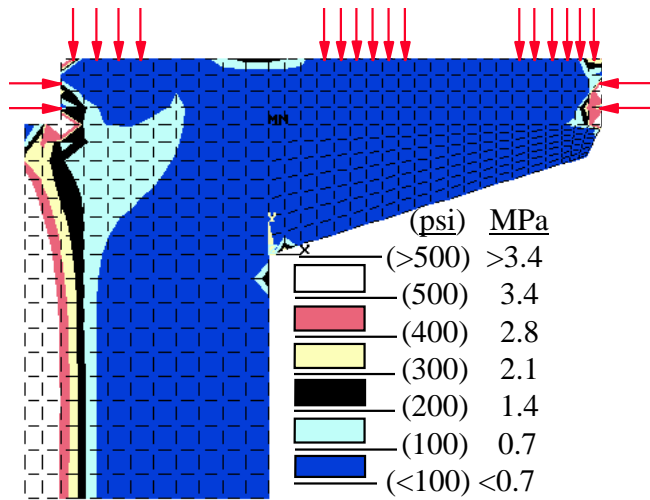


Figure 8.57 POJ-PS-100-RP2 - Overall Principal Tensile Stresses and Trajectories at Service Loads

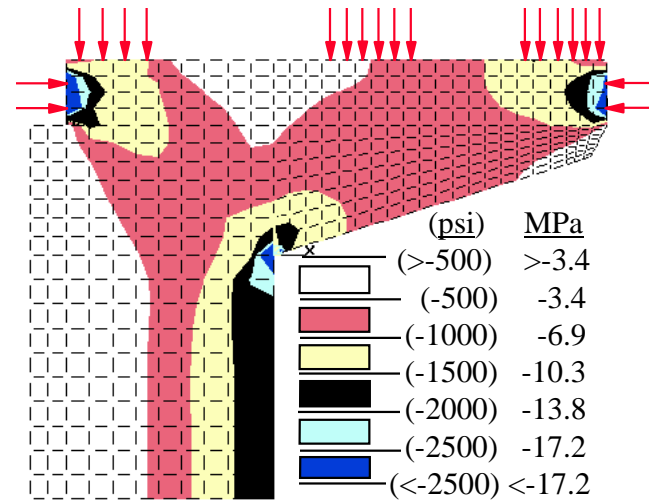
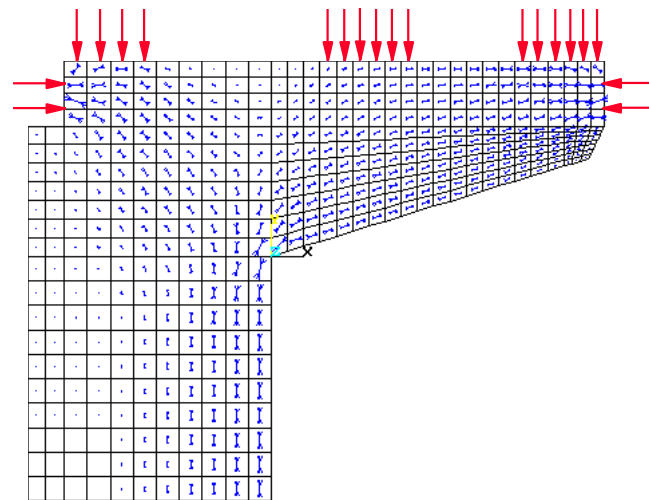
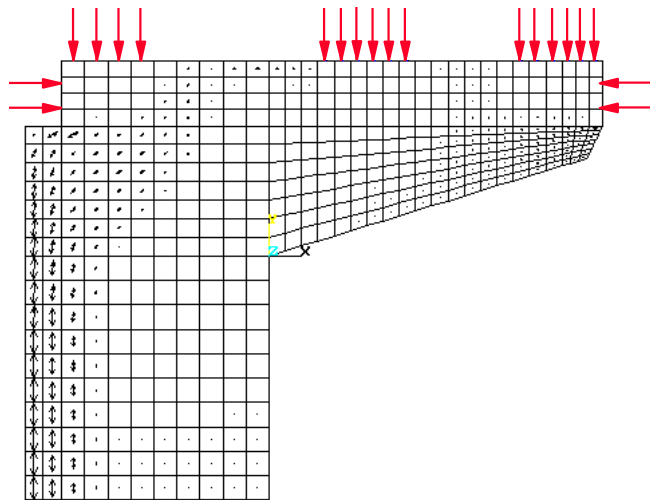


Figure 8.58 POJ-PS-100-RP2 - Overall Principal Compressive Stresses and Trajectories at Service Loads



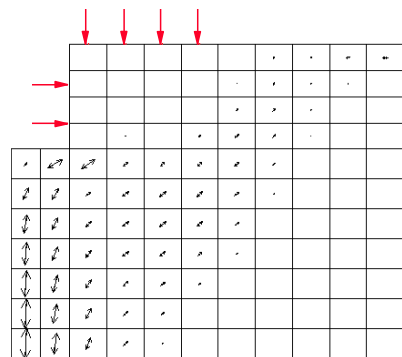
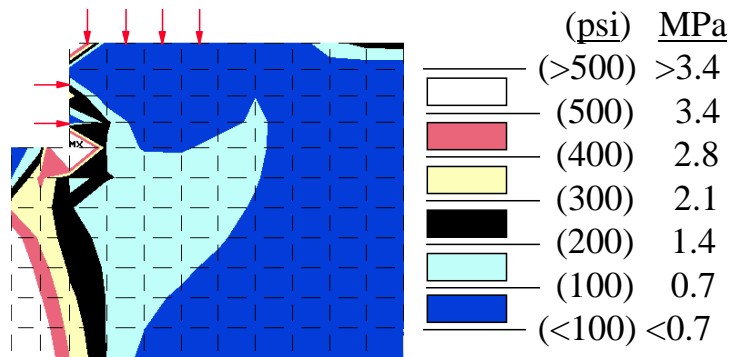


Figure 8.59 POJ-PS-100-RP2 - Joint Principal Tensile Stresses and Trajectories at Service Load

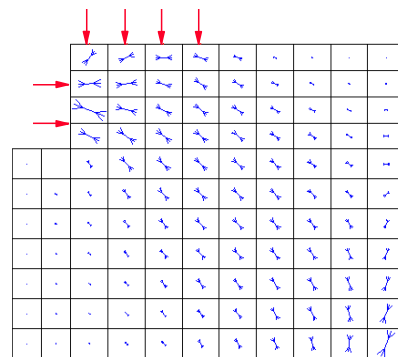
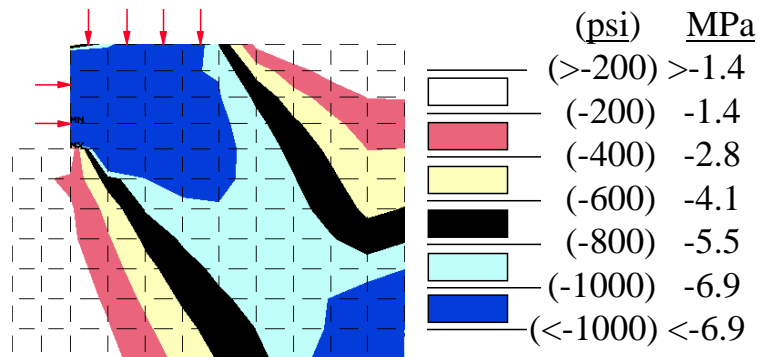


Figure 8.60 POJ-PS-100-RP2 - Joint Principal Tensile Stresses and Trajectories at Service Load

8.7.1.3. Design and Installation Details (POJ-PS-100-RP1 & RP2)

Design details for the external vertical post-tensioned repair are presented in Figure 8.61 through Figure 8.65. Positioning of the repair is shown from different views in Figure 8.61 through Figure 8.63. Detailed dimensions used for fabrication of the stiffened side plates and cap piece are presented in Figure 8.64 and Figure 8.65, respectively. Both repairs utilized the same plates and cap piece. Differences in the designs were limited to the quantity of post-tensioning force used.

Specimen POJ-PS-100-RP1 was designed assuming two layers of shear friction reinforcement were unbonded in the joint region. Twelve - 16 mm (5/8 in.) diameter Dywidag post-tensioning bars (two rows of four bars on each side) were used, providing a vertical post-tensioning force of $0.6 F_{pu}$ [1.34 MN (302 kips)] at service load and $0.75 F_{pu}$ [1.68 MN (378 kips)] at the onset of failure.

Specimen POJ-PS-100-RP2 used 8- 16 mm (5/8 in.) diameter Dywidag post-tensioning bars. Three bars on each side of the specimen were located adjacent to the specimen (in the near row of holes) and one bar was placed in the center hole on the outside row of holes (see Figure 8.63). Vertical post-tensioning force at service load was $0.6 F_{pu}$ [0.898 MN (202 kips)] and $0.75 F_{pu}$ [1.12 MN (252 kips)] at the onset of failure.

Fabrication of the repair hardware required a large quantity of steel plate and substantial welding. Fillet welds had a throat thickness of 0.6 cm (0.25 in.) and plug welds (1.2 cm (0.5 in.) in diameter) were used for the bottom plate of the cap piece. The cap piece was designed to resist a 1120 kN (252 kip) shear at ultimate loads and a 170 kN-m (1512 K-in.) moment. Confinement plates were welded to the cap piece to provide concrete confinement in the joint corner and reduce moments in the cap. The through-bolts in the pier region were designed to resist the 1120 kN (252 kip) shear and to resist the moment produced from the eccentric loading produced by the post-tensioning bars. All steel plates were specified to be Grade 50.

Twenty - 2.5 cm (1 in.) diameter cores were drilled through the pier, as shown Figure 8.61 and Figure 8.62. Small-diameter plastic tubes were used to pump cement grout

(with Interplast N expansive water reducing agent added) after the through-bolts were installed. Each bolt was torqued to 11.3 N-m (100 ft-lbs) after the grout had cured for two days.

The cap piece was seated by stressing the post-tensioning, thus pushing it down into contact with the specimen. Once the base plate of the cap was 2.5 cm (1 in.) above the top surface of the specimen, hydrostone was pooled under the cap piece and the cap piece was brought into full contact with the hydrostone.

After the cap was in place, silicone caulk was placed around the confinement plates of the cap and bottom side plates to provide a water-tight seal. Hydrostone was cast between the specimen and the plates to ensure uniform contact. Vertical post-tensioning bars were stressed in pairs, following a pattern that alternated the pair of bars that were being stressed. Two - 267 kN (60 Kip) capacity center-hole hydraulic rams were used for stressing the bars.

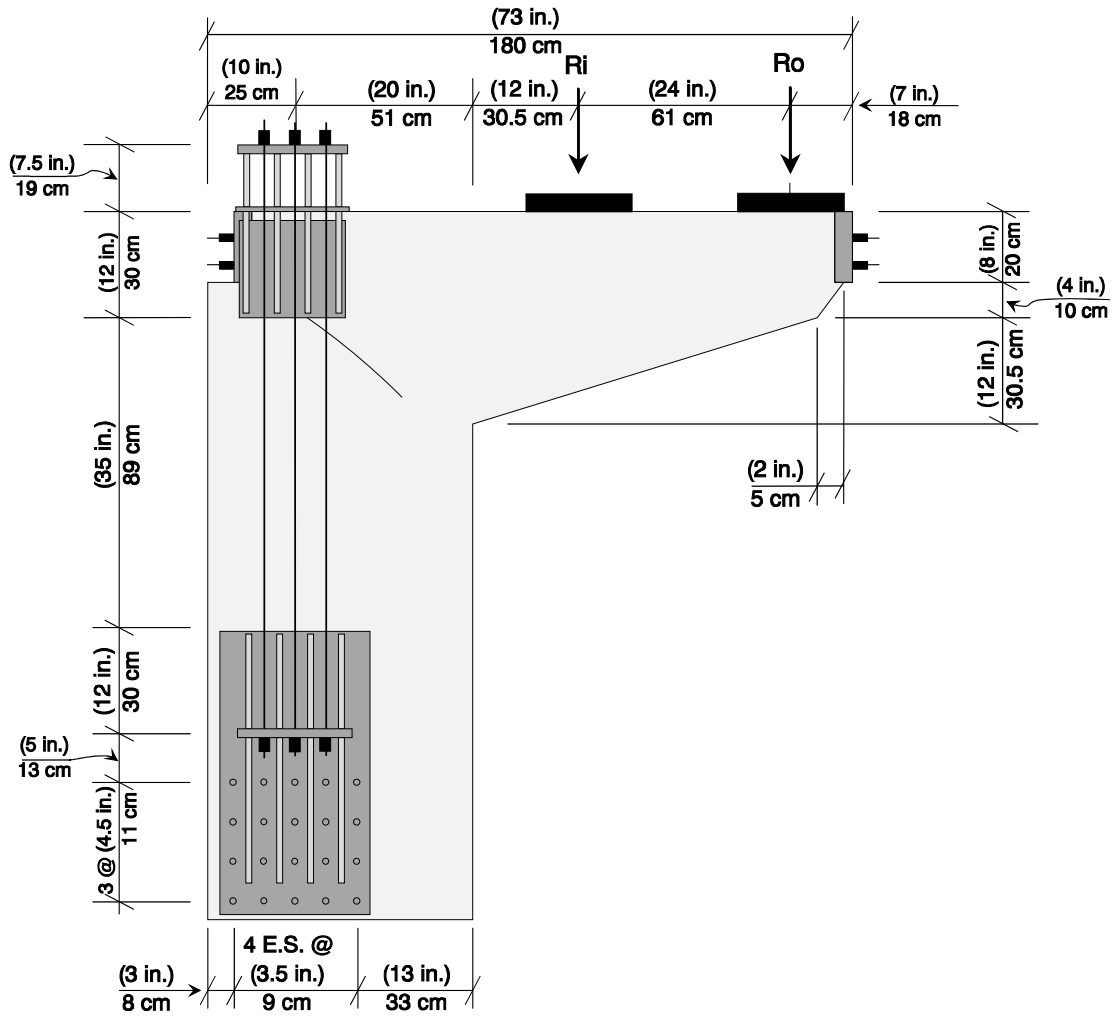


Figure 8.61 POJ-PS-100 Repair - Elevation

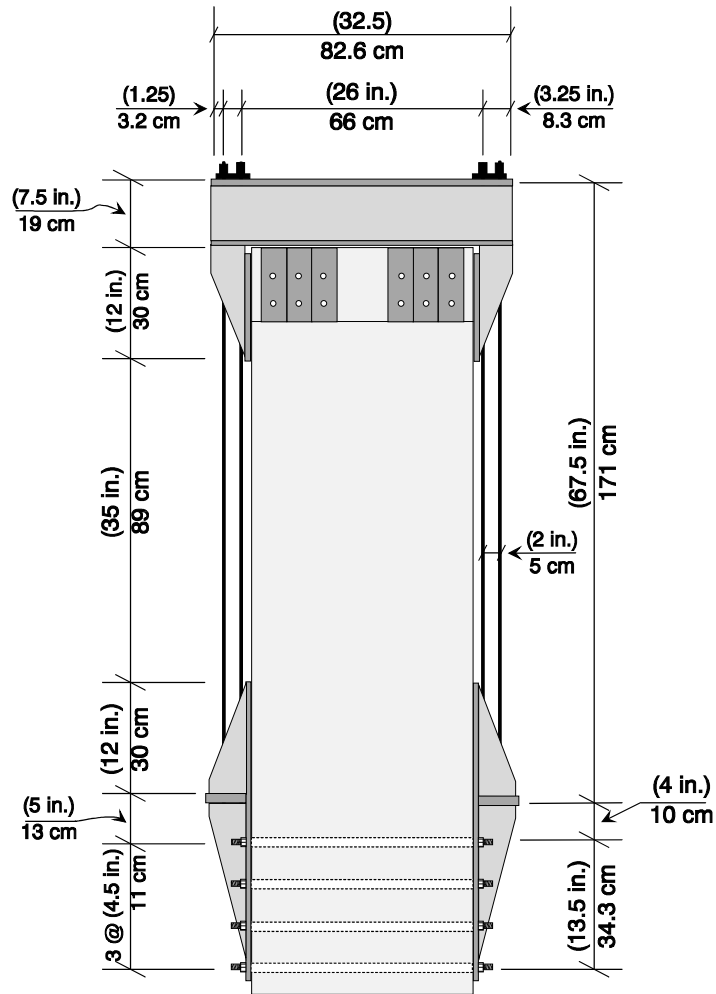


Figure 8.62 POJ-PS-100 Repair - End View

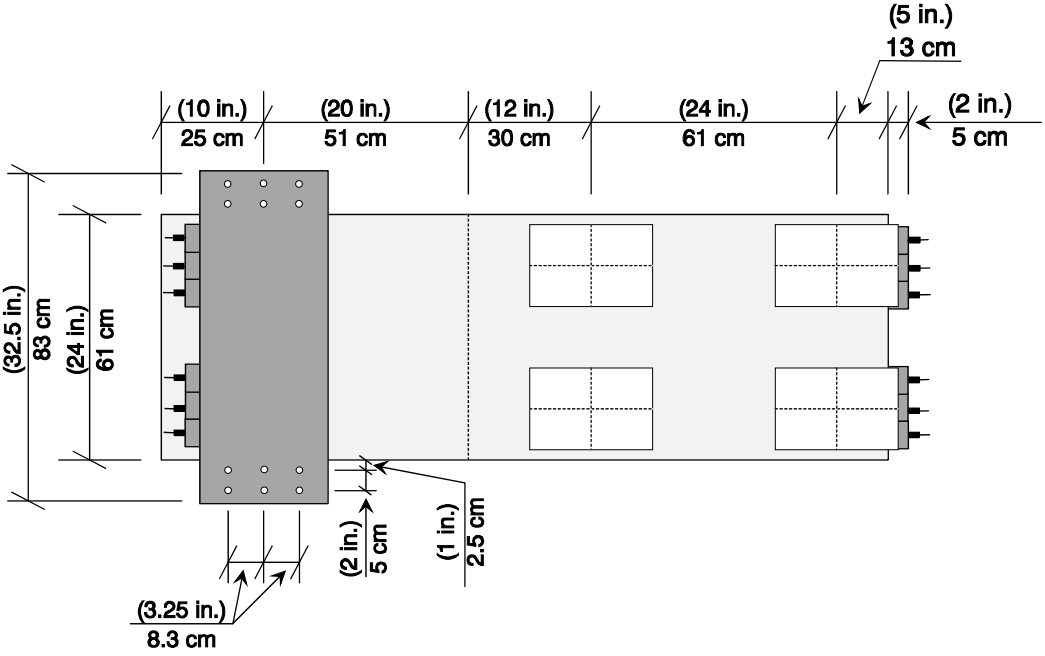


Figure 8.63 POJ-PS-100 Repair - Top View

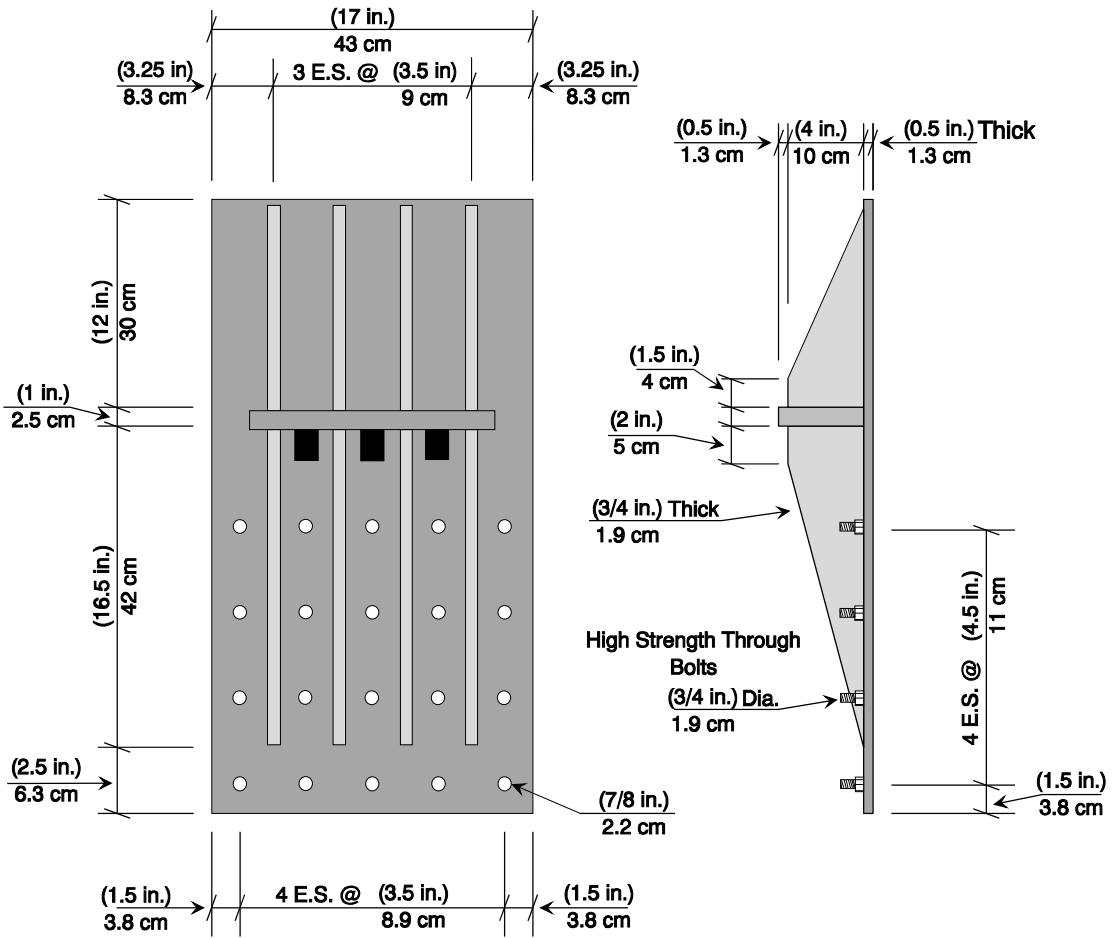


Figure 8.64 POJ-PS-100 Repair - Side Plate Dimensions and Details

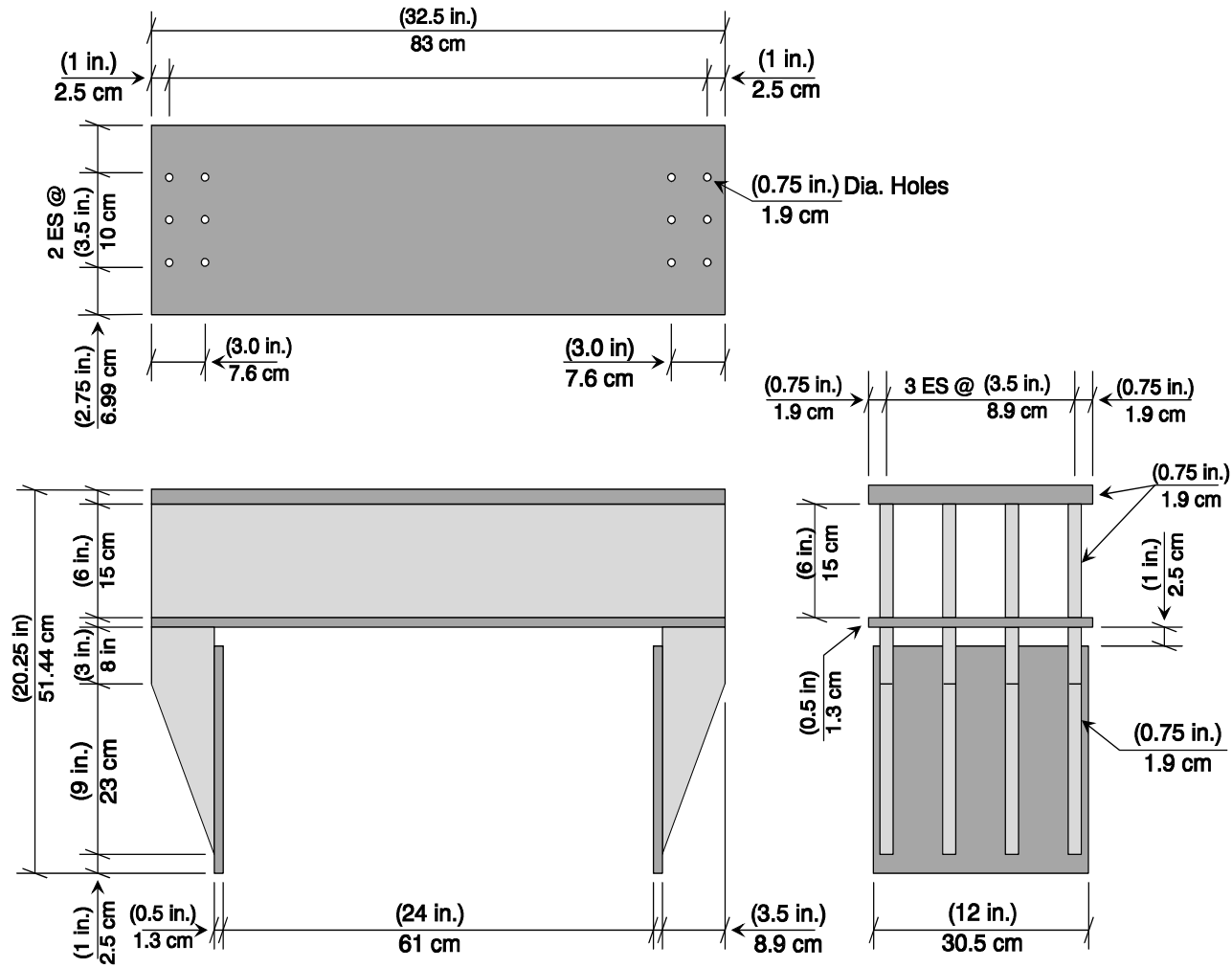


Figure 8.65 POJ-PS-100 Repair - Cap Beam Dimensions and Details

8.7.1.4. Behavior During Testing (POJ-PS-100-RP1 & RP2)

Repairs POJ-PS-100-RP1 and RP2 were installed after Specimen POJ-PS-100 was tested to the brink of failure, as discussed in Section 8.2.2. External post-tensioning bars were stressed with one-half dead load applied, and joint cracks were not epoxy injected before each test. Each repaired specimen was loaded incrementally to factored load/phi. Crack widths were measured before and after stressing the repair, at applied dead load, DL + 1/2 LL, DL + LL, and DL + 2LL. A detailed reporting of crack locations and crack-width measurements is presented by Scott [6].

Applied moment vs. overhang tip displacement responses for Specimens POJ-PS-100-RP1 and RP2 are presented in Figure 8.66 and Figure 8.67, respectively. Specimen POJ-PS-100-RP1 had a nearly linear moment-displacement response up to applied factored loads/phi. Loss of pressure in the interior loading ram (Ri) caused a brief drop in applied moment at 1.03 times factored loads. Repair POJ-PS-100-RP2 (with reduced post-tensioning force) also demonstrated nearly linear moment-displacement response to applied factored load / phi. This specimen was loaded beyond factored load / phi to determine failure load. Increased tip deflections (shown in Figure 8.67), increased post-tensioning strain (shown in Figure 8.69), and reduced stiffness at an applied load equal to 1.24 times factored load indicated the specimen was near failure. Additional load was not applied to preserve the unrepaired specimen for ultimate load testing, discussed in Section 8.2.2.5. Average recorded post-tensioning strains for both repairs indicated post-tensioning forces were below $0.6 F_{pu}$ at applied service loads and were at $0.60 F_{pu}$ and $0.62 F_{pu}$ at applied factored load/phi for Specimens POJ-PS-100-RP1 and RP2, respectively. Post-tensioning for Specimen POJ-PS-100-RP2 achieved $0.66 F_{pu}$ at 1.24 times applied factored loads. In conclusion, both repairs provided sufficient strength to resist factored load / phi.

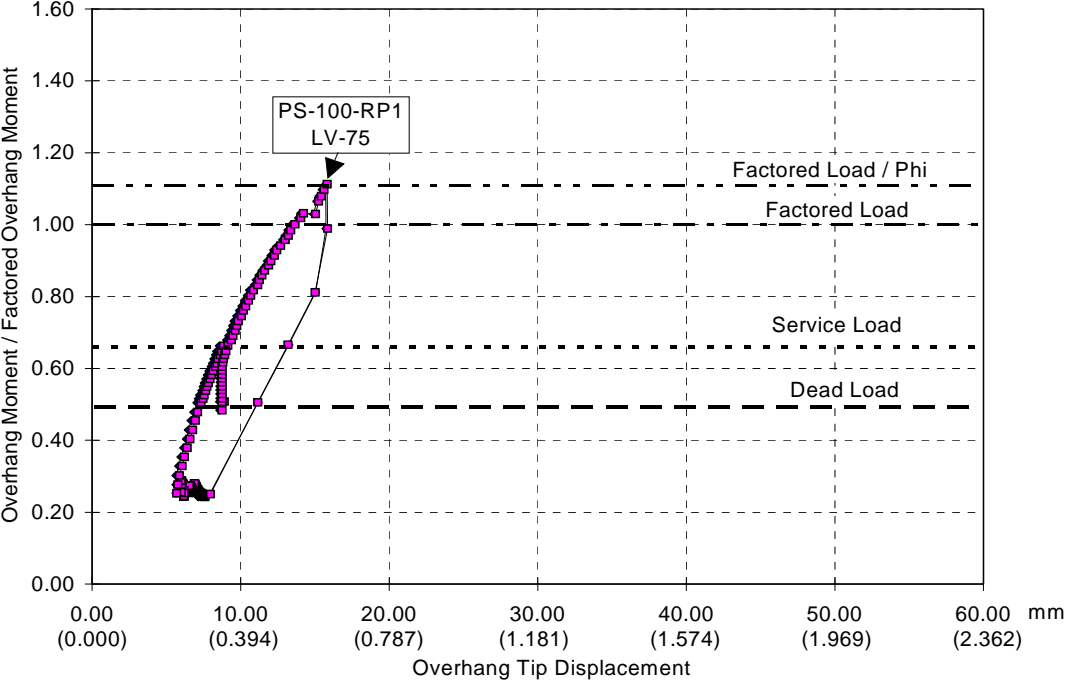


Figure 8.66 POJ-PS-100-RP1 Overhang Moment vs. Tip Deflection Response

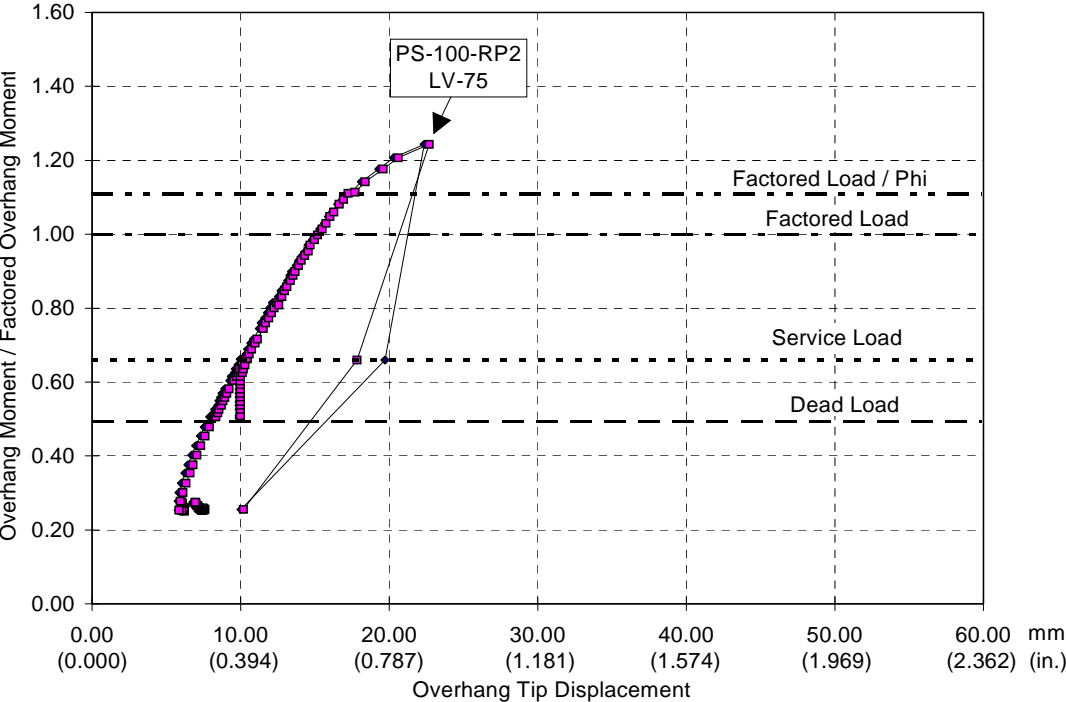


Figure 8.67 POJ-PS-100-RP2- Overhang Moment vs. Tip Deflection Response

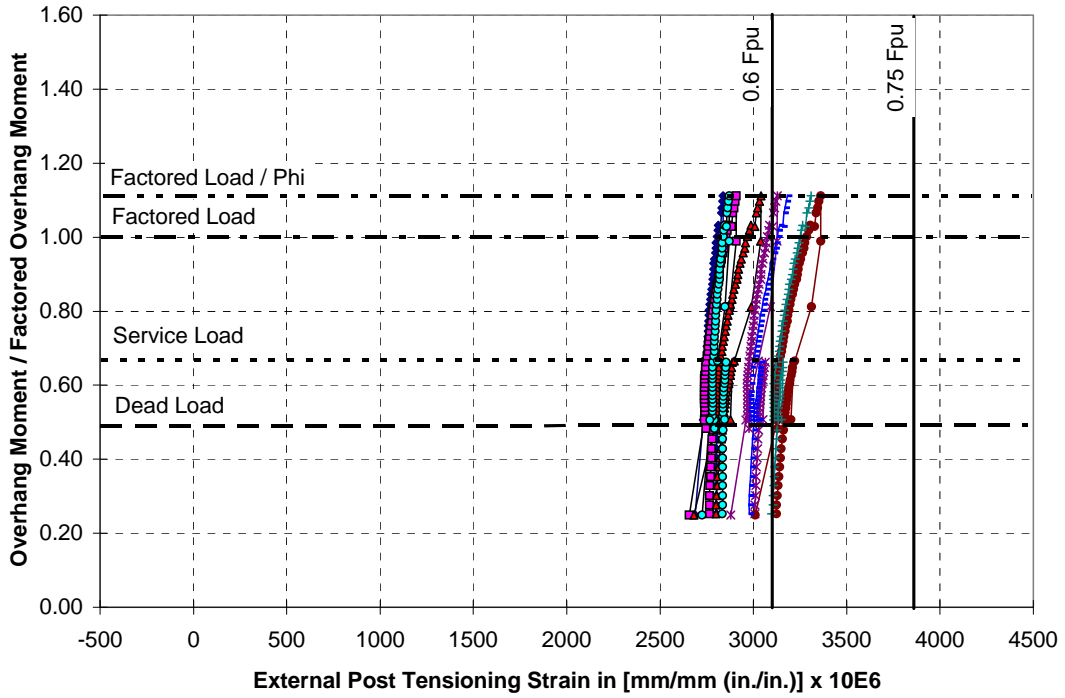


Figure 8.68 Recorded Strain in External PT Bars for POJ-PS-100-RP1

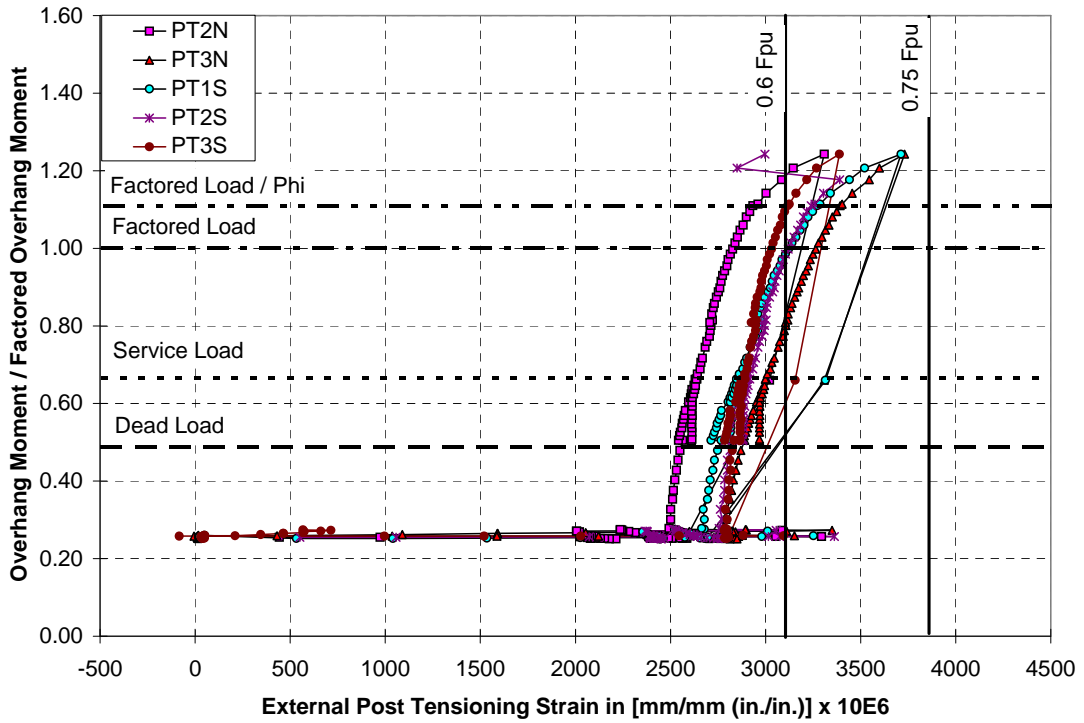


Figure 8.69 Recorded Strain in External PT Bars for POJ-PS-100-RP2

8.	377
8.7. Analysis and Behavior of Selected POJ-PS-100 Repairs	377
8.7.1. External Vertical Post-Tensioned Repairs (POJ-PS-100-RP1 & RP2)	377
8.7.1.1. Capacity Calculation (POJ-PS-100-RP1 & RP2)	379
8.7.1.2. Finite Element Analysis (POJ-PS-100-RP1 & RP2)	383
8.7.1.3. Design and Installation Details (POJ-PS-100-RP1 & RP2)	388
8.7.1.4. Behavior During Testing (POJ-PS-100-RP1 & RP2)	395
Figure 8.49 Elevation of POJ-PS-100-RP1 & RP2 External Vertical PT Repairs	378
Figure 8.50 POJ-PS-100-RP1- Free Body and Reinforcement Locations Used in Capacity Calculation	380
Figure 8.51: POJ-PS-100-RP2 Free Body and Reinforcement Locations Used in Capacity Calculation	381
Figure 8.52 Free Body Used to Determine Post-Tensioning Force for Specimens POJ-PS-100-RP1 & RP2	382
Figure 8.53 POJ-PS-100-RP1 -Overall Principal Tensile Stresses and Trajectories at Service Load	384
Figure 8.54 POJ-PS-100-RP1 - Overall Principal Compressive Stresses and Trajectories at Service Load	384
Figure 8.55 POJ-PS-100-RP1 - Joint Principal Tensile Stresses and Trajectories at Service Load	385
Figure 8.56 POJ-PS-100-RP1 - Joint Principal Compressive Stresses and Trajectories at Service Load	385
Figure 8.57 POJ-PS-100-RP2 - Overall Principal Tensile Stresses and Trajectories at Service Loads	386
Figure 8.58 POJ-PS-100-RP2 - Overall Principal Compressive Stresses and Trajectories at Service Loads	386
Figure 8.59 POJ-PS-100-RP2 - Joint Principal Tensile Stresses and Trajectories at Service Load	387

Figure 8.60 POJ-PS-100-RP2 - Joint Principal Tensile Stresses and Trajectories at Service Load	387
Figure 8.61 POJ-PS-100 Repair - Elevation	390
Figure 8.62 POJ-PS-100 Repair - End View	391
Figure 8.63 POJ-PS-100 Repair - Top View	392
Figure 8.64 POJ-PS-100 Repair - Side Plate Dimensions and Details	393
Figure 8.65 POJ-PS-100 Repair - Cap Beam Dimensions and Details.....	394
Figure 8.66 POJ-PS-100-RP1 Overhang Moment vs. Tip Deflection Response.....	396
Figure 8.67 POJ-PS-100-RP2- Overhang Moment vs. Tip Deflection Response	396
Figure 8.68 Recorded Strain in External PT Bars for POJ-PS-100-RP1	397
Figure 8.69 Recorded Strain in External PT Bars for POJ-PS-100-RP2	397

CHAPTER 9
ANALYSIS OF TEST RESULTS
FROM CANTILEVER BENT STRENGTHENING STUDY

9.1 Introduction

Three potential repair methods for the San Antonio ‘Y’ substructures were selected for study: an external vertical post-tensioned repair, an external diagonal post-tensioned repair, and an internal vertical post-tensioned repair. The prototype reinforced concrete specimen (POJ-RC-100-2) was strengthened using an external diagonal post-tensioned repair (POJ-RC-100-RP1) and an internal vertical post-tensioned repair (POJ-RC-100-RP2). The prototype prestressed concrete specimen (POJ-PS-100) was strengthened using different levels of external vertical post tensioning.

The purpose of the study was to evaluate the response of each repaired specimen at applied factored loads / ϕ (where $\phi = 0.9$). It was generally not possible to test the repairs to failure because Specimens POJ-RC-100-2 and POJ-PS-100 were each used for more than one repair. In addition to the capacity criterion, each repair was evaluated for constructability, estimated cost, durability, and aesthetics. A decision matrix was used to identify which repair method best met the design criteria.

9.2 Comparison of Overhang Moment vs. Tip Deflection Response

9.2.1 Specimen POJ-RC-100-2 and Repairs RP1 and RP2

The normalized overhang moment vs. deflection response for the external diagonal post-tensioned repair (POJ-RC-100-RP1) and the internal vertical post-tensioned repair (POJ-RC-100-RP2) are plotted with the response of the unrepaired test specimen (POJ-RC-100-2) in Figure 9.1. The POJ-RC-100-2 specimen failed at an applied load below service-level loads. It was concluded from the tests that both the external diagonal and internal vertical post-tensioned repairs (Specimens POJ-RC-100-RP1 and -RP2, respectively) satisfied the strength criterion. Moment-deflection response for both repaired specimens indicated limited reduction in stiffness throughout the entire response range.

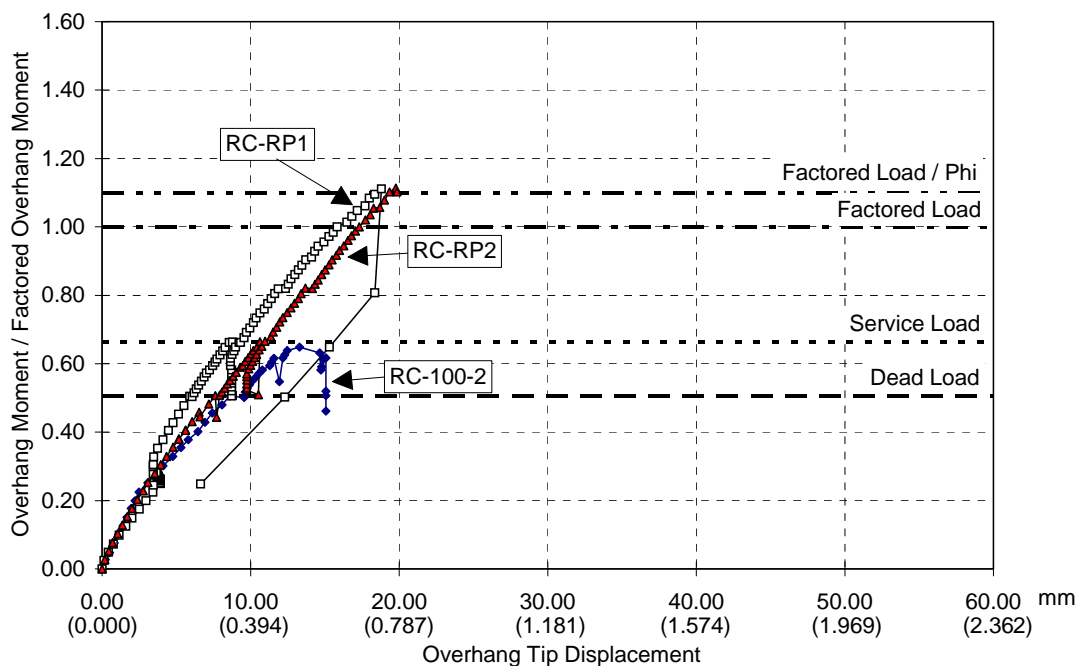


Figure 9.1 Comparison of Overhang Tip Displacement Response for Specimen POJ-RC-100-2, and Repairs RP1 and RP2

9.2.2 Specimen POJ-PS-100 and Repairs RP1 and RP2

Normalized overhang moment vs. deflection response for the external vertical post-tensioned repair (POJ-PS-100-RP1) and the external vertical repair with reduced post-tensioning (POJ-PS-100-RP2) are plotted with the response of the unrepaired specimen (POJ-PS-100) in Figure 9.2. Specimen POJ-PS-100-RP1 had a slightly stiffer moment-displacement response than Specimen POJ-PS-100-RP2, which is consistent with the larger external post-tensioning force and greater number of post-tensioning bars used in Specimen POJ-PS-100-RP2. Applied loads for Specimen POJ-PS-100-RP2 were increased beyond applied factored loads / phi in an attempt to determine the ultimate strength of one of the strengthened specimens. The change in slope of the moment-deflection response at loads exceeding factored load/phi in Figure 9.2 was indicative of non-linear behavior in the specimen. However, testing was discontinued in order to limit damage to Specimen POJ-PS-100, which was subsequently tested to failure. The results from these tests indicated both repairs satisfied the design-strength criterion.

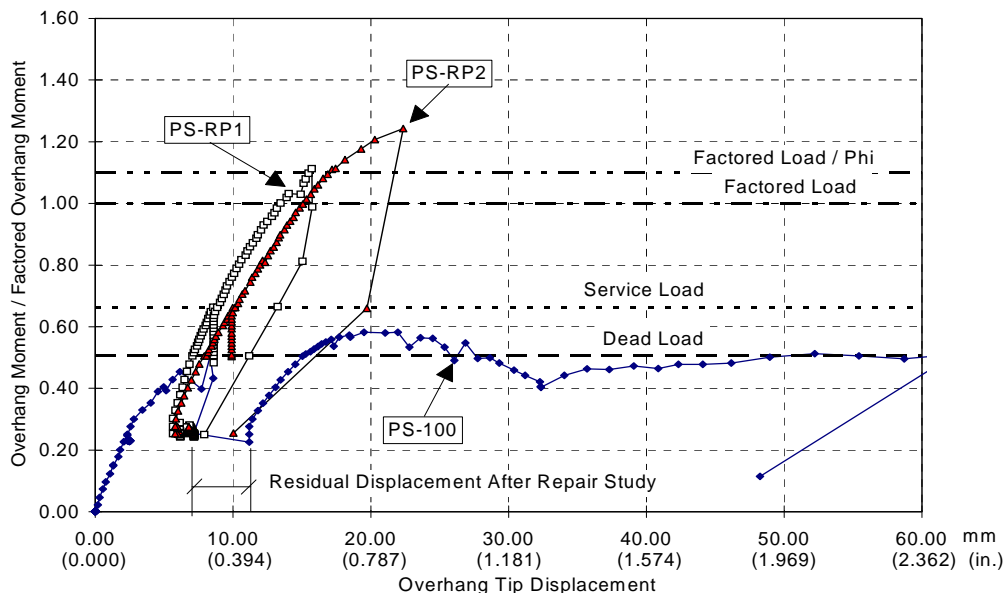


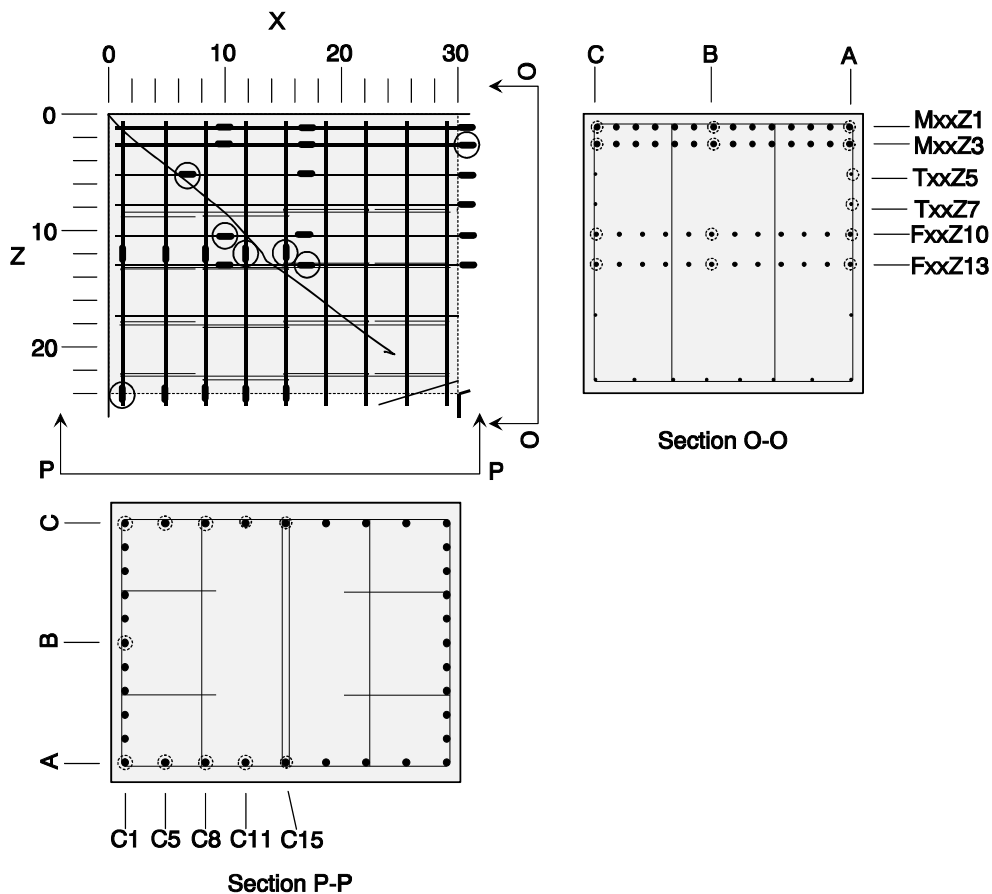
Figure 9.2 Comparison of Overhang Tip Displacement Behavior for Specimen POJ-PS-100 and Repairs RP1 and RP2

9.3 Comparison of Measured Strain Response

9.3.1 Reinforced Concrete Design (POJ-RC-100-2) Repairs

Strain gages were attached to the longitudinal and transverse reinforcement in Specimen POJ-RC-100-2 before the specimen was cast. Strain gage readings were monitored to determine if the two repairs reduced tensile stresses in the longitudinal reinforcement anchored in the joint region, and to determine if yielding or bond slip of the mild reinforcement occurred. The names and locations of strain gages in the joint are presented in Figure 9.3. Overhang moment vs. measured strain for Specimen POJ-RC-100-2 is compared with responses for the external diagonal post-tensioned repair (POJ-RC-100-RP1) and the internal vertical post-tensioned repair (POJ-RC-100-RP2) in Figure 9.4 through Figure 9.10. Strain responses plotted in Figure 9.4 through Figure 9.10 (gages T7Z5A, F10Z10A, F17Z13A, M31Z3A, C1Z24B, C11Z12C, and C15Z12A, respectively) are for seven strain gages located in highly stressed regions of the joint (gages circled in Figure 9.3).

Based on the moment vs. strain responses measured by the seven gages, it was concluded the longitudinal mild reinforcement experienced a reduction in tensile stresses due to the application of external post-tensioning. Bond failure of the joint reinforcement was not suspected because the moment-strain curves were continuous and did not contain increases in have increasing slope, which is indicative of slip. Strain gage T7Z5A (shown in Figure 9.4) had strains in excess of yield at applied factored load / ϕ , which was another indication that bar anchorage of these select reinforcing bars was adequate. Other measured strains were less than 75 percent of yield strain at applied factored load / ϕ .



Overhang Bars	Section X=7	Section X=10			Section X=17			Section X=31		
	A	A	B	C	A	B	C	A	B	C
Level Z1		M10Z1A	M10Z1B	M10Z1C	M17Z1A	M17Z1B	M17Z1C	M31Z1A	M31Z1B	M31Z1C
Level Z3		M10Z3A	M10Z3B	M10Z3C	M17Z3A	M17Z3B	M17Z3C	M31Z3A	M31Z3B	M31Z3C
Level Z5	T7Z5A							T31Z5A		
Level Z7								T31Z7A		
Level Z10		F10Z10A	F10Z10B	F10Z10C	F17Z10A	F17Z10B	F17Z10C	F31Z10A	F31Z10B	F31Z10C
Level Z13		F10Z13A		F10Z13C	F17Z13A	F17Z13B	F17Z13C	F31Z13A	F31Z13B	F31Z13C

Pier Bars	Section Z=12			Section Z=24		
	A	B	C	A	B	C
Level X1	C1Z12A	C1Z12B	C1Z12C	C1Z24A	C1Z24B	C1Z24C
Level X5	C5Z12A		C5Z12C	C5Z24A		C5Z24C
Level X8	C8Z12A		C8Z12C	C8Z24A		C8Z24C
Level X11	C11Z12A		C11Z12C	C11Z24A		C11Z24C
Level X15	C15Z12A		C15Z12C	C15Z24A		C15Z24C

Figure 9.3 POJ-RC-100-2 - Joint Region Strain Gage Locations and Labels

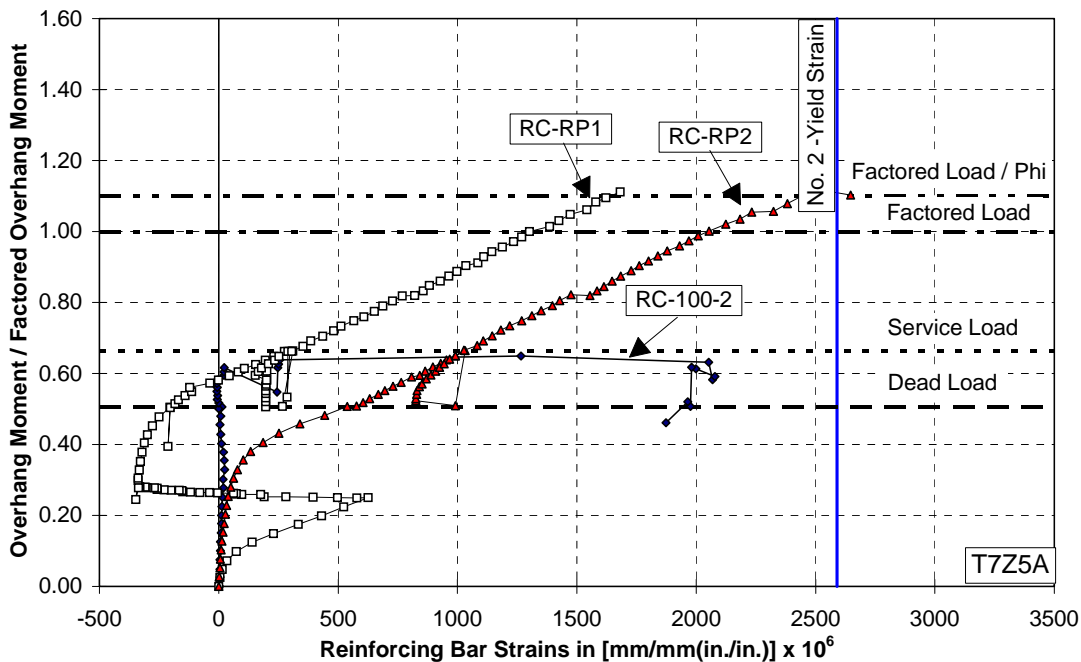


Figure 9.4 Comparison of Strain Gage T7Z5A Response for Specimen POJ-RC-100-2 and Repairs RP1 and RP2

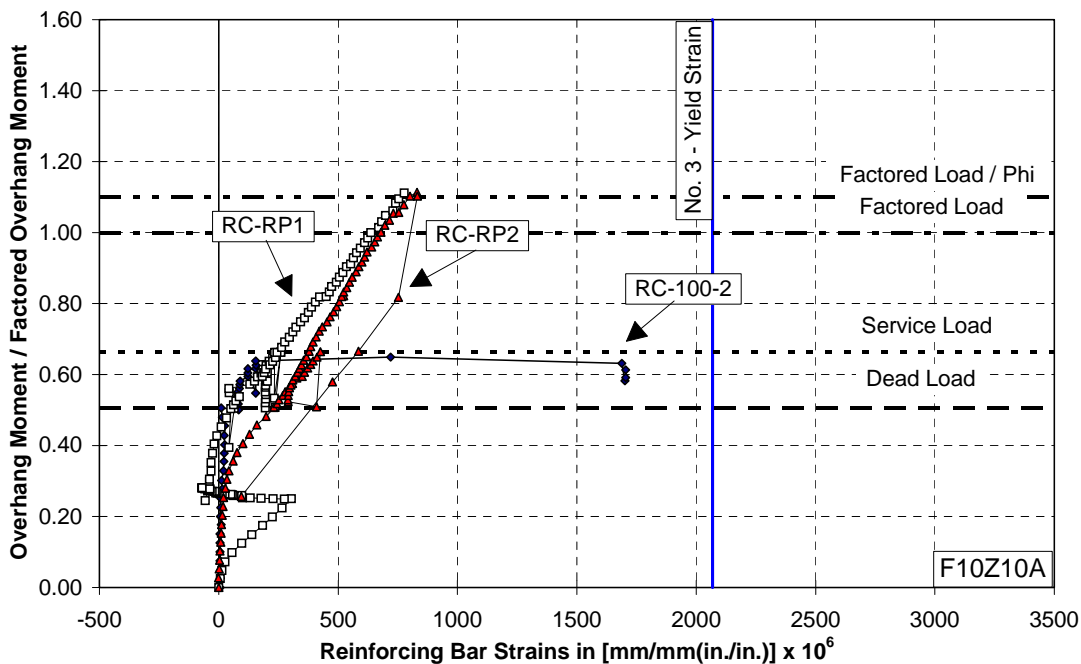


Figure 9.5 Comparison of Strain Gage F10Z10A Response for Specimen POJ-RC-100-2 and Repairs RP1 and RP2

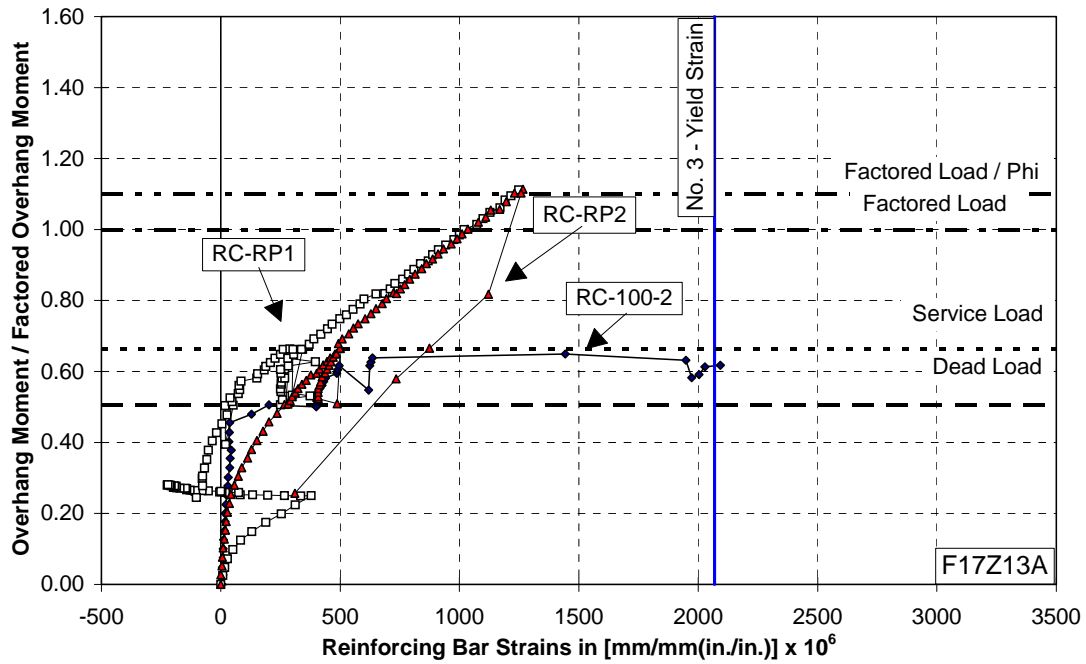


Figure 9.6 Comparison of Strain Gage F17Z13A Response for Specimen POJ-RC-100-2 and Repairs RP1 and RP2

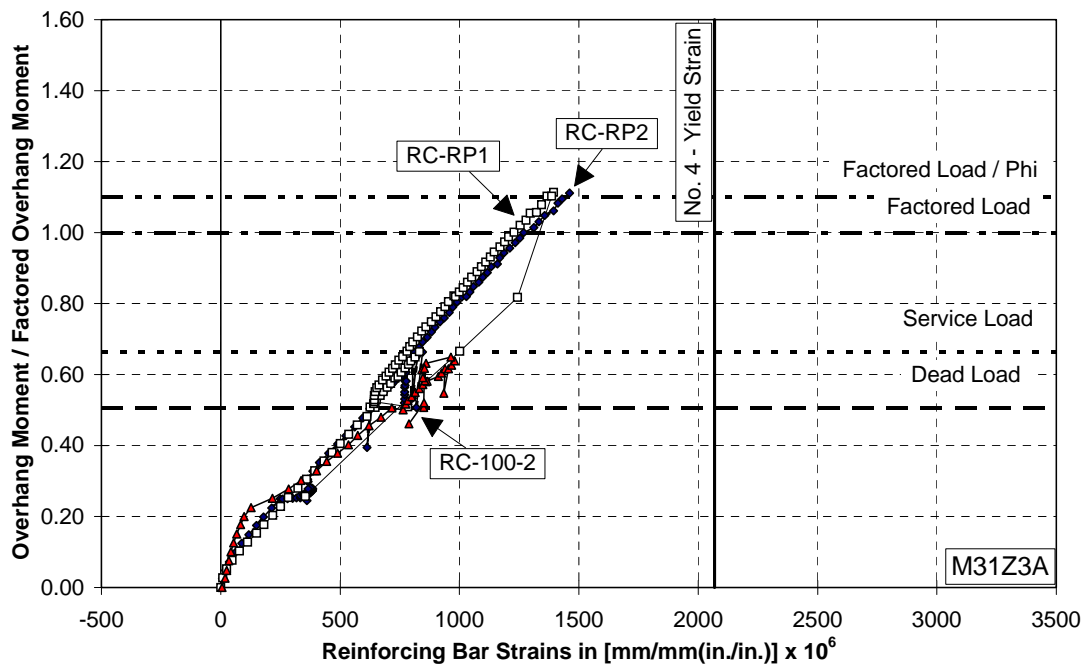


Figure 9.7 Comparison of Strain Gage M31Z3A Response for Specimen POJ-RC-100-2 and Repairs RP1 and RP2

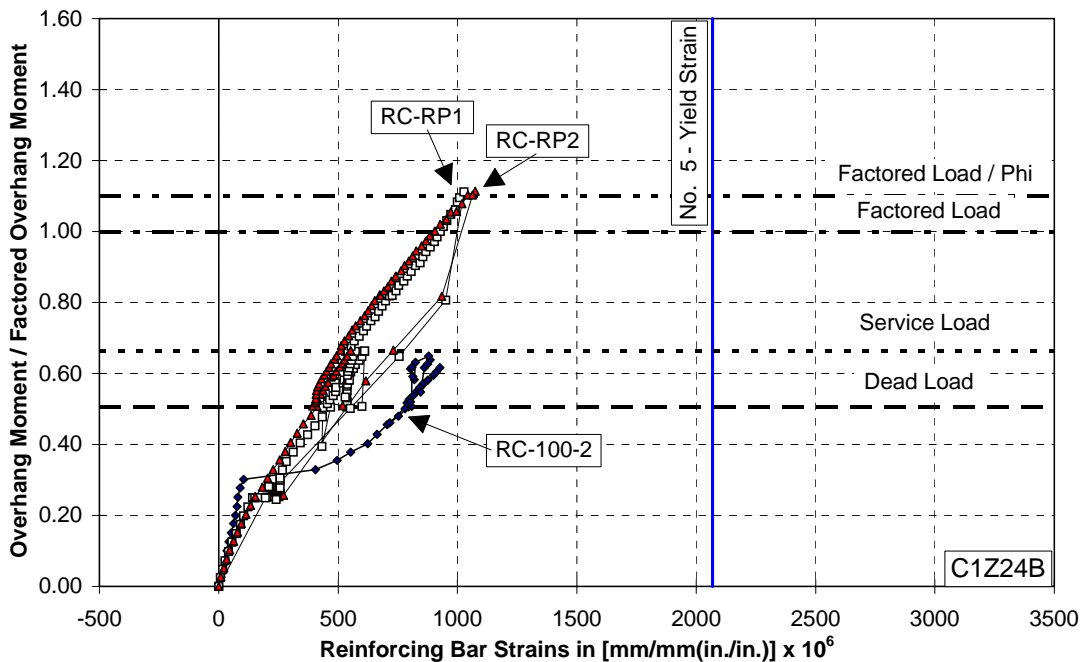


Figure 9.8 Comparison of Strain Gage C1Z24B Response for Specimen POJ-RC-100-2 and Repairs RP1 and RP2

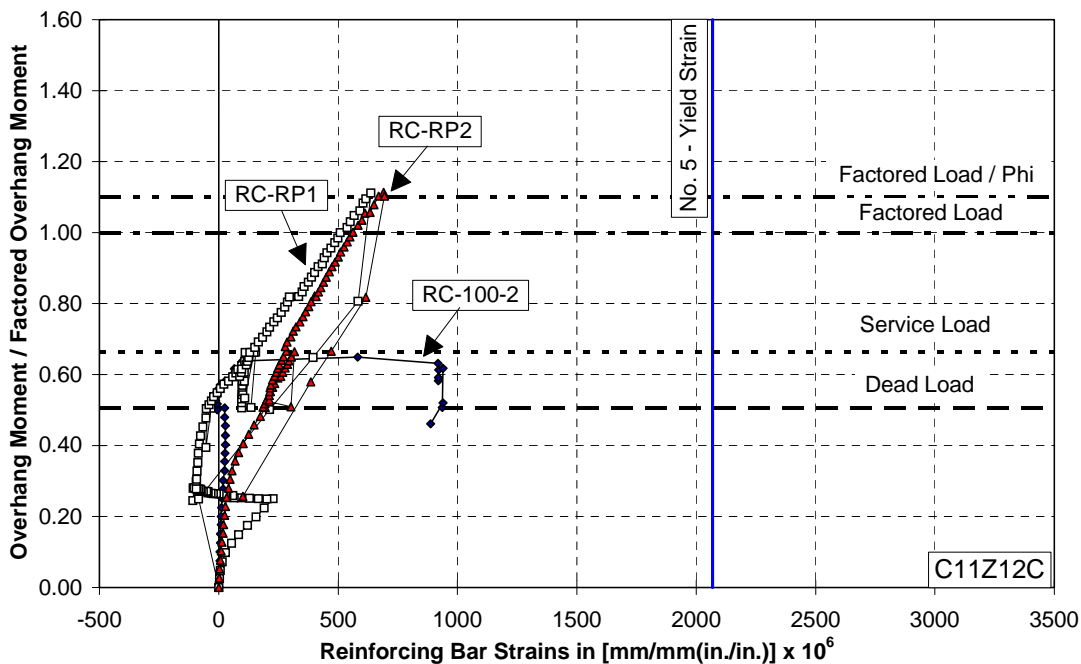


Figure 9.9 Comparison of Strain Gage C11Z12C Response for Specimen POJ-RC-100-2 and Repairs RP1 and RP2

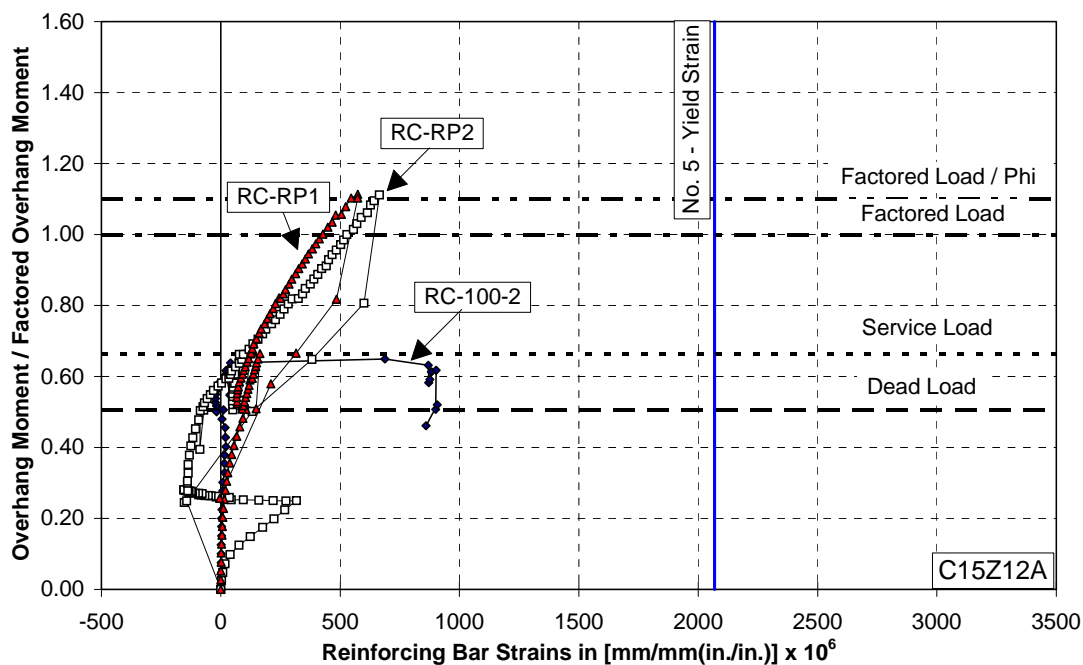


Figure 9.10 Comparison of Strain Gage C15Z12A Responses for Specimen POJ-RC-100-2 and Repairs RP1 and RP2

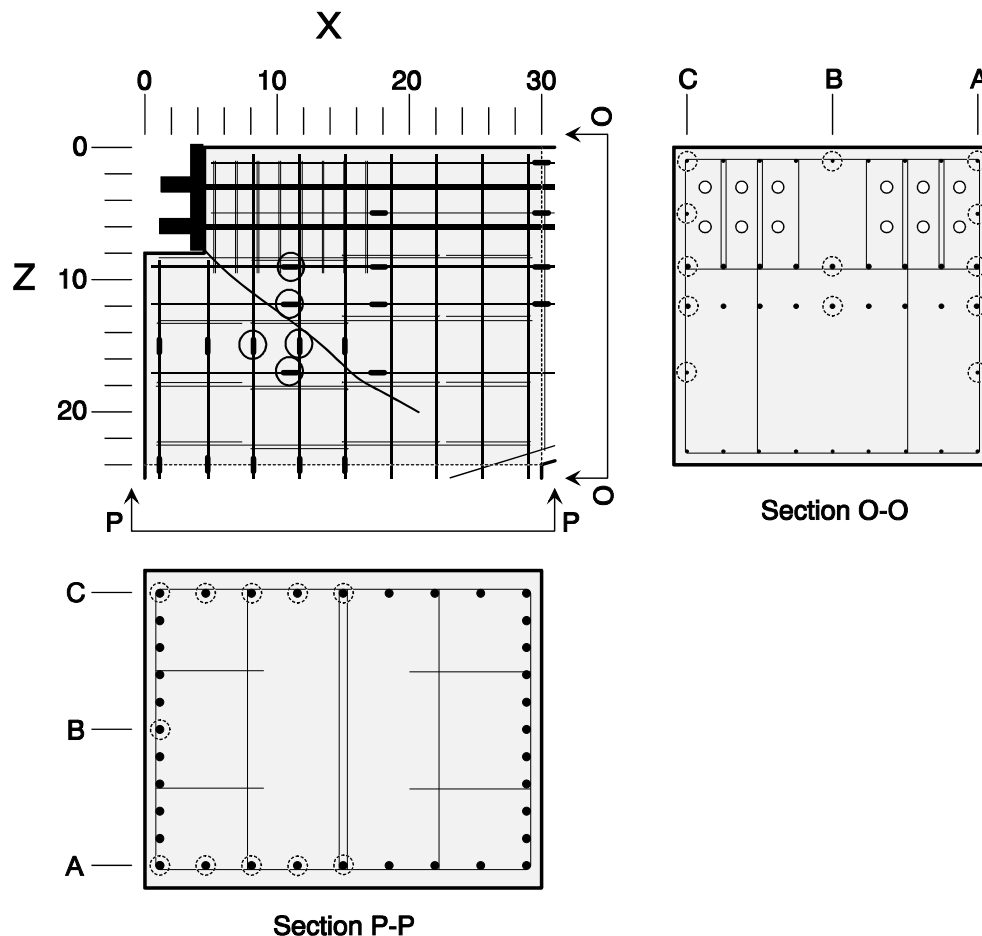
9.3.2 Specimen with Fully-Prestressed Overhang (POJ-PS-100) Repairs

Overhang moment vs. strain responses for Specimen POJ-PS-100 are compared with responses for the external vertical post-tensioned repair (POJ-PS-100-RP1) and the reduced force external vertical post-tensioned repair (POJ-PS-100-RP2) in Figure 9.12 through Figure 9.16. Strain gage labels and locations for gages in the joint region are presented in Figure 9.11. Strain gage responses plotted in Figure 9.12 through Figure 9.16 (gages T10Z17A, F10Z9B, F10Z12B, C8Z12A, C11Z12C, respectively) are for five strain gages located in highly stressed regions of the joint (identified in Figure 9.11).

Moment-strain response these strain gages indicated the two repairs provided a similar reduction of tensile stresses in the joint reinforcement. The reinforcing strains in the joint region were used to identify yielding or bond slippage of the mild reinforcing steel. The large external post-tensioning force used for the POJ-PS-100-RP1 repair reduced the strains in the reinforcing and reduced the size of all major joint and pier cracks. At applied service loads, the cracks opened and at that point measurable increases in reinforcing strains were

recorded. The reduced external post-tensioned repair (POJ-PS-100-RP2) provided adequate strength to resist applied factored loads / phi, but strains in the pier and joint reinforcing steel increased after dead loads were applied. The large strain increases in the C8Z12A and C11Z12C bars after factored loads / phi were applied indicated the specimen was near failure load. The moment-strain curves for both specimens were continuous and had a positive slope, indicating bond failure did not occur before each test was discontinued.

Finite element analyses of the POJ-PS-100-RP1 and RP2 specimens, described in Sections 8.7.1.2, indicated the level of principal tensile stresses in the region of the diagonal joint crack were less than the assumed cracking tensile stress of $7\sqrt{f'_c}$ [3.4 MPa (500 psi)]. The joint region was expected to remain uncracked under applied service loads, if the cracks were epoxy injected before testing each specimen.



Overhang Bar	Section X=10			Section X=17			Section X=31		
	A	B	C	A	B	C	A	B	C
Level Z1							T31Z1A	T31Z1B	T31Z1C
Level Z5				T17Z5A			T31Z5A		T31Z5C
Level Z9	F10Z9A	F10Z9B	F10Z9C	F17Z9A	F17Z9B	F17Z9C	F31Z9A	F31Z9B	F31Z9C
Level Z12	F10Z12A	F10Z12B	F10Z12C	F17Z12A	F17Z12B	F17Z12C	F31Z12A	F31Z12B	F31Z12C
Level Z17	T10Z17A			T17Z17A					

Pier Bars	Section Z=12			Section Z=24		
	A	B	C	A	B	C
Level X1	C1Z12A	C1Z12B	C1Z12C	C1Z24A	C1Z24B	C1Z24C
Level X5	C5Z12A		C5Z12C	C5Z24A		C5Z24C
Level X8	C8Z12A		C8Z12C	C8Z24A		C8Z24C
Level X11	C11Z12A		C11Z12C	C11Z24A		C11Z24C
Level X15	C15Z12A		C15Z12C	C15Z24A		C15Z24C

Figure 9.11 POJ-PS-100 Joint Strain Gage Locations and Labels

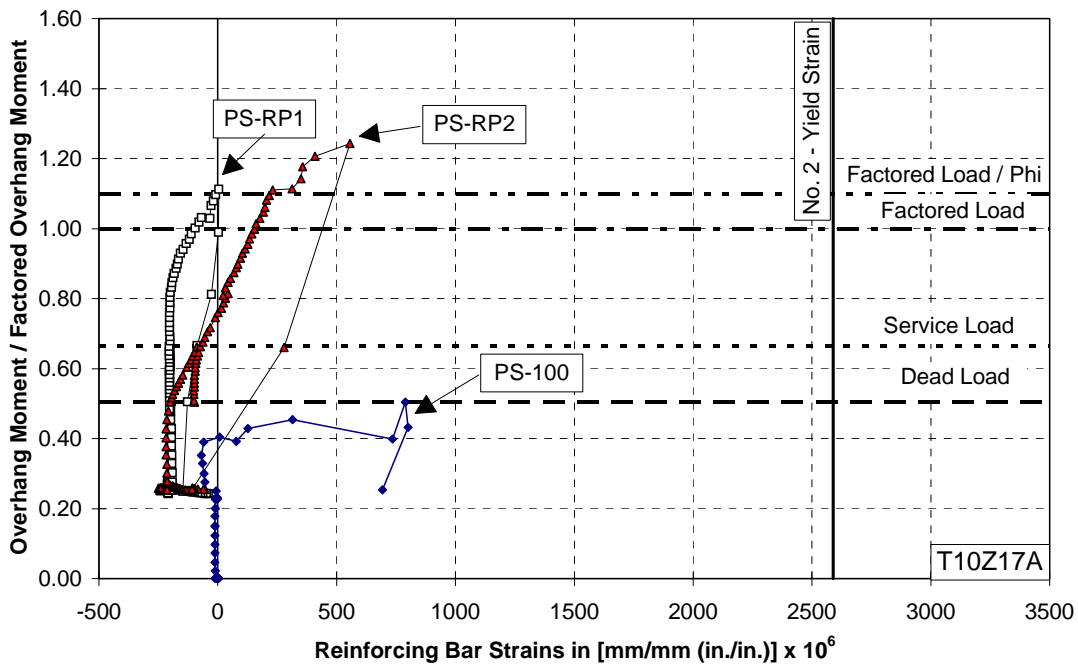


Figure 9.12 Comparison of Strain Gage T10Z17A Responses for Specimen POJ-PS-100 and Repairs RP1 and RP2

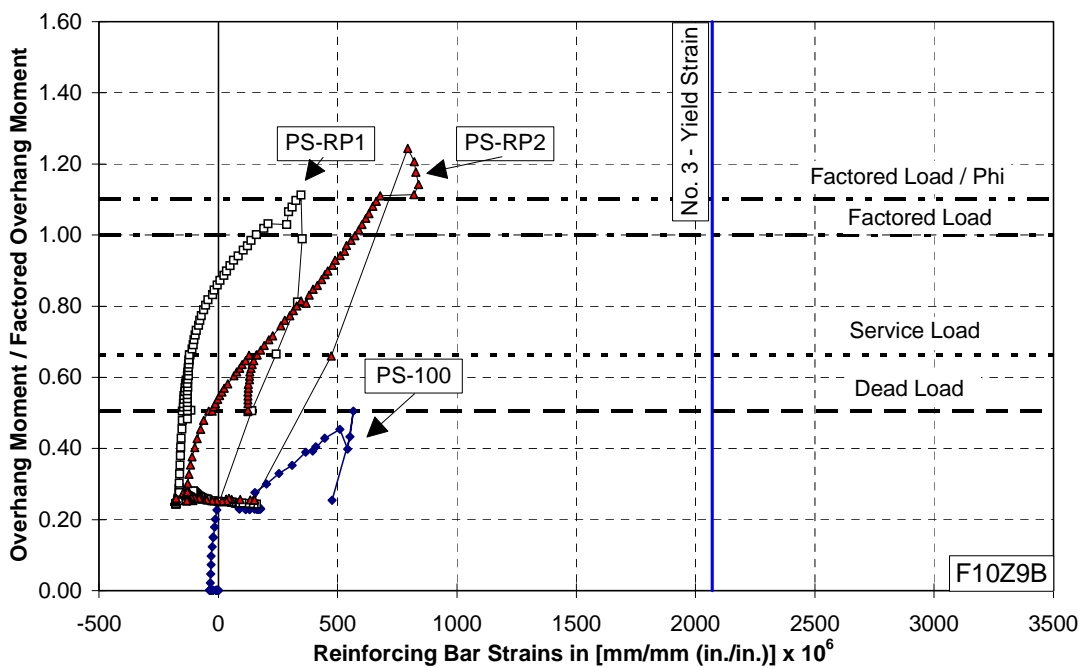


Figure 9.13 Comparison of Strain Gage F10Z9B Responses for Specimen POJ-PS-100 and Repairs RP1 and RP2

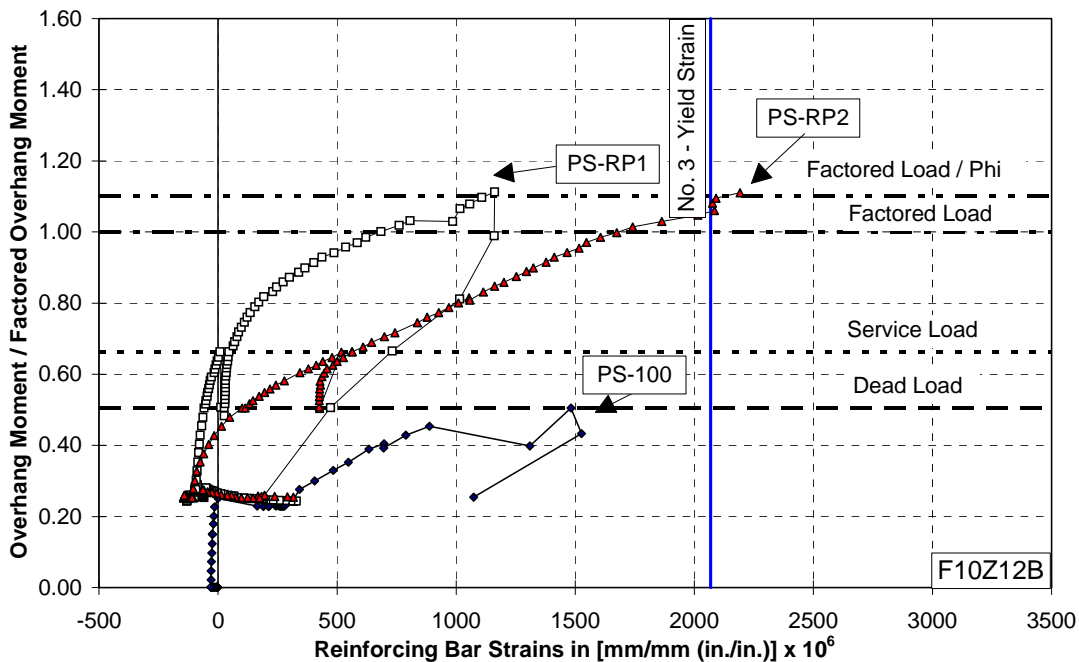


Figure 9.14 Comparison of Strain Gage F10Z12B Response for Specimen POJ-PS-100 and Repairs RP1 and RP2

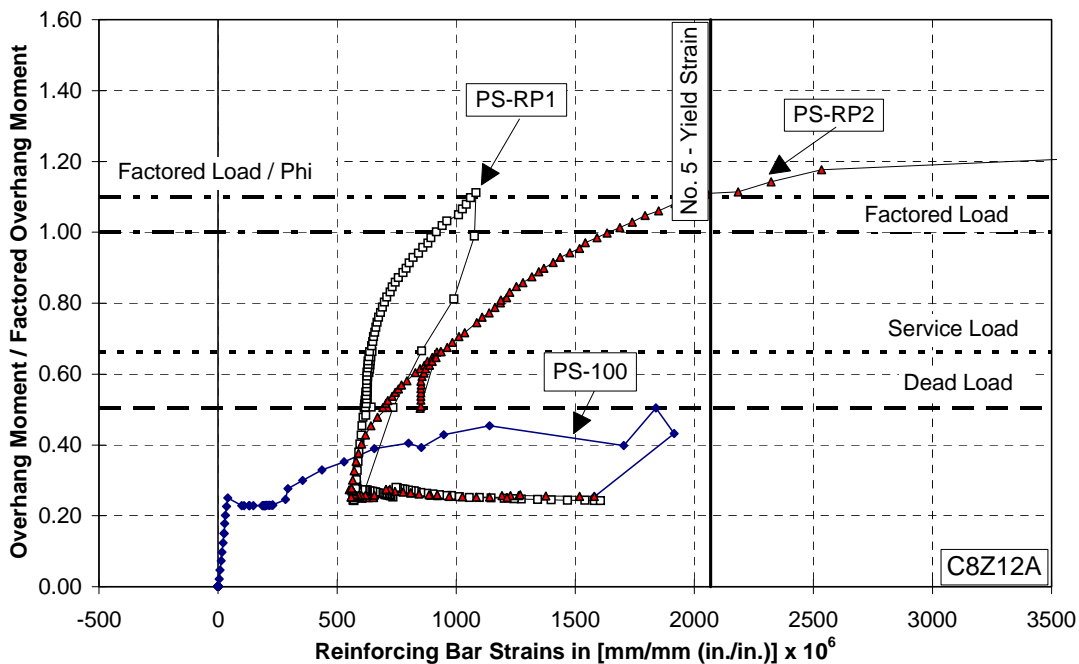


Figure 9.15 Comparison of Strain Gage C8Z12A Responses for Specimen POJ-PS-100 and Repairs RP1 and RP2

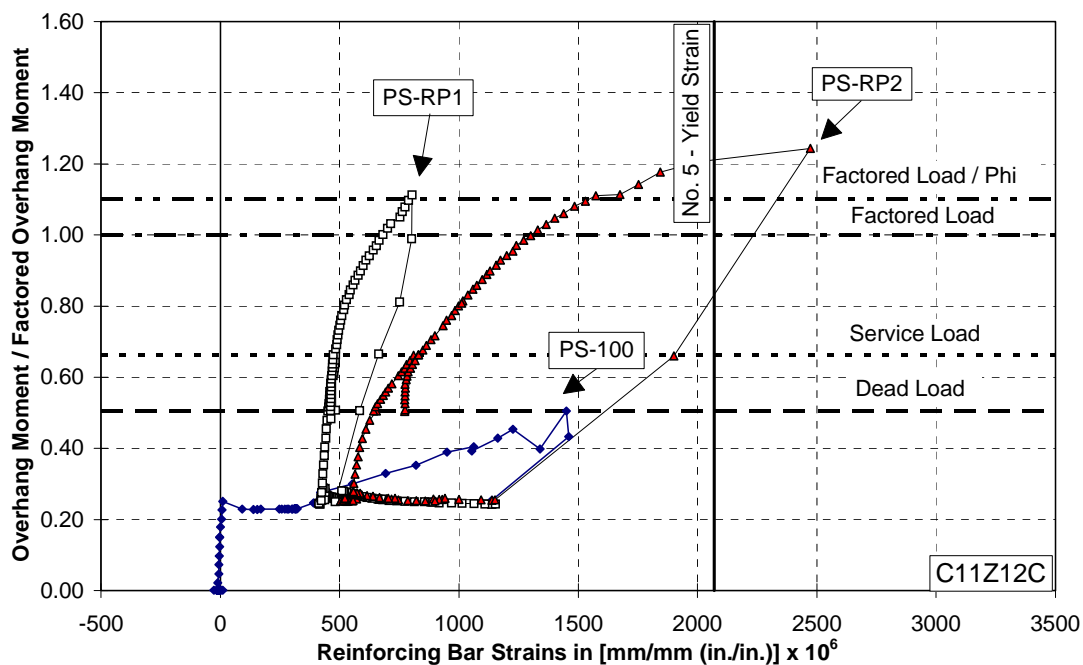


Figure 9.16 Comparison of Strain Gage C11Z12C Response for Specimen POJ-PS-100 and Repairs RP1 and RP2

9.3.3 Comparison of External Post-Tensioned Repair Strains

Strain response for the external post-tensioned repairs is presented using an averaged strain value compiled from the strain measurements taken from the gaged post-tensioning bars. The plot of averaged strains in the external post-tensioning bars, shown in Figure 9.17, indicates the initial post-tensioning bar stresses for the POJ-PS-100-RP1 and POJ-PS-100-RP2 specimens were less than the desired initial post-tensioning stress of $0.6 f_{pu}$. The large increase in the average strain for the POJ-RC-100-RP1 specimen indicates the diagonal post-tensioning force increased as the joint crack width grew in size. This indicates the repair was quite stiff and was capable of transmitting joint tensile forces (produced by the applied loads) into the pier. The average strain for the external post-tensioning did not reach the assumed yield strain corresponding with a stress of $0.75 f_{pu}$ ($3879 \mu\epsilon$), although the row of post-tensioning bars located near the extreme tensile fiber for both Specimens POJ-PS-100-RP1 and RP2 reached the assumed yield strain.

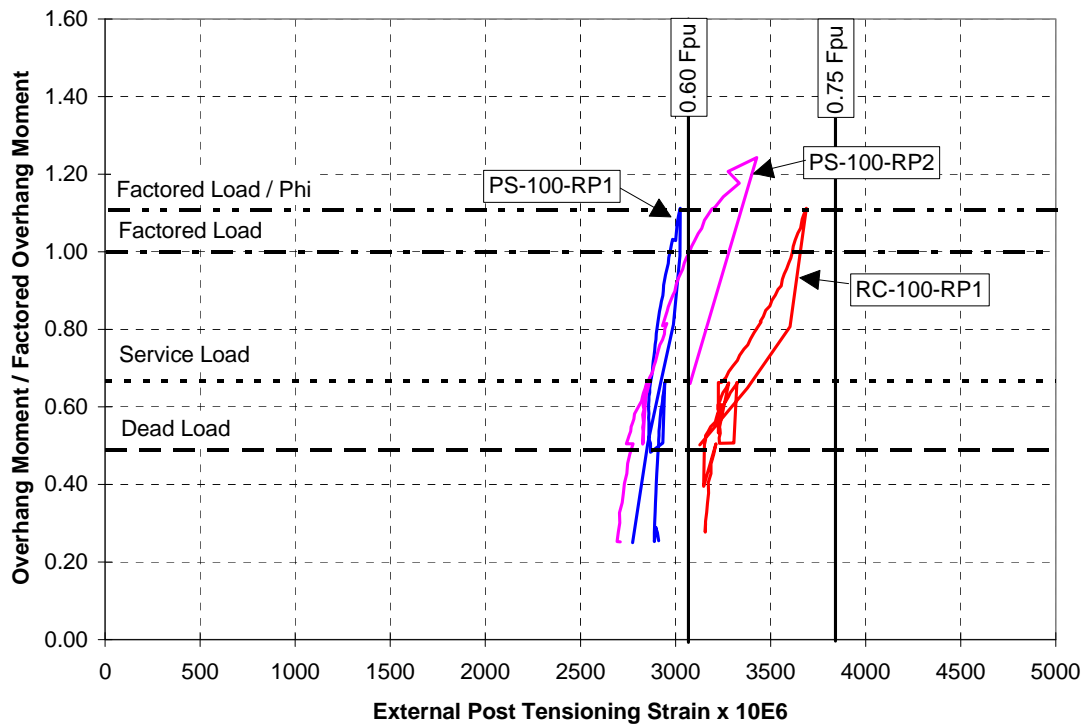


Figure 9.17 Average Recorded Strains in Post-Tensioned Bars for External Post-Tensioned Repairs

9.4 Constructability of the Repairs

Constructability of the repairs for the full-scale prototypes was estimated by extrapolating from the time and level of effort required to install each repair on the model specimens. Factors such as the number of operations, time required to complete each task, amount of equipment (coring drills, cranes, compressors, etc.), and skill level of the laborers were considered in the evaluation of constructability. Discussion of constructability of the repair methods is limited to those investigated in the experimental program. It should be noted that all of the repairs, if applied to an actual bent, would involve epoxy injection of the cracks after each repair is post tensioned.

9.4.1 External Diagonal Post-tensioning Repair

The external diagonal post-tensioned repair is a simple and non-invasive repair option. Installation requires drilling a short distance into the top and end faces of the joint to install undercut anchor bolts. Installation of the anchor bolts is not labor intensive, and drilling can be performed with an impact/rotary drill and carbide bit. Fabrication of the top and side plates is estimated to require a significant amount of time because of plate cutting and welding operations. Once the anchor bolts are installed and the top and side plates are fabricated, the plates can be lifted into place by a crane and anchored to the specimen. After the anchor bolts are torqued, the external post-tensioning bars can be stressed. It is estimated this type of repair would take one to two months to fabricate and install, and would require periodic inspections.

The disadvantages of the external diagonal post-tensioned repair are the visibility and reduced effectiveness of external post-tensioning bars (as opposed to bonded internal post-tensioned bars). Although the diagonal external PT repair is smaller than the vertical external PT repair, it will be quite visible from the ground. The external post-tensioning bars are not as effective as bonded internal post-tensioning bars because the entire length of the bars is strained as cracks develop, resulting in little increase in the post-tensioned bar force. By controlling the length and quantity of post-tensioning bar used, at failure loads the post-tensioning will achieve yield stress ($0.75 f_{pu}$).

9.4.2 External Vertical Post-Tensioned Repair

The main advantages of the external vertical post-tensioned repairs are minimized damage to the specimen in the joint region during installation and the ability to prefabricate the elements.

The disadvantages of this repair method are the high material and fabrication costs of \$4.40 per kilogram (\$2 per pound) for constructing and welding the steel sections, the time and labor required to core holes through the pier, the difficult installation process, and the visibility of the repair from the ground.

The installation of the repair involves several operations. After coring is completed and side plates are fabricated, the through-anchors are installed. Grouting the core holes in the pier after the through-anchors are installed is quite difficult because side plates cover the holes in the pier. To allow the grout to flow past the plate and into the core holes, small holes can be drilled through the side plates and small tubes inserted into the core holes.

After the core holes are grouted and the side plates installed, the cap piece is positioned. A crane is required to lift the large cap piece into position and lower it onto the top of the joint. Once the cap piece is in place, the post-tensioning bars are installed and stressed.

It is estimated that the external vertical post-tensioned repair requires over six months to complete and will require frequent inspections.

9.4.3 Internal Vertical Post-Tensioned Repair

The internal post-tensioned repair is judged to be a time-consuming and labor-intensive operation. By its very nature, internal post-tensioning requires coring into the structure to install the post-tensioning. It is estimated that it takes 1 hour to core a 9 cm (3.5 in.) diameter hole 31 cm (12 in.) into the concrete.

Coring for the vertical post-tensioning will be quite difficult for cases where the superstructure extends over the joint region. Because clearance between the bottom of the wing and the joint is 1.8 m (6 ft.) in the San Antonio ‘Y’ structure, coring would need to be done in small increments. When the post-tensioning is installed, it would have to be coupled at 1.8 m (6 ft.) intervals.

The use of a coupler has two effects on installation: 1) core holes need to be oversized to accommodate bar couplers and 2) time required for installation is critical. Because the epoxy packets used for anchoring the post-tensioning bars are mixed by “drilling” each post-tensioning bar through the epoxy packets, installation of the bars must be done expeditiously. In order for the epoxy anchorage to be effective, the epoxy at the base of each core hole must be mixed well in a very short period of time.

Once each post-tensioning bar is anchored into the specimen, stressing and final grouting procedures are completed. For some cases, slow-setting epoxy can be used in the length outside the anchorage zone to improve corrosion resistance and crack control.

The internal post-tensioned repair is believed to have excellent serviceability and aesthetics factors. The internal post-tensioning is grouted along the length of the core, which provides excellent crack control and long term corrosion-resistance. The main aesthetic advantage of the internal repair is that it is not visible to passing traffic. Given the publicity the deficient substructures received [26, 27], an invisible repair option is quite appealing, even at a greater cost. It is estimated that the repair will take five months to install and will not require frequent inspections.

9.5 Cost Estimates of Repair Methods

The cost estimates for the different repair methods were calculated for a full-scale prototype substructure. Dimensions of the external and internal repair options were determined by multiplying the dimensions of the repairs used for the model by the 2.75 scale factor. Costs of the materials, fabricated materials (such as welded plates), and costs for coring are presented as unit prices based on quotes from material suppliers [35, 38, 39, 40] and information provided by TxDOT [41].

The break-down of the unit costs are as follows:

Welded Steel Plate-	\$2.00 / lb
Coring-	
3.0" dia. Hole-	\$130 / ft.
3.5" dia. Hole-	\$150 / ft.
Fosrock Epoxy Cartridges-	
12 in. Yield Cartridge	\$31.20 ea.
Dywidag Post-Tensioning Hardware-	
1-3/8" Dia. Bar-	\$8.53 / ft.
1-3/8" Nuts.-	\$9.25 ea.
Steel Plates-	\$22.85 ea.
Drillco Undercut Anchors:	
1.25" Dia. Maxi-Bolt	\$225.00 ea.

9.5.1 External Diagonal Post-Tensioning

The diagonal external post-tensioning option is considered to be the most cost-effective method for repairing the cantilever bent. Materials comprise 67 percent of the total cost, and the total cost was is smallest for the three options investigated. Estimated costs for the external diagonal post-tensioned option are presented in Table 9.1.

Table 9.1 Estimated Cost for the External Diagonal Post-Tensioned Option

Top Plate	#	Width (in.)	Length (in.)	Thick. (in.)	Volume (in.3)	Sub Total (in.3)	Weight (lbs.)	Unit Cost (\$/unit)	Cost (\$)	
Base Plate	1	39.88	60.50	1.38	3,317		941			
Triangle Stiffeners	4	7.56	11.00	1.38	229		65			
I Beam Flanges	2	11.00	83.88	1.38	2,537		719			
I Beam Web	1	8.25	83.88	2.06	1,427		405			
Stiffeners	8	8.25	2.75	0.69	125		35			
						7,635	2,165	\$2.00	\$4,330.06	
Side Plates										
Base Plate	1	56.38	60.50	1.38	4,690		1,330			
Triangle Stiffeners	2	11.00	15.81	2.06	359		102			
Triangle Stiffeners	2	11.00	15.81	1.38	239		68			
I Beam Flanges	2	11.00	83.88	1.38	2,537		719			
I Beam Web	1	8.25	83.88	2.06	1,427		405			
Stiffeners	8	8.25	2.75	0.69	125		35			
						9,377	2,659	\$2.00	\$5,317.86	
Anchors	18	- 22" Long 1.25" Dia Maxi Bolts w/ 17.375" Embedment							\$225.00	\$4,050.00
Post Tensioning	4	- 1-3/8" Dia. 91 in. Long Dywidag Bar							\$64.61	\$258.44
	8	- 1-3/8" Nuts							\$9.25	\$74.00
	8	- Plates							\$22.85	\$182.80
									\$14,213.16	

9.5.2 External Vertical Post-Tensioning

The external vertical post-tensioned repair involves a great deal of welding and plate cutting to construct the three primary items: the cap piece and the two side plates. The through-anchors for the side plates require 20 cores, which results in an amount of coring almost equal to that used for the internal PT option. The combination of coring and extra steel components make the external vertical post-tensioned repair the most expensive repair option, with the fabricated materials comprising 65 percent of the total cost. The estimated costs for the external vertical post-tensioned option are presented in Table 9.2.

Table 9.2 Estimated Costs for the External Vertical Post-Tensioned Option

Vertical External Post Tensioning Repair									
Cap Piece	#	Width (in.)	Length (in.)	Thick. (in.)	Volume (in.3)	Sub Total (in.3)	Weight (lbs.)	Unit Cost (\$/unit)	Cost (\$)
Top Plate	1	34.38	89.38	2.06	6,337				
Rectangle Stiffener	4	16.50	89.38	2.06	12,166				
Base Plate	1	34.38	89.38	1.38	4,224				
Triangle Stiffeners	8	33.00	9.63	2.06	5,229				
Side Plate	2	33.00	33.00	1.38	2,995				
						30,951	8,777	\$2.00	\$17,553.14
Side Plates (2)									
Base Plate	2	46.75	88.00	1.38	11,314				
Triangle Stiffeners	8	31.63	11.00	2.06	5,740				
Rigid Plate	2	33.00	12.38	2.75	2,246				
Triangle Stiffeners	8	45.38	11.00	2.06	8,224				
						27,523	7,805	\$2.00	\$15,609.25
Anchors	20	- 72 in. Long 2.5" Dia H.S. Threaded Bar						\$100.80	\$2,016.00
Coring	20	- 66 in. Long 3." Dia. Core.						\$709.50	\$14,190.00
Post Tensioning	4	- 1-3/8" Dia. 201 in. Long Dywidag Bar						\$0.71	\$1,276.85
	8	- 1-3/8" Nuts						\$9.25	\$83.19
	8	- Plates						\$22.85	\$124.78
									\$50,853.21

9.5.3 Internal Vertical Post Tensioning

Eighty percent of the cost for the internal vertical post-tensioned repair option are due to coring costs. It was estimated that total construction time is 30 weeks, which is due to the time-consuming coring operations. Materials costs comprise 15 percent of the total repair cost. The estimated costs for the internal vertical post-tensioning option are shown in Table 9.3.

Table 9.3 Estimated Costs for Internal Vertical Post-Tensioned Option

Vertical Internal Post Tensioning Repair									
	#	Width (in.)	Length (in.)	Thick. (in.)	Volume (in.3)	Sub Total (in.3)	Weight (lbs.)	Unit Cost (\$/unit)	Cost (\$)
Top Plate	4	5.50	24.75	8.25	4,492				
						4,492	1,274	\$2.00	\$636.90
Anchors	16	- 5 minute Quick Set Epoxy Cartridges						\$31.20	\$499.13
	28	- 50 minute Slow Set Epoxy Cartridges						\$31.20	\$873.47
Post Tensioning	8	- 1-3/8" Dia. 187 in. Long Dywidag Bar						\$132.77	\$1,062.16
	8	- 1-3/8" Nuts						\$9.25	\$74.00
	8	- Plates						\$22.85	\$182.80
Coring	8	- 187 in. Long 3.5" Dia. Core.						\$2,346.85	\$18,780.41
									\$22,108.87

9.5.4 Repair Cost Comparison

Based on the stated unit prices, the external diagonal post-tensioned option is the lowest cost repair. Figure 9.18 illustrates the break-down of the material costs, fabricated material costs, and labor/coring costs. Welded steel items, such as the side plates are considered to be fabricated materials. Items that can be bought “off the shelf” are considered to be materials. Coring costs are displayed separately to illustrate the amount of coring required.

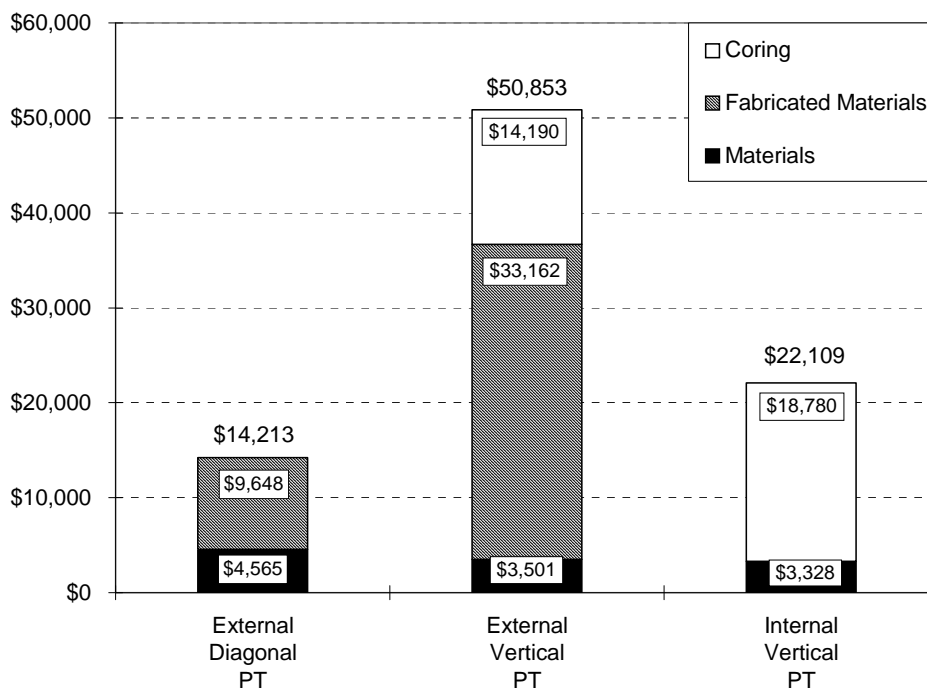


Figure 9.18 Cost Comparison of Proposed Repair Methods

9.6 Recommended Repair Method

Based on cost estimates, estimated construction time, durability, and aesthetics, the suggested repairs are either the internal vertical post-tensioned or diagonal external post-tensioned option. The decision matrix shown below was completed as part of the process to determine the best option. The ranges used for grading the different options were based on the extremes of the proposed repair options.

The price difference between the diagonal PT and internal PT options were not significant enough to overcome the improved durability and aesthetics of the internal PT option. Durability of the repairs was estimated based on the total area of exposed steel used for the repairs. Clearly the internal post-tensioned repair will have the best durability. Large weighting factors were placed on the durability and aesthetics of the repairs, given the publicity that the deficient substructures received. Grading of the repairs is given in Table 9.4.

Cost	10=	\$10,000
	0=	\$50,000
Time	10=	1 Month
	0=	6 Months
Durability	10=	Protected/ unexposed
	0=	Exposed to elements/ requires frequent inspection and maintenance
Aesthetics	10=	Totally Hidden/ Unobtrusive
	0=	Plain Sight/ Accessible to Vandals

Table 9.4 Decision Matrix for the Studied Repair Methods

Item	Cost	Time	Durability	Aesthetics	Total
Weight	4	1	2	3	100
Ext. Diag. PT	8.8	8	5	6	73.2
Ext. Vert. PT	0	0	2.5	0	5.0
Internal PT	6.7	2	10	10	78.8

The Texas Department of Transportation elected to repair the deficient bents in San Antonio using an internal vertical post-tensioned repair for the fully-prestressed overhang bents, as depicted in Figure 8.22 in Section 8.5.1. A combination of internal vertical and horizontal post-tensioning (shown in Figure 8.24 in Section 8.5.3) was used for the reinforced concrete bents.

9.1 Introduction	398
9.2 Comparison of Overhang Moment vs. Tip Deflection Response	399
9.2.1 Specimen POJ-RC-100-2 and Repairs RP1 and RP2.....	399
9.2.2 Specimen POJ-PS-100 and Repairs RP1 and RP2	400
9.3 Comparison of Measured Strain Response.....	401
9.3.1 Reinforced Concrete Design (POJ-RC-100-2) Repairs.....	401
9.3.2 Specimen with Fully-Prestressed Overhang (POJ-PS-100) Repairs	406
9.3.3 Comparison of External Post-Tensioned Repair Strains	411
9.4 Constructability of the Repairs	413
9.4.1 External Diagonal Post-tensioning Repair	413
9.4.2 External Vertical Post-Tensioned Repair	414
9.4.3 Internal Vertical Post-Tensioned Repair	415
9.5 Cost Estimates of Repair Methods	416
9.5.1 External Diagonal Post-Tensioning	417
9.5.2 External Vertical Post-Tensioning	418
9.5.3 Internal Vertical Post Tensioning.....	419
9.5.4 Repair Cost Comparison	420
9.6 Recommended Repair Method	421
Figure 9.1 Comparison of Overhang Tip Displacement Response for Specimen POJ-RC-100-2, and Repairs RP1 and RP2	399
Figure 9.2 Comparison of Overhang Tip Displacement Behavior for Specimen POJ-PS-100 and Repairs RP1 and RP2	400
Figure 9.3 POJ-RC-100-2 - Joint Region Strain Gage Locations and Labels	402
Figure 9.4 Comparison of Strain Gage T7Z5A Response for Specimen POJ-RC-100-2 and Repairs RP1 and RP2.....	403
Figure 9.5 Comparison of Strain Gage F10Z10A Response for Specimen POJ-RC-100-2 and Repairs RP1 and RP2.....	403
Figure 9.6 Comparison of Strain Gage F17Z13A Response for Specimen POJ-RC-100-2 and Repairs RP1 and RP2.....	404

Figure 9.7 Comparison of Strain Gage M31Z3A Response for Specimen POJ-RC-100-2 and Repairs RP1 and RP2.....	404
Figure 9.8 Comparison of Strain Gage C1Z24B Response for Specimen POJ-RC-100-2 and Repairs RP1 and RP2.....	405
Figure 9.9 Comparison of Strain Gage C11Z12C Response for Specimen POJ-RC-100-2 and Repairs RP1 and RP2.....	405
Figure 9.10 Comparison of Strain Gage C15Z12A Responses for Specimen POJ-RC-100-2 and Repairs RP1 and RP2.....	406
Figure 9.11 POJ-PS-100 Joint Strain Gage Locations and Labels	408
Figure 9.12 Comparison of Strain Gage T10Z17A Responses for Specimen POJ-PS-100 and Repairs RP1 and RP2.....	409
Figure 9.13 Comparison of Strain Gage F10Z9B Responses for Specimen POJ-PS-100 and Repairs RP1 and RP2.....	409
Figure 9.14 Comparison of Strain Gage F10Z12B Response for Specimen POJ-PS-100 and Repairs RP1 and RP2.....	410
Figure 9.15 Comparison of Strain Gage C8Z12A Responses for Specimen POJ-PS-100 and Repairs RP1 and RP2.....	410
Figure 9.16 Comparison of Strain Gage C11Z12C Response for Specimen POJ-PS-100 and Repairs RP1 and RP2.....	411
Figure 9.17 Average Recorded Strains in Post-Tensioned Bars for External Post-Tensioned Repairs	412
Figure 9.18 Cost Comparison of Proposed Repair Methods	420
Table 9.1 Estimated Cost for the External Diagonal Post-Tensioned Option.....	417
Table 9.2 Estimated Costs for the External Vertical Post-Tensioned Option.....	418
Table 9.3 Estimated Costs for Internal Vertical Post-Tensioned Option.....	419
Table 9.4 Decision Matrix for the Studied Repair Methods	421

CHAPTER 10

SUMMARY AND CONCLUSIONS

10.1 Summary

Large cantilever bents were designed and tested to evaluate AASHTO Standard Specifications, which provide separate treatment of design of reinforced and prestressed concrete elements. A specification is proposed here for an integrated design method for structural concrete. Two prototype model specimens that represent a reinforced concrete bent and a bent with a fully-prestressed overhang, and three integrated design specimens were designed and tested.

The prototype model reinforced concrete and fully-prestressed-overhang designs were structurally deficient. The reinforced concrete bent failed under applied loads equivalent to 0.76 times factored load, and the fully-prestress overhang failed under applied loads equivalent to 0.58 times factored load. A joint-capacity model was developed that used a uniform-bond stress model to compute bar anchorage in the joint and computed maximum applied load on the overhang. Computed capacities were within ± 10 percent of measured capacities.

The integrated-design specimens consisted of a reinforced concrete specimen, a 54 percent prestressed specimen, and a 74 percent prestressed specimen. The three-integrated design specimens used headed longitudinal reinforcement, and the partially-prestressed specimens contained tendons that were continuous through the overhang, joint, and pier. All three integrated-design specimens had capacities exceeding factored design loads. The reinforced concrete and 54 percent prestressed specimens were tested to failure (1.44 and 1.41 times factored loads, respectively), and measured capacities were 14 percent greater than predicted capacities, indicating the design and analysis procedures provided conservative designs. Specimen POJ-PU-74-TH was proof-tested to an applied load equivalent to 1.41 times factored loads.

The three integrated design specimens had superior strength because a strut-and-tie model was used to plot the force path through the bent. The strut-and-tie model indicated that the longitudinal reinforcement in the overhang and pier needed to be fully anchored in the joint corner. Headed reinforcement was used to fully anchor the longitudinal reinforcement in the joint corner and continuous post tensioning was placed through the joint. Had the engineers performed a strut-and-tie model of the full-scale bents, most notably the fully-prestressed overhang design, they would have recognized that there was no viable force path through the joint.

Serviceability of the three integrated-design specimens was evaluated using maximum measured crack widths and deflections. Maximum measured crack widths were within the historically-accepted range of ± 50 percent of crack widths predicted by using the proposed crack-width equation. It was clear from tests performed on integrated-design specimens that using a larger percentage of post-tensioning reduced the number of cracks that formed at service loads. The 74 percent prestressed specimen had excellent crack control and overall serviceability.

Subtle changes were recommended to the AASHTO LRFD Specifications. The bulk of the LRFD specifications were in-line with the procedures used in the design of the integrated-design specimens. As use of the integrated-design method and strut-and-tie analysis procedure becomes more prevalent, some existing design provisions for corbels, deep beams, and shear friction reinforcement may be phased out, as well as the AASHTO Standard Specifications.

In the experimental program, all integrated-design specimens were designed using resistance factors of 0.9 and 0.85 for flexure and shear, respectively. However, LRFD Specifications use resistance factors of 1.0 for flexure of prestressed concrete, 0.9 for flexure of reinforced concrete, and 0.9 for shear and torsion of reinforced or prestressed concrete. This research does not directly address the issue of resistance factors, but some consideration should be given to these factors during this code cycle. Results from three integrated-designs specimens support the conclusion that designs ranging from 72% prestressed to reinforced concrete can be designed with similar ultimate capacities, and a resistance factor for “flexure

and tension of structural concrete” should be proposed to replace the values for reinforced concrete and prestressed concrete. The shear resistance factor given in the LRFD Specifications is 0.9 which is equal to the resistance factor for flexure in reinforced concrete. Clearly design conservatism is reduced on two fronts if a fraction of the concrete tensile strength is included in the shear resistance calculation and an increased value for the resistance factor for shear is used. Maintaining resistance factor for shear at a currently recognized value of 0.85 is more appropriate if a fraction of concrete tensile strength is included in the shear resistance equation. It is suggested to use a resistance factor of 0.9 for flexure and 0.85 for shear.

There is concern that the quantity of transverse reinforcement in the bent was marginal if a concrete contribution for shear is included. However, it should be noted that the compression failure in the overhang preceded the shear failure of Specimen POJ-PU-54-TH and the overhang bents reported in Ref. 42. If compressive reinforcement above the minimum required for creep and shrinkage had been used in the overhang, the bent capacity would have been increased. If the concrete contribution for shear is not included, it will result in slightly more congested reinforcing cages.

Initial indicators are that the minimum column reinforcement provisions may not be modified from 1 percent of the gross column area [12]. The proposed column reinforcement provisions should recognize that axial creep in columns and creep in beam-columns are similar in nature. Minimum longitudinal and transverse reinforcement provisions should be developed and applied to the compression zones of all structural concrete members. In the case of the piers in the San Antonio ‘Y’ Project, minimum column reinforcement provision should apply to that region of the column subjected to constant compressive loads. This would have provided a considerable reduction in the quantity of longitudinal reinforcement required in the pier.

Premature failure of the prototype model reinforced concrete bent led to careful examination of the full-scale bents in the San Antonio. It was concluded from an evaluation of reinforced concrete cantilever bent I4-C and fully-prestressed overhang cantilever bent C11-C that capacities of some bents were severely deficient. Capacity of the I4-C bent was computed to be 69 percent of design factored loads, and the C11-C bent had a predicted

capacity equal to 50 percent of factored loads. The failure of C11-C during construction of the elevated expressway (under a load equivalent to that predicted by the joint bond-strength model) should have alerted designers that other bents might be deficient. TxDOT was alerted that test results indicated the San Antonio bents were deficient and that preliminary visual inspection of the San Antonio bents confirmed that joint cracks were visible from the ground. TxDOT quickly assembled an inspection crew to assist in the bent crack survey. After the survey was completed, it was clear that several bents were deficient and collapse of a portion of the elevated expressway due to an overload was a real possibility. Portions of the I-10 expressway were closed to traffic until braces could be installed to support the superstructure.[26,27]

Three strengthening schemes were quickly developed, fabricated, and installed on the prototype model specimens while the temporary supports were being installed on the full-scale bents. Each repaired specimen was proof tested to factored load/phi. A diagonal external post-tensioning scheme and vertical internal post-tensioning scheme were each installed and tested on the prototype model reinforced concrete specimen. Both strengthening schemes for the prototype model reinforced concrete design enabled the bent to develop factored load/phi. A vertical external post-tensioning scheme, using different quantities of external prestress, was installed on the prototype model fully-prestressed-overhang design. Both strengthening schemes for the fully-prestressed overhang design developed the desired strength, and the second test (using fewer external post-tensioning bars) confirmed the prediction of the strength model. Serviceability was not evaluated because multiple tests were performed on the same specimen, and cracks were not epoxy injected before each test.

Results of the repair study indicated that the external diagonal post-tensioned repair and internal vertical post-tensioned repair were the best repair options. TxDOT elected to use the internal vertical post-tensioned repair for the fully-prestressed overhang bents and a combined internal vertical and horizontal post-tensioned repair for the deficient reinforced concrete bents. The internal vertical post-tensioned repair was estimated to cost \$22,109 per bent.

10.2 Conclusions and Recommendations

- 1) Clearly, behavior of specimens designed using the integrated design procedure was much superior to that of specimens designed using the AASHTO Standard Specifications. Integrated-design specimens attained factored design loads for which they were designed, while prototype model reinforced concrete and fully-prestressed overhang designs resisted only 76 and 58 percent of factored design loads, respectively.
- 2) Serviceability of the integrated-design specimens was excellent when larger quantities of prestressed reinforcement was used. The 74 percent prestressed bent (POJ-PU-74-TH) had excellent crack control for all regions of the bent and limited service-level deflections. The 54 percent prestressed bent (POJ-PU-54-TH) had good crack control and deflections that were slightly greater than the limiting service-level deflections. The reinforced concrete bent with T-headed reinforcement (POJ-RC-100-TH) had some large cracks in the joint region, and service-level deflections were larger than the accepted limit. Modifications were proposed to improve serviceability of these bents.
- 3) Costs of integrated-design bents were estimated to be equal to the structurally deficient reinforced concrete prototype bent. Congestion of reinforcement was greatly reduced through the use of partially-prestressed designs and headed mild reinforcement. Estimated cost of the deficient prototype model fully-prestressed overhang design was 2.1 time more than the deficient prototype reinforced concrete design.
- 4) Costs, based on current construction costs estimates, increased with additional post-tensioning, however reduced reinforcement congestion should reduce concrete placement costs. Additionally, the premium associated with construction of prestressed concrete structures should decrease as more construction firms become adept at installing and stressing post-tensioned reinforcement. The superior serviceability and strength of Specimen POJ-PU-75-TH is well worth the small increase in cost for additional post-tensioned reinforcement.
- 5) Headed reinforcement reduced reinforcement congestion and facilitated anchorage of reinforcement in the joint region. Headed reinforcement is a commercially available

product [35] and specifications for anchorage of headed reinforcement should be provided in codes to promote more extensive use of the product. Additionally, anchor heads provide ideal nodes for anchoring tension ties and compression struts as visualized in strut-and-tie models.

- 6) Strut-and-tie modeling was the key analysis tool used in this study. It helped identify the flow of forces through the bent, and identified the criticality of bar anchorage in the joint region. Designers of the San Antonio ‘Y’ would have identified the problems with the joint details had a strut-and-tie model been used to design the bent. The inclusion of the strut-and-tie design method in the AASHTO LRFD Specifications clearly makes it a natural successor to the AASHTO Standard Specifications.
- 7) The proposed crack-width equation provided conservative estimates of crack widths, within the historically accepted range. The equation proved to be a valuable tool when it was used to evaluate serviceability of various design and compute required number of reinforcing bars to control crack widths. Integrated design specimens had excellent crack control when post-tensioning was located in regions of high tensile stresses. Given the uncertainty associated with crack-width measurements in general, it is understood that limits applied to crack widths should be conservative to prevent unsightly cracks from developing and to provide corrosion protection. An amendment to the AASHTO LRFD Specifications is provided.

- 8) Anchorage details used in joint of prototype model bents were inadequate and resulted in premature failure of the bent. A uniform bond-stress model was shown to represent the anchorage capacity for bars anchored in the joint region at failure. The uniform bond-stress model simply assumes that each bar can develop an anchorage force equal to the ratio of anchorage length to development length times the nominal capacity of the bar. In practice, equations from Orangun [29] or the ACI Committee 408 Summary Report [30] should be used to compute bar development lengths. The joint capacity model assumes that all reinforcement reached their capacity at maximum loads. A free-body calculation using the individual bar forces estimated capacities of the prototype model reinforced concrete and prestressed concrete bents within $\pm 10\%$ of measured bent capacity. Additionally, predicted capacity of the C11-C full-scale bent was in-line with the estimated load on the bent when it failed during construction.
- 9) Linear elastic finite element analyses proved invaluable for identification of peak tensile stress regions and determination of first-cracking load. Different reinforcement configurations can be assessed with a finite element model, and critical regions identified for further analysis. Further use of finite element modeling should be promoted and exercised in design offices.
- 10) Three strengthening methods were quickly developed, fabricated, and tested for two prototype model bents that were similar in design to full-scale bents constructed in the San Antonio 'Y' project. All repairs restored the strength of each model bent to at least factored loads/ ϕ . The external diagonal and internal vertical post-tensioned repairs were clearly the best repair options.

- 11) The cost of the internal post-tensioned repair was nearly twice the cost of the diagonal external post-tensioned repair. The external diagonal post-tensioned repair was an excellent repair option, however TxDOT elected to repair the San Antonio bents using the internal vertical post-tensioned repair. The internal vertical post-tensioned repair was selected because it was hidden from view and it was the repair solution used for the C11-C bent. In the event of an overload, crack widths in the joint would be best controlled using grouted post-tensioning, as opposed to external post-tensioning. The third repair option (external vertical post-tensioned repair) was aesthetically unappealing, expensive, and was prone to corrosion. It was not considered to be a viable repair option for bents in the San Antonio 'Y' Project.
- 12) Costs associated with bent replacement or failure under traffic loads was not considered in this study. Steps should be taken to disseminate the information contained in this dissertation to designers, to prevent similar design problems in the future.

10.1 Summary	423
10.2 Conclusions and Recommendations	427

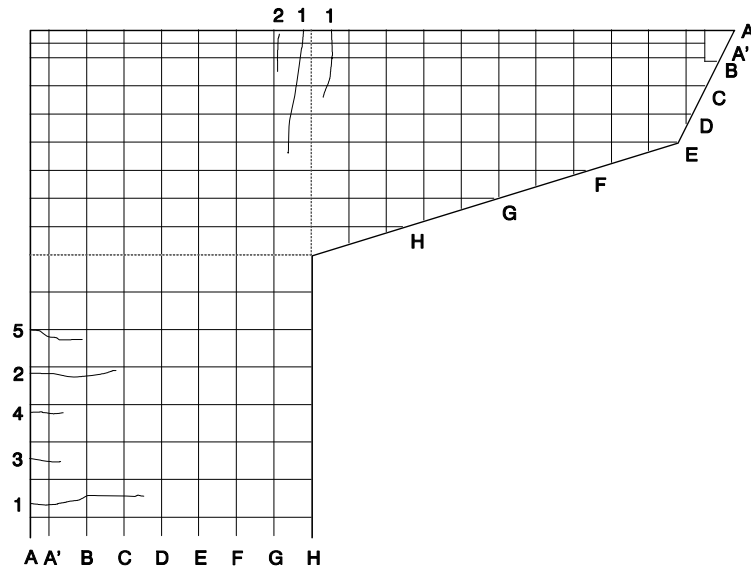


Figure A.43 Cracking Pattern on North Face of Specimen POJ-PU-54-TH at Dead Load

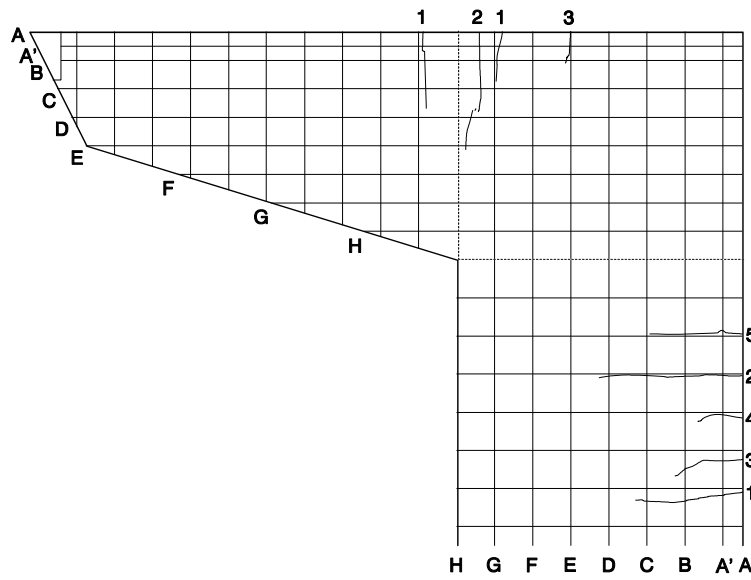


Figure A.44 Cracking Pattern on South Face of Specimen POJ-PU-54-TH at Dead Load

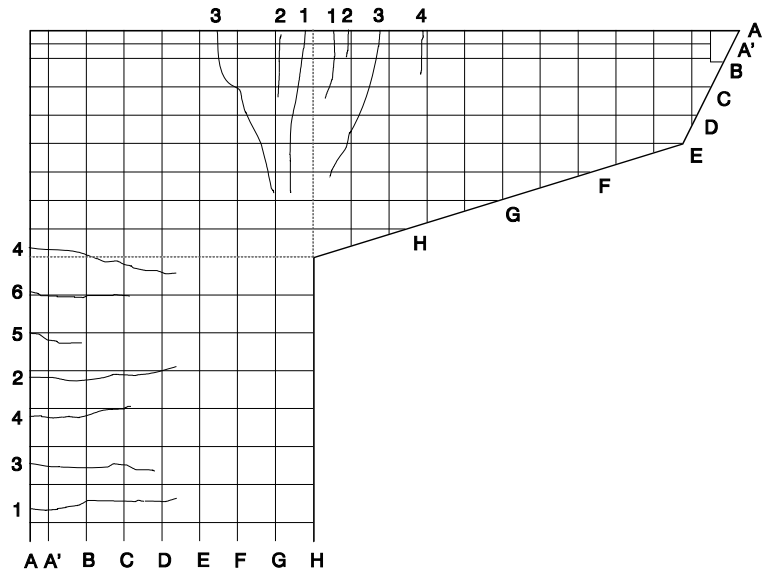


Figure A.45 Cracking Pattern on North Face of Specimen POJ-PU-54-TH at Service Load

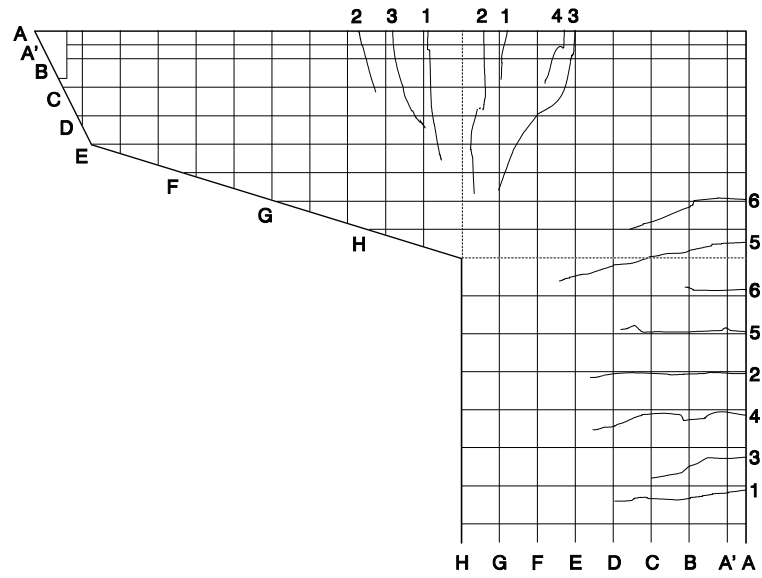


Figure A.46 Cracking Pattern on South Face of Specimen POJ-PU-54-TH at Service Load

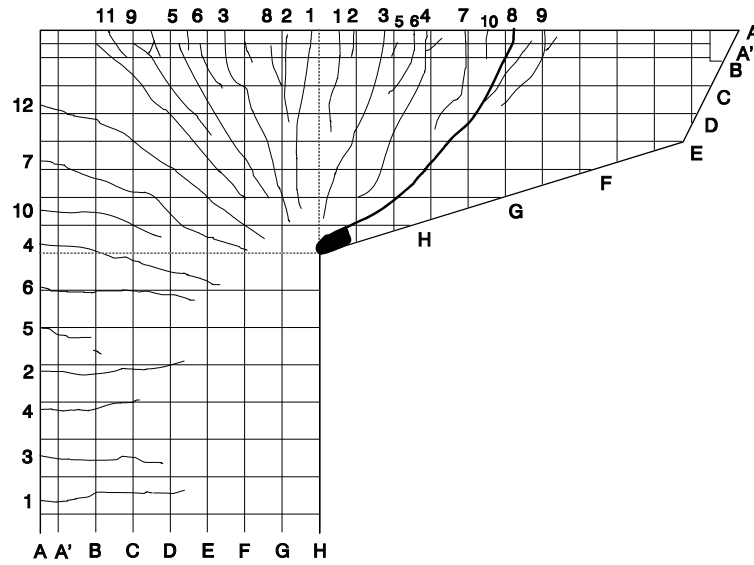


Figure A.47 Cracking Pattern on North Face of Specimen POJ-PU-54-TH at Failure

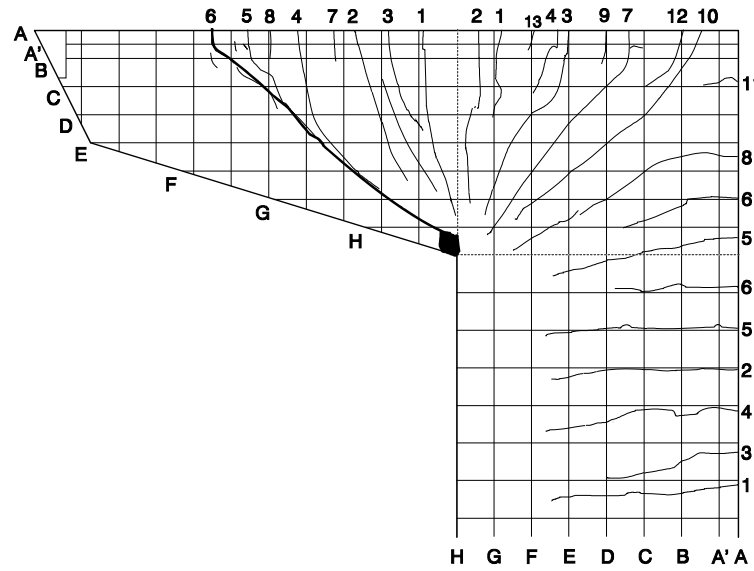


Figure A.48 Cracking Pattern on South Face of Specimen POJ-PU-54-TH at Failure

REFERENCES

- [1] American Association of State Highway Transportation Officials (AASHTO), Standard Specifications for Highway Bridges, Thirteenth Edition, 1983.
- [2] Bergmeister, K, Breen, J.E., Jirsa, J.O., and Kreger, M.E., "Detailing for Structural Concrete," Research Report 1127-3F Center for Transportation Research, The University of Texas at Austin, October 1990.
- [3] Armstrong, S.D., "Design and Behavior of Large Cantilever Overhangs with Combinations of Prestressed and Non-Prestressed Reinforcement," Unpublished Masters Thesis, The University of Texas at Austin, August 1994
- [4] Salas Pereira, R.M., "Behavior of Structural Concrete Cantilever Piers Using T-Headed Reinforcing Bars and Varied Prestressing Design Criteria," Unpublished Masters Thesis, The University of Texas at Austin, August 1994.
- [5] Billington, S.L., "Behavior of Two-Span Continuous Pier Caps with Varying Levels of Prestress," Unpublished Masters Thesis, The University of Texas at Austin, December 1994.
- [6] Scott, S.E., "An Evaluation of Repair Methods for Cantilever Bridge Piers," Unpublished Masters Thesis, The University of Texas at Austin, May 1997.
- [7] American Association of State Highway and Transportation Officials (ASSHTO), LRFD Bridge Specifications and Commentary, April 1996.
- [8] Schlaich, J., Schafer, K., and Jennewein, M., "Toward a Consistent Design of Reinforced and Prestressed Concrete Structures," PCI Journal, Vol. 32, No. 3, May-June 1987, pp. 74-151.
- [9] Breen, J.E., Burdet, O., Roberts, C., Sanders, D., and Wollmann, G., "Anchorage Zone Reinforcement for Post-Tensioned Concrete Girders," National Cooperative Highway Research Program, Report No. 356, August 1991.
- [10] Frantz G.C., and Breen J.E., "Control of Cracking on the Side Faces of Large Reinforced Concrete Beams," Research Report 198-1F Center for Transportation Research, The University of Texas at Austin, August 1992.
- [11] "Reinforced Concrete Column Investigation - Tentative Final Report of Committee 105," ACI Journal, Proceedings V. 20, No. 5, Feb. 1933, pp. 275-282.
- [12] Zeihl, P., "Minimum Mild Reinforcing Requirements for Concrete Columns," Unpublished Masters Thesis, The University of Texas at Austin, December 1997.

- [13] DeVries, R.A., "Anchorage of Headed Reinforcement in Concrete," Unpublished Doctoral Dissertation, The University of Texas at Austin, December 1996.
- [14] Dyken, T., and Kepp B., "Properties of T-Headed Reinforcing Bars in High Strength Concrete," Norway
- [15] Suri K.M. and Dilger W.H., "Crack Width of Partially Prestressed Concrete Members," ACI Journal, September-October, 1986.
- [16] Gergely P., and Lutz L.A., "Maximum Crack Width in Reinforced Concrete Flexural Members," Causes, Mechanism and Control of Cracking in Concrete, ACI Publication SP-20, American Concrete Institute, Detroit, 1973, pp. 87-117.
- [17] Yip, T.S.C. , "Discussion of Equations for Prediction of Flexural Crack Width in Prestressed Members," Departmental Report, University of Texas at Austin, December 1995.
- [18] American Concrete Institute (ACI), Building Code Requirements for Reinforced Concrete and Commentary - 318-89, Detroit, 1989.
- [19] West, J.D., "Durability Design of Post-Tensioned Substructure Elements," Unpublished Doctoral Dissertation, The University of Texas at Austin, December 1997.
- [20] Posten, R.W., "Improving Durability of Bridge Decks by Transverse Prestressing," Doctoral Dissertation, The University of Texas at Austin, December 1984.
- [21] Borges, F. and Lima, A., "Crack and Deformation Similitude in Reinforced Concrete," RILEM, No. 7, June 1960.
- [22] Sabnis, G.M., Harris, H.G., White, R.N., and Mirza, M.S., Structural Modeling and Experimental Techniques, Prentice-Hall Civil Engineering and Engineering Mechanics Series, 1983
- [23] Abeles, P.W., "Static and fatigue tests on partially prestressed concrete," ACI Journal, December 1954.
- [24] Abeles, P.W., "Philosophy of Partial Prestressing," American Concrete Institute SP-59, from 1976 Symposium on "Concrete Design: U.S. and European Practices", 1979, pp. 287-304.
- [25] Wollmann, G.P. , Yates, D.L., Breen, J.E., and Kreger, M.E., "Fretting Fatigue in Post-Tensioned Concrete," The University of Texas at Austin, Center for Transportation Research, Report No. 465-2F, November 1988.

- [26] “Cracks in columns force closing on I-10”, San Antonio Express-News, 5 April 1995, 2B.
- [27] “Eight columns on freeway set to be repaired”, San Antonio Express-News, 8 June 1995, 2B.
- [28] ACI, Building Code Requirements for Reinforced Concrete and Commentary - 318-63, Detroit, 1963.
- [29] Orangun, C.O., Jirsa, J.O, and Breen, J.E. “A Reevaluation of Test Data on Development Length and Splices,” ACI Journal, Proceedings V. 74, Mar. 1977, pp. 114-122.
- [30] ACI Committee 408, “Bond Stress - The State of the Art,” ACI Journal, Proceedings V. 63, No. 11, Nov. 1966, pp. 1161-1188.
- [31] Wang, C, Salmon, C.G., Reinforced Concrete Design, Fourth Edition, Harper & Row, New York 1985, pp. 208-211.
- [32] “ANSYS 5.0 Engineering Analysis System Command Reference Manual,” Swanson Analysis Systems Inc., Houston, PA, June 8, 1992.
- [33] Microsoft Excel Version 5.0, Microsoft Corporation, 1994.
- [34] Price Quotation for T-headed Bars, David Mitchell, Headed Reinforcement Canada, Inc. Mt. Pearl, Newfoundland, Canada, February 1996.
- [35] Price Quotation for Dywidag Hardware, Micki L. Torres, Dywidag-Systems International, February 1996.
- [36] American Association of State Highway Transportation Officials (AASHTO), Standard Specifications for Highway Bridges, Fifteenth Edition, 1992.
- [37] Proposed American Association of State Highway and Transportation Officials (ASSHTO), LRFD Bridge Specifications and Commentary, April 15 1992.
- [38] Procedure to Install Internal Post-Tensioning and Price Estimate, Gary Greenfield, Fosrock Inc., May 1995.
- [39] Price Quotation for Maxi Bolt Undercut Anchors, Chris Heinz, Drillco Devices LTD, Long Island City, NY, February 1996.
- [40] Price Quotation for Threaded Through-Anchors, Phone Quotation, Austin Bolt, February 1996.
- [41] Conversation w/ Scott Armstrong, TxDOT

- [42] Armstrong, S.D, Salas Pereira, R.M., Wood, B.A., Breen, J.E., Kreger, M.E., "Behavior and Design of Large Structural Concrete Bridge Pier Overhangs," Research Report 1364-1 Center for Transportation Research, The University of Texas at Austin, August 1996.

